UDK 669+666+678+53
ISSN 1580-2949
MTAEC9, 49(1)1–177(2015)

MATER. TEHNOL.	LETNIK VOLUME 49	ŠTEV. NO. 1	STR. P. 1–177	LJUBLJANA SLOVENIJA	JAN.–FEB. 2015

VSEBINA – CONTENTS

IZVIRNI ZNANSTVENI ČLANKI – ORIGINAL SCIENTIFIC ARTICLES

STROKOVNI ČLANKI – PROFESSIONAL ARTICLES

UDK 678.84
Original scientific article/Izvirni znanstveni članek

ISSN 1580-2949
MTAEC9, 49(1)3(2015)

BORON-DOPED HYDROGENATED AMORPHOUS SEMICONDUCTOR MEMS

Z BOROM DOPIRANI HIDROGENIRANI AMORFNI POLPREVODNIK MEMS

Margarita Galindo[1], Carlos Zúñiga[2], Rodolfo Palomino-Merino[1],
Francisco López[3], Wilfrido Calleja[2], Javier de la Hidalga[2], Victor M. Castaño[4]
[1]Facultad de Ciencias Físico-Matemáticas, Benemérita Universidad Autónoma de Puebla, Av. San Claudio y 18 Sur, Col. San Manuel, Ciudad Universitaria, 72570 Puebla, Mexico
[2]Instituto Nacional de Astrofísica, Óptica y Electrónica (INAOE), Luis E Erro # 1, Santa María Tonantzintla, Puebla, Mexico
[3]Facultad de Ciencias de la Electrónica, Benemérita Universidad Autónoma de Puebla, Av. San Claudio y 18 Sur, Col. San Manuel, Ciudad Universitaria, 72570 Puebla, Mexico
[4]Centro de Fisica Aplicada y Tecnologia Avanzada, Campus Juriquilla, Queretaro, Mexico (on sabbatical leave at CIATEQ-Queretaro)
meneses@unam.mx

Prejem rokopisa – received: 2013-01-28; sprejem za objavo – accepted for publication: 2014-01-17

A micromachining process for the fabrication of micro-electro-mechanical systems (MEMSs), using both boron-doped silicon and silicon-germanium amorphous films (a-SiB:H and a-Si0.50Ge0.50B:H) prepared with plasma-enhanced chemical vapor deposition (PECVD), at 110 kHz, 300 °C and a low pressure ($8 \cdot 10^{-4}$ mbar) is presented. These MEMSs were fabricated using a surface micromachining technology with wet and dry etching. The microstructures made of a-Si0.50Ge0.50B:H and a-SiB:H, with a structural single layer with a thickness of 1 μm were fabricated. Diamond, ring, V and Vernier-beam structures were included in the MEMS process. We found optical gaps of 1.55 eV and 0.97 eV for the a-SiB:H and a-Si0.50Ge0.50B:H films, respectively. We varied the boron doping concentration for the a-Si0.50Ge0.50B:H samples, causing a decrease in the resistance from 6.84 MΩ to 0.2 MΩ. A compressive stress of 13.44 MPa was obtained for the diamond-type microstructures of a-SiB:H. An improved mechanical stability and lateral definition were obtained for the a-Si0.50Ge0.50B:H microstructures, with a compressive stress of 10.66 MPa. These microstructures showed excellent characteristics for their integration in the production of MEMSs.

Keywords: MEMS, Vernier beam, diamond-type structure, amorphous silicon, amorphous silicon germanium, PECVD

Predstavljen je postopek mikroobdelave pri izdelavi mikroelektromehanskega sistema (MEMS) z borom dopiranih silicijevih in silicij-germanijevih amorfnih tankih plasti (a-SiB:H in a-Si0,50Ge0,50B:H), izdelanih s kemijskim postopkom nanašanja iz parne faze v plazmi (PECVD) pri 110 kHz in 300 °C pri tlaku $8 \cdot 10^{-4}$ mbar. MEMS so bili izdelani s tehnologijo mikroobdelave površine z mokrim in suhim jedkanjem. Izdelane so bile mikrostrukture iz a-Si0,50Ge0,50B:H in a-SiB:H, ki sestojijo iz ene plasti debeline 1 μm. V proces MEMS so bile vključene diamantne, obročaste, V in Vernierjeve stebraste strukture. V plasti a-SiB:H in a-Si0,50Ge0,50B:H smo našli optične vrzeli pri 1,55 eV in 0,97 eV. Spreminjanje koncentracije dopiranega bora v vzorcu a-Si0,50Ge0,50B:H je pripeljalo do zmanjšanja upornosti od 6,84 MΩ na 0,2 MΩ. Tlačna napetost 13,44 MPa je bila dosežena v diamantni mikrostrukturi a-SiB:H. Izboljšana mehanska stabilnost je bila dobljena pri mikrostrukturi a-Si0,50Ge0,50B:H s tlačno napetostjo 10,66 MPa. Te mikrostrukture kažejo odlične lastnosti za njihovo vključitev pri izdelavi MEMS.

Ključne besede: MEMS, Vernierjev steber, diamantna struktura, amorfni silicij, amorfni silicij-germanij, PECVD

1 INTRODUCTION

Recent advances in micromachining technologies related with the manufacturing of micro-electro-mechanical systems (MEMSs) made it necessary to investigate new materials to be used for the fabrication of modern devices[1–3]. Some materials can be deposited at the temperatures that are low enough (below 300 °C) to remain unaffected during a regular process involving a thermal load in the production of any complex microelectronics, for instance, when sensors and/or actuators (accelerometers, anemometers, gyroscopes, thermal devices, RF-transmitters, photodetectors, optical modulators, micromirrors[4–8]) must be integrated using a complementary metal-oxide semiconductor (CMOS) technology[9,10]. A variety of materials, such as amorphous Si (a-Si), amorphous Ge (a-Ge) and the amorphous Si-Ge alloy (a-SiGe), can be nowadays deposited onto different substrates, using plasma-enhanced chemical vapor deposition (PECVD)[11–13]. Currently, these materials are attracting the attention because their electrical and mechanical properties are suitable for manufacturing microstructures.

The a-SiGe films were developed mainly for the applications in optoelectronic devices. The optical band gap of an amorphous material is determined with the content ratio of Si/Ge in the film. In general, optical, electrical and mechanical properties can be varied according to the type and ratio of the introduced gases during the deposition. In particular, the mechanical properties provide a new property of amorphous semiconductors for fabricating microstructures.

On the other hand, most of the microstructures for MEMSs are made with polysilicon (i.e., polycrystalline silicon); however, this material is deposited and doped at 650 °C and 900 °C, respectively, and this affects the thermal budget of the process. Thus, on the basis of our knowledge of the PolyMEMSV process, we fabricated microstructures using a-SiGe films. We used this material because a-SiGe films, deposited at 300 °C, can show properties similar to those presented by polysilicon processed at much higher temperatures. Furthermore, the a-SiGe properties such as Young's modulus, bond content, thickness, resistivity and optical gap can be varied with the deposition conditions (frequency, pressure, temperature and gas-flow rate). It was found[14] that Si-Ge forms polymeric chains that do not alter at all the procedure explained in this article.

1.1 Mechanical structures for monitoring mechanical stress

One of the main problems in manufacturing surface microstructures is the presence of residual stresses. Residual stresses ($\sigma_i = E\varepsilon$) are internal mechanical forces that act on an isotropic material without the applications of external forces or temperature gradients. Residual stresses lead to mechanical deformations (ε) in the materials, resulting in fractional changes in the dimensions (linear, surface or volume)[12,13].

In order to develop a microsystem technology, we must include the structures for monitoring the efforts and residual stress on the film so that we are able to observe the presence of mechanical stresses due to the deformation. The presence of a mechanical stress causes an unpredictable behavior in static or dynamic structures. A bridge-type structure (clamped-clamped beam), under a compressive stress, presents a deformation along its structure when it is released (buckling). The critical deformation $\varepsilon_{\mathrm{cr}}$ can be estimated using Euler equation 1 for a beam with the critical length L_{cr}, as shown in **Figure 1**:

$$\varepsilon_{\mathrm{cr}} = \frac{\pi^2}{12L_{\mathrm{cr}}^2}(4D_z^2 + 4h^2) \tag{1}$$

In the above equation h is the thickness of the beam, L_{cr} is the critical length of the beam and D_{z} is the strain amplitude.

1.2 Young's modulus

Young's modulus is a measure of the stiffness of an elastic material. The residual stress (σ_i) is directly proportional to Young's modulus; therefore, a higher Young's modulus corresponds to a higher stress in the material. An ANSYS® finite-element simulator was used to calculate the Young's modulus for a-SiGe films[15,16] and this allowed a simulation of the dynamic behavior of the microstructure beams. A modal analysis was used to determine the first natural mode of the resonance frequency of the beam with the following conditions:

- The beam is considered as a harmonic oscillator.
- The beam is anchored at one end and free at the other end.
- The resonance frequency is proportional to the dimensions of the beam (L = 100 μm, h = 1 μm and w = 10 μm).
- The properties of the materials are: thermal-expansion coefficients, density, thermal conductivity[17,18].

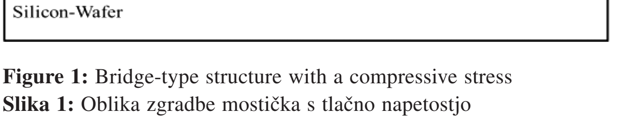

Figure 1: Bridge-type structure with a compressive stress
Slika 1: Oblika zgradbe mostička s tlačno napetostjo

The resonance frequency is a function of the dimensions and mechanical characteristics of the material:

$$F_{\mathrm{res}} = 0.1604\sqrt{\frac{E(1-\upsilon^2)}{\rho}}\,\frac{h}{L^2} \tag{2}$$

Here h is the thickness of the thin film, L is the length of the beam, ρ is the density of the material, E is Young's modulus, υ is Poisson's ratio and F_{res} is the resonance frequency of the beam[15].

1.3 Design and manufacturing of microstructures

Any PolyMEMSV chip includes passive structures such as bridge, diamond, ring, V and Vernier-beam structures acting as the monitors of the residual mechanical stress of a-SiB:H and a-$\mathrm{Si}_{0.50}\mathrm{Ge}_{0.50}$B:H films.

The microstructure manufacturing consists of deposition and etching of the materials, while the microstructure release is done with the chemical-etching techniques: wet and/or dry[16–23]. Surface micromachining is used to remove the material used as a sacrificial film[20–22]. In other cases, the bulk micromachining of silicon moves the wafer back[24]. Dry etching is done with the reactive-ion-etching system (RIE) or inductively coupled plasma (ICP). In contrast, wet etching uses chemical solutions, usually alkaline potassium hydroxide (KOH) and sodium hydroxide (NaOH). In the cases of both wet and dry etching, it is necessary to define the geometric patterns on the wafer to manufacture the microstructures with a photolithographic process.

The PolyMEMSV process is based on material deposition and wet and dry attacks for surface micromachining. Wet etching with potassium hydroxide and water (H_2O:KOH) at a temperature of 32 °C is used. Dry etching based on the reactive ion attack (RIE) is carried out with MicroRIE-800 from Technics Inc.[25]; CHF_3/O_2 and SF_6/O_2 gasses are used[24]. Photolithography with a positive photoresistance (ma-P1225) at 3000 r/min was applied for 30 s.[26] Our manufacturing processes are standardized to the level of a-SiGe of 1 μm on a phosphosilicate-glass (PSG) layer of 3 μm as the sacrificial material and an aluminum layer of 1 um.

1.4 Experimental setup

The experimental setup consisted of a silicon oxide (SiO_2) film as the electrical insulator, a PSG material as the sacrificial material (or a temporary mechanical support), an amorphous-film deposition and aluminum (Al) as the electrical conductor, and a crystalline silicon wafer used as the substrate. The manufacturing process is carried out in the following steps:

1. It begins with the growth of 200 nm SiO_2 films at a temperature of 1000 °C, for 30 min, in a H_2O vapor flow (**Figure 2a**).
2. A PSG sacrificial film 3 μm is deposited using an atmospheric-pressure chemical vapor deposition system (APCVD.) This film serves as a temporary mechanical support for the structures suspended. The conditions are: a temperature of 450 °C, nitrogen (N_2), silane (SiH_4) and phosphine (PH_3) flows, duration of 58 min (**Figure 2b**).

Lithography and wet etching are performed on the PSG film in order to deposit a microstructure film, applying a negative photoresistance (ma-1420) at 5000 r/min for 30 s, during an exposure time of 10 s.[25] Developed in 35 s and using a thermal annealing at 110 °C for 15 min, wet etching is performed with potassium hydroxide (KOH) to 10 % at a temperature of 32 °C for 3 min (**Figure 2c**).

The a-SiB:H and a-Si0.50Ge0.50B:H films 1 μm are deposited with the PECVD system under the following conditions: a temperature of 300 °C, a frequency of 110 kHz, a power of 500 W and a pressure of $8 \cdot 10^{-4}$ mbar. Silane (SiH_4), germane (GeH_4), hydrogen (H_2) and diborane (B_6H_4) flows are used (**Figure 2d**).

The microstructures of the a-Si1B:H and a-Si0.50Ge0.50B:H films are defined with lithography and dry etching in RIE. Sulfur tetrafluoride (SF_4) gas is used to generate the RIE plasma, with an electrical power of 200 W and the base pressure of $4 \cdot 10^{-1}$ mbar (**Figure 2e**).

Aluminum 1 μm used for electrical contacts is deposited with a physical vapor deposition system (PVD). Aluminum etching is performed using a chemical solution of H_3PO_4, CH_3COOH and HNO_3 for 7 min at 27 °C (**Figure 2f**).

The last step includes a removal of the PSG sacrificial layer to release the suspended microstructures. The technique used to release the microstructures consists of eliminating the PSG with a hydrofluoric acid solution (HF to 49 %) at room temperature for 4 min. The microstructure release is performed with 2-propanol at 62 °C, water DI at 62 °C and acetone at 62 °C to remove the residues in order to avoid a collapse (**Figure 2g**).

2 RESULTS AND DISCUSSION

The spectra of the optical absorption were measured with a UV/Vis 300 Spectronic-Unicam spectrometer[20]. The optical gap E_g of the films was extracted according to the empirical formula derived by Tauc[26–29]. **Figure 3** shows the band optical gap E_g versus the Ge content (X_g) for the films studied here. The values of the optical gap of 1.55 eV for the a-SiB:H film are also shown. As the Ge content increases from 0 to 0.25 the optical gap decreases rapidly from 1.55 eV to 1.06 eV for the a-Si0.75Ge0.25B:H films. When the Ge content $X_g > 0.5$ (a-Si0.50Ge0.50B:H) the change in the optical gap becomes slower, 0.97 eV and 0.78 eV for the a-GeB:H films.

The electrical and mechanical properties, the stress and roughness of a film are important in the fabrication of microstructures. The data obtained from the a-SiB:H thin films and the a-Si1-XGeXB:H alloy with different molar concentrations of Ge show that the optical gap

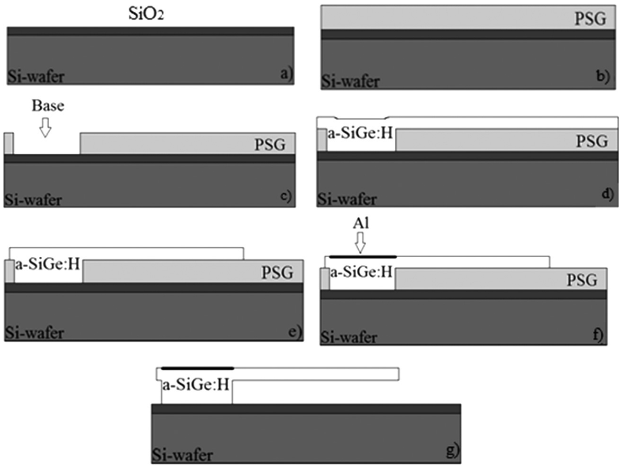

Figure 2: Sequence of the steps for the production of the microstructures of a-Si1B:H and a-Si0.50Ge0.50B:H with a thickness of 1 μm

Slika 2: Zaporedje korakov pri izdelavi mikrostrukture a-Si1B:H in a-Si0,50Ge0,50B:H debeline 1 μm

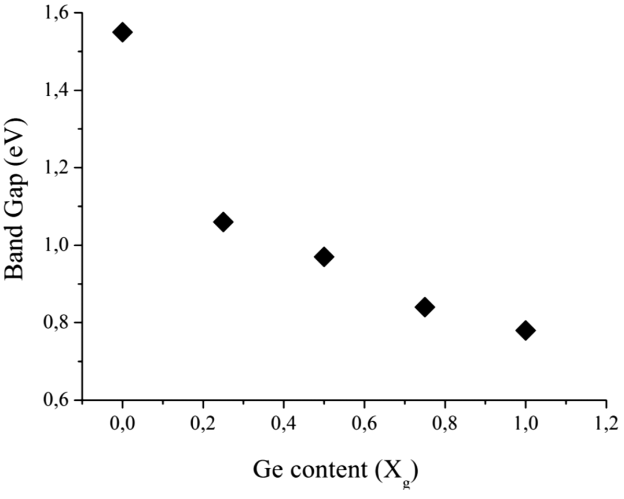

Figure 3: Band gap versus Ge content for a-Si1-XGeXB:H thin films

Slika 3: Energijska vrzel v tanki plasti a-Si1-XGeXB:H glede na vsebnost Ge

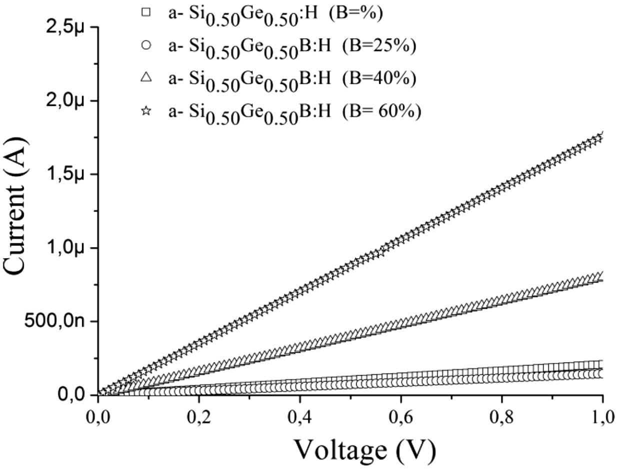

Figure 4: Current-voltage curves for the a-Si0.50Ge0.50B:H sample doped with different amounts of boron

Slika 4: Odvisnost toka od napetosti pri vzorcu a-Si0,50Ge0,50B:H, dopiranem z različnimi vsebnostmi bora

varies with the B content, but the preferential Ge incorporation in the solid phase is evident.

Figure 4 shows the current-voltage curves for the sample of a-Si0.50Ge0.50B:H doped with different amounts of boron; this graph shows that the slope of each curve changes in the range of 0.12 µA to 1.7 µA. These changes in the slope of the current-voltage curve between different samples are due to the variation in the electrical resistance of different samples. The electrical resistance decreases with the amount of boron present in the samples in the range of 6.84 MΩ to 0.514 MΩ. The a-Si0.50Ge0.50B:H sample doped with 60 % of boron has less electrical resistance. The result of an electrical characterization was obtained with a Keithley Model 2400 SourceMeter[16,30].

Figure 5 shows the resonance frequency obtained through the finite-element method using ANSYS®[16], allowing us to calculate the Young's modulus from Equation 2 as a function of the germanium concentration in the bridge-type microstructure.

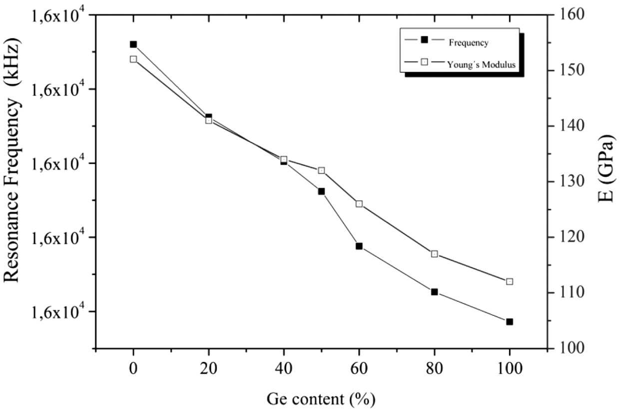

Figure 5: Resonant frequency and Young's modulus as functions of the concentration

Slika 5: Resonančna frekvenca in Youngov modul v odvisnosti od koncentracije

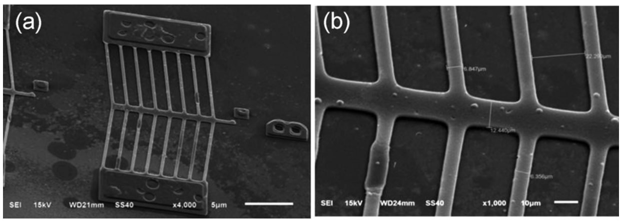

Figure 6: a) Geometric profile and b) close-to-TVM-type microstructure

Slika 6: a) Geometrijski profil in b) mikrostruktura blizu TVM

The analysis showed that Young's modulus can be assumed as a linear combination of the amounts of silicon and germanium in thin films.

We designed a microstructure-manufacturing process with the a-Si0.50Ge0.5B:H films deposited at the temperature of 300 °C to use it for post-processing MEMS with the CMOS technology. The SEM images were recorded at an acceleration voltage of 15 kV and in a high vacuum (HV) using a JEOL SEM model JSM-5610LV (Hitachi, Japan). The samples were placed on a specimen stub using a double-sided adhesive carbon tape.

The microstructures manufactured at a low temperature of 300 °C, with a structural level of hydrogenated amorphous silicon doped with boron (a-Si1B:H) exhibited a higher roughness on the surface and a poor definition at the edges of the structures; in addition to the chemical attack on the surface of the wafer and the structures, **Figure 6** shows SEM images of thermal microactuator chevron (TVM) type microstructures.

Additionally, when using thin films of a-Si0.50 Ge0.50B:H a direct dependence on the roughness and the definition of the edge is observed, while others do not show lateral etching on the structures or on the wafer. **Figure 7** shows the profiles of thermal bimorph micro-actuator (TBA) type microstructures manufactured with the a-Si0.50Ge0.50B:H films including a structural layer.

The microstructures of a-SiB:H and a-Si0.50Ge0.50 B:H show the presence of the residual stress (σ_i) of compression in suspended microstructures. **Figure 8**

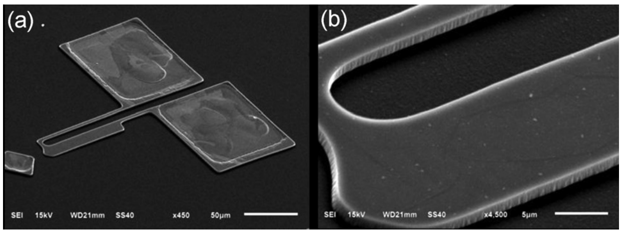

Figure 7: SEM images of the microstructure of a-Si0.50Ge0.50B:H: a) TBA-type microstructure, b) close up of the TBA-type microstructure

Slika 7: SEM-posnetka mikrostrukture a-Si0,50Ge0,50B:H: a) TBA-vrsta mikrostrukture, b) blizu TBA-vrsti mikrostrukture

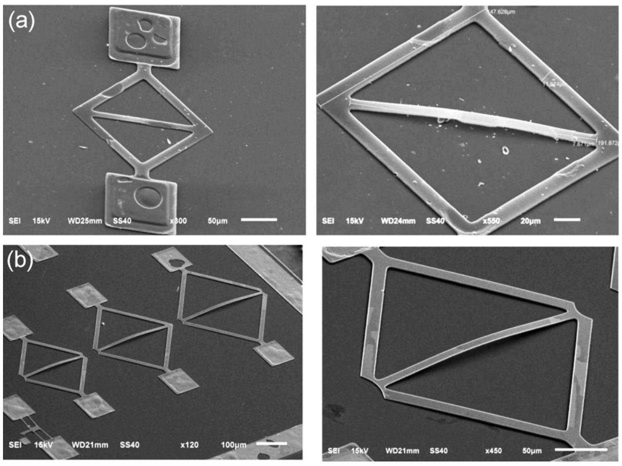

Figure 8: Compression stress $(-\sigma_i)$ for diamond-type microstructures: a) microstructure of a-SiB:H, b) microstructure of a-Si0.50Ge0.50B:H
Slika 8: Tlačna napetost $(-\sigma_i)$ za diamantno mikrostrukturo: a) mikrostruktura a-SiB:H, b) mikrostruktura a-Si0,50Ge0,50B:H

shows images of diamond-type structures with different lengths and a width of 10 μm across the central bar; the structures present an evident deformation known as the critical length of deformation (buckling), ε_{cr}.

According to Equation 1, the deformation of a-SiB:H diamond-type structures, with a length of 200 μm across the central bar and a width of 10 μm, is 89.363 μm, and the residual stress ($\sigma_i = \varepsilon E$) is calculated to be 13.444 MPa. The a-Si0.50Ge0.50B:H diamond-type structure does not show any lateral chemical attacks, but it indicates a compressive residual stress of 10.661 MPa (**Figure 8**).

Figure 9 shows that the stress is higher when the length of the central bar is smaller; this is because the deformation (ε_{cr}) is directly proportional to the length of the bar and the stress $-\sigma_i$ is directly proportional to the Young's modulus. The Young's modulus of a-Si:H is 160 GPa and for a-Si0.50Ge0.50B:H the Young's modulus is 130 GPa. So, the a-Si0.50Ge0.50B:H microstructures present less stress.

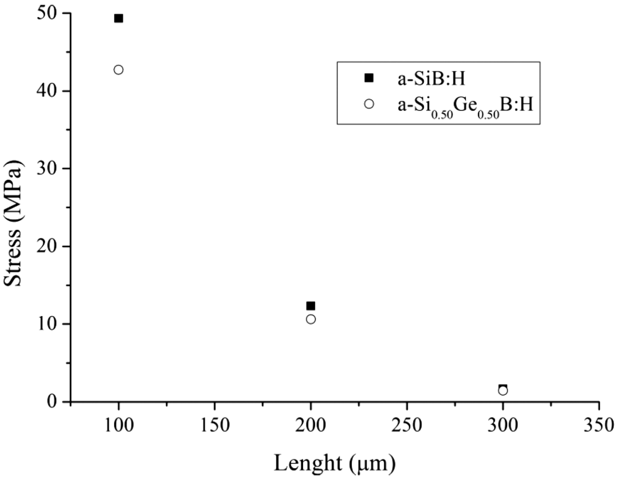

Figure 9: Compression residual stress of diamond-type microstructures versus the length
Slika 9: Zaostale tlačne napetosti pri diamantni mikrostrukturi v odvisnosti od dolžine

3 CONCLUSIONS

The work presents the results of manufacturing microstructures with a-SiB:H and a-Si0.50Ge0.50B:H films deposited with a PECVD system at a temperature of 300 °C. The electrical and optical characterization of a-Si1-XGeXB:H thin films was made. The value of the optical gap of the a-SiB:H film is 1.55 eV and for the a-Si0.50Ge0.50B:H film it is 0.97 eV. When germanium content increases, the optical gap decreases rapidly from 1.55 eV to 0.78 eV for a-GeB:H films. The electrical resistance of the a-Si0.50Ge0.50B:H film doped with different concentrations of boron becomes reduced from 6.84 MΩ to 0.56 MΩ. The Young's modulus of amorphous silicon-germanium alloys presents a linear behavior of the silicon/germanium content.

The a-Si0.50Ge0.50B:H suspended microstructures fabricated with a surface micromachining technique at a temperature of 300 °C provide an excellent definition of geometric patterns, having a high mechanical stability in contrast with the microstructures of a-Si1B:H. The advantage of working at low temperatures is a reduction of the residual stress and the intrinsic gradient present at high temperatures. However, diamond-type structures exhibit a compressive mechanical stress of 13.44 MPa for the a-SiB:H structural layer and 10.66 MPa for the a-Si0.50Ge0.50B:H structural layer. We can, therefore, conclude that the microstructures with the a-Si0.50 Ge0.50B:H structural layers deposited at 300 °C using PECVD with the heat treatments < 350 °C can be applied in post-CMOS processes and MEMSs as structural materials. In future we plan to integrate the manufacturing devices and microstructures within a die.

Acknowledgements

The work was supported by Consejo Naciuonal de Ciencia y Tecnología through grant 160164 and by Red Nacional de MEMS.

4 REFERENCES

[1] H. Baltes, O. Brand, A. Hierlemann, D. Lange, C. Hagleitner, CMOS MEMS – present and future, Proc. of the International conference on Micro Electro Mechanical Systems, Las Vegas, 2002, 459–466

[2] S. Beeby, G. Ensell, M. Kraft, N. White, MEMS mechanical sensors, Artech House, Norwood, MA 2004

[3] J. W. Judy, Microelectromechanical systems (MEMS): fabrication, design and applications, Journal of Smart Materials and Structures, 10 (**2001**), 1115–1134

[4] E. K. Petersen, Silicon as a mechanical material, Proceedings of the IEEE, 70 (**1982**), 420–455

[5] J. Stauth, Micromechanical electrostatic resonators in a standard post-CMOS process, UC Berkeley-EECS, 2005, 1–4

[6] F. Yuan, CMOS Current-Mode Circuits for Data Communications, Springer, 2007

[7] J. Laconte, D. Flandre, J. P. Raskin, Micromachined Thin-Film Sensors for SOICMOS Co-Integration, Springer, 2006, 47–103

[8] A. Witvrouw, F. Steenkiste, D. Maes, L. Haspeslagh, P. Gerwen, P. Moor, S. Sedky, C. Hoof, A. Vries, A. Verbist, A. Caussemaeker, B. Parmentier, K. Baert, Why CMOS integrated transducers? A review, Microsystem Technologies, 6 (**2000**), 192–199

[9] T. Hidekuni, S. Kazuaki, I. Makoto, Integrated inductors for RF transmitters in CMOS/MEMS smart microsensor systems, Sensors, 7 (**2007**), 1387–1398

[10] F. Mayer, A. Haberli, H. Jacobs, G. Ofner, H. Baltes, Single CHIP CMOS anemometer, International Electron Devices Meeting, Washington, 1997, 895–898

[11] H. Guckel, D. Burns, C. Rutigliano, E. Lovell, B. Choi, Diagnostic microstructures for the measurement of intrinsic strain in films, J. Micromech, Microeng, 2 (**1992**), 86–95

[12] H. Guckel, T. Randazzo, D. Burns, A simple technique for the determination of mechanical strain in thin films with applications to polysilicon, J. Appl. Phys., 57 (**1985**) 5, 1671–1675

[13] Research Institute. http://www.inaoep.mx/ (accessed 20 April 2010)

[14] G. Craciun, H. Yang, W. Van Zeijl, L. Pakula, A. Blauw, E. Van der Drift, J. French, Single step cryogenic SF6/O2 plasma etching process for the development of inertial devices, Proceedings on semiconductors sensors, Fabrication and characterization, 2002, 612–615

[15] W. Brostow, V. M. Castaño, G. Martinez-Barrera, J. M. Saiter, Pressure-volume-temperature properties of Ge_xSe_{1-x} inorganic polymeric glasses, Physica B, 334 (**2003**), 436–443

[16] F. López, A. Herrera, J. Estrada, C. Zúñiga, B. Cervantes, E. Soto, B. S. Soto-Cruz, Alternative Post-Processing on a CMOS Chip to Fabricate a Planar Microelectrode Array, Sensors, 11 (**2011**), 10940–10957

[17] Software products for engineering simulation, http://www.ansys.com/ (accessed in December 2009)

[18] W. Hernández, I. Zaldivar, C. Zúñiga, A. Torres, C. Reyes, A. Itzmoyol, Optical and compositional properties of amorphous silicon-germanium films by plasma processing for integrated photonics, Optical Materials Express, 2 (**2012**), 358–370

[19] Laboratory Equipments, Available online: http://www.echromtech.com (accessed in September 2011)

[20] B. Nelson, Y. Xu, D. Williamson, D. Han, R. Braunstein, M. Boshta, B. Alavi, Narrow gap a-SiGe:H grown by hot-wire chemical vapor deposition, Thin Solid Films, 430 (**2003**), 104–109

[21] Electronic Instruments, Available online: http://www.keithley.com (accessed in November 2011)

[22] M. Christian, H. Qiuting, A Low-Noise CMOS instrumentation amplifier for thermoelectric infrared detectors, IEEE Journal of Solid-State Circuits, 32 (**1997**), 968–976

[23] I. Toledo, R. Adler, Y. Knafo, O. Kalis, J. Kaplun, BCB etching process using high density plasma, CS MANTECH Conference, Chicago, Illinois, USA, 2008, 14–17

[24] M. Tsai, C. Sun, Y. Liu, C. Wang, W. Fang, Design and application of a metal wet-etching post-process for the improvement of CMOS-MEMS capacitive sensors, Journal of Micromechanics and Microengineering, 19 (**2009**), 1–7

[25] D. Fernández, J. Ricart, J. Madrenas, Experiments on the release of CMOS micromachined metal layers, Journal of Sensors, 2010 (**2010**), article ID 937301, 1–7

[26] P. Merz, H. Quenzer, H. Bernt, B. Wagner, M. Zoberbier, A novel micromachining technology for structuring borosilicate glass substrates, The 12th International Conference on Solid State Sensors, Actuators and Microsystems, Boston, MA, USA, 2003, 258–261

[27] H. Berney, M. Hill, D. Cotter, E. Hynes, M. O'Neill, A. Lane, Determination of the effect of processing steps on the CMOS compatibility of a surface micromachined pressure sensor, Journal of Micromechanics and Microengineering, 11 (**2001**), 402–408

[28] A. Jihwan, V. Brian, Micromachined nerve electrode array integrated with shape memory thin film position clamp, Proceedings of E240, 2007, 1–4

[29] T. Gregory, I. Nadimi, E. Kurt, Bulk micromachining of silicon, Proceedings of the IEEE, 86 (**1998**), 1536–1550

[30] Microresist Technology, Available online: http://www.microresist.de/home_en.htm (accessed in September 2011)

UDK 669.018.9:539.538:669.715
Original scientific article/Izvirni znanstveni članek

ISSN 1580-2949
MTAEC9, 49(1)9(2015)

WEAR BEHAVIOUR OF B_4C REINFORCED HYBRID ALUMINUM-MATRIX COMPOSITES

VEDENJE HIBRIDNEGA KOMPOZITA NA OSNOVI ALUMINIJA, OJAČANEGA Z B_4C, PRI OBRABI

Thirumalai Thiyagarajan[1], Ramanathan Subramanian[2], Somasundaram Dharmalingam[3], Nachiappan Radika[4], Annadurai Gowrisankar[2]

[1]Department of Mechanical Engineering, Erode Sengunthar Engineering College, Perundurai, Erode, India
[2]Department of Metallurgical Engineering, PSG College of Technology, Coimbatore, India
[3]Department of Mechanical Engineering, RVS Faculty of Engineering, Coimbatore, India
[4]School of Mechanical Engineering, Amrita Vishwa Vidyapeetham University, Coimbatore, India
thirumalaimet@gmail.com

Prejem rokopisa – received: 2013-08-12; sprejem za objavo – accepted for publication: 2014-03-24

Harnessing the benefits of aluminum hybrid composites requires strengthening of materials with better reinforcing materials. Hence, this investigation was carried out to identify the optimum level of B_4C reinforcement to enhance the wear resistance of aluminum alloys. Four amounts of B_4C reinforcement (3, 6, 9 and 12) % and a constant amount of 3 % graphite were mixed with an aluminum alloy to produce aluminum hybrid composites. The hybrid composites thus produced were tested for wear resistance at various loads and sliding speeds. The change in the wear resistance of the newly produced hybrid material was studied with SEM micrographs to confirm the results. Al-B_4C-Gr composites produced with the stir-casting method including various amounts of B_4C reinforcement show that the B_4C reinforcement of up to 9 % was found beneficial as it increased the wear resistance of the aluminum alloy. The addition of a constant amount of graphite provides for the lubrication effect, while B_4C increases the strength of the parent material (Al). SEM micrographs confirmed that aluminum hybrid composites showed less debris and finer grooves with delamination at lower loads and sliding speeds. Hence, 9 % B_4C reinforcement with 3 % graphite is a better way of increasing the wear resistance of aluminum alloys.

Keywords: aluminum-matrix composites, boron carbide, graphite, wear, stir casting, sliding distance

Izkoriščanje prednosti hibridnih kompozitov na osnovi aluminija zahteva ojačanje materiala z boljšimi materiali za utrjevanje. Zato je bila izvršena ta preiskava, da bi se ugotovil optimalni dodatek B_4C za povečanje obrabne odpornosti aluminijevih zlitin. Štiri vsebnosti B_4C (3, 6, 9 in 12) % kot dodatka za utrjevanje in 3 % grafita so bile dodane aluminijevi zlitini, da bi dobili aluminijeve hibridne kompozite. Tako izdelani hibridni kompoziti so bili preizkušeni v odpornosti proti obrabi pri različnih obtežbah in hitrostih drsenja. Potrditev rezultatov in spremembe v odpornosti proti obrabi hibridnih materialov so bile ugotavljane s SEM-posnetkov. Kompoziti Al-B_4C-Gr, izdelani z metodo vmešavanja v talino, z različno vsebnostjo sredstva za utrditev B_4C so pokazali, da je dodatek do 9 % B_4C ugoden in poveča obrabno odpornost aluminijeve zlitine. Dodatek enake količine grafita zagotavlja učinek mazanja, medtem ko B_4C daje višjo trdnost osnovnemu materialu (Al). SEM-posnetki hibridnih kompozitov aluminija so pokazali manj zlomnin in drobnejše opilke z delaminacijo pri manjših obtežbah in hitrostih drsenja. Torej je dodatek 9 % B_4C za ojačanje in 3 % grafita boljša tehnologija za povečanje obrabne odpornosti aluminijevih zlitin.

Ključne besede: kompoziti na osnovi aluminija, borov karbid, grafit, obraba, vmešavanje v talino, razdalja drsenja

1 INTRODUCTION

Aluminum-matrix composites (AMCs) have recently gained momentum due to their structural applications in aircraft, automotive, construction, packaging, electronics and military industries. Next to iron and steel, aluminium alloys are the most widely used metallic materials. They are used particularly in the manufacturing of automotive components such as cylinder liners, pistons, drive shafts, brake rotors, cylinder heads, cylinder blocks, intake manifolds, rear axles and differential housings[1–3]. Their high strength-to-weight ratio, high thermal conductivity and specific stiffness enhanced the interest of the researchers to further improve the material characteristics so that they are appropriate for all the applications. Aluminium represents around 8 % of the vehicle curb weight in today's cars, trucks and minivans. However, an inadequate wear resistance and low seizure loads prevent a direct use of aluminium alloys in automotive parts due to the intensive friction, high thermal and mechanical loading[4].

Boron carbide (B_4C) is found to be a promising ceramic material due to its high strength, low density (2.52 g/cm^3), extremely high hardness and better chemical stability. Extreme hardness of this material makes it a better alternative to silicon carbide (SiC) and aluminum oxide (Al_2O_3) for reinforcement with aluminum alloys. A hybrid aluminum-matrix composite combines the high strength and hardness of reinforcing materials with the ductility and toughness of light metals[5,6]. A study conducted to test the wear behaviour of Al-B_4C and Al-SiC composites fabricated with the stir-casting method revealed that the wear rate and friction coefficient of Al-B_4C were lower than those of Al-SiC[7]. The aluminum-matrix composite reinforced with B_4C particles and SiC particles through the pressureless-infiltration method indicated that the strength of the Al-B_4C composite was greater than that of the Al-SiC composite.[8] Hence, a decrease in the reinforcement particle size to the nanometer range can improve the mechanical and tribological properties of AMCs. The tribological behaviour of stir-cast Al-Si/SiC composites (15 % and 20 % volume fraction) against the automobile-brake-pad material using a pin-on-disc tribotester showed an inverse proportionality between the sliding speed and the wear rate[9]. Dry-sliding wear performance of a hypereutectic A390 Al-Si alloy reinforced with graphite particulates (4 % and 8 %) showed that both the wear rate and COF of the composites decreased considerably with the addition of graphite[10].

The fabrication and characterization of bulk Al-B$_4$C nanocomposites containing different mass fractions of B$_4$C w = (5, 10 and 15) % showed an increase in the wear resistance with the increasing B$_4$C amount[11]. The fabrication of mass fractions 40 % SiC/% Gr/Al composites with the additions of various amounts of graphite using the squeeze-casting technology showed that the addition of graphite decreased the friction coefficient of the composites and increased the wear resistance by 170 to 340 times[12]. A study on the influence of the sliding speed on dry-sliding wear behaviour and the extent of subsurface deformation in an Al 2219/15 % SiCp composite and an Al 2219/15 % SiCp-graphite hybrid composite due to liquid metallurgy reported that the wear rates of the composites remained almost unchanged with the increasing sliding speed up to 4.6 m/s, after which an increasing trend in the wear rate was observed[13].

Extensive researches on individual reinforcements of boron carbide and graphite improving the wear resistance and the strength of hybrid aluminum composites were carried out. However, very limited research was conducted in order to explore the combined effect of boron-carbide and graphite-particulate reinforcements on hybrid aluminum composites. Hence, this study was carried out i) to develop new hybrid aluminum composites with boron carbide and graphite and ii) to test the improvement in the wear resistance of the material under varying sliding speed and load.

2 MATERIALS AND METHODS

Hybrid aluminum composites with boron carbide (B$_4$C) in various amounts and constant graphite reinforcement were cast using the stir-casting method. The hybrid Al composites were reinforced with (3, 6, 9 and 12) % of B$_4$C and a constant amount of 3 % graphite. The boron-carbide and graphite particles with the average particle size of 25 µm to 75 µm were preheated up to 300 °C. Degassing tablets were added during the melting to remove gaseous molecules. Magnesium (w = 2 %) was added to the molten metal to improve the wettability between the reinforcements and aluminium.

The mixture of the molten alloy was mechanically stirred using a steel stirrer for 10 min to obtain a homogenous mixture. A speed of 400 r/min was maintained and a pouring temperature of 710 °C was maintained. After removing them from the metal dye, the specimens were collected and subjected to the wear tests performed with a pin-on-disc machine. The test specimens were in the form of pins having a diameter of 10 mm and a height of 40 mm. The ends of the specimens were polished with abrasive paper of grade 600 followed by grade 1000. The disc was made of EN-31 steel having a hardness of 63 HRc under dry conditions. The wear loss of the pin in microns was recorded during the wear test. The pin surface wore out during the rubbing with the counter disc, continuously moving down to have a contact with the surface of the disc. The tests were conducted as per ASTM G99-95a test standards with a constant sliding distance of 2500 m and a normal load of 10 N to 30 N. The sliding speed of 1 m/s to 3 m/s was tested under dry conditions and the wear resistance was recorded.

3 RESULTS AND DISCUSSIONS

Dry-sliding wear tests were conducted for the hybrid composites and an unreinforced aluminium alloy (the parent material) using a pin-on-disc apparatus at different normal loads (10 N to 30 N) and sliding speeds (1 m/s and 2 m/s) with a constant sliding distance of 2500 m. The wear rate was calculated by weighing the specimens before and after the test. The variation in the wear rate with varied levels of the normal load and reinforcement percentage at different sliding speeds is shown in the graphs (**Figures 1** to **4**). It can be observed that the wear loss increases with the increasing load and the highest wear is noted at the load of 30 N at both sliding speeds. Comparing various materials tested for the wear loss, it was evident that the maximum wear loss occurred on the parent material (Al) and the minimum wear loss occurred on 3 % Gr + 9 % B$_4$C + Al compo-

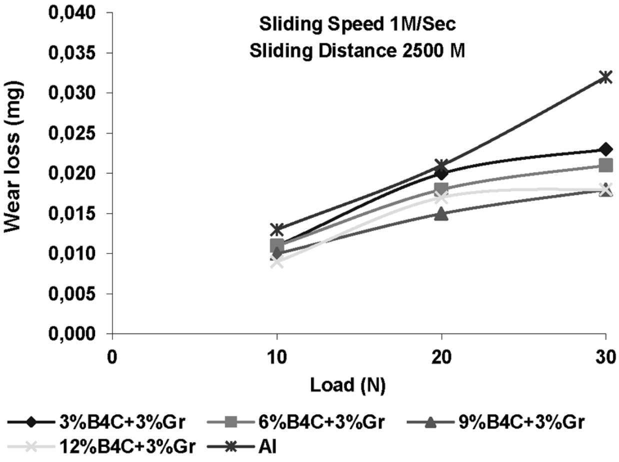

Figure 1: Wear loss of hybrid aluminum composites with load at 1 m/s sliding speed

Slika 1: Izguba zaradi obrabe hibridnega kompozita aluminija z obtežbo pri hitrosti drsenja 1 m/s sites (C3) which might have happened due to its better wear resistance.

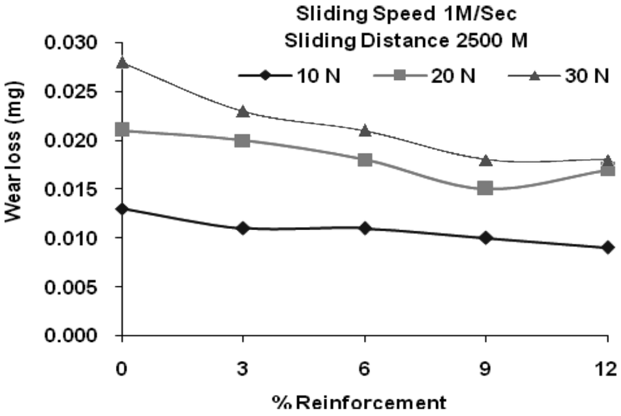

Figure 2: Wear loss of hybrid aluminum composites with reinforcement fraction at 1 m/s sliding speed

Slika 2: Izguba zaradi obrabe hibridnega kompozita aluminija z deležem ojačitvene faze pri hitrosti drsenja 1 m/s

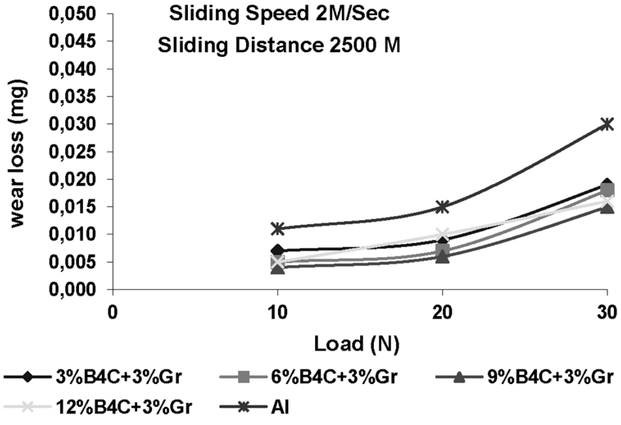

Figure 3: Wear loss of hybrid aluminum composites with load at 2 m/s sliding speed

Slika 3: Izguba zaradi obrabe hibridnega kompozita aluminija z deležem ojačitvene faze pri hitrosti drsenja 2 m/s

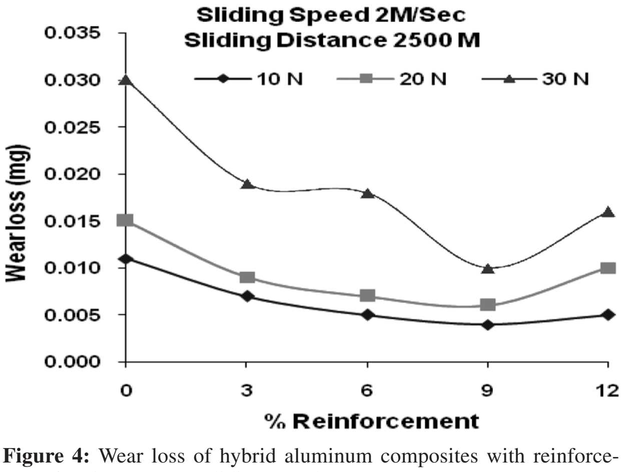

Figure 4: Wear loss of hybrid aluminum composites with reinforcement fraction at 2 m/s sliding speed

Slika 4: Izguba zaradi obrabe hibridnega kompozita aluminija z deležem ojačitvene faze pri hitrosti drsenja 2 m/s

The wear resistance increases with the increasing B_4C amount up to 9 % in the composites, but a mixture containing more than 9 % B_4C decreases the wear resistance. The beneficial effect noticed up to 9 % B_4C reinforcement could be due to its higher hardness, causing a better wear resistance of the composites[11]. Like the parent material, the other compositions, 3 % Gr + 3 % B_4C + Al (C1), 3 % Gr + 6 % B_4C + Al (C2) and 3 % Gr + 12 % B_4C + Al (C4), also showed higher wear losses which can be ascribed to larger quantities of the particles. Many investigators reported that the low density (2.52 g/cm^3), high hardness (HV = 30 GPa) and thermal stability of boron carbide might be possible reasons for the increased wear resistance[14–17]. A decreased wear resistance at a higher level of B_4C reinforcement (w = 12 %) could be due to a reduction in the interfacial strength. This reduction in the interfacial strength is attributed to the formation of a boron-rich Al-B phase at the grain boundaries[18,19]. The sliding speed is an important factor that needs to be tested to understand the wear loss of any new composite. Hence, two sliding speeds were tested under various loads and B_4C reinforcement percentages and the results revealed that the wear loss decreased with the increasing sliding speed irrespective of the reinforcement percentage and the load. The wear loss of the parent material was the highest at the higher load (30 N) and it decreased with the sliding speed which must have been due to the reduced particle retention time for abrasion[11,20]. The formation of the surface

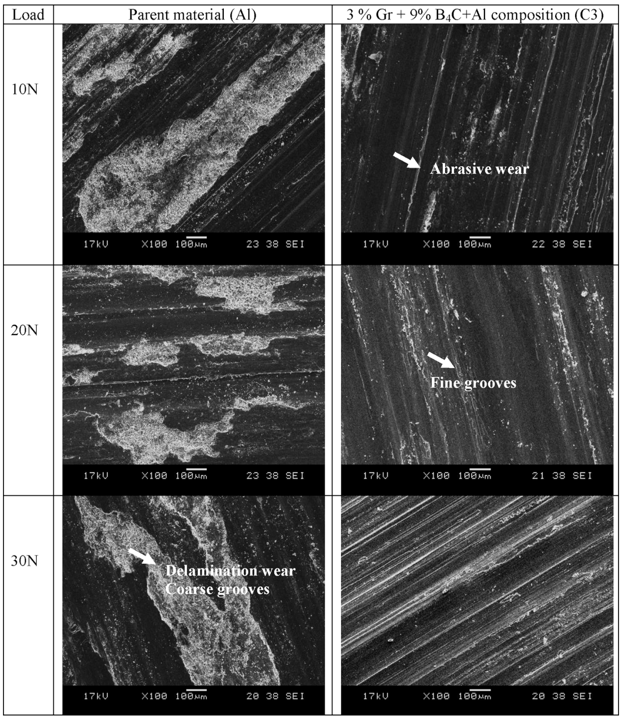

Figure 5: SEM micrographs of the worn surfaces of hybrid Al-B_4C composites and aluminum (sliding speed 1 m/s, sliding distance 2500 m)

Slika 5: SEM-posnetki obrabljene površine hibridnega kompozita Al-B_4C in aluminija (hitrost drsenja 1 m/s, razdalja drsenja 2500 m)

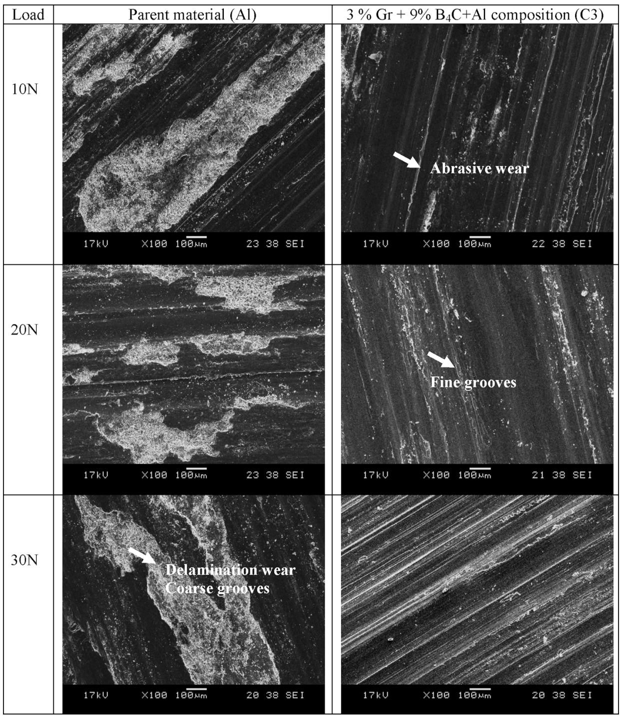

Figure 6: SEM micrographs of the worn surfaces of hybrid Al-B_4C composites and aluminum (sliding speed 2 m/s, sliding distance 2500 m)

Slika 6: SEM-posnetki obrabljene površine hibridnega kompozita Al-B_4C in aluminija (hitrost drsenja 2 m/s, razdalja drsenja 2500 m)

coatings of oxidized debris at the higher sliding speed might have reduced both the wear rate and the coefficient of friction.

Wear-track patterns of hybrid composites and the parent material at three different loads and two sliding speeds were studied by taking SEM micrographs. **Figures 5** and **6** show the typical wear-track patterns developed on the surfaces of the composites and the parent material. On the parent material, the increasing load increases the formation of coarse grooves, debris particles and surface delamination. At the lower load (10 N), more debris particles and abrasive wear of the surfaces were noticed. With the increased load (20 N) wider grooves and more debris were formed. Delamination, wider grooves with more debris and mixed adhesive wear were noticed when the parent material was subjected to the 30 N load[21,22].

Upon sliding, the higher speed caused abrasive wear which pulled some of the material from the surface and formed loose abrasive debris. As the sliding process proceeded with the increasing speed, the material attached to alumina was delaminated and defoliated to form more small debris and deep widened grooves. As the load increased, greater amounts of the material from the surfaces were defoliated, forming deep grooves with wider widths due to ploughing in the aluminum alloy[23]. In the case of major wear mechanisms, the abrasion wear was predominant at the lower load (10 N) while at the higher load (30 N) the adhesive wear was higher. In contrast, the reinforcement with B_4C and graphite showed a beneficial effect on the wear resistance of the composites.

The reinforced hybrid composites exhibited fine grooves and less debris at the 10 N load. Like in the case of the parent material, the increasing load increased the delamination and the adhesive wear of the composites to a lesser extent. The B_4C reinforcement decreased the groove width and debris formation due to an improvement in the load-carrying capacity of the composites, enhancing the abrasion resistance of the composites and, thus, decreasing the wear loss[24,25]. At the lower load and sliding speed (L = 10 N and S = 1 m/s) the worn pin surface predominantly revealed fine and shallow grooves in the sliding direction. Such features are characteristic of the abrasive wear, where hard asperities of the counter face plough into the hybrid composite pin, causing wear by removing small fragments of the material.

4 CONCLUSIONS

Al-B_4C-Gr composites were produced with the stir-casting method using various levels of B_4C reinforcement and a constant amount of 3 % graphite addition. An evaluation of the morphological properties and the wear showed that the B_4C reinforcement of up to 9 % was beneficial in increasing the wear resistance of aluminum hybrid composites. In the presence of graphite, B_4C made the parent material (Al) even stronger, resisting both the abrasive and the adhesive wear. Subjecting the composites and the unreinforced aluminum parent material to various levels of the load showed that the increased load increased the wear of the composites. At the lower load and sliding speed, less debris and fine grooves with delamination were formed which was confirmed with SEM micrographs. The improved wear resistance of the composites is due to the hardness of B_4C and the lubricating effect of graphite. Hence, 9 % B_4C reinforcement with 3 % graphite can be a better way of increasing the wear resistance of aluminum alloys.

5 REFERENCES

[1] W. S. Miller, L. Zhuang, J. Bottema, A. J. Wittebrood, P. D. Smet, A. Haszler, A. Vieregge, Recent development in aluminium alloys for the automotive industry, Materials Science & Engineering A, 280 (**2000**), 37–49

[2] I. Sinclair, P. J. Gregson, Structural performance of discontinuous metal matrix composites, Materials Science and Technology, 13 (**1997**), 709–726

[3] I. A. Ibrahim, F. A. Mohamed, E. J. Lavernia, Particulate Reinforced Metal Matrix Composites – A Review, Journal of Materials Science, 24 (**1991**), 1137–1156

[4] V. Kevorkijan, Engineering wear-resistant surfaces in automotive aluminium, JOM, 55 (**2003**), 32–34

[5] B. R. Henriksen, T. E. Johnsen, Influence of microstructure of fiber/matrix interface on mechanical properties of Al/SiC composites, Materials Science and Technology, 6 (**1990**), 857–863

[6] Y. H. Kim, C. S. Lee, K. S. Han, Fabrication and Mechanical Properties of Aluminum Matrix Composite Materials, Journal of Composite Materials, 26 (**1992**), 1062–1086

[7] K. M. Shorowordi, A. S. M. A. Haseeb, J. P. Celis, Tribo-surface characteristics of Al–B_4C and Al–SiC composites worn under different contact pressures, Wear, 261 (**2006**), 634–641

[8] K. B. Lee, H. S. Sim, S. Y. Cho, H. Kwon, Tensile properties of 5052 Al matrix composites reinforced with B_4C, Metall. Mater. Trans. A, 32 (**2001**), 2142–2147

[9] R. K. Uyyuru, M. K. Surappa, S. Brusethaug, Tribological behavior of Al-Si-SiCp composites/automobile brake pad system under dry sliding conditions, Tribology International, 40 (**2007**), 365–373

[10] T. S. Mahmoud, Tribological behaviour of A390/Gr_P metal-matrix composites fabricated using a combination of rheocasting and squeeze casting techniques, Journal of Mechanical Engineering Science, 222 (**2008**), 257–265

[11] E. Mohammad Sharifi, F. Karimzadeh, M. H. Enayati, Fabrication and evaluation of mechanical and tribological properties of boron carbide reinforced aluminum matrix nanocomposites, Materials and Design, 32 (**2011**), 3263–3271

[12] L. Jinfeng, J. Longtao, W. Gaohui, T. Shoufu, C. Guoqin, Effect of Graphite Particle Reinforcement on Dry Sliding Wear of SiC/Gr/Al Composites, Rare Metal Materials and Engineering, 38 (**2009**), 1894–1898

[13] S. Basavarajappa, G. Chandramohan, A. Mahadevan, M. Thangavelu, R. Subramanian, P. Gopalakrishnan, Influence of sliding speed on the dry sliding wear behaviour and the subsurface deformation on hybrid metal matrix composite, Wear, 262 (**2007**), 1007–1012

[14] S. Basavarajappa, G. Chandramohan, K. Mukund, M. Ashwin, M. Prabu, Dry Sliding Wear Behavior of Al 2219/SiC_p-Gr Hybrid Metal Matrix Composites, Journal of Materials Engineering and Performance, 15 (**2006**) 6, 668–674

[15] M. Gui, S. B. Kang, J. M. Lee, Dry sliding wear behavior of spray deposited AlCuMn alloy and AlCuMn/SiCp composite, Journal of Materials Science, 35 (**2000**), 4749–4762

[16] R. M. Mohanty, K. Balasubramanian, S. K. Seshadri, Boron carbide-reinforced alumnium 1100 matrix composites: fabrication and properties, Materials Science and Engineering A, 498 (**2008**), 42–52

[17] J. Oñoro, M. D. Salvador, L. E. G. Cambronero, High-temperature mechanical properties of aluminium alloys reinforced with boron carbide particles, Materials Science and Engineering A, 499 (**2009**), 421–426

[18] I. Kerti, F. Toptan, Micro structural variations in cast B4C-reinforced aluminium matrix composites (AMCs), Materials Letters, 62 (**2008**), 1215–1218

[19] U. B. Gopala Krishna, K. V. Sreenivas Rao, B. Vasudeva, Effect of boron carbide reinforcement on aluminium matrix composites, International Journal of Metallurgical & Materials Science and Engineering, 3 (**2013**), 41–48

[20] Y. Sahin, S. Murphy, The effect of sliding speed and microstructure on the dry wear properties of metal-matrix composites, Wear, 214 (**1998**), 98–106

[21] D. Poirier, R. A. L. Drew, M. L. Trudeau, R. Gauvin, Fabrication and properties of mechanically milled alumina/aluminum nanocomposites, Materials Science and Engineering A, 527 (**2010**), 7605–7614

[22] N. Hosseini, F. Karimzadeh, M. H. Abbasi, M. H. Enayati, Tribological properties of Al6061-Al_2O_3 nanocomposite prepared by milling and hot pressing, Mater. Des., 31 (**2010**), 4777–4785

[23] D. Cree, M. Pugh, Dry wear and friction properties of an A356/SiC foam interpenetrating phase composite, Wear, 272 (**2011**), 88–96

[24] M. Ramachandra, K. Radhakrishna, Effect of reinforcement of flyash on sliding wear, slurry erosive wear and corrosive behavior of aluminium matrix composite, Wear, 262 (**2007**), 1450–1462

[25] M. Jafari, M. H. Enayati, M. H. Abbasi, F. Karimzadeh, Compressive and wear behaviors of bulk nanostructured Al2024 alloy, Mater. Des., 31 (**2010**), 663–669

UDK 669.245:621.74.042:621.7.016.2
Original scientific article/Izvirni znanstveni članek

ISSN 1580-2949
MTAEC9, 49(1)15(2015)

INFLUENCE OF THE HIP PROCESS ON THE PROPERTIES OF AS-CAST Ni-BASED ALLOYS

VPLIV VROČEGA IZOSTATSKEGA STISKANJA NA LASTNOSTI Ni-ZLITIN Z LITO STRUKTURO

Jitka Malcharcziková[1], Martin Pohludka[1], Vít Michenka[2], Tomáš Čegan[1], Jan Juřica[1], Miroslav Kursa[1]
[1]VŠB-Technical University of Ostrava, Faculty of Metallurgy and Materials Engineering, Department of Non-Ferrous Metals, Refining Processes and Materials Recycling, Regional Materials Science and Technology Centre, 17. listopadu 15/2172, 708 33 Ostrava - Poruba, Czech Republic
[2]VÚHŽ a.s., Dobrá 240, 739 51 Dobrá, Czech Republic
jitka.malcharczikova@vsb.cz

Prejem rokopisa – received: 2013-09-30; sprejem za objavo – accepted for publication: 2014-01-30

The main goal of this work was to evaluate the application of the samples prepared by centrifugal casting as the test samples for a tensile test. Selected types of modified superalloys were prepared as experimental samples. The samples were molten by vacuum-induction melting and then cast centrifugally into a shaped graphite mould. The final castings had the shape corresponding approximately to the test specimens. Some of the samples were subjected to hot isostatic pressing (HIP). After HIP the castings contained substantially fewer casting defects. Selected mechanical properties were compared for the samples in the as-cast state and after HIP. For the majority of the investigated alloys the HIP process led to an increase in the strength and ductility.

Keywords: Ni-based alloys, centrifugal casting, hot isostatic pressing, mechanical properties

Glavni cilj tega dela je bila ocena uporabnosti vzorcev za natezni preizkus, izdelanih s centrifugalnim litjem. Preizkusni vzorci so bili izdelani iz izbrane vrste modificiranih superzlitin. Vzorci so bili staljeni v vakuumski indukcijski peči in centrifugalno uliti v izoblikovane grafitne forme. Ulitki so imeli obliko, ki ustreza vzorcem za natezne preizkuse. Del vzorcev je bil vroče izostatsko stisnjen (HIP). Ulitki so imeli po obdelavi HIP občutno manj livarskih napak. Izbrane mehanske lastnosti so bile primerjane pri vzorcih v litem stanju in po obdelavi HIP. Pri večini preiskovanih zlitin je obdelava HIP povzročila povečanje trdnosti in duktilnosti.

Ključne besede: Ni-zlitine, centrifugalno litje, vroče izostatsko stiskanje, mehanske lastnosti

1 INTRODUCTION

Ni-based alloys, including the alloys based on intermetallic compounds (IMC) and superalloys are still in the forefront of interest. These alloys that can be used even at high temperatures are continuously investigated thanks to their excellent mechanical and corrosion properties[1,2]. The technology of hot isostatic pressing (HIP) belongs, within the powder metallurgy, to the methods of hot sintering, during which the powder achieves the required properties as a result of the effect of predominantly physical processes. The HIP method is successfully used also for additional compacting of castings, ensuring a homogenisation of the structure and a reduction of the pores and shrinkage cavities. This method is used also for the alloys based on nickel and Ni_3Al. Numerous data were published on sintering powder-pressed pieces made of the materials based on Ni[3–6]. Kim[7] describes a procedure for additional compacting of the castings made of alloys IC396. Many problems occur when processing the samples with the usual production methods. The methodology for processing to the specified dimensions is highly demanding and expensive. A large amount of experimental material is damaged[8] and the testing of the mechanical properties of this type of material is, therefore, very difficult.

The most frequent use of hot isostatic pressing is a compaction of powder materials[4,9–12]. There are several papers dealing with the compaction of nickel-alloy castings with the HIP method[13–15]. Nickel-alloy castings consist of large and irregular grains of the γ' phase. This phase continues to coarse during the HIP process at a high temperature and pressure[4,9,12,15]. In some cases, carbides and the δ phase precipitate at the grain boundaries after a HIP process[11]. All of the above has a negative influence on the mechanical properties of nickel alloys. Therefore, after a HIP process, nickel alloys should be heat treated by solution annealing and aging[11,12].

2 EXPERIMENT

Selected types of modified superalloys IC50, IC396, IC221M and IC438 were prepared as the experimental samples. They were molten by vacuum-induction melting and then cast centrifugally into a shaped graphite mould (**Figure 1**). The final castings had the shape corresponding approximately to the test specimens

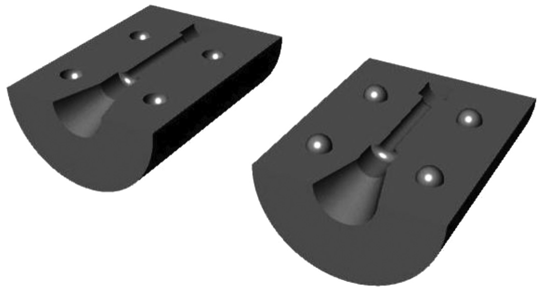

Figure 1: Graphite-mould drawing
Slika 1: Risba grafitne forme

(**Figure 2**). The compositions of the alloys were derived from the already verified and industrially used types of alloys for the given applications, and their compositions are presented in **Table 1** (A: the state after HIP, B: the as-cast state).

Table 1: Chemical composition of the used samples in mass fractions, *w*/%
Tabela 1: Kemijska sestava uporabljenih vzorcev v masnih deležih, *w*/%

Alloy	Sample	Amounts of elements					
		Al	Cr	Mo	Zr	B	Ni
IC50	3A, 3B	11.30	-	-	0.60	0.01	88.08
IC396	4A, 4B	7.98	7.72	3.02	0.85	0.01	80.42
IC221M	5A, 5B	8.00	7.70	1.43	1.70	0.01	81.10
IC438	6A, 6B	8.10	5.23	7.02	0.13	0.01	79.52

A flaw-detection method with X-ray radiation was used for determining the quality of the castings. The pattern of distribution and the type of casting defects were similar in all the centrifugally cast samples. **Figure 3** schematically shows their location and size. Defects occurred on the tapered part of the test piece (the tensile bar body), or in the direction towards the head, on the part of the casting without a riser.

2.1 Hot isostatic pressing (HIP)

It was established after a flaw-detection analysis, that the castings contained numerous casting defects. That is why some of the samples were subjected to hot isostatic pressing (HIP). The conditions for HIP were derived from the literature sources[3–7]. Hot isostatic pressing was performed on a press of the EPSI company. In the first stage of the additional compacting we chose a pressure of 100 MPa, the time of 4 h and a temperature of 1100 °C. Using flaw detection, we established that the castings subjected to HIP under the pressure of 100 MPa still contained a considerable amount of casting defects. For this reason we increased the pressure to 150 MPa for the HIP process, while the time of 4 h and the temperature of 1100 °C remained unchanged. However, even after applying a higher pressure the castings still contained casting defects, but to a much smaller extent than in the state just after centrifugal casting.

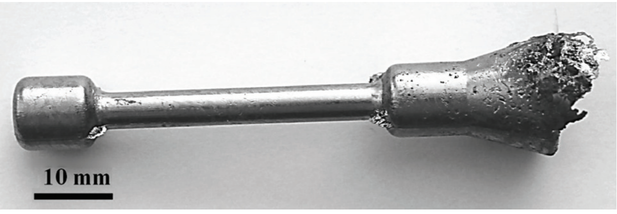

Figure 2: Sample after the casting
Slika 2: Vzorec po ulivanju

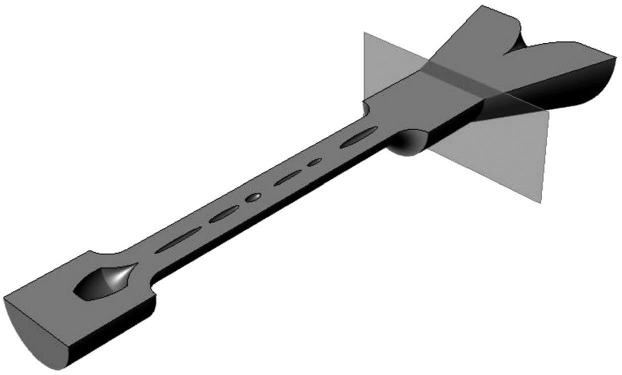

Figure 3: Scheme of casting defects
Slika 3: Shematski prikaz livarskih napak

Due to sufficient compaction, hot isostatic pressing can create a homogenous structure with a reduced number of pores and casting defects (shrinkage cavities and contractions) even in castings. This was confirmed in our case as well. After HIP, the castings contained substantially fewer casting defects.

2.2 Testing of the mechanical properties

Some of the samples in the as-cast state and the samples after HIP were ground to precise dimensions of the test piece and the tensile testing was performed. Short tensile bars with a length of 55 mm and a diameter of the central part of the bar of 5 mm were prepared by lathe turning. The strain rate was approximately $9.1 \cdot 10^{-4}$ s^{-1} for all the samples. **Table 2** gives the measured values of the tensile stress at yield, the ultimate engineering stress and the proportional elongation after braking. The table also contains the average values of the porosity and micro-hardness.

Table 2: Obtained mechanical characteristics
Tabela 2: Dobljene mehanske lastnosti

Sample No.	$R_{p0.2}$/ MPa	R_m/ MPa	A/ %	Porosity %	HV 0.05
3A	239	949	32	0.0309	302
3B	313	824	19	0.0393	249
4A	539	668	6	0.0123	353
4B	720	754	6	0.0743	336
5A	550	995	28	0.0486	354
5B	653	776	7	0.0496	324
6A	463	807	10	0.0589	359
6B	771	817	5	0.0614	351

3 DISCUSSION

We performed a comparison of the selected mechanical properties in the as-cast state and after HIP. In the majority of the investigated alloys the HIP process led to an increase in the determined strength and elongation. It is evident from the comparison of the values in **Table 2** that a significant enhancement of the mechanical properties after the HIP process occurred in samples 3 and 5, while no significant improvement of these values took place in samples 4 and 6. The R_{m} value of sample 4 does not correspond to the expected values. The casting probably contained a larger volume of casting defects before the HIP process. **Figure 4** shows the stress-strain curves for samples 3 and 5 in the as-cast state and after HIP. It may be concluded from the results that the process of additional compaction of the castings with the HIP method under the given conditions has a positive influence.

Figures 5 to **8** show the structures of samples 3 and 5 in the as-cast state and after HIP. The HIP process caused a coarsening of the grains as observed on **Figures 5** and **7**. This change in the structure was reflected by the changes in the yield strength. The value of the yield strength dropped for all the types of alloys (**Table 2, Figure 4**). The gained results were already confirmed in the conclusions of the papers of other authors[4–15]. According to these results every nickel alloy reacts differently to the HIP process. To avoid a decrease in the mechanical properties of the castings, their grains should be as small as possible and the microstructural changes

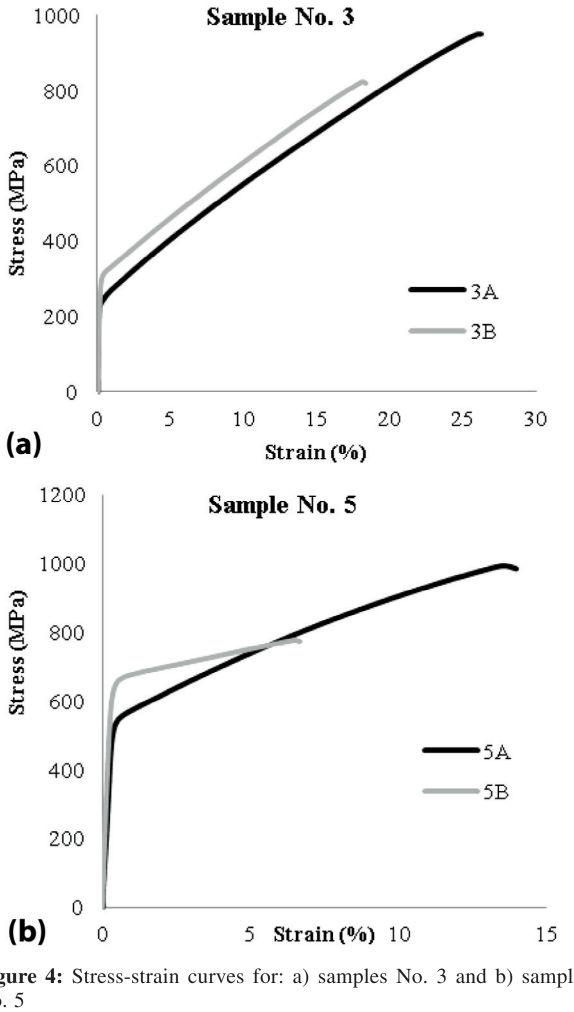

Figure 4: Stress-strain curves for: a) samples No. 3 and b) samples No. 5
Slika 4: Krivulje napetost – raztezek za: a) vzorca št. 3 in b) vzorca št. 5

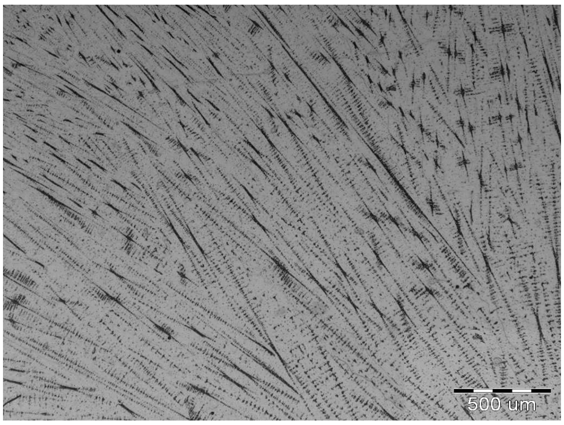

Figure 5: Microstructure of sample 3A
Slika 5: Mikrostruktura vzorca 3A

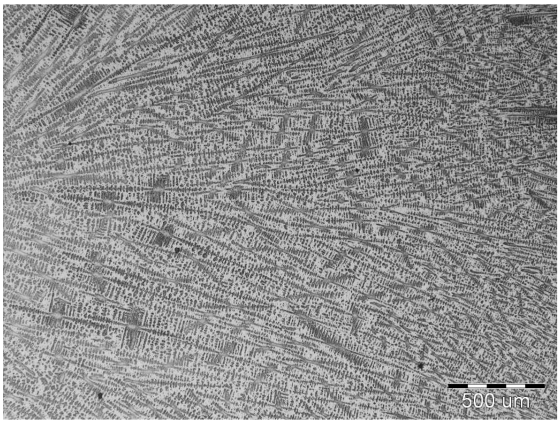

Figure 6: Microstructure of sample 3B
Slika 6: Mikrostruktura vzorca 3B

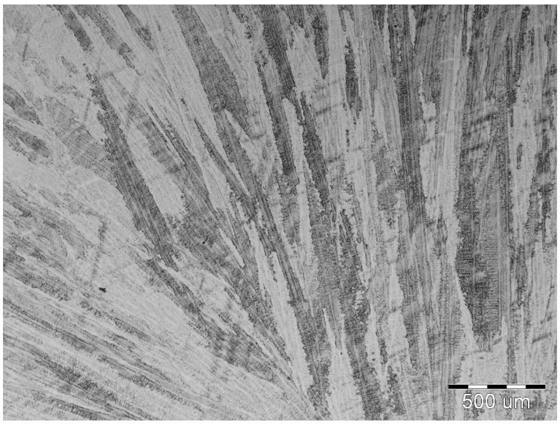

Figure 7: Microstructure of sample 5A
Slika 7: Mikrostruktura vzorca 5A

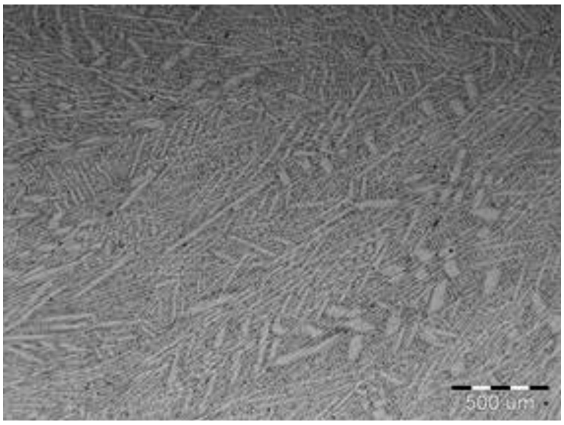

Figure 8: Microstructure of sample 5B
Slika 8: Mikrostruktura vzorca 5B

of these alloys should be studied during the HIP process. The porosity and micro-hardness are approximately the same for both the as-cast state and the HIP state. However, for all the experimental alloys the value of porosity decreased after the HIP process.

In practise it is possible to prepare the samples for evaluating the selected mechanical properties using the method of centrifugal casting of precision castings. The use of precision castings as the test specimens brings considerable savings of the materials and machining costs. The alloys of this type are used for high-temperature applications and a modification of the alloy composition is still performed[16].

4 CONCLUSIONS

Modified Ni superalloys were prepared as the experimental samples. The samples were molten by vacuum-induction melting and then cast centrifugally into a shaped graphite mould. The final castings had the shape corresponding to the test specimens. After a flaw-detection analysis, it was established that the castings contained numerous casting defects. As a result, some of the samples were subjected to hot isostatic pressing (HIP). Hot isostatic pressing reduced the number of the pores and casting defects in the castings. We performed a comparison of selected mechanical properties in the as-cast state and after HIP. For the majority of the investigated alloys, the HIP process led to an increase in the strength and ductility.

Acknowledgement

The presented results were obtained within research project TA 01011128 "Research and development of centrifugal casting technology of the Ni-based inter-metallic compounds" and project CZ.1.05/2.1.00/01.0040 "Regional materials science and technology centre".

5 REFERENCES

[1] A. Milosavljevic et al., The influence of the heat-treatment regime on a fracture surface of nickel-based supperalloys, Mater. Tehnol., 46 (**2012**) 4, 411–417

[2] M. Oruč et al., Alloys with modified characteristics, Mater. Tehnol., 45 (**2011**) 5, 483–487

[3] C. García et al., Improvement of the ductility of a bimodal micro-structured PM Ni3Al by thermal treatment, Materials Science and Engineering A, 303 (**2001**), 11–18

[4] J. G. Berriocanal et al., Microstructure and mechanical properties of Ni3Al base alloy reinforced with Cr particles produced by powder metallurgy, Intermetallics, 14 (**2006**), 456–463

[5] V. A. C. Haanappel et al., The cyclic oxidation behavior of PM Ni3Al in air at elevated temperatures: the effect of Cr- and Y-implantation, Intermetallics, 6 (**1998**), 347–356

[6] P. Pérez et al., Influence of the powder particle size on tensile properties of Ni_3Al processed by rapid solidification and hot isostatic pressing, Materials Science and Engineering A, 199 (**1995**), 211–218

[7] H. K. Kim et al., High temperature deformation and fracture mechanism in a dendritic Ni_3Al alloy, Acta Metallurgica et Materialia, 42 (**1994**), 679–687

[8] J. Malcharcziková et al., Non-alloyed Ni3Al based alloys – preparation and evaluation of mechanical properties, Metalurgija, 52 (**2013**), 309–312

[9] C. L. Qui et al., Influence of hot isostatic pressing temperature on microstructure and tensile properties of a nickel-based superalloy powder, Materials Science and Engineering A, 564 (**2013**), 176–185

[10] L. S. Ng et al., Cold-hot isostatic pressing of Mar M200 superalloy powder, Journal of Materials Processing Technology, 67 (**1997**), 143–149

[11] L. Chang et al., Effect of heat treatment on microstructure and mechanical properties of the hot-isostatic-pressed Inconel 718 powder compact, Journal of Alloys and Compounds, 590 (**2014**), 227–232

[12] C. Qiu et al., Influence of heat treatment on microstructure and tensile behaviour of a hot isostatically pressed nickel-based superalloy, Journal of Alloys and Compounds, 578 (**2013**), 454–464

[13] M. T. Kim et al., Effect of high pressure on the solid-liquid phase change of a nickel base superalloy during hot isostatic pressing, Journal of Alloys and Compounds, 477 (**2009**), 224–232

[14] M. T. Kim et al., Effect of γ' precipitation during hot isostatic pressing on the mechanical property of a nickel-based superalloy, Materials Science and Engineering A, 480 (**2008**), 218–225

[15] H. Y. Bor et al., Influence of isostatic pressing on the fracture transitions in the fine grain MAR-M247 superalloys, Materials Chemistry and Physics, 84 (**2004**), 284–290

[16] J. Malcharcziková et al., Evaluation of structure characteristics of centrifugally cast alloy based on Ni3Al, 21st International Conference on Metallurgy and Materials, Metal 2012, Brno, 2012, 1280–1287

UDK 669.14.018.8:621.793:620.193
Original scientific article/Izvirni znanstveni članek

ISSN 1580-2949
MTAEC9, 49(1)19(2015)

CORROSION OF CrN-COATED STAINLESS STEEL IN A NaCl SOLUTION (w = 3 %)

KOROZIJA NERJAVNEGA JEKLA S CrN-PREVLEKO V RAZTOPINI NaCl (w = 3 %)

Israfil Kucuk, Cevat Sarioglu

Marmara University, Dept. of Metallurgical and Materials Engineering, Göztepe kampusu, 34722 Kadiköy-Istanbul, Turkey
cevat.sarioglu@marmara.edu.tr

Prejem rokopisa – received: 2013-09-30; sprejem za objavo – accepted for publication: 2014-02-12

A CrN coating deposited by arc PVD was characterized by XRD and SEM. The in-situ measurement of the corrosion of the CrN-coated substrate was made by corrosion potential (Cor. Pot.), the polarization resistance (PR) method and electrochemical impedance spectroscopy (EIS) in a NaCl solution w = 3 % as a function of the immersion time (about 24 h). A semiconductor scale that formed on the CrN was identified by Mott-Shottky analysis as a p-type semiconductor with flat band potentials, 0.49 V (SCE). The CrN coating (0.5 µm thick) consisted of a mixture of cubic Cr and hexagonal Cr_2N phases exhibiting equiaxed grains and a dense coating with a small quantity of pinholes, voids and porosities. The "transition in corrosion resistance" for the CrN coatings at an early stage was found based on Cor. Pot., PR and EIS data. The CrN did not exhibit any pitting for about 24 h, while the corrosion resistance (R_p and R_{total}) decreased rapidly with time after 5 h of incubation. The transition from high resistance (3 MΩ cm^2) to low resistance (0.24 MΩ cm^2) was explained as a result of the penetration of the electrolyte through the Cr_2O_3 oxide layer to the Cr_2O_3/CrN interface. The resistance of the CrN against pitting corrosion was explained based on the blocking character of the equiaxed, dense, CrN coating against the penetration of the electrolyte.

Keywords: stainless steel, coating, CrN, EIS, polarization resistance, pitting corrosion

CrN-prevleka, nanesena z obločnim PVD-postopkom, je bila pregledana z XRD in SEM. In-situ merjenje korozije podlage s CrN-prevleko je bilo izvršeno z metodo korozijskega potenciala (Cor. Pot.), metodo polarizacijske upornosti (PR) in z elektrokemijsko impedančno spektroskopijo (EIS) v raztopini NaCl (w = 3 %) v odvisnosti od časa namakanja (okrog 24 h). Mott-Shottkyjeva analiza je odkrila nastanek p-vrste polprevodniške plasti s ploščinskim potencialom 0,49 V (SCE). CrN-prevleka (debela 0,5 µm) je sestavljena iz mešanice kubičnega Cr in heksagonalne faze Cr_2N ter ima enakoosna zrna, je gosta, z majhno količino luknjic, praznin in poroznostjo. Na podlagi podatkov Cor. Pot., PR in EIS je bil že v zgodnji fazi ugotovljen "prehod v obstojnost proti koroziji". CrN ni pokazal korozijskih jamic po 24 h, medtem ko se je korozijska upornost (R_p in R_{total}) hitro zmanjšala po 5 h inkubacijskega časa. Prehod iz velike upornosti (3 MΩ cm^2) v majhno (0,24 MΩ cm^2) se razlaga kot rezultat penetracije elektrolita skozi sloj oksida Cr_2O_3 na mejo Cr_2O_3/CrN. Odpornost CrN proti jamičasti koroziji je razložena z zadrževalnim značajem goste, enakoosne prevleke CrN za penetracijo elektrolita.

Ključne besede: nerjavno jeklo, prevleka, CrN, EIS, polarizacijska upornost, jamičasta korozija

1 INTRODUCTION

Hard ceramic coatings such as CrN have mainly been used for tribological applications (e.g., the injection molds for plastic and metals and forming dies).[1–4] CrN coatings possess excellent wear and oxidation resistance and low coefficients of friction. In addition, CrN has been used for decorative applications (particularly for replacing decorative electroplating chrome coatings).[5,6]

Besides the excellent mechanical properties and oxidation resistance, CrN coated on metallic substrates (steel and stainless steels) possesses significant corrosion resistance in saline solutions compared to other hard coatings such as TiN and TiAlN.[7–15] Even though the corrosion resistance of a CrN coating is superior to other coatings, the corrosion resistance of CrN-coated substrates degrades with time.[9,14,15] Generally, this degradation ends up with pitting corrosion by galvanic corrosion between the substrate and the coatings.[14,15] In the literature there has not been sufficient research into degradation and pitting-corrosion mechanisms and the relationships with microstructure.

Martensitic stainless steels (used in this work, EN 1.4034) generally used for blades in kitchen appliances, were coated for both decorative (chrome appearance) and wear-resistance requirements. The corrosion of the CrN coating deposited by arc PVD on a stainless-steel substrate was studied in detail with corrosion potential (Cor. Pot), polarization resistance (PR) and electrochemical impedance spectroscopy (EIS) techniques. The mechanism of corrosion was evaluated with respect to the microstructure of the CrN coating and EIS modelling.

2 EXPERIMENTAL PROCEDURES

The substrate material obtained from ThyssenKrupp was EN 1.4034 (X46Cr13) stainless steel. The composition analysed by optical emission spectroscopy (Q4 Tasman Bruker) was 0.40 C, 0. 44 Si, 0.53 Mn, 14.05 Cr and Fe (balance) (all in mass fractions, w/%). The 4034 stainless steel belonged to the martensitic group of stainless steels and was commercially available annealed and cold-rolled thin-plate form (1.5 mm thickness). The specimens were cut into widths 50 mm and lengths 100 mm. All the specimens were electropolished for 10 min in a solution containing 30 % H_2SO_4, 60 % H_3PO_4 and 10 % Neutral H_2O at 50 °C with a voltage of 10 V, and then ultrasonically cleaned at 60 °C, dumped in distilled water and dried with nitrogen in order to obtain a clean and smooth corrosion-resistant surface. The electropolished 4034 stainless-steel substrate is subsequently referred to as "substrate" in this paper.

The coating of the substrates was performed in an industrial-sized arc PVD coating chamber (AFS ltd. Cop., Turkey) equipped with six evaporators (cathodes) and rotating substrate holders. During the deposition, four round cathodes (opposing each other) were in use. An Ar glow discharge at a –600 V bias for 10 min was formed in the chamber in order to clean the surface of the substrates. The heating of the substrates was performed with Cr cathodes at about a –800 V bias for about 15 min until the starting temperature reached 350 °C. Then the electropolished specimens were coated with a Cr interlayer for 1 min to improve the adhesion of the coating and later with the CrN layer for 20 min at 1.1×10^{-3} mbar nitrogen pressure and a total pressure of 10^{-2} mbar with a bias voltage of –200 V. The final deposition temperature was 250 °C. The argon gas was purged into the chamber before opening the chamber door.

Electrochemical corrosion units used to perform the EIS, polarization resistance and Mott-Shottky scan were a Gamry PC14/750 Poteniostat/Galvanostat/ZRA System equipped with DC105 corrosion testing and an EIS300 A/C (10 mHz to 300 kHz). All the tests were performed in a NaCl 0.5 M (w = 3 %) aerated water solution at 25 °C using a three-electrode system (working (sample), auxiliary (graphite) and reference (standard calomel electrode (SCE)) using a Gamry paint cell unit. This Gamry Paint cell unit, presented in **Figure 1** and used for flat plate samples, consisted of a hollow glass cylinder (capacity 50 mL) mounted on a plate sample using a stainless-steel clamp with an O-ring. The exposed surface area of all the samples was kept at 15 cm^2, the maximum value without using a mask in order to incorporate a statistically significant number of defects in the CrN coatings. The computer-controlled automatic measurements (corrosion potential, polarization resistance and EIS) were carried out in the following order: 10 min cor. pot; 2.7 min PR; 5 min waiting period; and 8 min EIS meas. for each cycle 68 min during a total of about 24 h of exposure after the corrosion potential was stable. The amplitude of the AC voltage was selected to be 10 mV with respect to the corrosion potential in the EIS. During the polarization resistance scan the corrosion potential was changed by 20 mV with a 0.25 mV/s scan rate from the cathodic to the anodic polarization directions. Mott-Shottky analyses at a frequency of 1 Hz between +430 mV and –570 mV were performed on a CrN-coated substrate after the corrosion potential was stable.

A microstructural analysis of the uncoated and coated samples was performed before and after the corrosion using a scanning electron microscope (SEM, Jeol, JSM-5910LV) and energy-dispersive spectroscopy (EDS). The cross-section of the coatings was observed after fracture in liquid nitrogen. X-ray diffraction (Rigaku, D-MAX 2200, Cu K_α radiation) was used to identify the structure of the coatings deposited on the substrate.

3 RESULTS

3.1 Microstructural characterization of CrN coated substrate

The 4034 EP stainless-steel substrate possessed a ferritic structure (α-Fe) matrix (**Figure 2**) with a homogenous distribution of the carbide phases (Cr and C-rich phase identified by EDS). After coating with CrN at 1.1×10^{-3} mbar of N_2 partial pressure, the surface morphology of the CrN coatings reflected the morphology of

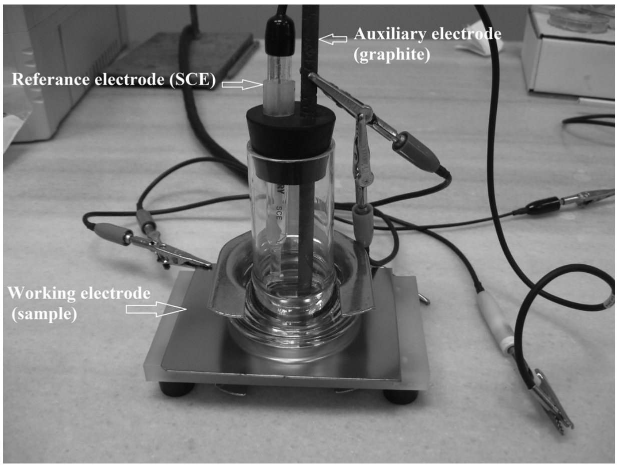

Figure 1: Gamry paint cell used in this work for electrochemical measurements

Slika 1: Elektrokemijske meritve so bile izvršene z Gamryjevo celico za preizkušanje barvnih premazov

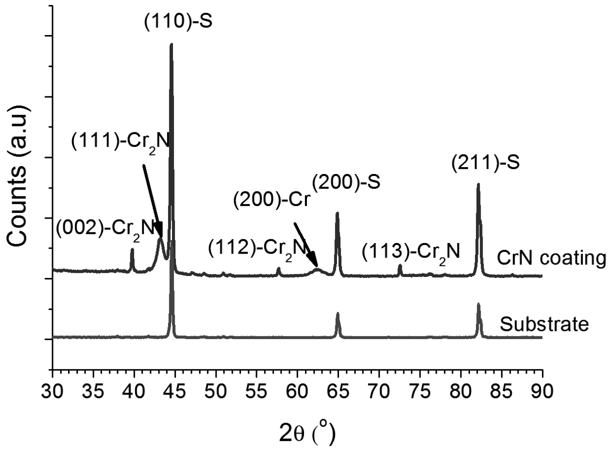

Figure 2: 2θ scan obtained from EP 4034 steel substrate and CrN-coated substrates using Bragg-Brentano symmetric X-ray diffraction

Slika 2: Posnetek 2θ z Bragg-Brentanovo simetrično rentgensko difrakcijo podlage iz jekla EP 4034 in iz podlage s prevleko CrN

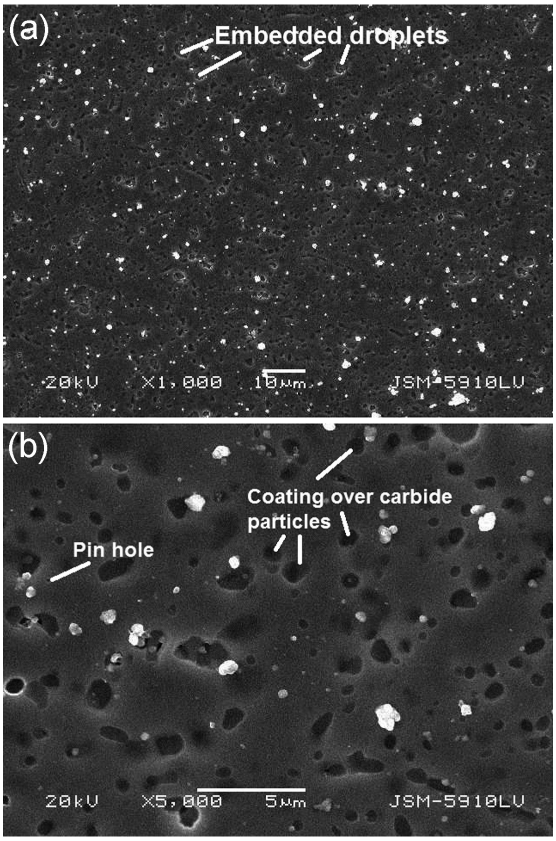

Figure 3: SEM (SEI) micrographs taken from the CrN coating surface at: a) low magnification and b) high magnification. The CrN coating deposited on the carbide phases was distinguished with a depression over the surface at a) and b) and was marked at b). Embedded droplets were marked at a). Bright particles on coating surface at a) and b) were un-embedded droplets (spherical particles).

Slika 3: SEM (SEI)-posnetka površine prevleke CrN pri: a) majhni povečavi in b) veliki povečavi. CrN-prevleke na karbidnih fazah so ločene s poglobitvijo na površini a) in b) in označene na b). Vgnezdene kapljice so označene na a). Svetli delci na površini prevleke a) in b) so nevgnezdene kapljice (sferični delci).

the EP substrate surface where etched carbide phases were covered by the CrN coating (**Figure 3**). The same observations were made for the cross-section micrographs of the CrN-coated substrates where the coatings formed on the carbide phases represented a hemispheric depression (**Figure 4**). Based on a detailed surface and cross-section investigation, it was found that the CrN coatings (**Figures 3** and **4**) exhibited a dense coating morphology (a small quantity of pinholes and porosities) with equiaxed grains (less than 100 nm grain size) and smooth coverage over the carbide precipitates and matrix. The thickness of the CrN coatings measured from the cross-section (**Figure 4**) was about 0.5 µm.

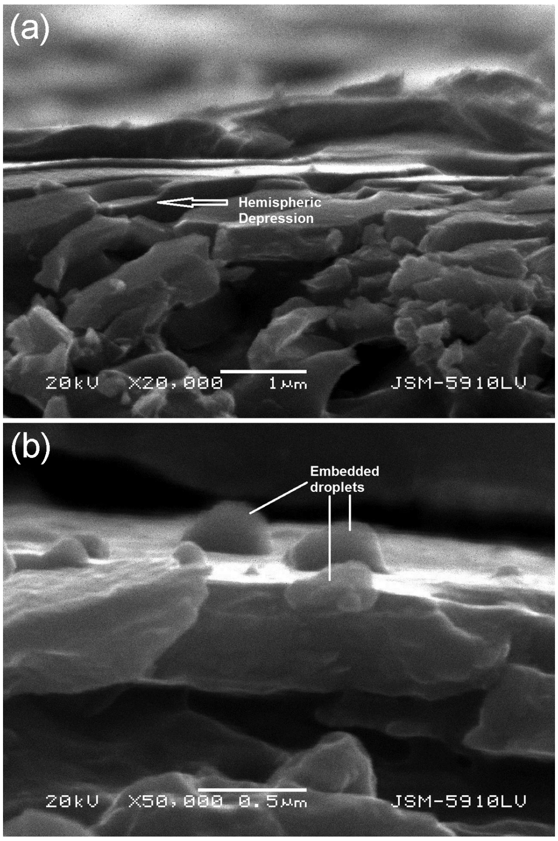

Figure 4: SEM (SEI) micrographs of fractured surface (in liquid nitrogen) of CrN coating from different areas a) and b). Equiaxed grains through the fractured coating were seen at high magnification b). Embedded particles were marked at b). Hemispheric depression in fractured coating was shown at a).

Slika 4: SEM (SEI)-posnetka površine preloma (v tekočem dušiku) CrN-prevleke z različnih področij a) in b). Pri veliki povečavi so vidna enakoosna zrna na prelomu prevleke. Vgnezdeni delci so označeni na b). Polkrožna poglobitev na prelomu prevleke je prikazana na a).

Due to the arc PVD process, droplets formed on the surface of the CrN-coated substrate. There were two different types of droplets found on the surface of the CrN coatings, the droplets embedded in the scale, the coating and the un-embedded macro-particles (spherical bright particles) (**Figures 3** and **4**). They were believed to deposit on the surface as a result of vapour-phase precipitation after the coating was finished (when a bias was interrupted). Both types of droplets analysed by EDS contained mainly Cr and N (Cr-rich particles). The CrN coating contained cubic Cr and hexagonal Cr_2N phases. The Cr peak exhibited line broadening and a shift in the line position of the (200) peak due to the dissolution of nitrogen in the Cr and a small crystallite size (**Figure 2**).

3.2 In-situ measurement of the corrosion of the CrN-coated substrate during 24 h of exposure with corrosion potentials, PR- and EIS-measurements

The corrosion potentials were plotted as a function of exposure time in **Figure 5**. The corrosion potential of the substrate (–468 mV (SCE) at 20 min) dropped rapidly and reached a steady-state value of –620 mV (SCE) within 180 min (3 h) (**Figure 5**). The corrosion potential of the CrN remained at around –150 mV (SCE) up to 267 min before decreasing to a level close to the substrate's potential value (**Figure 5**). At all times the corrosion potential of the substrate was lower compared to the

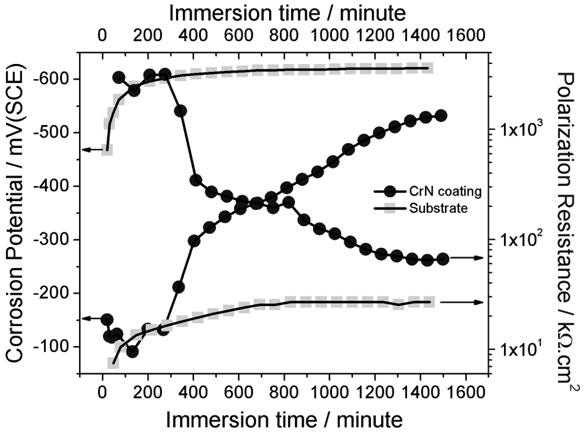

Figure 5: Corrosion potentials and polarization resistance (R_p) of the substrate and CrN-coated substrates determined from polarization resistance scan in NaCl (w = 3 %) solution as a function of immersion time

Slika 5: Korozijski potenciali in polarizacijska upornost (R_p) podlage in CrN-prevleke, določeni s posnetka polarizacijske upornosti v raztopini NaCl (w = 3 %) v odvisnosti od časa namakanja

CrN coating during about 24 h of exposure. The surface appearance of the uncoated substrate and the CrN-coated substrate did not vary during the 24 h of exposure.

The polarization-resistance values (R_p) were determined using the polarization resistance method and plotted (**Figure 5**). The polarization resistance (R_p) of the CrN coatings (**Figure 5**), deduced from the plots in **Figure 6**, remained at a high level of 3 MΩ cm^2 until 267 min and then rapidly decreased from 3 MΩ cm^2 to 0.24 MΩ cm^2 within the next 272 min. This decrease could be detected in the polarization plots (expansion of the *x*-axis) (**Figure 6**). After 1491 min the polarization resistance decreased to 66 kΩ cm^2. The plateau in the polarization resistance up to 267 min matched with the plateau in the corrosion potentials in the same exposure range (**Figure 5**). The polarization resistance (R_p) of the substrate increased up to 27 kΩ cm^2 with time (**Figure 5**). After about 24 h the R_p of the CrN coating was two times greater than the R_p of the substrate (**Figure 5**).

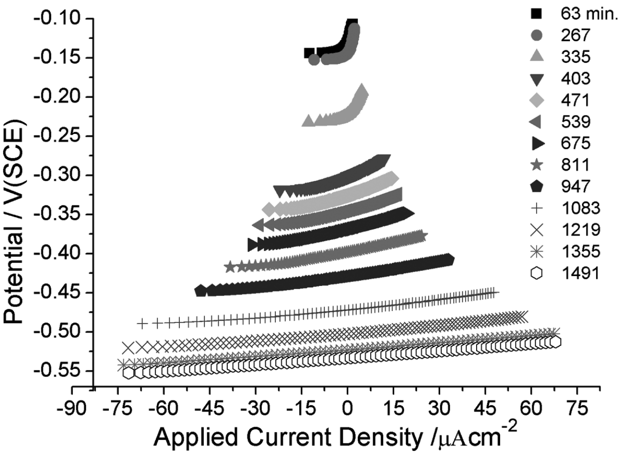

Figure 6: Polarization resistance scan of CrN coating in NaCl (w = 3 %) solution as a function of immersion time

Slika 6: Posnetek polarizacijske upornosti CrN-prevleke v raztopini NaCl (w = 3 %) v odvisnosti od časa namakanja

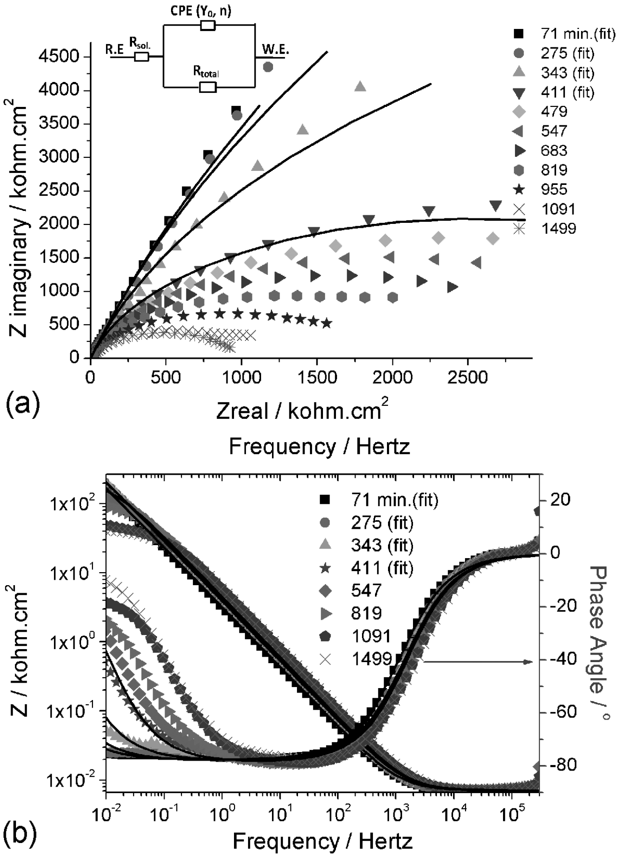

Figure 7: EIS data of CrN coating for selected immersion time: a) Nyquist plots and b) the Bode plots

Slika 7: EIS-podatki za CrN-prevleko pri izbranih časih namakanja: a) Nyquistov diagram in b) Bodejev diagram

The Bode and Nyquist plots of the CrN coatings from the EIS measurements are shown in **Figure 7**. At the beginning of the immersion in the salt solution, the Bode and Nyquist plots exhibited a strong capacitive behaviour. In the Bode plot (**Figure 7b**), the plateau in the phase shift (at about –80°) extended to the whole low-frequency region and the almost perpendicular line in the Nyquist plot indicated a strong imaginary part of the impedance (a strong capacitive character) (**Figure 7a**). Between 275 min and 411 min, the Bode and Nyquist plots changed noticeably, the plateau in the low-frequency region shrank and the Nyquist plot's shape changed from a line to an arch (**Figure 7a**). The evolution of the impedance spectrum coincided with the change in the corrosion potential (**Figure 5**) and the polarization resistance during the first 411 min of exposure in the salt solution (**Figures 5** and **6**). The one time constant clearly appeared in the Bode plot (**Figure 7b**). The imaginary impedance values decreased, resulting in the shrinkage of the arch in the Nyquist plot (**Figure 7a**). During 24 h of exposure to the salt solution there were no pits and no colour changes on the surface of the CrN coatings, while the impedance values continued to decrease (**Figure 7**).

3.3 The Mott-Shottky measurements

The Mott-Shottky measurements were made for the CrN coating and plotted in **Figure 8**. Before the Mott-Shottky measurement was made the corrosion potential was stable and the EIS data indicated a strong capacitive response at an early stage of the exposure (after 60 min). The plot for CrN (**Figure 8**) showed a linear part with a negative slope between 110 mV and 435 mV (SCE). The negative slope implied that there was a p-type semiconductor oxide layer on the CrN surface.

4 DISCUSSION

4.1 Structure of CrN coating

The CrN coating exhibited a mixture of two phases of Cr and Cr_2N in the N_2 partial pressure of 1.1×10^{-3} mbar (**Figure 2**). Significant peak broadening of the (200) plane and a shift in the peak position were observed for Cr. Similar results were found by Barata.[16] With increasing nitrogen content, Cr, Cr_2N, CrN and mixtures of these phases were obtained, based on reports in[16–21]. The Cr phase was soft, while the Cr_2N phase was hard.[16,18,22] The CrN coatings in this work exhibited significant ductility, as can be seen from the fractured cross-section (**Figure 4**). Droplets, considered as a preferential site for pitting in[8], were found on the CrN coating (**Figures 3** and **4**). The CrN coating exhibited a very dense and very smooth surface over the substrate, including etched carbide phases and droplets, resulting in less porosity and fewer pinholes. Thus, the CrN coating could effectively prevent the electrolyte from reaching the CrN coating/substrate interface directly.

The development of an equiaxed grain morphology (**Figure 4**) requires significant mobility of the adatoms during the growth of the coating according to the structure zone model (SZM).[8] The equiaxed grain morphology was observed for similar coating conditions in[6,14,15]. In addition, from the surface and cross-section micrographs (**Figures 3** and **4**) it was clear that the CrN coating was dense and provided smooth coverage over the etched carbide phases, indicating significant surface mobility of the adatoms. In the structure Zone Model, the T_S/T_M ratio, where T_S is the substrate deposition temperature (taken as an average of 300 °C) and T_M is the melting temperature of the coating, determines the morphology of coatings (equiaxed vs. columnar) together with the bias voltage and the total pressure.[3] As the ratio increases the coating morphology becomes more equiaxed due to an increase in the surface mobility.[3] When the melting point of the CrN coatings is taken as T_M (Cr) = 1907 °C [23] and T_M (Cr_2N) = 1500 °C [24], the ratio of T_S/T_M for CrN is in the range 0.26–0.32. For this ratio range we expected to observe significant surface mobility for the CrN coatings according to SZM[3], supporting the observation of equiaxed grains, and the denser and smoother coverage of the CrN coating.

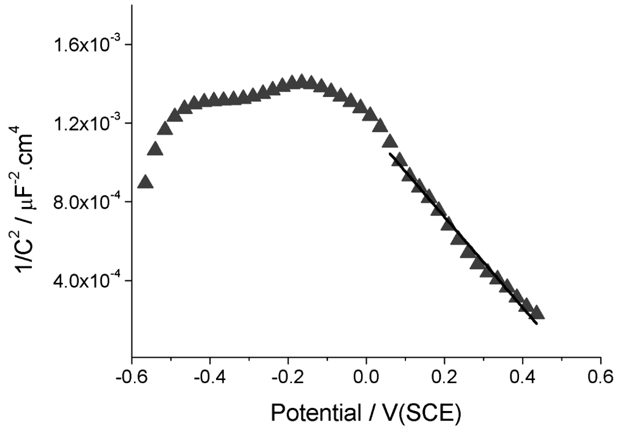

Figure 8: The Mott-Shottky measurements made for CrN coatings at frequency of 1 Hz in NaCl (w = 3 %) solution

Slika 8: Mott-Shottkyjeva meritev CrN-prevleke pri frekvenci 1 Hz v raztopini NaCl (w = 3 %)

4.2 Mott-Shottky analysis of CrN coatings

In the literature, the Mott-Shottky analysis has been used to characterize the semiconductor layer formed on the surface of the materials and coatings.[9,25–30] Based on **Figure 8**, it was concluded that the semiconductor layer formed on the CrN-coated substrate was p-type (presumably Cr_2O_3). In agreement with this result, Lavigne[31] and Mendibide[9] found p-type Cr_2O_3 on the CrN coating deposited by PVD on glass substrates.

The Mott-Shottky equation on page 127 in[25] was used to determine the flat band potential and the density of the charge (the density of acceptors for the p-type semiconductor) in the space-charge region. After taking the dielectric constant of the Cr_2O_3 as 30 (cited in[26] as ref. 17), the flat band potentials and the density of charges were determined from the linear portion of the plot in **Figure 8** using the equation in[25]. The density of acceptors in the space-charge region in the p-type Cr_2O_3 was 2.14×10^{25} cm^{-3}. Lavigne[31] obtained a density of the acceptors of 1.3×10^{20} cm^{-3} for the p-type oxide scale (mainly Cr_2O_3) formed on the CrN coating in a solution of Na_2SO_4 0.07 M and a small addition of H_2SO_4 with pH = 4. The Cr_2O_3 scales with the high charge densities ($10^{20–25}$ cm^{-3}) in the space-charge layer were considered as highly doped semiconductor layers.[25] The flat bond potentials indicated the position of the valance-band edge for the p-type Cr_2O_3 since the Fermi levels were generally close to the valance-band edge for the p-type.[25] The calculated flat band potentials from the intercept of the plots (**Figure 8**) was +0.49 V (SCE) for the p-type Cr_2O_3. The flat band potential reported for the oxide scale for a similar coating and nitrogen pressure by Lavigne[31] was in agreement with this result after considering the pH effect.

4.3 Corrosion of CrN-coated substrate and EIS modelling

Even though there was no colour change or pitting on the CrN-coated substrate during immersion, the transition in PR and EIS data (this transition was reproduced) from more resistance to less resistance at the early stage between 275 min and 411 min was found simultaneously using the EIS and PR measurements (**Figures 5** and **7**). The EIS data was modelled as a one-time constant (**Figure 7a**), the same as the EIS model for the substrate since there was no pitting corrosion and the EIS data exhibited one time constant (**Figure 7**). The total polarization resistance ($R_{\text{total}} = R_{\text{passive}} + R_{\text{pore}}$) included the resistance of the passive layer (R_{passive}) and the pore resistance (R_{pore}) to where the electrolyte gained access. The fitted EIS data are presented in **Figure 7** and **Table 1**. The $\chi 2$ values were in the range of $2–10 \times 10^{-3}$, while the n value was about 0.88 and remained constant with time. The polarization resistance (R_{p}) and the total resistance (R_{total}) determined from the EIS data were almost the same (**Figure 9**). The R_{total} values dropped rapidly from about 2.62 MΩ cm^2 levels to 0.33 MΩ cm^2 levels between 275 min and 411 min (in about 2 h) (**Figure 9**). In the same time interval, the admittance, Y_0 (**Figure 10** and **Table 1**), decreased from 34.6 µcm^{-2} s^{n} Ω to 29.7 µcm^{-2} s^{n} Ω by 14 %, indicating an increase in the capacitive behaviour of the passive layer (Cr_2O_3). The total resistance of the capacitive layer R_{total} and R_{p} continued to decrease gradually after 411 min until the end of the exposure (1499 min) to the level of 60 kΩ cm^2 without any observation of pitting on the CrN surface (**Figures 5** and **9**). The corrosion potential also followed the same trend with the EIS and PR results (**Figures 5** and **9**).

Table 1: The EIS fit parameters of the CrN coating from the electrical circuit model (EC model); Y_0, n, $R_{\text{sol.}}$ and R_{total} were determined by the best non-linear least-square fit with a goodness of the fit value ($\chi 2$)

Tabela 1: EIS-parametri CrN-prevleke iz modela električnega tokokroga (EC-model); Y_0, n, $R_{\text{sol.}}$ in R_{total} so bili določeni z najboljšim ujemanjem nelinearnih najmanjših kvadratov z vrednostjo ujemanja ($\chi 2$)

Immersion time (min)	R_{sol}/ (Ω cm^2)	R_{total}/ (kΩ cm^2)	Y_0/ (µcm^{-2} s^n Ω)	n	Goodness of Fit ($\chi 2 \times 10^{+3}$)
71	10.6	3457.5	42.8	0.86	2.143
275	10.6	2632.5	34.6	0.87	4.065
343	10.6	1054.5	33.1	0.87	4.014
411	10.6	340.5	29.7	0.88	3.299
819	10.7	195	24.6	0.88	2.72
1091	10.7	109.5	22.7	0.88	10.18
1499	10.6	63	23	0.88	2.237

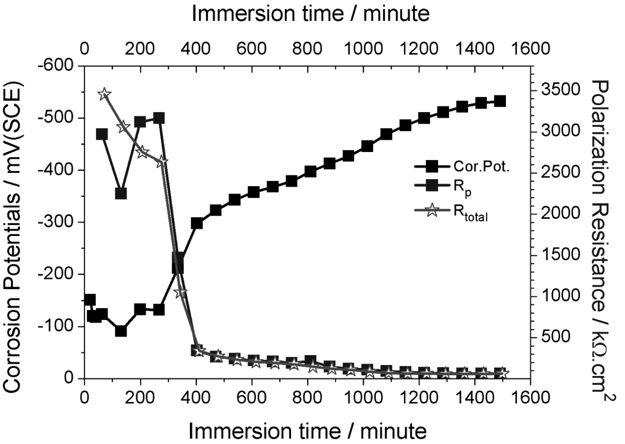

Figure 9: Corrosion potential (Cor. Pot.), polarization resistance (R_{p} and R_{total} calculated from EIS data) for the CrN coating in NaCl (w = 3 %) solution as a function of immersion time

Slika 9: Korozijski potencial (Cor. Pot.), polarizacijska upornost (R_{p} in R_{total}, izračunani iz podatkov EIS) CrN-prevleke v raztopini NaCl (w = 3 %) v odvisnosti od časa namakanja

It was believed that a rapid drop in the corrosion potential and the polarization resistance (R_{p} and R_{total}) of the passive oxide (Cr_2O_3) between 275 min and 411 min (in the transition period) (**Figure 9**) was due to penetration of the electrolyte into the CrN coating/Cr_2O_3 interface. Once the electrolyte reached this interface, the galvanic coupling between the passive layer (Cr_2O_3) and the bare mixture of the Cr and Cr_2N surfaces (CrN surface) proceeded and polarization on both areas (the cathodic polarization on the Cr_2O_3 scale, the anodic polarization on the bare CrN coatings) took place. The new corrosion potential established (more cathodic, more negative) as observed (**Figures 5** and **9**).

After 411 min, the polarization resistance (R_{p} and R_{total}) and the corrosion potential continued to drop gradually (**Figures 5** and **9**). This could be explained as follows. The anodic areas of the bare exposed surface in the CrN scale increased with the penetration of the electrolyte into the Cr_2O_3/CrN interface and towards the substrate/CrN coating interface through equiaxed grain boundaries, pinholes and embedded droplets. The increase in the anodic areas increased the anodic currents

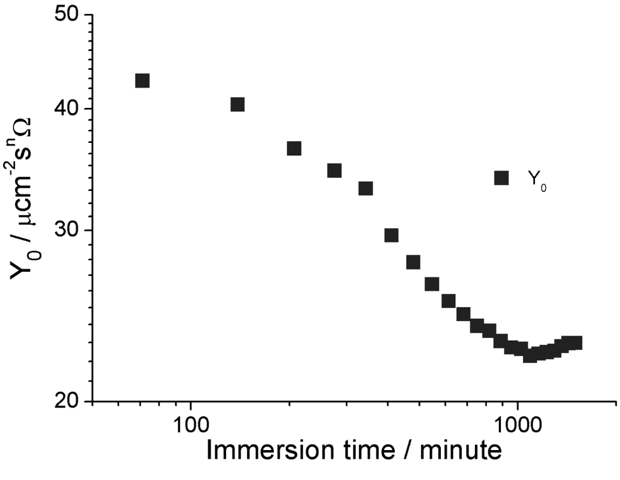

Figure 10: Admittance (Y_0) for the CrN coating in NaCl (w = 3 %) solution as a function of immersion time

Slika 10: Admitanca (Y_0) za CrN prevleko v raztopini NaCl (w = 3 %) v odvisnosti od časa namakanja and cathodic currents, resulting in a more cathodic polarization of the Cr_2O_3 surface as bare surfaces of CrN coating continued to be exposed to the electrolyte with the immersion time. As a result of this, the polarization resistance and corrosion potentials decreased, as was observed (**Figures 5** and **9**).

In aerated salt solution (w(NaCl) = 3 %) with pH = 8 and at the corrosion potential range (**Figure 5**), the Pourbaix diagram for the Cr indicated that the Cr could exhibit passivation and the anodic polarization of surface could result in passivation.[32] Mixture phases (Cr and Cr_2N) of the CrN coating were thought to behave in a similar way to the pure Cr phase when the surface was anodically polarized in the saline solution. In support of this, Lavigne[31] observed a passive layer on the Cr and Cr + Cr_2N coating in a pH = 4 solution. Passivation could continue with time until the substrate containing Fe is reached. The electrolyte was believed to not yet reach the substrate/CrN interface since no pit or Fe oxide residue (brownish colour residue) on the surface after 24 h was observed.

The Y_0 (measure of capacity) value decreased with time logarithmically up to 1091 min (**Figure 10**). The capacity (C) decreases either with a decrease in the dielectric constant of the Cr_2O_3 passive film and the area of the passive film or an increase in the thickness of the Cr_2O_3 oxide layer. Both the area of the passive layer could increase (as explained above) and the passive film of Cr_2O_3 on Cr or Cr_2N coating could grow in this solution of pH = 8 during immersion in a 3 NaCl (w = 3 %) solution.

The corrosion resistance of the CrN was greater than the substrate during about 24 h of exposure (**Figure 5**), indicating more resistance to the passive scale on the CrN-coated substrate in the NaCl (w = 3 %) solution. Also, the corrosion resistance of the CrN coating was more resistance than that of the TiN coating under similar deposition conditions.[33] Similar results were reported in the literature for different PVD processes and coating conditions.[8–15] There were two main differences in the microstructural morphologies between the TiN and CrN coatings for the same deposition condition.[14,15,33] First, the CrN exhibited equiaxed grains (**Figure 4**), while the TiN coating was columnar. Second, the CrN coating was denser (contained a smaller quantity of pinholes and fewer porosities) compared to the TiN coating. The CrN coatings with equiaxed grains were believed to suppress the time for the electrolyte to reach the substrate interface by increasing the diffusion length (more grain boundaries) (**Figure 4**).[14,15] In addition to this, with denser and better coverage of the CrN coatings over the substrate, it resisted more against the penetration of the electrolyte, delaying the pitting corrosion (**Figures 3** and **4**). On the other hand, the TiN coating with columnar grain boundaries extending from the surface to the substrate interface and containing more porosity (pinholes, voids, cracks and less coverage) allowed the electrolyte to reach the interface easily. As a result of this, the pitting formation and growth as captured by the PR and EIS measurements took place on the TiN coating as quickly as after 1 h. In conclusion, the blocking character of the coating against the penetration of the electrolyte driven by galvanic corrosion was found to be the predominant factor in the corrosion of CrN and TiN.

5 CONCLUSIONS

1. The corrosion of CrN is directly related to the coating defects and coating structure. The CrN coating deposited on the substrate consisted of a mixture of cubic Cr and hexagonal Cr_2N and a passive p-type oxide (presumably Cr_2O_3) film, determined by Mott-Shottky analysis. The CrN coating consisted of equiaxed grains and a smooth coverage over the substrate surface, resulting in a dense coating morphology with a small quantity of pin holes and porosities.
2. The CrN did not exhibit any pitting for about 24 h, while the corrosion resistance (R_p and R_{total}) decreased rapidly with time after 5 h of incubation time. Based on the PR and EIS results, the transition from high resistance (3 MΩ cm^2) to low resistance (0.24 MΩ cm^2) was explained as a result of the penetration of the electrolyte through the Cr_2O_3 oxide layer to the Cr_2O_3/CrN interface.
3. The corrosion resistance (R_p and R_{total}) of CrN was greater than that of the TiN and the substrate during about 24 h of immersion in NaCl (w = 3 %) solution. The cause of the greater corrosion resistance of the CrN was explained on the basis of the greater blocking character of the equiaxed, dense, CrN coating against the penetration of the electrolyte through the coatings compared to the columnar, porous, TiN coating.

Acknowledgement

Marmara University is greatly acknowledged for financial support through the Contract (No: FEN-KPS-080808-0178).

6 REFERENCES

[1] B. Warchholinski, A. Gilewicz, Surface Engineering, 27 (**2011**) 7, 491–497

[2] E. Lugscheider, K. Bobzin, Th. Horning, M. Macs, Thin Solid Films, 420–421 (**2002**), 318–323

[3] C. Ducros, V. Benevent, F. Sanchette, Surface and Coatings Technology, 163–164 (**2003**), 681–688

[4] L. Hultman, J. E. Sundgren, Structure/property relationships for hard coatings, In: R. F. Bunshah (ed.), Handbook of Hard Coatings, William Andrew Publishing, New York 2001, 108–180

[5] B. Navinsek, P. Panjan, I. Milosev, Surf. Cot. Tech., 116–119 (**1999**), 476–487

[6] A. Hurkmans, D. B. Lewis, W. D. Munz, Surface Engineering, 19 (**2003**) 3, 205–210

[7] H. A. Jehn, Surface and Coatings Technology, 125 (**2000**), 212–217

[8] M. Fenker, M. Balzer, H. Kappl, Thin Solid Films, 515 (**2006**) 1, 27–32
[9] C. Mendibide, P. Steyer, J. P. Millet, Surface and Coatings Technology, 200 (**2005**), 109–112
[10] M. Urgen, A. F. Cakir, Surface and Coatings Technology, 96 (**1997**), 236–244
[11] M. A. M. Ibrahim, S. F. Korablov, M. Yoshimura, Corrosion Science, 44 (**2002**), 815–828
[12] V. K. William Grips, H. C. Barshilia, V. Ezhil Selvi, Kalavati, K. S. Rajam, Thin Solid Films, 514 (**2006**), 204–211
[13] L. Cunha, M. Andritschky, L. Rebouta, R. Silva, Thin Solid Films, 317 (**1998**), 351–355
[14] C. Liu, Q. Bi, A. Leyland, A. Matthews, Corrosion Science, 45 (**2003**), 1243–1256
[15] C. Liu, Q. Bi, A. Leyland, A. Matthews, Corrosion Science, 45 (**2003**), 1257–1273
[16] A. Barata, L. Cunha, C. Moura, Thin Solid Films, 398–399 (**2001**), 501–506
[17] E. Forniés, R. Escobar Galindo, O. Sánchez, J. M. Albella, Surface and Coatings Technology, 200 (**2006**), 6047–6053
[18] S. K. Pradhan, C. Nouveau, T. A. Vasin, M. A. Djouadi, Surface and Coatings Technology, 200 (**2005**), 141–145
[19] Z. B. Zhaoa, Z. U. Rekb, S. M. Yalisovec, J. C. Bilell, Surface and Coatings Technology, 185 (**2004**), 329–339
[20] B. C. Ruden, E. Restrepo-Parra, A. U. Paladines, F. Sequeda, Applied Surface Science, 270 (**2013**), 150–156
[21] P. Hones, R. Sanjines, F. Levy, Surface and Coatings Technology, 91–95 (**1997**), 398–402
[22] P. Engel, G. Schwarz, G. K. Wolf, Surface and Coatings Technology, 98 (**1998**), 1002–1007
[23] R. T. DeHoff, Thermodynamics in materials science, McGraw-Hill, Inc., 1993
[24] W. Kim, C. Y. Suh, K. M. Roh, J. W. Lim, S. L. Du, I. J. Shan, Materials Transactions, 53 (**2012**) 8, 1543–1546
[25] S. Roy Morrison, Electrochemistry at Semiconductor and Oxidized Metal Electrodes, Plenum Press, New York 1980
[26] S. Rudenja, C. Leygraf, J. Pan, P. Kulu, E. Talimets, V. Mikli, Surface and Coatings Technology, 114 (**1999**), 129–136
[27] J. Wielant, V. Goossens, R. Hausbrand, H. Terryn, Electrochimca Acta, 52 (**2007**), 7617–7625
[28] K. S. Raja, D. A. Jones, Corrosion Science, 48 (**2006**), 1623–1638
[29] N. E. Hakiki, M. F. Montemor, M. G. S. Ferreira, M. da Cunha Belo, Corrosion Science, 42 (**2000**), 687–702
[30] G. Goodlet, S. Faty, S. Cardoso, P. P. Freitas, A. M. P. Simoes, M. G. S. Ferreira, M. Da Cunha Belo, Corrosion Science, 46 (**2004**), 1479–1499
[31] O. Lavigne, C. Alemany-Dumont, B. Normand, M. H. Berger, C. Duhamel, P. Dekichere, Corrosion Science, 53 (**2011**), 2087–2096
[32] D. A. Jones, Principles and Prevention of Corrosion, Prentice hall, Inc., 1992
[33] I. Kucuk, Corrosion of hard ceramic (TiN, CrN) coatings deposited on stainless steels, Master Thesis, Sakarya University, Turkey, 2009

UDK 669.017.12:621.74.046:66.046.51
Original scientific article/Izvirni znanstveni članek

ISSN 1580-2949
MTAEC9, 49(1)27(2015)

PREPARATION AND PROPERTIES OF MASTER ALLOYS Nb-Al AND Ta-Al FOR MELTING AND CASTING OF γ-TiAl INTERMETALLICS

PRIPRAVA IN LASTNOSTI PREDZLITIN Nb-Al IN Ta-Al ZA TALJENJE IN ULIVANJE INTERMETALNIH ZLITIN γ-TiAl

Jan Jurica, Tomáš Čegan, Kateřina Skotnicová, Daniel Petlák, Bedřich Smetana, Vlastimil Matějka

VŠB – Technical University of Ostrava, Faculty of Metallurgy and Materials Engineering, Department of RMSTC, 17. listopadu 15,
70833 Ostrava-Poruba, Czech Republic
jan.jurica@vsb.cz

Prejem rokopisa – received: 2013-09-30; sprejem za objavo – accepted for publication: 2014-03-10

The advantages of gamma TiAl-based alloys including their specific modulus, specific high-temperature strength and oxidation resistance make them attractive candidates as high-temperature structural materials in the automotive, aerospace and power industries. Currently most attention is paid to the alloys of the third and fourth generations. However, this type of alloys contains relatively high amounts of refractory metals such as Nb and Ta. The high melting points of these metals (2477 and 3017) °C are problematic for the preparation of these products with the conventional casting, because it is necessary to use higher temperatures and thus, generally, longer total melting times. This may result in increased oxygen amounts in the products and in decreased mechanical properties. The use of Nb-Al and Ta-Al master alloys for the preparation of the resulting Ti-Al-Nb and Ti-Al-Ta alloys is highly suitable because of the reduction in the temperature during melting.

This article describes the preparation of selected master alloys Nb-60Al and Ta-80Al (x/%) with the melting points of about 1600–1650 °C using plasma melting. The optimum conditions for the preparation of these master alloys (current density, feed speed, distribution and size of charge) were characterised in order to maximise the purity and homogeneity. The prepared alloys were studied with light microscopy (LM), backscattered scanning electron microscopy (BSE), energy-dispersive spectrometry (EDS), and the melting temperature was evaluated with a differential thermal analysis (DTA).

Keywords: intermetallics, plasma melting, microstructure, differential thermal analysis (DTA)

Prednost zlitin na osnovi gama Ti-Al je v specifičnem modulu, specifični visokotemperaturni trdnosti in odpornosti proti oksidaciji, kar jih dela zanimive za izdelavo visokotemperaturnih komponent v avtomobilski industriji, letalstvu in energetiki. Sedaj se največ pozornosti namenja zlitinam tretje ali četrte generacije. Ta vrsta zlitin vsebuje relativno veliko količino ognjevarnih kovin, kot sta Nb in Ta. Visoko tališče teh materialov (2477 in 3017) °C otežuje izdelavo teh zlitin s klasičnim ulivanjem, ker je treba uporabiti višje temperature in s tem daljše čase taljenja. To lahko povzroči povečanje vsebnosti kisika v proizvodih in poslabšanje mehanskih lastnosti. Uporaba predzlitin Nb-Al in Ta-Al za izdelavo zlitin Ti-Al-Nb in Ti-Al-Ta je zelo primerna zaradi znižanja temperature pri taljenju.

Članek opisuje pripravo izbranih predzlitin Nb-60Al in Ta-80Al (x/%) s tališčem okrog 1600–1650 °C s taljenjem v plazmi. Za maksimiranje čistosti in homogenosti so bili določeni optimalni pogoji za pripravo teh predzlitin (gostota, hitrost dodajanja, razporeditev in velikost zatehte). Pripravljene zlitine so bile preiskane s svetlobno mikroskopijo (LM), vrstično elektronsko mikroskopijo s povratno sipanimi elektroni (BSE), energijsko disperzijsko spektroskopijo (EDS), temperatura taljenja pa je bila določena z diferenčno termično analizo (DTA).

Ključne besede: intermetalne zlitine, taljenje s plazmo, mikrostruktura, diferenčna termična analiza (DTA)

1 INTRODUCTION

The binary diagrams shown in **Figures 1a** and **1b** demonstrate the objective of this experiment, e.i., how to transform refractory Ta or Nb into the master alloys, suitable for the preparation of the γ-TiAl intermetallics of the third or fourth generations that usually contain 5–10 % of these metals[1–4]. Suitable master alloys should have the melting temperature of approximately 1600 °C, high purity and low amount of interstitial elements, particularly oxygen. The chosen chemical compositions of the master alloys were Nb-60Al and Ta-80Al (amount-of-substance fractions, x/%). As it can be seen in the binary diagrams, the master alloys with these compositions are characterised by both an acceptable melting temperature and a chemical composition that can be considered as suitable for the preparation of the γ-TiAl alloys with respect to an easy preparation of the charges.

2 EXPERIMENTAL WORK

For the preparation of the Al-Nb and Al-Ta alloys we used the possibility of re-melting in a plasma furnace with a horizontal mould. The charge consisted of a lump material including pure metals in the form of plates, wires and rods. The charge was uniformly distributed in a water-cooled copper mould placed in the furnace. The melting was performed using a quadruple passage through the zone (twice on each side) for the Nb-60Al alloy and a sextuple passage through the zone (three times on each side) for the Ta-80Al alloy. An inert

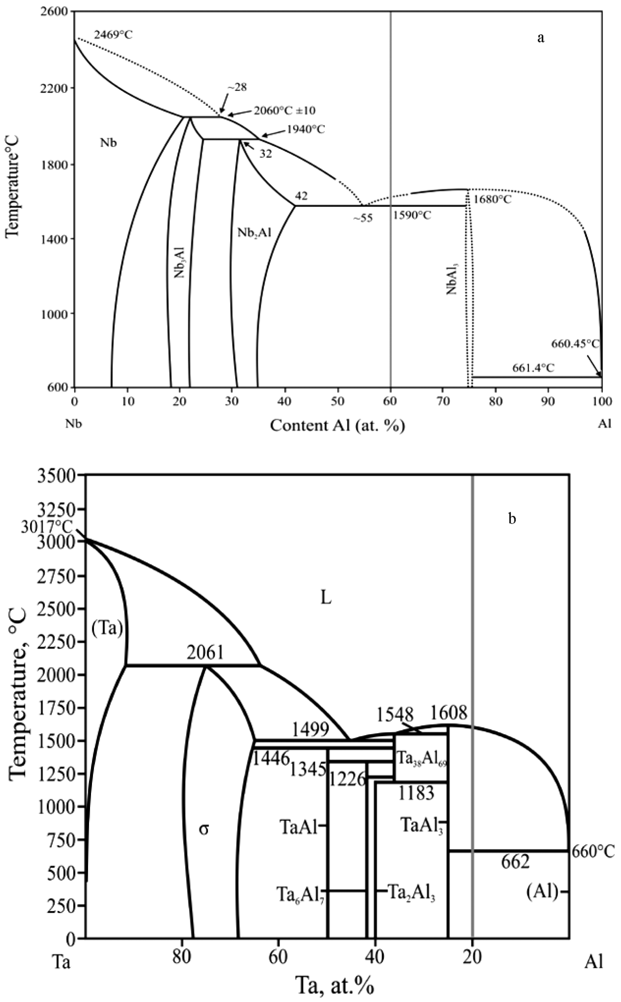

Figure 1: Binary-phase diagrams for: a) Nb-Al and b) Ta-Al with indicated chemical compositions[3,4]

Slika 1: Binarna fazna diagrama: a) Nb-Al in b) Ta-Al z označeno kemijsko sestavo[3,4]

atmosphere was ensured during the melting using an argon flow with a flow rate of 27 L/min through the furnace chamber. The rate of shift of the mould was 0.5 cm/min and the current intensity was up to 800 A.

The samples for metallographic observations were prepared with the standard metallographic method including the initial grinding on the sandpapers with the granularities from 60 to 2000, and polishing with an Al_2O_3 suspension with the particles of the sizes from 1 µm to 0.3 µm. For the observation of the microstructure and the analysis of the chemical composition we used a scanning electron microscope QUANTA FEG 450 equipped with an EDAX APOLLO X probe. The samples for the X-ray diffraction analysis were prepared by cutting them in an electro-spark cutter. X-ray diffraction patterns were obtained with a diffractometer Bruker D8 Advance equipped with a detector VÅNTEC 1. The measurements were performed in the reflection mode. The phase composition was evaluated using the PDF-2 2004 database from the International Centre for Diffraction Data. The oxygen amount was measured with the thermo-evolution method using an ELTRA ONH–2000 instrument. For the measurement we always used at least three pieces from each sample. The DTA analysis was performed with the experimental equipment Setaram SetSys 1750. The samples with the dimensions of 3 mm × 3 mm × 3 mm, prepared by electro-spark cutting and by wet grinding them on the sandpaper with a granularity of 600 were analysed in corundum crucibles with an internal coating of Y_2O_3 at a heating rate of 10 °C/min and in an atmosphere of argon with the purity of 6 N.

3 RESULTS AND DISCUSSION

Table 1 shows the chemical compositions, determined with the EDS method, of individual sections of the prepared ingots of the master alloys. The sections were always taken from the front and rear parts of an ingot. It was established that a slight loss of mass occurred during the melting, which was probably a result of the evaporation of the Al part, due to the high temperature of the melt (the melting point of Ta is 3017 °C, the evaporation temperature of Al is 2519 °C). A similar phenomenon was also observed during the melting of alloy Ti46Al8Ta[5] and during the melting of γ-TiAl intermetallics in ceramic crucibles[6]. This loss of mass was approximately 1 g for alloys NbAl-1 and NbAl-2, and 2 g for alloy TaAl-1. The loss of mass was probably a result of the evaporation of the Al part due to a very high temperature of the melt. A higher loss of mass in the case of master alloy TaAl-1 also corresponds with it, since higher outputs were used. The following charges were, therefore, modified. This modification consisted of an increase in the Al amount by 1 g for the charge of master alloy NbAl-3, and by 2 g for the charges of the TaAl-2 and TaAl-3 master alloys. It follows from **Table 1** that in the cases of the master alloys whose Al amounts in the charges were not increased, the Al amounts decreased. For the master alloys, whose charges were thus increased, the decrease of Al was lower. This confirms the fact that a loss of mass after melting was caused by the evaporation of the Al part. Nevertheless, for all the master alloys, with the exception of the TaAl-3 master alloy, the determined amount of Al was lower than for the nominal composition. The determined values

Table 1: Al amounts in different parts of the ingots detected with EDS

Tabela 1: Vsebnost Al v različnih delih ingota, določena z EDS

Alloy	The nominal composition (x/%)	EDS-measured composition (x/%)	
		Front part	Rear part
NbAl-1	Nb-60Al	56.82 ± 0.58	58.41 ± 0.24
NbAl-2	Nb-60Al	57.93 ± 0.46	59.46 ± 0.12
NbAl-3	Nb-60Al	58.98 ± 0.51	59.73 ± 0.39
TaAl-1	Ta-80Al	76.79 ± 3.00	78.43 ± 3.86
TaAl-2	Ta-80Al	78.87 ± 2.98	79.23 ± 3.02
TaAl-3	Ta-80Al	79.01 ± 4.01	81.72 ± 3.28

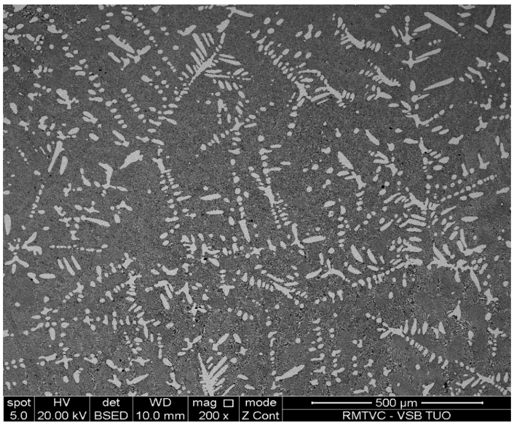

Figure 2: Microstructure of master alloy NbAl-2
Slika 2: Mikrostruktura predzlitine NbAl-2

of chemical compositions also manifest substantial differences between individual parts of an ingot. This can be explained with a slow shift of the mould and a segregation of Al. However, a non-homogenous distribution of the elements in the ingots of the master alloys does not represent the principal problem, since we always used whole ingots for the preparation of the TiAlNb and TiAlTa alloys. The determined amounts of oxygen in the prepared master alloys were very low, (29 ± 2) μg/g for the Nb-60Al master alloy and (123 ± 21) μg/g for the Ta-80Al master alloy.

The microstructures of the Nb-60Al master alloys are shown in **Figures 2** and **3**. In principle, these microstructures correspond to the binary diagram (**Figure 1a**) consisting of Nb_2Al dendrites, presented as light areas, and a regular eutectic consisting of Nb_2Al and $NbAl_3$ phases. The $NbAl_3$ phase is presented, in the micrographs below, as darker areas. The average amounts of the elements in individual phases or areas, calculated from the measured chemical composition according to EDS, are presented in **Table 2**.

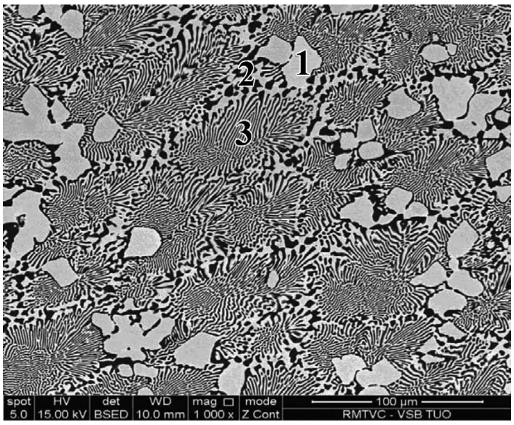

Figure 3: Microstructure of master alloy NbAl-1
Slika 3: Mikrostruktura predzlitine NbAl-1

Table 2: Al amounts measured in individual structural fields shown in **Figure 3**
Tabela 2: Vsebnost Al, izmerjena na posameznih področjih strukture, prikazanih na **sliki 3**

	Al amount by EDS (x/%)		
Ingot	Nb_2Al (1)	$NbAl_3$ (2)	Eutectic (3)
NbAl-1	46.80 ± 0.33	71.68 ± 1.34	59.66 ± 0.50
NbAl-2	46.48 ± 0.15	76.05 ± 0.41	60.62 ± 0.22
NbAl-3	46.39 ± 0.11	75.58 ± 0.39	60.88 ± 0.34

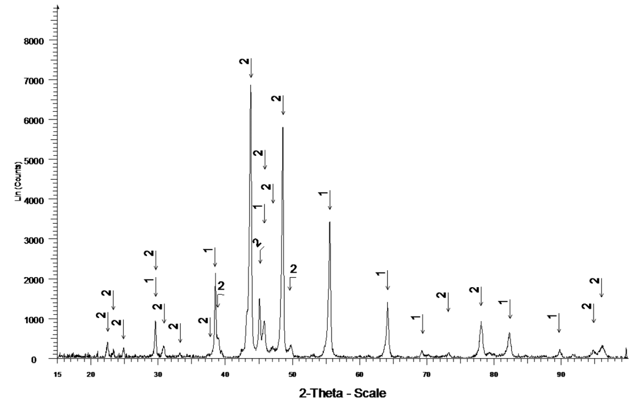

Figure 4: Diffraction pattern of NbAl-2 master alloys: 1-$NbAl_3$, 2-σ Nb_2Al
Slika 4: Uklonska slika predzlitin NbAl-2: 1-$NbAl_3$, 2-σ Nb_2Al

The occurrence of the Nb_2Al and $NbAl_3$ phases was also confirmed with the X-ray diffraction pattern shown in **Figure 4**.

Figures 5 and **6** show BSE images of the microstructure of the TaAl-2 master alloy. The microstructures of all the prepared master alloys were dendritic, not showing any significant changes between individual ingots and parts of the ingots. The established chemical composition of dendrites and interdendritic areas is presented in **Table 3**. According to the binary diagram of the Ta-Al binary system (**Figure 1b**), the chemical composition of dendrites corresponds to the $TaAl_3$ phase, and the chemical composition of interdendritic areas corresponds to the solid solution of Ta and Al. The occurrence of these two phases was also confirmed with the X-ray diffraction analysis (**Figure 7**).

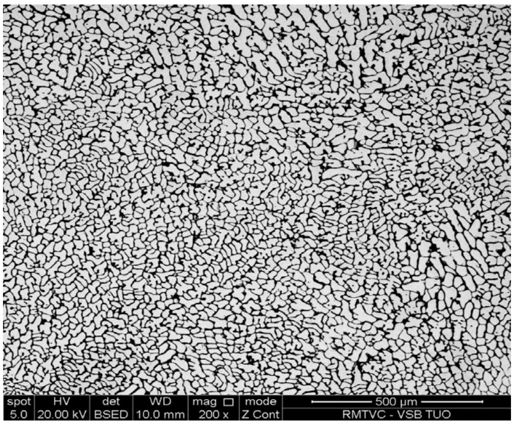

Figure 5: Microstructure of master alloy TaAl-2
Slika 5: Mikrostruktura predzlitine TaAl-2

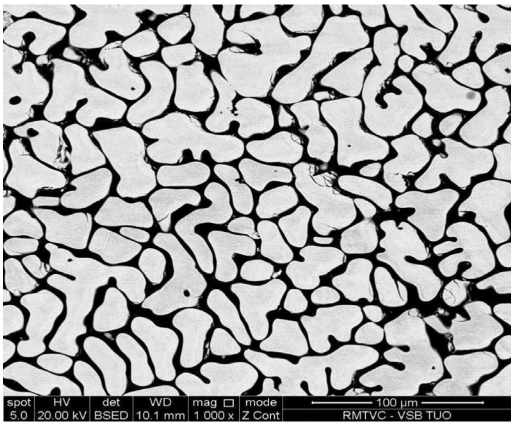

Figure 6: Microstructure of master alloy TaAl-3
Slika 6: Mikrostruktura predzlitine TaAl-3

Table 3: Al amounts measured in individual structural fields shown in **Figure 6**
Tabela 3: Vsebnost Al, izmerjena na posameznih področjih strukture, prikazanih na **sliki 6**

Al amount by EDS (x/%)		
Ingot	Dendrites	Interdendritic space
TaAl-1	75.08 ± 0.19	99.73 ± 0.13
TaAl-2	75.18 ± 0.27	99.56 ± 0.35
TaAl-3	75.15 ± 0.21	99.71 ± 0.28

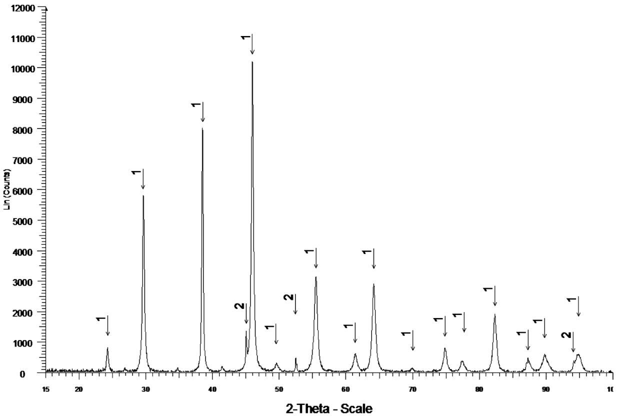

Figure 7: Diffraction pattern of TaAl-2 master alloys: 1-$TaAl_3$, 2-Al
Slika 7: Uklonska slika predzlitin TaAl-2: 1-$TaAl_3$, 2-Al

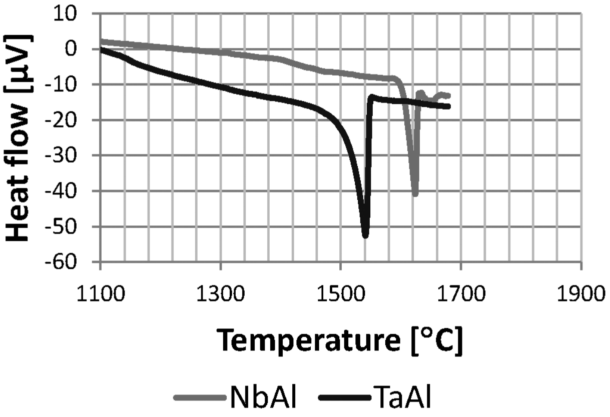

Figure 8: DTA curves of NbAl and TaAl master alloys
Slika 8: DTA-krivulji predzlitin NbAl in TaAl

The results of the differential thermal analysis of the master alloys are shown in **Figure 8**. The determined temperature of the liquidus of the NbAl alloy was 1624 °C and the temperature of the liquidus of the TaAl alloy was 1541 °C. The temperatures presented in **Figure 8** are not corrected and must be corrected to the melting temperature of pure Pd (5N, a calibration standard). We obtained the melting temperature of Pd under identical conditions. After the correction, the determined liquidus temperature of NbAl was 1615 °C and that of TaAl was 1532 °C.

4 CONCLUSION

Master alloys of NbAl and TaAl with the nominal compositions of Nb-60Al and Ta-80Al (x/%) were prepared by melting in a plasma furnace. These master alloys contain very low amounts of oxygen, namely, (29 ± 2) µg/g for the Nb-60Al master alloy and (123 ± 21) µg/g for the Ta-80Al master alloy. The melting temperatures of these master alloys were 1615 °C for NbAl and 1532 °C for TaAl. The DTA analysis, therefore, confirmed low melting temperatures of the prepared master alloys and, thus, their suitability for the preparation of γ-TiAl alloys alloyed with Nb or Ta.

Acknowledgement

This paper was created within projects No. CZ.1.05/2.1.00/01.0040 "Regional Materials Science and Technology Centre" within the frame of the operational programme "Research and Development for Innovations" financed by the Structural Funds and the state budget of the Czech Republic and SP2013/64 "Specific research in metallurgy, materials and process engineering".

5 REFERENCES

[1] V. Imayev, Advanced Engineering Materials, 10 (**2008**), 1095–1100
[2] D. Hu, Intermetallics, 15 (**2007**), 327–332
[3] T. Takeuchi [cit. 2013-08-27], http://www.nims.go.jp/smcMetal/takeuchi.html
[4] ASM International phase diagram database [cit. 2013-08-27] http://www1.asminternational.org/asmenterprise/apd/
[5] K. Frkáňová, Conference proceedings METAL, Brno, 2011
[6] F. Gomes, Materials Science Forum, 730–732 (**2012**), 697–702

UDK 669.15-194.56:539.4.016:621.78
Original scientific article/Izvirni znanstveni članek

ISSN 1580-2949
MTAEC9, 49(1)31(2015)

DECREASING THE CARBONITRIDE SIZE AND AMOUNT IN AUSTENITIC STEEL WITH HEAT TREATMENT AND THERMOMECHANICAL PROCESSING

ZMANJŠANJE VELIKOSTI KARBONITRIDOV V AVSTENITNEM JEKLU S TOPLOTNO OBDELAVO IN TERMOMEHANSKO PREDELAVO

Petr Martínek, Pavel Podaný, Jan Nacházel
COMTES FHT a.s., Dobřany, Czech Republic
pmartinek@comtesfht.cz

Prejem rokopisa – received: 2013-10-01; sprejem za objavo – accepted for publication: 2014-03-07

The article deals with the heat treatment and forging of AISI 321 austenitic stainless steel with a combination of the main alloying elements, Cr-Ni, in the mass ratio of about 18 : 10 and its variants used in the energy industry. The experiment was focused on the influence of heat treatment and thermomechanical processing on the microstructure and, especially, on the distribution of titanium carbo/nitrides and their agglomerations. Three experimental heats with various amounts of carbon, titanium and boron were prepared and subjected to different heat-treatment regimes. Also, different solution-annealing treatments were applied after the forging. The distribution of titanium carbo/nitrides was analyzed in different areas of the tested ingots. The microstructure of the samples was analyzed by means of light and scanning electron microscopy. A numerical simulation in the DEFORM HT software was used for simulating the cooling in different environments after the forging.

Keywords: austenitic steels, heat treatment, titanium carbonitrides

Članek obravnava toplotno obdelavo in kovanje avstenitnega nerjavnega jekla AISI 321 s kombinacijo glavnih legirnih elementov Cr-Ni v masnem razmerju 18 : 10 in njegovih različic, ki se uporabljajo v energetiki. Preizkus je bil usmerjen na vpliv toplotne obdelave in termomehanske predelave na mikrostrukturo in predvsem na razporeditev titanovih karbonitridov in njihovo grupiranje. Pripravljene so bile tri eksperimentalne taline z različno vsebnostjo ogljika, titana in bora ter izpostavljene različnim načinom toplotne obdelave. Po kovanju so bila izvršena različna raztopna žarjenja. Na različnih področjih eksperimentalmih ingotov je bila analizirana razporeditev titanovih karbonitridov. Mikrostruktura vzorcev je bila analizirana s svetlobno in vrstično elektronsko mikroskopijo. Za simulacijo ohlajanja v različnih okoljih po kovanju je bila uporabljena numerična simulacija s programsko opremo DEFORM HT.

Ključne besede: avstenitna jekla, toplotna obdelava, titanovi karbonitridi

1 INTRODUCTION

Stainless steels with an austenitic microstructure and an approximate composition of mass fractions $w = 18\ \%$ chromium, 10 % nickel and additions of molybdenum, titanium or niobium are today widely used in the components designed for high-temperature applications like nuclear power stations, boilers or superheaters.[1] AISI 321 is a typical austenitic stainless steel with this combination of the main alloying elements of Cr-Ni.

The main goal of this study was to reduce the amount of large carbo/nitride agglomerations. Large agglomerations usually cause echoes during ultrasonic inspections and, thus, almost finished products have to be rejected.

In normal practice, a sufficient amount of titanium is added to steel to combine with all the carbon. Titanium prevents the formation of $Cr_{23}C_6$ carbides, which locally deplete the matrix of chromium[2]; however, a reduction in the carbon amount below $w = 0.03\ \%$ does more to improve the sensitization resistance than an increase in the Ti amount.[3]

Titanium and niobium carbides are much less soluble in austenite than chromium carbide, so they form at much higher temperatures as relatively stable particles. These should remain relatively inert during commercial heat treatments involving solution temperatures no higher than 1050 °C, thus minimizing the possible nucleation of $Cr_{23}C_6$. However, TiC and NbC have some solubility in austenite at 1050 °C and can subsequently precipitate at lower temperatures. During high-temperature processes, these carbides dissolve to a greater extent in austenite and can then reprecipitate at lower temperatures. Therefore, NbC and TiC do not always form inert dispersions and are often likely to be redistributed due to heat treatment. They do, however, have a great advantage of not depleting the matrix of chromium, particularly in the sensitive areas such as grain boundaries.[4]

The precipitation of carbides and nitrides also occurs during the rapid quenching from high solution temperatures;[4] nevertheless, if only the final heat treatment is applied on thermomechanically processed products (long-time annealing at the temperatures above 1150 °C), grain coarsening can be observed. $M_{23}C_6$ particles precipitated predominantly at the grain boundaries, causing an earlier onset of an abnormal grain growth as compared to the samples, in which precipitation occurred in the interior of the grains (at the lowest temperature, 1090 °C). This effect is associated with the stability and kinetics of the dissolution of $M_{23}C_6$ particles.[5]

The solution heat treatment in the range of 1100–1250 °C also has a beneficial effect on the creep resistance due to the subsequent precipitation of MX precipitates.[6]

2 EXPERIMENT

Three different heats of austenitic stainless steel were prepared. The chemical composition meets the requirement of the Russian standard 08Ch18N10T and American standards AISI 321 and AISI 321H (in the case of a heat enrichment with boron). The chemical composition of the experimental material is summarized in **Table 1**.

Table 1: Chemical composition of experimental heats
Tabela 1: Kemijska sestava eksperimentalnih talin

Element	Heat number		
(*w*/%)	46471	46736	46777
C	**0.0400**	**0.0400**	**0.0600**
Mn	1.5100	1.6100	1.7000
Si	0.5300	0.5100	0.5700
P	0.0250	0.0220	0.0210
S	0.0070	0.0020	0.0020
Cr	17.600	17.650	17.600
Ni	10.300	10.100	10.100
Ti	**0.2200**	**0.2800**	**0.3900**
B	**0.0001**	**0.0037**	**0.0045**
N	0.0215	0.0265	0.0116

The main variation of the chemical composition consists of different amounts of titanium, carbon and boron. The experiment was mainly focused on the microstructure examination and image analysis. This was done on the ingots. The ingot size and shape were 8K 1.1 with a mass of 1000 kg (the mean diameter was about 500 mm, the length without the head was 1120 mm). The microstructure was inspected in three localities (the ingot axis – 1; the half of radius – 2; the edge – 3), of the ingots after different heat treatments, on the samples forged from the ingots and cooled in two different environments and on these samples after the high-temperature annealing. The microstructure examination and image analyses were focused on the amount and distribution of titanium carbonitrides, on the volume fraction of delta ferrite and the grain size after forging and heat treatment. The particular parameters of the experiment described above are shown in **Table 2**. All the samples for the microstructure documentation were cut in a cubic shape with the dimensions of about 12 mm × 12 mm × 12 mm.

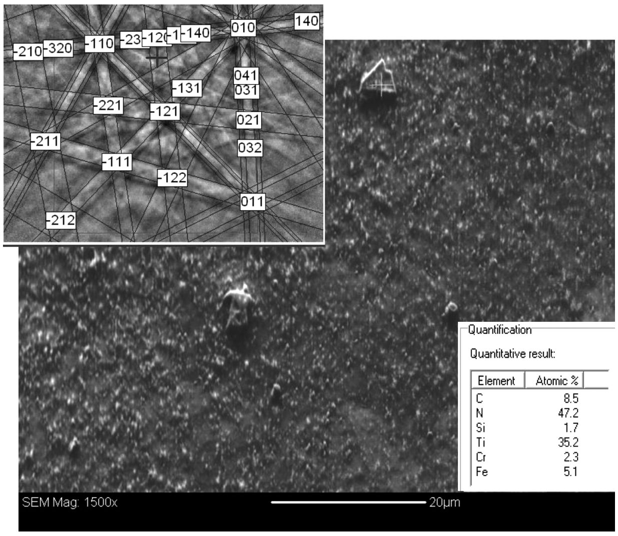

Element	Atomic %
C	8.5
N	47.2
Si	1.7
Ti	35.2
Cr	2.3
Fe	5.1

Figure 1: EBSD and EDX analysis of TiCN
Slika 1: EBSD- in EDX-analiza TiCN

Table 2: Parameters of the experiment (for the samples from ingots and the samples forged from ingots)
Tabela 2: Parametri preizkusa (na vzorcih iz ingotov in na kovanih vzorcih iz ingotov)

Experimental procedure	Experiments on ingots		Experiments on forged samples	
	Heat treatment of the samples from ingots (solution annealing)		Cooling after forging (forging at 1200 °C)	Annealing temperature (°C)
Parameters	Temp. (°C)	Time (h)	Vermiculite or water quenching	1020 or 1100
	900	1; 5; 10		
	1100	1; 5; 10		
	1300	1; 5; 10		
Analyses	Microstructure examination and image analysis			

The ingots were cut with a conventional cutting saw. The samples for the microstructure examination were subjected to a conventional metallographic procedure (grinding and subsequent polishing with an alumina suspension). The Beraha 2 etchant was used for revealing delta ferrite. Austenite grains were revealed by means of the V2A etchant.

The identification of carbonitrides was done by means of an HKL Nordlyss EBSD camera and EDS detector INCAx-sight on a JEOL 7400F scanning electron microscope (**Figure 1**).

The image analysis was made with a Nikon MA 200 light microscope with the NIS Elements software for image analyses.

All the samples were evaluated at a 500× magnification and inspected in 30 image fields of each sample (one image field represents an area of 0.022728 mm^2).

The entire experimental heat treatment was done with an annealing furnace Heraus. The forging of the samples from the experimental ingots was done with a hydraulic press Zeulenroda (PYE 40).

3 RESULTS AND DISCUSSION

3.1 Microstructure of the ingots

A quantitative image analysis of the carbonitride count and the carbonitride size found that there is no essential difference between particular heats. However, it was found that there are substantial differences between the localities within an ingot. The highest amount of carbonitrides was concentrated on the edge (near the surface) of an ingot. On the other hand, the size (the average area) of these particles near the surface is the lowest (see **Figure 2** where locality 1 is the ingot axis, locality 2 is at the half of its radius and locality 3 is on the edge of the ingot). The term "object count" in the figure represents the amount of particles per analysed image field, while "object area" represents the average area of one particle.

Agglomerations of carbonitrides are classified as one large carbonitride during the image analyses. Histograms show the distribution of carbonitrides into 10 size factors on the *x*-axis (from 0 μm^2 to 10 μm^2 with a 1 μm^2 step). Class "other" indicates carbonitride agglomerations. It is clearly visible that the amount (the *y*-axis) of large carbonitride agglomerations decreases from the ingot axis to its surface (**Figure 3**).

Delta ferrite formed a complex network around the as-cast grains in the middle of the ingot (**Figures 4** and

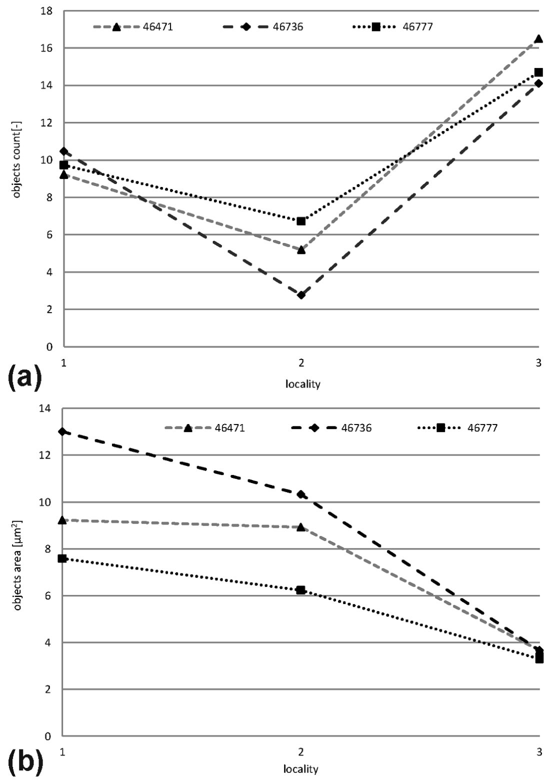

Figure 2: Amount of carbonitride particles and the average area of carbonitride particles in ingots: a) amount of particles per field, b) average area of particles

Slika 2: Delež delcev karbonitridov in povprečna velikost karbonitridnih delcev v ingotih: a) količina delcev v enem polju, b) povprečna velikost področja delcev

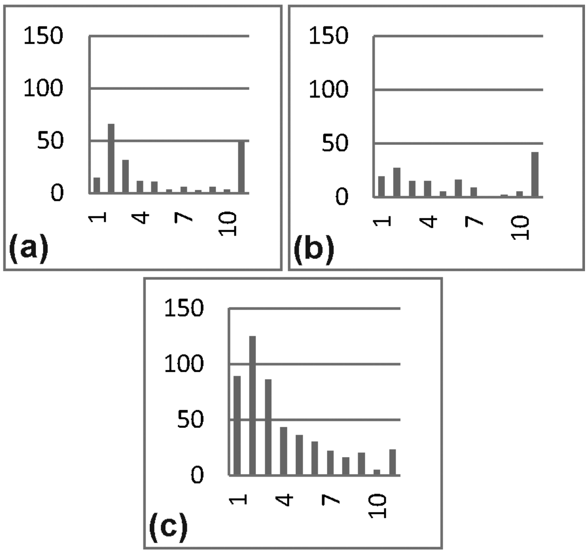

Figure 3: Histograms of carbonitride classification for ingot 46471: a) ingot axis, b) half of radius, c) edge of ingot

Slika 3: Histogrami razporeditve velikosti karbonitridov v ingotu 46471: a) os ingota, b) polovica polmera ingota, c) rob ingota

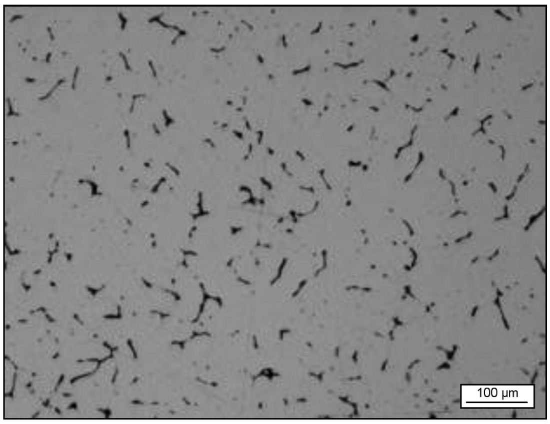

Figure 4: Size and distribution of delta ferrite in ingot 46471 – the middle part of the ingot, Beraha 2 etchant

Slika 4: Velikost in razporeditev delta ferita v ingotu 46471 – sredina ingota, jedkalo Beraha 2

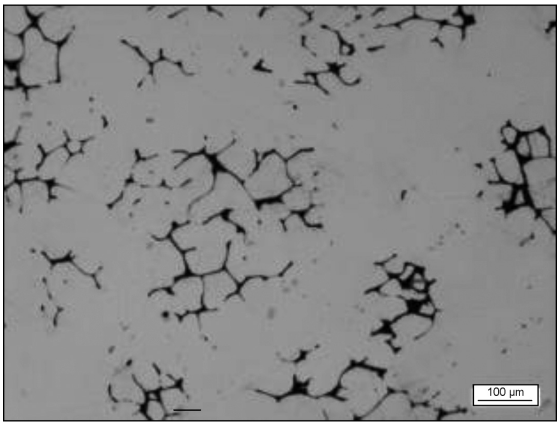

Figure 5: Size and distribution of delta ferrite in ingot 46471 – the edge of the ingot, Beraha 2 etchant

Slika 5: Velikost in razporeditev delta ferita v ingotu 46471 – rob ingota, jedkalo Beraha 2

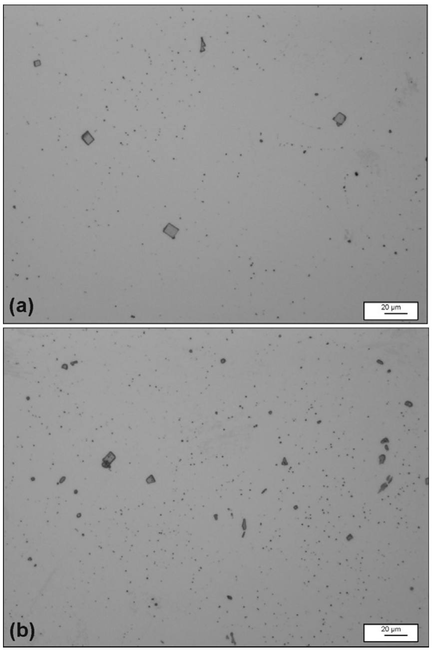

Figure 6: Size and distribution of carbonitrides in ingot 46471: a) initial state, as polished, b) after the heat treatment (1300 °C, 5 hours), as polished

Slika 6: Velikost in razporeditev karbonitridov v ingotu 46471: a) začetno stanje, polirano, b) po toplotni obdelavi (1300 °C, 5 h), polirano

5). Near the edge of the ingot, delta ferrite forms more separate islands and its volume fraction is lower. Both delta-ferrite and carbonitride distribution within the ingot are related to the ingot solidification. Carbonitrides form agglomerations due to the reduced speed of solidification and delta ferrite is formed due to the segregation of the alpha-phase-forming elements.

3.2 Heat treatment of ingots

The samples from the ingots were annealed at (900, 1100 and 1300) °C for (1, 5 or 10) h. The results of the image analyses after the solution annealing are shown **Table 3**.

The annealing at 900 °C for a short time (1 h and 5 h) does not substantially affect the size and count of carbonitrides. The effect of annealing on this temperature is only visible after the annealing for 10 h when the amount of carbonitrides decreases and its average area slightly increases.

An increase in the solution temperature to 1100 °C led to a similar effect on the particle size even after 1 h. But the average amount of carbonitrides per inspected field did not change substantially. A longer annealing at this temperature did not bring any other effect.

The best result was obtained with the annealing at 1300 °C for 1 h and 5 h (**Figure 6**). The average area of one particle decreased and the average count of particles increased. However, the annealing prolonged to 10 h gave almost the same values of the particle count and the average area was the same as in the initial state before the annealing. Nevertheless, the annealing at this temperature for 10 h led to a more homogeneous distribution of carbonitrides.

The best result was reached after the annealing at 1300 °C for 1 h and 5 h when the average area of particles decreased and the average amount of particles per inspected image field increased.

3.3 Forging of the samples from the ingots and different cooling processes

The samples made from the edges of the ingots were heated up to 1200 °C and solution annealed for 2 h and after that they were forged, with a degree of reduction of 2.5. Two different cooling processes were applied: quenching in water and simulation of cooling a whole forged bar with a 250 mm diameter in the air. An insertion of a forged sample into insulating vermiculite simulated this process. The condition of cooling was verified by means of the DEFORM HT software, which proved a similarity of the cooling conditions for a small sample in vermiculite. The influence of forging and the way of cooling on the carbonitride size and distribution were then studied. The forging itself has a substantial

Table 3: Results of the image analyses after the solution annealing (object count represents the amount of particles per analysed image field, object area represents the average area of one particle)

Tabela 3: Rezultati analize slik po raztopnem žarjenju ("število objektov" pomeni število delcev na enem analiziranem polju, velikost področja pomeni povprečno velikost enega delca)

TiCN		46471		46736		46777	
		Obj. count	Obj. area	Obj. count	Obj. area	Obj. count	Obj. area
Temperature	Time	(–)	(µm^2)	(–)	(µm^2)	(–)	(µm^2)
	0	13.00	3.49	14.1	3.67	14.70	3.31
900 °C	1	12.10	3.48	12.2	3.21	14.17	3.05
	5	12.87	3.37	13.67	3.04	14.47	3.33
	10	10.57	5.40	6.8	5.90	14.53	5.33
1100 °C	1	16.57	4.15	8.93	5.77	12.80	4.88
	5	16.33	4.60	10.53	4.68	18.33	5.67
	10	12.37	4.06	7.67	6.64	14.77	5.32
1300 °C	1	36.13	1.72	30.13	2.10	25.43	2.05
	5	37.03	1.98	28.23	2.31	26.27	1.84
	10	20.53	2.50	12.77	3.44	15.20	2.60

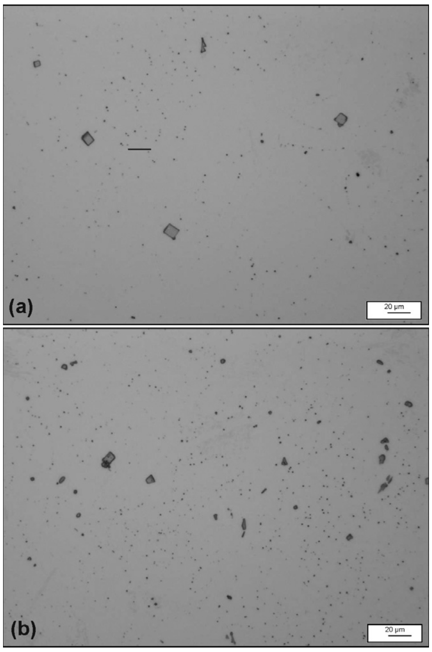

Figure 7: Microstructure of a forged sample after forging, cooling in vermiculite and annealing: a) heat 46736 annealed at 1020 °C, polished, b) heat 46777 annealed at 1020 °C, polished

Slika 7: Mikrostruktura kovanega vzorca po kovanju, ohlajanju v vermikulitu in žarjenju: a) talina 46736, žarjena pri 1020 °C, polirano, b) talina 46777, žarjena pri 1020 °C, polirano

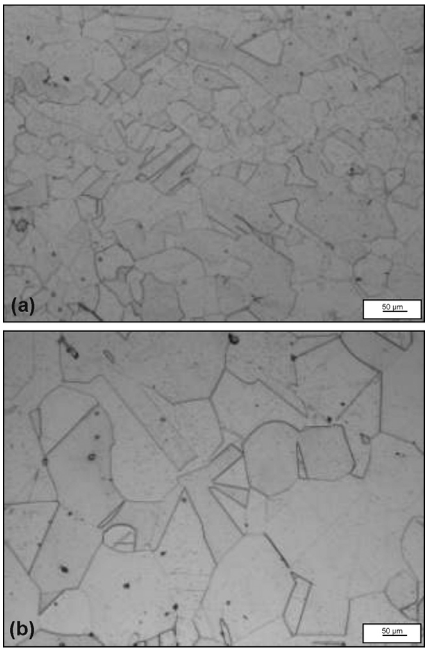

Figure 8: Microstructure of a forged sample after forging, cooling in vermiculite and annealing: a) heat 46736 annealed at 1020 °C, V2A etchant, b) heat 46736 annealed at 1100 °C, V2A etchant

Slika 8: Mikrostruktura kovanega vzorca po kovanju, ohlajanju v vermikulitu in žarjenju: a) talina 46736, žarjena pri 1020 °C, jedkalo V2A, b) talina 46736, žarjena pri 1100 °C, jedkalo V2A

influence on the size and distribution of carbonitrides. An increase in the amount of carbonitrides was observed for all three heats. Heat 46777 showed the strongest increase in carbonitrides due to forging. The observed particles were unfortunately too small for an EDS analysis. But with respect to their positioning within the grain interior, the carbides are not detrimental. Only a low increase in the particle count was observed after the cooling in vermiculite in comparison to the cooling in water. The forging of all the samples led to a decrease in the size of carbonitrides.

3.4 Annealing of forged samples

The forged samples were afterwards annealed at two different temperatures, 1020 °C and 1100 °C, to achieve a further dissolution of carbonitrides. It was found that in the case of heats 46736 and 46777 annealing the forgings quenched in water at 1020 °C led to a further increase in the particle count (**Figure 7**) and a decrease in the average area of particles (**Table 4**).

Increasing the annealing temperature for these heats was beneficial for a further particle refinement but negligible for the final grain size. The grain size increased from 8 (after the forging) to 5 (after the annealing at 1100 °C) according to ASTM E 112 (**Figure 8**). This result was the same for all the heats, there were only minor differences between them.

3.5 Mechanical testing

There was not enough material for standard mechanical testing, thus, mini-tensile test samples were made

Table 4: Average values of the particle count and size for the initial state, after the forging (1 – quenching in water, 2 – cooling in vermiculite) and annealing

Tabela 4: Povprečne vrednosti štetja delcev in velikost v začetnem stanju, po kovanju (1 – ohlajanje v vodi, 2 – ohlajanje v vermikulitu) in po žarjenju

TiCN	46471		46736		46777	
	Obj. count	Obj. area	Obj. count	Obj. area	Obj. count	Obj. area
state	–	µm^2	–	µm^2	–	µm^2
initial state	13.0	3.49	14.1	3.67	14.70	3.31
forging 1	27.97	2.17	18.13	2.86	166.53	0.92
1020 °C	23.9	2.63	24.87	2.83	192.57	0.90
1100 °C	23.73	2.95	45.13	2.10	203.83	0.89
forging 2	25.7	3.05	46.20	2.70	171.73	0.95
1020 °C	23.03	2.81	32.73	1.98	180.37	0.97
1100 °C	19.43	3.05	57.23	1.56	215.57	0.90

from the forged specimens. A sample for the mini-tensile testing is flat, with very small dimensions (the functional-body length is in units of millimetres). The tests were done on a mini-tensile test machine MTS with a video-extensometer MESSPHYSIK. The results of testing the samples annealed at 1020 °C are in **Table 5**. The yield strength increases due to the increasing count of carbonitride particles (precipitation strengthening). Thus, heat 46777 shows the highest *YS* and *TS* of all the heats. The mechanical test of the samples annealed at 1100 °C was not performed because of insufficient grain size.

Table 5: Results of mechanical testing after forging 1 (subsequent quenching in water) and annealing at 1020 °C

Tabela 5: Rezultati mehanskih preizkusov po kovanju 1 (sledilo je ohlajanje v vodi) in žarjenju pri 1020 °C

Specimen	$R_{p0.2}$/MPa	R_m/MPa	A/%
46471	295.5	609.3	70.5
46736	323.4	595.4	56.7
46777	343.2	628.7	63.0

4 CONCLUSIONS

Complex experiments were performed on austenitic stainless steel. Three experimental heats of AISI 321(H) with various amounts of carbon, titanium and boron were subjected to a particular annealing heat treatment, forging with various cooling procedures and a further annealing. Three different temperatures of solution annealing were applied on the ingots – (900, 1100 and 1300) °C, with different holding times – (1, 5 and 10) h. The forged samples were cooled in two different environments – rapid quenching in water and slow cooling in vermiculite. The last heat treatment – solution annealing – was applied on the forged samples – at 1020 °C and 1100 °C for 1 h.

The highest amount of carbonitrides is concentrated on the edge (near the surface) of an ingot where rapid solidification takes place. Carbonitrides become coarsened, forming agglomerations towards the ingot axis, together with the decreasing solidification velocity. Delta ferrite forms a network structure near the ingot axis; it divides into separate islands near the ingot surface.

A substantial decrease in the carbonitride amount was reached after the heat treatment of the ingots at the temperature 1300 °C for 1 h or 5 h when the average area of particles decreased and the average amount of particles per inspected image field increased. Increasing both the annealing temperature and the holding time led to a substantial decrease in the delta-ferrite volume fraction. No substantial differences between the amounts of the observed carbonitrides, in dependence of particular carbon and titanium amounts in the ingots were observed.

Further experiments were concentrated on the samples taken from the edges of the ingots. Thermomechanical processing – the forging itself – substantially decreased the size of particles in all the heats. On the other hand, the amount of carbonitrides increased. The minimum increase was observed on heat 46471 with the lowest carbon and titanium amounts. The highest increase in the carbonitride amount was observed on heat 4677 with the highest titanium, carbon and boron amounts. Considering the difference between the cooling procedures in two environments, a substantial increase in the particle count was observed for heat 46736 after the cooling in vermiculite in comparison to the cooling in water. However, the differences for the other heats were not crucial.

The highest increase in carbonitrides after the solution annealing at 1020 °C was observed in heat 46777 (the heat with the highest carbon and boron amounts). Using a higher annealing temperature (1100 °C) was not beneficial because of the coarsening of the grain size. The grain size increased from 8 (after the forging) to 5 (after the annealing at 1100 °C) according to ASTM E 112. This correlates with the other studies[5]. The heats with higher titanium and boron amounts (46736 and 46777) exhibited good mechanical properties. The precipitation of very fine carbonitrides has a positive effect on the yield strength, as previously stated by Sourmail[6].

Acknowledgments

The results presented in this paper were supported by: project FR-TI1/222 of the Ministry of Industry and Trade of the Czech Republic and project West-Bohemian Centre of Materials and Metallurgy CZ.1.05/2.1.00/03.0077, co-funded by the European Regional Development Fund.

5 REFERENCES

[1] G. Kaishu et al., Effect of aging at 700 °C on precipitation and toughness of AISI 321 and AISI 347 austenitic stainless steel welds, Nuclear Engineering and Design, 235 (**2005**), 2485–2494

[2] K. Kaneko et al., Formation of $M_{23}C_6$-type precipitates and chromium-depleted zones in austenite stainless steel, Scripta Materialia, 65 (**2011**) 6, 509–512

[3] A. Pardo et al., Influence of Ti, C and N concentration on the intergranular corrosion behaviour of AISI 316Ti and 321 stainless steels, Acta Materialia, 55 (**2007**), 2239–2251

[4] W. K. Honeycombe, H. K. D. H. Bhadeshia, Steels: Microstructure and Properties, 3rd Ed., Elsevier Ltd., 2006, 267

[5] J. C. Dutra et al., Interaction Between Second-Phase Particle Dissolution and Abnormal Grain Growth in an Austenitic Stainless Steel, Materials Research, 5 (**2002**) 3, 379–384

[6] T. Sourmail, Precipitation in creep resistant austenitic stainless steels, Materials Science and Technology, 17 (**2001**) 1, 1–14

UDK 621.78.08:539.538
Original scientific article/Izvirni znanstveni članek

ISSN 1580-2949
MTAEC9, 49(1)37(2015)

DEEP CRYOGENIC TREATMENT OF H11 HOT-WORKING TOOL STEEL

GLOBOKA KRIOGENSKA OBDELAVA ORODNEGA JEKLA H11 ZA DELO V VROČEM

Pavel Suchmann[1], Dagmar Jandova[2], Jana Niznanska[1]
[1]COMTES FHT a. s., Průmyslová 995, 334 41 Dobrany, Czech Republic
[2]VZU PLZEN s. r. o., Tylova 46, 323 00 Plzen, Czech Republic
pavel.suchmann@comtesfht.cz

Prejem rokopisa – received: 2013-10-02; sprejem za objavo – accepted for publication: 2014-02-07

Unlike a conventional cold treatment, which is commonly used for the elimination of retained austenite, a deep cryogenic treatment (DCT) primarily improves the wear resistance of tools. This effect is supposed to result from the preferential precipitation of fine η-carbides, whose formation mechanism has been the subject of several recent investigations, performed mainly on high-speed steels. This article describes the influence of a DCT on the microstructure and properties of X37CrMoV5-1 (H11) hot-working tool steel. The wear resistance of specimens treated using DCT was analysed using a pin-on-disc wear tester and compared to that of specimens treated using standard quenching and tempering. In addition, the specimens' microstructures were analysed by TEM. The results show a significant improvement in the wear resistance as a consequence of the DCT, especially at the high sliding velocities that are typical of many industrial applications for hot-working steels (e.g., closed die forging). Apart from this, some effects of DCT on the microstructure were found, which contributed to a better understanding of this process.

Keywords: tool steel, wear resistance, microstructure

Različno od konvencionalnega podhlajevanja, ki se navadno uporablja za odpravo zaostalega avstenita, se kriogena obdelava (DCT) uporablja predvsem za povečanje obrabne odpornosti jekla. Domneva se, da to izvira iz preferenčnega izločanja drobnih η-karbidov. Mehanizem njihovega nastanka je predmet številnih raziskav, narejenih predvsem pri hitroreznih jeklih. Članek opisuje vpliv DCT na mikrostrukturo in lastnosti X37CrMoV5-1 (H11) orodnega jekla za delo v vročem. Obrabna odpornost vzorcev, obdelanih z DCT, je bila določena na napravi za določanje obrabe "pin-on-disc" in primerjana z obrabno odpornostjo vzorcev, obdelanih z navadnim kaljenjem in popuščanjem. Mikrostruktura vzorcev je bila analizirana s TEM. Rezultati kažejo občutno izboljšanje odpornosti proti obrabi pri DCT-obdelavi, posebno pri velikih hitrostih drsenja, ki so značilne pri mnogih vrstah industrijske uporabe jekel za delo v vročem (npr. kovanje v utopih). Poleg tega so bili ugotovljeni vplivi DCT na mikrostrukturo, kar prispeva k boljšemu razumevanju tega procesa.

Ključne besede: orodno jeklo, odpornost proti obrabi, mikrostruktura

1 INTRODUCTION

The deep cryogenic treatment of steels has been the subject of numerous research and experimental studies over the past twenty years. Its practical significance has been growing with new findings, which suggest that the process may substantially extend the life of various types of tools. From the technical viewpoint, a deep cryogenic treatment is a single processing operation that immediately follows the conventional quenching (and precedes tempering). One should, however, distinguish between a deep cryogenic treatment and a conventional cold treatment. The latter has been commonly used in industry since the 1950s. The purpose of a cold treatment (same as in multiple tempering) is to eliminate the retained austenite from the microstructure of the hardened steel. In high-alloyed tool steels the retained austenite remains stable down to the approximate temperature range –80 °C to –120 °C. In a cold treatment, a temperature below this level is reached only once in the process. The treatment improves the material's mechanical properties (i.e., the strength) and enhances the dimensional stability for tools processed in this manner.

In contrast, in a deep cryogenic treatment the elimination of retained austenite is no more than a side effect. A number of reports suggest that in steels the supercooling below –150 °C and a subsequent long holding time (of the order of hours or tens of hours) at the low temperature leads to a substantial improvement in their resistance wear in service. This applies even in comparison with materials subjected to a conventional cold treatment (i.e., materials with a zero retained austenite content).

The improvement in tool life due to a deep cryogenic treatment has recently been reported in various types of forming and cutting tools.[1,2] In forging dies from the X37CrMoV5-1 (H11) steel, an improvement in service life by 40 % was proven repeatedly,[2] when compared to conventional quenching and tempering without a deep cryogenic treatment. An extensive series of experiments on various types of punching tools, milling cutters and drill bits from several types of tool steels demonstrated a definite contribution of the deep cryogenic treatment to a longer tool life.[3] Another widely published series of experiments was conducted on turning tools made from HS10-4-3-10 high-speed steel.[4] In this case, too, the improvement in the cutting edge's life thanks to a deep cryogenic treatment was demonstrated.

The microstructural aspects of these effects were explored in the 1990s by Collins and other researchers.[5–8] In the case of the X155CrVMo12-1 steel (the nearest equivalent grade: D2), a large content of fine secondary carbides was found in the deep cryogenically treated material, in addition to its improved wear resistance over that of the conventionally quenched and tempered material. The changes in microstructure taking place in the course of the deep cryogenic treatment are summarised and described by Collins as a cold treatment modification of martensite. The author believes that the modification consists of the formation of a large number of lattice defects that serve as nuclei for the precipitation of these fine carbides during tempering. It should be noted that all these conclusions have been drawn on the basis of nothing more than a quantitative image analysis of optical micrographs. From today's perspective, this is an insufficiently detailed analysis of the microstructure.

Another in-depth investigation of the behaviour of X155CrVMo12-1 steel (the nearest equivalent grade: D2) after a deep cryogenic treatment was reported by Das et al.[9–11] Tests of the wear resistance revealed its improvement by 12–39 % after cold treatment and by 34–88 % after a deep cryogenic treatment, when compared to conventional quenching and tempering. Das reported that a deep cryogenic treatment leads to a permanent change in the carbide precipitation kinetics. According to his report, the material upon deep cryogenic treatment contains 22 % more carbides per unit volume than the conventionally quenched and tempered material.

The most recent findings on deep cryogenic treatment were reported in 2011 by Oppenkowski,[1] who carried out an in-depth analysis of several types of high-speed steels that were processed using various technologies, including cold and deep cryogenic treatments. He proved that steels, after various hardening procedures, contain different types of martensite. According to his findings, deep cryogenically treated materials are characterized by a higher content of martensite with less tetragonal distortion and finer twin structures. These microstructural changes are probably the cause of the precipitation of a large amount of fine carbides during the subsequent tempering.

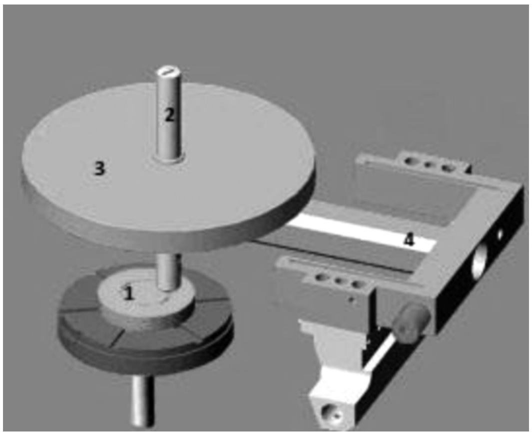

Figure 1: Pin-on-disc equipment: 1-test sample, 2-indenter holder with ball indenter, 3-weight, 4-flexible arm

Slika 1: Naprava "pin-on-disc": 1-vzorec, 2-nosilec kroglastega utiskovalnika, 3-utež, 4-gibljiva ročica

The present paper describes the investigation procedure and the results of exploring the impact of a deep cryogenic treatment on the wear resistance and microstructure of the X37CrMoV5-1 (H11) hot-work steel. The wear resistance was measured at 400 °C using the pin-on-disc method with a rotary tribometer. The microstructure of the steel was examined using light and transmission electron microscopes.

2 EXPERIMENTAL

2.1 Heat Treating

The experimental specimens of the X37CrMoV5-1 (H11) tool steel had a diameter of 55 mm and a height of 10 mm. These specimens were treated using the schedules listed in **Table 1**. Two specimens were prepared with each schedule. One was used for wear-resistance testing and the other for microstructural observations. The hardness of all the heat-treated specimens was 52 HRC.

Table 1: Experimental heat-treatment schedules

Tabela 1: Pregled eksperimentalnih toplotnih obdelav

Specimen Designation	Heat Treating Schedule
1 (H+2T)	Heating to 1030 °C, quenching in oil, double tempering (610 °C)
2 (H+6C+2T)	Heating to 1030 °C, quenching in oil, deep freezing at –160 °C for 6 h, double tempering (610 °C)
3 (H+12C+2T)	Heating to 1030 °C, quenching in oil, deep freezing at –160 °C for 12 h, double tempering (610 °C)
4 (H+20C+2T)	Heating to 1030 °C, quenching in oil, deep freezing at –160 °C for 20 h, double tempering (610 °C)

2.2 Wear Resistance

The wear-resistance tests were performed using the pin-on-disc method. The principle of this test is forcing a ceramic ball into the surface of a rotating flat specimen. The holder with the ball indenter is pressed using a defined force (exerted by a weight) against the specimen. The holder is attached to a flexible arm, through which the dependence of the friction coefficient on the length of the ball's path is recorded by means of strain gauges. The testing equipment is schematically shown in **Figure 1**.

After the test, the profile of the resulting wear track is measured using a contact profilometer. The wear of the

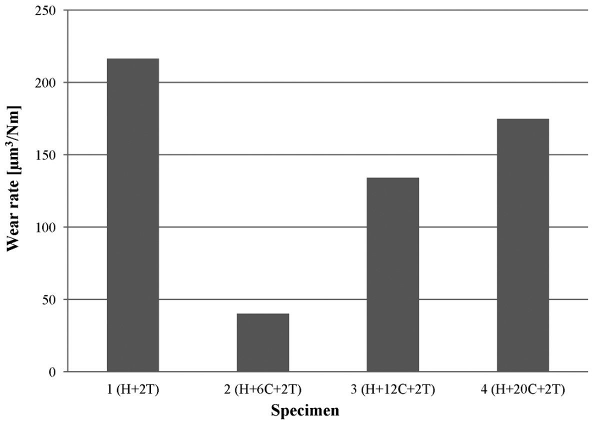

Figure 2: Wear rates of pin-on-disc test specimens
Slika 2: Hitrost obrabe na preizkušancih "pin-on-disc"

test specimen is calculated from the measured data as follows:

$$W/(\mu m^3/N\ m) = \frac{\text{Wear track volume } (\mu m^3)}{\text{Load (N)} \cdot \text{Path travelled by ball indenter (m)}}$$

The specimens of X37CrMoV5-1 (H11) were tested with the following parameters:

- Indenter holder with a ball indenter (Si_3N_4) with the diameter of $D = 6$ mm
- Wear-track diameter: $r = 3.00$ mm
- Temperature: 400 °C
- Load: 10 N
- 5000 cycles (specimen revolutions)

The choice of a temperature of 400 °C is based on the conditions for the most frequent industrial applications of the steel in question: forging dies, injection moulds and other tools whose surfaces may experience a high temperature in service. For example, during closed-die forging, the temperatures of the die surface may reach approximately 250–500 °C.

The wear rates of the specimens tested are given in **Figure 2**. The results of the measurement suggest that a deep cryogenic treatment dramatically improves the material's wear resistance. However, with the holding time at the deep cryogenic temperature becoming longer, the resistance declines again. This occurrence was mentioned in several reports (e.g.,[1]) but no satisfactory theoretical explanation has been found.

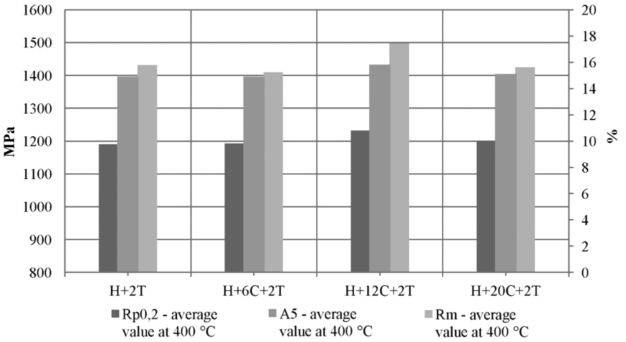

Figure 4: Results of tensile tests
Slika 4: Rezultati nateznih preizkusov

2.3 Tensile tests

Standard tensile tests of specimens treated according to **Table 1** were performed at room temperature and at 400 °C. For each testing temperature, three specimens were tested. As the following results (**Figures 3** and **4**) show, no significant influence of the deep cryogenic treatment on the tensile strength or the elongation was found.

2.4 Impact tests

Standard specimens (10 mm × 10 mm × 55 mm, with a U-formed notch, the radius of the notch is 1 mm, the depth of the notch is 5 mm) treated according to the above-mentioned regimes undertook the Charpy impact tests at 20 °C and 400 °C. Similar to the results of the tensile tests, no significant influence of the deep cryogenic treatment on the notch toughness of the investigated material was observed (**Figure 5**).

2.5 Light Microscopy Observation

The specimens were prepared using a standard metallographic procedure: grinding and subsequent polishing.

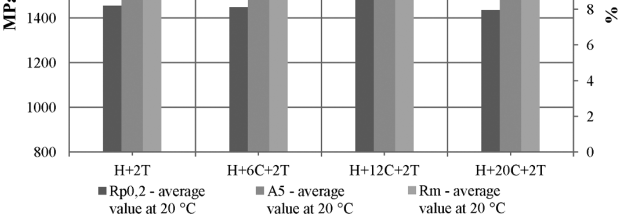

Figure 3: Results of tensile tests
Slika 3: Rezultati nateznih preizkusov

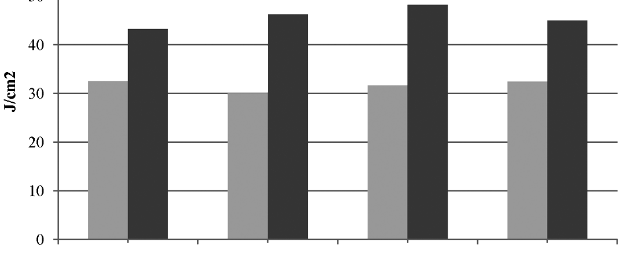

Figure 5: Results of impact tests
Slika 5: Rezultati udarnih preizkusov

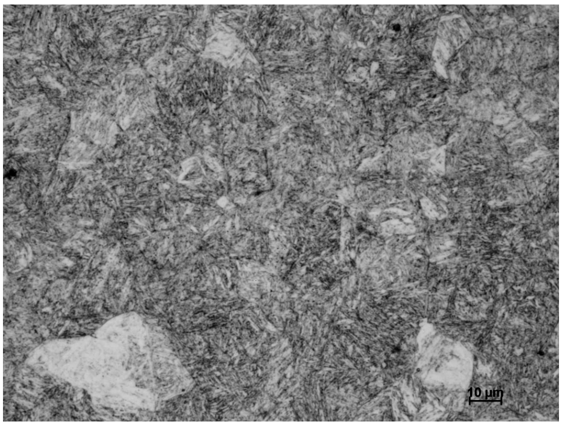

Figure 6: Microstructure of specimen 1 (H+2T); etched in nital 3 %
Slika 6: Mikrostruktura vzorca 1 (H+2T); jedkano v nitalu 3 %

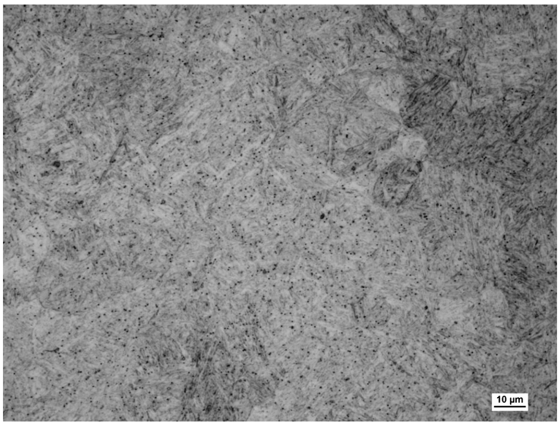

Figure 7: Microstructure of specimen 2 (H+6C+2T); etched in nital 3 %
Slika 7: Mikrostruktura vzorca 2 (H+6C+2T); jedkano v nitalu 3 %

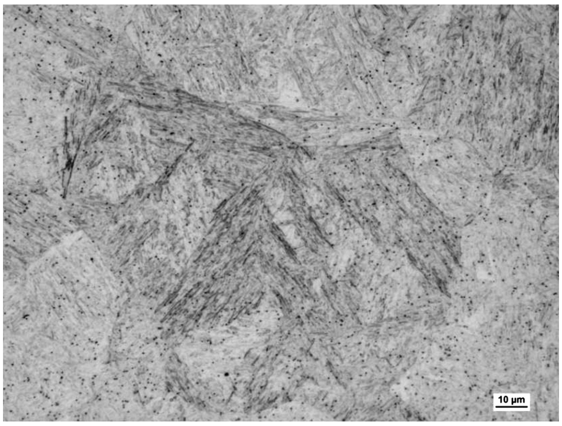

Figure 8: Microstructure of specimen 3 (H+12C+2T); etched in nital 3 %
Slika 8: Mikrostruktura vzorca 3 (H+12C+2T); jedkano v nitalu 3 %

Their microstructures were revealed by etching with nital 3 % and photographed using a NIKON EPIPHOT 200 light microscope. As the micrographs below show, the microstructures in all the specimens examined are very similar. They consist in all cases of martensite laths, within which some fine carbides can be found. Neither non-metallic inclusions nor other microstructure deficiencies were revealed. Micrographs of the individual specimens are shown in **Figures 6** to **9**.

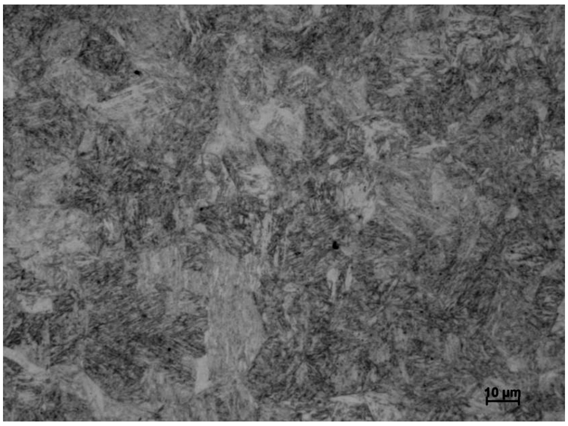

Figure 9: Microstructure of specimen 4 (H+20C+2T); etched in nital 3 %
Slika 9: Mikrostruktura vzorca 4 (H+20C+2T); jedkano v nitalu 3 %

2.6 Transmission Electron Microscopy Observation

In order to document the impact of a deep cryogenic treatment on the martensite morphology more accurately, the tempering at 610 °C was omitted in the case of specimens for transmission electron microscopy observation. The reason was that some recent reports (e.g.,[1]) claim that at higher tempering temperatures, the precipitation of fine carbides in tool steels is accompanied by a gradual annihilation of some types of lattice imperfections formed during the deep cryogenic treatment. For this reason, only low-temperature tempering at 180 °C was applied. The heat-treatment schedules for the specimens investigated by means of transmission electron microscopy are detailed in **Table 2**.

Table 2: Heat treatment of specimens for transmission electron microscopy observation
Tabela 2: Toplotna obdelava vzorcev za presevno elektronsko mikroskopijo

Specimen Code	Heat Treating Schedule
1T (H+2T)	Heating to 1030 °C, quenching in oil, tempering (180 °C)
2T (H+6C+2T)	Heating to 1030 °C, quenching in oil, deep freezing at –160 °C for 6 h, tempering (180 °C)

The microstructures of specimens 1T and 2T consist of tempered martensite. No significant differences between these specimens were observed in the light microscope (**Figure 10** – etched with Vilella-Bain reagent). The bands occur in both samples as a result of the segregation of alloying elements – this is a typical phenomenon in the forgings of hot-working tool steels. A Widmannstätten structure was evident in the more intensively etched regions (bands), whereas a rather featureless structure with a high density of precipitates was found in adjacent regions.

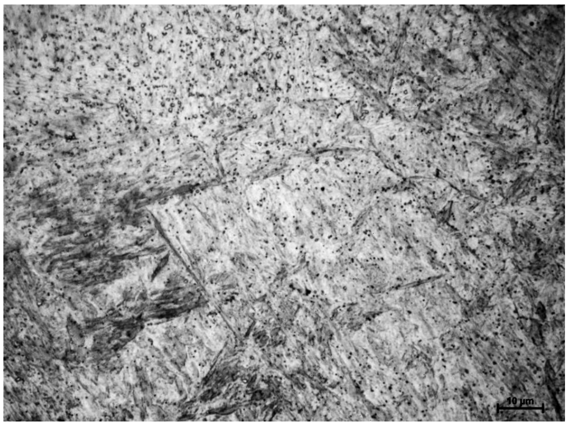

Figure 10: Microstructure of 2T specimen; etched in Vilella-Bain
Slika 10: Mikrostruktura vzorca 2T; jedkano z jedkalom Vilella-Bain

Thin foils for the transmission electron microscopy observations were prepared from specimens 1T and 2T using jet electrolytic polishing in a 6 % solution of perchloric acid in methanol at a temperature of approximately –50 °C. Thin areas, transparent to electrons, accelerated by a voltage of 120 kV were found predominantly in the above-mentioned bands of the featureless structure. Two different substructures were observed. Tempered martensite of plate-like, rather than lath-like, character with very thin twins (a width of several tens of nanometres) was observed in foils from both specimens (**Figure 11**). In the 2T specimen, very fine precipitates at boundaries of the ferritic laths and twins were observed. A crystallographic investigation has not been performed yet, as the electron-diffraction patterns obtained are still not finished and ready for a reliable phase identification. The second type of substructure revealed a specific striped contrast and diffraction patterns with streaks typical for structures after spinodal decomposition (**Figure 12**). In these areas, some globular and relatively coarse particles were observed – probably those that were also observed using the light microscope.

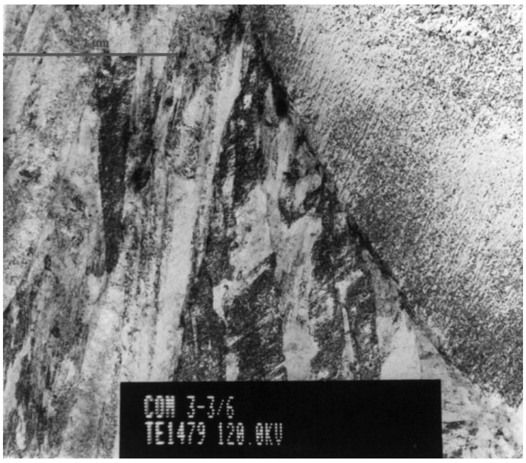

Figure 11: TEM image of specimen 1T
Slika 11: TEM-posnetek vzorca 1T

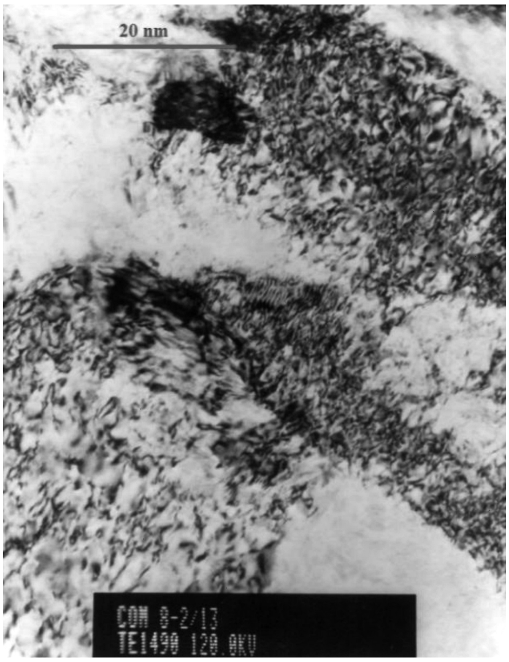

Figure 12: TEM image of specimen 2T
Slika 12: TEM-posnetek vzorca 2T

It seems that both phase transformations occur in the steel during a deep cryogenic treatment: the displacive martensitic transformation and the spinodal decomposition. It can be supposed that the spinodal decomposition occurred predominately in areas enriched with carbon and other alloying elements. Furthermore, the above-described substructures seem to promote the nucleation of very fine carbides during the annealing of the investigated steel.

3 CONCLUSIONS

Tests carried out in this study have shown that a deep cryogenic treatment of the X37CrMoV5-1 (H11) steel has no influence on its tensile strength and notch toughness, but it dramatically improves its resistance to wear at high temperatures (as determined by the pin-on-disc test). However, the length of the holding time at the temperature of the deep cryogenic treatment is crucial. The optimum time appears to be 6 hours. A microstructural observation in a light microscope did not reveal any substantial differences between the specimens hardened in the conventional manner and the specimens after a deep cryogenic treatment. On the other hand, the analysis of specimens upon deep cryogenic treatment by means of transmission electron microscopy found two types of substructure, which are likely to facilitate the precipitation of fine carbides during the final tempering of the steel. At this point, the impact of longer holding times at the deep cryogenic temperature on this substructure has not been analysed. The cause of the decline in the wear resistance with extended holding times cannot thus be determined.

4 REFERENCES

[1] A. Oppenkowski, Cryobehandlung von Werkzeugstahl, PhD thesis, Ruhr-Universität Bochum, 2011

[2] P. Šuchmann, A. Ciski, Enhancing of lifetime of forging dies by means of deep cryogenic treatment, 19th International Forging Congress, Chicago, USA, 2008

[3] F. P. Stratton, Optimizing nano-carbide precipitation in tool steels, Materials Science and Engineering, A449 (**2007**), 809–812

[4] G. R. Tated, R. S. Kajale, K. Iyer, Improvement in tool life of cutting tools by application of deep cryogenic treatment, 7th International Tooling Conference, Torino, Italy, 2006

[5] N. D. Collins, G. O'Rourke, Response of Tool Steels to Deep Cryogenic Treatment, Effect of Alloying Elements, ASM International, Materials Park, OH 1999

[6] N. D. Collins, Deep Cryogenic Treatment of Tool Steels: a Review, Heat Treatment of Metals, (**1996**), 40–42

[7] N. D. Collins, J. Dormer, Deep Cryogenic Treatment of a D2 Cold-Work Tool Steel, Heat Treatment of Metals, (**1997**), 71–74

[8] K. Moore, N. D. Collins, Cryogenic Treatment of Three Heat-Treated Tool Steels, Key Engineering Materials, 86-87 (**1993**), 47–54

[9] D. Das, K. A. Dutta, V. Toppo, K. K. Ray, Effect of deep cryogenic treatment on the carbide precipitation and tribological behavior of D2 steel, Materials and Manufactirung Processes, 22 (**2007**) 4, 474–480

[10] D. Das, K. A. Dutta, K. K. Ray, Correlation of microstructure with wear behavior of deep cryogenically treated AISI D2 steel, Wear, 267 (**2009**) 9–10, 1371–1380

[11] D. Das, K. A. Dutta, V. Toppo, K. K. Ray, Inconsistent wear behavior of cryotreated tool steels: the role of mode and mechanism, Materials Science and Technology, 25 (**2009**) 10, 1249–1257

UDK 519.61/.64:621.785.53:669.017.12
Original scientific article/Izvirni znanstveni članek

ISSN 1580-2949
MTAEC9, 49(1)43(2015)

NUMERICAL PREDICTION OF THE COMPOUND LAYER GROWTH DURING THE GAS NITRIDING OF Fe-M BINARY ALLOYS

NUMERIČNO NAPOVEDOVANJE RASTI SPOJINSKE PLASTI MED PLINSKIM NITRIRANJEM BINARNIH ZLITIN Fe-M

Ramdhane Kouba, Mourad Keddam

Laboratoire de Technologie des Matériaux, Département SDM, Faculté de Génie Mécanique et Génie des Procédés, USTHB BP 32 El-Alia
16111 Alger, Algeria
r_kouba11@yahoo.fr

Prejem rokopisa – received: 2013-10-03; sprejem za objavo – accepted for publication: 2014-01-20

A numerical model was developed to simulate the gas nitriding of Fe-M binary alloys. The suggested model takes into account the nitrogen diffusion in the compound layer and in the diffusion zone as well as the displacement of the (γ'/α) interface. The precipitation of fine MN nitrides in the diffusion zone was also considered during the modelling. A numerical resolution of the problem was done with the front-tracking method via the finite-difference technique. The model was capable of predicting the growth of the γ'-compound layer and also the nitrogen-depth profile.

In order to validate the model, the compound-layer thicknesses obtained with the simulation were compared with those obtained experimentally for the nitrided Fe-Cr binary alloys. Good concordance between the numerical results and the experimental data was noticed.

Keywords: gas nitriding, modelling, compound layer, front-tracking method

Razvit je bil numerični model za simulacijo plinskega nitriranja binarnih zlitin Fe-M. Predlagani model upošteva difuzijo dušika v spojinski plasti in tudi v difuzijski plasti, kot tudi premik stika (γ'/α). Model upošteva tudi izločanje drobnih MN-nitridov v difuzijski coni. Numerična rešitev problema je bila izvršena z uporabo metode sledenja fronte z uporabo tehnike končnih diferenc. Model je sposoben predvidevanja rasti γ' spojinskega sloja in tudi profila dušika v globino.

Za oceno modela je bila pri simulaciji dobljena debelina spojinske plasti primerjana z eksperimentalno dobljeno debelino pri nitriranih binarnih zlitinah Fe-Cr. Ugotovljeno je dobro ujemanje med numeričnimi rezultati in eksperimentalnimi podatki.

Ključne besede: nitriranje v plinu, modeliranje, spojinski sloj, metoda sledenja fronte

1 INTRODUCTION

Gas nitriding is a thermochemical process in which nitrogen atoms diffuse into the material surface after the dissociation of ammonia gas. The nitriding temperature varies between 500 °C and 600 °C with the time duration ranging from a few hours to a few days.

After this treatment, the nitride layers are formed and we can distinguish a compound layer and a diffusion zone. The compound layer, also called the white layer, generally contains two sublayers: the γ' phase, mainly composed of iron nitride (Fe_4N) and the ε phase as Fe_2N_{1-x}. The thickness of the compound layer can reach a value of 50 µm. Beneath the compound layer, the diffusion zone can extend up to a depth of 1200 µm. For binary alloys, the diffusion zone is a ferrite which contains atomic nitrogen dissolved interstitially, with dispersed fine metallic nitrides of the MN type where M is a nitride-forming element. This diffusion zone is responsible for increasing the resistance to fatigue observed after nitriding.

The main objective of modelling nitriding is to quantitatively describe different phenomena occurring during the gas-nitriding treatment. Several models[1–7] were reported in the literature, describing the nitriding process for iron alloys and steels. These models allowed the prediction of the nitriding kinetics and microstructure of the nitrided zone.

Most of these models focus on the diffusion zone, in which nitrogen diffusion takes place simultaneously with the precipitation of the nitrides of the MN type (where M is an alloying element). In the case of steels, the presence of carbides and carbonitrides was also considered in the modelling[5] on the basis of the appropriate thermodynamic data.

However, these models did not take into account the presence of the compound layer, despite the fact that the formation of this layer has an important influence on the properties of a nitrided material. Indeed, the white layer can lead to a significant improvement in tribological and anti-corrosion properties[8]. In the case of the nitriding of steels, it has been shown that the microstructure of the compound layer has an influence on the hardening depth in the diffusion zone[9]. With respect to these considerations, it is interesting to include this layer in the modelling.

The prediction of the nitriding process including several phases (ε, γ' and α) was already achieved for the case of nitrided pure iron. This modelling was performed analytically and reported on in[10–13], while the numerically performed modelling was described in[14–18]. However, a corresponding model of nitriding a multi-component system, such as Fe-M binary alloys and steels, is not yet available.

The main objective of the present work is to present such a model, relating to the gas nitriding of a Fe-M binary alloy. However, the numerical approach developed in the present work only deals with a single compound layer consisting of γ' nitride.

2 MATHEMATICAL FORMULATION OF THE MODEL

During the gas nitriding of pure iron and binary alloys or even steels, the formation of the compound layer depends on the operating parameters, particularly, the nitriding potential r_N (see references[15,16] for further details). In fact, three configurations are possible:

- the absence of the compound layer (and therefore the treatment is completed in the ferritic phase)
- the compound zone with a single-phase γ'
- the compound zone with a dual-phase (ε/γ').

In the present work, the aim was to simulate the nitriding process with the presence of only γ' in the compound zone. Therefore, the chosen value of r_N must correspond to this configuration according to the Lehrer diagram[16].

During the nitriding treatment, if the thermodynamic conditions are satisfied, γ' precipitates appear in the vicinity of the external surface if the solubility limit of nitrogen in ferrite is reached. Thereafter, the γ' phase tends to grow at the expense of the ferrite. This phase transformation ($\alpha \rightarrow \gamma$') involves a displacement of the (γ'/α) interface.

A diffusion problem, with one or more moving boundaries, is commonly called the Stefan problem. Its solving is usually performed with the use of one of the front-tracking methods.

In[19–22] several models based on this approach are presented in order to simulate phase transformations in metals and alloys. The model presented in[20] was implemented in the DICTRA software and used to simulate the nitriding process in a Fe-N system[13,14].

In the present work, a new front-tracking method is presented considering both the long-range diffusion in the diffusion zone and the interstitial diffusion of nitrogen within the iron nitrides. The nitrogen diffusion takes place simultaneously with the advancement of the (γ'/α) nterface.

It should be noted that the diffusion of heavy elements (Fe, M) was neglected as the nitrogen diffusion controls the growth of the compound layer. This hypothesis has already been adopted by several authors[1–7].

The main objective of the present model is to simulate the growth of the γ' layer at the expense of ferrite. However, in the diffusion zone, the nitrogen diffusion occurs simultaneously with the precipitation of MN nitrides which also affect the growth kinetics of the γ' layer. For this reason, this precipitation phenomenon was also included in the modelling.

After the γ' phase is precipitated, the problem can be represented schematically as shown in **Figure 1**, where the two phases, γ' and α, are henceforth adjacent. At any time t, the position of the interface (γ'/α) is represented by the distance λ from the origin (z = 0) which corresponds to the (γ'/gas) interface.

The nitrogen diffusion in each phase is governed by the Fick's second law. The system of Equations 1 and 2 can be established in the one-dimensional space as:

$$\frac{\partial N_{\gamma'}}{\partial t} = \frac{\partial}{\partial z}\left(D_{\gamma'}(N_{\gamma'})\frac{\partial N_{\gamma'}}{\partial z}\right) \quad \text{in the } \gamma' \text{ phase} \qquad (1)$$

$$\frac{\partial N_{\alpha}}{\partial t} = \frac{\partial}{\partial z}\left(D_{\alpha}(N_{\alpha})\frac{\partial N_{\alpha}}{\partial z}\right) \quad \text{in the } \alpha \text{ phase} \qquad (2)$$

where $N_{\gamma'}$ and N_α represent, respectively, the nitrogen concentrations in the γ' and α phases. These concentrations are expressed as the numbers of moles per unit volume and they are dependent on the depth (z) and time (t). The nitrogen amount can also be expressed as a nitrogen mole fraction ($X_{\gamma'}$, X_α) using the relations: $N_{\gamma'} = X_{\gamma'}/V_{\gamma'}$ and $N_\alpha = X_\alpha / V_\alpha$, where $V_{\gamma'}$ and V_α are the molar volumes of the two phases that are considered independent of the compositions. The concentration may also be converted into mass fractions.

$D_{\gamma'}(N_{\gamma'})$ and $D_\alpha(N_\alpha)$ are defined as the nitrogen diffusion coefficients dependent on the N amount.

During the incremental time dt the interface position advances with the value of dλ. In order to conserve the number of nitrogen moles and considering the nitrogen flux arriving at the interface and the nitrogen flux leaving the interface, the following balance equation can be established (Equation 3):

$$(X_{\gamma'\alpha} - X_{\alpha\gamma'})\frac{v}{V_{\gamma'}} = \left[-D_{\gamma'}\frac{\partial N_{\gamma'}}{\partial z}\right]_{z=\lambda} - \left[-D_{\alpha}\frac{\partial N_{\alpha}}{\partial z}\right]_{z=\lambda} \qquad (3)$$

Where v is the interface velocity expressed as v = dλ/dt.

The terms $X_{\alpha\gamma'}$ and $X_{\gamma'\alpha}$ are the nitrogen molar fractions at the interface of the two phases, α and γ', respectively (refer to **Figure 1**). It is assumed that the thermodynamic equilibrium is continuously established between the two phases, α and γ' at the considered interface. So, $X_{\alpha\gamma'}$ and $X_{\gamma'\alpha}$ can be read from the corresponding phase diagram.

The diffusion problem with the moving boundaries is then governed by the set of three partial differential equations (Equations 1, 2 and 3). The solving of the problem of interest requires the knowledge of the following boundary conditions:

In the external surface (z = 0), the nitrogen concentration in γ' is considered constant (N_s) corresponding to the equilibrium between γ' and the gas mixture. Therefore, at $z = 0$, $N_{\gamma'}(0,t) = N_s$, at $z = \lambda$, $N_{\gamma'}(\lambda,t) = N_{\gamma'\alpha}$ and $N_\alpha(\lambda,t) = N_{\alpha\gamma'}$.

For greater depths (i.e., $z > 1200$ µm), this zone corresponds to the non-nitrided core where the nitrogen amount in the matrix is neglected. Therefore, at $z = +\infty$, $N_\alpha(\infty,t) = 0$.

3 NUMERICAL SOLVING OF THE PROBLEM

The finite-difference method is used to solve the problem of the nitrogen diffusion with a moving boundary. For this purpose, the zones occupied by both phases, γ' and α, are divided into the cells with thicknesses $\Delta z_{\gamma'}$ and Δz_α, respectively, as shown in **Figure 1**. Two adjacent cells are separated by a node. It is assumed that at time t, the number of nodes in the γ' phase is $n_{\gamma'}$ and in α it is n_α (the numbers of cells in both phases will then be $(n_{\gamma'} - 1)$ and $(n_\alpha - 1)$, respectively).

The thicknesses of all the cells are kept constant except for the last cell in γ' and the first cell in the α phase, which are considered as time-dependent during the simulation process (**Figure 1**). Indeed, as the interface advances, there is an expansion of the left cell and shrinkage of the one on the right. By introducing these two variable cells, it becomes possible to follow the progress of the γ'/α interface during the numerical calculation as explained below.

When using the finite-difference method, the time is also discretized with an equal time step (Δt). The solution is assumed to be known at time t, then it is calculated at the next time step ($t + \Delta t$). At the instant t, the nitrogen concentration in each node is known for both γ' and α and so are the sizes of the two variable cells, $d_{\gamma'}(t)$ and $d_\alpha(t)$.

In order to determine these values at time ($t + \Delta t$), the process can be divided in two steps: first, a diffusion step where the nitrogen diffusion occurs in γ' and α by considering the displacement of the (γ'/α) interface.

In the diffusion step, the resolution consists of separate solutions of diffusion Equations 1 and 2 in their corresponding areas. This allows a determination of the nitrogen concentration profile for the whole nitrided zone.

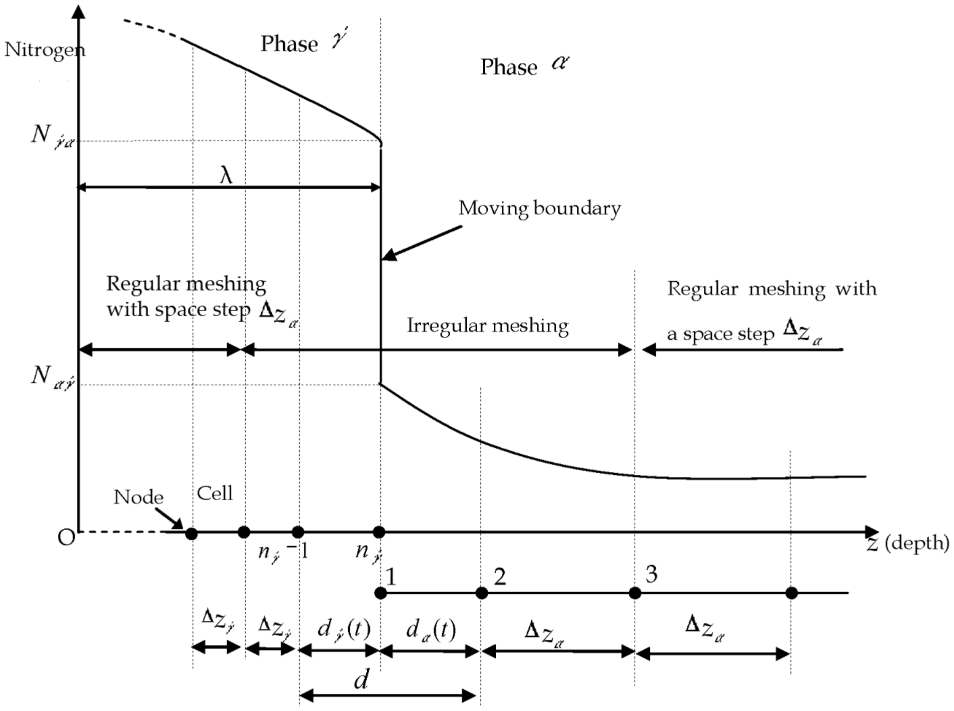

Figure 1: Schematic diagram illustrating the problem of nitriding with the presence of γ'as the compound layer. In order to carry out a numerical resolution, the zone occupied by the two phases, γ' and α, is divided into small cells. Two adjacent cells are separated by a node also called a grid point. It is supposed that the number of nodes is equal to $n_{\gamma'}$ and n_α in the γ' phase and α phase, respectively. In order to consider the displacement of the interface, the thicknesses of the last cell in γ' and the first cell in α are considered variable during the process. When the cell on the right-hand side dilates, the left one shrinks, while the sum ($d_{\gamma'} + d_\alpha$) remains constant being equal to d.

It should be noted that all the nodes of the grid are immobile, except for the last node in γ' and the first one in α, which are mobile. At the interface, the N concentration is kept constant in both phases with the values of $N_{\gamma'\alpha}$ and $N_{\alpha\gamma'}$. The corresponding N mole fractions (i.e., $X_{\gamma'\alpha}$ and $X_{\alpha\gamma'}$) can be read from the phase diagram.

Slika 1: Shematski prikaz problema pri nitriranju s prisotnostjo spojinske plasti γ'. Za numerično resolucijo je bila plast, v kateri sta dve fazi, γ' in α, razdeljena v majhne celice. Dve sosednji celici sta ločeni z vozlom oz. točko v mreži. Predvideva se, da je število vozlov enako $n_{\gamma'}$ in n_α v γ'-fazi in α-fazi. Da bi upoštevali premik stične ploskve, se kot spremenljivki v procesu vzameta debelina zadnje celice v γ' in prve celice v α. Medtem ko se celica na desni strani širi, se na levi oži. Medtem pa vsota ($d_{\gamma'} + d_\alpha$) ostaja konstantna in je enaka d.

Treba je omeniti, da so vsi vozli v mreži nemobilni, razen zadnjega vozla v γ' in prvega v α, ki sta mobilna. Na stiku je koncentracija N konstantna v obeh fazah z vrednostima $N_{\gamma'\alpha}$ in $N_{\alpha\gamma'}$ Ustrezni molski delež N (to je $X_{\gamma'\alpha}$ in $X_{\alpha\gamma'}$) se prebere iz faznega diagrama.

In order to solve the diffusion equation in γ' using the finite-difference technique, Equation 1 is rewritten in the following form:

$$\frac{\partial N_{\gamma'}}{\partial t} = D_{\gamma'}(N_{\gamma'})\frac{\partial^2 N_{\gamma'}}{\partial z^2} + \left(\frac{\partial D_{\gamma'}(N_{\gamma'})}{\partial z}\right)\left(\frac{\partial N_{\gamma'}}{\partial z}\right) \tag{4}$$

When the implicit scheme is used, a relation between the unknown nitrogen concentrations in three successive nodes (i – 1, i and i + 1) can be found. This is done simply by replacing the partial derivatives, which appear in Equation 4, with their corresponding finite differences[23,24]. The following relation can be established:

$$\begin{aligned} &A_i N_{\gamma'}(i-1, t+\Delta t) + B_i N_{\gamma'}(i, t+\Delta t) + C_i N_{\gamma'}(i+1, t+\Delta t) = \\ &= N_{\gamma'}(i,t) \quad 2 \le i \le n_{\gamma'} - 2 \end{aligned} \tag{5}$$

The values for A_i, B_i and C_i are obtained with the following expressions:

$$A_i = \frac{\left[D_{\gamma'}(i+1) - D_{\gamma'}(i+1) - 4D_{\gamma'}(i)\right]\Delta t}{4(\Delta z_{\gamma'})^2}$$

$$B_i = 1 + \frac{2D_{\gamma'}(i)\Delta t}{(\Delta z_{\gamma'})^2}$$

$$C_i = -\frac{\left[D_{\gamma'}(i+1) + D_{\gamma'}(i+1) + 4D_{\gamma'}(i)\right]\Delta t}{4(\Delta z_{\gamma'})^2}$$

Obviously, the diffusion coefficient $D_{\gamma'}$ changes along the depth, so the term $D_{\gamma'}(i)$ corresponds to its value at the node i. The variation of the diffusion coefficient in γ' with the nitrogen amount is described in **Appendix 1**.

Equation 5 is valid for a regular meshing with the same cell size, $\Delta z_{\gamma'}$. However, in the vicinity of the γ'/α interface, due to the presence of the variable cell, the mesh is irregular. Therefore, the relation between the N concentrations in the last three nodes in γ' is not given by Equation 5. An equivalent equation can be obtained by replacing partial derivatives with finite differences in Equation 4 as follows:

$$\begin{aligned} \left.\frac{\partial^2 N_{\gamma'}}{\partial z^2}\right|_{z=z_{n\gamma'-1}} &= \frac{2N_{\gamma'}(n_{\gamma'}-2, t+\Delta t)}{\Delta z_{\gamma'}\left[d_{\gamma'} + \Delta z_{\gamma'}\right]} - \\ &- \frac{2N_{\gamma'}(n_{\gamma'}-1, t+\Delta t)}{\Delta z_{\gamma'} d_{\gamma'}} + \frac{2N_{\gamma'}(n_{\gamma'}, t+\Delta t)}{d_{\gamma'}\left[d_{\gamma'} + \Delta z_{\gamma'}\right]} \end{aligned} \tag{6}$$

$$\left.\frac{\partial N_{\gamma'}}{\partial z}\right|_{z=z_{n\gamma'-1}} = \frac{N_{\gamma'}(n_{\gamma'}, t+\Delta t) - N_{\gamma'}(n_{\gamma'}-2, t)}{d_{\gamma'} + \Delta z_{\gamma'}} \tag{7}$$

$$\left.\frac{\partial D_{\gamma'}}{\partial z}\right|_{z=z_{n\gamma'-1}} = \frac{D_{\gamma'}(n_{\gamma'}) - D_{\gamma'}(n_{\gamma'}-2)}{d_{\gamma'} + \Delta z_{\gamma'}} \tag{8}$$

$$\left.\frac{\partial N_{\gamma'}}{\partial t}\right|_{z=z_{n\gamma'-1}} = \frac{N_{\gamma'}(n_{\gamma'}-1, t+\Delta t) - N_{\gamma'}(n_{\gamma'}-1, t)}{\Delta t} \tag{9}$$

By substituting these relations (6 to 9) in Equation 4, Equation 10 can be obtained as follows:

$$\begin{aligned} &A_{n_{\gamma'}-1} N_{\gamma'}(n_{\gamma'}-2, t+\Delta t) + B_{n_{\gamma'}-1} N_{\gamma'}(n_{\gamma'}-1, t+\Delta t) + \\ &+ C_{n_{\gamma'}-1} N_{\gamma'\alpha} = N_{\gamma'}(n_{\gamma'}-1, t) \end{aligned} \tag{10}$$

$$A_{n_{\gamma'}-1} = \left[\frac{D_{\gamma'}(n_{\gamma'}) - D_{\gamma'}(n_{\gamma'}-2)}{(d_{\gamma'} + \Delta z_{\gamma'})^2} - \frac{2D_{\gamma'}(n_{\gamma'})}{\Delta z_{\gamma'}(d_{\gamma'} + \Delta z_{\gamma'})}\right]\Delta t$$

$$B_{n_{\gamma'}-1} = 1 + \frac{2D_{\gamma'}(n_{\gamma'})\Delta t}{\Delta z_{\gamma'} d_{\gamma'}}$$

$$C_{n_{\gamma'}-1} = \left[\frac{D_{\gamma'}(n_{\gamma'}-2) - D_{\gamma'}(n_{\gamma'})}{(d_{\gamma'} + \Delta z_{\gamma'})^2} - \frac{2D_{\gamma'}(n_{\gamma'})}{\Delta z_{\gamma'}(d_{\gamma'} + \Delta z_{\gamma'})}\right]\Delta t$$

Equations 5 and 10 represent a set of ($n_{\gamma'}$ – 2) equations with ($n_{\gamma'}$ – 2) unknowns. In order to determine the nitrogen concentrations in the nodes at time (t + Δt) this set of equations must be solved using the tridiagonal matrix algorithm (TDMA)[23].

The same analysis can be applied for the numerical solution of the diffusion equation in the ferritic phase (Equation 2). However, it was shown in several references[15–18] that the dependence of the diffusion coefficient on the composition of ferrite is weak. So, in the present paper, a constant value for diffusivity is adopted and noted as D_α.

The following relation can be established for the first three nodes in the ferritic phase (irregular mesh, similar to Relation 10):

$$\begin{aligned} &A_2^\alpha N_{\alpha\gamma'} + B_2^\alpha N_\alpha(2, t+\Delta t) + \\ &+ C_2^\alpha N_\alpha(3, t+\Delta t) = N_\alpha(2,t) \end{aligned} \tag{11}$$

$$A_2^\alpha = \frac{-2D_\alpha \Delta t}{d_\alpha(d_\alpha + \Delta z_\alpha)}, \quad B_2^\alpha = 1 + \frac{2D_\alpha \Delta t}{\Delta z_\alpha d_\alpha},$$

$$C_2^\alpha = \frac{-2D_\alpha \Delta t}{\Delta z_\alpha(d_\alpha + \Delta z_\alpha)}$$

For the other nodes (for i = 2 to n_α – 1) a relationship similar to (5) can be given:

$$\begin{aligned} &-r_\alpha N_\alpha(i-1, t+\Delta t) + (1+2r_\alpha)N_\alpha(i, t+\Delta t) - \\ &-r_{\alpha'} N_\alpha(i+1, t+\Delta t) = N_\alpha(i,t) \end{aligned} \tag{12}$$

where $r_\alpha = \dfrac{D_\alpha \Delta t}{(\Delta z_\alpha)^2}$

As for the γ' phase, the resolution of the set of Equations 11 and 12 indicates the nitrogen concentration in each node of the ferritic phase at time (t + Δt).

4 CONSIDERING THE DISPLACEMENT OF THE (γ'/α) INTERFACE

After the diffusion step, the nitrogen concentration in both phases is modified. The change in the nitrogen profile leads to a displacement of the corresponding interface so that the nitrogen-amount balance is conserved.

Equation 3 which gives the interface velocity must then be included into the resolution.

The main feature associated with the present model and compared to most of the other front-tracking methods (given, for example, in[19–21]) is the inclusion of the diffusion near the interface. The diffusion process near the interface region was already considered in the modelling from reference[22]. In the present work, the simplest method is used to take this phenomenon into account. For this purpose, it is supposed that the interface is governed not only by Relation 3 but also by Diffusion Equations 1 and 2. In fact, near the interface, the three partial differential equations, 1, 2 and 3, are solved simultaneously.

The technique used in the resolution consists of replacing the partial derivatives with their finite differences. But at this time, the sizes of variable cells are time-dependent and are still unknown at $t + \Delta t$.

For example, to get the diffusion equation for γ', in the finite-difference form near the interface, (according to an implicit scheme), we simply substitute Relations 6 to 9 into 4 given that the term $d_{\gamma'}$ is considered at the time $t + \Delta t$ and not at t. The following equation can be obtained:

$$\begin{aligned}&\frac{N_{\gamma'}(n_{\gamma'}-1,t+\Delta t)-N_{\gamma'}(n_{\gamma'}-1,t)}{\Delta t}=2D_{\gamma'}(n_{\gamma'}-1)\cdot\\&\left\{\frac{N_{\gamma'}(n_{\gamma'}-2,t+\Delta t)}{\Delta z_{\gamma'}\left[d_{\gamma'}(t+\Delta t)+\Delta z_{\gamma'}\right]}-\frac{N_{\gamma'}(n_{\gamma'}-1,t+\Delta t)}{\Delta z_{\gamma'}d_{\gamma'}(t+\Delta t)}\cdot\right.\\&\left.\cdot\frac{N_{\gamma'\alpha}}{d_{\gamma'}(t+\Delta t)\left[d_{\gamma'}(t+\Delta t)+\Delta z_{\gamma'}\right]}\right\}+\\&\frac{\left[N_{\gamma'\alpha}-N_{\gamma'}(n_{\gamma'}-2,t+\Delta t)\right]\cdot\left[D_{\gamma'}(n_{\gamma'})-D_{\gamma'}(n_{\gamma'}-2)\right]}{\left[d_{\gamma'}(t+\Delta t)+\Delta z_{\gamma'}\right]^2}\end{aligned}\tag{13}$$

It should be noted that this relationship is similar to 10, but in this case $d_{\gamma'}$ is still unknown at the $(t + \Delta t)$ instant.

Similarly, the diffusion Equation 2 can be written near the interface as finite differences. Then the following relation can be established:

$$\begin{aligned}&\frac{N_\alpha(2,t+\Delta t)-N_\alpha(2,t)}{\Delta t}=\\&=2D_\alpha\left\{\frac{N_{\alpha\gamma'}}{d_\alpha(t+\Delta t)\left[d_\alpha(t+\Delta t)+\Delta z_\alpha\right]}-\frac{N_\alpha(2,t+\Delta t)}{\Delta z_\alpha d_\alpha(t+\Delta t)}+\right.\\&\left.+\frac{N_\alpha(3,t+\Delta t)}{\Delta z_\alpha\left[d_\alpha(t+\Delta t)+\Delta z_\alpha\right]}\right\}\end{aligned}\tag{14}$$

The thickness of the shrinking cell $d_\alpha\,(t + \Delta t)$ is not an independent variable, but it is related to $d_{\gamma'}(t + \Delta t)$ with the following relation (**Figure 1**):

$$d_\alpha(t+\Delta t)=d-d_{\gamma'}(t+\Delta t)\tag{15}$$

By substituting Equation 15 into 14, the discrete form of Equation 2 can be given near the interface as follows:

$$\begin{aligned}&\frac{N_\alpha(2,t+\Delta t)-N_\alpha(2,t)}{\Delta t}=\\&=2D_\alpha\left\{\frac{N_{\alpha\gamma'}}{\left[d-d_{\gamma'}(t+\Delta t)\right]\cdot\left[d-d_{\gamma'}(t+\Delta t)+\Delta z_\alpha\right]}-\right.\\&\left.-\frac{N_\alpha(2,t+\Delta t)}{\Delta z_\alpha\left[d-d_{\gamma'}(t+\Delta t)\right]}+\frac{N_\alpha(3,t+\Delta t)}{\Delta z_\alpha\left[d-d_{\gamma'}(t+\Delta t)+\Delta z_\alpha\right]}\right\}\end{aligned}\tag{16}$$

Finite differences are also determined in the case of Equation 3 and the following relations can then be written:

$$\left.\frac{\partial N_{\gamma'}}{\partial z}\right|_{z=\lambda}=\frac{N_{\gamma'\alpha}-N_{\gamma'}(n_{\gamma'}-1,t+\Delta t)}{d_{\gamma'}(t+\Delta t)}\tag{17}$$

$$\left.\frac{\partial N_\alpha}{\partial z}\right|_{z=\lambda}=\frac{N_\alpha(2,t+\Delta t)-N_{\alpha\gamma'}}{d_\alpha(t+\Delta t)}\tag{18}$$

In order to write the derivative $\mathrm{d}\lambda/\mathrm{d}t$ as a finite difference, it is worth noting that the change in the position of the interface is related only to the change in the expanding cell size. So, the following relation can be written:

$$\frac{\mathrm{d}\lambda}{\mathrm{d}t}=\frac{\mathrm{d}(d_{\gamma'})}{\mathrm{d}t}=\frac{d_{\gamma'}(t+\Delta t)-d_{\gamma'}(t)}{\Delta t}\tag{19}$$

Substituting these three last relations (17, 18 and 19) into Equation 3, the following relation can be obtained:

$$\begin{aligned}&d_{\gamma'}(t+\Delta t)-d_{\gamma'}(t)=\frac{\Delta t V_{\gamma'}}{(X_{\gamma'\alpha}-X_{\alpha\gamma'})}\cdot\\&\cdot\left\{D_{\gamma'}(n_{\gamma'})\frac{N_{\gamma'}(n_{\gamma'}-1,t+\Delta t)-N_{\gamma'\alpha}}{d_{\gamma'}(t+\Delta t)}-D_\alpha\frac{N_{\alpha\gamma'}-N_\alpha(2,t+\Delta t)}{\left[d-d_{\gamma'}(t+\Delta t)\right]}\right\}\end{aligned}\tag{20}$$

The above analysis has finally led to the set of three nonlinear equations (13, 16 and 20) with the following unknowns: $d_{\gamma'}(t + \Delta t)$, $N_{\gamma'}(n_{\gamma'} - 1,t + \Delta t)$ and $N_{\gamma'}(2,t + \Delta t)$. So, after the diffusion step, the consideration of the interface displacement is performed by solving this set of equations in order to determine the corresponding unknowns. The resolution requires the use of an iterative algorithm with the Newton-Raphson method.

Once the resolution is achieved (i.e., $d_{\gamma'}(t + \Delta t)$ is calculated), the interface position at the time $(t + \Delta t)$ can be determined from Equation 21:

$$\lambda(t+\Delta t)=\lambda(t)+d_{\gamma'}(t+\Delta t)-d_{\gamma'}(t)\tag{21}$$

The term $\Delta\lambda = d_{\gamma'}(t + \Delta t) - d_{\gamma'}(t)$ represents the advancement of the interface during a time step.

The thickness of the shrinking cell is also calculated by using Relation 15.

The two steps of the resolution (i.e., the nitrogen diffusion and the interface displacement) are afterwards repeated for the next time step.

It should be mentioned that the nitrogen concentration in the first neighbouring nodes of the interface (i.e., $N_{\gamma'}(n_{\gamma'} - 1, t + \Delta t)$ and $N_{\gamma'}(2, t + \Delta t)$ is computed in both diffusion step and interface-displacement step. For the next time step, only the values resulting from the interface-displacement analysis are retained.

During the simulation process, there is an expansion of the left cell and shrinkage of the one on the right. However, this process cannot continue indefinitely and the remeshing may become necessary if $d_{\gamma'}$ is too large or d_α becomes too small. So, the two following criteria have been adopted: The expanding cell splits into two cells if its size becomes 1.5 times greater than the original size. This division is performed by inserting a new node inside the cell. The nitrogen concentration in the new node is obtained with a linear interpolation from the concentration in the neighbouring nodes. Similarly, if the shrinking cell reaches half of its original size, a grid point is removed from α in order to increase d_α to its initial value. It can be seen that when the simulation process is performed, there is a creation of nodes and cells in phase γ' and a disappearance of others in α.

5 APPLICATION OF THE MODEL FOR THE NITRIDED Fe-M BINARY ALLOYS

In fact, the configuration presented in **Figure 1** does not appear at the first instant at the beginning of the nitriding process, but there is a period of nitrogen enrichment in the ferrite which precedes the formation of the compound layer.

This incubation time is more important when the M alloying element is present in the ferritic matrix because of the consumption of a large amount of nitrogen in the MN nitride precipitation. In addition, if the nitriding potential r_N is not too high, as assumed in the present work, the incubation time is even longer[25]. For these reasons, the early stage of the process, which takes place completely in the ferritic phase, must be considered.

Before the γ' formation, the diffusion of nitrogen is carried out exclusively in the ferrite zone according to Equation 2. In this case, at $z = 0$, there is a ferrite/gas contact. The transfer of nitrogen from the gas mixture to the metal is expressed with the following relationship:

At $z = 0$,

$$-D_\alpha \left.\frac{\partial N_\alpha}{\partial z}\right|_{z=0} = K_\alpha \left[N_{\mathrm{eq}\alpha} - N_\alpha(0,t) \right] \qquad (22)$$

Equation 22 is obtained by considering a thermodynamic equilibrium between the solid (the α phase) and the gas mixture. The term $N_{eq\alpha}$ indicates the nitrogen concentration in ferrite at the thermodynamic equilibrium between α and the gas mixture. $N_\alpha(0,t)$ represents the actual concentration at the surface and K_α is the kinetic constant. Equation 22 is regarded as an external boundary condition when solving the diffusion problem in the preliminary stage.

The nitriding process during the preliminary stage can be regarded as the nitrogen diffusion in one phase (ferrite) coupled to the precipitation of fine MN nitrides. The details of the calculation procedure are given in[1]. After the diffusion step which causes a modification of the nitrogen profile, a test of the MN precipitation is realized at each depth using the solubility-product method. So, the amount of the nitrogen precipitated as MN and the quantity which remains dissolved in the ferrite can be calculated. It is also possible to determine the proportion of M consumed by the precipitation and the residual part dissolved in the matrix[1].

The nitrogen transfer from the gas mixture to the sample, according to Equation 22, means that the N concentration in the ferrite at $z = 0$ increases with time. The formation of γ' takes place when the surface concentration reaches the solubility limit of the nitrogen in ferrite. Therefore, the condition of the precipitation of γ' on the top of α, at $z = 0$, is satisfied if: $N_\alpha(0,t) \geq N_{\alpha\gamma'}$. This test is performed for each time step during the calculation process in the preliminary stage.

It should be noted that the kinetic considerations related to the γ' nucleation have been neglected which makes the formation of the compound layer take place as soon as the nitrogen solubility limit is reached.

Subsequently, a small γ' layer with a thickness not exceeding 0.1 µm is inserted at the top of the first cell of α having an initial thickness of 1 µm.

The introduction of a small thickness of the γ' layer is the beginning of the diffusion problem with a moving boundary. Thereafter, the front-tracking solving process is conducted as explained in detail in Sections 3 and 4.

However, when solving a diffusion problem with moving boundaries for binary alloys, there is not just the nitrogen diffusion in the phase (ferrite) on the right, but

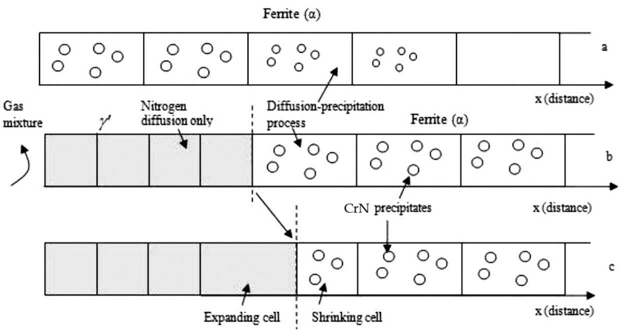

Figure 2: Schematic diagram illustrating a full simulation of nitriding Fe-Cr alloys. The diagram shows the formation of CrN precipitates and evolution of the variable cell size: a) during the early stage, b) after the formation of the compound layer (at time t_1), c) for a time $t_2 > t_1$

Slika 2: Shematski prikaz polne simulacije nitriranja zlitin Fe-Cr. Diagram prikazuje nastanek izločkov CrN in razvoj spremenljivke velikosti celic: a) v začetni fazi, b) po nastanku spojinske plasti (v času t_1), c) za čas $t_2 > t_1$

also the precipitation of MN nitrides which continues to occur after the γ' formation. The precipitation of MN nitrides is considered during the simulation in the same way as in the preliminary stage.

A schematic illustration of a full simulation of the gas nitriding of Fe-M binary alloys is shown in **Figure 2**. A general scheme giving different steps of the calculation is presented in **Figure 3**. A computer code written in the MATLAB language was used to achieve the numerical resolution and the necessary data for the implementation of the simulation are presented and discussed in **Appendix 2**.

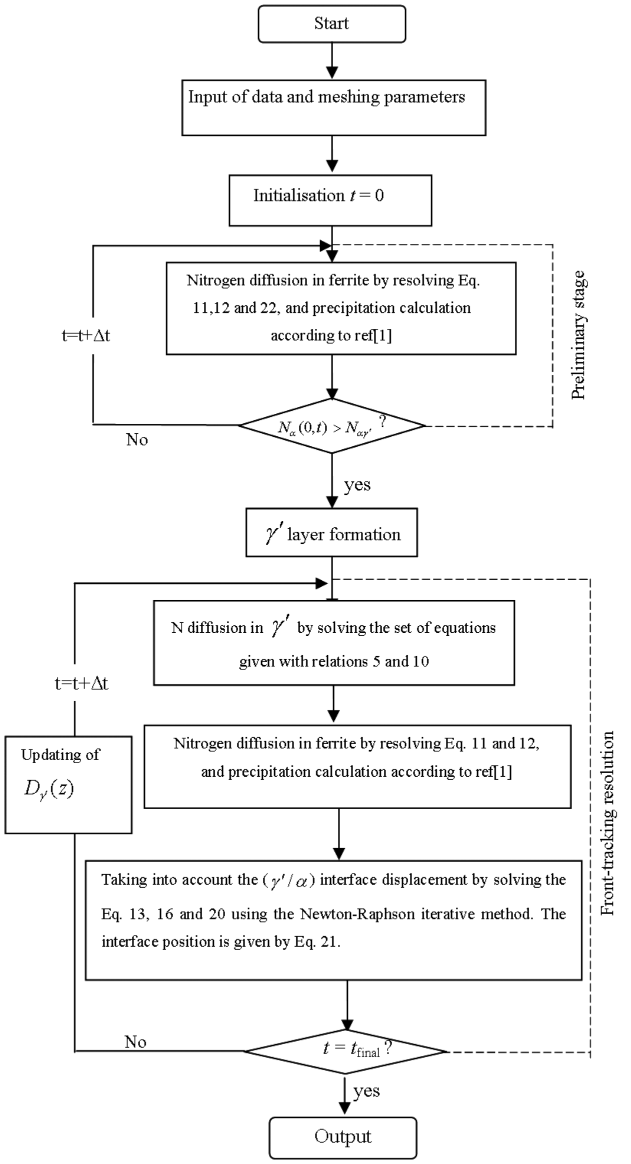

Figure 3: Flow chart showing a global scheme of the simulation of the nitriding process

Slika 3: Diagram prikazuje celotno shemo simulacije poteka postopka nitriranja

6 SIMULATION RESULT

Before presenting the results of the model for nitriding Fe-Cr binary alloys, the model was first applied to a Fe-N binary system. The case of nitriding pure iron is quite interesting since the analytical solution of the problem is already available[10–12]. Therefore, a comparison between the results of the analytical model[11] and those obtained with the present work for Cr % = 0 is possible. For this purpose, a constant diffusion coefficient was adopted for γ' instead of the composition-dependent diffusivity. The same data, used in[11], was adopted for the numerical resolution and the incubation time was also ignored.

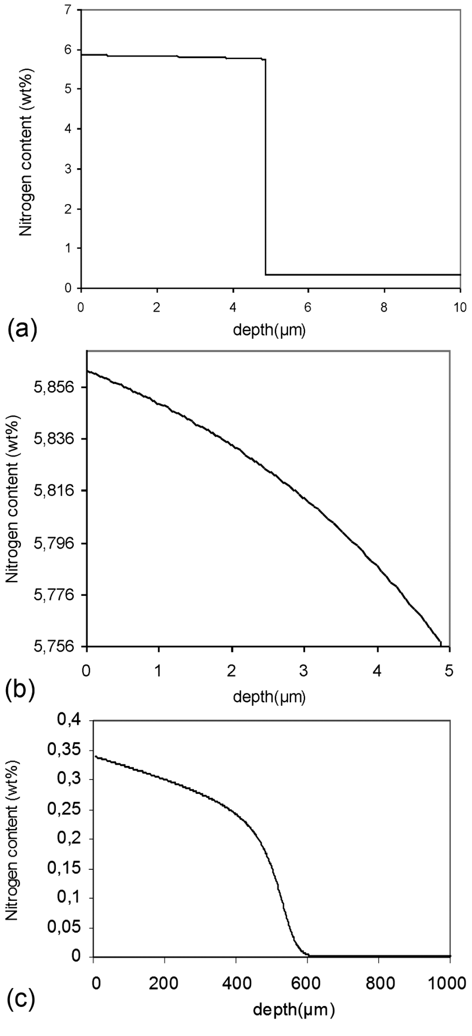

Figure 4: Results given by the model for the nitriding of Fe – 1 % Cr binary alloy for the given nitriding conditions: T = 550 °C, r_N = 0.7 bar$^{-1/2}$, time = 16 h: a) nitrogen-concentration profile for the compound layer and the beginning of the diffusion zone, b) profile of nitrogen inside the compound layer, c) total nitrogen profile for the diffusion zone

Slika 4: Rezultati, ki jih da model za nitriranje binarne zlitine Fe – 1 % Cr v danih razmerah nitriranja: T = 550 °C, r_N = 0,7 bar$^{-1/2}$, trajanje = 16 h: a) profil koncentracije dušika v spojinski plasti in začetek difuzijske cone, b) profil koncentracije dušika v spojinski plasti, c) skupni profil dušika v difuzijski coni

It is noticed that the numerical solution converges towards the analytical one provided that the spatial and temporal discretization steps are as small as possible. Indeed, the following parameters ($\Delta z_{\gamma'}$ = 0.1 μm, Δz_{α} = 0.1 μm and Δt = 0.1 s) provide a good accuracy. These parameters were adopted for all the numerical calculations done in the present study. A good agreement between the numerical and analytical results represents, in fact, the first step in the validation of the model.

Figure 4a shows the simulated nitrogen-concentration profiles through the γ' layer and the beginning of the diffusion zone obtained after nitriding the Fe – 1 % Cr binary alloys (for the following conditions: T = 550 °C, K_N = 0.7 bar$^{-1/2}$ and t = 16 h).

For the compound layer, despite the narrow composition range, **Figure 4b** shows that the profiles are not linear, in contrast to the assumption made in[15].

Figure 4c shows the total nitrogen profile within the diffusion zone. The major part of nitrogen is in the form of the CrN precipitate. The results are the same as those obtained in[1].

In this last reference[1], the experimental nitrogen profile fits well with the simulation results despite the fact that some aspects of the problem were not taken into account (for example, the nitrogen excess and the nucleation and growth kinetic of the formation of MN precipitates). These considerations can be seen as part of the validation of the present model with respect to the diffusion zone as long as the same solubility product K_{CrN} is used.

Figure 5 shows, for the same alloy and for two different temperatures (520 °C and 550 °C) the evolution of simulated compound-layer thickness versus time. In this figure, it is possible to deduce the corresponding values of incubation times, and to confirm the parabolic regime of the growth law of the γ' layer.

In the same figure, the growth of the γ' layer in the case of the Fe-N system (w(Cr) = 0 %) is also presented.

It can be seen that the presence of alloying element Cr slows down the growth of the compound layer. This result can be attributed to the CrN precipitation. Indeed, on the one hand, the precipitation reaction near the outer surface during the preliminary phase delays the formation of iron nitrides by increasing the corresponding incubation time. On the other hand, the CrN precipitation accentuates the nitrogen concentration gradient in the ferrite near the interface (on the right-hand side) because of the consumption of a large amount of nitrogen initially dissolved in the ferrite. Thereafter, the nitrogen flux leaving the interface is increased which leads to a reduction in the interface velocity.

7 EXPERIMENTAL VALIDATION OF THE MODEL

In order to validate the model, nitriding experiments were carried out on the Fe – 1 % Cr binary alloy. The measurements of the compound-layer thicknesses were subsequently realized with the purpose of comparing them with the simulated results.

The samples of the Fe – 1 % Cr alloy were gas nitrided in the laboratory nitriding furnace at 520 °C and 550 °C during different treatment times for the same nitriding potential (K_N = 0.7 bar$^{-1/2}$). The identification of the phases formed after nitriding was performed using X-ray diffraction. The measurements of the thicknesses were performed using a scanning electron microscope at different locations of the cross-sections of the nitrided samples. The mean value of the compound-layer thickness was then taken from different measurements.

Figure 6 shows a micrograph of the nitrided zone, where one can distinguish the compound layer and the beginning of the diffusion zone. **Figure 7** shows the X-ray diffraction pattern of the gas-nitrided sample at T

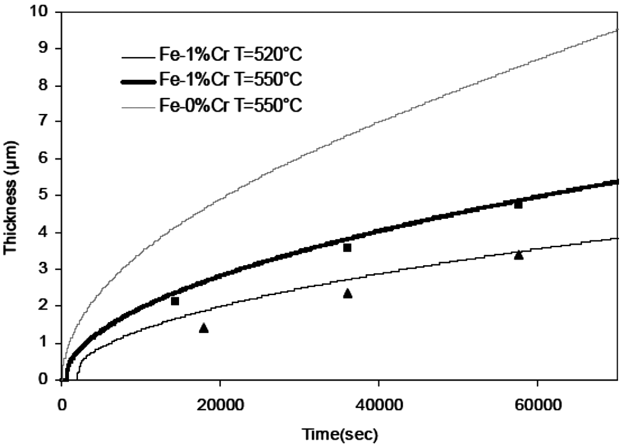

Figure 5: Comparison between the γ' layer thicknesses obtained with the model (curve) and those measured experimentally (marks) for r_N = 0.7 bar$^{-1/2}$

Slika 5: Primerjava med debelino plasti γ', dobljene z modelom (krivulja) in eksperimentalno izmerjene (točke) pri r_N = 0,7 bar$^{-1/2}$

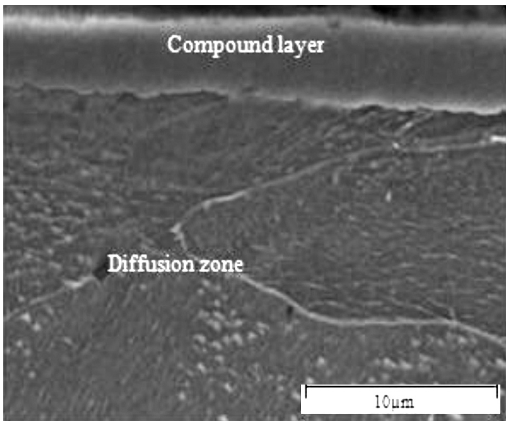

Figure 6: SEM micrograph of the cross-section of nitrided Fe – 1 % Cr alloy for the nitriding conditions: (T = 550 °C, t = 10 h, K_N = 0.7 bar$^{-1/2}$)

Slika 6: SEM-posnetek prereza nitrirane zlitine Fe – 1 % Cr pri razmerah nitriranja: (T = 550 °C, t = 10 h, K_N = 0,7 bar$^{-1/2}$)

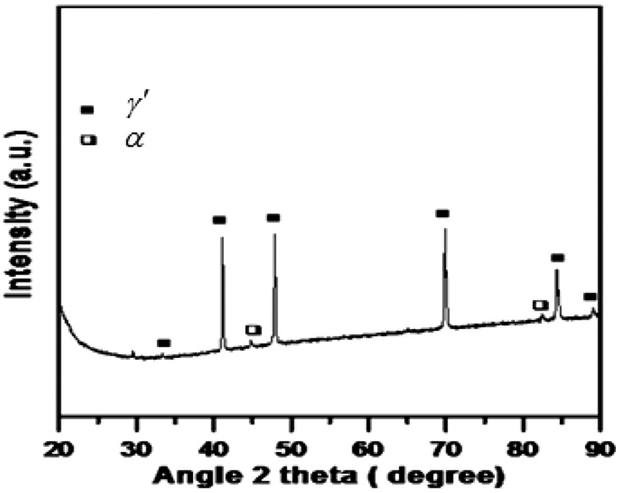

Figure 7: X-ray diffraction pattern of the surface of gas-nitrided Fe – 1 % Cr alloy at $T = 550$ °C during 10 h of treatment
Slika 7: Rentgenska difrakcija površine plinsko nitrirane zlitine Fe – 1 % Cr 10 h pri $T = 550$ °C

= 550 °C during 10 h of treatment. It can be seen that the detected phase includes γ'nitride and ferrite with no CrN which is probably due to its small fraction. It can also be seen that the nitriding conditions did not allow the formation of ε nitride.

The comparison between the experimental values of the γ' layer thicknesses and those calculated by the model is shown in **Figure 5**. It can be seen that there is good agreement between the experimental thicknesses and the simulated ones. This comparison leads to the conclusion that the model predicts, in a good way, the growth kinetics of the compound zone.

8 FURTHER POSSIBILITIES OF THE MODEL

The model provides good results concerning the growth of the compound layer, at least for the considered range of nitriding conditions and for low concentrations of the Cr alloying element. The model can be extended to perform a bilayer configuration (ε/γ') of the compound zone. The model can also be extended to simulate the nitriding of alloyed steel.

This requires a method for handling, the presence of several alloying elements with the possibility of different types of MN precipitates. The modeling of nitriding steels necessitates, especially, the consideration of the carbon element which brings significant changes to the microstructure before and during nitriding.

For example, it is reported in several studies[5,26] that the alloyed carbides transform into nitrides or carbonitrides during the process and that the nitrogen interstitial diffusion is accelerated by that of carbon.

One of the solutions that can be adopted to simulate the nitriding of steels is to combine the present model with a thermodynamic model using the CALPHAD approach as shown in[5] for the diffusion zone.

If the present model is interfaced with appropriate thermodynamic and kinetic data (resulting from thermodynamic calculations) it becomes a more complete model for the nitriding of steels. Such a model is able to predict nitrogen profiles in the diffusion zone and also in the compound layer.

Furthermore, the present model can be extended to study other processes involving moving boundaries, such as phase transformations and solidification. The model can even be extended to consider a case of a multicomponent system where several elements are able to diffuse as reported in[20–22]. However, it requires the use of a comprehensive thermodynamic description necessary to determine different diffusivities and chemical potentials required for handling a diffusion process. However, in the present work, the model was restricted to the simulation of a nitriding process for binary alloys.

9 CONCLUSION

A numerical model for a simulation of the gas nitriding of Fe-M binary alloys is presented. The model takes into account both the diffusion precipitation in the diffusion zone and the nitrogen within the iron nitride γ', also considering the (γ'/α) interface displacement. The diffusion problem with a moving boundary formulated in this way is solved through the front-tracking approach. Because of the presence of the M alloying element, the model also considers the precipitation of the MN nitrides in the diffusion zone. The numerical solving was achieved using the finite-difference method via an implicit scheme.

The numerical resolution allows a determination of the nitrogen profile along the depth as well as the interface position which makes it possible to follow the growth kinetics of the compound layer. There is a good concordance between the numerical calculations and the experimental results in the case of nitriding the Fe – 1 % Cr alloy.

Despite the fact that the model is limited to the case of a monolayer compound zone, it can be used as a tool for controlling the nitriding process and optimizing the desired properties.

Moreover, the applicability of the model can be extended to simulate the nitriding of steels using an appropriate thermodynamic and kinetic database in the simulation.

APPENDIX 1: VARIATION IN THE DIFFUSION COEFFICIENT IN γ' WITH THE COMPOSITION

The implementation of the model requires a determination of the dependence of the intrinsic diffusion coefficient on the nitrogen amount in the γ' phase. On the basis of thermodynamic and kinetic considerations, the following expression can be established:

$$D_{\gamma'}(N_{\gamma'}) = D^{*}_{\gamma'} \frac{\mathrm{d}\ln a_{\mathrm{N}}}{\mathrm{d}\ln N_{\gamma'}} \tag{A1}$$

where a_{N} is the nitrogen activity in γ' and $D^{*}_{\gamma'}$ is the nitrogen-tracer diffusion coefficient which is considered independent of the composition. The term $\Phi = \frac{\mathrm{d}\ln a_{\mathrm{N}}}{\mathrm{d}\ln N_{\gamma'}}$ is often called the thermodynamic factor.

During the gas nitriding process with the presence of a gas mixture (NH_3/H_2), it is assumed there is a thermodynamic equilibrium between the solid (γ') and the atmosphere. It was shown that the activity of nitrogen is proportional to the nitriding potential of $r_{\mathrm{N}} = P_{\mathrm{NH3}}/P_{\mathrm{H2}}$ [15,16]. The thermodynamic factor can then be rewritten as follows:

$$\Phi = \frac{\mathrm{d}\ln r_{\mathrm{N}}}{\mathrm{d}\ln N_{\gamma'}} \tag{A2}$$

Using the absorption-isotherm theory, Somers et al.[15] gave the relation between the nitrogen amount in γ'and the nitriding potential, expressed with the following equation:

$$y_{N,\gamma'} = \frac{1}{4}\left\{1 + \left[\exp\left(-\frac{7558}{T} + 2.978\right)\right] \cdot \left[\frac{r_{\mathrm{N}}}{r^{0}_{\mathrm{N},\gamma'}} - \frac{r^{0}_{\mathrm{N},\gamma'}}{r_{\mathrm{N}}}\right]\right\} \tag{A3}$$

where $y_{N,\gamma'}$ is the nitrogen amount expressed as a site fraction. The meanings and values of the constants appearing in A3 are given in the same reference[15]. In order to obtain the nitrogen concentration (the number of moles per volume), the following relationship can be used:

$$N_{\gamma'} = \frac{y_{\mathrm{N},\gamma'}}{V_{\gamma'}(1 + y_{\mathrm{N},\gamma'})} \tag{A4}$$

For each composition, Relations A3 and A4 can be combined and derived in order to calculate the thermodynamic factor Φ (according to A2) and then the corresponding diffusivity (according to A1). In this way, the composition dependence of diffusivity was taken into account in the model and implemented as explained above.

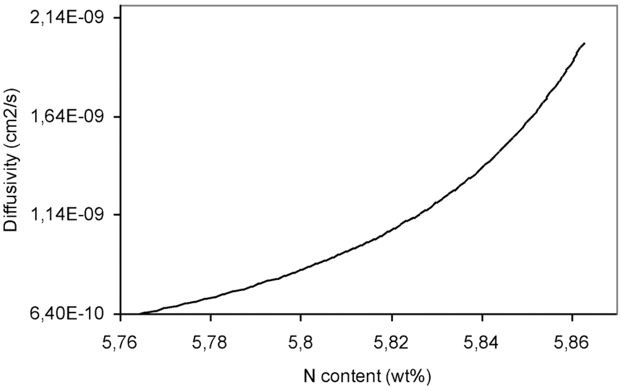

Figure 8: Evolution of the diffusion coefficient $D_{\gamma'}(N)$ versus the nitrogen concentration in γ' (T = 550 °C, r_{N} = 0.7 bar$^{-1/2}$)

Slika 8: Razvoj koeficienta difuzije $D_{\gamma'}(N)$ v odvisnosti od koncentracije dušika v γ' (T = 550 °C, r_{N} = 0,7 bar$^{-1/2}$)

Figure 8 shows the evolution of the diffusion coefficient $D_{\gamma'}$ versus the mass fraction of N, at T = 550 °C and r_{N} = 0.7 bar$^{-1/2}$. A strong dependence on the concentration can be observed.

APPENDIX 2: DATA USED IN THE SIMULATION

The data required for the simulation are gathered in **Table 1**.[1,13,15,16,18,27] It is worth noting that when considering the nitrogen concentrations in both the external surface (N_s) and at the interface ($N_{\gamma'\alpha}$, $N_{\alpha\gamma'}$), the Fe-N binary phase diagram was used instead of an isothermal section of the Fe-N-Cr phase diagram.

Table 1: Different constants used for implementing the model with their source references

Tabela 1: Različne konstante, uporabljene v modelu in reference njihovega izvora

Constant	Value at 520 °C	Value at 550 °C	References
K_α/(cm/s)	5.3332 E–6	7.6047 E–6	27
$w(N_{eq\alpha})$/%	0.1807	0.2742	15,16
$w(N_s)$/%	5.8630	5.8621	15,16
$x(X_{\gamma'\alpha})$/%	0.1973	0.1964	15,16
$x(X_{\alpha\gamma'})$/%	0.0026	0.0032	15,16
$w(K_{\mathrm{CrN}})/\%^{-2}$	0.0019	0.0033	1
D_α/(cm^2/s)	4.9183 E–8	7.5636 E–8	15,16
$D_{\gamma'}$/(cm^2/s)	8.3870 E–12	1.3303 E–11	18
V_α/(cm^3/mol)	7.14	7.14	13
$V_{\gamma'}$/(cm^3/mol)	8.22	8.22	13

mass fraction, w/%
amount (= mol) fraction, x/%

This was possible because during the preliminary phase the CrN precipitation near the external surface consumes practically all the dissolved Cr so that γ' nitride precipitates, thereafter, from the ferrite containing almost no alloying element. The CrN nitride is thermodynamically stable and assumed to be stoichiometric. This simplification was already adopted in[1].

In addition, in the Fe-N system the boundaries between phases were considered as a function of the nitriding potential instead of the total nitrogen amount. This phase diagram is called the Lehrer diagram and the corresponding thermodynamic description can be found in[15,16].

10 REFERENCES

[1] Y. Sun, T. Bell, Materials Science and Engineering A, 224 (**1997**), 33–47

[2] M. Gouné, T. Belmonte, J. M. Fiorani, S. Chomer, H. Michel, Thin Solid Films, 377–378 (**2000**), 543–549

[3] H. P. Van Landeghem, M. Gouné, A. Redjaimia, Journal of Crystal Growth, 341 (**2012**), 53–60

[4] R. Schacherl, P. C. J. Graat, E. J. Mittemeijer, Metall. Mater. Trans., 35A (**2004**), 3387

[5] S. Jegou, PhD thesis, ENSAM, Aix En Provence, France, 2009

[6] J. D. Kamminga, G. C. A. M. Janssen, Surface and Coatings Technology, 200 (**2006**), 5896–5901

[7] R. Kouba, M. Keddam, M. E. Djeghlal, Journal of Alloys and Compounds, 536 (**2012**), 124–131

[8] H. C. F. Rozendaal, P. F. Coljin, E. J. Mittemeijer, Surface Engineering, 1 (**1985**), 30–43

[9] J. Ratajski, R. Olik, Advanced Materials Research, 83–86 (**2010**), 1025–1034

[10] M. Keddam, M. E. Djeghlal, L. Barralier, Materials Science and Engineering A, 378 (**2004**), 475–478

[11] L. Torchane, P. Bilger, J. Dulcy, M. Gantois, Metallurgical and Materials Transactions A, 27A (**1996**), 1823–1834

[12] M. Keddam, M. E. Djeghlal, L. Barralier, E. Salhi, Annales de Chimie-Science des Matériaux, 28 (**2003**), 53–61

[13] H. Du, J. Ågren, Metallurgical and Materials Transactions A, 27A (**1996**), 1073–1080

[14] H. Du, J. Ågren, Z. Metallkunde, 86 (**1995**), 522–529

[15] M. A. Somers, E. J. Mittemeijer, Metallurgical and Materials Transactions A, 26A (**1995**), 57–74

[16] E. J. Mittemeijer, M. A. J. Somers, Surface Engineering A, 13 (**1997**), 483–497

[17] P. B. Friehling, M. A. J Somers, HTM J, 57 (**2002**), 415–420

[18] T. Belmonte, M. Gouné, H. Michel, Materials Science and Engineering A, 302 (**2001**), 246–251

[19] T. C. Illingworth, I. O. Golosnoy, Journal of Computational Physics, 209 (**2005**), 207–225

[20] S. Crusius, G. Inden, U. Knoop, L. Höglund, J. Ågren, Zeitschrift für Metallkunde, 83 (**1992**), 673–678

[21] H. Larsson, R. C. Reed, Acta Materialia, 56 (**2008**), 3754–3760

[22] J. Svoboda, E. Gamsjager, F. D. Fischer, Y. Liu, E. Kozeschnik, Acta Materialia, 59 (**2011**), 4775–4786

[23] L. V. Fausett, Applied Numerical Analysis Using Matlab, Prentice Hall, New Jersey 1999

[24] J. W. Thomas, Numerical partial differential equations: Texts in Applied Mathematics, vol. 33, Springer, New York 1999

[25] P. B. Friehling, F. W. Poulsen, M. A. J. Somers, Z. Metallkd, 92 (**2001**), 589–593

[26] S. Jegou, L. Barralier, R. Kubler, Acta Materialia, 58 (**2010**), 2666–2676

[27] H. C. F. Rozendaal, E. J. Mittemeijer, P. F. Colijn, P. J. Van Der Schaff, Metallurgical and Materials Transactions A, 14A (**1983**), 395–399

UDK 678.7:66.017:620.3
Original scientific article/Izvirni znanstveni članek

ISSN 1580-2949
MTAEC9, 49(1)55(2015)

ANTIBACTERIAL COMPOSITE BASED ON NANOSTRUCTURED ZnO MESOSCALE PARTICLES AND A POLY(VINYL CHLORIDE) MATRIX

PROTIBAKTERIJSKI KOMPOZIT NA OSNOVI NANOSTRUKTURNIH DELCEV ZnO IN OSNOVE IZ POLIVINIL KLORIDA

Jakub Sedlák[1,2], Pavel Bažant[1,2], Jiří Klofáč[1,2], Miroslav Pastorek[1,3], Ivo Kuřitka[1,2]

[1]Centre of Polymer Systems, University Institute, Tomas Bata University in Zlin, Nad Ovcirnou 3685, 760 01 Zlin, Czech Republic
[2]Polymer Centre, Faculty of Technology, Tomas Bata University in Zlin, Namesti T.G. Masaryka 275, 762 72 Zlin, Czech Republic
[3]Department of Polymer Engineering, Faculty of Technology, Tomas Bata University in Zlin, Namesti T.G. Masaryka 275, 762 72 Zlin, Czech Republic
j1sedlak@ft.utb.cz

Prejem rokopisa – received: 2013-10-04; sprejem za objavo – accepted for publication: 2014-03-10

The microwave-assisted solvothermal synthesis of inorganic ZnO nanoparticles is a facile method yielding a broad variety of active fillers with specific properties. The synthesis of hierarchical nanostructured zinc oxide mesoscale particles was carried out under continuous microwave irradiation from soluble zinc acetate as the precursor in a diethylene glycol solvent. The prepared ZnO particles were characterized with X-ray diffractometry, scanning electron microscopy and UV-VIS spectrometry. A composite was obtained by mixing these particles with the softened medical-grade poly(vinyl chloride) as a model polymer matrix to develop an antibacterial polymer system with a possible application for plastic medical devices. The testing of the antibacterial activity of the composite confirmed an excellent performance against *Escherichia coli* (gram-negative) and sufficient activity against *Staphylococcus aureus* (gram-positive) bacteria according to ISO 22196: 2007. In addition, no adverse effects of the filler on the mechanical properties of the composite were observed in comparison with the neat PVC resin. Therefore, the prepared composites can be considered as suitable candidates for application in plastic medical devices and other industries.

Keywords: antibacterial, PVC, composite, ZnO, nanoparticles

Solvotermična sinteza anorganskih delcev ZnO v mikrovalovni pečici je lahka metoda za izdelavo različnih polnil s posebnimi lastnostmi. Sinteza delcev cinkovega oksida s hierarhično nanostrukturo je bila izvršena s kontinuirnim mikrovalovnim obsevanjem v mikrovalovni pečici iz predhodno raztopljenega cink acetata v raztopini dietilen glikola. Pripravljeni delci ZnO so bili karakterizirani z rentgensko difrakcijo, vrstično elektronsko mikroskopijo in z UV-VIS-spektrometrijo. Kompozit je bil izdelan z mešanjem teh delcev v zmehčan medicinski polivinil klorid kot modelno polimerno osnovo za razvoj protibakterijskega polimernega sistema z možnostjo uporabe za plastične medicinske naprave. Preizkušanje protibakterijske aktivnosti kompozita je pokazalo odlično vedenje pri *Escherichia coli* (gram-negativne) in zadovoljivo aktivnost proti bakterijam *Staphylococcus aureus* (gram-pozitivne) skladno z ISO 22196: 2007. Dodatno pa v primerjavi s čisto PVC-smolo ni bil ugotovljen neželen učinek polnila na mehanske lastnosti kompozita. Zato je pripravljeni kompozit primeren kandidat za uporabo v plastičnih medicinskih napravah in v drugih industrijah.

Ključne besede: protibakterijski, PVC, kompozit, ZnO, nanodelci

1 INTRODUCTION

Nosocomial infections have become a serious problem of today's hospital environment. The prevalence of medical-devices-related infections (MDIs) rapidly grows among hospital-acquired infections and high health risks are especially associated with the devices which are in close contact with the inner parts of a patient's body.[1] As the polymers are the most frequently used materials in medical devices, the prevention against bacterial adhesion and growth on their surfaces is an absolute imperative.[2] There are two principally different strategies of how to resolve this problem. The first approach uses organic antimicrobial additives to plastics. They are very efficient; however, their mechanism of action requires diffusion out of the plastic surface and they can be classified as migratory additives. In contrast, the second approach uses inorganic additives with a very low solubility which ensures sufficient surface antibacterial activity and a minimum leakage of the active species into the patients body.[3] Therefore, a utilization of inorganic antibacterial nanopowders by compounding them with commercial polymer resins seems to be the simplest way leading to an enhanced antibacterial activity of a polymer composite system.

In recent years, a great effort has been made by the community of researchers for the synthesis and utilization of nanomaterials in the field of medical materials.[4] Zinc oxide is one of the promising candidates from the group of metal oxides (e.g., CaO, MgO, TiO_2, Cu_2O) that can be obtained with various properties depending on the nanoparticle size and shape as the crucial parameters.[5] ZnO is a biocompatible material exhibiting antimicrobial properties against the gram-negative as well as gram-positive bacteria. The mechanisms of the antibacterial action are still not perfectly understood, but there are several proposals for the explanation of the microbial inhibition such as the generation of reactive oxygen species (ROS) like hydroxyl radicals and singlet oxygen, or the release of Zn^{2+} cations.[6,7]

Up to now, a large variety of physical and chemical methods have been developed for the ZnO-nanoparticle preparation such as thermal decomposition, hydrothermal, solvothermal or microwave-assisted syntheses. The last mentioned microwave energy exclusively reduces the reaction time as well as the energy demands of the process.[8–12]

Here we report on a fast and simple solvothermal microwave-assisted synthesis of hierarchical nanostructured mesoscale ZnO aggregates, their compounding into medical-grade plasticized PVC as a model polymer matrix suitable for utilization in medical devices and an evaluation of the surface antimicrobial and mechanical properties of the final composites.

2 EXPERIMENTAL WORK

2.1 Materials

All the chemical reagents used in the experiment were of the analytical grade and used as received without further purification: zinc acetate dihydrate, p.a., (a purity of 99 %, Penta, The Czech Republic), diethylene glycol, p.a., (a purity of 99 %, Penta, The Czech Republic). Azeotropic denatured ethanol (The Czech Republic) was used for washing the product. The medical-grade softened PVC resin RB-3 (Modenplast Medical, Italy) was used as the polymer matrix.

2.2 Synthesis of the ZnO antibacterial filler

At first 2.195 g of $Zn(CH_3COO)_2 \cdot 2H_2O$ was completely dissolved in 100 mL of diethylene glycol at a temperature of about 100 °C during a 30 min agitation on a magnetic stirrer. The obtained solution was transferred to a 250 mL boiling flask and irradiated under reflux for 5 min using microwaves. The product was cooled down naturally after turning off the microwave oven. The powder was collected with centrifugation, washed with ethanol and air-dried up to the constant mass. The microwave reaction was performed in a microwave open-vessel system MWG1K-10 (Radan, The Czech Republic, 800 W, 2.45 GHz), based on modifying a domestic microwave oven by drilling a hole in the ceiling for external cooling and equipped with an external source of microwave energy that allows a control of the duty cycle. The reaction mixture was heated in a quasi-continuous mode at the maximum heating power.

2.3 Compounding the ZnO filler with the PVC matrix

The PVC-filler compounds were prepared with a melt-mixing process using a Brabender Plasti-Corder machine (Brabender, Germany) equipped with a 50 cm^3 mixing chamber and the mixing elements working in a contra-rotating mode. In this way, four mixtures differing from each other with respect to the load of the filler in the polymer matrix were compounded with the compositions as follows: w = (0.5, 1, 2 and 3) %. The compounding process consisted of three continuous phases. The first started by feeding the mixing chamber with PVC pellets and synthesized filler in the form of a fine powder at 20 r/min for two minutes. In the next step, after the feeding of the chamber was finished, the engine speed was continuously increased from 20 r/min up to 50 r/min within 1 min. The last part of the mixing was done at 50 r/min for 5 min. The mixing process was monitored by measuring the torque of the drive engine. The processing time of 8 min was enough to obtain a constant torque value for all the samples. No resin discoloration or other signs of a polymer deterioration connected with the use of the ZnO filler were observed under the used mixing conditions. The prepared compounds were compression molded to square-shaped sheets with the dimensions of 50 mm × 50 mm × 1 mm at 180 °C for 2.5 min. Blank samples without any filler were prepared in the same way as the filled ones.

2.4 Characterization

The synthesized powder was characterized with X-ray powder diffraction (XRD) using an X´Pert PRO (PANalytical, The Netherlands) with a Cu K_α radiation source (λ = 0.1540598 nm). The micrographs of the prepared powder and cross-section surfaces of the composites were taken with a scanning electron microscope Vega II (Tescan, The Czech Republic) and the UV-VIS absorption spectra were collected with an Avaspec UV-VIS spectrometer (Avantes, The Netherlands) with an AvaLight-DHS-DUV source type and an integrating sphere ($BaSO_4$ coated) was used for the diffuse reflectance measurement. The mechanical properties of the composites were evaluated with the tensile tests performed on a Testometric universal testing machine M350-5CP (LABOR machine Ltd., The Czech Republic) according to the ISO 37: 2005 standard with a type-2 testing specimen. The speed of the moving clamps was 250 mm/min. All the sample measurements were replicated six times.

2.5 Antibacterial testing

An evaluation of the surface antibacterial activity of the composites against bacterial adherence and growth was performed according to the ISO 22196: 2007 (formerly known as JIS Z-2801) standard. Gram-positive bacteria were represented by *Staphylococcus aureus* ATCC 6538P and gram-negative by *Escherichia coli* ATCC 8739, both obtained from The Czech Collection of Microorganisms (The Czech Republic). The size of the test specimens was 50 mm × 50 mm × 1 mm. A HERAcell 150i incubator (Thermo Scientific, USA) was used for the cultivation. The antibacterial activity R was calculated using Equation 1:

$$R = (U_t - U_0) - (A_t - U_0) = U_t - A_t \qquad (1)$$

where R is the antibacterial activity; U_0 is the average of the common logarithm of the number of viable bacteria cells in 1/cm^2, recovered from the untreated test specimens immediately after the inoculation; U_t is the average of the logarithm of the number of viable bacteria cells in 1/cm^2, recovered from the untreated test specimens immediately after 48 h; and A_t is the average of the logarithm of the number of viable bacteria cells in 1/cm^2, recovered from the treated test specimens immediately after 48 h. The colonies were counted after 24 h and checked after 48 h for a presence of slowly growing colonies on both untreated and treated test specimens, improving the original standard protocol. All the tests were repeated in triplicates.

3 RESULTS AND DISCUSSION

The crystalline-phase structure of the synthesized filler is shown on the diffractogram in **Figure 1**. By comparison with JCDD PDF-2 entry 01-079-0207, diffraction peaks were labelled as (100), (002), (101), (102), (110), (103), (200), (112), (201), (004), (202) and (104) and assigned to the hexagonal ZnO wurtzite structure. Moreover, the evident broadness of diffraction lines implies that the synthesized particles are of nano-scale dimensions.

Figure 2 shows the diffuse reflectance UV-VIS (DR-UV-VIS) spectrum of the prepared ZnO nanocrystals that exhibit a strong absorption with the maximum below 380 nm. This peak is slightly blue-shifted from the typical position of bulk ZnO[13] which points towards the nanosized particles, similarly as with the XRD analysis. The morphology of the prepared filler is presented in the SEM image in **Figure 3a**. As can be seen, the material consists of globular-like particle aggregates with a diameter ranging from 200 nm up to 1 μm. According to the XRD analysis and DR-UV-VIS measurement it can be concluded that these aggregates are assembled from much smaller nanocrystals.

The filler dispersion in the prepared composites was achieved at the aggregate level and its good distribution in the PVC matrix is shown in the SEM image in **Figure 3b**, for the sample with w = 2 % of the filler. There are no visible agglomerates of the globular aggregates within the polymer matrix. On the other hand, the aggregates were not disaggregated during the mixing procedure.

The mechanical properties of the prepared composites were characterized with tensile tests, and the Young's modulus, elongation at break and tensile strength were chosen as the three representative quantities for evaluating the filler-amount effects on the composite performance. As summarized in **Table 1**, no significant changes in the mechanical properties were observed across all the samples. Thus, it can be concluded that (i) the incorporation of the inorganic ZnO filler up to w = 3 % did not change the properties of the

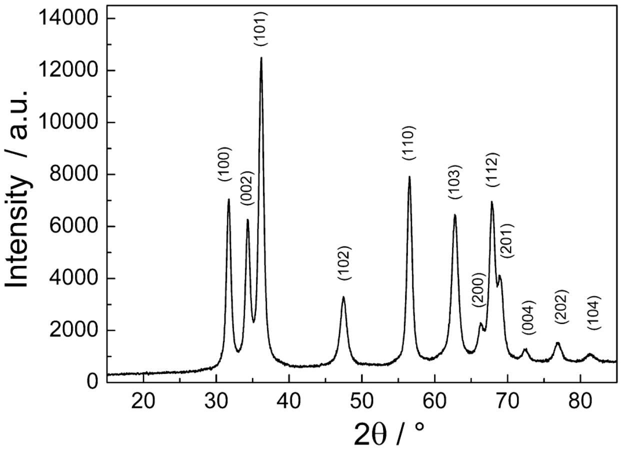

Figure 1: X-ray diffractogram of the prepared ZnO filler
Slika 1: Rentgenski difraktogram pripravljenega ZnO-polnila

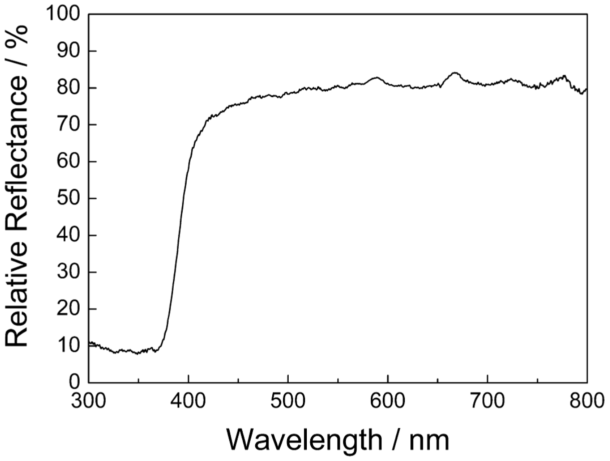

Figure 2: UV-VIS diffuse-reflectance spectrum of the prepared ZnO filler. Relative reflectance is plotted versus wavelength.
Slika 2: UV-VIS-spekter razpršene odbojnosti pripravljenega ZnO-polnila. Relativna odbojnost je prikazana v odvisnosti od valovne dolžine.

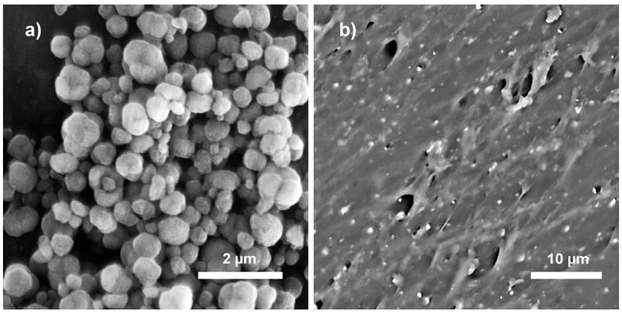

Figure 3: SEM images of: a) prepared ZnO filler and b) cross-section of the prepared composite material with w = 2 % of ZnO filler
Slika 3: SEM-posnetka: a) pripravljeno ZnO-polnilo in b) prerez pripravljenega kompozitnega materiala z masnim deležem ZnO-polnila 2 %

neat medical-grade plasticized PVC matrix which was already designed by its producer to be an optimally flexible material for medical devices such as urinal catheters or blood bags, and that (ii) the filler had no adverse influence on the application potential of the prepared antibacterial composite.

Table 1: Summary of the selected mechanical properties of the prepared composites and their standard deviations
Tabela 1: Povzetek izbranih mehanskih lastnosti pripravljenih kompozitov in njihov standardni odmik

Concentration of ZnO filler (*w*/%)	Young's modulus (MPa)	Elongation at break (%)	Tensile strength (MPa)
0	9.9 ± 0.2	501 ± 17	19.1 ± 0.9
0.5	9.8 ± 0.2	494 ± 30	19.0 ± 1.1
1	10.3 ± 0.3	500 ± 20	19.4 ± 0.8
2	10.1 ± 0.3	497 ± 9	19.4 ± 0.8
3	9.2 ± 1.0	520 ± 20	18.4 ± 0.4

The quantitative evaluation of the surface antibacterial activity of the as-prepared ZnO/PVC composites is summarized in **Table 2**. The obtained R values representing the antibacterial activity of the composites against both bacteria are high enough for the composites filled with $w = 2$ % and 3 %. The R value should not be lower than 2 for the materials that can be classified as the ones exhibiting an antibacterial surface suitable, for instance, for hygienic applications or less demanding applications. However, medical devices are more demanding with respect to the antibacterial performance of the used materials. The R-values of 5 or even 6 are expected for current high-end commercial materials, especially those with organic additives intended to be used in indwelling medical devices.[3] The surface antibacterial activity of the composites containing $w = 2$ % or 3 % of the filler against *E. coli* meet these highest requirements, while the activity against *S. aureus* is not so high. A similar antibacterial performance was recently obtained for the antibacterial systems containing hybrid Ag/ZnO filler employing nanosilver in addition to nanostructured ZnO.[14] On the other hand, *S. aureus* is a very vital and resistant bacterium, so it is difficult to suppress it and inhibit its growth. Concurrent studies reported reductions with respect to the control samples by about 70–95 % for much higher nano-ZnO loadings in PVC matrices, which means that the R values of less than 2 were claimed as success by their authors.[4] However, other strains were used throughout these studies and the surface-activity-estimation methods were similar but not identical to ISO 22196: 2007. From this point of view, and with a full awareness of the peculiar comparability among different published results, the performance of our prepared composites seems to be sufficiently high. Next, as the bacteria gain antibiotic resistance, the organic molecular additives in antimicrobial polymer systems may be found to be inefficient or ineffective and the inorganic nanofillers will serve as the last line of defense.

4 CONCLUSIONS

The present study describes a microwave-assisted synthetic route leading to the development of a hierarchical nanostructured ZnO mesoscale filler. The synthesized powder was clearly identified to have a ZnO hexagonal wurtzite structure and globular morphology of the aggregated nanocrystals. The composite materials compounded of medical-grade softened PVC and an as-prepared filler showed excellent antibacterial-activity values against *E. coli* and satisfactory antibacterial-activity values against *S. aureus*. Moreover, the obtained composites kept the mechanical properties of the neat PVC resin suitable as they were deteriorated neither by the processing nor by the effects of the nanofiller. These facts suggest that the prepared nanostructured mesoscale ZnO/PVC composite has an application potential in medicine as the material for medical devices being in the direct contact with the human body, besides many other possible utilizations.

Acknowledgment

The authors wish to thank for the internal grant of TBU in Zlin, No. IGA/FT/2013/026, funded from the resources for specific university research.

This article was written with the support of the Operational Program "Research and Development for Innovations" co-funded by the European Regional Development Fund (ERDF) and the national budget of the Czech Republic, within the Centre of Polymer Systems project (reg. number: CZ.1.05/2.1.00/03.0111).

This article was written with the support of the Operational Program "Education for Competitiveness"

Table 2: Summary of the surface-antibacterial-activity-evaluation results obtained for the prepared composites
Tabela 2: Povzetek rezultatov ocene površinske protibakterijske aktivnosti za pripravljene kompozite

Concentration of ZnO filler (*w*/%)	Treated specimens after 48 h *E. coli* N/(cfu cm^{-2})	Treated specimens after 48 h *S. aureus* N/(cfu cm^{-2})	Antibacterial activity (lg CFU) *E. coli*, $R = U_t - A_t$	Antibacterial activity (lg CFU) *S. aureus*, $R = U_t - A_t$
0	4.0×10^6	7.5×10^4	$U_t = 6.6$	$U_t = 4.9$
0.5	1.5×10^5	8.0×10^4	1.4	0
1	1.7×10^5	1.0×10^0	1.4	4.9
2	< 1	2.2×10^0	> 6.6	4.5
3	< 1	1.3×10^0	> 6.6	4.8

co-funded by the European Social Fund (ESF) and the national budget of the Czech Republic, within the Advanced Theoretical and Experimental Studies of Polymer Systems project (reg. number: CZ.1.07/2.3.00/20.0104).

5 REFERENCES

[1] P. M. Sivakumar, S. Balaji, V. Prabhawathi et al., Carbohydrate Polymers, 79 (**2010**), 717–723

[2] X. Y. Ma, W. D. Zhang, Polymer Degradation and Stability, 94 (**2009**), 1103–1109

[3] A. Jones, Plastics Engineering, 64 (**2008**), 34–40

[4] B. M. Geilich, T. J. Webster, International Journal of Nanomedicine, 8 (**2013**), 1177–1184

[5] J. Sawai, Journal of Microbiological Methods, 54 (**2003**), 177–182

[6] N. Padmavathy, R. Vijayaraghavan, Science and Technology of Advanced Materials, 9 (**2008**) 3, 035004, 7 pp

[7] K. H. Tam, A. B. Djurisic, C. M. N. Chan et al., Thin Solid Films, 516 (**2008**), 6167–6174

[8] Y. Yang, H. Chen, B. Zhao et al., Journal of Crystal Growth, 263 (**2004**), 447–453

[9] H. Lu, S. Wang, L. Zhao et al., Journal of Materials Chemistry, 21 (**2011**), 4228–4234

[10] P. Tonto, O. Mekasuwandumrong, S. Phatanasri et al., Ceramics International, 34 (**2008**), 57–62

[11] J. Zhu, J. Zhang, H. Zhou et al., Trans. Nonferrous Met. Soc. China, 19 (**2009**), 1578–1582

[12] A. Phuruangrat, T. Thongtem, S. Thongtem, Materials Letters, 63 (**2009**), 1224–1226

[13] N. S. Pesika, K. J. Stebe, P. C. Searson, J. Phys. Chem. B, 107 (**2003**), 10412–10415

[14] P. Bazant, I. Kuritka, O. Hudecek, M. Machovsky, M. Mrlik, T. Sedlacek, Polymer Composites, 35 (**2014**) 1, 19–26

UDK 621.74.043:621.743
Original scientific article/Izvirni znanstveni članek

ISSN 1580-2949
MTAEC9, 49(1)61(2015)

WATER-SOLUBLE CORES – VERIFYING DEVELOPMENT TRENDS

JEDRA, TOPNA V VODI – PREVERJANJE SMERI RAZVOJA

Eliška Adámková, Petr Jelínek, Jaroslav Beňo, František Mikšovský
VŠB-Technical University of Ostrava, Faculty of Metallurgy and Materials Engineering, Department of Metallurgy and Foundry, Czech Republic
eliska.adamkova@vsb.cz

Prejem rokopisa – received: 2013-10-07; sprejem za objavo – accepted for publication: 2014-01-17

Application of pure inorganic salt-based cores has been known since the end of the 20th century, especially in the field of gravity and low-pressure die casting. The contemporary trend in technology leads to the use of the cores in the field of non-ferrous-alloy high-pressure die casting. The main methods of the core production include high-pressure squeezing and shooting (warm core box). During research processes it was shown that pure-salt application is not very suitable for high-pressure casting. That is why a composite salt-based matrix of defined properties was started to be used. The aim of the paper is to verify the influences of the chemical composition, shape and morphology of the grains of various NaCl compounds on the mechanical properties (the bending strength) of water-soluble salt cores used for Al-alloy high-pressure die casting and to evaluate their properties resulting from the squeezing and shooting methods.

Keywords: salt cores, inorganic salts, die casting, warm box, non-ferrous metals

Uporaba jeder iz čistih anorganskih soli je poznana že od konca 20. stoletja, še posebno na področju gravitacijskega in nizkotlačnega litja. Podobne usmeritve in tehnologije vodijo k uporabi jeder na področju visokotlačnega litja neželeznih zlitin. Med glavnimi metodami izdelave jeder sta visokotlačno iztiskanje in vbrizganje (segreti jedrnik). Raziskava je pokazala, da uporaba čiste soli ni najbolj primerna za visokotlačno litje. To je razlog za začetek uporabe kompozitnih jeder na osnovi soli. Namen članka je preveriti vpliv kemijske sestave, oblike in morfologije zrn različnih vrst NaCl na mehanske lastnosti (upogibna trdnost) in uporabnost v vodi topnih jeder za visokotlačno litje Al-zlitin ter oceniti njihove lastnosti po stiskanju ali vbrizgavanju.

Ključne besede: jedra iz soli, anorganske soli, tlačno litje, segret jedrnik, neželezne kovine

1 INTRODUCTION

Together with the development in various technical fields (the automotive industry) the demand for more and more difficult and challenging castings increases; these are mechanically cleanable only with large difficulties. The application of the technology of disposable, inorganic, water-soluble salt cores is one of the solutions for the difficulty of a core removal from the areas that are hardly accessible for mechanical cleaning.[1] A reverse crystallization of the salt from a water solution is enabled due to the core water solubility, which is a requirement for creating an environmentally friendly closed circuit of the core production.

The usage of water-soluble salt cores has been so far known in the field of non-ferrous-alloy gravity and low-pressure die casting.[2] Promising possibilities can be created by focusing the investigation on the development of water-soluble salt-core application technology in the field of Al-alloy high-pressure die casting.[3,4] At present, two salt-core manufacturing techniques are being developed: high-pressure squeezing with the use of the recrystallization process and shooting with the use of inorganic binders, e.g., alkaline silicates.[5,6] Considering the material-purchase costs for the production of salt cores from chemically pure salts, it is necessary to look for more suitable solutions for crating the basic salt matrix.

The aim of this paper is to verify the applicability of NaCl (from the vast range of the common salts commercially available in the Czech market), with the main focus on the possibility to replace the more expensive chemically pure salt with a cheaper common salt. The influences of various salt origins (rock, Alpine or sea salt), chemical compositions, shapes and surface morphologies of the grains on the mechanical properties (the bending strength) of the salt cores manufactured with the high-pressure squeezing and shooting methods are investigated.

2 SELECTION OF THE USED SALTS

To evaluate the cores manufactured with the squeezing and shooting methods, the tested cores were prepared from technical (common) and chemically pure (standard) salts. The salts for the core production were chosen according to the chemical composition declared by the manufacturer on the packaging (**Table 1**). From the wide range of commercially available salts six types of salts were finally chosen for the observation performed in this experiment. Each of the salts was of a different chemical composition, grain shape and surface morphology. These aspects and the selected salt-core-production technologies had significant influences on the final mechanical properties of the cores.

The chemical composition of the selected types of salts can be evaluated from two important viewpoints:

- Health
- Technology

With respect to health, salts contain healthy elements – iodine, fluorine – in the form of chemical compounds (KIO_3, KI, NaF) in the amount of 15–58 (max. 250) mg/kg. However, more important for the salt-core production is the technology (the chemical composition) that affects the quality of the manufactured cores. Some of the commercially available salts contain the additives that prevent the grains from sticking, i.e., the anti-sintering additives. These are K_2CO_3, $CaCO_3$, $MgCO_3$, SiO_2, $K_4[Fe(CN_6)] \cdot 3H_20$. Alpine salts feature substantial amounts of carbonates. These components added for the purposes of trouble-free storage, transport and manipulation have significant influences on the core-production technology and strength properties. The mechanisms of grain sticking and further recrystallization are disturbed and the strength of squeezed cores is decreased. Similarly, in the case of shot cores a decrease in the bending properties of the salt grains and alkaline silicate occurs.

3 MECHANICAL PROPERTIES OF SALT CORES

The criterion for evaluating the mechanical properties of squeezed and shot cores was the bending strength which was measured as follows:

- after 24 h in the air (the primary strength)
- after drying at 160 °C 1 h (105 °C 1 h)

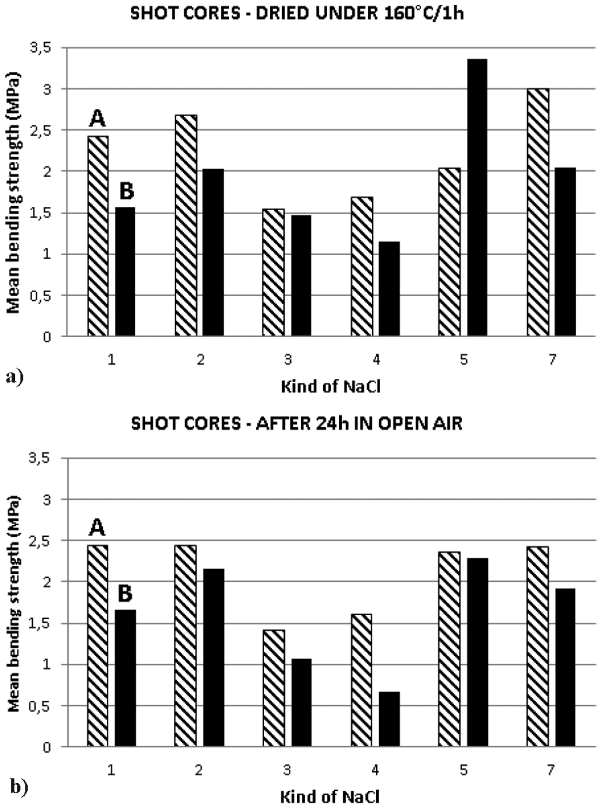

Figure 1: Comparison of the mean bending strengths of 6 types of shot salt: a) after drying and b) after 24 h in the open air (the mean value for 6 cores; A – original granularity, B – fraction of 0.063–1.0 mm)

Slika 1: Primerjava povprečne upogibne trdnosti 6 vrst vbrizganih soli: a) po sušenju in b) po zadržanju 24 h na zraku (srednja vrednost 6 jeder; A – originalna zrnatost, B – frakcija od 0,063 mm do 1,0 mm)

Table 1: Chemical compositions of the selected salts as declared by the manufacturers

Tabela 1: Kemijska sestava izbranih soli po navedbi proizvajalca

Salt sample	Commercial name	Additives		Presence of compounds
1	Rock salt with iodine and fluorine, edible (fine ground)	F I	max. 250 mg/kg 27 ± 7 mg/kg	NaF KIO_3
2	Rock salt with iodine (fine ground)	I	20–35 mg/kg	KI KIO_3
3	Alpine salt with iodine (vacuum packed)	NaCl $CaCO_3$ $MgCO_3$ KIO_3 I	98.8 % min. 0.9 % min. 0.2 % 33–58 mg/kg 20–34 mg/kg	$CaCO_3$ $MgCO_3$ KIO_3
4	Alpine salt with fluorine and iodine (vacuum packed)	NaCl $CaCO_3$ $MgCO_3$ KIO_3 I F	98.0 % min. 0.7 % min. 0.1 % 33–58 mg/kg 20–34 mg/kg max. 250 mg/kg	KIO_3 $CaCO_3$ $MgCO_3$ NaF
5	Fine sea salt with iodine (evaporated from sea water)	I	15–35 mg/kg	KIO_3
6	NaCl, p.a. (chemically pure)	Fe Heavy metals (Pb) SO_4 Ca Mg I Br	max. 0.0003 % max. 0.0005 % max. 0.005 % max. 0.005 % max. 0.002 % max. 0.008 % max. 0.01 %	

3.1 Shot cores

For the shot-core production a mixture of the originally supplied granulometry and a mesh fraction of 0.063–1.0 mm was used. The conditions for the shot-core production are as follows:

- Mixture composition: 100 mass parts of NaCl; 5 mass parts of Na – sodium silicate (M = 1.85)
- Hardening time: 50 s
- Core-box temperature: 190 °C
- Shooting speed: 7.5 s
- Air pressure: 7.5–8 bar

From **Figure 1** it is evident that for all the salts, except the sea salt with iodine (sample No. 5), the removal of dust proportion (< 0.063 mm) led to a bending-strength decrease. The final drying of the cores (160 °C/1 h) led to a bending-strength increase only for the NaCl sample (No. 5). Strengths comparable to the standard strength were achieved for rock salts with I and IF (Nos. 1, 2). The lowest strengths were achieved for the cores made of Alpine salt with I and IF (samples Nos. 3, 4). It was shown that the salt grain shape and the grain-surface quality are of the highest importance.

The apparent porosity *m* was calculated with the following relation:

$$m = \frac{\rho_{\mathrm{NaCl}} - \rho_{\mathrm{v}}}{\rho_{\mathrm{NaCl}}} \cdot 100\ (\%) \tag{1}$$

where:

ρ_{v} = bulk density of cores (g/cm^3)

The apparent porosity of shot cores ranged from 35 % to 45 %. After sieving the dust (< 0.063 mm) off the apparent porosity, an increase (a decrease in the volume mass ρ_v and strength) occurred for all the salt samples except for sample No. 5 (sea salt with I), which underwent an extreme increase in the bending strength, especially after being dried at 160 °C 1 h **(Figure 2)**.

3.2 Squeezed cores

For the production of squeezed cores, a mixture granulometry adjustment was carried out: the fraction of 0.063–1.0 mm. The conditions for the squeezed-core production are as follows:

- NaCl humidity: 0.65–1.04 %
- squeezing force: 200 kN
- squeezing tension: 104 MPa
- load rate: 9 kN/s

After the squeezing significantly higher strengths were achieved for all the salt samples **(Figure 3)**. The increase in the strength (together with a decrease in the apparent porosity) was evident for dried cores (105 °C 1 h). It was shown that the lowest strengths were achieved for the cores made of the salts with regular,

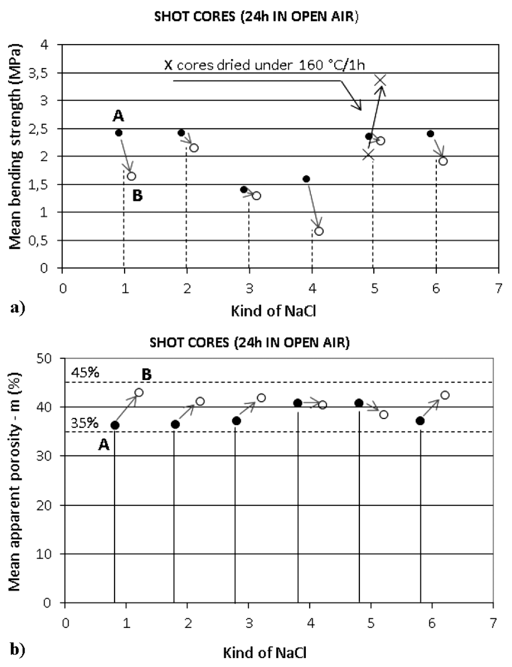

Figure 2: Comparison of: a) the mean bending strengths and b) apparent porosities of 6 types of shot salts after 24 h in the open air (the mean value for 6 cores; A – original granularity, B – fraction of 0.063–1.0 mm)

Slika 2: Primerjava: a) povprečne upogibne trdnosti in b) navidezne poroznosti 6 vrst vbrizganih soli po 24 h zadržanju na zraku (srednja vrednost 6 jeder; A – originalna zrnatost, B – frakcija od 0,063 mm do 1,0 mm)

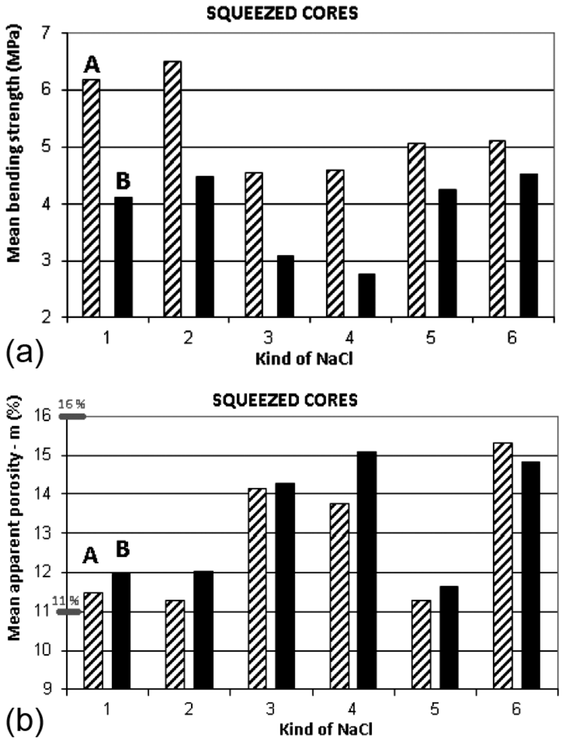

Figure 3: Comparison of: a) the mean bending strengths and b) apparent porosities of 6 types of squeezed salts (the mean value for 6 cores; A – cores additionally dried at 105 °C 1 h, B – 24 h in the open air)

Slika 3: Primerjava: a) povprečne upogibne trdnosti in b) navidezne poroznosti 6 vrst iztiskanih soli (povprečna vrednost 6 jeder; A – jedra dodatno sušena 1 h pri 105 °C, B – 24 h na zraku) cubic grain shape (Alpine salt, samples Nos. 3, 4 – recrystallized salts), whereas the highest strengths were achieved for the cores made of crushed-rock salts (samples Nos. 1, 2) and sea salt (sample No. 5). However, this does not apply to the standard salt (NaCl, p. a., sample No. 7). Regular, dipyramidal grain shape allows high strengths of the squeezed cores as well as of the shot ones. This shape is the closest to the globular silica-sand grain shape.

4 GRAIN SHAPE AND GRAIN-SURFACE MORPHOLOGY (SEM AND EDX ANALYSES)

A comparison of the chemical compositions declared on salt packagings and the real compositions determined with the use of an EDX microprobe is shown in **Table 2**.

In most cases, the grain shapes and surface morphologies of the selected salts vary significantly. The differences are due to different salt-production technologies, e.g., crushing and milling of the rock salt or the salt recrystallized from a solution – Alpine or sea salt. **Figures 4** to **7** below show grain shapes and surface morphologies, together with an EDX analysis of the investigated salts.

The differences between the salt-core strengths are explained with a detailed investigation of the salts using the SEM and EDX analyses. The low strengths of Alpine salts are caused by their lower quality of grain surfaces catching the blocking additives of $MgCO_3$ and $CaCO_3$; their presence was proven with the EDX analysis (**Figure 5**).

The dipyramidal grain shape of the chemically pure NaCl, p.a., is distinctive for its high grain coordination number, resembling the grain shape of SiO_2 sand grains, and being different from the regular, cubic Alpine-salt grains. This shape is more suitable for both core squeezing and core shooting.

Table 2: Comparison of declared chemical compositions and EDX microanalysis of the investigated real compositions
Tabela 2: Primerjava deklarirane kemijske sestave in EDX-mikroanaliza preiskovanih realnih sestav

	Type	Anti-sticking additives		F-additive	I-additive
COMPOSITION DECLARED BY THE MANUFACTURER	1 - Rock salt with iodine and fluorine (fine ground)			NaF	KIO_3
	2 - Rock salt with iodine, edible (fine ground)				KI, KIO_3
	3 - Alpine salt with iodine (vacuum packed)	$CaCO_3$	min. 0.9 %		KIO_3
		$MgCO_3$	min. 0.2 %		
	4 - Alpine salt with fluorine and iodine (vacuum packed)	$CaCO_3$	min. 0.7 %	NaF	KIO_3
		$MgCO_3$	min. 0.1 %		
	5 - Fine sea salt with iodine (evaporation of sea water)				KIO_3
	7 - NaCl, p.a. (chemically pure)				
		Elements observed with the EDX microprobe			
EDX ANALYSIS	1 - Rock salt with iodine and fluorine (fine ground)	Mg, C, O		F	
	2 - Rock salt with iodine, edible (fine ground)	Ca, C, O			K
	3 - Alpine salt with iodine (vacuum packed)	Mg, Ca, C, O			K
	4 - Alpine salt with fluorine and iodine (vacuum packed)	Mg, Ca, C, O		F	K
	5 - Fine sea salt with iodine (evaporation of sea water)	Mg, Ca, Si			K
	7 - NaCl, p.a. (chemically pure)				K

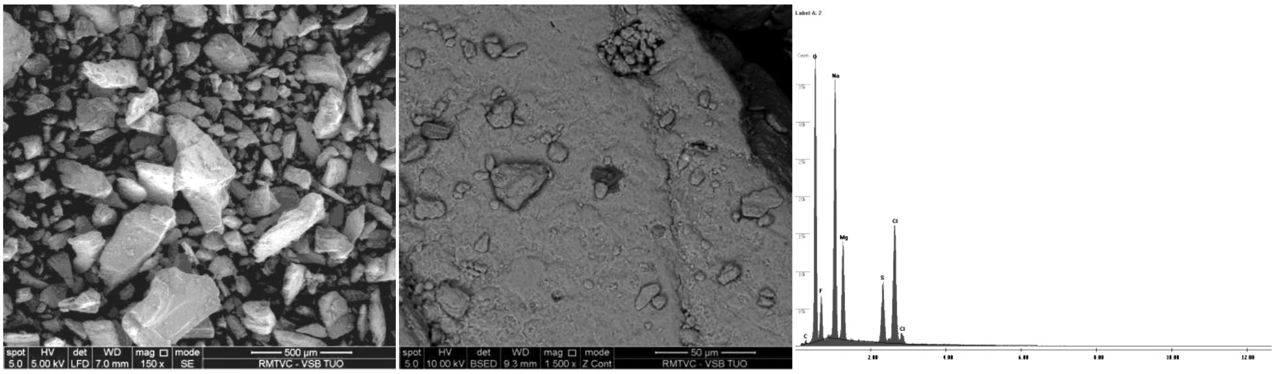

Figure 4: Shattered surface of crushed-rock salts (samples Nos. 1, 2) and EDX analysis of its chemical composition
Slika 4: Razbita površina drobljene kamene soli (vzorca št. 1 in 2) in EDX-analiza kemijske sestave

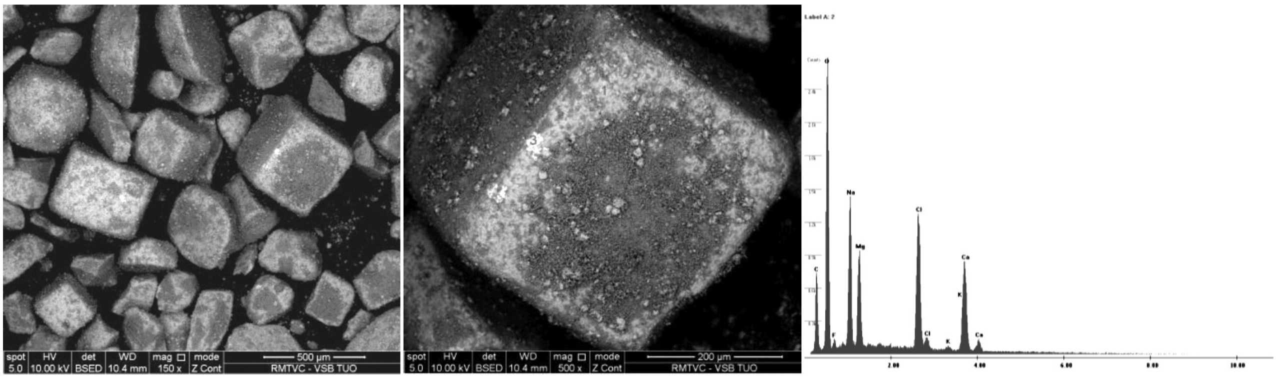

Figure 5: Regular cubic grains of Alpine salts (samples Nos. 3, 4) and EDX analysis confirming the presence of anticaking agents on the salt grain surface ($MgCO_3$, $CaCO_3$)
Slika 5: Pravilna kockasta zrna soli Alpine (vzorca št. 3 in 4) in EDX-analiza, ki potrjuje prisotnost sredstva proti sprijemanju na površini zrn soli ($MgCO_3$, $CaCO_3$)

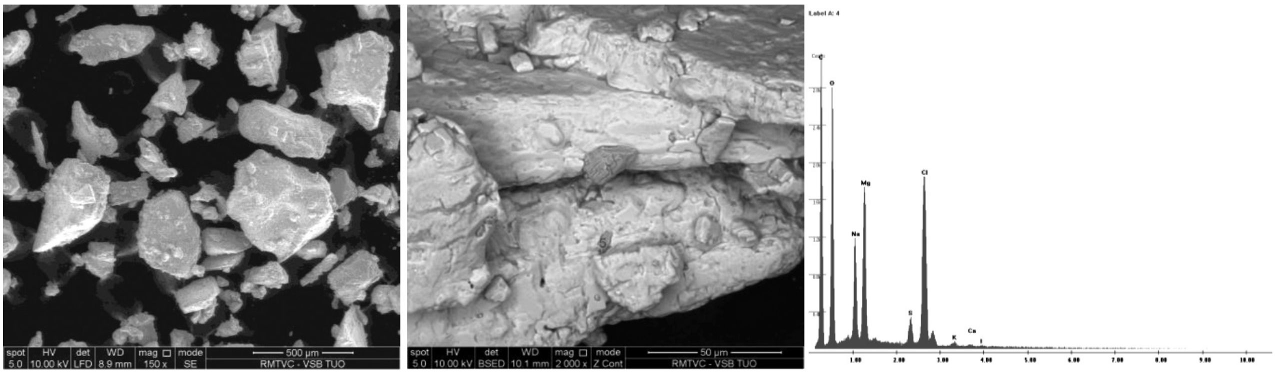

Figure 6: Oval form of sea-salt grains (sample No. 5) and EDX analysis of its chemical composition
Slika 6: Ovalna oblika zrn morske soli (vzorec št. 5) in EDX-analiza kemijske sestave

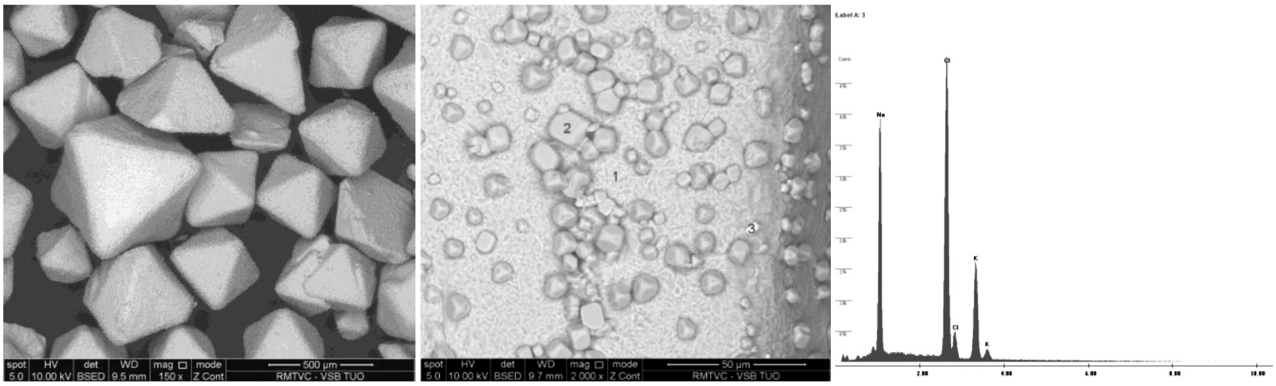

Figure 7: Regular dipyramidal form of NaCl, p. a. – standard (sample No. 7) and EDX analysis of its chemical composition
Slika 7: Dvopiramidna pravilna oblika NaCl, p. a. – standard (vzorec št. 7) in EDX-analiza kemijske sestave

5 HYGROSCOPICITY OF CORES

Hygroscopicity of common-salt cores and chemically pure salt cores was investigated using the weight-change measurement. The cores were stored in various climate conditions including the humidity of 35–58 % RV, the temperature of 20.7–24.9 °C and normal pressure. Hygroscopicity was observed for 23 d.

The results of the measurements given in **Figure 8** show different hygroscopic behaviours of squeezed and shot cores. The porosity and, at the same time, the strength of the cores are considerably influenced by the used manufacturing technology. It is evident that the hygroscopicity increases with the growing porosity (shot cores) while the strength is on a decrease. In the case of a lower porosity, hygroscopicity is less evident for the squeezed cores. But in both cases the growth of weight is not considerable, only sufficient for short-time storing

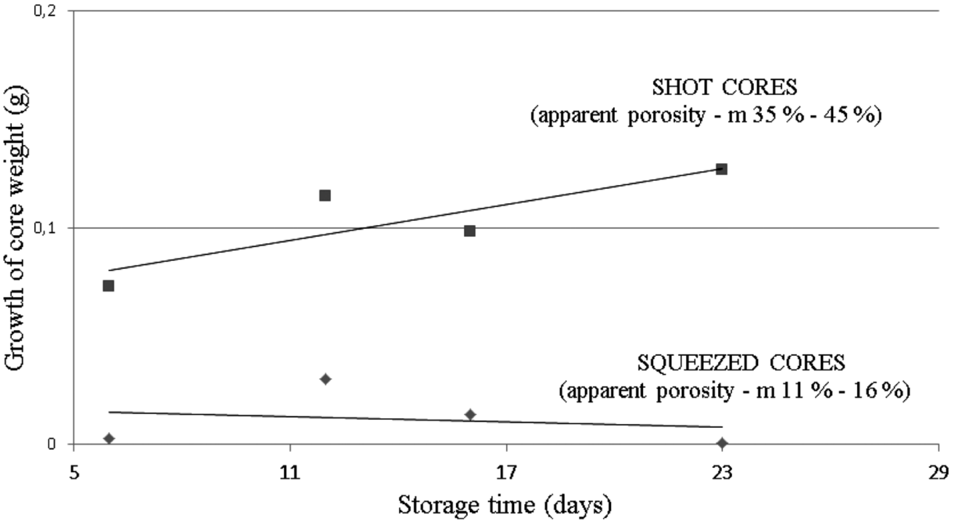

Figure 8: Different hygroscopicity trends for squeezed and shot cores
Slika 8: Različna usmeritev higroskopičnosti iztisnjenega in vbrizganega jedra

the salt cores destined for immediate use in the manufacturing process of castings.

6 INFLUENCE OF PRODUCTION TECHNOLOGY ON THE SALT-CORE POROSITY

The actual porosity, the pore size and pore distribution, was measured with a Micromeritics Instrument Corporation mercury porosimeter investigating the salt cores, based on NaCl and squeezed with a pressure of 200 kN (104 MPa) or shot with a pressure of 7.5–8 bar. The results are shown in **Table 3**.

Table 3: Properties of different salt cores
Tabela 3: Lastnosti različnih jeder iz soli

	Sample	Total volume of pores (cm^3/g)	Mean diameter of pores (µm)	Porosity (%)	Bulk density (g/cm^3)
Shot	2	0.1482	0.3240	24.20	1.6329
	5	0.1443	0.4207	23.52	1.6299
	7	0.2278	0.2409	19.10	0.8383
Squeezed	2	0.0320	0.2416	6.51	2.0351
	5	0.0354	0.2216	6.98	1.9734
	7	0.0635	0.5525	12.06	1.8977

The porosity of the squeezed cores is 6–12 % (a correlation with the apparent-porosity calculated value) while the porosity of the shot cores is 19–24 %, i.e., about four times higher. The overall volume of pores is one order lower for the squeezed cores.

From the resulting values it is evident that the applied production technology has a significant influence on the core actual porosity. This is important for the penetration of metal into the cores, especially in the case of high-pressure die casting, where the cores are extremely stressed by the metal pressure.

7 DISCUSSION

On the basis of the results achieved during the investigation of commercial salts (different origins, granulometries, grain shapes and chemical compositions) the following can be stated:

- In all the cases the cores made with the squeezing method achieved 2–3 times higher bending strengths than the shot cores **(Figure 4)**. They had a lower hygroscopicity (lower porosity) and lower water solubility so that only simple geometrical forms can be manufactured with this method.
- Shot cores are highly water soluble. It is possible to utilize the existing shooting-core foundry machines. However, there is a negative aspect of the high hygroscopicity correlating with the porosity and it is, therefore, necessary to protect the core surfaces against the penetration with coatings and lubricants.
- Due to the removal of the parts < 0.063 mm in the case of all the cores, the apparent porosity increased and the strength decreased, with the exception of sample No. 5 – the sea salt. An explanation is offered involving the granulometry of the bought sea salt that contained, unlike the other salts, almost no dust parts. The grains are highly oval, having no sharp edges.
- Dipyramid (sample No. 7 – standard) seems to be the most suitable grain shape giving high strengths to both the shot cores and squeezed ones. It enables the highest coordination number of the grains and, most of all, it is close to the shape of the SiO_2 base sand. For that reason this shape seems to be advantageous for squeezing and shooting the cores.
- An adverse influence of the anticaking agents ($CaCO_3$, $MgCO_3$, SiO_2, $K_4[Fe(CN_6)]\cdot3H_2O$) in combination with the regular, cubic shape of Alpine salts resulted in a strength decrease for both methods of the core production (squeezing and shooting). The

presence of undesirable additives on the grain surfaces does not enable binding with alkali silicate (shooting) and sticking of the grains with the following recrystallization along the grain boundaries (squeezing).

8 CONCLUSION

The aim of the research was to investigate the possibility of replacing the expensive chemically pure salt with common salt for the production of foundry cores applied in gravity, low-pressure, and possibly also high-pressure die casting of non-ferrous alloys.

The best strength results were achieved for crushed salts (rock salt) used for squeezing and shooting. The occurrence of fine-dust fractions contributes to achieving higher core strengths. The salts with recrystallized grains (Alpine salts) of a regular, cubic shape are less suitable, with the exception of dipyramidal shapes (chemically pure salts). Additions of the anti-sintering additives (SiO_2, $MgCO_3$, $CaCO_3$, $K_4[Fe(CN_6)]\cdot 3H_2O$) (for Alpine salts) deteriorate the strength properties.

A comparison of the core-production methods shows that the squeezed cores have higher mechanical properties (the bending strength) and the minimum hygroscopicity (decreased actual porosity).

The investigation proved that chemically pure salt can be adequately replaced with rock salt that is up to 50-times cheaper.

Acknowledgement

The research was performed with the financial support of the Technology Agency of the Czech Republic within the Alfa programme, TA 02011314.

9 REFERENCES

[1] H. Michels et al., Suitability of lost cores in rheocasting process, Trans. Nonferrous Met. Soc. China, 20 (**2010**), s948–s953

[2] P. Stingl, G. Schiller, Leichte und rückstandfreie Entkernung, Giesserei Erfahrungsaustausch, 6 (**2009**), 4–8

[3] P. Jelínek et al., Salt cores in high-pressure die-casting technology, In: 5. Holečkova's conference, 1 edition, Czech Foundry Society, Brno 2013, 63–67 (in Czech)

[4] E. Adámková et al., Technology of Water Soluble Cores for Foundry Applications, Proceedings of XX. International Student's Day of Metallurgy, Cracow, Poland, 2013, 8 p. (CD-ROM)

[5] P. Jelínek et. al., Development of technology of salt cores manufacture, Slévárenství, LXI (**2013**) 1–2, 28–31 (in Czech)

[6] P. Jelínek et. al., Influencing the strength characteristics of salt cores soluble in water, Slévárenství, LX (**2012**) 3–4, 85–89 (in Czech)

UDK 519.61/.64:621.7.016.2
Original scientific article/Izvirni znanstveni članek

ISSN 1580-2949
MTAEC9, 49(1)69(2015)

MATHEMATICAL MODELLING AND PHYSICAL SIMULATION OF THE HOT PLASTIC DEFORMATION AND RECRYSTALLIZATION OF STEEL WITH MICRO-ADDITIVES

MATEMATIČNO MODELIRANJE IN FIZIKALNA SIMULACIJA VROČE PLASTIČNE PREDELAVE IN REKRISTALIZACIJE JEKLA Z MIKRODODATKI

Elżbieta Kalinowska-Ozgowicz[1], **Wojciech Wajda**[2], **Wojciech Ozgowicz**[1]

[1]Institute of Engineering Materials and Biomaterials, Silesian University of Technology, ul. Konarskiego 18a, 44-100 Gliwice, Poland
[2]Institute of Metallurgy and Materials Science, Polish Academy of Science, ul. Reymonta 25, Kraków, Poland
wojciech.ozgowicz@polsl.pl

Prejem rokopisa – received: 2013-10-07; sprejem za objavo – accepted for publication: 2014-02-06

This paper deals with the possibility of optimizing the parameters for a thermomechanical treatment of structural steel with micro-additives, particularly in the processes of the controlled rolling of economical profiles type [240E by means of mathematical modelling of the flow stress (σ_p) and the physical simulation of this process based on the results of investigations obtained by plastometric hot-torsion tests. In the description of the flow stress the rheological model suggested by C. M. Sellars is applied in the paper, in the form $\sigma_p = f(\varepsilon,\dot{\varepsilon},T)$. Based on this model, the cause of the experimental and theoretical flow stress-strain curves was verified, applying the minimum of the goal function in order to determine most accurately the matching of the analysed curves of the investigated steels. It was found that the applied rheological model achieves a good matching of the experimental and theoretical curves, whereas a physical simulation permits a complementary verification of the optimal parameters of the controlled rolling of the manufactured products.

Keywords: flow stress, plastometric torsion test, rheological model, physical simulation, thermomechanical controlled processing (TMCP)

Članek obravnava možnost optimizacije parametrov termomehanske obdelave konstrukcijskega jekla z mikrododatki, posebno procese kontroliranega valjanja ekonomskih profilov vrste [240E, z uporabo matematičnega modeliranja napetosti tečenja (σ_p) in fizikalne simulacije tega procesa na osnovi rezultatov raziskav, dobljenih s preizkusi na vročem torzijskem plastometru. V tem članku je bil za opis napetosti tečenja uporabljen reološki model, ki ga je predlagal C. M. Sellars, v obliki $\sigma_p = f(\varepsilon,\dot{\varepsilon},T)$. Na podlagi tega modela so bile preizkušene eksperimentalne in teoretične krivulje tečenje – raztezek z uporabo minimuma ciljne funkcije, da bi določili najboljše ujemanje analiziranih krivulj preiskovanih jekel. Ugotovljeno je, da uporabljeni reološki model zagotavlja dobro ujemanje eksperimentalnih in teoretičnih krivulj, medtem ko fizikalna simulacija dopolnjuje preverjanje optimalnih parametrov kontroliranega valjanja proizvodov.

Ključne besede: napetost tečenja, plastometrični torzijski preizkus, reološki model, fizikalna simulacija, termomehansko kontrolirana predelava (TMCP)

1 INTRODUCTION

Mathematical modelling is an essential and economical tool in the application of new techniques for the hot plastic deformation of metals and alloys. It makes it possible not only to reduce the number of technical experiments, but also to assess the interaction of the technological parameters of the investigated processes determining the usability of the final products. Therefore, it integrates, in most cases, the thermal, mechanical and microstructural processes. In the future modelling will constitute the basis of a system for controlling most technological processes. The constructed models will be applied simultaneously in an off-line simulation and on-line control of the processes[1–3].

The determination of the parameters of force in thermomechanically controlled processing (TMCP), particularly in the controlled rolling of new profiles, requires a knowledge of the values of the flow stress of the steel under the specific conditions of the deformation. One of numerous methods for determining these stresses is the hot plastometric torsion test, which also permits a physical simulation of the sequential rolling deformation. Thus, it becomes possible to determine the values of the flow stress in successive roll passes, separated by interpass times in which thermally activated processes occur, removing the results of the strain hardening[4].

The paper presents possibilities for the mathematical modelling of hot plastic deformation concerning some selected products obtained by rolling structural steels with micro-additives in the range of technological parameters simulating such processes in the plastometric torsion test. Special attention was paid to the verification of the rheological model developed by C. M. Sellars et al.[5,6] describing the flow stress as a function of the deformation and temperature, as well as strain rate and the effect of dynamic recrystallization, which dominates in the hot deformation for the investigated structural steels with micro-additives of Nb, V, Ti and N.

2 EXPERIMENTAL PROCEDURE

2.1 Materials

The tests were carried out on industrial melts of structural steels with micro-additives, the chemical composition of which is shown in **Table 1**.

Plastometric tests of the steel were performed applying the hot-torsion method. The tested samples had a diameter of 6 mm and a basis length of 10 mm. They were cut out from slabs with dimensions of 200 mm × 220 mm × 5300 mm provided after the hot rolling. By means of continuous torsion, the characteristics of plasticity for the investigated steels were determined in the $\sigma - \varepsilon$ system, depending on the temperature of austenitization (1150–1200 °C) and deformation (800–1050 °C) as well as on the strain rate within the range 0.15 s^{-1} to 10 s^{-1}. The testing was conducted on a torsion plastometer that was designed at the Institute of Iron Metallurgy in Gliwice, Poland. The conversion of torque-twist to stress-strain was generally based on a Fields and Backofen[7] analysis, commonly quoted in[8].

2.2 Rheological model

In constitutive equations, actually applied for the purpose of modelling the processes of hot plastic working, the effects of dynamic recovery and dynamic recrystallization are not always conveyed explicitly. The equation in which both components are distinctly separated, elaborated at the University of Sheffield by C. M. Sellars et al.[5,6], takes the following form:

$$\sigma = \sigma_0 + (\sigma_{SS(e)} - \sigma_0)\left[1 - \exp\left(\frac{\varepsilon}{\varepsilon_r}\right)\right]^{1/2} - R \tag{1}$$

where the respective variables are defined as follows:

$$R = \begin{cases} 0 & \text{for } \varepsilon \le \varepsilon_C \\ (\sigma_{SS(e)} - \sigma_{SS})\left\{1 - \exp\left[-\left(\dfrac{\varepsilon - \varepsilon_C}{\varepsilon_{xr} - \varepsilon_C}\right)^2\right]\right\} & \varepsilon > \varepsilon_C \end{cases} \tag{1a}$$

$$\sigma_0 = \frac{1}{\alpha_0}\sinh^{-1}\left(\frac{Z}{A_0}\right)^{\frac{1}{n_0}} \tag{1b}$$

$$\sigma_{SS(e)} = \frac{1}{\alpha_{SS(e)}}\sinh^{-1}\left(\frac{Z}{A_{SS(e)}}\right)^{\frac{1}{n_{SS(e)}}} \tag{1c}$$

$$\sigma_{SS} = \frac{1}{\alpha_{SS}}\sinh^{-1}\left(\frac{Z}{A_{SS}}\right)^{\frac{1}{n_{SS}}} \tag{1d}$$

$$\varepsilon_r = 0.31\left[q_1 + q_2(\sigma_{SS(e)})^2\right] \tag{1e}$$

$$\varepsilon_{xr} - \varepsilon_C = \frac{\varepsilon_{xs} - \varepsilon_C}{1.98} \tag{1f}$$

$$\varepsilon_C = C_0\left(\frac{Z}{\sigma^2_{SS(e)}}\right)^{Ne} \tag{1g}$$

$$\varepsilon_{xs} - \varepsilon_C = C_x\left(\frac{Z}{\sigma^2_{SS(e)}}\right)^{Nx} \tag{1h}$$

$$Z = \dot{\varepsilon}\exp\left(\frac{Q_{def}}{RT_{def}}\right) \tag{1i}$$

The variables in Equation (1) are as follows:

σ_p – flow stress
σ_0 – the maximum stress when the plastic strain $\varepsilon = 0$
$\sigma_{SS(e)}$ – the onset of steady-state conditions in the extrapolated curve
σ_{SS} – the onset of steady-state conditions on the experimental flow stress curve
ε – plastic deformation
ε_C – strain for the onset of dynamic recrystallization
ε_r – the "transient strain constant" and effectively defines the curvature of the flow-stress curve between σ_p and $\sigma_{SS(e)}$ where the equation saturates
ε_{xr} – the strain required to reach a fixed amount of softening, measured in terms of $\Delta\sigma/\Delta\sigma_S$. This term effectively defines the rate of softening as a result of the dynamic recrystallization
ε_{xs} – the strain at the "onset" of steady state when dynamic recrystallization occurs
$\dot{\varepsilon}$ – strain rate
Z – Zener – Hollomon parameter
R – the universal gas constant
R_x – a term expressing the dynamic recrystallization
Q_{def} – the activation energy for the deformation
A, α, n, q, C, N – constants for each characteristic stress σ_p.

Table 1: Chemical composition of the tested steels
Tabela 1: Kemijska sestava uporabljenih jekel

Steel	Concentration of the element in mass fractions, *w*/%										
	C	Mn	Si	Cr	P	S	Nb	V	Ti	N	Al
B1	0.15	1.03	0.25	–	0.018	0.009	0.017	0.05	–	0.0070	0.040
B2	0.16	1.25	0.32	–	0.023	0.019	0.030	0.01	–	0.0060	0.042
S9	0.38	1.52	0.63	0.56	0.027	0.012	0.030	–	0.11	–	–
S1	0.66	1.02	0.26	0.30	0.029	0.021	–	0.10	–	0.0080	–

The presented model illustrates more distinctly the behaviour of the material in the course of dynamic recrystallization, because it makes it possible to describe the point of deflection ($\varepsilon_{\mathrm{peak}}$) on the curves $\sigma - \varepsilon$ and the procedure of flow stress beginning at the peak strain up to the achievement of the value of the stresses in the steady state (σ_{SS}). The coefficients of this constitutive equation are usually determined based on the results of plastometric tests within a wide range of temperature and strain rates.

This allows us to model various structural materials over a wide range of conditions for hot plastic deformation. The main difficulty in applying this model lies in the large number of parameters, which have to be unambiguously identified. One of the main factors limiting the application of the mode simulating the processes of plastic working is the difficulty in determining these coefficients, the values of which depend on the kind of applied material. Nevertheless, Equation (1) has been used in this study for the investigated microalloyed steels.

For the optimization of the parameters of the applied model of C. M. Sellars[5,6], describing stress–strain curves, making use of the goal function ϕ in the form:

$$\phi=\sum_{i=1}^{N_{\mathrm{p}}}\sqrt{\frac{1}{N_{\mathrm{p}}}\left(\frac{\sigma_{\mathrm{m}i}-\sigma_{\mathrm{C}i}}{\sigma_{\mathrm{m}i}}\right)^{2}} \qquad (2)$$

where:

σ_{m} – measured stress

σ_{c} – calculated stress

N_{p} – number of measurement points of all the curves in the i-th experiment

For the purpose of the minimum of Equation (2), the Nelder and Mead Simplex algorithm was used. The calculations were performed by means of Scilab's calculation packet.[9] In results of the optimization for the appropriate parameters of Equation (1) were found.

3 EXPERIMENTAL RESULTS AND DISCUSSION

The results of the mathematical modelling of the process of high-temperature plastic deformation for the investigated micro-alloyed steels allowed us to verify analytically the assumed Eqation (1) of the type $\sigma_{\mathrm{p}} = \sigma_{\mathrm{p}}(\varepsilon, \dot{\varepsilon}, T)$ describing the flow stress (σ_{p}) on the experimental flow-stress curves, making use of the plastometric method for metals and alloys with a low stacking-fault energy (SFE), which in the course of hot deformation display the phenomenon of dynamic recrystallization. Modelling was applied for some selected microalloyed steels of the type HSLA with various contents of the micro-additive Nb (steel B1 and B2), as well as an average-carbon structural steel (0.38 % C) with a binary system of micro-additives of Nb and Ti and a structural rail steel containing about 0.66 % carbon with the micro-additive V (0.10 %). The performed numerical calculations were based on the results of a hot-torsion test, analysing about 80 stress-strain curves recorded with a wide range of external variables, particularly the temperature and the strain rate. A comparison of the experimental flow curves with those in the model concerning the investigated steels is presented in the diagrams in **Figures 1** to **4**. In order to obtain a universal description of the flow curves, the complete data of measurements $\sigma_{\mathrm{p}}(\varepsilon, \dot{\varepsilon}, T)$ concerning the respective kinds of steel were optimized. The influence of the varying distribution of strains on the radius of the twisted sample, as well as the changes in the temperature at the cross-section of a massive sample have, in the process of optimization, not been taken into account. This might perturb the obtained results, particularly the identified parameters of the rheological model, as has been shown in[10]. The elimination of the effect of the homogeneity of deformation and other errors in the measurements ensures the identification of the parameters of the model, applying the inverse method[11,12]. The paper[10] analyses, however, only the application of this method in the case of various types of hot-compression tests. Future plans will include the application of the inverse method in dealing with the results of hot torsion tests. The numerically determined values of the coefficients assumed in the model, taking into account the Simplex algorithm

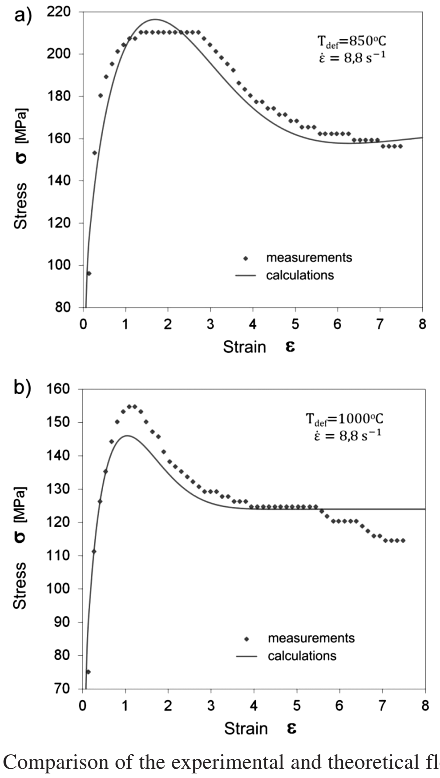

Figure 1: Comparison of the experimental and theoretical flow curves of microalloyed steel B1, hot deformed in compliance with the torsion method at a strain rate of 8.8 s^{-1} and at: a) T_{def} = 850 °C and b) T_{def} = 1000 °C

Slika 1: Primerjava eksperimentalne in teoretične krivulje tečenja vroče deformiranega mikrolegiranega jekla B1 v primerjavi z metodo torzije pri hitrosti deformacije 8,8 s^{-1} pri: a) T_{def} = 850 °C in b) T_{def} = 1000 °C

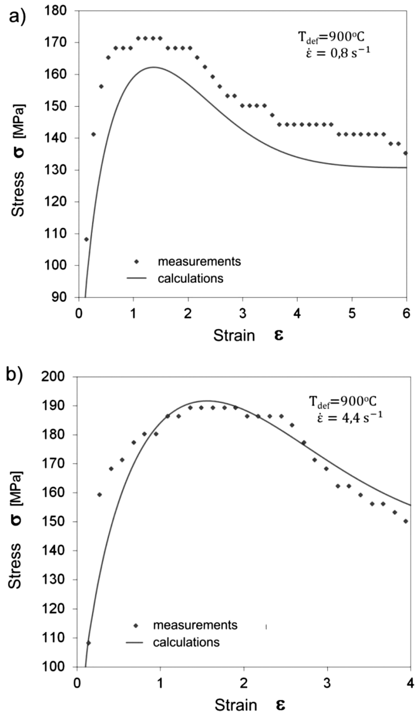

Figure 2: Experimental and modelled flow curves of microalloyed steel B2, hot twisted at T_{def} = 900 °C and a strain rate of: a) $\dot{\varepsilon} = 0.8\ \mathrm{s}^{-1}$ and b) $\dot{\varepsilon} = 4.45\ \mathrm{s}^{-1}$

Slika 2: Eksperimentalna in modelirana krivulja tečenja jekla B2, vroče zvijanega pri T_{def} = 900 °C in hitrosti deformacije: a) $\dot{\varepsilon} = 0{,}8\ \mathrm{s}^{-1}$ in b) $\dot{\varepsilon} = 4{,}45\ \mathrm{s}^{-1}$

concerning the analysed stress-strain curves are shown in **Table 2**, which also contains the values of the energy of activation of the process of deformation and the final values of the goal function ϕ, representing the accuracy of the modelling solution. Due to measurement errors and limitations with the model, different values were obtained for the goal function (Equation (2)) concerning the particular types of investigated steels. However, the median square error of the calculation remains within 2–5 % limits. This proves that the assumed model fits well with the experimental results. The flow curves of the investigated steels indicate principally the characteristic procedure of the continuous dynamic recrystallization. Their analysis permits us to state that this process is essentially influenced by the temperatures (**Figure 1**) and the strain rate (**Figure 2**), as well as the chemical composition of the steel (**Figures 1** to **4**). The effect of these factors concerns, first of all, changes in the value of the maximum flow stress and the stresses in the steady state (σ_{ss}), and also the values of critical deformations (ε_{f}), generally assumed to be in compliance with the criterion of the plasticity of steel in the process of hot deformation. It has been generally assumed that the stresses in the flow of the investigated steels increase with the drop in the temperature and the increasing strain rate. It has also been found that the best compatibility in matching the experimental and theoretical curves is achieved in the case of steel S9 (**Figure 3**), with the

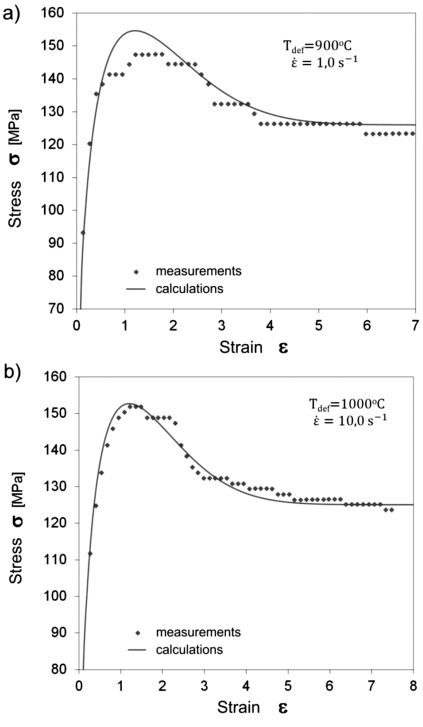

Figure 3: Comparison of experimental and modelled flow curves of steel S9 in a hot torsion test: a) T_{def} = 900 °C, $\dot{\varepsilon} = 1\ \mathrm{s}^{-1}$, b) T_{def} = 1000 °C, $\dot{\varepsilon} = 10\ \mathrm{s}^{-1}$

Slika 3: Primerjava eksperimentalne in modelirane krivulje tečenja jekla S9 pri preizkusu vroče torzije: a) T_{def} = 900 °C, $\dot{\varepsilon} = 1\ \mathrm{s}^{-1}$, b) T_{def} = 1000 °C, $\dot{\varepsilon} = 10\ \mathrm{s}^{-1}$

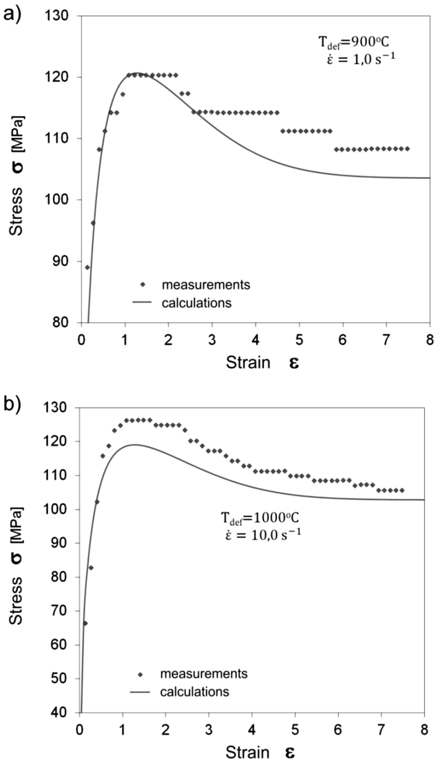

Figure 4: Experimental and modelled flow curves of steel S1, hot twisted at: a) T_{def} = 900 °C, $\dot{\varepsilon} = 1\ \mathrm{s}^{-1}$, b) T_{def} = 1000 °C, $\dot{\varepsilon} = 10\ \mathrm{s}^{-1}$

Slika 4: Eksperimentalna in modelirana krivulja tečenja jekla S1, vroče zvijanega pri: a) T_{def} = 900 °C, $\dot{\varepsilon} = 1\ \mathrm{s}^{-1}$, b) T_{def} = 1000 °C, $\dot{\varepsilon} = 10\ \mathrm{s}^{-1}$

Table 2: Optimal coefficients of the rheological model obtained as a result of Simplex optimization concerning the investigated steels with micro-additives
Tabela 2: Optimalni koeficienti reološkega modela, dobljeni kot rezultati optimizacije Simplex preiskovanih jekel z mikrododatki

Steel No.	Rheology – σ_o			Activation energy Q/(J/mol)	Goal function ϕ
	Coefficients				
	A_o	n_o	α_o		
B1	$4.1200 \cdot 10^{11}$	0.0525	2.2969	278323.4	0.0489
B2	$1.7800 \cdot 10^{13}$	0.1223	0.8931	330559.2	0.0399
S9	$2.2300 \cdot 10^{8}$	0.0535	36.5915	297570.7	0.0336
S1	$3.7700 \cdot 10^{10}$	0.0193	21.2038	296973.7	0.0518
Steel No.	Rheology – strain hardening and dynamic recovery				
	A_{sse}	n_{sse}	α_{sse}	q_1	q_2
B1	$3.19 \cdot 10^{13}$	4.2182	0.0028	0.1668	$0.0067 \cdot 10^{-2}$
B2	$6.38 \cdot 10^{19}$	4.3216	0.0039	$0.0024 \cdot 10^{-2}$	$0.0075 \cdot 10^{-2}$
S9	$2.81 \cdot 10^{13}$	5.3884	0.0049	0.6791	$0.0026 \cdot 10^{-2}$
S1	$1.86 \cdot 10^{11}$	2.4098	0.0203	1.2176	$0.0001 \cdot 10^{-2}$

Steel No.	Rheology – strain hardening and dynamic recrystallization						
	A_{ss}	n_{ss}	α_{ss}	C_c	N_c	C_x	N_x
B1	$1.80 \cdot 10^{9}$	2.4377	0.029	0.000036	0.0244	0.0234	0.279958
B2	$1.22 \cdot 10^{10}$	2.5560	0.0365	0.0433	0.0079	0.0812	0.1763
S9	$5.99 \cdot 10^{8}$	3.6426	0.0279	0.0944	0.0378	0.6839	0.0957
S1	$1.21 \cdot 10^{9}$	3.9124	0.0302	$0.0018 \cdot 10^{-2}$	0.0427	1.4927	0.0670

Table 3: Characteristics of the process of rolling the profile [240E
Tabela 3: Značilnosti postopka valjanja profila [240E

Table of roll passes				Profile [240E				
Slab: 200 mm × 200 mm × 6000 mm; S_o = 382 cm^2								
Stand	Roll Pass No.	Working pass No.	ε_s/%	ε_h/%	Pass input temp. T/°C	S_k/cm^2	v_l/(m/s)	φ/s^{-1}
BD	1	4	2.9	2.5	1150–1180	371.0	2.52	1.32
Z1	2	1	17.0	24.6	1140–1170	307.9	4.54	10.30
Z1	3	2	29.4	34.3	–	217.3	5.35	17.56
Z1	4	3	29.3	30.6	–	153.6	6.12	21.86
Z1	5	4	28.3	29.9	–	110.2	6.84	28.36
Z1	6	5	19.8	21.3	1050–1080	88.4	6.89	25.54
Z2	7	6	26.2	27.0	1020–1055	65.2	9.01	47.80
Z2	8	7	25.9	25.9	–	48.3	9.09	54.36
Z2	9	8	19.0	21.5	950–1020	39.1	8.83	52.60
D1	10	9	15.3	12.7	960–1050	33.9	6.97	34.57
D2	11	10	10.0	8.8	920–950	30.5	6.93	29.16

ε_s, ε_h indices for the deformation of the rolled channel section [240E
S_k – running cross-section of the rolled band
v_l – linear velocity of the rolling
φ – strain rate of the rolled band

values of goal function ϕ = 0.0336, within the entire range of the temperature and deformations.

In the case of simulative investigations, some constitutive equations were applied, concerning the modelling of the microstructure[13,14], as well as the kinetics of dynamic recrystallization, developed based on data obtained in plastometric tests for a varying size of the primary austenite grain. As in the rheological model, the kinetics of dynamic recrystallization was taken into account, and it was included in the function of the yield stress, expressed by Equation (1). Thus, in the Sellars model the stress depends on the size of the austenite grain. This model predicts a more accurate flow of the material, particularly in the processes of reiterated deformations in the case of hot rolling.

The rolling of channel iron [240E of type B2 steel was physically simulated based on the parameters of the rolling mill collected in **Table 3**. These parameters served as the output data for the physical simulation realized on a torsional plastometer in a test of hot torsion, applying the sequential method at a strain rate amounting to about 4.0 s^{-1}. The analysed flow curves were compared with the $\sigma - \varepsilon$ curves that were determined in the course of continuous torsion tests in order to determine the effect of global cycles of deformation on the initiation and progress of the activated thermal processes occurring during the intervals between the roll passes. The results of the kinetic investigations, including an analysis of the share of the decay of strain hardening during the interpass times, are presented in the

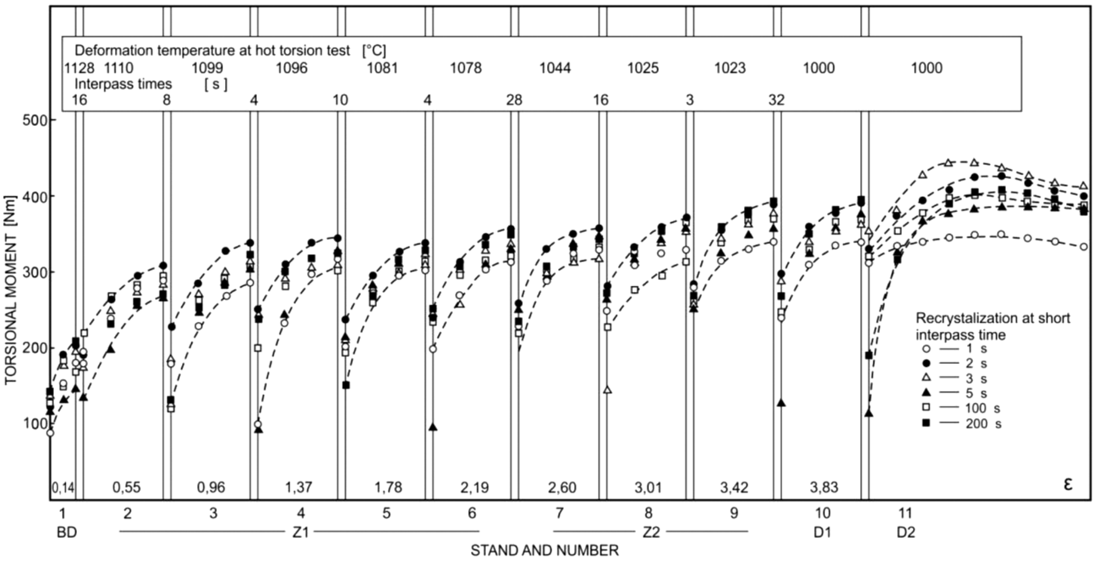

Figure 5: Deformation schedules for channel section type [240E; rolling simulations of microalloyed steel B2
Slika 5: Zaporedje deformacij v kanalskem delu vrste [240E; simulacija valjanja mikrolegiranega jekla B2

diagrams in **Figure 5**. The deformations in the respective sequential roll passes were found to be less than the critical values required for the initiation of dynamic recrystallization determined by continuous $\sigma - \varepsilon$ curves, similar to the case in tests of physical simulations, whereas global deformations in the respective roll passes exceeded the values $\varepsilon_{\rm cd}$. Thus we can assume that in the case of the last roll passes on the flushing stand D1 and D2 the strain hardening is accumulated. This character of the deformation changes determines the occurrence of both static and meta-dynamic recrystallization, and consequently a grain refinement of the investigated steels.

4 CONCLUSIONS

The mathematical modelling of flow stress in the course of high-temperature deformation allows us to obtain the optimal parameters for the thermomechanically controlled processing of the tested structural steels with micro-additives.

Sellars's rheological model provides good matching of the experimental and theoretical flow curves in the investigated steels, determined on the basis of hot plastometric torsion tests.

A correct model describing the behaviour of HSLA steel type B2 during high-temperature plastic deformation process ensured an accurate simulation of the sequential rolling schedule for a selected economical section of the type [240E.

A physical simulation of the rolling schedule of a channel section [240E by the means of hot torsion tests ensures the yield stress values $\sigma_{\rm p}$ in consecutive roll passes and calculates the force and energy parameters in the controlled rolling process.

A kinetic analysis of thermally activated phenomena occurring in the course of high-temperature plastic deformation and interpass times ensures the possibility of shaping the structure of the investigated steels and to determine the mechanical properties of the final products.

5 REFERENCES

[1] P. D. Hodgson, PhD Thesis, Univ. of Queensland, 1993
[2] D. Martin, Mater. Sci. Technol., 10 (**1994**) 10, 855–861
[3] R. Kuziak, Institute for Ferrous Metallurgy, Gliwice, 2005 (in Polish)
[4] Z. Kuzminski, A. Nowakowski, M. Gębala, Hutnik – Wiadomości Hutnicze, 8–9 (**2006**), 394–399
[5] S. Davenport, N. Silk, C. Sparks, C. M. Sellars, Mater. Sci. Technol., 16 (**2000**), 539–546
[6] B. Kowalski, C. M. Sellars, M. Pietrzyk, ISIJ Int., 40 (**2000**), 1230–1236
[7] D. S. Fields, W. A. Backofen, 40 (**2000**) 1, 35
[8] F. Grosman, E. Hadasik, Silesian University of Technology, Gliwice, 2005 (in Polish)
[9] http://www.scilab.org/
[10] D. Szeliga, M. Pietrzyk, Arch. Civ. Mech. Eng., 7 (**2007**) 1, 35
[11] J. Lenard, M. Pietrzyk, L. Cser, Mathematical and physical simulation of the properties of hot rolled products, Elsevier, Amsterdam 1999
[12] D. Szyndler, PhD Thesis, AGH, Kraków, 2001 (in Polish)
[13] R. Kuziak et.al., Transaction of the Institute for Ferrous Metallurgy, 1 (**2012**), 17–23
[14] E. Kalinowska-Ozgowicz, Structural and mechanical factors of the strengthening and recrystalization of hot plastic deformation of steels with microadditives, Open Access Library, 20 (**2013**) 2, 1–246

UDK 620.3:66.017:669.018.9
Original scientific article/Izvirni znanstveni članek

ISSN 1580-2949
MTAEC9, 49(1)75(2015)

SYNTHESIS OF NiTi/Ni-TiO$_2$ COMPOSITE NANOPARTICLES VIA ULTRASONIC SPRAY PYROLYSIS

SINTEZA KOMPOZITNIH NANODELCEV NiTi/Ni-TiO$_2$ Z ULTRAZVOČNO RAZPRŠILNO PIROLIZO

Peter Majerič[1], Rebeka Rudolf[1,2], Ivan Anžel[1], Jelena Bogović[3], Srečko Stopić[3], Bernd Friedrich[3]

[1]Faculty of Mechanical Engineering, Smetanova 17, 2000 Maribor, Slovenia
[2]Zlatarna Celje d.d., Kersnikova 19, 3000 Celje, Slovenia
[3]IME Process Metallurgy and Metal Recycling, RWTH University Aachen, Intzestrasse 3, Aachen, Germany
peter.majeric@um.si

Prejem rokopisa – received: 2013-10-09; sprejem za objavo – accepted for publication: 2014-02-26

In this paper we present the production of NiTi/Ni-TiO$_2$ composite nanoparticles via the synthesis method called ultrasonic spray pyrolysis (USP). The precursor solution for the synthesis of spherical NiTi particles was prepared from an orthodontic wire with a chemical composition of Ni (amount fraction $x = 51.46$ %) and Ti ($x = 48.54$ %). TEM microscopy, in combination with EDX analyses, was used for a detailed characterization of the obtained NiTi nanoparticles. The results showed the nanoparticle sizes ranging from 60 nm to 600 nm, depending on the parameters of the production procedure. This showed the versatility of the new USP synthesis procedure, proving its usefulness for different materials and applications.

Keywords: ultrasonic spray pyrolysis, NiTi/Ni-TiO$_2$ composite nanoparticles, characterization, TEM microscopy

V tem prispevku je predstavljena izdelava NiTi/Ni-TiO$_2$ kompozitnih nanodelcev po metodi ultrazvočne razpršilne pirolize (USP). Sferični nanodelci NiTi so bili izdelani iz ortodontske žice s kemijsko sestavo Ni (množinski delež $x = 51{,}46$ %) in Ti ($x = 48{,}54$ %). Za karakterizacijo nanodelcev je bila uporabljena TEM-mikroskopija v kombinaciji z EDX-analizo. Rezultati meritev so pokazali velikostno porazdelitev narejenih nanodelcev v razponu od 60 nm do 600 nm v odvisnosti od parametrov izdelave. To potrjuje vsestranskost novega izdelovalnega postopka USP in njegovo uporabnost za različne materiale in aplikacije.

Ključne besede: ultrazvočna razpršilna piroliza, kompozitni nanodelci NiTi/Ni-TiO$_2$, karakterizacija, TEM-mikroskopija

1 INTRODUCTION

During the recent swarm of nanosized materials in the last decade, nanosized particles of nickel titanium, a shape-memory alloy in the macroscopic world, have not been overlooked. The potential of the nanoparticles of NiTi lies in their biocompatibility, magnetic and photocatalytic properties.[1] As such, they have a potential for applications in the anode of solid-oxide fuel cells or in the conductive electrolytic layer of proton-exchange-membrane fuel cells. Replacing platinum with nickel titanium nanoparticles in automotive catalytic converters would also significantly reduce their costs. They also have a potential in coatings, plastics, nanowires, nanofibers and textiles or as a temperature-control system.[2]

The most widely used method for producing nickel titanium nanoparticles is laser ablation of the alloy in a liquid. Laser ablation has some advantages as a production method, such as a disperse distribution of the colloids in the solvent, no use of toxic chemical precursors, chemically pure nanoparticles and its applicability for different materials.[3] The produced NiTi nanoparticles form a titanium oxide layer on the surface, creating a core-shell structure of the nanoparticles. The thickness of the layer varies, depending on the organic liquids used for the suspension.[4] Other production methods of NiTi nanoparticles include ultrasonic electrolysis, mechanically assisted synthesis (nickel and titanium powders in a planetary ball mill),[5] electro-explosion of a NiTi wire with spark-plasma sintering,[6] gas-flash evaporation,[7] thin-film deposition in combination with nanosphere lithography,[8] electric-discharge plasma in liquid[9] and biosynthesis/bioreduction.[10]

For the purposes of positioning the teeth to a desired location in orthodontics, NiTi wires have been proved to be very useful. This alloy's shape-memory effect and superelasticity provide a good combination of care for the patient and a reasonable treatment duration.[11] Even though nickel is considered toxic, the nickel titanium alloy is biocompatible due to the high reactivity of titanium in oxygenated environments. As such, a titanium dioxide layer is formed on the surface of a shape-memory alloy, providing a good corrosion resistance and preventing nickel from migrating outwards from the alloy, causing biocompatibility of the alloy. To further improve the handling of such orthodontic tools, a project involving nickel titanium nanoparticles for orthodontics was proposed. A replacement for the bulk nickel titanium wire with a textile or polymer fiber coated with NiTi nanoparticles via electrospinning and then removing the fiber could produce a hollow wire for orthodontic purposes. This wire could potentially have the same shape-memory and superelasticity properties, while possibly reducing the material needed for the wire production. After producing such a hollow NiTi wire, its properties would have to be compared with the original NiTi orthodontic wire already in use.

In our research of the nanoparticle production, we had some successes with the production of gold nanoparticles with the ultrasonic-spray-pyrolysis method (USP).[12] This is a simple, low-cost process, available to produce nanoparticles from different materials. The concept of USP is to produce aerosol droplets of a solution with a dissolved material, desired for the nanoparticles. These micro-sized droplets of the precursor solution are generated by the ultrasound. The frequency of the ultrasound and the surface tension of the solution determine the size of the droplets. The droplets are a few micrometers in diameter and are produced as the ultrasound reaches the surface of the liquid, generating cavitation (a formation, growth and implosive collapse of the bubbles in a liquid).[13,14] The generated droplets are then carried by a carrier gas into the furnace, where the reactions for the nanoparticle formation occur. The gas can be a mixture of a carrier gas and a reaction gas or, in some cases, a single gas acting as the carrier and reaction gas at the same time. When the droplets reach the furnace, the heightened temperature starts to evaporate the solvent and the droplets shrink in size. The dissolved material required for the nanoparticles starts to diffuse into the core of the droplet. The solvent evaporates completely and the dried porous particle then reacts with the reduction gas. The reacted particle is then sintered into the solid final particle, which is then carried away by the carrier gas into the collection bottles.[15] This is the principle of the one-particle-per-droplet mechanism.

The final size of the particle is thus mainly dependent on the size of the droplets, the precursor concentration and the reactor temperature. The droplet size is controlled with the ultrasound frequency, as higher frequencies produce smaller droplets. Higher precursor concentrations cause a higher concentration in a droplet and a bigger final particle size.[12] The temperature must be high enough for the reactions to occur. However, very high temperatures evaporate the solvent faster, leaving less time for the diffusion of the material. When this occurs, the result is the creation of porous particles and particles with irregular shapes. In some cases the material reaction occurs on the surface of the droplets, creating shell structures. In the case of creating ideally spherical particles, an ideal temperature must be found, low enough to allow the time for diffusion, while still high enough for the required reactions to occur. This could be done experimentally or theoretically, where a lot of diffusion and reaction data would have to be acquired. A two-step USP process can also be employed, capable of creating core-shell structures with two different materials.[13]

In this work we present the results of our first experimental work in the field of NiTi/Ni-TiO_2 composite-nanoparticle production via USP. With this research we want to simplify the field of nanotechnology, allowing a transfer of this production to the industrial level.

2 MATERIALS AND METHODS

For the synthesis of NiTi/Ni-TiO_2 composite nanoparticles, we used an orthodontic wire composed of amount fraction of Ni x = 51.46 % and x = 48.54 % of Ti. To prepare the precursor for USP, the wire was dissolved in aqua regia (12 mL or 24 mL of HNO_3 + 3HCl) and the resulting solution was topped off to the required volume with water (a total volume of 500 mL).

The resulting solution was then used for generating aerosol droplets with a USP device assembled at the IME Process Metallurgy and Metal Recycling, RWTH Aachen University, Germany. The device contains an ultrasonic atomizer with an ultrasound generator and a reservoir for the precursor, a thermostat for keeping the precursor solution at a constant temperature, a quartz tube and furnace for the reaction of precursor droplets, some tubing leading the aerosol into and out of the furnace, and collection bottles with alcohol and water for the nanoparticle collection (**Figure 1**). The ultrasonic atomizer (Gapusol 9001, RBI/France) was producing aerosol droplets with one transducer at the selected frequency of 2.5 MHz.

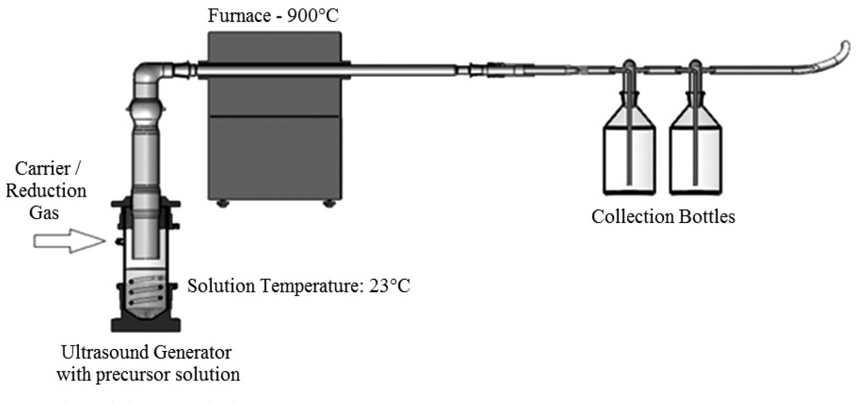

Figure 1: Schematic presentation of the USP device
Slika 1: Shematska predstavitev USP-naprave

The experiment of the USP procedure was run in several steps. First, nitrogen was flushed into the system at a rate of 1 L/min to remove air from the tubes. When the furnace reached the selected temperature, hydrogen was added to the flow of nitrogen, at a rate of 1.5 L/min. After a while, a steady flow of nitrogen and hydrogen was established. At this time, the ultrasonic generator was turned on, creating aerosol droplets from the precursor solution. The droplets were then carried via gas into the furnace, where the reactions occurred, and the final particles were then carried out of the furnace and collected in the collection bottles. The retention time of the droplets/particles in the quartz tube of 1 m length and 20 mm diameter was about 30 s. The temperature of the precursor solution was kept at 23 °C and the furnace temperature at 900 °C. The system parameters (the solution temperature, furnace temperature, steady volume of the solution in the ultrasonic atomizer, etc.) were being monitored for the duration of the experiment. The collection bottles in the first experiments contained water and, in later experiments, alcohol for the prevention of agglomeration and titanium oxide formation. The experiment parameters are provided in **Table 1**.

Table 1: Technological parameters of the performed experiments
Tabela 1: Tehnološki parametri opravljenih eksperimentov

Experiment	Concentration (g/L)	Temperature (°C)	Gas flow N_2 (L/min)	Gas flow H_2 (L/min)	Time (h)	Collection
1	0.5	900	1	1.5	5.5	Water
2	0.25	900	1	1.5	5.5	Water
3	0.5	900	1	1.5	5.0	Ethanol
4	0.25	900	1	1.5	5.0	Ethanol

A transmission electron microscope (TEM) with an EDX analysis was used for the characterization of the obtained nanoparticles and analysis of their morphology.

3 RESULTS

The NiTi/Ni-TiO$_2$ composite orthodontic wire was dissolved in aqua regia (HNO$_3$ + 3HCl) and diluted with water. The oxidizing properties of chloride ions and chlorine etch away nickel and titanium from the lattice, creating nickel chlorides NiCl$_2$ and titanium chlorides TiCl$_4$. The addition of hydrogen gas inside the furnace then reduces the chlorides and creates particles with nickel and titanium. The resulting sizes of the produced nanoparticles are dependent on the precursor concentration and ultrasound frequency used for the creation of aerosol droplets, as reported previously.[12] The obtained solution was left overnight for particle sedimentation. The excess fluid was removed and the resulting samples were characterized with TEM and EDX analysis. The analysis showed nearly ideally spherical nanoparticles with different sizes (**Figure 2**), according to the concentration and the ultrasound frequency. The obtained nanoparticles consisted of titanium, nickel and oxygen (**Fig-**

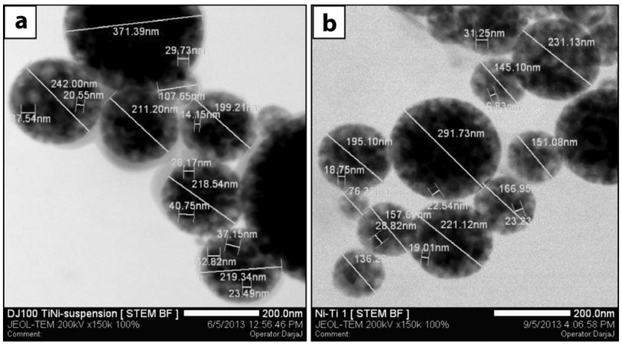

Figure 2: Sizes of NiTi/Ni-TiO$_2$ composite nanoparticles depending on the precursor concentration: a) 0.5 g/L NiTi, experiment numbers 1 and 3, b) 0.25 g/L NiTi, experiment numbers 2 and 4

Slika 2: Velikosti kompozitnih nanodelcev NiTi/Ni-TiO$_2$ pri različnih koncentracijah prekurzorja: a) 0,5 g/L NiTi, številki poskusov 1 in 3, b) 0,25 g/L NiTi, številki poskusov 2 in 4

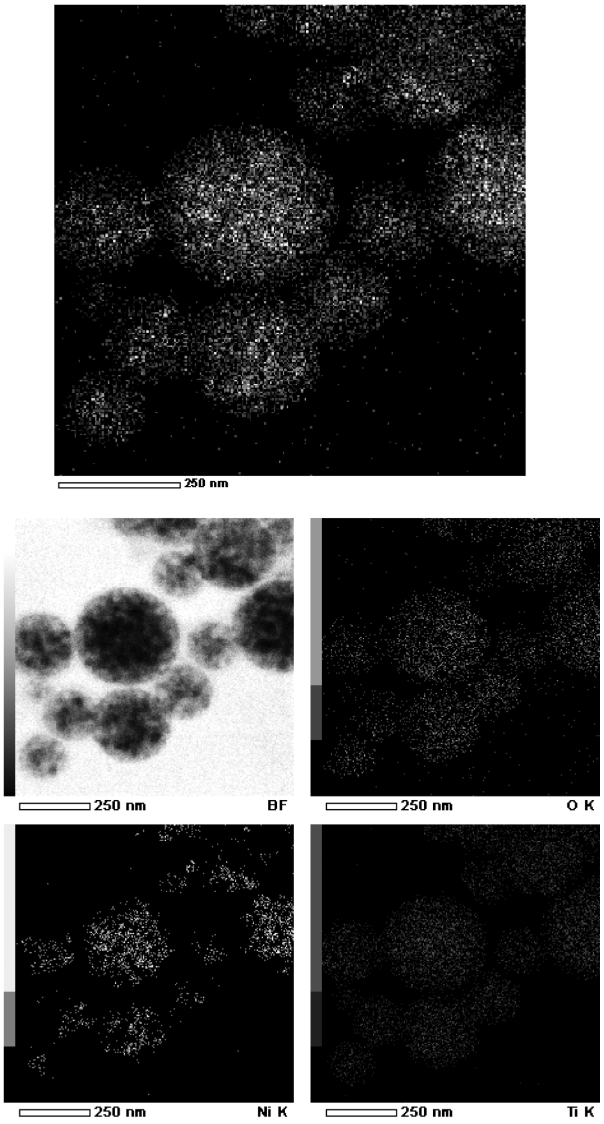

Figure 3: Element mapping of NiTi/Ni-TiO$_2$ composite nanoparticles (No. 1)

Slika 3: Porazdelitev elementov pri kompozitnih nanodelcih NiTi/Ni-TiO$_2$ (št. 1)

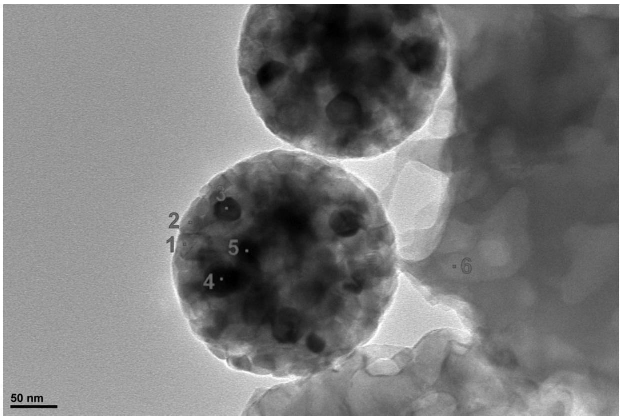

Figure 4: Points for the EDX analysis on the NiTi/Ni-TiO_2 composite nanoparticles' surface (No. 1)
Slika 4: Mesta na površini kompozitnih nanodelcev NiTi/Ni-TiO_2 (št. 1), kjer je bila izvršena EDX-analiza

ure 3). The ratio between nickel and titanium was lower than expected; with the orthodontic wire used for the experiments it was about 1 : 1, while with the nanoparticles the values for the nickel amount were much lower (**Figure 4** and **Table 2**).

Table 2: Chemical composition of the points on the NiTi nanoparticles' surface form **Figure 4**
Tabela 2: Kemijska sestava točk na površini nanodelcev NiTi s **slike 4**

Point	x(Ni)/%	x(Ti)/%	x(O)/%
1	/	44.29	54.05
2	/	41.72	56.60
3	31.22	28.21	39.36
4	40.78	20.65	38.02
5	21.78	26.88	50.70

4 DISCUSSION

The production steps for the synthesis of nanoparticles from an orthodontic NiTi wire and their usage with the process of electrospinning are shown in **Figure 5**. With electrospinning the particles are spun onto fibers like building blocks, producing a thin shell with the properties of the nanoparticle material. The fibers could then be removed, for example, with chemical etching, producing new, otherwise hard-to-obtain shapes.

The high reactivity of titanium with oxygen is a problem for pure nickel titanium nanoparticle formation. The results suggest that the nanoparticles are formed from titanium oxide with smaller amounts of nickel. Even though the reaction takes place in a hydrogen/nitrogen atmosphere, a high amount of oxygen also comes from the water of the precursor, as the reaction runs at a high temperature. Some effort was made to reduce the amount of titanium oxide formation with the use of alcohol in the collection bottles. A smaller amount of oxygen in alcohol allowed this reduction to occur to a certain degree, while the total elimination of the titanium oxide formation from the particles was not achieved. To obtain such particles, a different solution would be required for the dissolution of the NiTi wire. Organic compounds and alcohol were used previously; however, the results of such experiments were unsatisfactory. The use of such solutions as the precursor resulted in destroyed particles or no particles being collected in the collection bottles, or alcohol complexes being formed. The use of organic compounds would also increase the cost and complexity of the process, while not producing the desired product.

The analysis of the particles also showed that the larger particles contain more nickel than the smaller ones. This can also be seen from the TEM figures (**Figure 2**), where the darker, blackened areas represent nickel in the particles, whereas the lighter, grayer areas represent titanium dioxide. The different shades in the figure are the result of different densities shown by the TEM imagery; nickel is darker because it has about twice the density of titanium dioxide (the nickel density is 8.9 g/cm^3 versus titanium dioxide with 4.23 g/cm^3). Smaller particles, up to about 180 nm, are grayer, which suggests there is a smaller amount of nickel, and this is supported by the EDX analysis. In **Figure 3**, less nickel is seen in smaller particles. As such, the bigger particles (more than 180 nm) have a core of nickel and a coating of titanium dioxide. A further analysis is required for determining whether the core of the bigger particles is purely nickel or the desired nickel titanium alloy.

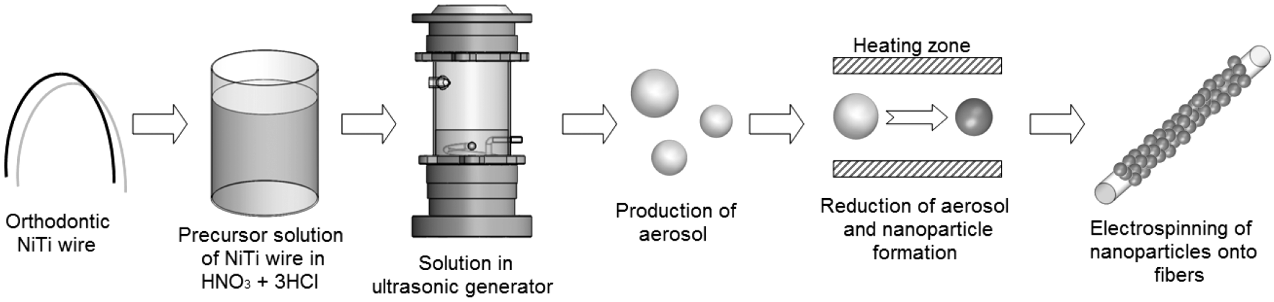

Figure 5: Production steps for the synthesis of nanoparticles from an orthodontic NiTi wire and their usage in electrospinning
Slika 5: Koraki pri sintezi nanodelcev iz ortodontske NiTi-žice in njihova uporaba pri elektropredenju

It is very difficult to obtain pure nickel titanium particles with USP due to the high reactivity of titanium with oxygen. Even though pure nickel titanium particles could be obtained, they would have to be stored in a virtually oxygen-free environment to prevent a titanium oxide formation on the surface of pure particles. As a source for nickel titanium used in these experiments, the orthodontic NiTi wire already has an outside layer of titanium dioxide. In order to use this wire as a precursor the layer would have to be removed. This would complicate the process of creating the precursor to more than just dissolving the wire in aqua regia. At this point, using different sources for nickel and titanium, such as nickel and titanium powders, would probably be more reasonable. Further research into the available precursor solutions for NiTi nanoparticles and collection media has to be performed.

Even though the resulted particles were not pure NiTi, but rather Ni-TiO_2, such particles do have some promising properties.[1,16,17] They have a photocatalytic function and can be used as a nickel titania nanocomposite coating, providing a good corrosion resistance and also a heightened hardness. The nickel containing TiO_2 nanoparticles is also promising as the material for high-temperature fuel-cell electrodes, as well as the catalyst for hydrogen cleavage in hydrogenation processes. Nickel titania particles were synthesized with a number of processes, such as adsorption of Ni to TiO_2, sol-gel methods, gas condensation and photodeposition of nickel nanoparticles on titanium dioxide.[1,16–19] However, with this experiment, the USP process was proven to be a versatile process, capable of creating nanoparticles of various materials.

5 CONCLUSION

Particles of Ni-TiO_2 were synthesized with USP, using a dissolved orthodontic NiTi wire as the precursor. The particles were formed at 900 °C, with nitrogen as the carrier gas and hydrogen as the reduction gas and were collected in water or alcohol. The TEM and EDX analysis showed that spherical particles with different compositions were created. The particles larger than 180 nm were composed of nickel with an outside layer of titanium dioxide, while the smaller particles were mainly composed of titanium dioxide. Further research and analysis of the particles obtained are needed for a better understanding of the particle formation with the experiment parameters used. With the current selection of the precursors, reaction gas and collection medium, it is difficult to obtain pure NiTi particles, which are desired. For this reason, an investigation of different precursor solutions, gases and collection media should be conducted.

Acknowledgement

We would like to thank the Institute for Metallurgical Processes and Metal Recycling (IME), RWTH Aachen University and the Institute of Metals and Technology Ljubljana (Dr. Darja Jenko) for their support. This research was made possible by the Slovenian Research Agency (ARRS) as part of the applied Project L2-4212, Research Program P2-0120 and the Young Researcher Program.

6 REFERENCES

[1] H. Chang, Y. C. Hsu, Fabrication and material properties of NiTi nanofluid, Journal of Vacuum Science & Technology B: Microelectronics and Nanometer Structures, 25 (**2007**) 3, 935–939

[2] Nickel-Titanium, Nitinol (NiTi) Nanoparticles – Properties, Applications [Online], Available: http://www.azonano.com/article.aspx?ArticleID=3383#1 [Accessed: 23-Sep-2013]

[3] S. Barcikowski, M. Hustedt, B. N. Chichkov, Nanocomposite Manufacturing using Ultrashort-Pulsed Laser Ablation in Solvents and Monomers, Polimery, 53 (**2008**) 9, 657–662

[4] M. Chakif, A. Ostendorf, A. Essaidi, M. Epple, O. Prymak, Generation of Nanoparticles by Laser Ablation in Liquids: Stoichiometry/Composition and Characterization of NiTi-Nanoparticles, The International Conference on Shape Memory and Superelastic Technologies (SMST), Prague, 2013, 201–202

[5] D. D. Radev, Mechanical synthesis of nanostructured titanium–nickel alloys, Advanced Powder Technology, 21 (**2010**) 4, 477–482

[6] C. Shearwood, Y. Q. Fu, L. Yu, K. A. Khor, Spark plasma sintering of TiNi nano-powder, Scripta Materialia, 52 (**2005**) 6, 455–460

[7] M. Kurumada, Y. Kimura, H. Suzuki, O. Kido, Y. Saito, C. Kaito, TEM study of early Ni4Ti3 precipitation and R-phase in Ni-rich NiTi nanoparticles, Scripta Materialia, 50 (**2004**) 11, 1413–1416

[8] W. Crone, W. Drugan, A. Ellis, J. Perepezko, Final Technical Report: Nanostructured Shape Memory Alloys, 841686, 2005

[9] S. Yatsu, H. Takahashi, H. Sasaki, N. Sakaguchi, K. Ohkubo, T. Muramoto, S. Watanabe, Fabrication of Nanoparticles by Electric Discharge Plasma in Liquid, Archives of Metallurgy and Materials, 58 (**2013**) 2, 425–429

[10] H. B. Liu, G. Canizal, P. S. Schabes-Retchkiman, J. A. Ascencio, Structural Selection and Amorphization of Small Ni-Ti Bimetallic Clusters, J. Phys. Chem. B, 110 (**2006**) 25, 12333–12339

[11] J. Ferčec, B. Glišić, I. Šćepan, E. Marković, D. Stamenković, I. Anžel, J. Flašker, R. Rudolf, Determination of Stresses and Forces on the Orthodontic System by Using Numerical Simulation of the Finite Elements Method, Acta Physica Polonica A, 122 (**2012**) 4, 659–665

[12] S. Stopic, R. Rudolf, J. Bogović, P. Majerič, M. Čolić, S. Tomić, M. Jenko, B. Friedrich, Synthesis of Au nanoparticles prepared with ultrasonic spray pyrolysis and hydrogen reduction, Mater. Tehnol., 47 (**2013**) 5, 577–583

[13] Nanostructured Materials Through Ultrasonic Spray Pyrolysis, Sigma-Aldrich [Online], Available: http://www.sigmaaldrich.com/technical-documents/articles/material-matters/ultrasonic-spray-pyrolysis.html [Accessed: 05-Sep-2013]

[14] J. Bogovic, A. Schwinger, S. Stopic, J. Schroeder, V. Gaukel, H. P. Schuchmenn, B. Friedrich, Controlled droplet size distribution in ultrasonic spray pyrolysis, Metall, 65 (**2011**) 10, 455–459

[15] J. Bogović, S. Stopić, B. Friedrich, Nanosized metallic oxide produced by Ultrasonic Spray Pyrolysis, Proceedings of European Metallurgical Conference, Düsseldorf/D, 2011, 1–12

[16] X. Shu, J. He, D. Chen, Visible-Light-Induced Photocatalyst Based on Nickel Titanate Nanoparticles, Ind. Eng. Chem. Res., 47 (**2008**) 14, 4750–4753

[17] K. E. Engates, H. J. Shipley, Adsorption of Pb, Cd, Cu, Zn, and Ni to titanium dioxide nanoparticles: effect of particle size, solid concentration, and exhaustion, Environ. Sci. Pollut. Res., 18 (**2011**) 3, 386–395

[18] F. A. Sheikh, J. Macossay, M. A. Kanjwal, A. Abdal-hay, M. A. Tantry, H. Kim, Titanium Dioxide Nanofibers and Microparticles Containing Nickel Nanoparticles, ISRN Nanomaterials, 2012 (**2012**), article ID 816474, 1–8

[19] J. L. Rodríguez, F. Pola, M. A. Valenzuela, T. Poznyak, Photocatalytic Deposition of Nickel Nanoparticles on Titanium Dioxide, Materials Research Society Symposium Proceedings, 1279 (**2010**), 19–25

UDK 621.793/.795:669.295
Original scientific article/Izvirni znanstveni članek

ISSN 1580-2949
MTAEC9, 49(1)81(2015)

HYDROXYAPATITE COATINGS ON Cp-TITANIUM GRADE-2 SURFACES PREPARED WITH PLASMA SPRAYING

NANOS HIDROKSIAPATITA NA POVRŠINO Cp-TITANA GRADE-2 Z NABRIZGAVANJEM S PLAZMO

Rebeka Rudolf[1], Dragoslav Stamenković[2], Zoran Aleksić[2], Monika Jenko[3], Igor Đordević[2], Aleksandar Todorović[2], Vukoman Jokanović[4], Karlo T. Raić[5]
[1]University of Maribor, Faculty of Mechanical Engineering, Maribor, Slovenia
[2]University of Belgrade, School of Dental Medicine, Belgrade, Serbia
[3]Institute of Metals and Technology, Ljubljana, Slovenia
[4]University of Belgrade, VINCA Institute of Nuclear Sciences, Belgrade, Serbia
[5]University of Belgrade, Faculty of Technology and Metallurgy, Belgrade, Serbia
karlo@tmf.bg.ac.rs

Prejem rokopisa – received: 2013-10-09; sprejem za objavo – accepted for publication: 2014-03-24

Thin hydroxyapatite coatings were produced on Cp-Titanium Grade-2 samples, with new high-voltage pulse-power equipment PJ-100 (Plasma Jet, Serbia) in order to get a more stable implant structure appropriate for further clinical applications. A comparative analysis of differently prepared surfaces of the Cp-Titanium Grade-2 samples was done before the hydroxyapatite was applied.

Microstructural observation of the modified hydroxyapatite/implant surface was done using scanning-electron-microscopy imaging and Auger electron spectroscopy, with the aim of detecting the morphology and the elements contained in the new surfaces of the samples. The results confirmed that the surface of Cp-Titanium Grade-2 modified with hydroxyapatite is very similar to the bone structure.

Keywords: Cp-Ti2 material, hydroxyapatite (HA), plasma-spray coating, characterization

Z novo, visokonapetostno pulzirajočo plazemsko napravo PJ-100 (plasma Jet, Serbia) je bil pripravljen tanek nanos hidroksiapatita na vzorce iz Cp-Titan Grade-2, da bi dobili bolj stabilno strukturo vsadka za klinično uporabo. Izvršena je bila primerjalna analiza različno pripravljenih površin vzorcev iz Cp-Titana Grade-2, preden je bil izvršen nanos hidroksiapatita.

Opazovanje mikrostrukture s hidroksiapatitom modificirane površine vsadka je bilo izvršeno z vrstično elektronsko mikroskopijo, kot tudi z Augerjevo elektronsko spektroskopijo, z namenom odkritja morfologije in razporeditve elementov na novi površini vzorca. Rezultati so potrdili, da je modificirana površina Cp-Titana Grade-2 s hidroksiapatitom zelo podobna strukturi kosti.

Ključne besede: material Cp-Ti2, hidroksiapatit (HA), s plazmo nabrizgan nanos, karakterizacija

1 INTRODUCTION

Titanium (Ti) has two most useful metal properties: corrosion resistance and the highest strength-to-weight ratio compared to other metals. Moreover, when in the unalloyed condition, it is stronger than some other similar materials, such as contemporary steel, and it is more than 40 % lighter. Ti can be alloyed with various elements (Al, V, Nb, Zr) that can additionally improve its strength, while maintaining high temperature performance, creep resistance, weldability, response to ageing heat treatments and formability. Ti and its alloys are resistant to corrosion because of the formation of an insoluble and continuous titanium-oxide layer on the surface having one of the highest heats of reaction: $\Delta H = -912$ kJ/mol. In air, an oxide (usually TiO_2) begins to form within nanoseconds (10^{-9} s) and reaches a thickness of 2–10 nm already in 1 s. This oxide is very adherent to the parent Ti, protecting the metal from other impurities and it is impenetrable to oxygen[1]. Moreover, this oxide on the Ti-surface gives Ti its excellent biocompatibility[2]. Commercially pure (Cp) Ti is available in four grades (1–4) that vary with respect to oxygen ($w = 0.18–0.40$ %) and iron ($w = 0.20–0.50$ %) amounts. These slight concentration differences have a substantial effect on the physical properties of the metal. Oxygen, in particular, has a great influence on the ductility and strength of Ti[3]. In our investigation we used Cp-Titanium Grade-2 (Cp-Ti2) materials which have the medium value of O. Cp-Ti2 is used widely because it combines excellent formability and moderate strength with superior corrosion resistance. This combination of properties makes Cp-Ti2 a good candidate for medical applications, i.e., implant manufacturing.

These materials are classified as biologically inert biomaterials. This means that they remain essentially unchanged when implanted into human bodies[4–6]. The human body is able to recognise these materials as foreign and tries to isolate them by encasing them in fibrous tissues. However, they do not cause any adverse reactions and are tolerated well by the human tissues[7]. Although the bulk properties of biomaterials are important with respect to their biointegration, the biological responses of the surrounding tissues to dental implants are controlled mostly with their surface characteristics (chemistry and structure) because biorecognition takes place at the interface of an implant and the host tissue. Biological tissues mainly interact with the outermost atomic layers of an implant, which are about 0.1–1 nm thick. The molecular and cellular events at the bone-implant interface are well described[8], but many crucial aspects are still far from being understood. A justification of the surface modification of implants is, therefore, straightforward: to retain the key physical properties of an implant while modifying only the outermost surface to control the bio-interaction. As a result, a lot of research work is devoted to elaborate methods of modifying the surfaces of the existing implants (biomaterials) to achieve the desired biological responses.

With respect to the presented problems of the state-of-the-art implant surface, the main question of our research was how to prepare the ideal micro-topography of the selected Cp-Ti2 material. In this framework we took into consideration that the most common physicochemical treatments are chemical surface reactions (e.g., oxidation, acid-etching), sand blasting, ion implantation, laser ablation, coating the surface with inorganic hydroxyapatite, etc. These methods alter the energy, charge and composition of the existing surface, but they can also provide the surfaces with modified roughness and morphology[9].

Although more accurate knowledge is required, typical Cp-Ti2 surfaces were treated with different high-voltage-plasma process parameters. In this manner we wanted to test the experimental presentation of the thin hydroxyapatite (HA) coating on the Cp-Ti2 samples using a specific plasma installation[10]. The aim of this work was, namely, to produce a thin HA coating with the new methods in order to get a more stable surface structure of Cp-Ti2 that could be used for further clinical applications. Finally, a comparative analysis was done using the classical preparation method, chemical etching, in order to acquire the information about the new plasma technology.

2 MATERIALS AND METHODS

The samples for the experiments were made from the Cp-Ti2 material (ASTM F 67-100) with a chemical composition in mass fractions as follows: $w(\mathrm{C})_{\max} = 0.08$ %, $w(\mathrm{N})_{\max} = 0.030$ %, $w(\mathrm{O})_{\max} = 0.25$ %, $w(\mathrm{Fe})_{\max} = 0.30$ %, $w(\mathrm{H}) = 0.015$ %. The properties of Cp-Ti2 are: the melting point of 1668 °C, a Vickers hardness of 180 HV, a 0.2 % yield strength of 275–450 MPa, a tensile strength of > 350 MPa, an elongation of > 20 %, a density of 4.5 g/cm^3, the coefficient of thermal expansion of 25–400 °C 9.4 × 10^{-6}/K, and elasticity modulus of 110 GPa. The samples were produced in the shape of discs with the dimension of $\phi = 10$ mm and a thickness of 2 mm.

It is well known that the adhesion between a ceramic coating (HA) and a metal implant is strongly influenced by the metal surface roughness. Therefore, the process of roughening is adjusted to the optimum level with several parameters: pressure of water, air flow, corundum granulation and diameter of the nozzle for roughening. The chamber for roughening was constructed in-house from hardened steel. The tool for capturing the samples (also our own construction) was used as a separate set of tools, rotating at more than 1000 r/min. The roughening of the samples was done under the following conditions: a fluid pressure of 8 bar, a nozzle diameter of ≈ 10 mm and a corundum granulation of 1–2 mm. The obtained surface roughness (R_a) was in the range from 4.72 µm to 5.28 µm (a Perthen Perthometer). After the roughening, the samples were washed with toluene and acetone to remove the traces of oil from the compressor. The specimens were then immersed in 5.0 mL of 5 M NaOH aqueous solution for 24 h. Afterwards they were removed from the solution and washed gently with distilled water, followed by drying at 40 °C for 24 h in an air atmosphere. The treated metal was then heated up to 300 °C (Sample F_1), 500 °C (Sample F_2), 700 °C (Sample F_3) and 800 °C (Sample F_4) at a rate of 5 °C/min in an Ni–Cr electrical furnace in an air atmosphere over 5 h. After the thermal treatment all the samples were cooled to room temperature in the furnace. An untreated sample (Sample F_0) was used for obtaining a better insight into the differences between the treated and untreated samples.

The plasma installation PJ-100 (Plasma Jet, Serbia) was used for the plasma-spray process[10,11]. The basic parameters of the installation used for applying HA depositions were: a power of (52.0 ±1.5) kW, a voltage of (120±2) V, a current of (430±5) A, an argon flow of (38.5±1.2) L/min, powder carrier gas, air of 8 L/min and a powder-mass input of (2.0±0.1) g/s. The samples were placed on a drum ($\phi = 200$ mm) of the plasma installation (a rotation velocity of 3.7 r/s) for the HA deposition. The complete coating process was performed in 2–3 short intervals taking 7 s to 10 s each, with a break rate of a few minutes between the cycles of deposition. Before the plasma treatment Ti disks were heated at a temperature of 200 °C, which was found to be the optimum for obtaining the maximum partition of the HA crystalline phase in the process of its deposition. Two commercially available HA powders were used: HA powder XPT-D-703 (Sulzer Metco, USA) and HA powder Captal 90 (Plasma Biotal, UK). The granulations of the powders were obtained from the manufacturers' specifications.

A microstructural characterization of the samples was carried out with scanning electron microscopy (SEM-Sirion 400 NC), in addition to an energy-dispersive X-ray (EDX) analysis (Oxford INCA 350). The specimens were observed directly without any surface preparation.

Detailed microstructure observations of the obtained surfaces were done using field-emission Auger electron spectroscopy (FE-AES) – a Thermo Scientific Microlab

310-F spectrometer equipped with a spherical-sector analyser and a field-emission electron gun with a thermally assisted Schottky field-emission source providing a stable electron beam in an accelerating voltage range of (0.5–25) keV.

3 RESULTS AND DISCUSSION

3.1 Microstructure observation of Cp-Ti2 surfaces

Typical microstructures of the Cp-Ti2 surfaces after different processes of roughening are shown in **Figure 1**.

From the pictures it can be concluded that immersion in NaOH represents a technique which results in obtaining a high surface roughness (**Figure 1a**). On the other hand, the thermal treatment at different temperatures represents the attainable method for surface roughness. At lower temperatures the roughness is lower (**Figures 1b, 1c, 1d**) and, consequently, at higher temperatures the roughness is higher (**Figure 1e**).

This is very important for the quality of the HA coating textures on dental Cp-Ti2 implants. The ideal microtopography of a Cp-Ti surface is still unknown because it is very difficult to associate Cp-Ti/HA interface properties with clinical results[12].

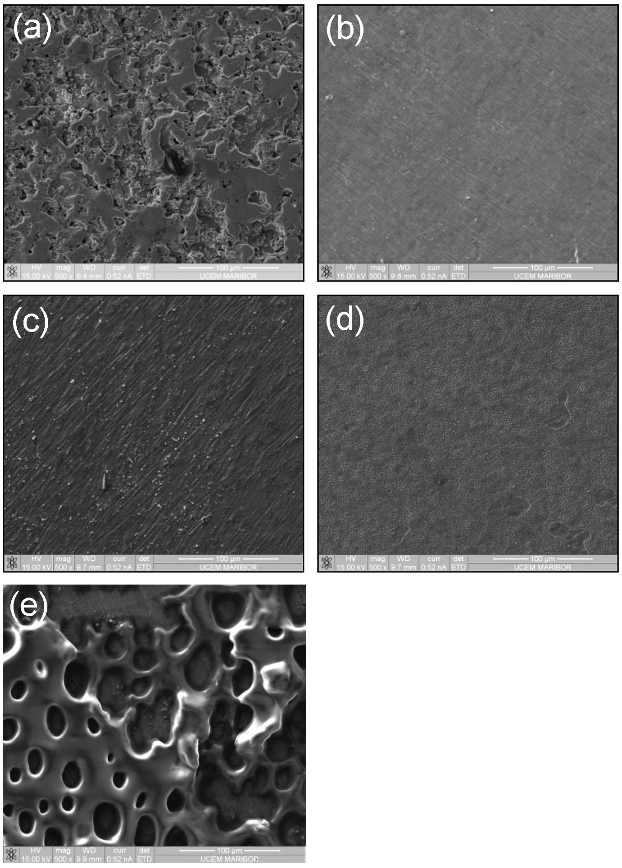

Figure 1: SEM micrographs of Cp-Ti2 surfaces: a) F_0, b) F_1, c) F_2, d) F_3 and e) F_4

Slika 1: SEM-posnetki površine Cp-Ti2: a) F_0, b) F_1, c) F_2, d) F_3 in e) F_4

3.2 Microstructure observation of HA/Cp-Ti2 surfaces

Using FE-AES spectroscopy we discovered that the cross-sections of the HA coatings for samples F_0-F_4 obtained with plasma-jet deposition clearly show their depths, as shown in **Table 1**.

Table 1: HA coating depth

Tabela 1: Debelina HA-nanosa

Sample label	Average depth, nm	Maximum depth, nm	Minimum depth, nm	Maximum deviation from the average value, nm
F_0	206	221.7	192.9	15.7
F_1	205.8	216.2	191.4	14.4
F_2	152.4	172.2	138.5	19.8
F_3	156.2	167.4	140.7	15.4
F_4	156.1	164.3	146.5	9.7

According to the data given in **Table 1** there are no significant differences in the depth of these coatings. For the same sample (the same conditions of their plasma treatment) the variety of the depths along the entire section was in the range of ± 20 nm. These values show a very uniform depth of the coating for each sample, with the maximum depth deviation (from its average value) between (9.7 and 19.8) nm.

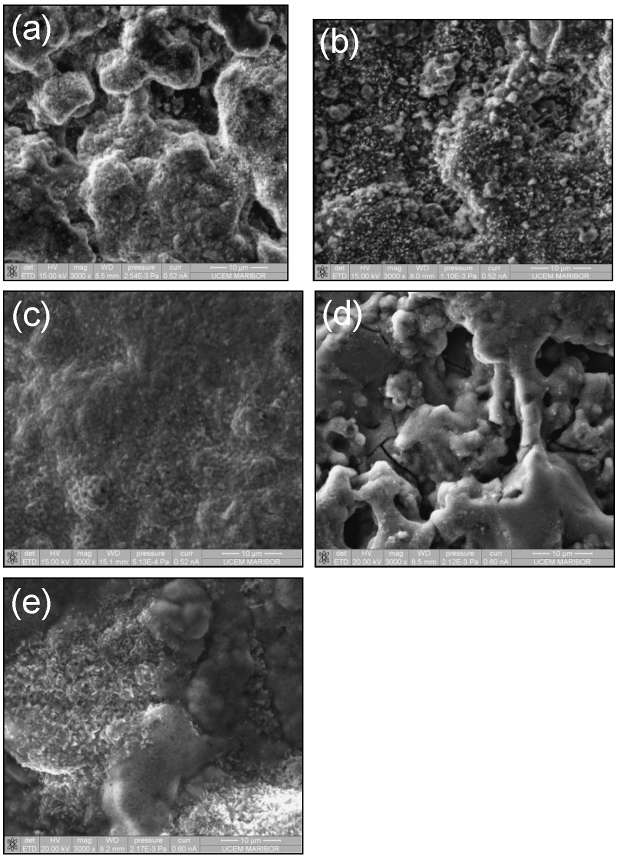

Figure 2: SEM micrographs of HA coating on different substrates: a) F_0, b) F_1, c) F_2, d) F_3 and e) F_4

Slika 2: SEM-posnetki HA nanosa na različnih podlagah: a) F_0, b) F_1, c) F_2, d) F_3 in e) F_4

The HA coating of sample F_0 (**Figure 2a**) shows a typical, very rough surface, with a very interesting morphology. The smallest sizes of the mosaic details were only a few µm, while very large and mutually interconnected parts were dominant. The obtained form is typical for quickly cooled systems that were exposed to melting at the edges of various particles. The specific form of the surface topology seems to be very promising for the cell adhesion. The structure is layered showing strongly exposed hills and valleys. In some places very deep voids can be observed. The mosaic details with an irregular form of very large agglomerates show the dimensions of about 50 µm.

The HA coating of sample F_1 (**Figure 2b**) shows a fairly homogenous surface with almost parallel patterns that look like textile fibres. The motifs are more discreet. The intertwined details are very ordered, with slightly raised or lowered parts. The details have the size of about 1 µm or less.

The HA coating of sample F_2 (**Figure 2c**) has a very rough surface with almost parallel patterns and it is sprinkled with white and black motifs resembling furrows, with the corresponding typical morphology. Very light details show individual particle sizes between (0.7 and 2.9) µm.

The HA coating of sample F_3 (**Figure 2d**) shows a specific surface morphology with a worm-like structure and finer, more expressed grains than in the previous cases. Individual particles are clearly visible. Their values are between 0.3 µm and 0.6 µm. The mosaic is very uniform. The grains are elongated and of a prismatic form. There are no visible voids and it seems that the layers of HA were sorted properly, without a build-up causing the creation of valleys and hills, as shown for samples F_0-F_2.

The HA coating of sample F_4 (**Figure 2e**) shows a very specific layout of cavities and elevations. It looks like a very nicely knitted network with several visible layers and holes with the dimensions of 7–36 µm. The depths of the continuous, interconnected parts of the network are of fairly similar dimensions. These morphologies show the first layer below the perforated layers (the ropes in network) with a fairly flat surface and small parallel patterns. The sizes of individual particles are between 0.25 µm and 1.45 µm.

The EDS analysis of the HA coating (**Figure 3**) shows all the elements present inside the coating from the titanium substrate to the top of the coating. The part of the substrate changed during the plasma-jet deposition can be also seen on the corresponding picture.

The concentrations of various elements given in the above diagrams show very similar data: the boundaries between the Ti substrate and HA coatings are clearly visible. In all the cases, small quantities of oxygen and aluminum are noticed, while the concentration of Ti deceases strongly, reaching a zero value. On the left side

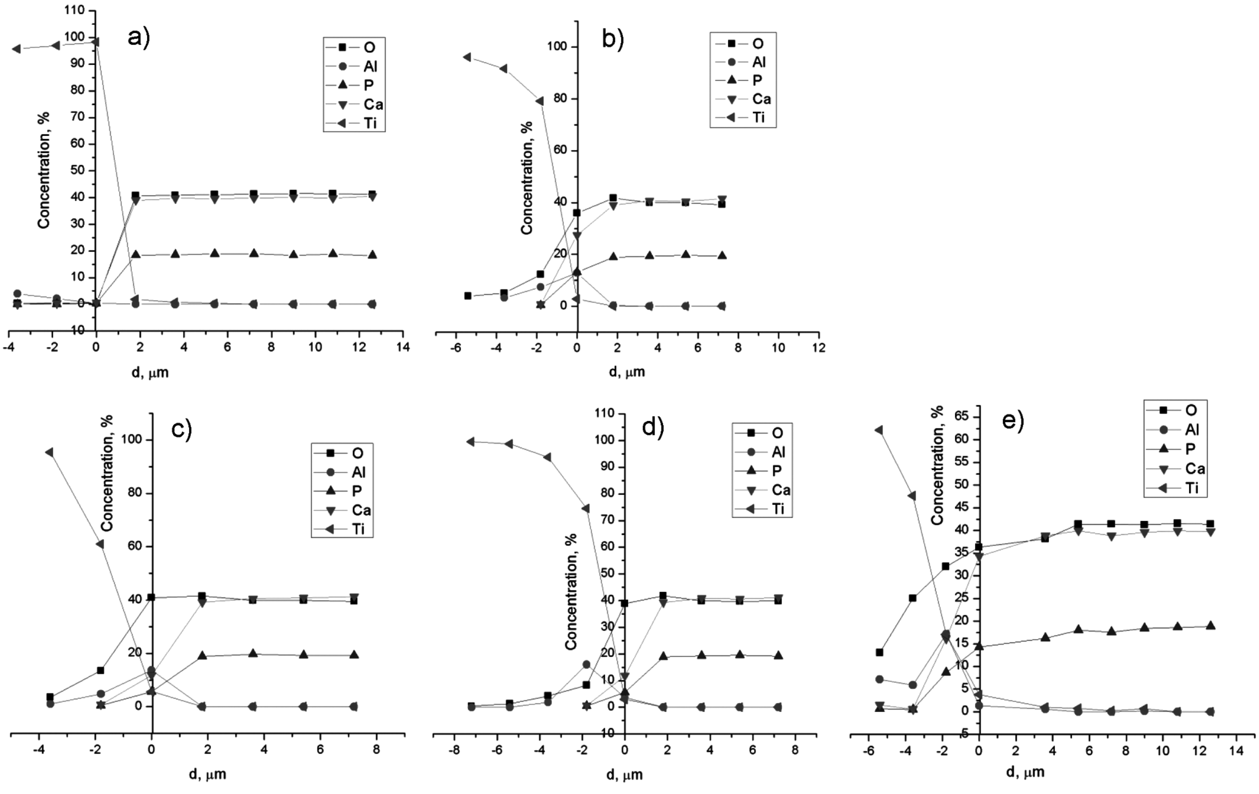

Figure 3: EDS analysis of the cross-sections of various samples of HA coatings: a) F_0, b) F_1, c) F_2, d) F_3 and e) F_4 depending on the distance from the left or right side of the boundary

Slika 3: EDS-analiza prereza različnih vzorcev HA-nanosa: a) F_0, b) F_1, c) F_2, d) F_3 in e) F_4, v odvisnosti od razdalje od meje levo ali desno of the boundary, small quantities of calcium and phosphorous were registered. Also, in this area, at a distance of 3.6 µm, the highest level of Al was noticed for sample F_0 (w = 3.95 %), while for F_1, F_2, F_3 and F_4 the highest levels of Al were noticed at the following boundaries: w =12.8 % for F_1, w = 13.7 % for F_2, w = 16 % for F_3 and w = 17 % for F_4. The oxygen level was very low on the left side of the boundary for the untreated sample F_0, while for sample F_1 it was between w = 3.9 % at a distance of 3.6 µm left of the substrate boundary and w = 35 % at the boundary; for sample F_2 it was w = 1.1 % at a distance of 3.6 µm left of the boundary and w = 13.7 % at the boundary; for sample F_3 it was w = 1.9 % at a distance of 1.8 µm left of the boundary and w = 16 % at the boundary; and for F_4 it was w = 20.45 % at a distance of 3.6 µm left of the boundary and w = 41.5 % at the boundary. The boundary was narrower or wider, and the mixing of ions from the right and left sides of the boundary was clearly visible at a distance of 1.8 µm left of the boundary (for samples F_2, F_3 and F_0). For samples F_1 and F_4 the boundary was narrower and the decrease in Ti was very sharp. The maximum depth of penetration of Ca and P ions in all the cases was about 3.8 µm inside the substrate depth. These values show good agreement for all the samples. Inside the HA coatings, at a distance of 1.8 µm on the right, there was no more interference, i.e., the mixing of the ions from the Ti substrate with the ions contained inside the HA coating. In deeper layers of HA coatings the concentrations of Ca, P and O ions reached

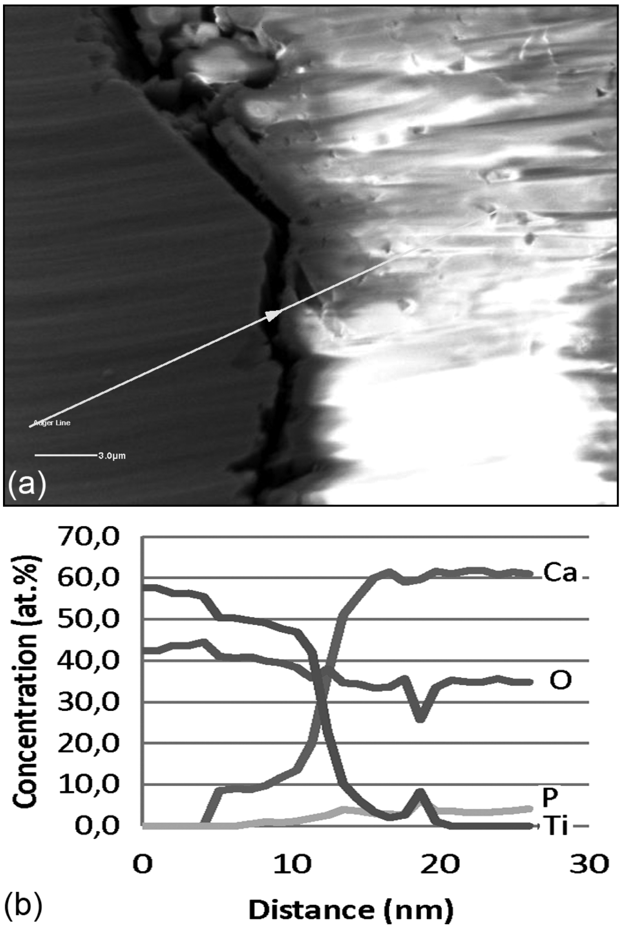

Figure 4: a) SEM image of the interface, line-scanned with AES, between the substrate and HA layer for sample F_1, b) AES line scan of the interface between HA and the substrate indicating the concentrations of Ca, O, Ti and P

Slika 4: a) SEM-posnetek stika, kjer je bila izvršena AES linijska analiza med podlago in HA-nanosom pri vzorcu F_1, b) AES linijska analiza stika HA in podlage, ki prikazuje koncentracijo elementov Ca, O, Ti in P

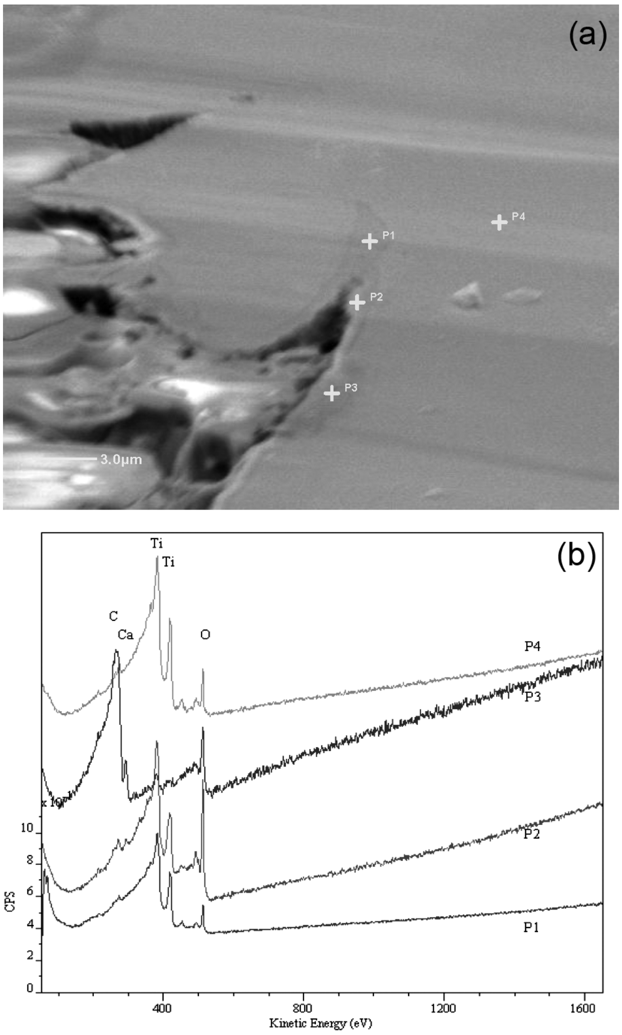

Figure 5: a) SEM image with marked places of AES, b) AE spectra for the spots in a)

Slika 5: a) SEM-posnetek točk AES-analize, b) AES-spektri v točkah iz a)

Table 2: Measured elements using AES, amount-of-substance, x/%

Tabela 2: Merjenje elementov z AES, množinski delež, x/%

	Concentration, x/%			
Spot	C	Ca	O	Ti
P1	11.2	0.0	35.2	53.6
P2	12.2	6.5	60.4	20.9
P3	46.3	25.6	24.3	3.8
P4	17.6	3.6	31.0	47.8

saturation, becoming uniform with a further increase in the distance.

A typical secondary electron image (SEI) of the interface, line-scanned with Auger electron spectroscopy (AES), between the substrate and HA coatings for sample F_1, and a spectrogram of the distributions of Ca, O, Ti and P are given in **Figure 4**.

This figure clearly shows a decrease in the Ti amount (present until the depth of the coating reaches a value of 20 nm) and an increase in the Ca in the coating between 4 nm and 17.5 nm. Both of these curves are typical S curves, inversely relative to one another. The oxygen amount decreases slightly, showing its highest value inside the chemically and thermally treated part of titanium (between 0 nm and 4 nm). In the area of the HA coating its amount reduces slightly by 4 nm and 10 nm (the part in which Ca atoms are propagated due to a high velocity of the calcium-hydroxide particles melted on the surfaces by the plasma jet). Afterwards, the oxygen amount varies statistically within certain limits.

Similar results are shown in **Figure 5**, where the concentrations of various elements, measured in counts per second (CPS), are explained with respect to the kinetic energy of the back-scattering electrons. Particular values of these energies prove the presence of Ca, Ti and O, showing their changes between sites P_1–P_4 (the sites at various distances from the boundary with hydroxyapatite). Besides, these values are given in **Table 2** for each of the observed sites.

Finally, as reported by Kokubo[13] and Kim[14], the calcium-phosphate deposition obeys the nucleation process. The electric-charge interaction also heavily favours this process. A higher surface energy favours the calcium phosphate initiating nucleation and the basic TiOH with the negative charge can adsorb the positively charged calcium ion (Ca^{2+}) first adsorbed to neutralize the surface charge until too much charge accumulates producing a positive layer of calcium titanate. Then, this positive layer interacts further with the negatively charged phosphate ion (PO_4^{3-}) to form the amorphous calcium phosphate, which will be crystallized further into an OCP phase despite the fraction of the amorphous calcium-phosphate residue.

4 CONCLUSIONS

The innovative plasma-jet process of hydroxyapatite deposition with a previous preparation of titanium substrates with NaOH etching and a subsequent thermal treatment is shown in this paper. In addition, the as-deposited coatings were composed mainly of the HA phase with the crystallite sizes between 15.5 nm and 31 nm.

Furthermore, Auger electron spectroscopy, through Ca-ion implantation in the depth of the oxide area of the substrate, shows the processing advantages that, consequently, led to the increased adhesion strength. Therefore, this improved plasma-jet method, with an unusually high kinetic energy of the plasma, seems to be promising for the fabrication of nanostructured HA coatings with unique microstructural features, which are desirable for enhancing the biological properties of HA coatings.

Research confirms a high potential of a deposition of HA on titanium substrates via a new plasma installation for any medical purpose.

Acknowledgements

This work was supported by the Ministry of Education, Science and Technological Development of the Republic of Serbia (Project 172026) and EUREKA Programme CELL-TI E!5831.

5 REFERENCES

[1] E. P. Lautenschlager, P. Monaghan, Titanium and titanium alloys as dental materials, Int Dent J, 43 (**1993**) 3, 245–53

[2] B. D. Ratner, A. S. Hoffman, F. J. Schoen, J. E. Lemons, Biomaterials science: an introduction to materials in medicine, Academic Press, New York 1996

[3] H. M. Kim et al., Thin film of low-crystalline calcium phosphate apatite formed at low temperature, Biomaterials, 21 (**2000**), 1129–1134

[4] L. Le Guehennec, A. Soueidan, P. Layrolle, Y. Amouriq, Surface treatments of titanium dental implants for rapid osseointegration, Dental Materials, 23 (**2007**), 844–854

[5] G. Daculsi, O. Laboux, O. Malard, P. Weiss, Current state of the art of biphasic calcium phosphate bioceramics, Journal of Materials Science: Materials in Medicine, 14 (**2003**), 195–200

[6] Z. T. Sul et al., The bone response of oxidized bioactive and non-bioactive titanium implants, Biomaterials, 24 (**2003**), 3893–3907

[7] K. Turzo, Surface Aspects of Titanium Dental Implants, In: R. H. Sammour (ed.), Biotechnology – Molecular Studies and Novel Applications for Improved Quality of Human Life, InTech, Rijeka 2012, 237 (www.intechopen.com)

[8] D. A. Puleo, A. Nanci, Understanding and controlling the bone-implant interface, Biomaterials, 20 (**1999**), 2311–2321

[9] B. Kasemo, Biological surface science, Surface Science, 500 (**2002**), 656–677

[10] M. Vilotijević, Dc plasma arc generator with increasing volt-ampere characteristic, RS Patent No 49, 7062007, 2007

[11] J. Ružic et al., Understanding plasma spraying process and characteristics of DC-arc plasma gun (PJ-100), Metallurgical & Materials Engineering, 18 (**2012**), 273–282

[12] I. Milinković et al., Aspects of titanium-implant surface modification at the micro and nano levels, Mater. Tehnol., 46 (**2012**) 3, 251–256

[13] T. Kokubo, H. M. Kim, M. Kawashita, Novel bioactive materials with different mechanical properties, Biomaterials, 24 (**2003**) 13, 2161–2175

[14] H. M. Kim et al., Surface potential change in bioactive titanium metal during the process of apatite formation in simulated body fluid, Journal of Biomedical Materials Research, Part A, 67A (**2003**) 4, 1305–1309

UDK 519.61/.64:536.2:620.3
Original scientific article/Izvirni znanstveni članek

ISSN 1580-2949
MTAEC9, 49(1)87(2015)

HEAT-TRANSFER CHARACTERISTICS OF A NON-NEWTONIAN Au NANOFLUID IN A CUBICAL ENCLOSURE WITH DIFFERENTIALLY HEATED SIDE WALLS

ZNAČILNOSTI PRENOSA TOPLOTE NENEWTONSKE Au NANOTEKOČINE V KOCKASTEM OHIŠJU Z RAZLIČNO GRETIMA STRANSKIMA STENAMA

Primož Ternik[1], Rebeka Rudolf[2,3], Zoran Žunič[4]
[1]Private Researcher, Bresterniška ulica 163, 2354 Bresternica, Slovenia
[2]University of Maribor, Faculty of Mechanical Engineering, Smetanova 17, 2000 Maribor, Slovenia
[3]Zlatarna Celje, d. d., Kersnikova ul.19, 3000 Celje, Slovenia
[4]AVL-AST, Trg Leona Štuklja 5, 2000 Maribor, Slovenia
pternik@pt-rtd.eu

Prejem rokopisa – received: 2013-10-14; sprejem za objavo – accepted for publication: 2014-02-17

The present work deals with the laminar natural convection in a cubical cavity filled with a homogenous aqueous solution of carboxymethyl cellulose (CMC) based gold (Au) nanofluid obeying the power-law rheological model. The cavity is heated on the vertical and cooled from the adjacent wall, while the other walls are adiabatic. The governing differential equations were solved with the standard finite-volume method and the hydrodynamic and thermal fields are coupled using the Boussinesq approximation.

The main objective of this study is to investigate the influence of the nanoparticle volume fraction on the heat-transfer characteristics of CMC-based Au nanofluid over a wide range of the base-fluid Rayleigh number.

Accurate numerical results are presented in the form of dimensionless temperature and velocity variations, the mean Nusselt number and the heat-transfer rate. It is shown that adding nanoparticles to the base fluid delays the onset of natural convection. In addition, numerical simulations showed that, just after the onset of natural convection, adding nanoparticles reduces the mean Nusselt number value for any given base-fluid Rayleigh number.

Keywords: natural convection, CMC-Au nanofluid, heat transfer, Nusselt number

Prispevek obravnava naravno konvekcijo v kockastem ohišju, napolnjenem s homogeno nanotekočino karboksimetil celuloza (CMC)-zlato (Au), z reološkim vedenjem, opisanim s potenčnim zakonom. Ohišje je greto na navpični in hlajeno na priležni steni, medtem ko so druge stene adiabatne. Vodilne diferencialne enačbe so bile rešene s standardno metodo končnih prostornin, pri čemer sta hidrodinamično in temperaturno polje sklopljena z Boussinesqovo aproksimacijo.

Glavni cilj prispevka je raziskati vpliv prostorninskega deleža nanodelcev na značilnosti prenosa toplote CMC-Au nanotekočine za široko območje vrednosti Rayleighjevega števila nosilne tekočine.

Natančni rezultati so predstavljeni v obliki spreminjanja brezdimenzijske temperature in hitrosti, srednje vrednosti Nusseltovega števila in hitrosti prenosa toplote. Pokazano je, da dodajanje nanodelcev v nosilno tekočino zakasni začetek naravne konvekcije. Poleg tega so numerične simulacije pokazale, da takoj za pojavom naravne konvekcije dodajanje nanodelcev zmanjšuje srednjo vrednost Nusseltovega števila za katero koli vrednost Rayleighjevega števila nosilne tekočine.

Ključne besede: naravna konvekcija, nanotekočina CMC-Au, prenos toplote, Nusseltovo število

1 INTRODUCTION

In recent years, nanosized particles dispersed in a base fluid, known as nanofluid[1], have been used and researched extensively to enhance the heat transfer in many engineering applications. While the presence of nanoparticles shows an unquestionable heat-transfer enhancement in forced-convection applications[2] there is still a dispute on the influence of nanoparticles on the heat-transfer enhancement of a buoyancy-driven flow.

Natural convection (i.e., a flow caused by temperature-induced density variations) is one of the most extensively analysed configurations because of its fundamental importance as the "benchmark" problem for studying convection effects (and comparing as well as validating numerical techniques). In addition to the obvious academic interest, a thermally driven flow is the strategy preferred by heat-transfer designers when a small power consumption, a negligible operating noise and a high reliability of a system are the main concerns (e.g., a reduction of the cooling time, manufacturing cost and an improvement of the product quality in the injection-moulding industry[3]). Although various configurations of the enclosure problem are possible[4–8], one of the most studied cases (involving nanofluids) is a two-dimensional square enclosure with differentially heated isothermal vertical walls and adiabatic horizontal walls[9–11]. Recent numerical studies[12,13] illustrated that the suspended nanoparticles substantially increase the heat-transfer rate for any given Rayleigh number. In addition, it is shown that the heat-transfer rate in water-based nanofluids increases with an increasing volume fraction of Al_2O_3, Cu, TiO_2 or Au nanoparticles. On the other hand, an apparently paradoxical behaviour of the heat-transfer deterioration was observed in many experimental studies: e.g., Putra et al.[14] reported that the presence of Al_2O_3 nanoparticles in a base fluid reduces the natural-convective heat transfer. However, they did not clearly explain why the natural-convective heat transfer decreases with an increase in the volume fraction of nanoparticles. This was later explained by the work of Ternik and Rudolf[4].

Regarding the natural convection in a 3D cubic cavity, most (if not all) of the work was done for the Newtonian fluid. For example, Tric et al.[15] studied the natural convection in a 3D cubic enclosure using a pseudo-spectra Chebyshev algorithm based on the projection-diffusion method with the spatial resolution supplied by polynomial expansions. Lo et al.[16] also studied the same problem under different inclination angles using the differential-quadrature method to solve the velocity-vorticity formulation of the Navier-Stokes equation employing higher-order polynomials to approximate differential operators.

The above review of the existing literature shows that the problem of natural convection in a cubical cavity filled with a nanofluid is an issue still far from being tackled and solved. Framed in this general background, the purpose of the present study is to examine the effect of adding Au nanoparticles to a non-Newtonian base fluid on the conduction and convection heat-transfer characteristics in a differentially heated cubical cavity heated over a wide range of the base-fluid Rayleigh number ($10^1 \le Ra_{\mathrm{bf}} \le 10^6$) and the volume fraction of nanoparticles ($0\ \% \le \varphi \le 10\ \%$).

2 NUMERICAL MODELLING

The standard finite-volume method is used to solve the coupled conservation equations of mass, momentum and energy. In this framework, a second-order central differencing scheme is used for the diffusive terms and a second-order upwind scheme for the convective terms. The coupling of the pressure and velocity is achieved using the SIMPLE algorithm. The convergence criteria were set to 10^{-8} for all the relative (scaled) residuals.

2.1 Governing equations

For the present study, a steady-state flow of an incompressible non-Newtonian CMC-Au nanofluid is considered. It is assumed that both the fluid phase and nanoparticles are in thermal and chemical equilibrium. Except for the density, the properties of the nanoparticles and the fluid (presented in **Table 1**) are taken to be constant. The Boussinesq approximation is invoked for the nanofluid properties to relate the density changes to the temperature changes, and to couple the temperature field with the velocity field.

The governing equations (mass, momentum and energy conservation) of such a flow are[9]:

$$\frac{\partial v_i}{\partial x_i} = 0 \tag{1}$$

$$\begin{aligned} &\rho_{\mathrm{nf}} v_j \frac{\partial v_i}{\partial x_j} - \frac{\partial}{\partial x_j}\left(\eta_{\mathrm{nf}}\left(|\dot{\gamma}|\right)\frac{\partial v_i}{\partial x_j}\right) = \\ &= -\frac{\partial p}{\partial x_i} + (\rho\beta)_{\mathrm{nf}}\, g(T - T_C) + \frac{\partial}{\partial x_j}\left(\eta_{\mathrm{nf}}\left(|\dot{\gamma}|\right)\frac{\partial v_j}{\partial x_i}\right) \end{aligned} \tag{2}$$

$$(\rho c_{\mathrm{p}})_{\mathrm{nf}}\, v_j \frac{\partial \mathrm{T}}{\partial x_j} = \frac{\partial}{\partial x_j}\left(k_{\mathrm{nf}} \frac{\partial T}{\partial x_j}\right) \tag{3}$$

where the cold-wall temperature T_{C} is taken to be the reference temperature for evaluating the buoyancy term $(\rho\beta)_{\mathrm{nf}} g(T - T_{\mathrm{C}})$ in the momentum-conservation equation.

In the momentum-balance law (Equation 2) the constitutive (i.e., rheological) equation is required for the viscous function $\eta_{\mathrm{nf}}\left(|\dot{\gamma}|\right)$, which, for the power-law model, reads as:

$$\eta_{\mathrm{nf}}\left(|\dot{\gamma}|\right) = K|\dot{\gamma}|^{n-1} \tag{4}$$

where $|\dot{\gamma}| = \sqrt{\frac{1}{2}\sum_i \sum_j \dot{\gamma}_{ij}\dot{\gamma}_{ji}}$ is the II invariant of the symmetrical rate-of-deformation tensor with Cartesian components $\dot{\gamma}_{ij} = (\partial v_i/\partial x_j) + (\partial v_j/\partial x_i)$, K is the consistency and n is the dimensionless power-law index with experimentally determined values (for a $w = 0.4\ \%$ aqueous CMC solution) of $K = 0.048$ Pas^n and $n = 0.882$.

The relationships between the properties of the nanofluid (nf), the base fluid (bf) and pure solid (s) are given with the following empirical models[4,8–13]:

- Dynamic viscosity:
  $\eta_{\mathrm{nf}} = \eta_{\mathrm{bf}} / (1-\varphi)^{2.5}$
- Density:
  $\rho_{\mathrm{nf}} = (1-\varphi)\rho_{\mathrm{bf}} + \varphi\rho_{\mathrm{s}}$
- Thermal expansion:
  $(\rho\beta)_{\mathrm{nf}} = (1-\varphi)(\rho\beta)_{\mathrm{bf}} + \varphi(\rho\beta)_{\mathrm{s}}$
- Heat capacitance:
  $(\rho c_{\mathrm{p}})_{\mathrm{nf}} = (1-\varphi)(\rho c_{\mathrm{p}})_{\mathrm{bf}} + \varphi(\rho c_{\mathrm{p}})_{\mathrm{s}}$
- Thermal conductivity:
  $k_{\mathrm{nf}} = k_{\mathrm{bf}} \dfrac{k_{\mathrm{s}} + 2k_{\mathrm{bf}} - 2\varphi(k_{\mathrm{bf}} - k_{\mathrm{s}})}{k_{\mathrm{s}} + 2k_{\mathrm{bf}} + \varphi(k_{\mathrm{bf}} - k_{\mathrm{s}})}$

Table 1: Thermophysical properties of CMC-Au nanofluid[9]
Tabela 1: Toplotno-fizikalne lastnosti CMC-Au nanotekočine[9]

	ρ (kg/m^3)	C_{p} (J/kg K)	k (W/m K)	β (1/K)
0.4 % CMC	997.1	4179	0.613	2.1×10^{-4}
Au	19320	128.8	314.4	1.416×10^{-7}

2.2 Geometry and boundary conditions

The simulation domain is shown schematically in **Figure 1**. The two horizontal walls of the square enclo-

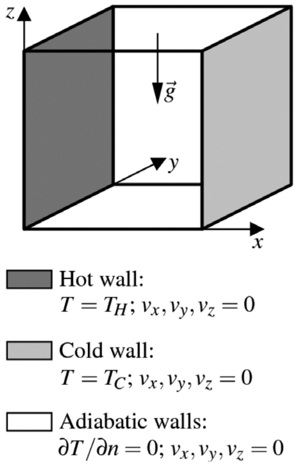

Figure 1: Schematic diagram of the simulation domain
Slika 1: Shematski prikaz območja simulacije

sure are kept at different constant temperatures ($T_H > T_C$), whereas the other boundaries are considered to be adiabatic. All the velocity components (i.e., v_x, v_y and v_z) are identically zero on each boundary because of the no-slip condition and the impenetrability of the rigid boundaries.

To study the heat-transfer characteristics due to the natural convection in nanofluids, the local Nusselt number (along the vertical hot wall) is defined as[15]:

$$Nu(y,z)=\frac{Q_{\mathrm{nf,conv}}}{Q_{\mathrm{nf,cond}}}=\frac{h_{\mathrm{nf}}L}{k_{\mathrm{nf}}}=-\frac{L}{T_{\mathrm{H}}-T_{\mathrm{C}}}\left.\frac{\partial T(y,z)}{\partial x}\right|_{x=0} \quad (5)$$

where $Nu(y,z)$ presents the ratio of the heat-transfer rate by convection to that by the conduction in the nanofluid in question, k_{nf} is the thermal conductivity and h_{nf} is the convection heat-transfer coefficient of the nanofluid:

$$h_{\mathrm{nf}}=-k_{\mathrm{nf}}\left.\frac{\partial T(y,z)}{\partial x}\right|_{x=0}\frac{1}{T_{\mathrm{H}}-T_{\mathrm{C}}} \quad (6)$$

Finally, in the present study, the heat-transfer characteristics are analysed in terms of the mean Nusselt number:

$$\overline{Nu}=\frac{1}{L^2}\int_0^L\int_0^L Nu(y,z)\mathrm{d}y\mathrm{d}z \quad (7)$$

and the ratio of the nanofluid heat-transfer rate to the base-fluid one:

$$\frac{Q_{\mathrm{nf}}}{Q_{\mathrm{bf}}}=\frac{k_{\mathrm{nf}}\overline{Nu}_{\mathrm{nf}}}{k_{\mathrm{bf}}\overline{Nu}_{\mathrm{bf}}} \quad (8)$$

at the same value of the base-fluid Rayleigh number.

In order to investigate the influence of solid-particle volume fraction φ on the heat-transfer characteristics, the Rayleigh number (Ra_{nf}) and Prandtl number (Pr_{nf}) of the CMC-based nanofluid (obeying the power-law viscous behaviour) are expressed as follows:

$$\begin{aligned} Ra_{\mathrm{nf}} &= \frac{\rho_{\mathrm{nf}}(\rho c_{\mathrm{p}})^{\mathrm{n}}_{\mathrm{nf}}\, g\beta_{\mathrm{nf}}\,\Delta T L^{2\mathrm{n}+1}}{k^{\mathrm{n}}_{\mathrm{nf}}K} \\ Pr_{\mathrm{nf}} &= \frac{K}{\rho_{\mathrm{nf}}}\left(\frac{k}{\rho c_{\mathrm{p}}}\right)^{\mathrm{n}-2}_{\mathrm{nf}} L^{2-2\mathrm{n}} \end{aligned} \quad (9)$$

Using Equation 9 we show that $Ra_{\mathrm{nf}} < Ra_{\mathrm{bf}}$ (**Figure 2a**) and $Pr_{\mathrm{nf}} < Pr_{\mathrm{bf}}$ (**Figure 2b**) for all the values of φ. The ratio of the CMC-based nanofluid Rayleigh and Prandtl numbers to the base-fluid Rayleigh and Prandtl numbers decreases with the increasing volume fraction of the nanoparticles; i.e., for the fixed values of Ra_{bf} and Pr_{bf}, the value of Ra_{nf} and Pr_{nf} decrease when adding nanoparticles.

2.3 Grid refinement and numerical accuracy

The grid independence of the present results was established with a detailed analysis using three different non-uniform meshes (the elements were concentrated towards each solid wall), the details of which are presented in **Table 2**. The table includes the numbers of the elements in a particular direction as well as the normalized minimum cell size.

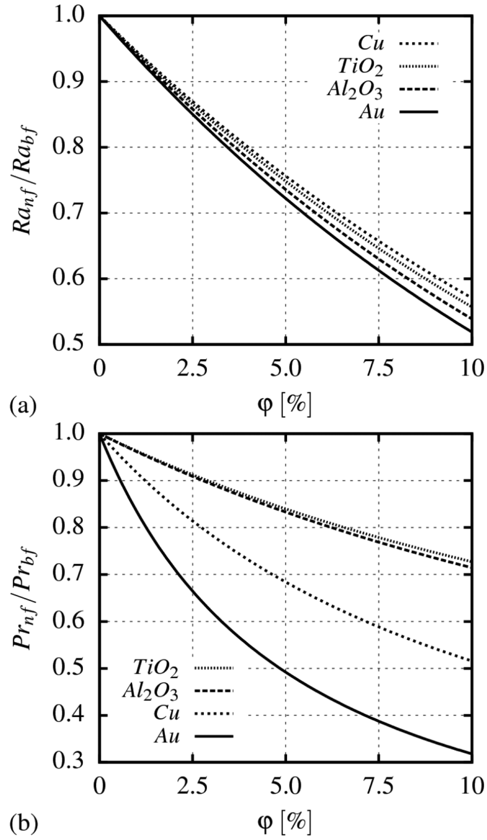

Figure 2: Variation of the dimensionless numbers of the CMC-based nanofluids with the volume fraction of nanoparticles: a) Rayleigh number and b) Prandtl number
Slika 2: Spreminjanje brezdimenzijskih števil CMC nanotekočin v odvisnosti prostorninskega deleža nanodelcev: a) Rayleighjevo število in b) Prandtlovo število

With each grid refinement the number of the elements (i.e., the control volumes) in a particular direction is increased and the element size is reduced. Such a procedure is useful for applying Richardson's extrapolation technique (a method for obtaining a higher-order estimate of the flow value from a series of lower-order discrete values) encountered in many numerical studies[8–12,17].

Table 2: Computational-mesh characteristics
Tabela 2: Značilnosti računskih mrež

	Mesh I	Mesh II	Mesh III
$N_x \times N_y \times N_z$	40 × 40 × 40	60 × 60 × 60	90 × 90 × 90
$\Delta_{\min}/L$	2.250×10^{-3}	1.500×10^{-3}	1.000×10^{-3}

For a general primitive variable ϕ the grid-converged value (i.e., extrapolated to the zero element size) is given as[8–12]: $\phi_{\mathrm{ext}} = \phi_{\mathrm{M3}} - (\phi_{\mathrm{M2}} - \phi_{\mathrm{M3}})/(r^{p} - 1)$ where ϕ_{M3} is obtained on the basis of the finest grid and ϕ_{M2} is the solution based on the next level of the coarse grid; r = 1.5 indicates the ratio between the coarse- and fine-grid spacings and p = 2 indicates the order of accuracy.

The numerical error $e = \left|(\phi_{\mathrm{M2}} - \phi_{\mathrm{ext}} / \phi_{\mathrm{ext}}\right|$ for the mean Nusselt number $\overline{Nu}$ is presented in **Table 3**. It can be seen that the differences in the grid refinement are exceedingly small and the agreement between Mesh II and the extrapolated value is extremely good (the discretisation error is below 0.20 %). Based on this estimation, the simulations in the remainder of the paper were conducted on Mesh II that provided a reasonable compromise between high accuracy and computational effort.

Table 3: Effect of the mesh refinement upon the mean Nusselt number (φ = 10 %, $Ra_{\mathrm{bf}} = 10^6$)
Tabela 3: Vpliv zgoščevanja mreže na srednjo vrednost Nusseltovega števila (φ = 10 %, $Ra_{\mathrm{bf}} = 10^6$)

Mesh I	Mesh II	Mesh III	$\overline{Nu}_{\mathrm{ext}}$	e
10.075	10.089	10.095	10.099	0.109 %

2.4 Benchmark comparison

In addition to the aforementioned grid-dependency study, the present results were also checked against the results of other authors[15,16] for the natural convection of air in a cubic enclosure (Pr = 0.71). The comparisons between the present simulation results and the corresponding benchmark values (**Table 4**) are very good and entirely consistent with our grid-dependency studies.

Table 4: Comparison of the present results for $\overline{Nu}$ with the benchmark results
Tabela 4: Primerjava dobljenih rezultatov za $\overline{Nu}$ z referenčnimi rezultati

	$Ra = 10^3$	$Ra = 10^4$	$Ra = 10^5$	$Ra = 10^6$
Present study	1070	2.048	4.327	8.627
Tric et al.[15]	1.070	2.054	4.337	8.641
Lo et al.[16]	1.071	2.054	4.333	8.666

3 RESULTS AND DISCUSSION

3.1 Temperature and velocity-flow field

It is useful to inspect the variations in dimensionless temperature θ and dimensionless vertical velocity v_z^* in order to understand the influences of Ra_{bf} and φ on the heat-transfer characteristics during the natural convection of the CMC-Au nanofluid in the cubical enclosure.

It is evident from **Figure 3a** that the distributions of θ become increasingly non-linear with the increasing values of Ra_{bf}. This statement is supported by the data plotted in **Figure 3b**, which demonstrates that the magnitude of the velocity component increases significantly with the increasing Ra_{bf}. For a given set of values of φ an increase in Ra_{bf} gives rise to a strengthening of the buoyancy forces in comparison to the viscous forces, which can be seen from **Figure 3b**, where the magnitude of v_z^* increases with the increasing Ra_{bf}. As the convective transport strengthens with the increasing Ra_{bf} the distribution of θ becomes significantly more non-linear with the increasing Ra_{bf} (**Figure 3a**).

Furthermore, **Figure 3a** illustrates that the thermal-boundary-layer thickness next to the heated wall is influenced by the addition of nanoparticles to the base fluid. This sensitivity of the thermal-boundary-layer

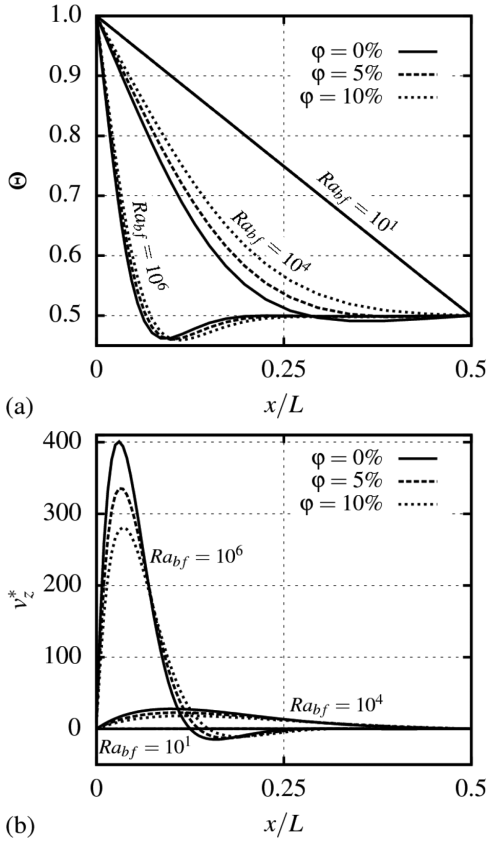

Figure 3: a) Variations in the non-dimensional temperature and b) non-dimensional vertical velocity component
Slika 3: a) Spreminjanje brezdimenzijske temperature in b) brezdimenzijske navpične komponente hitrosti

thickness to the volume fraction of the nanoparticles is related to the increased thermal conductivity of the CMC-based Au nanofluid. As a matter of fact, the increased values of the thermal conductivity are accompanied by higher values of the thermal diffusivity and these higher values of the thermal diffusivity result in a reduction in the temperature gradients and, accordingly, an increase in the thermal-boundary thickness as demonstrated in **Figure 3a**. Finally, this increase in the thermal-boundary-layer thickness reduces the Nusselt-number values.

3.2 Mean Nusselt number

Figure 4 presents the variation in the mean Nusselt number with the Rayleigh number. For smaller values of the base-fluid and nanofluid Rayleigh numbers there is no convection in the nanofluid or the base fluid, and the heat transfer occurs due to pure conduction; the mean Nusselt number equals 1.0 and its value is independent of the Rayleigh number. As the value of Ra_{bf} increases, the nanofluid remains in the conductive-heat-transfer regime, while the convective-heat-transfer regime appears in the base fluid.

The onset of the heat convection[4] (i.e., the critical value of the base-fluid Rayleigh number, at which the mean Nusselt number equals 1.01) depends on the volume fraction of the Au nanoparticles. The higher is the value of φ, the more delayed is the occurrence of the convective-heat-transfer regime (**Figure 5a**). When the nanofluid is in the convective-heat-transfer regime, the mean Nusselt number monotonically increases with the Rayleigh number (**Figures 4** and **5**), attaining lower values for the higher nanoparticle volume fraction (**Figure 4**) at a given base-fluid Rayleigh number.

On the other hand, it is interesting to notice that the onset of the convection occurs at the same critical value of the nanofluid Rayleigh number, i.e., $Ra_{\mathrm{nf,cr}} \cong 281$ (**Figure 5b**). Moreover, the value of the mean Nusselt number at a given nanofluid Rayleigh number is practically independent of the nanoparticle volume fraction (**Figure 4b**), which is consistent with the earlier findings in the context of the natural convection of generalized Newtonian fluids[18] as well as Au nanofluids[4] in a side wall, differentially heated, 2D square enclosure.

This finding is a reflection of the nanofluid Prandtl-number values considered in the present study and for this range of Prandtl-number values (i.e., $Pr_{\mathrm{nf}} > 1$) the

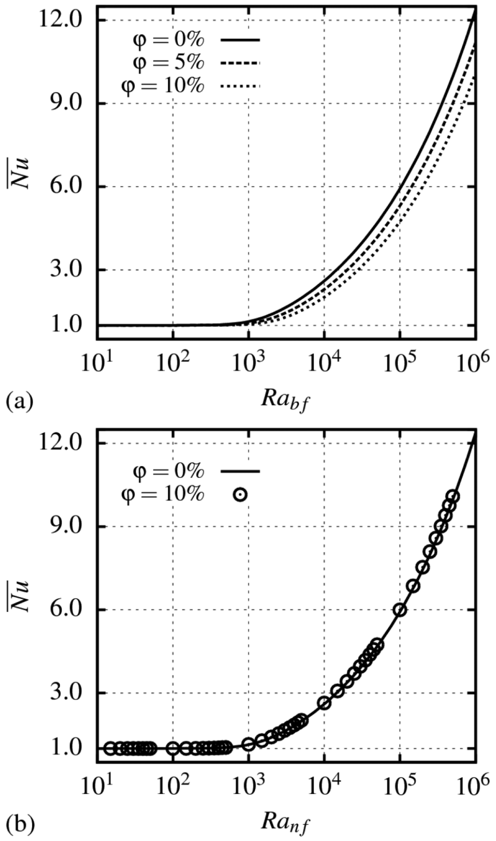

Figure 4: Variation in the mean Nusselt number with the: a) base-fluid Rayleigh number and b) nanofluid Rayleigh number

Slika 4: Spreminjanje srednjega Nusseltovega števila v odvisnosti z: a) Rayleighjevim številom nosilne tekočine in b) Rayleighjevim številom nanotekočine

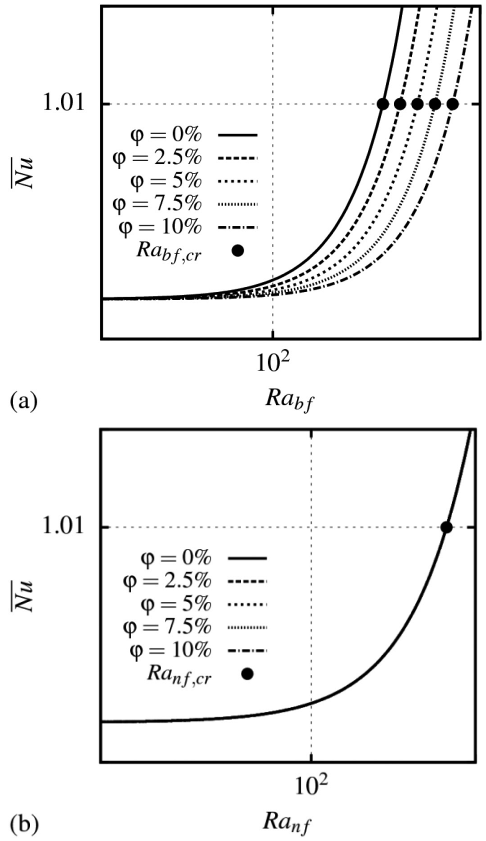

Figure 5: Onset of the heat-transfer convection as a function of the: a) base-fluid Rayleigh number and b) nanofluid Rayleigh number

Slika 5: Nastop konvektivnega prenosa toplote v odvisnosti od: a) Rayleighjevega števila nosilne tekočine in b) Rayleighjevega števila nanotekočine hydrodynamic-boundary-layer thickness remains much greater than the thermal-boundary-layer thickness, and thus the transport characteristics are driven primarily by the buoyancy and viscous forces, which is reflected in the weak Prandtl-number dependence on the mean Nusselt number.

3.3 Heat-transfer rate

Figure 6 shows the effect of the base-fluid Rayleigh number Ra_{bf} on the ratio of the heat-transfer rates for the CMC-based Au nanofluid for different values of the volume fraction.

In the range of $Ra_{\mathrm{bf}} \leq 281$ the heat transfer occurs due to pure conduction and the mean Nusselt number equals $\overline{Nu} = 1$. Consequently, the ratio of the heat transfer is equal to the ratio of thermal conductivities and it is constant and independent of the base-fluid Rayleigh number. For $Ra_{\mathrm{nf}} \leq 281$ and $Ra_{\mathrm{bf}} > 281$ the nanofluid remains in the conductive-heat-transfer regime, while the convection appears in the base fluid. The heat transfer is more important in the base fluid than in the nanofluid and the ratio of the heat-transfer rates is on a decrease.

After the onset of the convective-heat-transfer regime in the nanofluid, the ratio of the heat-transfer rates is on an increase but remains lower than the ratio obtained when both the nanofluid and the base fluid are in the conductive regime.

Last but not least, the present conclusions can be extrapolated to the other CMC-based nanofluids (e.g., Cu, TiO_2 and Al_2O_3) since their nanofluid Rayleigh- and Prandtl-number values are within the range of the present (i.e., CMC-based Au nanoparticles) Rayleigh- and Prandtl-number values.

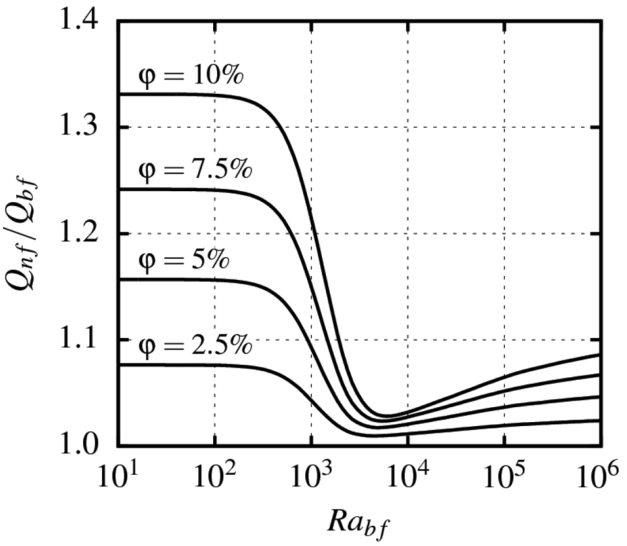

Figure 6: Heat-transfer rate variation with the base-fluid Rayleigh number and nanoparticle volume fraction

Slika 6: Spreminjanje razmerja prenosa toplote z Rayleighjevim številom nosilne tekočine in prostorninskim deležem nanodelcev

4 CONCLUSIONS

In the present study, a steady laminar natural convection of a non-Newtonian (i.e., CMC-based Au) nanofluid obeying the power-law rheological model in a cubical enclosure with differentially heated side walls, subjected to constant wall temperatures was analysed with numerical means. The effects of the base-fluid Rayleigh number ($10^1 \leq Ra_{\mathrm{bf}} \leq 10^6$) and the solid volume fraction ($0\ \% \leq \varphi \leq 10\ \%$) on the momentum and heat-transfer characteristics were systematically investigated in detail.

The influence of the computational grid refinement on the present numerical predictions was studied throughout the examination of the grid convergence at $Ra_{\mathrm{bf}} = 10^6$ and $\varphi = 10\ \%$. By utilizing extremely fine meshes, the resulting discretisation error for $\overline{Nu}$ is well below 0.2 %.

The present numerical method was validated for the case of the natural convection of air in a cubical cavity, for which the results of other authors are available in the available literature. Remarkable agreement of the present results with the benchmark results yields sufficient confidence in the presented numerical procedure and results.

Highly accurate numerical results allow some important conclusions such as:

Just after the onset of the convection, there is more heat transfer in the base fluid than in the nanofluid. At a fixed value of the base-fluid Rayleigh number Ra_{bf}, the nanofluid Rayleigh number Ra_{nf} decreases with the volume fraction of the nanoparticles. Thus, the nanoparticles delay the onset of the convection.

In the convective-heat-transfer regime the mean Nusselt number $\overline{Nu}$ is found to increase with the increasing values of the base-fluid Rayleigh number Ra_{bf}, but the $\overline{Nu}$ values obtained for the higher values of the nanoparticle volume fraction φ are smaller than those obtained in the case of the base fluid ($\varphi = 0\ \%$) at the same nominal values of Ra_{bf}.

The transition from the conductive to the convective heat-transfer regime occurs at the same value of the nanofluid Rayleigh number, i.e., $Ra_{\mathrm{nf}} \leq 281$.

The values of the mean Nusselt number at a given Ra_{nf} are practically independent of the nanoparticle volume fraction.

The heat-transfer rate can decrease or increase depending on the value of the Rayleigh number. So, an addition of nanoparticles increases the heat transfer only for the given values of the temperature difference.

Acknowledgements

The research leading to these results was carried out within the framework of research project "Production technology of Au nano-particles" (L2-4212) and it received the funding from the Slovenian Research Agency (ARRS).

5 REFERENCES

[1] S. U. S. Choi, Enhancing thermal conductivity of fluids with nanoparticles, Developments Applications of Non-Newtonian Flows, 66 (**1995**), 99–105

[2] W. Daungthongsuk, S. Wongwises, A critical review of convective heat transfer in nanofluids, Renewable & Sustainable Energy Reviews, 11 (**2009**), 797–817

[3] F. H. Hsu, K. Wang, C. T. Huang, R. Y. Chang, Investigation on conformal cooling system design in injection molding, Advances in Production Engineering & Management, 8 (**2013**), 107–115

[4] P. Ternik, R. Rudolf, Conduction and convection heat transfer characteristics of water-based Au nanofluids in a square cavity with differentially heated side walls subjected to constant temperatures, Thermal Science, 18 (**2014**), 189–200

[5] G. Huelsz, R. Rechtman, Heat transfer due to natural convection in an inclined square cavity using the lattice Boltzmann equation method, International Journal of Thermal Sciences, 65 (**2013**), 111–119

[6] M. N. Hasan, S. C. Saha, Y. T. Gu, Unsteady natural convection within a differentially heated enclosure of sinusoidal corrugated side walls, International Journal of Heat and Mass Transfer, 55 (**2012**), 5696–5708

[7] G. Yesiloz, O. Aydin, Laminar natural convection in right-angled triangular enclosures heated and cooled on adjacent walls, International Journal of Heat and Mass Transfer, 60 (**2013**), 365–374

[8] P. Ternik, R. Rudolf, Z. Žunič, Numerical study of Rayleigh-Benard natural convection heat transfer characteristics of water-based Au nanofluids, Mater. Tehnol., 47 (**2013**) 2, 211–215

[9] P. Ternik, R. Rudolf, Laminar natural convection of non-Newtonian nanofluids in a square enclosure with differentially heated side walls, International Journal of Simulation Modelling, 12 (**2013**), 5–16

[10] O. Turan, R. J. Poole, N. Chakraborty, Influences of boundary conditions on laminar natural convection in rectangular enclosures with differentially heated side walls, International Journal of Heat and Fluid Flow, 33 (**2012**), 131–146

[11] P. Ternik, R. Rudolf, Heat transfer enhancement for natural convection flow of water-based nanofluids in a square enclosure, International Journal of Simulation Modelling, 11 (**2012**), 29–39

[12] P. Ternik, R. Rudolf, Z. Žunič, Numerical study of heat transfer enhancement of homogeneous water-Au nanofluid under natural convection, Mater. Tehnol., 46 (**2012**) 3, 257–261

[13] H. F. Oztop, E. Abu-Nada, Y. Varol, K. Al-Salem, Computational analysis of non-isothermal temperature distribution on natural convection in nanofluid filled enclosures, Superlattices and Microstructures, 49 (**2011**), 453–467

[14] N. Putra, W. Roetzel, S. K. Das, Natural convection of nano-fluids, Heat and Mass Transfer, 39 (**2002**), 775–784

[15] E. Tric, G. Labrosse, M. Betrouni, A first incursion into the 3D structure of natural convection of air in a differentially heated cubic cavity, from accurate numerical simulations, International Journal of Heat and Mass Transfer, 43 (**2000**), 4034–4056

[16] D. C. Lo, D. L. Young, K. Murugesan, GDQ method for natural convection in a cubic cavity using velocity-vorticity formulation, Numerical Heat Transfer, Part B, 48 (**2005**), 363–386

[17] I. Biluš, M. Morgut, E. Nobile, Simulation of Sheet and Cloud Cavitation with Homogenous Transport Models, International Journal of Simulation Modelling, 13 (**2013**), 94–106

[18] O. Turan, A. Sachdeva, N. Chakraborty, R. J. Poole, Laminar natural convection of power-law fluids in a square enclosure with differentially heated side walls subjected to constant temperatures, Journal of Non-Newtonian Fluid Mechanics, 166 (**2011**), 1049–1063

UDK 519.61/.64:620.179.1:681.586.773
Original scientific article/Izvirni znanstveni članek

ISSN 1580-2949
MTAEC9, 49(1)95(2015)

AMPLITUDE–FREQUENCY RESPONSE OF AN ALUMINIUM CANTILEVER BEAM DETERMINED WITH PIEZOELECTRIC TRANSDUCERS

AMPLITUDNO-FREKVENČNI ODZIV KONZOLNEGA NOSILCA IZ ALUMINIJA, UGOTOVLJEN S PIEZOELEKTRIČNIMI PRETVORNIKI

Zuzana Lašová[1], Robert Zemčík[2]
[1]University of West Bohemia in Pilsen, Department of Mechanics, Univerzitní 22, 306 14, Plzeň, Czech Republic
[2]European Centre of Excellence NTIS – New Technologies for Information Society, Faculty of Applied Sciences, University of West Bohemia, Univerzitní 22, 306 14, Plzeň, Czech Republic
zlasova@kme.zcu.cz

Prejem rokopisa – received: 2013-10-16; sprejem za objavo – accepted for publication: 2014-02-13

This work is focused on the creation of an appropriate finite-element model of an aluminum cantilever beam using a pair of piezoelectric patch transducers. Thanks to the reversible behavior of the piezoelectric effect each patch transducer can represent either an actuator or a sensor. For a precise prediction of the amplitude values in the numerical simulations each transducer is calibrated before being attached to the beam with strain gauges. From these experiments piezoelectric properties of each piezoelectric patch are obtained. The cantilever beam is actuated with a voltage signal applied to one of the patches. The signal is a linear chirp (sine wave with a swept frequency) with a sufficient range to affect the selected natural frequencies. The time response of the beam from the piezoelectric sensor and, alternatively, from the laser position sensor is transformed with the STFT algorithm to obtain the characteristics of the time-frequency domain (spectrogram). The finite-element model of the cantilever beam with the piezoelectric patches was created using 3D solid structural and piezoelectric bricks in Ansys. The time response of the model to the chirp voltage signal was determined with a transient analysis. The amplitude/frequency characteristics are compared with the experimental results.

Keywords: piezoelectric materials, frequency spectrum, finite-element analysis

To delo obravnava izdelavo primernega modela z metodo končnih elementov konzolnega nosilca iz aluminija z uporabo para piezoelektričnih pretvornikov v obliki obliža. Zaradi reverzibilnega vedenja piezoelektričnega pojava je lahko vsak obližast pretvornik aktuator ali senzor. Za natančno napovedovanje vrednosti amplitude pri numeričnih simulacijah je bil vsak pretvornik pred namestitvijo na nosilec kalibriran z napetostnimi lističi. Iz teh preizkusov so dobljene piezoelektrične lastnosti vsakega piezoelektričnega obliža. Konzolni nosilec je bil aktiviran s signalom električne napetosti, uporabljene na enem od obližev. Signal je linearno cvrčanje (sinus s šablonirano frekvenco) s primernim območjem, da se vpliva na izbrane naravne frekvence. Časovni odziv nosilca iz piezoelektričnega senzorja in alternativno s položaja laserskega senzorja je pretvorjen s STFT-algoritmom, da se dobi značilnosti vedenja čas – frekvenca (spektrogram). Izdelan je bil model s končnimi elementi konzolnega nosilca s piezoelektričnimi obliži. Z uporabo 3D strukturnih in piezoelektričnih opek v Ansys in z uporabo končnih elementov je bil izdelan model konzolnega nosilca s piezoelektričnimi obliži. Časovni odziv modela na cvrčeč signal napetosti je bil določen s prehodno analizo. Značilnosti amplitude in frekvence so primerjane z eksperimentalnimi rezultati.

Ključne besede: piezoelektrični material, spekter frekvenc, analiza končnih elementov

1 INTRODUCTION

Automatic detection of impacts and hidden defects in structures (denoted as structural health monitoring, SHM) is the present-day trend in the non-destructive testing. The data obtained from the sensors applied to a structure are transmitted to the control system, which evaluates the state of the structure and responses appropriately (e.g, it enables the warning system). Especially the structures made of composite materials affected by hidden defects such as fibre debonding or delamination[1] call for an integration of the novel SHM methods.

Two approaches are usually distinguished in SHM: the passive and active ones. In a passive system "natural" impulses like impacts or crack propagation create stress waves that are sensed by a grid of sensors. The source can be then localized and reconstructed.[2] In an active SHM system the health of a structure is assessed by evaluating its response to specific actuating signals. One way of establishing damage is by detecting the changes in a structure's modal properties (particularly the basic natural frequency),[3] providing the global information on its state. Another way, denoted as the pitch-catch technique, uses the scattering of stress waves when the actuating signal approaches a structural defect.[4]

The sensors and actuators in SHM systems are made of smart materials that have a capability to convert various kinds of energy, e.g., piezoelectric materials (Rochelle salt, tourmaline or artificially produced ceramics) respond to a mechanical deformation by generating electric voltage and vice versa. Therefore, piezoelectric materials can be used as both sensors and actuators.

This work is focused on creating a reliable FE model of a piezoelectric transducer used in SHM. The model is then tested in the case when two patches are applied to a cantilever beam. An appropriate FE model of a piezoelectric patch is the key part for designing a future SHM system.

2 MODEL OF THE PIEZOELECTRIC MATERIAL

The piezoelectric material can be described with a set of constitutive equations:

$$\begin{bmatrix}\sigma\\ D\end{bmatrix}=\begin{bmatrix}C & -e^{\mathrm{T}}\\ e & \mu\end{bmatrix}\cdot\begin{bmatrix}\varepsilon\\ E\end{bmatrix} \tag{1}$$

where σ [Pa] is stress vector 6 × 1, C [Pa] is the matrix of elastic coefficients 6 × 6, ε is strain vector 6 × 1, D [C/m^2] is electric displacement vector 3 × 1, E [V/m] is electric-field intensity vector 3 × 1, μ is dielectric matrix 3 × 3 (with electric permittivity constants on its diagonal) and e [C/m^2] is piezoelectric stress matrix 3 × 6:

$$e=\begin{bmatrix}0 & 0 & 0 & 0 & e_{15} & 0\\ 0 & 0 & 0 & e_{24} & 0 & 0\\ e_{31} & e_{32} & e_{33} & 0 & 0 & 0\end{bmatrix} \tag{2}$$

The rows of matrix e denote the direction of the electric field and the columns refer to the strain components, e.g., constant e_{32} of the piezoelectric actuator quantifies strain ε_2 induced by the electric field in transversal direction 3.

In the producer's datasheet piezoelectric strain matrix d is listed instead of e. These matrices are related using the stiffness matrix:

$$e^{\mathrm{T}}=Cd^{\mathrm{T}} \tag{3}$$

A transversally isotropic material model is considered for the piezoelectric ceramic with the main direction of anisotropy identical with the direction of polarity. Stiffness matrix C is obtained with the inversion of compliance matrix S:

$$S=\begin{bmatrix}\frac{1}{E_1} & -\frac{v_{21}}{E_2} & -\frac{v_{31}}{E_3} & 0 & 0 & 0\\ -\frac{v_{12}}{E_1} & \frac{1}{E_2} & -\frac{v_{32}}{E_3} & 0 & 0 & 0\\ -\frac{v_{13}}{E_1} & -\frac{v_{23}}{E_2} & \frac{1}{E_3} & 0 & 0 & 0\\ 0 & 0 & 0 & \frac{1}{G_{23}} & 0 & 0\\ 0 & 0 & 0 & 0 & \frac{1}{G_{13}} & 0\\ 0 & 0 & 0 & 0 & 0 & \frac{1}{G_{12}}\end{bmatrix} \tag{4}$$

where E_1 is the Young's modulus in the direction perpendicular to the plane of isotropy, while $E_2 = E_3$ are the Young's moduli in the plane of isotropy. $G_{12} = G_{13}$ are the shear moduli in the planes perpendicular to the plane of isotropy, $G_{23} = G_{32}$ are the shear moduli in the plane of isotropy and are defined with:

$$G_{23}=\frac{E_2}{2(1+v_{23})}=\frac{E_3}{2(1+v_{32})} \tag{5}$$

Poisson's ratios $v_{12} = v_{13}$ give a measure of the extension (compression) in the plane of isotropy due to the extension (compression) in the direction perpendicular to this plane and vice versa. $v_{23} = v_{32}$ are the Poisson's ratios in the plane of isotropy.

3 DETERMINATION OF PIEZOELECTRIC COEFFICIENTS OF THE PATCHES

The piezoelectric patches used in the experiments are DuraAct P-876.A12 with a layer of piezoelectric ceramic (type PIC-255 [5]) with the dimensions of 50 mm × 30 mm × 0.2 mm. The top and bottom surfaces of the ceramic are silvered and connected to the soldering pads. Due to the high fragility the ceramic is embedded in a protective polymeric foil with the dimensions of 61 mm × 35 mm × 0.5 mm. The mechanical and electrical properties of the constituent materials are presented in **Tables 1** and **2**. Material properties of the piezoelectric ceramic were determined by the producer.[5]

Table 1: Material properties
Tabela 1: Lastnosti materiala

		Units	PZT	Foil	Al
Young's modulus	E	[GPa]	See Tab.2	3	68
Poisson's ratio	v	[–]		0.3	0.3
Density	ρ	[kg/m^3]	7800	1580	2777
Relative electric permittivity	μ_1/μ_0*	[–]	1650	–	–
	μ_2/μ_0	[–]	1650		
	μ_3/μ_0	[–]	1750		
Piezoelectric coefficients	e_{31},e_{32}	[C/m]	6.4	–	–
	e_{33}	[C/m]	–20.5	–	–
* μ_0 = 8.85418 × 10^{-12} F/m is vacuum permittivity					

Table 2: Elastic parameters of piezoelectric ceramic PIC-255
Tabela 2: Parametri elastičnosti piezoelektrične keramike PIC-255

E_1	[GPa]	62.1
$E_2 = E_3$	[GPa]	48.3
$v_{12} = v_{13}$	[–]	0.34
$v_{23} = v_{32}$	[–]	0.34
$G_{12} = G_{13}$	[GPa]	23.1
$G_{23} = G_{32}$	[GPa]	17.9

Although geometric and material properties of the piezoelectric patches are supposed to be similar for one type and production set, various results with differences up to 20 % were obtained using two patches of the same type and set. For this reason the piezoelectric properties of the patches used in following experiment need to be determined.

In the first experiment two pairs of strain gauges (HBM rosettes 6/650 RY91) were glued on the two

Figure 1: Piezoelectric patch with the applied strain gauges, one on the front side and one on the back side
Slika 1: Piezoelektrični obliž z napetostnimi lističi: eden spredaj in eden zadaj

piezoelectric patches (**Figure 1**), one on each side of a patch, to eliminate the influence of the minor patch curvature. The strain response to the applied static-electric voltage was measured and these values are presented in **Table 3**. The difference between these two patches loaded with 100 V was 14.4 %.

Table 3: Measured strains of the two patches (loaded with 100 V)
Tabela 3: Izmerjene napetosti dveh obližev (obremenjenih s 100 V)

Patch	1 / sensor	2 / actuator
ε_{11} by SG 1	10.27×10^{-5}	11.74×10^{-5}
ε_{11} by SG 2	9.38×10^{-5}	11.23×10^{-5}
ε_{11} – averaged	9.83×10^{-5}	11.49×10^{-5}

The piezoelectric-matrix coefficients were identified using a FE model in Ansys v.14. The model was created using 3D hexagonal elements: 20-node piezoelectric bricks (SOLID 226) for PZT and 20-node structural bricks (SOLID 186) for the protective foil. The piezoelectric elements have an additional degree of freedom for the electric potential in each node. One layer of these elements was used, which was sufficient for an approximation of the electric potential across the thickness of a patch. The nodes of the piezoelectric elements in the top and bottom surfaces are represented by the silver electrodes, where the relevant electric potential is applied.

The model parameter e_{31} was optimized to match the experimental data. Coefficients e_{32} and e_{33} were calculated as $e_{32} = e_{31}$ and e_{33} was chosen to maintain the mutual ratio of $e_{33}/e_{31} \approx -2.5$. The resulting values are presented in **Table 4**.

Table 4: Identified piezoelectric coefficients of the two patches
Tabela 4: Ugotovljeni piezoelektrični koeficienti pri dveh obližih

Patch	1 / sensor	2 / actuator
e_{31}, e_{32} [C/m]	7.1	8.3
e_{33} [C/m]	–17.8	–20.8

4 FREQUENCY RESPONSE OF THE CANTILEVER BEAM

The calibrated patches were glued to an aluminium beam with the dimensions of 1000 mm × 30 mm × 3 mm, each on one side. The beam was clamped at 100 mm of its length and 10 mm from the patches.

The patches were connected to the National Instruments data acquisition system (NI CompactDAQ) supplied with an actuating module NI 9215, sensing module NI 9236 and an amplifier. The beam was actuated by one of the patches and the vibration was sensed by another patch and laser position sensor OptoNCDT. The experimental set-up is presented in **Figure 2**.

The actuating signal was a linear chirp (sine wave with a linearly swept frequency) defined with the following equation:

$$x(t) = X \cdot \sin\left[\varphi_0 + 2\pi\left(f_0 + \frac{k}{2}t^2\right)\right] \tag{6}$$

where X is the amplitude, φ_0 is the initial phase, f_0 is the initial frequency, k is the chirp rate defined by:

$$k = \frac{f_1 - f_0}{t_1} \tag{7}$$

where f_1 denotes the final frequency and t_1 is the final time.

Table 5: Parameters of the actuating signal
Tabela 5: Parametri vzbujevalnega signala

Amplitude	X	[V]	75
Initial phase	φ_0	[rad]	0
Initial frequency	f_0	[Hz]	0
Final frequency	f_1	[Hz]	100
Final time	t_1	[s]	20
Sampling frequency	f_s	[Hz]	50000

The properties of the actuating chirp signal are presented in **Table 5**. The range of frequencies was chosen to contain the lowest natural frequencies of the beam for the relevant two out-of-plane bending modes.

The time-voltage responses of the piezoelectric sensor and laser sensor were recorded (**Figure 3**). A short-time Fourier transform (STFT) was performed to obtain a spectrogram (**Figure 4**). The length of the Hanning window in STFT was set to 10^5 samples providing a frequency precision of 0.5 Hz. The two lowest natural

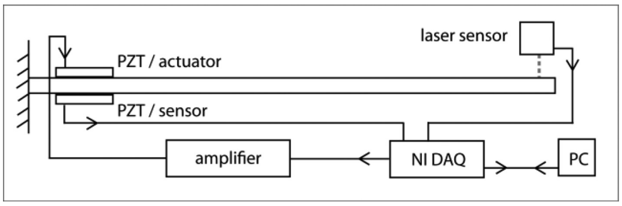

Figure 2: Experimental set-up
Slika 2: Eksperimentalni sestav

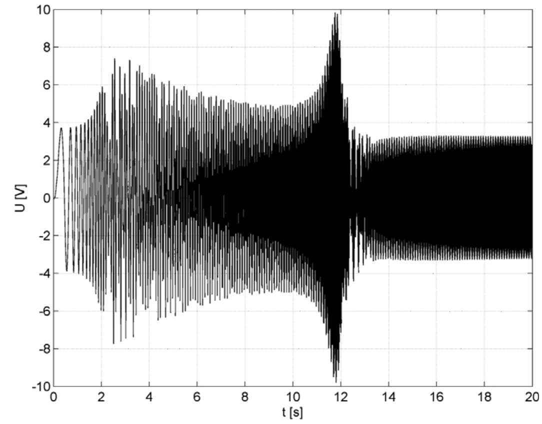

Figure 3: Time response of the cantilever beam measured with PZT
Slika 3: Časovni odziv konzolnega nosilca, izmerjen s PZT

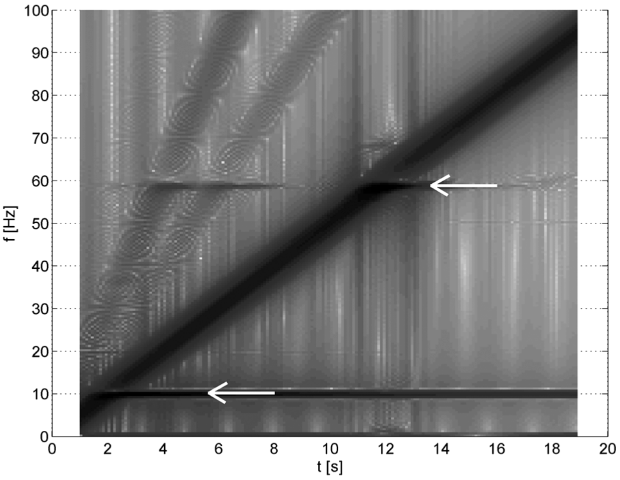

Figure 4: Spectrogram of the cantilever beam, the two lowest natural frequencies are marked with arrows
Slika 4: Spektrogram konzolnega nosilca; puščici prikazujeta dve najnižji naravni frekvenci

frequencies can be detected in the spectrogram. In **Table 6** the experimental results are compared with the numerically calculated natural frequencies.

Table 6: Comparison of natural frequencies
Tabela 6: Primerjava naravnih frekvenc

	FEM [Hz]	Experiment [Hz]
1st	9.9	10.0
2nd	60.5	60.0

5 AMPLITUDE RESPONSE OF THE CANTILEVER BEAM TO THE HARMONIC LOADING

To obtain the amplitude response the structure was loaded with a harmonic sine wave with a low frequency (1 Hz) with a duration of 40 s to approach steady oscillations. The amplitude was 100 V and the sampling frequency was 25 kHz. The deflection of the beam tip was measured with the laser sensor and compared with the results of the FE static analysis (**Table 7**). The difference between the experiment and FE was 2.4 %.

Table 7: Comparison of the experimental and numerical results
Tabela 7: Primerjava eksperimentalnih in numeričnih rezultatov

	Beam-tip deflection u_z
Experiment	0.206 mm
FEA	0.201 mm
Difference	2.4 %

6 CONCLUSION

A numerical model of a piezoelectric transducer was created in Ansys using three-dimensional piezoelectric and structural finite elements. The piezoelectric coefficients of each patch were calibrated using strain gauges and it was found that they differ by 14 %.

The FE model of the piezoelectric transducer was tested on a problem of bending an aluminum cantilever beam. The two lowest natural frequencies were determined experimentally and compared with the results of the FE modal analysis with sufficient match for the given frequency precision.

The amplitude of deflection of the beam loaded with the low-frequency voltage was measured with the laser sensor and compared to the result of the FE static analysis with a difference of 2.4 %.

This numerical model proved to be suitable for designing the SHM systems based on the change in the structure's natural frequencies. The reliability of the model will be further tested for the case of transient problems such as those used in the pitch-catch SHM systems.

Acknowledgement

The work was supported by projects SGS-2013-036 and GA P101/11/0288.

7 REFERENCES

[1] V. Laš, R. Zemčík, Progressive damage of unidirectional composite panels, Journal of Composite Materials, 42 (**2008**) 1, 25–44

[2] R. Zemčík, V. Laš, T. Kroupa, J. Bartošek, Reconstruction of Impact on Textile Composite Plate Using Piezoelectric Sensors, Proceedings of the Ninth International Workshop on Structural Health Monitoring, Stanford, 2013, 393–400

[3] R. Zemčík, R. Kottner, V. Laš, T. Plundrich, Identification of material properties of quasi-unidirectional carbon-epoxy composite using modal analysis, Mater. Tehnol., 43 (**2009**) 5, 257–260

[4] V. Giurgiutiu, Structural Health Monitoring with Piezoelectric wafer active sensors, Academic Press, Burlington 2008, 468–474

[5] Piezo Material Data, Physik Instrumemte (PI), [cited 2013-09-25] Available online on www.piceramic.com

UDK 66.017:669.018.9:620.178.3
Original scientific article/Izvirni znanstveni članek

ISSN 1580-2949
MTAEC9, 49(1)99(2015)

MICROMECHANICAL MODEL OF THE SUBSTITUENTS OF A UNIDIRECTIONAL FIBER-REINFORCED COMPOSITE AND ITS RESPONSE TO THE TENSILE CYCLIC LOADING

MIKROMEHANSKI MODEL NADOMESTKOV KOMPOZITOV, OJAČANIH Z ENOSMERNIMI VLAKNI, IN NJIHOV ODGOVOR NA CIKLIČNO NATEZNO OBREMENJEVANJE

Tomáš Kroupa[1], Hana Srbová[2], Robert Zemčík[1]
[1]University of West Bohemia in Pilsen, NTIS – New Technologies for the Information Society, Univerzitní 22, 306 14, Plzeň, Czech Republic
[2]University of West Bohemia in Pilsen, Department of Mechanics, Univerzitní 22, 306 14 Plzeň, Czech Republic
kroupa@kme.zcu.cz

Prejem rokopisa – received: 2013-11-08; sprejem za objavo – accepted for publication: 2014-02-13

A micromechanical model respecting the behavior of a long-fiber unidirectional composite subjected to the cyclic tensile loading was proposed. The so-called unit cell representing the structure of the composite material was created using the finite-element-analysis software. Material models of the fibers and matrix proposed in this work are based on the non-linear elastic and elasto-plastic behavior of real materials. The material and geometric parameters of the model are found by minimizing the difference between the numerical and experimental results.

Keywords: unidirectional fiber composite, cyclic tensile test, micromodel, material parameters, non-linear, elasto-plastic

Predlagan je mikromehanski model, ki obravnava vedenje kompozita z dolgimi enosmernimi vlakni pri cikličnemu nateznemu obremenjevanju. Osnovna celica, ki pomeni zgradbo kompozita, je bila izdelana s programsko opremo za analizo končnih elementov. Predlagani model materiala vlaken in osnove temelji na nelinearnem elasto-plastičnem vedenju realnih materialov. Material in geometrijski parametri modela so dobljeni z zmanjševanjem razlike med numeričnimi in eksperimentalnimi rezultati.

Ključne besede: kompozit z enosmernimi vlakni, ciklični natezni preizkus, mikromodel, parametri materiala, nelinearno, elasto-plastično

1 INTRODUCTION

Due to advantages, such as stiffness-to-weight and strength-to-weight ratios, carbon-fiber-reinforced composites are widely used for load-carrying structures in various kinds of industries such as aerospace, automotive, etc.

The behavior of composite materials can be modeled on the micro-, meso- and macro-scale levels. The micromechanical approach gives the most detailed information about the constituents. The constituents and the resulting composite exhibit, in general, a significantly non-linear response. In this work, the material models of the constituents include non-linear elastic and elasto-plastic effects. The goal is to capture the response of a unidirectional composite to the cyclic loading.

2 EXPERIMENT

In this work carbon-epoxy unidirectional continuous-fiber-composite-coupons were subjected to the tensile cyclic loading. Rectangular specimens (coupons) were cut with a water jet from a composite plate made of eight equally oriented layers, the so-called prepregs, HexPly 913C with fiber Tenax HTS 5631. With respect to the loading direction five specimens were tested for each of the following fiber orientations: 10°, 20°, 30°, 40°, 50°, 60°, 70°, 80° and 90° (**Figure 1**). Only two specimens were successfully tested for the fiber orientation of 0°. All the specimens were loaded in tension

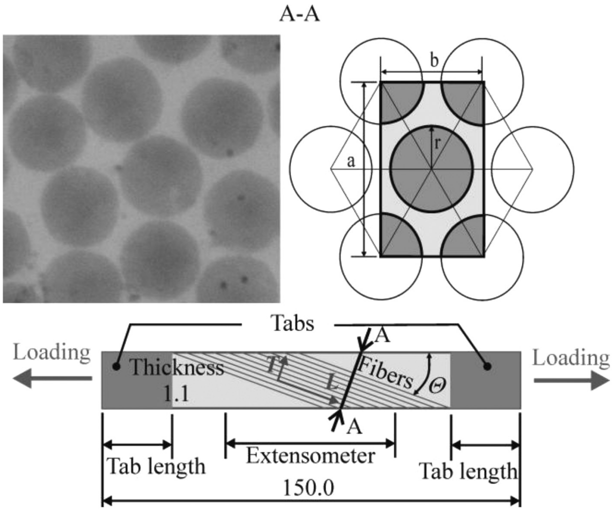

Figure 1: Geometry of the coupons (mm), real and idealized parts of the composite cross-section with a unit cell

Slika 1: Geometrija vzorcev (mm), realen in idealiziran del prereza kompozita z osnovno celico with the constantly increasing cycles up to failure. The test control parameter was the applied load.

The force-displacement dependencies obtained from the experiment were measured on the coupons with the glass-textile (0°) or aluminum tabs (10°, 20°, 30°, 40°, 50°, 60°) bonded with epoxy high-strength and tough adhesive Spabond 345. In the cases of the specimens with the fiber orientations of 70°, 80° and 90° a non-bonded emery cloth was used as the interface between the grip and the coupon. The tab configuration summarized in **Table 1** produced the required gage-section tensile failure (**Figure 2**).[1]

Table 1: Experiment configuration
Tabela 1: Konfiguracija eksperimenta

Fiber orientation (°)	Tab material	Tab length (mm)	Extensometer length (mm)
0	glass textile	60.0	10.0
10, 20, 30, 40, 50, 60	aluminum	25.0	60.0
70, 80, 90	emery cloth	25.0	60.0

2.1 Micromodel (finite-element model)

A three-dimensional idealized micromechanical model of the composite material was proposed in the form of a unit cell representing the periodical array of the composite. The unit cell consists of two parts, the part of the matrix and the part of the fibers. The fibers and the matrix are perfectly bonded.

A perfect honeycomb distribution of the fibers is assumed and the ratio of $r{:}a{:}b$ (**Figure 1**) is given by the fiber volume ratio V_f. The finite-strain theory was used.

The global coordinate system xyz is given by the loading direction x and the direction perpendicular to the composite surface z. The local coordinate system 123 is defined by the unit-cell edges, where the axis direction 1 corresponds to the fiber direction, direction 3 is identical to the axis direction z and 2 is perpendicular to axes 1 and 3 (**Figure 3**).

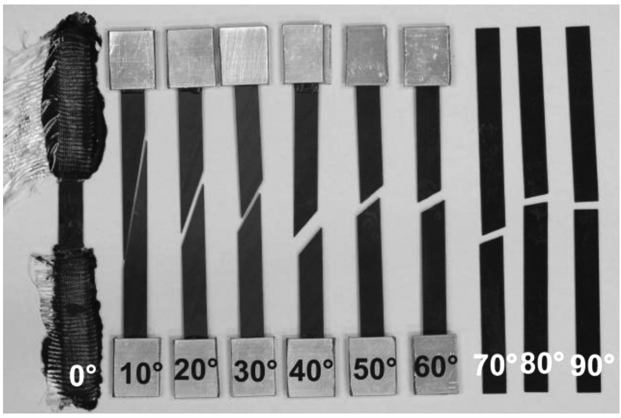

Figure 2: Cracked specimens. Final crack direction is parallel to the fibers in the directions of 10°–90° and perpendicular for the direction of 0°.
Slika 2: Vzorci z razpoko. Končna smer razpoke je vzporedna z vlakni pri smereh 10°–90° in pravokotna pri smeri 0°.

Assuming a uniaxial stress across the whole specimen, the behavior of the material can be simulated by loading the unit cell with a normal stress:

$$\sigma_x = \frac{F}{A} \tag{1}$$

where F is the external force and A is the cross-section of the specimen.

The effect of the loading force is transformed to the local coordinate system using the transformation:

$$\begin{bmatrix} \sigma_1 \\ \sigma_2 \\ \tau_{12} \end{bmatrix} = \begin{bmatrix} \cos^2\theta & \sin^2\theta & 2\sin\theta\cos\theta \\ \sin^2\theta & \cos^2\theta & -2\sin\theta\cos\theta \\ -\sin\theta\cos\theta & \sin\theta\cos\theta & \cos^2\theta - \sin^2\theta \end{bmatrix} \cdot \begin{bmatrix} \sigma_x \\ 0 \\ 0 \end{bmatrix} \tag{2}$$

where θ is the angle of rotation between the local and global coordinate systems.[2]

The results from the finite-element analysis (strains) are transformed back to the global coordinate system using the transformation:

$$\begin{bmatrix} \varepsilon_x \\ \varepsilon_y \\ \gamma_{xy} \end{bmatrix} = \begin{bmatrix} \cos^2\theta & \sin^2\theta & -\sin\theta\cos\theta \\ \sin^2\theta & \cos^2\theta & \sin\theta\cos\theta \\ 2\sin\theta\cos\theta & -2\sin\theta\cos\theta & \cos^2\theta - \sin^2\theta \end{bmatrix} \cdot \begin{bmatrix} \varepsilon_1 \\ \varepsilon_2 \\ \gamma_{12} \end{bmatrix} \tag{3}$$

Periodical boundary conditions were applied to ensure that there was no separation or overlap between the neighboring unit cells after the deformation.[2,3]

The micromodel was built in Abaqus/CAE (Complete Abaqus Environment), consisting of eight-node brick elements. The finite-element analysis was solved as a quasistatic process using the Abaqus/standard solver. The loading respected the experimentally obtained envelope; however, only four cycles were prescribed to reduce the computational time.

2.2 Material model of the fibers

The fibers were modeled as a transversely isotropic, elastic material, respecting the non-linear behavior in the axis direction. The nonlinearity is ensured with the form of the stress-strain relationships:

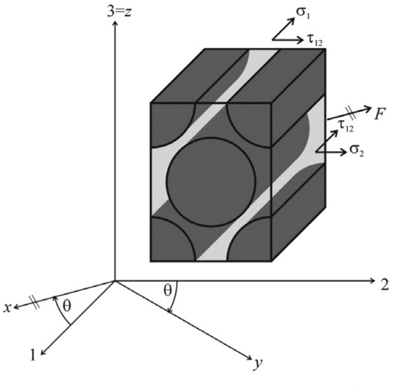

Figure 3: Rotated coordinate systems and loading of the unit cell
Slika 3: Zavrteni koordinatni sistemi in obremenitev osnovne celice

$$
\begin{aligned}
\sigma_{11} &= C_{11}(1+\tfrac{1}{2}\xi\varepsilon_{11})\varepsilon_{11}+C_{12}(\varepsilon_{22}+\varepsilon_{33})\\
\sigma_{22} &= C_{12}\varepsilon_{11}+C_{22}\varepsilon_{22}+C_{23}\varepsilon_{23}\\
\sigma_{33} &= C_{12}\varepsilon_{11}+C_{23}\varepsilon_{22}+C_{22}\varepsilon_{33}\\
\tau_{12} &= G_{12}\gamma_{12}\\
\tau_{13} &= G_{12}\gamma_{13}\\
\tau_{23} &= G_{23}\gamma_{23}
\end{aligned}
\tag{4}
$$

where ξ is the coefficient describing the measure of nonlinearity with the growing strain ε_{11} in the fiber direction, while ε_{22} and ε_{33} are the strains in the directions transverse to the fibers. G_{12} and G_{13} are the shear moduli in planes 12 and 13, respectively. The remaining elastic constants are:

$$
\begin{aligned}
C_{11} &= \frac{E_1(1-\nu_{23}^2)}{1-\nu_{12}\nu_{21}-\nu_{23}^2-2\nu_{21}^2\nu_{23}}\\
C_{12} &= \frac{E_1\nu_{21}(1+\nu_{23})}{1-\nu_{12}\nu_{21}-\nu_{23}^2-2\nu_{21}^2\nu_{23}}\\
C_{13} &= C_{12}\\
C_{22} &= \frac{E_2(1-\nu_{31}\nu_{12})}{1-\nu_{12}\nu_{21}-\nu_{23}^2-2\nu_{21}^2\nu_{23}}\\
C_{23} &= \frac{E_2(\nu_{23}+\nu_{21}\nu_{12})}{1-\nu_{12}\nu_{21}-\nu_{23}^2-2\nu_{21}^2\nu_{23}}\\
C_{33} &= C_{22}
\end{aligned}
\tag{5}
$$

where E_1 is the Young's modulus in the fiber direction, E_2 is the Young's modulus in the direction transverse to the fibers and ν_{12}, ν_{21} and ν_{23} are Poisson's ratios.[4]

2.3 Material model of the matrix

The matrix was modeled as an isotropic, elasto-plastic material. The elastic parameters were Young's modulus E_{m} and Poisson's ratio ν_{m}. Von Mises plasticity was used with the isotropic-hardening and work-hardening functions proposed in the form of:

$$\sigma^y = \sigma_0^y + \beta(\bar{\varepsilon}_{\mathrm{p}})^\alpha \tag{6}$$

where σ^y is the yield stress, $\bar{\varepsilon}_{\mathrm{p}}$ is the equivalent plastic strain, σ_0^y is the initial yield stress, and β and α are the shape parameters.

2.4 Identification process

The experimental results from the tensile cyclic tests were processed using the Python programming language. For each set of experiments belonging to the fiber direction θ, the arithmetic mean of displacement values at the maximum point of each cycle, was found. By connecting these averaged points with lines, the envelope curve was obtained. Tangent k of a particular cycle was determined by approximating the peak points with a linear function:

$$F = k\Delta l + q \tag{7}$$

individually for each experiment (**Figure 4**).

During the process of material-parameter optimization, the residuum describing the difference between the experimentally obtained envelope curve consisting of N points and the numerical force-displacement data for the cyclic tensile test:

$$r = \sum_{\theta}\sum_{i=1}^{N}\left(\frac{\Delta l^{\exp}(\theta, F_i) - \Delta l^{\mathrm{num}}(\theta, F_i)}{\Delta l_N^{\exp}(\theta)}\right)^2 \tag{8}$$

is minimized.

3 RESULTS

Material parameters were found for $V_{\mathrm{f}} = 0.55$ and $r{:}a{:}b$ = 1:1.28:2.22 (**Tables 2** and **3**). Moreover, the inaccuracy of the cutting orientation of the samples from the plate was determined to be $\Delta\theta = 1.7°$.

The work-hardening function is shown in **Figure 5**. Note that the force-displacement dependencies resulting from the numerical analysis are in good agreement with the dependencies obtained experimentally (**Figures 6** and **7**). However, there is not sufficient agreement between the cycle tangents (**Figure 8**).

Table 2: Material parameters of fibers
Tabela 2: Parametri materiala vlaken

Parameter	Units	Value
E_1	(GPa)	155.77
ξ	(-)	14.44
E_2	(GPa)	16.41
ν_{12}	(-)	0.30
ν_{23}	(-)	0.40
G_{12}	(GPa)	50.35

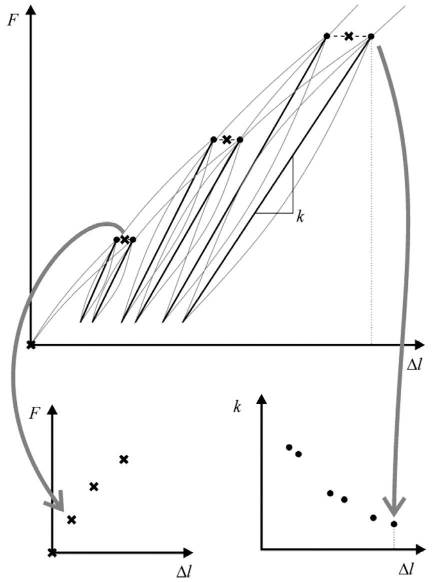

Figure 4: Principle of processing the data experimentally obtained from multiple experiments into envelope curve $F(\Delta l)$ and cycle tangents $k(\Delta l)$
Slika 4: Način pridobitve eksperimentalnih podatkov iz večkratnih preizkusov v skupno krivuljo $F(\Delta l)$ in tangento ciklov $k(\Delta l)$

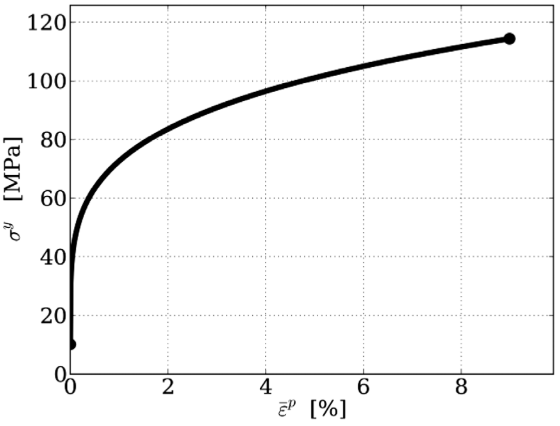

Figure 5: Matrix work-hardening function
Slika 5: Funkcija utrjevanja osnove

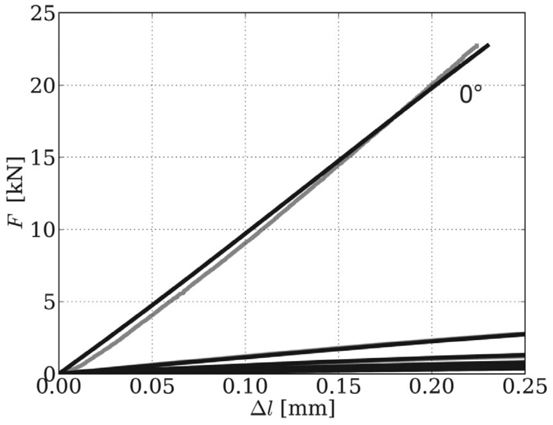

Figure 6: Force-displacement diagrams for the 0° specimen (black – determined, gray – experiments)
Slika 6: Diagrami sila – raztezek pri vzorcu 0° (črno – določeno, sivo – eksperimenti)

Table 3: Matrix-material parameters
Tabela 3: Parametri osnovnega materiala

Parameter	Units	Value
E_m	(GPa)	3.97
ν_m	(–)	0.40
σ_0^y	(MPa)	10.14
α	(–)	0.23
β	(MPa)	182.71

4 CONCLUSION

Finite-element analyses of the cyclic tensile tests were performed on unidirectional composite specimens with various fiber orientations. Material parameters of the orthotropic non-linear elastic material of the fibers and of the non-linear elasto-plastic material of the matrix were determined and good agreement with the experiments was achieved.

In future work a degradation of the matrix will be included into the material model in order to achieve better agreement between the determined and experimentally obtained cycle tangents.

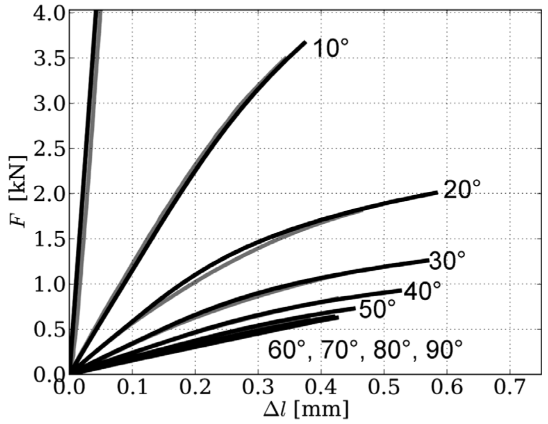

Figure 7: Force-displacement diagrams for 10° to 90° specimens (black – determined, gray – experiments)
Slika 7: Diagrami sila – raztezek pri vzorcih od 10° do 90° (črno – določeno, sivo – eksperimenti)

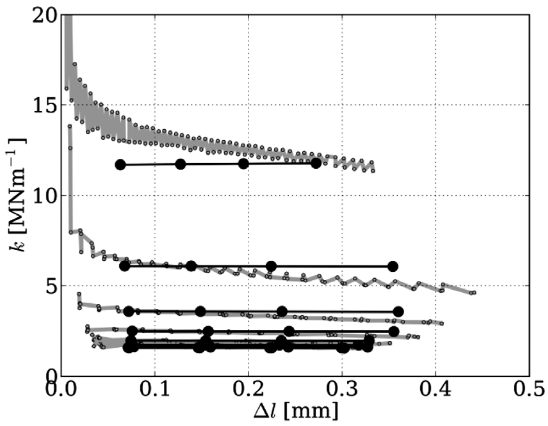

Figure 8: Tangents of the force-displacement cycles (black – determined, gray – experiments)
Slika 8: Tangente ciklov sila – raztezek (črno –določeno, sivo – eksperimenti)

Acknowledgement

The work was supported by projects SGS-2013-036 and European Regional Development Fund (ERDF), project "NTIS - New Technologies for the Information Society", European Centre of Excellence, CZ.1.05/1.1.00/02.0090.

5 REFERENCES

[1] ASTM Standard D 3039/D 3039M - 08, 2008, Standard Test Method for Tensile Properties of Polymer Matrix Composite Materials, ASTM International, West Conshohocken, PA 19428-2959, 2003, www.astm.org

[2] H. Srbová, T. Kroupa, R. Zemčík, Identification of the Material Parameters of a Unidirectional Fiber Composite Using a Micromodel, Mater. Tehnol., 46 (**2012**) 5, 431–434

[3] S. W. Tsai, P. D. Shah, Strength & Life of Composites, Department of Aeronautics & Astronautics, Stanford University, 2008

[4] V. Laš, Mechanics of Composite Materials, University of Bohemia, Plzeň, 2004 (in Czech)

UDK 621.93:621.936.6:622.35
Original scientific article/Izvirni znanstveni članek

ISSN 1580-2949
MTAEC9, 49(1)103(2015)

DRY-CUTTING OPTIONS WITH A CHAINSAW AT THE HOTAVLJE I NATURAL-STONE QUARRY

MOŽNOSTI SUHEGA REZANJA Z VERIŽNO ŽAGO V KAMNOLOMU NARAVNEGA KAMNA HOTAVLJE I.

Jože Kortnik[1], Boštjan Markoli[2]

[1]University of Ljubljana, Faculty of Natural Sciences and Engineering, Department of Geotechnology and Mining, Aškerčeva 12, Ljubljana, Slovenia
[2]University of Ljubljana, Faculty of Natural Sciences and Engineering, Department of Materials and Metallurgy, Aškerčeva 12, Ljubljana, Slovenia
joze.kortnik@guest.arnes.si

Prejem rokopisa – received: 2013-12-10; sprejem za objavo – accepted for publication: 2014-01-17

This paper presents the results of a study on the possibility of replacing cutting inserts and introducing dry-cutting mode (without water rinsing) with a chainsaw machine in the underground structures of the Hotavlje I quarry. In the experiment a column-driven chainsaw machine Fantini G.70 was used with tungsten-carbide-based cutting inserts. The article presents the physico-mechanical properties of the natural stone called the Hotaveljčan limestone and the state of discontinuities, which has a significant impact on the efficiency of stone cutting. In the experiment the cutting characteristics of two types of inserts, type H-13A and type H6T, were compared. The specimens of both types of the used inserts were subjected to a detailed metallographic investigation to evaluate the changes in the surface structure and hardness, the results of which are presented in detail.

Keywords: tungsten-carbide inserts, chainsaw machine, dimensional stone

V članku so podani rezultati raziskave možnosti zamenjave rezalnih ploščic in vpeljave suhega načina rezanja (brez izpiranja z vodo) naravnega kamna z verižno žago v podzemnih prostorih kamnoloma Hotavlje I. V poskusu je bila uporabljena verižna žaga Fantini G.70 na hidravličnih stojkah. V članku so predstavljene tudi fizikalno-mehanske lastnosti naravnega kamna, t. i. pisanega apnenca "Hotaveljčana", in stanje diskontinuitet, kar pomembno vpliva na učinkovitost rezanja naravnega kamna. Pri poskusu so bile primerjane rezalne karakteristike dveh vrst rezalnih ploščic tipa H-13A in H6T. Materiala obeh tipov rezalnih ploščic sta bila po poskusu detajlno metalurško preiskana glede spremembe trdote površine, rezultati pa so tudi podrobneje prikazani.

Ključne besede: rezalne ploščice, verižni zasekovalni stroj, okrasni kamen

1 INTRODUCTION

The efforts to study and understand the cutting mechanisms applied to hard limestone using chainsaw machines are not new in Slovenia. The first chainsaw machines were introduced in Slovenian natural-stone quarries in the late nineties; they were originally equipped with carbide cutting tools and later progressively replaced with the new generation of tools. The new generation of tools for metal machining included inserts of tungsten carbide coated with a thin film of a hard material that was chemically deposited on the substrate and welded to the metal shank.

Until now, no research project aiming at a better understanding of the stone-cutting mechanisms using a chainsaw has been initiated in Slovenian natural-stone quarries. For example, in Belgium the first results obtained with this technique were widely published in specialized literature[1–9]: Mingels (1971)[10] and Focant (1977)[11] described sawing applications in Belgian red marble; Boxho (1971)[12], Brych (1975)[13] and Neerdael (1975)[14] worked with Belgian blue stone. Later, very few scientific publications were dedicated to the chainsaw-cutting problems.

Research objectives were at first aimed at decreasing the exploitation costs of the chainsaw machines and then at optimizing the technological parameters in order to correctly set up the cutting machines. The very first studies tried to investigate the machine's performance with respect to the intrinsic properties of the stone being cut, comparing it with the results of the cutting tests performed in a laboratory. These studies highlighted the considerable losses of the machines due to the friction generated at the contact between the chain and the arm of the machine, and also the losses in the hydraulic system driving the machine.

Although the sawing techniques have been particularly improved in the last 20 years, they are still problematic when hard and/or abrasive stones are cut. The main problems encountered with this type of materials are a low productivity, a high consumption of cutting tools and, thus, the related high production costs.

2 EXTRACTION OF NATURAL STONE FROM THE HOTAVLJE I QUARRY

For the hard materials such as Hotavlje calcareous limestone, brittle breakage is typical. This means that this kind of material, when burdened with an additional load, can only sustain a minor degree of plastic strains (approximately 5 %). Thus, it can instantly break in a plastic zone[8]. Because of these characteristic, the areas with plastic zones are considered unstable and dangerous for the stability of the underground structure.

The occurrence of cracking requires a consideration of the rocks with cracks and their statuses. Thus, an observed rock is called a mound. It is the cracks that cause local differences in the mechanical properties of the rock which differ considerably from those measured in the laboratory. Examinations of mechanical and physical properties of natural stone were carried out in accordance with European Union standards EN 12058:2004 (Natural stone products – Slabs for floors and stairs – Requirements). **Table 1** shows the physico-mechanical properties of three color variations of natural decorative stone called Hotaveljčan.[15]

Table 1: Mechanical properties of natural stone called Hotaveljčan[15]
Tabela 1: Mehanske lastnosti naravnega kamna, imenovanega "Hotaveljčan"[15]

Type of investigation	Unit	Hotavlje red	Hotavlje gray	Hotavlje gray-pink
Density without pores and cavities	t m^{-3}	2.90	2.74	2.73
Density	t m^{-3}	2.74	2.71	2.71
Coefficient of density		0.94	0.99	0.99
Porosity	%	0.06	0.01	0.70
Water absorption	%	0.36	0.23	0.25
Grinding wear	cm^3 50 cm^{-2}	29.5	27.1	
Modulus of elasticity	GPa	25.0	25.0	25.0
Angle of internal friction	°	22–35	–	–
Bending tensile strength	MPa	–	14.7	
Bending tensile strength after 48 freeze/thaw cycles	MPa	–	13.6	
Average compressive strength:			90.2	
– dry	MPa	137.8	114.0	–
– wet	MPa	150.8	156.0	–
– after 25 freeze/thaw cycles	MPa	187.8	118.0	–

Since the knowledge on rock-mass fracturing is very important in our case in order to determine the geomechanical properties of a rock mass, it has to be described by means of a statistical examination of the dispersion of the measured cracks in the quarry and wells, and a description of its occurrence. The main statistical characteristic of a particular occurrence of a large statistical dispersion indicates that random cracks and crevices thicken considerably with a mild dip to the northeast.

Figure 1: Column-driven chainsaw machine Fantini G.70 on the location in the Hotavlje I quarry
Slika 1: Verižna žaga Fantini G.70 na hidravličnih/vpenjalnih stebrih na lokaciji poskusa v kamnolomu Hotavlje I.

There are two quarries of colored calcareous stone in the Hotavlje deposit. The Hotavlje I quarry, also called the lower quarry, is the older and larger quarry, operating in the northern part of the deposit, 435 m to 450 m above sea level. In the central part of the deposit a new and smaller quarry is in its opening phase. The Hotavlje II quarry, also called the upper quarry, lies between 478 m and 488 m above sea level. Both quarries are situated on the steep eastern side of the Srednje Brdo Mountain[16].

In 1993, in the colored-calcareous-stone Hotavlje I quarry, a new method of natural-stone-block production was introduced, called the underground stopping, which, until then, had not been used in the Republic of Slovenia. This method was proposed because of the geological structure and the state of the quarry, and also due to an increasing demand for this particular stone. Extraction in the gallery is done with a diamond-wire saw and chainsaw combined. This method proved to be the most efficient one (**Figure 1**).

For the extraction of natural stone from the Hotavlje I underground quarry a chain machine with hydraulic/clamping columns is used (**Figure 2**). Hydraulic pillars allow the machine blade with the cutting chain to move in both horizontal and vertical directions. The cutting chain machine is placed directly in front of the stope-face and is it rigidly attached. Horizontal cuts are first made at the bottom and top and finally on the sides. Process water is used for cooling the saw chain and washing the stone slurry out of the cut.

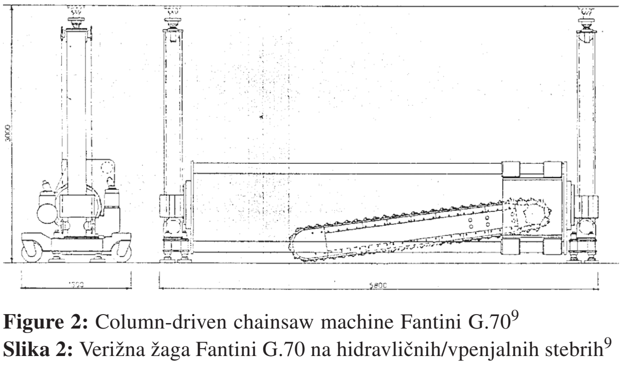

Figure 2: Column-driven chainsaw machine Fantini G.70[9]
Slika 2: Verižna žaga Fantini G.70 na hidravličnih/vpenjalnih stebrih[9]

Table 2 shows technical details/characteristics of the column-driven chainsaw machine Fantini G.70 used in underground quarries.

Table 2: Technical properties of column-driven chainsaw machine Fantini G.70[9]

Tabela 2: Tehnični podatki verižne žage Fantini G.70 s hidravličnimi/vpenjalnimi stebri[9]

Weight of the chainsaw/Weight of the hydraulic unit	6000 kg/2000 kg
Total installed power	52.2 kW (70 HP)
Chain rotation speed	0–0.71 m s^{-1}
Arm/blade cutting-speed rate	0–0.07 m^2 min^{-1}
Cutting width	38 mm
Arm/blade length	2900 mm
Water consumption	20 L min^{-1}
Cutting speed	2–4 m^2 h^{-1}

As presented in **Table 2** the cutting speed is between 2 m^2 h^{-1} and 4 m^2 h^{-1}, the cut width is 38 mm and the cut depth is 2.40 m or more. The speed of the blade movement is up to 0.07 m min^{-1} and the chain speed is up to 0.7 m s^{-1}. The minimum stope-face width is 5.80 m. The cutting method is based on cutting the rock using widia or diamond plates that are mounted on the cutting chain machine's blade. The cutting machine's blade moves along the cogged rail and guiding rails. Process water is used for cooling the saw chain and washing the stone slurry out of the cut.

3 THEORY OF NATURAL-STONE CUTTING

An improvement of the sawing techniques in the Hotavlje I quarry initially requires an understanding of the cutting responses of the tools currently available on the market. This implies a development of the working methodology, making it possible to correctly characterize the performances of cutting configurations independently of the machines, the operators and any other parameters that can influence the operations of the machines. The field experimental approach was selected because it makes it possible to very quickly estimate the performances of various types of cutting tools used in a quarry.

Rake angle α: Cutting and normal forces decrease monotonically with the increasing rake angle as seen in **Figure 3**. Most of the benefit to the insert forces is achieved at a rake angle of 20°, beyond which a further marginal improvement weakens the cutting insert's strength and its potential to survive. The rake angle can be either positive or negative. The rake angles between +20° and +30° can be chosen for cutting weak rocks and coal. High rake angles may not be beneficial since the inserts with these angles are more susceptible to a gross failure.

Wear angle φ: The wear flat is almost parallel to the cutting direction; however, it generally tends to incline in the opposite direction forming a wear angle. This angle is only a few degrees and it becomes smaller for the hardest and strongest materials. The occurrence of the wear flat changes the tool-tip geometry and, consequently, results in the generation of higher tool forces. The normal force is the component most affected by the wear, e.g., a wear flat of around 1.0 mm can drastically increase the F_n/F_t ratio. It is also reported that a large clearance angle relieves the wear effect and provides a better overall efficiency even if, as a consequence, a small or slightly negative rake angle is introduced.

Clearance angle β: The clearance angle, which is between the lower surface of the insert and the plane parallel to the cutting direction, also has pronounced effects on the cutting insert's forces. The investigations showed that the tool forces drop sharply after a value of around 5° and stay sensibly constant. To meet the kinematic needs, the clearance angle is generally designed to be around 10°.

When cutting stone with a chainsaw two forces are acting on the cutting inserts (**Figure 3**):

- Axial (thrust) force of the chainsaw arm/blade F_n, which allows the cutting inserts to progress from the surface of the stone into the depth d,
- Force of the chain rotation F_t, which allows the cutting and progression of the chainsaw arm/blade to the depth d of the cutting grooves.

The cutting depth of individual cuts depends on the axial force F_n which is proportional to and decreases with the increasing cutting surface and the cutting resistance of the rock (strength, toughness and hardness of the rock). Rock cutting begins when the critical pressure is reached, which must be greater than the strength of the rock.

A chip formation can be described as a destruction of the stone consistency using a tool. In the literature, the models based on simple geometries of the cutting edges divide the process of forming a cut into two mechanisms[1,2]. The cutting mechanism of marble is explained as a plastic deformation (a crushed zone) and a brittle

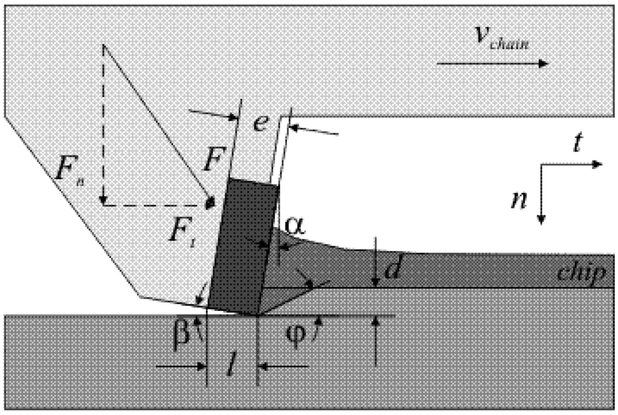

Figure 3: Forces active during the chainsaw cutting of natural stone (α – rake angle, φ – wear angle, β – clearance angle)

Slika 3: Delovanje sil pri žaganju naravnega kamna z verižno žago (α – kot strganja, φ – strižni kot, β – kot praznjenja rezi) fracture of stone[2,17]. The plastic deformation and the brittle fracture are influenced by the cutting conditions such as the depth of cut, the tip shape of the cutting tool, and the properties of the stone. When cutting stone with diamond tools, the mechanical interaction of the tool and the workpiece results in the process forces, mainly caused by the following factors:

- elastic and plastic workpiece deformation by the cutting edges;
- friction between the stone and the matrix;
- friction between the swarf and the matrix.

In front of the grains engaged in the process, stresses are caused by tangential forces. In this zone, the insert is forced out through the grooves in front of and beside the grains. While the rock shows elastic characteristics up to its ultimate stresses, it is necessary for the cutting to reach a certain minimum grinding thickness. The material to be cut is deformed by the compressive stress conducted below the diamond. When the load is removed, an elastic reversion leads to critical tensile stresses, which cause a brittle fracture. This mechanism affected by tensile stresses is termed the secondary chip formation. The general insert is carried away by the coolant. The following factors influencing this process are directly or indirectly contained in the model:

- physical material properties of the stone;
- forces between the diamonds and the materials;
- stress distribution in the rock;
- temperatures at the tool/workpiece interface.

The cutting force and energy play important roles in all the stone-machining processes. They are functions of the maximum chip thickness and the geometry of the idealized sawing chip.

The axial (thrust) force of the chainsaw arm/blade, F_n, was calculated by Purtić[18]:

$$F_\mathrm{n} = \frac{\sigma_\mathrm{u} \cdot l \cdot d \cdot \sin(\alpha + 2\varphi)}{\cos\alpha \cdot \cos^2\varphi} = k \cdot \sigma_\mathrm{u} \cdot l \cdot d \tag{1}$$

where

σ_u (MPa) – compressive strength of the rock

l (m) – length (thickness) of the cutting inserts

d (m) – depth of the insert penetration into the rock

k (m) – coefficient of friction.

Coefficient of friction:

$$k = \frac{\cos\alpha \cdot \cos^2\varphi}{\sin(\alpha + 2\varphi)} \tag{2}$$

The value of coefficient of friction k is dependent on the angle of the rock internal friction φ and the rake angle α:

Coefficient of friction k	0.27	0.30	0.36	0.44
Angle of rock internal friction φ/°	15	17	20	22

The cutting speed v_cut is usually obtained with the following equation:

$$v_\mathrm{cut} = d \cdot m \cdot v_\mathrm{chain} \quad (\mathrm{m^2\ s^{-1}}) \tag{3}$$

where

d (mm) – depth of cutting

m (–) – number of cutting inserts

v_chain (m $\mathrm{s^{-1}}$) – speed of the chain with cutting inserts.

The depth of cutting is strongly dependent on the compressive strength of the rock and the force of the chainsaw arm or blade (**Figure 4**). Specific energy is also a very important factor in determining the efficiency of cutting systems and it is defined as the work required to excavate a unit volume of a rock. Hughes[19] and Mellor[20] demonstrated that specific energy can be formulated in the following way:

$$S_\mathrm{E} = \frac{\sigma_\mathrm{u}^2}{2E} \tag{4}$$

where

S_E – specific energy

σ_u – compressive strength of the rock

E – elasticity modulus.

The work done with the cutting force F_n is the work needed to excavate a unit volume of yield. Dependent on rock strength and toughness, degree of fracturing, machine type and method of operation, cutting insert type and condition, available tool forces (machine size and power) and penetration depth, the specific energy amounts to:

$$S_\mathrm{E} = \frac{\sigma_\mathrm{u}^2}{2E} = \frac{90.2^2\ \mathrm{MPa}}{2 \cdot 25.000\ \mathrm{MPa}} = 162.7\ \mathrm{kPa}$$

Stone cutting is the result of the interference between the insert grits and hard stone at the stone-tool interface. The traditional tool is constituted of diamond grits that are joined to the metal shank with the metal matrix. The new-generation tools in metal machining are constituted of inserts of tungsten carbide, coated with a thin film of diamond that was chemically deposited on the substrate

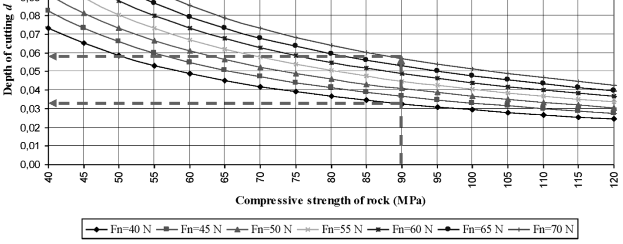

Figure 4: Graph of the expected depth d of the insert penetration at different compressive strengths of natural stone and the axial (thrust) force of the chainsaw arm/blade F_n

Slika 4: Graf pričakovanih globin d penetracije rezalnih ploščic v naravnih kamnih različnih tlačnih trdnosti in različnih v naravnega kamna ter z različnimi osnimi (potisnimi) silami meča verižne žage F_n

(chemical-vapor-deposition (CVD) diamond inserts) and welded to the metal shank$^{2-4}$.

4 EXPERIMENTAL WORK: IN-SITU ATTEMPTS TO USE DIFFERENT INSERTS

The presented research undertaken at the Faculty of Natural Sciences and Engineering, the University of Ljubljana, in 2009/2012 in collaboration with the Marmor Hotavlje company was conducted to understand the main problems encountered while cutting hard limestones such as Hotaveljčan and to propose technical solutions for increasing the competitiveness of the column-driven chainsaw machine Fantini G.70 in the Hotavlje I quarry (**Figure 1**).

The main objectives of the research were as follows:

- Increasing the machine's performance so that it reaches a higher productivity when cutting the hard Hotaveljčan limestone. The operators usually empirically determined the operating parameters of the machines on the basis of their personal experiences. Consequently, the performance was strongly influenced. The determination of the optimum parameters that should increase the performance required a fundamental scientific study.
- Identifying the potential implementation of dry cutting without the use of process water for rinsing the stone debris from the cut and cooling the inserts.
- Increasing the lifespan of the cutting tools and reducing the maintenance costs of the chain-saw machines.

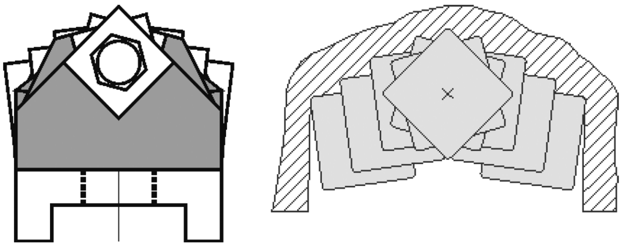

Figure 5: Cutting configuration with 13 mm wide square cutters/inserts (a system of 7 holders (n0–n6))

Slika 5: Postavitev rezanja 13 mm kvadratnih rezalnih ploščic (sistem s 7 nosilci (n0–n6))

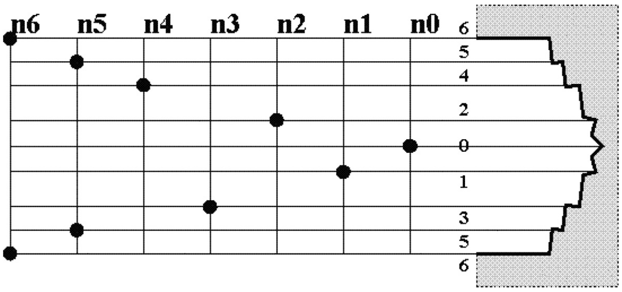

Figure 6: Schematic view of the cutting system with 7 cutting insert holders and their positions on the chainsaw chain (on the right, a schematic view of the cutting grooves)

Slika 6: Shematski prikaz sistema razporeda 7 nosilcev in lege nosilcev rezalnih ploščic na verigi verižne žage (na desni shematski prikaz rezalne brazde)

Figure 7: Detail of the chain and arm/blade of the chainsaw machine

Slika 7: Detajl verige in zobnika roke/meča verižne žage

Two different values of the side rake angle, at the insert/tool holders from n1–n6, angle –6° and at the insert/tool holder n0, angle –25°, were adopted. These were used to simulate the actual engagement between the insert and stone during sawing and, therefore, the cracking phenomena between the insert and stone during sawing. A scheme of the tool engaged in stone cutting is shown in **Figures 5** and **6**, while **Figure 7** depicts a detail of the actual set up of the cutting machine. The cutting force along the cutting direction F_n and the cutting force F_t perpendicular to the cutting direction were evaluated from **Figure 3**.

In the experiment, two types of inserts were used, namely:

- Fantini Sandvik H6T CT30 insert grade (a hardness of 1753 HV) and
- Fantini Segatrice H-13A insert grade (a hardness of 1310 HV).

The cutting force along the cutting direction F_n and the cutting force F_t perpendicular to the cutting direction were calculated using the data from **Table 3**.

Table 3: Data on the cutting parameters used for the calculations

Tabela 3: Podatki o parametrih rezanja, uporabljenih za izračune

v_{chain}	Rotation speed of the chain with tungsten-carbide inserts Hitrost verige z rezilnimi ploščicami	0–6.000 cm min^{-1}
	Arm/blade cutting speed rate Hitrost pomika meča pri žaganju	0–10 cm min^{-1}
v_{cut}	Average chain cutting speed Povprečna hitrost rezanja verižne žage	0–8 m^2 h^{-1}
	Width of the cut Širina reza	38–42 mm

In addition to the data from **Table 3**, the values of the cutting speed (0–60 m min^{-1} (the average of 55 m min^{-1}))

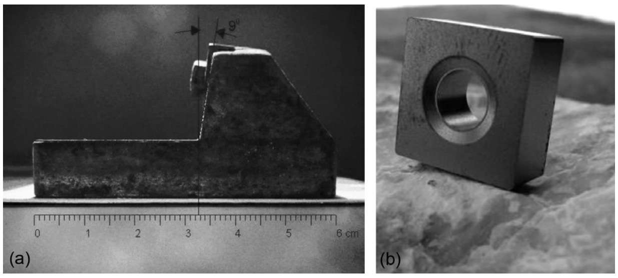

Figure 8: a) Insert holder n5 with a rake angle α = 9° and b) a tungsten-carbide insert

Slika 8: a) Nosilec rezalne ploščice n5 s kotom strganja α = 9° in b) volfram-karbidna rezalna ploščica

and many different values of the depth of cut (between 0.03 mm and 0.06 mm) were also used.

The forces exerted on the cutting inserts, as presented in **Figure 8**, led to the wear of these inserts during the cutting operation, presented in **Figure 9**.

The chainsaw cutting machine (Fantini G-70) operates using the following stepwise procedure to cut natural stone: It starts in Position 0 (**Figure 9**) where the initial cut using only the tip of the cutting blade is made and it is then forced into Position 1 (a blade angle of 10° to 72°). Then the blade is repositioned into Position 2 where it starts to move towards Position 3 (a blade angle of 72° to 81°). In this arrangement the chain with the cutting inserts is cutting the stone piece along the whole of the width, i.e., from 0–250, generating the highest forces exerted on the blade and on the cutting chain. When Position 3 is finally reached, the blade starts to rotate slightly so as to move into Position 4 (a blade angle of 81° to 107°). Finally, it moves into Position 5 (a blade angle of 107° to 166°). This is done in a manner very similar to the one at the beginning of the cutting process. The extent of horizontal cuts is limited to a depth of 2.50 m and the minimum length of 5.75 m. Vertical cuts are limited to a depth of 2.5 m and a height of 4.6 m. The construction of the cutting machine also enables the cuts to be made under different angles, exerting additional forces on the blade and the chain, thus leading to premature wear of the cutting inserts.

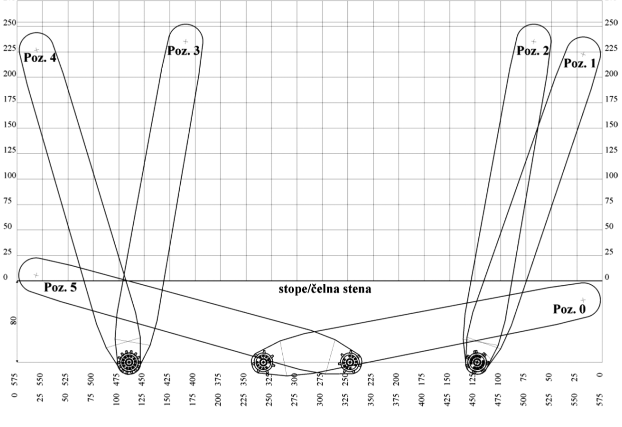

Figure 9: Stages (Pos. 0 to Pos. 5) of making a horizontal cut with two types of cutting inserts

Slika 9: Faze (Poz. 0 do Poz. 5) rezanja horizontalnega reza z različnima tipoma rezalnih ploščic

5 RESULTS AND DISCUSSION

The results of the cutting process described in the section about the experimental work associated with **Figure 9** are depicted in **Figures 10** and **11**. Two different cutting inserts were employed for the cutting purposes. Both cutting inserts were mounted on the same chain of the Fantini G-70 cutting machine so as to make the comparison of the cutting inserts as reliable as possible. **Figure 10** shows the behavior of the H6T C30 Fantini Sandvik cutting inserts mounted on the cutting chain cutting the natural stone from the Hotavlje quarry in the horizontal manner. For this purpose the following process parameters were used: the chain speed varied from 53.0 m min^{-1} to 55.3 m min^{-1} and the average cutting speed increased from 3.5 m^2 h^{-1} to 5.5 m^2 h^{-1}. The entire duration of the pure horizontal cut with the chainsaw took 186 minutes. Throughout the cutting process, the consumption of time was also recorded. In the case of the cutting inserts H-13A Fantini Segatrice (**Figure 11**) the horizontal cutting manner was also applied and the chain speed varied from 51.5 m min^{-1} to 55.6 m min^{-1}, while the average cutting speed varied from 6.3 m^2 h^{-1} to 7.9 m^2 h^{-1}. The entire duration of the pure horizontal cut with the chainsaw took 169 min. A comparison of the results from **Figures 10** and **11** indicated that the yield in the case of the H-13A cutting inserts was higher in relation to the average cutting speeds, whilst the time consumption was pretty much the same. However, the variation in the chain speed was smaller in the case of the H6T cutting inserts which applies to the average cutting speeds as well. In the case of H6T, these showed less dissipation or variation in all the positions or incisions (Pos. 0 to Pos. 5) which inevitably led to less pronounced wear of the cutting inserts due to fragmentation than in the case of the H-13A cutting inserts. When the H-13A cutting inserts were used, the variations in the chain speeds were much more obvious as the

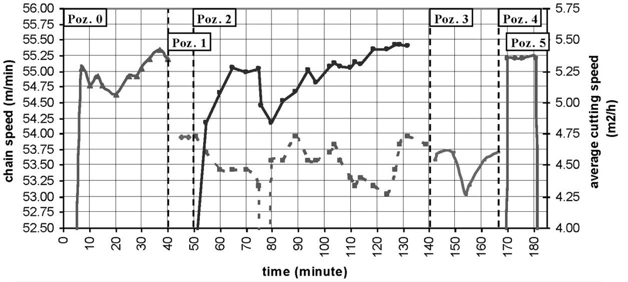

Figure 10: Results of a horizontal cut with the H6T cutting inserts

Slika 10: Rezultati rezanja horizontalnega reza z rezalnimi ploščicami H6T

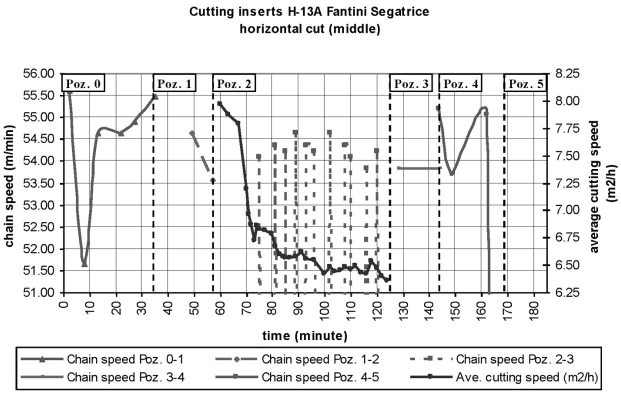

Figure 11: Results of a horizontal cut with the H-13A cutting inserts
Slika 11: Rezultati rezanja horizontalnega reza z rezalnimi ploščicami H-13A

speeds varied, for all the incisions (Pos. 0 to Pos. 5), with sharp peaks and drops.

This led to less uniform wear and a more frequent deformation of the cutting inserts due to fragmentation. The recorded peaks and drops in the chain speeds in the case of H-13A are visible in **Figure 12** showing an array of grooves made in a stepwise manner as the mechanical properties of the natural stone were changing locally, as were the mechanical properties of the cutting inserts.

The measurements of the surface and subsurface microhardness of the cutting inserts showed that the degradation of the surface hardness was severe but it was, in all the cases, limited to an area within a few tenths of a millimeter under the surface (**Table 4**).

A brief metallographic overview of the applied cutting plates provided us with a definite proof of surface and subsurface degradation. This was observed using LM and the microhardness measurements made on the surface and, in a stepwise manner, also under the surface. **Table 4** summarizes the Vickers hardness measurements with the average number of measurements of 5.

Table 4: Microhardness measurements of HV 0.05 for H-13A and H6T CT30 cutting inserts
Tabela 4: Mikrotrdote HV 0,05 rezalnih ploščic H-13A in H6T CT30

Cutting insert	Average hardness on the surface	Average hardness 0.1 mm under the surface
Grade H-13A	1240.75	1471.40
Grade H6T CT30	1269.00	1614.67

Figure 12: Visible grooves or a cut profile made by the cutting inserts
Slika 12: Vidni kanal oziroma profil reza, ki nastaja med rezanjem z rezalnimi ploščicami

It is clear that in both cases the hardness degrades quite rapidly and dramatically from the surface towards the inner region of a cutting plate, which is a consequence of the thermomechanical load on the surface of the cutting plate. On the micrographs of the H-13A cutting inserts in **Figures 13a** and **13b** severe material wear can be observed on the cutting edges of the cutting inserts due to a complete rounding and cracking of the initially rectangular edges. On the top (**Figure 13b**), the indents of the diamond pyramid can still be seen allowing clear indications of the places where the microhardness HV measurements were made. The protective TiN layer of the surface and the edges of H6T CT30 is still intact, which was also confirmed with the HV measurements showing a higher hardness of the cutting inserts after the operation (**Figure 13c**). It has to be noted here that the H-13A cutting inserts were used for the so-called dry cutting, whereas the H6T CT30 inserts were water cooled. Namely, the H-13A cutting inserts were constructed to be used for dry cutting although we believe that the use of a lubricant or coolant would most likely prolong their service time too.

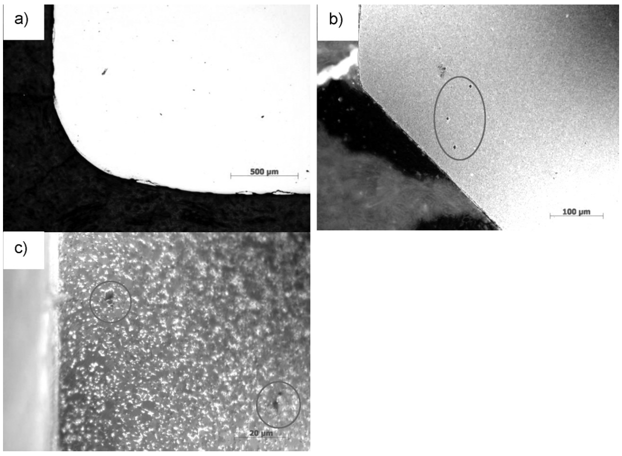

Figure 13: LM micrographs of the cutting inserts after the operation: a) cutting edges of H-13A cutting inserts and b) with clear positions of the indents (circle) of the diamond pyramid used in HV measurements. Uniformity in the grain size of WC can be seen in b). The surface of H6T CT30 exhibits fewer defects and still has the protective layer of TiN. Positions of the indents caused by the diamond pyramid are visible in c).
Slika 13: LM-posnetki uporabljenih rezalnih ploščic: a) rezalni robovi ploščic H-13A in b) z lepo vidnimi vtiski po uporabi diamantne piramide v okviru HV-meritev. Na sliki b) je prikazana enakomerna velikost delcev WC. Površina rezalne ploščice H6T CT30 izkazuje veliko število majhnih poškodb na še vedno prisotni zaščitni plasti iz TiN. Na sliki c) so vidna mesta z diamantno piramido nastalih vtiskov.

6 CONCLUSIONS

The present work shows that tungsten-carbide H-13A inserts allow an increase in the cutting efficiency by more than 66 % and, therefore, a decrease in the amounts of force and energy involved in stone sawing. This means that the tool is exposed to the stresses lower than those affecting a tungsten-carbide insert probably causing a reduction of tool wear. Moreover, the cutting power of the tungsten carbide H-13A inserts is lower than that of the tungsten-carbide H6T CT30 inserts.

A single model describes well the actual cutting force caused by the interaction between a tungsten-carbide insert and stone. This means that a unique simple equation can represent the relationship between the cutting force and the chip-cutting area.

An analysis of the tungsten-carbide insert wear over time and of the relationship between the tungsten-carbide wear and the cutting-force value compared to the behavior of the chemical-vapor-deposition (CVD) diamond inserts is currently the topic of further studies in order to verify that this type of tool is suitable for sawing the Hotaveljčan limestone.

Acknowledgement

Special thanks go to Marmor Hotavlje; despite the fact that the study was not formally funded, they unselfishly shared their knowledge and contributed a lot of voluntary work, engaging their human resources and their hardware.

7 REFERENCES

[1] F. I. Dagrain, Understanding stone cutting mechanisms for the design of new cutting tools sequences and the cutting optimization of chain saw machines in Belgian blue stone quarries, Diamante, Aplicazioni & Technologia, 17 (**2011**) 66, 55–67

[2] S. Turchetta, L. Carrino, W. Polini, CVD diamond insert in stone cutting, Diamond and Related Materials, 14 (**2005**) 3–7, 641–645

[3] H. K. Tönshoff, H. Hillmann-Apman, J. Asce, Diamond tools in stone and civil engineering industry: cutting principles, wear and application, Diamond and Related Materials, 11 (**2002**) 3–6, 736–741

[4] Y. Li, H. Huang, J. Y. Shen, X. P. Xu, Y. S. Gao, Cost-effective machining of granite by reducing tribological interactions, Journal of Materials Processing Technology, 129 (**2002**) 1–3, 389–394

[5] H. D. Jerro, S. S. Pang, C. Yang, R. A. Mirshams, Kinematics analysis of the chipping process using the circular diamond saw blade, Journal of Manufacturing Science and Engineering, 121 (**1999**) 2, 257–264

[6] K. Brach, D. M. Pai, E. Ratterman, M. C. Shaw, Grinding forces and energy, Journal of Manufacturing Science and Engineering, 110 (**1988**) 1, 25–31

[7] H. K. Tönshoff, J. Peters, I. Inasaki, T. Paul, Modelling and simulation of grinding processes, Annals of the CIRP, 41 (**1992**) 2, 677–688

[8] T. W. Hwang, S. Malkin, Grinding mechanisms and energy balance for ceramics, Journal of Manufacturing Science and Engineering, 121 (**1999**) 4, 623–631

[9] Fantini Technical Paper, 2002, 4

[10] C. Mingels, Utilisation d'une haveuse Perrier dans une carriere de marbre, Annales des Mines de Belgique, 2 (**1971**) 1, 121–130

[11] J. Focant, Utilisation des haveuses Perrier dans I'exploitation des carrieres de Marbres Rouge, Annales des Mines de Belgique, 9 (**1977**) 2, 819–823

[12] J. Boxho, Essai d'una haveuse Perrier dans le Petit Granit, Annales des Mines de Belgique, 2 (**1971**) 3, 131–142

[13] J. Brych, Les outils autoaffutants au service du havage des roches dures, Annales des Mines de Belgique, 2 (**1975**) 1, 165–180

[14] B. Neerdael, Contribution ill'etude de la destructibilite des roches dures telles que les callcaires crino'idiques de Soignies, Faculte Polytechnique de Mons, Travail de fin d'etudes, 1975, 5–18

[15] K. Fifer, Natural stone "Hotavlje" geotechnical report / Poročilo o preiskavi naravnega kamna "Hotavlje", ZAG, Department of materials, Ljubljana 2005, 35

[16] U. Bajželj, J. Kortnik, B. Petkovšek, K. Fifer, Environment friendly underground excavation of dimension stone, 27th International Symposium on Computer Applications in the Mineral Industries, London, 1998, 11–22

[17] J. Kortnik, U. Bajželj, Underground mining of natural stone in Slovenia, 20th World Mining Congress, Tehran, 2005, 277–286

[18] N. Purtić, Drilling and Blasting/Bušenje i miniranje, Rudarsko-geološki fakultet, Beograd 1991, 20–22

[19] H. Hughes, Some aspects of rock machining, Int. J. Rock Mech. Min. Sci., 9 (**1972**) 2, 205–211

[20] M. Mellor, Normalization of specific energy values, Int. J. Rock Mech. Min. Sci., 9 (**1972**) 5, 661–663

UDK 621.785.53:620.178.1:539.92
Original scientific article/Izvirni znanstveni članek

ISSN 1580-2949
MTAEC9, 49(1)111(2015)

EFFECT OF SLIDING SPEED ON THE FRICTIONAL BEHAVIOR AND WEAR PERFORMANCE OF BORIDED AND PLASMA-NITRIDED W9Mo3Cr4V HIGH-SPEED STEEL

VPLIV HITROSTI DRSENJA NA VEDENJE IN OBRABO BORIRANEGA IN V PLAZMI NITRIRANEGA HITROREZNEGA JEKLA W9Mo3Cr4V

Ibrahim Gunes

Department of Metallurgical and Materials Engineering, Faculty of Technology, Afyon Kocatepe University, 03200 Afyonkarahisar, Turkey
igunes@aku.edu.tr

Prejem rokopisa – received: 2013-12-11; sprejem za objavo – accepted for publication: 2014-02-06

This study investigated the effect of sliding speed on the friction and wear behaviors of plasma-nitrided (PN) and borided (W9Mo3Cr4V) steels. The PN process was carried out in a dc-plasma system at a temperature of 923 K for 6 h in a gas mixture of 80 % N_2-20 % H_2 under a constant pressure of 5 mbar. The boriding process was carried out in Ekabor-II powder at a temperature of 1223 K for 6 h. X-ray diffraction analysis on the surface of the PN and borided steels revealed the presence of FeB, Fe_2B, CrB, MoB, WB, FeN, Fe_2N, Fe_3N and Fe_4N compounds. The wear tests were carried out in a ball-disc arrangement under dry friction conditions at room temperature with an applied load of 10 N and with sliding speeds of (0.1, 0.3 and 0.5) m/s at a sliding distance of 1000 m. The wear surfaces of the samples at the different sliding speeds were analyzed using SEM microscopy and X-ray energy-dispersive spectroscopy EDS. The friction coefficients of the nitrided and borided W9Mo3Cr4V steels varied from 0.42 to 0.61, and from 0.33 to 0.52, respectively. As a result of the wear, the friction coefficient was observed to decrease with an increase in the sliding speeds of the PN and the borided AISI W9Mo3Cr4V steel while an increase was observed in the wear resistance.

Keywords: plasma nitriding, boriding, W9Mo3Cr4V, sliding speed, wear rate

V tej študiji je bil preučevan vpliv hitrosti drsenja na trenje in vedenje v plazmi nitriranega (PN) in boriranega jekla (W9Mo3Cr4V). PN-postopek je bil izvršen v enosmernem plazemskem sistemu 6 h na temperaturi 923 K in v plinski mešanici 80 % N_2-20 % H_2 pri konstantnem tlaku 5 mbar. Postopek boriranja je bil izvršen s prahom Ekabor-II pri temperaturi 1223 K in trajanju 6 h. Rentgenska difrakcijska analiza na površini PN in boriranega jekla je odkrila spojine FeB, Fe_2B, CrB, MoB, WB, FeN, Fe_2N, Fe_3N in Fe_4N. Preizkus obrabe je bil izvršen na napravi s kroglo na plošči pri suhem trenju na sobni temperaturi z obtežbo 10 N in s hitrostjo drsenja (0,1, 0,3 in 0,5) m/s pri razdalji drsenja 1000 m. Obraba na površini pri vzorcih z različno hitrostjo drsenja je bila analizirana s SEM-mikroskopijo in rentgensko energijsko disperzijsko spektroskopijo. Koeficient trenja nitriranega in boriranega jekla W9Mo3Cr4V je bil med 0,42 in 0,61 oziroma 0,33 in 0,52. Kot rezultat obrabe PN in boriranega jekla AISI W9Mo3Cr4V se je koeficient trenja zmanjševal pri naraščanju hitrosti drsenja, odpornost proti obrabi pa se je povečala.

Ključne besede: nitriranje v plazmi, boriranje, W9Mo3Cr4V, hitrost drsenja, stopnja obrabe

1 INTRODUCTION

Plasma nitriding and boriding are thermo-chemical surface treatments widely used to improve the tribo-mechanical properties of engineering components via a modification of their surface microstructure.[1–6] During the plasma-nitriding process, the nitriding reaction not only occurs on the surface but also in the sub-surface owing to the long-distance diffusion of nitrogen atoms from the surface towards the core. Nitrogen diffused into a steel surface is combined with alloying elements to form a fine dispersion of alloy nitrides.[7,8] As a result, two different structures have been identified, the so-called "white" or "compound" layer and the "diffusion zone". The first one is the outermost layer, and consists of one or two iron nitrides (Fe_4N–$Fe_{2-3}N$), depending on the process parameters. The second layer results from the reactions produced by the N diffusion, such as precipitation of nitrides, α-Fe saturation, changes in the residual tensions and C redistributions.[9,10]

During the boriding process, boron atoms can diffuse into ferrous alloys due to their relatively small size and very mobile nature. They can dissolve in iron interstitially, but can react with it to form FeB and Fe_2B intermetalic compounds. Depending on the potential of the medium and the chemical compositions of the base materials, a single or a duplex layer may be formed. Borided steel components display excellent performance in several tribological applications in the mechanical engineering and automotive industries.[11–14]

Plasma nitriding and boriding are used in numerous applications in industries such as the manufacture of machine parts for plastics and food processing, packaging and tooling, as well as pumps and hydraulic machine parts, crankshafts, rolls and heavy gears, motor and car construction, cold- and hot-working dies and cutting tools. The wear behavior of plasma-nitrided and borided steels has been evaluated by a number of researchers.[15–20] However, there is no information about the effect of sliding speed on the friction and wear behaviors of plasma-nitrided and borided W9Mo3Cr4V steel. The main objective of this study was to investigate the effect of sliding speed on the friction and wear behaviors of plasma-nitrided and borided W9Mo3Cr4V steel. Structural and tribological properties were investigated using light microscopy, XRD, SEM, EDS, microhardness tests and a ball-on-disc tribotester.

2 EXPERIMENTAL METHOD

2.1 Plasma Nitriding, Boriding and Characterization

The W9Mo3Cr4V steel contained mass fractions (*w*) 0.82 % C, 4.10 % Cr, 3.80 % Mo, 7.40 % W and 1.30 % V. The test samples were cut into Ø 25 mm × 8 mm dimensions and ground up to 1000 G and polished using a diamond solution. The PN process was carried out in a dc plasma system at a temperature of 923 K for 6 h in a gas mixture of 80 % N_2-20 % H_2 under a constant pressure of 5 mbar. The boriding heat treatment was carried out by using a solid boriding method with commercial Ekabor-II powders. The samples that were to be borided were packed in the powder mixture and sealed in a stainless-steel container. The boriding heat treatment was performed in an electrical resistance furnace under atmospheric pressure at 1223 K for 6 h followed by air cooling.

The microstructures of the polished and etched cross-sections of the samples were observed under an Olympus BX-60 light microscope. The presence of nitrides and borides formed in the coating layer was detected by means of X-ray diffraction equipment (Shimadzu XRD 6000) using Cu K_α radiation. The diffusion zone on the nitrided sample and the thickness of borides were measured by means of a digital thickness measuring instrument attached to a light microscope (Olympus BX60). Micro-hardness measurements were performed from the surface to the interior along a line in order to see variations in the hardness of the nitride and boride layers, the transition zone and the matrix, respectively. The microhardness of the boride layers was measured at 8 different locations at the same distance from the surface by means of a Shimadzu HMV-2 Vickers indenter with a load of 50 g and the average value was taken as the hardness.

2.2 Friction and Wear

A ball-on-disc test device was used to perform the friction and wear tests of the borided samples. In the wear tests, WC-Co balls of 8 mm in diameter supplied by H. C. Starck Ceramics GmbH were used. Errors caused by the distortion of the surface were eliminated by using a separate abrasion element (WC-Co ball) for each test. The wear experiments were carried out in a ball-disc arrangement under dry friction conditions at room temperature with an applied load of 10 N and with sliding speeds of (0.1, 0.3 and 0.5) m/s at a sliding distance of 1000 m. Before and after each wear test, each sample and abrasion element was cleaned with alcohol. After the test, the wear volumes of the samples were quantified by multiplying the cross-sectional areas of the wear by the width of the wear track obtained from the Taylor-Hobson Rugosimeter Surtronic 25 device. The wear rate was calculated using the following formula:

$$W_k = W_v/(M \cdot S) \quad \mathrm{mm^3/(N\ m)} \qquad (1)$$

where W_k is the wear rate, W_v the worn volume, *M* is the applied load and *S* is the sliding distance.

Friction coefficients depending on the sliding distance were obtained through a friction coefficient program. Surface profiles of the wear tracks on the samples and surface roughness were measured by a Taylor-Hobson Rugosimeter Surtronic 25. The worn surfaces were investigated by scanning electron microscopy and energy-dispersive X-ray spectroscopy (EDS).

3 RESULTS AND DISCUSSION

3.1 Characterization of Plasma Nitriding and Boriding Coatings

The cross-sections of the optical micrographs of the nitrided and borided W9Mo3Cr4V steel are given in

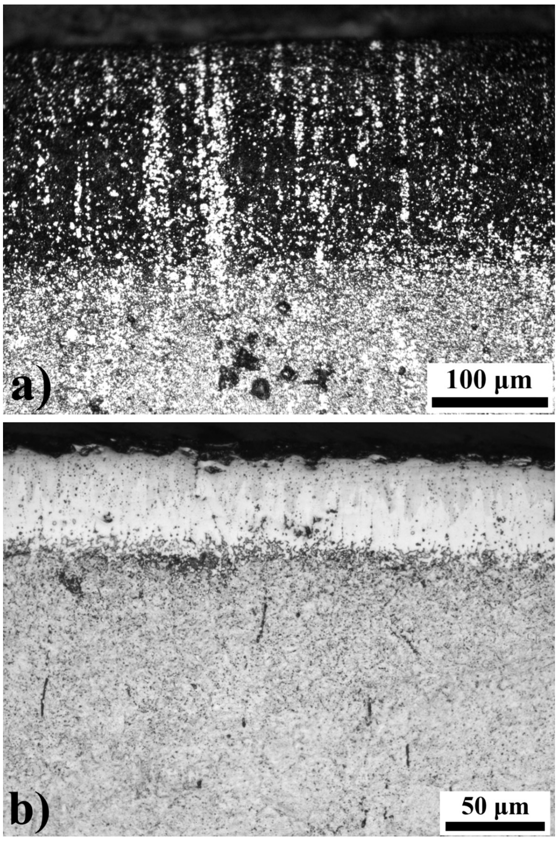

Figure 1: Cross-section of plasma-nitrided and borided W9Mo3Cr4V steel: a) PN, b) borided

Slika 1: Prerez v plazmi nitriranega in boriranega jekla W9Mo3Cr4V: a) PN, b) borirano

Figure 1. A typical light photograph of the cross-sectional microstructure of the plasma nitrided W9Mo3Cr4V sample is given in **Figure 1a**. This photograph shows the formation of a diffusion zone on the sample. However, the formation of a continuous compound (white) layer on top of the nitrided layer of the sample is not visible in **Figure 1a**. Following etching with a 3 % nital reagent, the nitrided (diffusion) layer appears as a dark zone on the sample. Around 250 µm depth of diffusion was obtained from the plasma-nitrided sample. As can be seen in **Figure 1b**, the boride layer was formed on the W9Mo3Cr4V steel borided with a solid boriding method. Depending on the process time, the temperature and the chemical composition of substrates, the thickness of the boride layer was found to be 55 µm.

The X-ray diffraction patterns of the nitrided and borided W9Mo3Cr4V steel are given in **Figure 2**. The XRD results showed that the nitrided W9Mo3Cr4 steel contained FeN, Fe_2N, Fe_3N, Fe_4N and M_6C phases (**Figure 2a**). The XRD results showed that the boride layers formed on the W9Mo3Cr4V steel contained FeB, Fe_2B, CrB, MoB and WB phases in **Figure 2b.** The microhardness and the wear resistance of the nitride and boride layers formed on the steel surface are to a large extent known with the help of these phases.[21–24]

Microhardness measurements were carried out on the cross-sections from the surface to the interior along a line, as can be seen in **Figure 3**. The hardness of the nitrided W9Mo3Cr4V steel varied between 995 $HV_{0.05}$ and 1286 $HV_{0.05}$. The hardness of the boride layer on the W9Mo3Cr4V steel varied between 1378 $HV_{0.05}$ and 1814 $HV_{0.05}$. On the other hand, the Vickers hardness values were 230 $HV_{0.05}$ for the untreated W9Mo3Cr4V steel. When the hardnesses of the nitride and boride layers are compared with the matrix, the nitride layer's hardness is approximately five times greater and the boride layer's hardness is approximately eight times greater than that of the matrix.

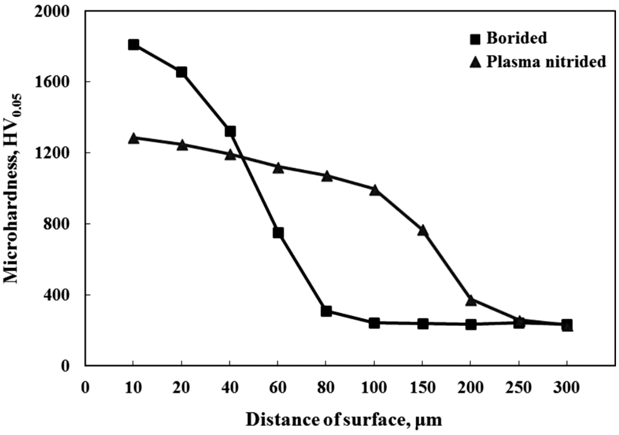

Figure 3: The variation of hardness depth in the plasma-nitrided and borided W9Mo3Cr4V steel

Slika 3: Spreminjanje trdote po globini v plazmi nitriranega in boriranega jekla W9Mo3Cr4V

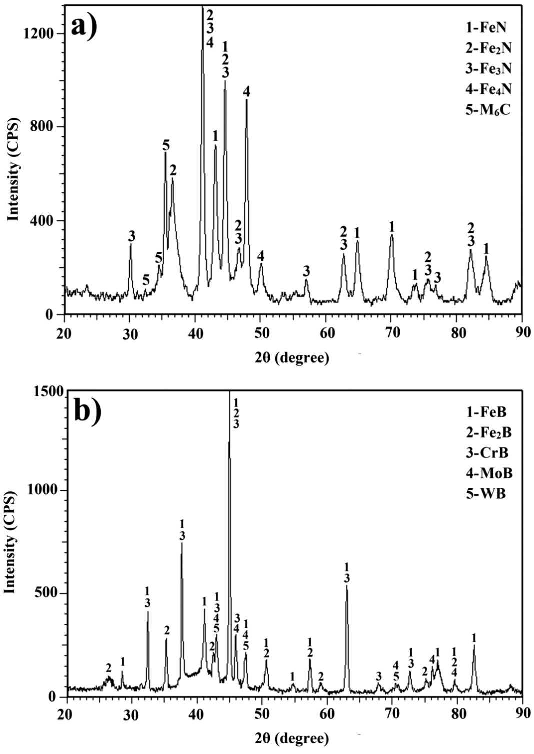

Figure 2: X-ray diffraction patterns of plasma-nitrided and borided W9Mo3Cr4V steel: a) PN, b) borided

Slika 2: Rentgenska difrakcija v plazmi nitriranega in boriranega jekla W9Mo3Cr4V: a) PN, b) borirano

3.2 Friction and Wear Behavior

The wear mechanism is defined as the physical and chemical phenomena that take place during wear. Abrasive wear refers to the mechanism where two bodies rubbing against each other break off pieces from each other. The hardness, shape and size or roughness of the

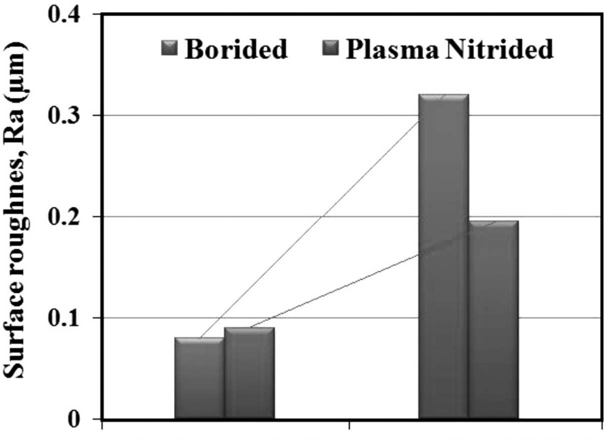

Figure 4: Surface roughness values of the plasma-nitrided and borided W9Mo3Cr4V steel

Slika 4: Hrapavost površine v plazmi nitriranega in boriranega jekla W9Mo3Cr4V abrasive material, the angle of contact, the normal load applied, the sliding speed and the fracture toughness of the material are all among the important factors in wear mechanisms.[25] **Figure 4** shows the surface roughness values of the nitrided and borided and unborided W9Mo3Cr4V steel. For the nitrided and borided W9Mo3Cr4V steel, it was observed that the surface roughness values increased, as can be seen in **Figure 4**. It was observed that the surface roughness of the nitrided W9Mo3Cr4V steel was higher than that of the borided W9Mo3Cr4V. These results indicate that both nitriding and boriding treatments affect the surface roughness of the specimens. While the surface roughness value of the borided sample is 0.84 μm, it increased to 0.33 μm as a result of the boriding process. While the roughness level of the surface of the non-nitrided sample is 0.93 μm at the end of the boriding process, it has increased to 0.198 μm.

Figure 5 shows the friction coefficients of the nitrided and borided W9Mo3Cr4V steels at different sliding speeds. The friction coefficients of the nitrided and borided W9Mo3Cr4V steels varied from 0.61 to 0.42 and from 0.52 to 0.33, respectively. The friction coefficients of both borided and nitrided W9Mo3Cr4V steels reduced with the increase of the sliding speed up to 0.5 m/s. The reason behind this may be the oxides on the surface of the sample. During the wear test, oxides formed on the steel surface, allowing for low friction coefficients. The wear tracks on the samples may have been oxidized due to the frictional heat.

As the sliding speed increased, the steady-state friction coefficient values slightly decreased. This may be explained by a decrease in the shear strength at the sliding interface. Decreasing the shear strength may occur in two ways. Firstly, the hardness and hence the shear strength of the coatings decrease with increasing temperature. It is reported that the hardness of the boride coatings decreases by a factor of more than two with increasing temperature up to 1000 °C.[12] Secondly, oxidation products (iron, boron, molybdenum, wolfram and chromium oxides) can reduce the friction. In fact, many of the oxides have high friction.

Figure 6 shows the effect of sliding speed on the wear rate of plasma-nitrided and borided W9Mo3Cr4V steel. It was observed that the borided W9Mo3Cr4V steel had a lower wear rate than that of the plasma-nitrided W9Mo3Cr4V steel. For the microhardness of the FeB, CrB and WB phases, the borided steel showed more resistance to wear due to the nitrided steel. The wear test results indicated that the wear resistance of the nitrided and borided steels was higher than that of the untreated steel. It is well known that the hardness of the nitride and boride layers plays an important role in the improvement of the wear resistance.

As shown in **Figures 3** and **6**, the relationship between the microhardness and the wear resistance of the nitrided and borided samples also confirms that the wear resistance was improved by the increase in the hardness. This is in agreement with reports of previous studies.[26–33] In addition, reductions in wear rates were observed with an increasing rate of sliding speed. The oxides formed on the samples borided at high sliding speeds may have caused a reduction in the friction coefficient and an increase in the wear rate because oxides on the sample surface act as a solid lubricant. Molinari et al.[34] investigated the tribological properties of a plasma-nitrided Ti-6A14V alloy at different loads and sliding speeds. It was observed that the increase in the sliding speed at low loads did not significantly affect the wear volume, while the wear volume decreased with an increase in the sliding speed at high loads. Straffelini et al.[35] investigated the impact of sliding speed and contact pressure on the oxidative wear of austempered ductile iron and reported that the friction coefficient and wear rate decreased with an increasing rate of sliding speed.

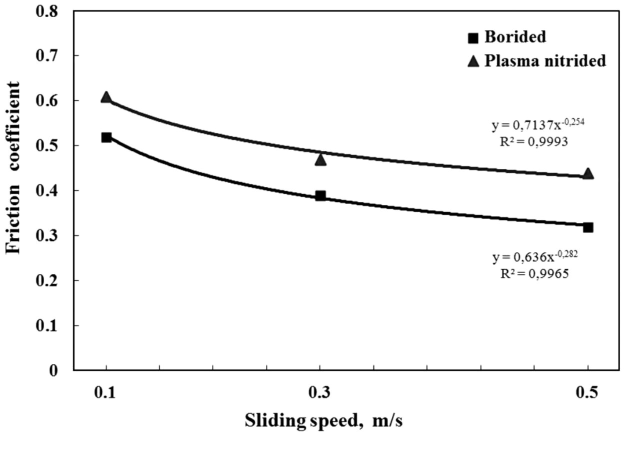

Figure 5: The effect of the sliding speed on the friction coefficient of the plasma-nitrided and borided W9Mo3Cr4V steel

Slika 5: Vpliv hitrosti drsenja na koeficient trenja jekla W9Mo3Cr4V, nitriranega v plazmi ali boriranega

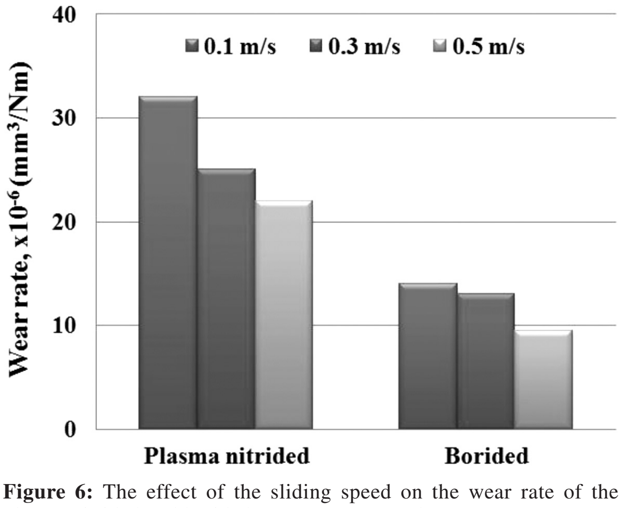

Figure 6: The effect of the sliding speed on the wear rate of the plasma-nitrided and borided W9Mo3Cr4V steel

Slika 6: Vpliv hitrosti drsenja na stopnjo obrabe v plazmi nitriranega ali boriranega jekla W9Mo3Cr4V

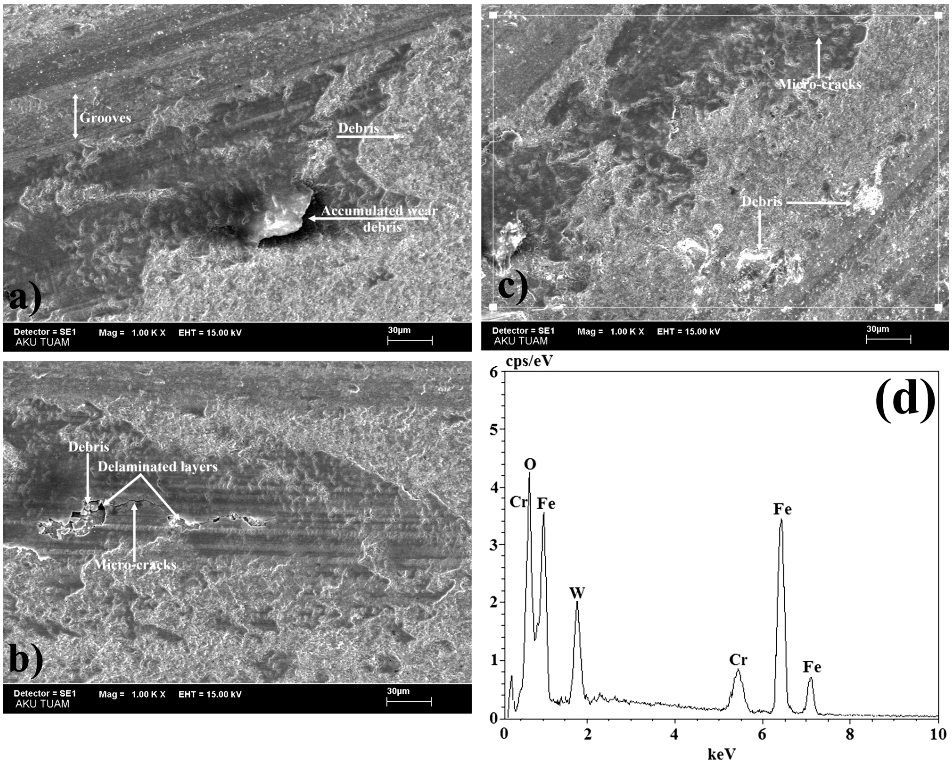

Figure 7: Sliding-speed-dependent SEM micrographs of the wear surfaces of the nitrided W9Mo3Cr4V steel at 923 K for 6 h: a) 0.1 m/s, b) 0.3 m/s, c) 0.5 m/s, d) EDS analysis

Slika 7: SEM-posnetki obrabljene površine v odvisnosti od hitrosti drsenja za 6 h nitrirano jeklo W9Mo3Cr4V pri 923 K: a) 0,1 m/s, b) 0,3 m/s, c) 0,5 m/s, d) EDS-analiza

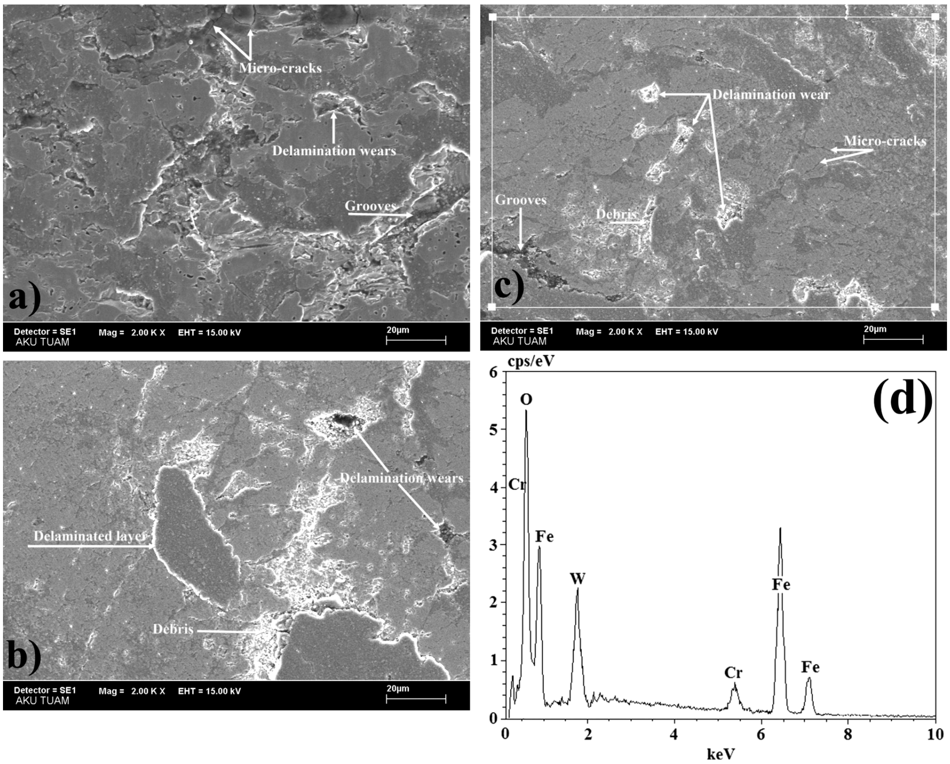

Figure 8: Sliding-speed-dependent SEM micrographs of the wear surfaces of the borided W9Mo3Cr4V steel at 1223 K for 6 h: a) 0.1 m/s, b) 0.3 m/s, c) 0.5 m/s, d) EDS analysis

Slika 8: SEM-posnetki obrabljene površine v odvisnosti od hitrosti drsenja za 6 h borirano jeklo W9Mo3Cr4V pri 1223 K: a) 0,1 m/s, b) 0,3 m/s, c) 0,5 m/s, d) EDS-analiza

The SEM micrographs and X-ray energy-dispersive spectroscopy EDS of the worn surfaces of the nitrided and borided samples are illustrated in **Figures 7** and **8**. **Figure 7** shows the SEM micrographs of the wear surfaces of nitrided W9Mo3Cr4V steel worn at different sliding speeds. The wear region of the nitrided samples, debris, surface grooves and cracks on the layer are shown in **Figures 7a** to **7c**. It was observed that delamination wears, which form as a result of the progress of microcracks, occurred on the wear tracks of the nitrided samples. The wear intensity on the surfaces of the nitrided samples was observed to decrease with an increase in the sliding speed (**Figures 7a** to **7c**). Oxidation products (iron, boron, wolfram and chromium oxides) formed as a result of the wear test in **Figure 7d**.

Figure 8 shows the SEM micrographs of the wear surfaces of borided W9Mo3Cr4V steel worn at different sliding speeds. There were microcracks, abrasive particles and small holes on the worn surface of the boride coatings (**Figures 8a** to **8c**). In the wear region of the borided W9Mo3Cr4V steel, there were cavities probably formed as a result of layer fatigue (**Figure 8b**) and cracks concluded in the delaminating wear (**Figure 8c**). It was observed that delamination wear, which forms as a result of the progress of microcracks, occurred on the wear tracks of the borided samples. Oxide layers formed as a result of the wear test in **Figure 8d**. The spallation of the oxide layers in the sliding direction and their orientation extending along the wear track were identified (**Figures 7d** and **8d**).

4 CONCLUSIONS

The following conclusions may be drawn from the present study.

- The multiphase nitride coating that thermo-chemically occurred on the W9Mo3Cr4V steel consisted of FeN, Fe_2N, Fe_3N, Fe_4N and M_6C phases, while the boride coating consisted of FeB, Fe_2B, CrB, MoB and WB phases.
- The surface hardness of the nitrided W9Mo3Cr4V steel was in the range of 995–1286 $HV_{0.05}$, the surface hardness of the borided W9Mo3Cr4V steel was in the range 1378–1814 $HV_{0.05}$ and the untreated W9Mo3Cr4V steel substrate was 230 $HV_{0.05}$.
- The surface roughness values of both the plasma-nitrided and borided W9Mo3Cr4V steel increased compared to the untreated W9Mo3Cr4V steel.
- The friction coefficients of the plasma-nitrided and borided W9Mo3Cr4V steel varied from 0.42 to 0.61, and from 0.33 to 0.52, respectively.
- Reductions were observed in the wear rates of both the nitrided and borided W9Mo3Cr4V steel.
- As a result of an increase in the sliding speed, it was observed that the friction coefficient decreased while the wear resistance of the plasma nitrided and borided W9Mo3Cr4V steel increased.

5 REFERENCES

[1] A. G. von Matuschka, Boronizing, Heyden and Son Inc., Philadelphia, USA 1980, 11

[2] C. Bindal, A. H. Ucisik, Surface and Coatings Technology, 122 (**1999**), 208

[3] A. Akbari, R. Mohammadzadeh, C. Templier, J. P. Riviere, Surface and Coatings Technology, 204 (**2010**), 4114

[4] A. Alsaran, A. Celik, C. Celik, Surface and Coatings Technology, 160 (**2002**), 219

[5] M. Hudakova, M. Kusy, V. Sedlicka, P. Grgac, Mater. Tehnol., 41 (**2007**) 2, 81–84

[6] N. Ucar, O. B. Aytar, A. Calik, Mater. Tehnol., 46 (**2012**) 6, 621–625

[7] S. Y. Sirin, E. Kaluc, Materials and Design, 36 (**2012**), 741

[8] S. Y. Sirin, K. Sirin, E. Kaluc, Materials Characterization, 59 (**2008**), 351

[9] P. Corengia, G. Ybarra, C. Moina, A. Cabo, E. Broitman, Surface and Coatings Technology, 200 (**2005**), 2391

[10] M. B. Karamis, Wear, 150 (**1991**), 331

[11] S. Taktak, Materials and Design, 28 (**2007**), 1836

[12] S. Taktak, Surface and Coatings Technology, 201 (**2006**), 2230

[13] C. Bindal, A. H. Ucisik, Surface and Coatings Technology, 94–95 (**1997**), 561

[14] C. Martini, G. Palombarini, G. Poli, D. Prandstraller, Wear, 256 (**2004**), 608

[15] A. Alsaran, Materials Characterization, 49 (**2003**), 171

[16] B. Podgornik, J. Vizintin, V. Leskovsek, Surface and Coatings Technology, 108–109 (**1998**), 454

[17] M. Ulutan, M. M. Yildirim, O. N. Celik, S. Buytoz, Tribology Letters, 38 (**2010**), 231

[18] T. Eyre, Wear, 34 (**1975**), 383

[19] A. Çelik, Ö. Bayrak, A. Alsaran, I. Kaymaz, A. F. Yetim, Surface and Coatings Technology, 202 (**2008**), 2433

[20] F. Yıldız, A. F. Yetim, A. Alsaran, A. Çelik, I. Kaymaz, Tribology International, 44 (**2011**), 1979

[21] I. Gunes, S. Ulker, S. Taktak, Materials and Design, 32 (**2011**), 2380

[22] L. G. Yu, X. J. Chen, K. A. Khor, G. Sundararajan, Acta Materialia, 53 (**2005**), 2361

[23] I. Gunes, Transactions of the Indian Institute of Metals, 67 (**2014**), 359

[24] Y. T. Xi, D. X. Liu, D. Han, Surface and Coatings Technology, 202 (**2008**), 2577

[25] M. Tabur, M. Izciler, F. Gül, I. Karacan, Wear, 266 (**2009**), 1106

[26] E. Atik, U. Yunker, C. Meric, Tribology International, 36 (**2003**), 155

[27] D. C. Wen, Surface and Coatings Technology, 204 (**2009**), 511

[28] I. Gunes, A. Dalar, Journal of Balkan Tribology Association, 19 (**2013**), 325

[29] B. Selcuk, R. Ipek, M. B. Karamıs, Journal of Materials Processing Technology, 141 (**2003**), 189

[30] C. Li, B. Shen, G. Li, C. Yang, Surface and Coatings Technology, 202 (**2008**), 5882

[31] S. Ulker, I. Gunes, S. Taktak, Indian Journal of Engineering Materials Science, 18 (**2011**), 370

[32] M. B. Karamiş, E. Gerçekcioğlu, Wear, 243 (**2000**), 76

[33] I. Gunes, Journal of Materials Science and Technology, 29 (**2013**), 662

[34] A. Molinari, G. Straffelini, B. Tesi, T. Bacci, G. Pradelli, Wear, 203–204 (**1997**), 447

[35] G. Straffelini, M. Pellizzari, L. Maines, Wear, 270 (**2011**), 714

UDK 539.92:669.018.9:66.017
Original scientific article/Izvirni znanstveni članek

ISSN 1580-2949
MTAEC9, 49(1)117(2015)

TRIBOLOGICAL BEHAVIOUR OF A356/10SiC/3Gr HYBRID COMPOSITE IN DRY-SLIDING CONDITIONS

TRIBOLOŠKO VEDENJE HIBRIDNEGA KOMPOZITA A356/10SiC/3Gr PRI SUHEM DRSENJU

Blaža Stojanović, Miroslav Babić, Nenad Miloradović, Slobodan Mitrović
Faculty of Engineering, University of Kragujevac, Sestre Janjic 6, 34000 Kragujevac, Serbia
blaza@kg.ac.rs

Prejem rokopisa – received: 2014-01-21; sprejem za objavo – accepted for publication: 2014-03-12

The paper presents tribological behaviour of hybrid aluminium composite A356/10SiC/3Gr in dry-sliding conditions. Hybrid composites were made with a modified compocasting procedure and tribological tests were conducted on a tribometer with a block-on-disc contact geometry. An analysis of the effects of three sliding speeds ((0.25, 0.5 and 1) m/s) and two normal loads (10 N and 20 N) on the wear volume and wear rate was conducted for different sliding distances. The total sliding distance was 300 m. SEM and an EDS analysis of the wear surfaces of the tested material were also performed. The analysis of the wear surfaces shows an intensive adhesive wear of hybrid composites. Also, the appearance of mechanically mixed layers (MMLs) was confirmed, i.e., an increase in the concentration of iron in the hybrid composite material.

Keywords: hybrid composites, wear, aluminium, SiC, graphite, testing

Članek opisuje tribološko vedenje hibridnega aluminijevega kompozitnega materiala A356/10SiC/3Gr pri suhem drsenju. Hibridni kompoziti so bili izdelani s prilagojenim postopkom "kompokasting", tribološki preizkusi pa so bili opravljeni na tribometru s kontaktno geometrijo "blok na disku". Opravljena je analiza vpliva treh drsnih hitrosti ((0,25, 0,5 in 1) m/s) in dveh normalnih obremenitev (10 N in 20 N) na intenzivnost in velikost obrabe pri različnih dolžinah drsenja. Skupna dolžina drsenja je bila 300 m. Hkrati sta bili izvršeni tudi SEM-mikroskopija in EDS-analiza obrabljene površine preizkušanega materiala. Analiza odrgnjenih površin pokaže intenzivno adhezivno obrabo hibridnega kompozita. Potrjen je bil pojav mehansko mešanih plasti (MML) oziroma povečane koncentracije železa v hibridnem kompozitnem materialu.

Ključne besede: hibridni kompoziti, obraba, aluminij, SiC, grafit, preizkušanje

1 INTRODUCTION

Composite materials with aluminium bases have an increasing application in the automotive, airline and aerospace industries. In the automotive industry, these materials are used for building engines, cylinder linings, valve tappets, brakes, cardan shafts, etc. An improvement in the mechanical and tribological characteristics is achieved by adding appropriate reinforcements to these materials. Graphite (Gr), silicon carbide (SiC) and alumina (Al_2O_3) are commonly used as reinforcements. By combining two types of reinforcements, hybrid composites with improved characteristics with regard to the basic material are obtained. The composites reinforced with SiC and graphite are called Al/SiC/Gr hybrid composites[1–5].

Tribological behaviour of the hybrid composites with Al2219 aluminium bases and reinforced with (5, 10 and 15) % SiC and 3 % Gr was investigated by Basavarajappa et al.[6] The composite materials were made with the liquid-metallurgy procedure. Tribological tests were realized on a tribometer with a pin-on-disc contact geometry in accordance with the ASTM G99-95 standard and they showed that an increase in the SiC fraction increases the wear resistance of hybrid composites and the wear is decreased. The wear rate increases with the increasing sliding speed and normal load.

Mahdavi and Akhlaghi[7] tested the tribological characteristics of Al/SiC/Gr hybrid composites obtained with an in-situ powder-metallurgy technique. A hybrid composite had a matrix made of the Al6061 aluminium alloy reinforced with 9 % Gr and (0–40) % SiC. The wear rate of the tested composites decreased with an increase in the SiC amount up to 20 %. A further increase in the SiC amount increased the wear. Other investigations of the same authors relate to the hybrid composites with 30 % SiC and a variable amount of graphite (0–13 %). The results of the tribological investigations showed that the wear rate also increases with the increasing sliding distance and the increasing graphite amount.

Suresha and Sridhara[8] investigated the tribological behaviour of the hybrid composites obtained using a stir-casting procedure, with variable SiC and Gr amounts (0–5 %) and the total ratio of 10 %. Ravindran et al.[9] investigated the tribological behaviour of the hybrid composites with aluminium alloy A2024 bases. The hybrid composites were obtained with powder metallurgy using 5 % of SiC and (0. 5 or 10) % of Gr. Hybrid composite Al/5SiC/5Gr (5 % SiC and 5 % Gr) showed the best tribological characteristics, while a further increase in the graphite amount increased the wear.

The literature gives a small amount of information about the effect of graphite and SiC particles on wear properties. Considering the previous statements, the aims of this paper are to investigate the tribological behaviour of the hybrid composites with an A356-aluminium-alloy base reinforced with SiC and Gr and to provide new information and knowledge. The compocasting procedure was selected to obtain hybrid composites because it is economical and it enables a good distribution of the reinforcements and a favourable composite structure. The quality/price ratio of the obtained composites is the best for this procedure, which is also very important. An investigation of tribological characteristics was conducted by varying normal loads and sliding speeds for different sliding distances in dry-sliding conditions. An analysis of the wear was conducted on the basis of the obtained values of the wear rates and SEM and EDS analyses of the test samples. Within the framework of this investigation, the tribological behaviour of the Al/SiC/Gr hybrid composites obtained with the compocasting procedure and an A356-aluminium-alloy base reinforced with 10 % SiC and 3 % Gr is presented.

2 EXPERIMENT

2.1 Procedure for obtaining the composites

Hybrid composites were obtained with the compocasting procedure or with an infiltration of the particles into the half-hardened melt of the A356 alloy. The preparation of the materials consisted of the chemical cleaning of the base (the A356 alloy) and its infiltration into a previously preheated electro-resistance furnace crucible, the melting and overheating up to 650 °C (the liquid-phase domain) to clean the slag. In order to obtain a hybrid composite (A356 alloy + 10 w(SiC) + 3 w(Gr)), the measured quantities of SiC and Gr were previously homogeneously mixed in the solid state, then preheated at 150 °C and later used in the infiltration process. The commercial procedure T6 was used for the heat treatment, consisting of solution annealing at 540 °C (for 6 h), water quenching and artificial aging at a temperature of 160 °C for 6 h. The mean value of the SiC-particle diameter was 39 μm and for the graphite-particle diameter it was 35 μm. The newly obtained composite had w(SiC) = 10 % and w = 3 % of graphite.

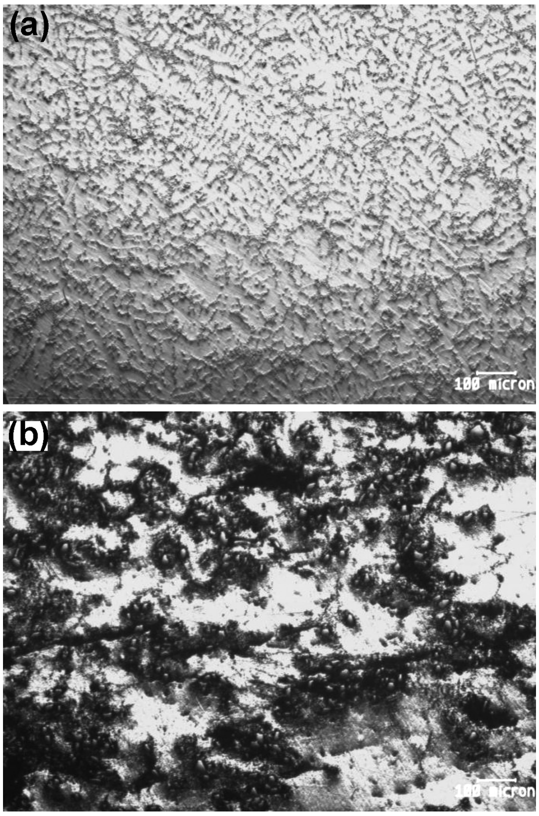

Figure 1: Metallographic structure of: a) basic material A356, b) A356/10SiC/3Gr hybrid composite

Slika 1: Mikrostruktura: a) osnovni material A356, b) hibridni kompozit A356/10SiC/3Gr

Figure 1a presents the structure of the basic material and **Figure 1b** shows the structure of the Al/10SiC/3Gr composite. In the hybrid composite, it is noticed that the base is well filled with the reinforcement particles, so that the base surface without any particles is decreased, which indicates a good distribution of the particles in the base. The soft particles of graphite did not sustain their mean value (35 μm) during the procedure of obtaining the composite. In fact, their erosion and size reduction occurred in the process of preparation (mixing them with the SiC particles).

2.2 Description of the experiment and equipment

The wear behaviour of a block was monitored in terms of the wear-scar width (**Figure 2**). Using the wear-scar width and the geometry of the contact pair, the wear volume (in accordance with ASTM G77-83) and the wear rate (expressed in mm^3/m) were calculated.

The tested blocks were made of the basic A356 material and the A356/10SiC/3Gr hybrid composite. The block dimensions were 6.35 mm × 15.75 mm × 10.16 mm, while the roughness of the ground contact surface was R_a = 0.2 μm. The counter body (disc) was made of 90MnCrV8 steel with a hardness of 62–64 HRC, a diameter of 35 mm and a width of 6.35 mm. The roughness of the contact surface of the disc was R_a = 0.3 μm. Tribo-

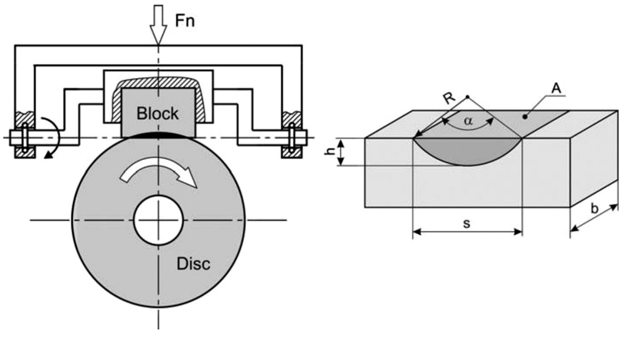

Figure 2: Scheme of the contact-pair geometry

Slika 2: Shematski prikaz geometrije kontakta logical tests were conducted in dry-sliding conditions for different sliding speeds ((0.25, 0.5 and 1.0) m/s) and loads (10 N and 20 N). All the experiments were repeated 5 times.

The tests were performed for a sliding distance of 300 m. The first tests were used to form wear-rate curves, while the other tests were conducted without stopping.

3 EXPERIMENT TEST RESULTS

The results of tribological tests were obtained for different sliding speeds and different normal loads in dry-sliding conditions and they are presented in the following diagrams. The diagrams showing the dependence between the material wear volume and the sliding distance were obtained on the basis of the wear-scar widths. The wear-scar widths were measured after the (30, 60, 90, 150 and 300) m of the sliding distance. **Figure 3** shows the variations in the wear volume in relation to the sliding distance for all three sliding speeds ((0.25, 0.5 and 1.0) m/s). Full lines show the results for the basic A356 material, while dashed lines present the results for the A356/10SiC/3Gr hybrid composite.

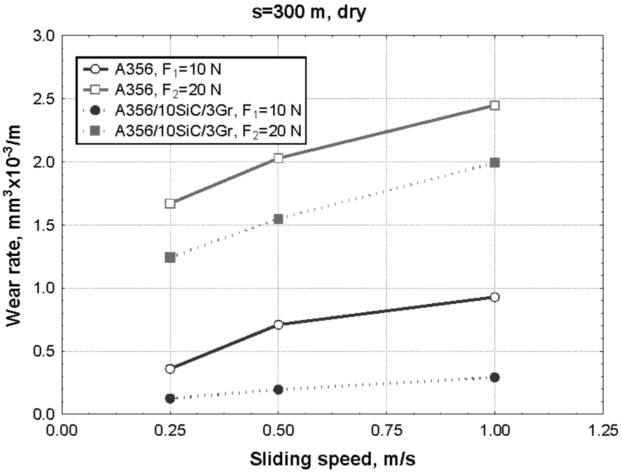

Figure 4: Dependence between the wear rate and the sliding speed
Slika 4: Odvisnost med obrabo in hitrostjo drsenja

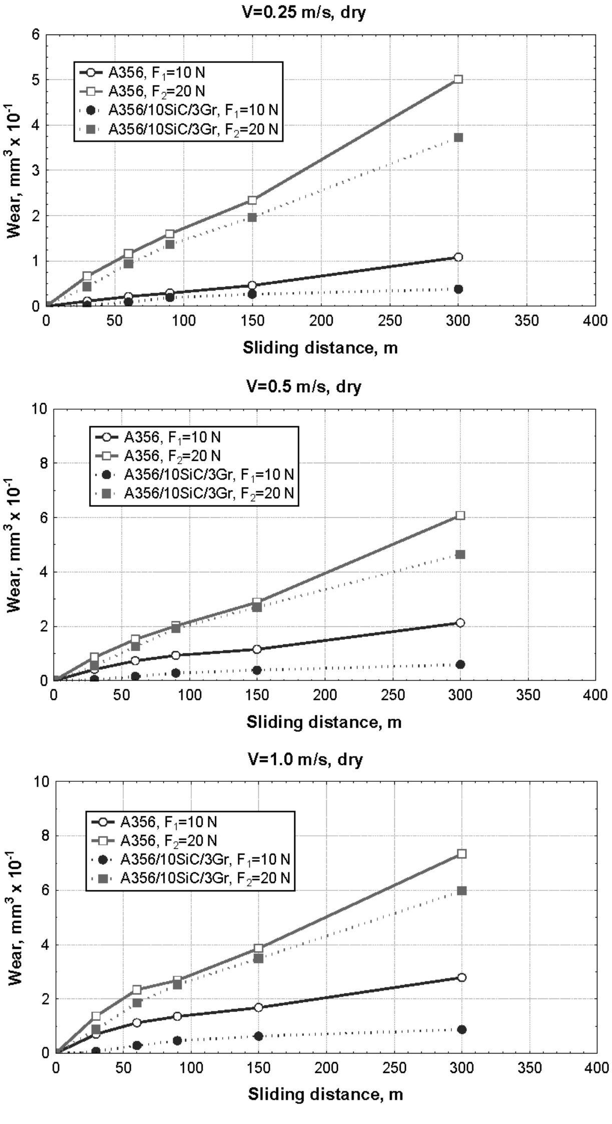

Figure 3: Dependence between the wear volume and the sliding distance for all three sliding speeds
Slika 3: Odvisnost med volumnom obrabe in dolžino poti drsenja za vse tri hitrosti drsenja

The run-in distance for the tested materials depends on the sliding speeds and normal loads and its range was between 50 m and 100 m. This is best seen on the wear-rate curves or the curves showing the dependence between the wear-scar widths and the sliding distance[10]. After this sliding distance, the tested materials entered the period of normal wear. When analysing the obtained diagrams, it became clear that the curves obtained for the base material were steeper than the curves for the hybrid composite. It was obvious that an addition of SiC and Gr prolonged the period of normal wear of the tested hybrid materials.

The effects of the sliding speed and normal loads on the wear rate of the tested materials for a sliding distance of 300 m are shown in **Figures 4** and **5**. With an increase in the sliding speed, the intensity of the wear increases for both the base A356 material and for the hybrid A356/10SiC/3Gr material. The dependence between the wear and the sliding speed is almost linear (**Figure 4**).

Figure 5 shows that an increase in normal load induces an increase in the wear rate for all the test regimes, i.e., for all the sliding speeds. According to the positions of the curves, it may be concluded that the effect of normal load on the wear rate is quite pronounced. Also, according to the positions of the curves, it is obvious that the wear rate of the hybrid composite with SiC and graphite is considerably smaller than the wear rate of the base material, especially at the normal load of 10 N. The wear rate of the basic A356 material for the normal load of 20 N is (on average) three times higher than the wear rate for the normal load of 10 N.

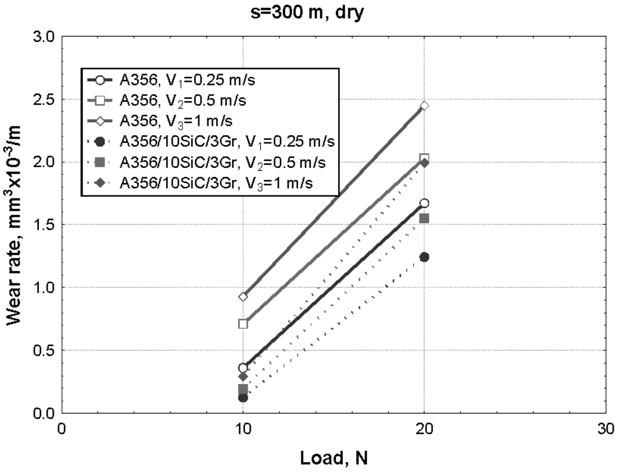

Figure 5: Dependence between the wear rate and normal load
Slika 5: Odvisnost med obrabo in obremenitvijo

The wear rate of the A356/10SiC/3Gr hybrid composite for the normal load of 20 N is (on average) seven times higher than the wear rate for the normal load of 10 N.

4 DISCUSSION

For a more complete analysis, **Figures 6a** and **6b** show the SEM microphotographs of the worn surfaces of the tested materials. These microphotographs were obtained during the tribological tests with the sliding speed of 0.25 m/s and the normal load of 10 N.

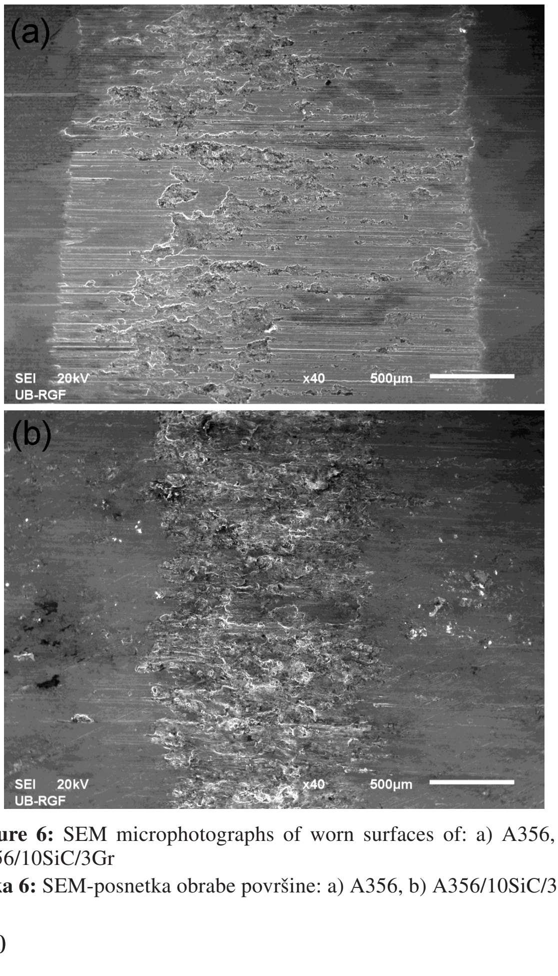

Figure 6: SEM microphotographs of worn surfaces of: a) A356, b) A356/10SiC/3Gr
Slika 6: SEM-posnetka obrabe površine: a) A356, b) A356/10SiC/3Gr

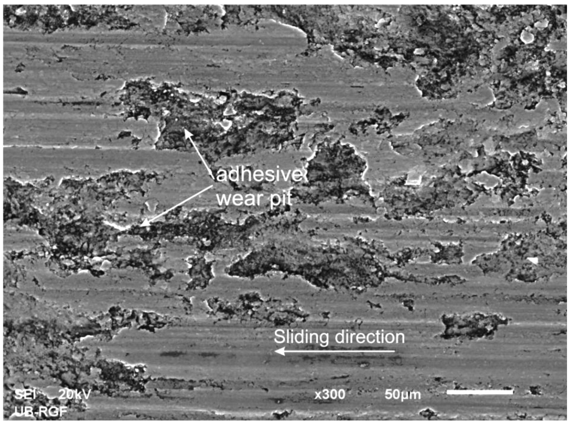

Figure 7: Forming of the adhesive-wear pits
Slika 7: Nastanek jamic zaradi adhezivne obrabe

When observing the samples, it is clear that the adhesive wear is the basic wear mechanism. Adhesive wear occurred as a result of an alternate formation and destruction of the frictional connections caused by an atomic and intermolecular interaction of the boundary layers of the contact bodies. Due to the adhesive wear, there is a pulling of the material out of the contact surface of the composite material (block). As a consequence of the adhesive wear, pits of irregular shapes and depths are visible on the surface of the block[6] and in **Figure 7**. A tribolayer was formed on the surface of the A356/10SiC/3Gr composite during sliding and it formed a protective lubricating film preventing a direct contact between the aluminium matrix and the steel counter body. High-volume-fraction ceramic particles act as load-bearing elements, preventing the subsurface damage during sliding and suppressing the spalling of tribolayers from the surface.

In order to rationalize the wear behaviour of the observed composite, it is important to analyze the composition of the microstructure of the tribolayer formed during the wear process. The EDS analysis was performed together with the SEM of the tested material. The EDS analysis was employed to determine the elements on the worn surface, as shown in **Figure 8**. An occurrence of iron (Fe) and oxygen (O) may be spotted on the analyzed samples. The presence of iron and its oxide confirms that the wear of the steel disc occurred. The disc wear occurs due to the effects of SiC from the composite material as well as of the Si phase from the A356 aluminium matrix. Worn particles of iron enter the surface layer of the composite causing a formation of a mechanically mixed layer (MML) which is characteristic for a MMC with an aluminium matrix[7,11–13]. The presence of iron and its oxides is confirmed by EDS Spectrum 2 in **Figure 8**. Spectrum 1 in **Figure 8** shows the presence of SiC in the hybrid composite. The lubrication

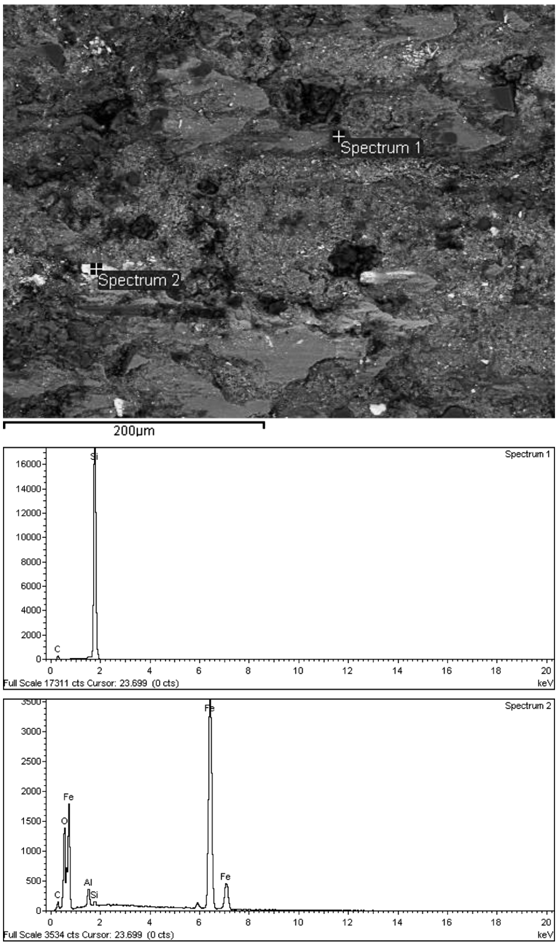

Figure 8: EDS analysis of hybrid A356/10SiC/3Gr composite
Slika 8: EDS-analiza hibridnega kompozita A356/10SiC/3Gr

layer is composed of the Al, Si, Fe, O and C elements. The occurrence of oxygen implies that the surface elements, such as Fe, were at least partially oxidized during the sliding. Thus, it may be concluded that the tribolayer is composed of a mixture of iron oxides, graphite and fractured SiC particles and some fine particles containing aluminium.

5 CONCLUSIONS

The testing of the tribological behaviour of the hybrid A356/10SiC/3Gr composite in dry-sliding conditions shows superior characteristics of this material compared to those of the base A356 material. With an increase in the sliding distance, the amount of the wear or wear rate of the hybrid composite is always smaller than that of the base material. The run-in sliding distance of the tested materials ranges between 50 m to 100 m, after which the materials enter the period of normal wear. The wear rate of the tested materials increases with the increasing sliding speed and normal load for all the test regimes. SEM confirms a homogenous distribution of SiC particles within the hybrid composite. Additionally, SEM microphotographs and an EDS analysis show the presence of Fe and its oxides as well as the formation of a mechanically mixed layer (MML).

Acknowledgement

This paper presents the results obtained during the research within the framework of project TR35021 supported by the Ministry of Education, Science and Technological Development of the Republic of Serbia.

6 REFERENCES

[1] A. Vencl, Tribology of the Al-Si alloy based MMCs and their application in automotive industry, In: L. Magagnin (ed.), Engineered Metal Matrix Composites: Forming Methods, Material Properties and Industrial Applications, Nova Science Publishers, Inc., New York, USA 2012, 127–166

[2] B. Stojanović, M. Babić, S. Mitrović, A. Vencl, N. Miloradović, M. Pantić, Tribological characteristics of aluminium hybrid composites reinforced with silicon carbide and graphite, A review, Journal of the Balkan Tribological Association, 19 (**2013**) 1, 83–96

[3] M. Babić, B. Stojanović, S. Mitrović, I. Bobić, N. Miloradović, M. Pantić, D. Džunić, Wear Properties of A356/10SiC/1Gr Hybrid Composites in Lubricated Sliding Conditions, Tribology in Industry, 35 (**2013**) 2, 148–154

[4] S. Mitrović, M. Babić, B. Stojanović, N. Miloradović, M. Pantić, D. Džunić, Tribological Potential of Hybrid Composites Based on Zinc and Aluminium Alloys Reinforced with SiC and Graphite Particles, Tribology in Industry, 34 (**2012**) 4, 177–185

[5] A. Vencl, I. Bobic, S. Arostegui, B. Bobic, A. Marinkovic, M. Babic, Structural, mechanical and tribological properties of A356 aluminium alloy reinforced with Al_2O_3, SiC and SiC + graphite particles, Journal of Alloys and Compounds, 506 (**2010**) 2, 631–639

[6] S. Basavarajappa, G. Chandramohan, A. Mahadevan, Influence of sliding speed on the dry sliding wear behaviour and the subsurface deformation on hybrid metal matrix composite, Wear, 262 (**2007**) 7–8, 1007–1012

[7] S. Mahdavi, F. Akhlaghi, Effect of the Graphite Content on the Tribological Behavior of Al/Gr and Al/30SiC/Gr Composites Processed by In Situ Powder Metallurgy (IPM) Method, Tribology Letters, 44 (**2011**) 1, 1–12

[8] S. Suresha, B. K. Sridhara, Friction characteristics of aluminium silicon carbide graphite hybrid composites, Materials & Design, 34 (**2012**), 576–583

[9] K. Ravindran, R. Manisekar, P. Narayanasamy, N. Narayanasamy, Tribological behaviour of powder metallurgy-processed aluminium hybrid composites with the addition of graphite solid lubricant, Ceramics International, 39 (**2013**) 2, 1169–1182

[10] S. Mitrović, N. Miloradović, M. Babić, I. Bobić, B. Stojanović, D. Džunić, Wear behaviour of hybrid ZA27/SiC/graphite composites under dry sliding conditions, Tribological Journal Bultrib, 3 (**2013**) 1, 142–147

[11] J. Rodriguez, P. Poza, M. A. Garrido, A. Rico, Dry sliding wear behaviour of aluminium–lithium alloys reinforced with SiC particles, Wear, 262 (**2007**) 3–4, 292–300

[12] R. N. Rao, S. Das, D. P. Mondal, G. Dixit, Effect of heat treatment on the sliding wear behaviour of aluminium alloy (Al–Zn–Mg) hard particle composite, Tribology International, 43 (**2010**) 1–2, 330–339

[13] A. K. Mondal, S. Kumar, Dry sliding wear behaviour of magnesium alloy based hybrid composites in the longitudinal direction, Wear, 267 (**2009**) 1–4, 458–466

UDK 678.7:544.6.018.47-036.5
Original scientific article/Izvirni znanstveni članek

ISSN 1580-2949
MTAEC9, 49(1)123(2015)

NEW SOLID-POLYMER-ELECTROLYTE MATERIAL FOR DYE-SENSITIZED SOLAR CELLS

NOVI ELEKTROLITNI MATERIAL NA OSNOVI TRDNEGA POLIMERA ZA SONČNE CELICE, OBČUTLJIVE ZA SVETLOBO

Vivek K. Singh, Bhaskar Bhattacharya, Shashank Shukla, Pramod K. Singh
Material research laboratory, School of Basic Sciences & Research, Sharda University, G. Noida 201310, India
vivekv445@gmail.com; singhpk71@gmail.com

Prejem rokopisa – received: 2014-02-08; sprejem za objavo – accepted for publication: 2014-02-26

A solid-polymer electrolyte consisting of polyvinylpyrrolidone (PVP) doped with ammonium iodide (NH_4I) was developed and characterized for a possible application in a dye-sensitized solar cell. Complex impedance spectroscopy revealed an increase in the conductivity and the maximum conductivity was obtained at the w = 50 % NH_4I mass concentration. Light photographs confirmed an enhancement in the amorphous nature of the host which was affirmed by XRD measurement. The composite nature of the polymer-electrolyte film was also confirmed with the FTIR spectrum. A dye-sensitized solar cell (DSSC) was fabricated using the most conductive film that showed an efficiency of 0.025 % at the 1 sun condition.

Keywords: polymer electrolyte, conductivity, FTIR, XRD, dye-sensitized solar cell

Razvit in karakteriziran je bil trdni polimerni elektrolit, ki ga sestavlja polivinil pirolidon (PVP), dopiran z amonijevim iodidom (NH_4I), za morebitno uporabo za sončne celice, občutljive za svetlobo. Kompleksna impedančna spektroskopija je odkrila povečano prevodnost z maksimumom pri masni koncentraciji w = 50 % NH_4I. Posnetki s svetlobno mikroskopijo so odkrili povečanje deleža amorfne osnove, kar so potrdile tudi XRD-meritve. Kompozitno naravo polimerne elektrolitne plasti je potrdil tudi FTIR-spekter. Sončne celice, občutljive za svetlobo (DSSC), so bile izdelane z uporabo najbolj prevodne plasti, ki je pokazala učinkovitost 0,025 % v razmerah 1 sun.

Ključne besede: polimerni elektrolit, prevodnost, FTIR, XRD, za svetlobo občutljive sončne celice

1 INTRODUCTION

Polymer electrolytes are promising candidates for electromechanical-device applications chiefly because they mechanically behave like solids but their internal structure and, consequently, the conductivity behavior closely resemble the liquid state.[1] The main advantages of polymeric electrolytes are satisfactory mechanical properties, easy fabrication of thin films and an ability to form a good electrode/electrolyte contact.[2–5]

Polyvinylpyrrolidone (PVP), also commonly called polyvidone or povidone, is a polymer made of N-vinylpyrrolidone monomer. PVP was first synthesized by Prof. Walter Reppe and a patent was filed in 1939. When dry it is a light flaky powder, which readily absorbs up to 40 % of its weight in atmospheric water. PVP is soluble in water and other polar solvents. Since it has excellent wetting properties and readily forms films, it makes a good coating or an additive to coatings. PVP is used in a wide variety of applications in medicine, pharmacy, cosmetics and industrial production. When added to iodine, PVP forms a complex called povidone-iodine exhibiting disinfectant properties and being beneficial for dye-sensitized solar-cell applications where iodide/polyiodide redox couple is frequently added to the electrolyte. Dye-sensitized solar cells (DSSCs) were first reported by O'Regan and Grätzel in 1991.[6]

Over the past decade, DSSCs have been intensely investigated as potential alternatives to the conventional inorganic photovoltaic devices due to their low production cost and good efficiency for a conversion of solar energy into electricity. A typical cell consists of a nanocrystalline mesoporous titanium dioxide film sensitized with a monolayer dye, an electrolyte containing iodide/triiodide as the redox couple and a platinum counter electrode. Liquid electrolytes were replaced with solid-polymer electrolytes because the former lead to corrosion, evaporation and leakage. Thus, the solid-polymer electrolytes improved the long-term stability of DSSCs.

In the present paper, we report on new solid-polymer electrolyte films of a polyvinylpyrrolidone (PVP) complex with ammonium iodide (NH_4I) and a DSSC that was fabricated using the film with the maximum electrical conductivity.

2 MATERIALS AND METHOD

Polyvinylpyrrolidone (PVP, Mw = 130,000), ammonium iodide (NH_4I) and iodine (I_2) were purchased from Sigma-Aldrich, USA while methanol was purchased from Qualikems Fine Chem. Pvt. Ltd., Vadodara, India.

The following approach was taken to prepare the electrolytes. PVP (500 mg) was dissolved in about 4 mL of methanol under continuous magnetic stirring (≈ 30 min) or until complete dissolution at room temperature. Then an appropriate quantity of NH_4I salts was added to the PVP methanolic solution and stirred continuously. After the solvent evaporation the polymer-salt complex was poured into polypropylene Petri dishes. Free-standing films of different PVP compositions – $w(NH_4I)/\%$ (where $w = (10, 20, 30, 40, 50, 60, 70)\ \%$) – were obtained and further characterized using various characterization tools.

A dye-sensitized solar cell with an active area of 0.72 cm^2 was fabricated with the procedure reported elsewhere.[7] With the common procedure the TiO_2 paste was applied on the fluorine-doped SnO_2 substrate (FTO) using the doctor-blade method. The adhesive scotch tape was used to control the thickness of the as-coated TiO_2 film with a thickness of ≈ 50 µm, followed by a heat treatment at 500 °C for 30 min. The porous TiO_2 film formed on the FTO substrate was 10 µm thick and a pore had a diameter of 10–15 nm.[8–13] The porous TiO_2 film on the FTO substrate was then immersed in a ruthenium sensitizer dye solution (0.5 mmol N-719, Solaronix, in ethanol) and left overnight to allow a sufficient dye adsorption. This TiO_2 working electrode with the dye was then rinsed off with distilled water and ethanol solution. A Pt-thin-film-coated counter electrode was prepared separately by spin-coating the H_2PtCl_6 solution onto the FTO substrate. The viscous polymer-electrolyte solution (≈ 400 µL) containing $PVP{:}NH_4I + I_2$ (the maximum σ) was finally cast on the working electrode (a two-step casting) and sandwiched between the platinized counter electrode and the TiO_2 working electrode.

3 RESULTS AND DISCUSSIONS

3.1 Conductivity measurement

Ionic conductivity of the polyvinylpyrrolidone-based polymer-electrolyte film was measured using a CH Instruments workstation (model 604D, USA) over a frequency range of 100–10^5 Hz.

We used steel electrodes as contacts to measure the ionic conductivity (σ) and we calculated ionic-conductivity values using the following formula:

$$\sigma = G \cdot l/A \qquad (1)$$

where σ is the ionic conductivity, G is the conductance (in the case of $1/R_b$, R_b is the bulk resistance where the Nyquist plot intercepts with the real axis), l is the thickness of the sample and A is the area of the given sample.

The cole-cole plot (complex impedance plot) of a typical sample of the PVP + $w(NH_4I)$ 50 % polymer electrolyte is shown in **Figure 1**. The room-temperature ionic conductivity (deduced from different cole-cole plots) of polymer electrolytes as a function of the NH_4I concentration is shown in **Figure 2** and its values are listed in **Table 1**.

Table 1: Room-temperature ionic conductivity of the $PVP{:}NH_4I$ polymer electrolyte system

Tabela 1: Ionska prevodnost $PVP{:}NH_4I$ polimernega elektrolitskega sistema pri sobni temperaturi

Composition ($w(NH_4I)/\%$)	Conductivity (S cm^{-1})
10	2.24×10^{-5}
20	2.57×10^{-5}
30	2.63×10^{-5}
40	1.09×10^{-4}
50	7.55×10^{-4}
60	4.85×10^{-4}
70	7.45×10^{-5}

As observed in **Figure 2** and **Table 1**, the ionic conductivity (σ) increases with the increase in the NH_4I concentration and reaches its maximum at the $w(NH_4I)$ = 50 % ($\sigma = 7.55 \times 10^{-4}$ S/cm) concentration and then it decreases. The increase in the ionic conductivity with the increasing NH_4I concentration can be related to the increase in the number of mobile charge carriers, while the possible decrease in the ionic conductivity at a NH_4I mass concentration greater than 50 % can be attributed to the formation of ion multiples.

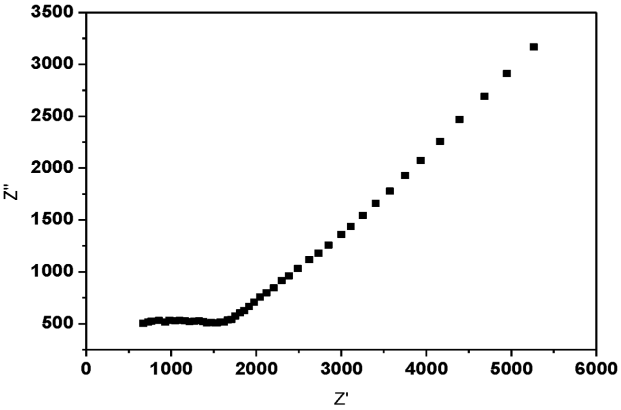

Figure 1: Cole-cole plot of the PVP + $w(NH_4I)$ 50 % polymer-electrolyte system

Slika 1: Cole-cole-diagram polimernega elektrolitnega sistema PVP + $w(NH_4I)$ 50 %

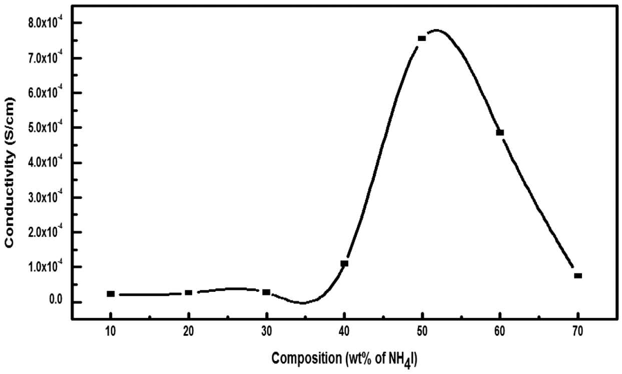

Figure 2: Effect of the NH_4I amount on the conductivity of the polymer electrolyte ($PVP{:}NH_4I$) measured at room temperature

Slika 2: Vpliv vsebnosti NH_4I na prevodnost polimernega elektrolita ($PVP{:}NH_4I$), izmerjeno pri sobni temperaturi

The ionic conductivity (σ) in the case of an electrolyte system is given as:

$$\sigma = n\, q\, \mu \tag{2}$$

where n is the charge carrier density, q is the charge of the carrier and μ is the mobility of the carriers. Therefore, any increase in either n or q will certainly affect the value of ionic conductivity.

3.2 X-ray diffraction

The crystallinity of the polymer electrolyte was further affirmed by X-ray diffraction patterns (XRD) using a Rigaku D/max-2500 XRD diffractometer at a scan rate of 5° min. The recorded X-ray diffraction patterns of pure PVP and NH_4I doped PVP polymer electrolytes are shown in **Figure 3**. It is clear that pure PVP shows well-known amorphous peaks around 2θ values of 23°. The incorporation of NH4I into the PVP matrix decreases the intensity of the peaks (the suppression in crystallinity). It also appears that the XRD data relating to the NH_4I doped PVP polymer electrolyte shows only the peaks related to either PVP or NH_4I, which clearly affirms the composite nature of the polymer-electrolyte system. Additionally, the PVP-NH_4I data does not contain any other peaks related to the NH_4I sample, affirming a complete dissolution of NH_4I in the Sago Palm matrix.

3.3 FTIR spectroscopy

The FTIR spectra of pristine PVP, NH_4I and the PVP doped with NH_4I were recorded between 4000 cm^{-1} and 400 cm^{-1} on a PerkinElmer Spectrophotometer 883 as shown in **Figure 4**. Pure NH_4I shows well defined peaks at (3131, 1622 and 1398) cm^{-1}, where the first peak corresponds to the N-H stretch, while the other two correspond to the N-H bending. In the spectrum of pure PVP, the peaks at (847, 895 and 934) cm^{-1} correspond to para-, di-substituted and mono-substituted C-H bendings. The bands between 1450 cm^{-1} and 1600 cm^{-1} correspond to the C=C stretching. The peaks at 1075 cm^{-1} and 2135 cm^{-1} correspond to the C-N stretching, while the ones at 1018 cm^{-1} and 1172 cm^{-1} correspond to the C-C stretching. The CH_3 bending is shown at 1375 cm^{-1}. The peak at 1835 cm^{-1} corresponds to the presence of C=O bonds. In the spectrum of PVP + NH_4I the peaks at 843 cm^{-1} and 934 cm^{-1} correspond to the C-H bending. The peaks at 1100–1300 cm^{-1} correspond to the C-C stretching. The C-N stretching is shown at 1074 cm^{-1}. The CH_2 bending is given by the peak at 1439 cm^{-1}. The bands between 1550 cm^{-1} and 1640 cm^{-1} correspond to the N-H bending. The peak at 1848 cm^{-1} corresponds to the C=O stretching, while the C=C peaks are indicated by the peaks between 1450 cm^{-1} and 1600 cm^{-1}.

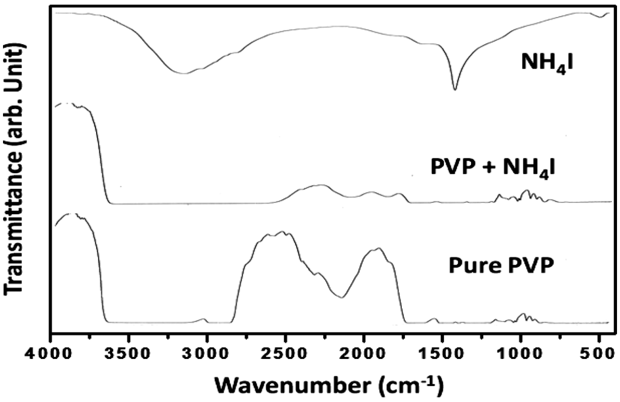

Figure 4: FTIR spectra of pure PVP, NH_4I and PVP + NH_4I polymer electrolyte

Slika 4: FTIR-spektri čistega PVP, NH_4I in PVP + NH_4I polimernega elektrolita

It is also clear from the figure that almost all the peaks related to the host materials (PVP and NH_4I) are present in the NH_4I doped PVP polymer-electrolyte sample. The disappearance of any new peaks other than those of the host materials clearly affirms the composite nature of the samples, also supported by our XRD data.

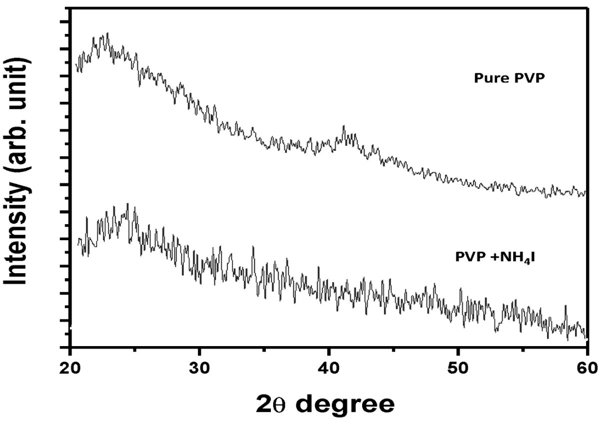

Figure 3: XRD pattern of pure PVP and PVP + NH_4I polymer electrolyte

Slika 3: XRD-posnetek čistega PVP in PVP + NH_4I polimernega elektrolita

3.4 Light microscopy

Light microscopy (LM) of a polymer-electrolyte sample with the dimensions of 1 cm × 1 cm was carried out using a Leica Leitz DMRX light microscope. The obtained photographs are shown in **Figure 5**. It is noted that the pure PVP film (**Figure 5a**) shows well-ordered patches, confirming its semicrystalline nature. This pattern is a bit different from the micrographs of the PEO matrix. Due to an addition of NH_4I to the PVP matrix (**Figure 5b**) the patch size becomes random and the crystallinity seems to be disturbed. The decrease in the crystallinity (an ordered pattern) showed a further increase in the amorphicity (a non-ordered pattern) where different sizes of rough patches are distributed randomly within the polymer matrix. It is believed that the amorphous regions (the non-ordered pattern) are conductivity-rich regions and, hence, our light micro-

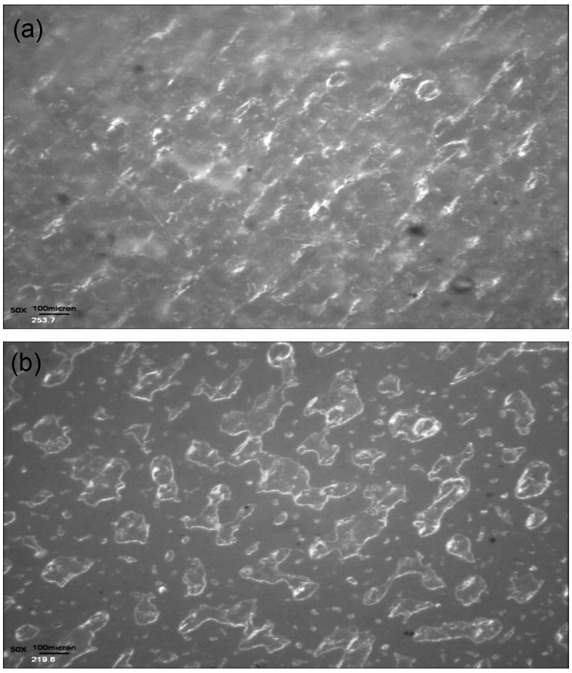

Figure 5: Light microscope photographs of: a) pure PVP, b) PVP + 40 % NH_4I polymer-electrolyte matrix

Slika 5: Posnetka s svetlobnim mikroskopom: a) čisti PVP, b) PVP + 40 % NH_4I osnova polimernega elektrolita

graphs showed good agreement with the ionic-conductivity data.

To further specify the nature of the charge carriers (ionic or electronic) we carried out the ionic-transference-number measurement. **Figure 6** shows the current-versus-time measurement for a typical sample of the arrowroot-60 % NH_4I polymer-electrolyte matrix. In this study we applied a fixed DC voltage and the current was recorded with respect to time following a well-established formula:

$$t_{\text{ion}} = \frac{I_{\text{initial}} - I_{\text{final}}}{I_{\text{initial}}} \qquad (3)$$

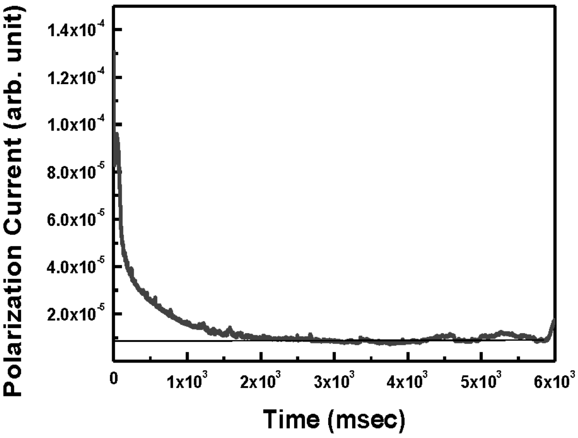

Figure 6: Current-versus-time plot (t_{ion} measurement) of a typical $PVP:NH_4I$ polymer-electrolyte matrix measured at room temperature

Slika 6: Odvisnost toka od časa (t_{ion} meritev) značilne $PVP:NH_4I$ osnove polimernega elektrolita, izmerjena pri sobni temperaturi

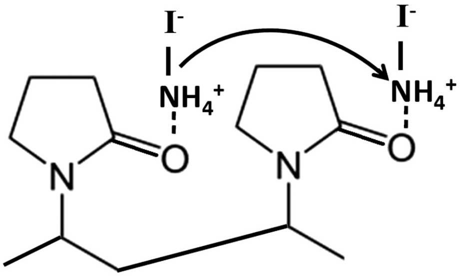

Figure 7: Mechanism of ion transport in the $PVP:NH_4I$ polymer-electrolyte matrix

Slika 7: Mehanizem potovanja ionov v osnovi polimernega elektrolita $PVP:NH_4I$

where I_{initial} is the initial current and I_{final} is the final residual current.

The observed ionic-transference number is 0.93 showing that our biopolymer electrolyte is essentially an ion-conducting system.[10]

3.5 Ion-transport mechanism

The ion-transport mechanism in the PVP polymer-electrolyte matrix can be easily understood using **Figure 7**. According to the literature, in most of the polyethers incorporated with alkali halides the anion contribution is more dominant.[14] However, in the case of the polyethers doped with the other salts like NH_4ClO_4 the cationic part is more dominating[15,16]. The NH_4^+ ions of NH_4I are coordinated with the ether oxygen of PVP and I^- anions hang outside. The weakly bonded H in NH_4^+ can be easily dissociated under the influence of a DC electric field forming H^+ ions. These H^+ or NH_4^+ ions can jump via each coordinating site as shown in **Figure 7**.

3.6 DSSC performance

A dye-sensitized solar cell (DSSC) was prepared with the $PVP:NH_4I/I_2$ polymer electrolyte with the maximum ionic conductivity ($w(NH_4I) = 50$ %). Iodine was also added to prepare the redox couple (10 % with respect to the iodide salt). The recorded J-V characteristic is shown in **Figure 8**. The fabricated DSSC shows

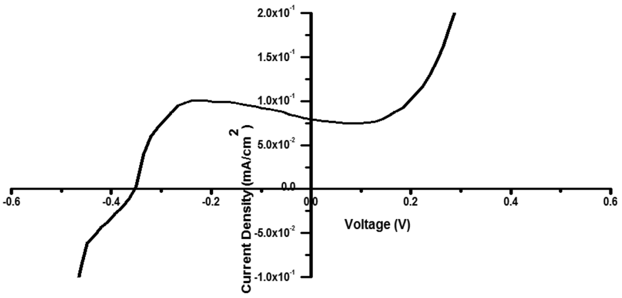

Figure 8: Current density versus voltage characteristic of the PVP:50 % NH_4I/I_2 polymer-electrolyte film at the 1 sun condition

Slika 8: Gostota toka v odvisnosti od značilnosti napetosti v plasti polimernega elektrolita PVP:50 % NH_4I/I_2 v razmerah 1 sun an open-circuit voltage (V_{oc}) of 0.35 V and a short-circuit-current density (J_{sc}) of 0.1 mA/cm^2 with the overall efficiency of 0.025 %.

The observed efficiency was much lower when compared to the other polymeric systems reported in[11–13]. This was expected since the observed conductivity in the present case was much lower (by ≈ 1–2 order of magnitude).

4 CONCLUSION

A solid polymer-electrolyte film consisting of PVP doped with the NH_4I salt was successfully prepared and characterized. It was observed that NH_4I doping enhances the ionic conductivity and the conductivity maximum was obtained at the 50 % NH_4I salt mass concentration with the conductivity value of 7.55×10^{-4} S/cm. XRD and IR affirmed the composite nature of the polymer electrolyte, while optical micrograph and XRD affirmed the reduction in the crystallinity due to the NH_4I doping. Using a solid polymer electrolyte with the maximum ionic conductivity, we fabricated a DSSC that shows a reasonable photo response at the 1 sun condition.

Acknowledgments

This work was supported by a DST project (DST/TSG/PT/2012/51) of the Government of India.

5 REFERENCES

[1] D. E. Fenton, J. M. Parker, P. V. Wright, Polymer, 14 (**1973**), 589

[2] K. N. Kumar, T. Sreekanth, M. J. Reddy, U. V. S. Rao, J. Power Sources, 101 (**2001**), 130–133

[3] T. M. W. J. Winjendra, P. Ekanayake, M. A. K. L. Dissanayake, I. Albinsson, B. E. Mellander, J. Solid State Electrochem., 14 (**2010**), 1221–1226

[4] R. Chandrasekaran, S. Selladurai, J. Solid State Electrochem., 5 (**2001**), 355–361

[5] X. Li, D. Zhang, X. J. Yin, S. Chen, J. Shi, Z. Sun, S. Huang, J. Solid State, Electrochem., 15 (**2011**), 1271–1277

[6] B. O'Regan, M. Grätzel, Nature, 353 (**1991**), 737–740

[7] M. Singh, V. K. Singh, K. Surana, N. A. Jadhav, P. K. Singh, B. Bhattacharya, H. W. Rhee, J. Ind. Eng. Chem., 19 (**2013**), 819–822

[8] A. F. Nogueira, J. R. Durrant, M. A. De Paoli, Advanced Materials, 13 (**2001**), 826–830

[9] M. Saito, S. Fujihara, Energy & Environmental Science, 1 (**2008**), 280–283

[10] A. Saxena, P. K. Singh, B. Bhattacharya, Mater. Tehnol., 47 (**2013**) 6, 799–802

[11] P. Kumar, P. K. Singh, B. Bhattacharya, Ionics, 17 (**2011**), 721–725

[12] P. K. Singh, B. Bhattacharya, R. K. Nagarale, J. Appl. Polym. Sci., 118 (**2010**), 2976–2980

[13] P. K. Singh, B. Bhattacharya, R. M. Mehra, H. W. Rhee, Current Applied Physics, 11 (**2011**), 616–619

[14] B. Bhattacharya, R. K. Nagarale, P. K. Singh, High Performance Polymers, 22 (**2010**), 498–512

[15] S. A. Hashmi, A. Kumar, K. K. Maurya, S. Chandra, J. Phys. D: Appl. Phys., 23 (**1990**), 1307–1314

[16] A. Sachdeva, R. Singh, P. K. Singh, B. Bhattacharya, Mater. Tehnol., 47 (**2013**) 4, 467–471

UDK 669.715:621.762:621.762.5
Original scientific article/Izvirni znanstveni članek

ISSN 1580-2949
MTAEC9, 49(1)129(2015)

COMPACTING THE POWDER OF Al-Cr-Mn ALLOY WITH SPS

KOMPAKTIRANJE PRAHU ZLITINE Al-Cr-Mn S SPS

Tomáš František Kubatík[1], Zdeněk Pala[1], Pavel Novák[2]
[1]Institute of Plasma Physics AS CR, Za Slovankou 1782/3, 182 00 Prague 8, Czech Republic
[2]Department of Metals and Corrosion Engineering, Institute of Chemical Technology, Technická 5, 166 28 Prague 6, Czech Republic
kubatik@ipp.cas.cz

Prejem rokopisa – received: 2014-02-11; sprejem za objavo – accepted for publication: 2014-02-26

Rapidly solidified powder AlCr6Fe2(Mn, Si, Ti) obtained with the melt atomization contained a solid solution of the alloying elements in aluminium and $Al_{57}Mn_{12}$, $Al_{42}Cr_7$(Fe) and Al_2Cr_3(Fe) intermetallic phases. The addition of chromium to aluminium alloys is acknowledged to efficiently inhibit the growth of refined Al grains. Spark-plasma sintering (SPS) is a modern method where the diffusion and decomposition of metastable intermetallics are limited due to the high speed of the process and lower sintering temperatures. This work investigates a compaction of Al-Cr-Fe-Si alloy powders using this method.

Keywords: aluminium alloy, intermetallics, powder metalurgy, spark-plasma sintering

Hitro strjen prah AlCr6Fe2(Mn, Si, Ti), dobljen z atomizacijo taline, je vseboval trdno raztopino legirnih elementov v aluminiju in intermetalne faze $Al_{57}Mn_{12}$, $Al_{42}Cr_7$(Fe), Al_2Cr_3(Fe). Dodatek kroma aluminiju učinkovito zadržuje rast drobnih zrn Al. Sintranje z iskrasto plazmo (SPS) je sodobna metoda, kjer je omejena difuzija in razgradnja metastabilnih intermetalnih zlitin zaradi velike hitrosti procesa in nižjih temperatur sintranja. V tem delu se raziskuje kompaktiranje prahov zlitine Al-Cr-Fe-Si po metodi SPS.

Ključne besede: aluminijeva zlitina, intermetalne faze, prašna metalurgija, sintranje z iskrasto plazmo

1 INTRODUCTION

Aluminium alloys with transition metals (e.g., Fe, Cr) have been known as attractive materials with an excellent combination of the tensile strength and thermal stability,[1] which makes them useful for the applications at elevated temperatures in the automotive and aerospace industries.[1] Their thermal stability is attributed to both the fact that these alloying elements have a low diffusion coefficient and their solubility in aluminium. However, these features make these alloys difficult to prepare using conventional metallurgy with a large amount of alloying elements. Therefore, these materials are made with powder metallurgy (PM) using rapidly solidified powders. A general feature of rapidly solidified Al-Cr and Al-Mn based alloys is the presence of many intermetallic phases, including quasi crystals (Q-phases),[2,3] in the intensively cooled alloys.

In the literature, the presence of multiple species of icosahedral quasicrystal phases $Al_{95}Fe_4Cr$ (Ti, Si), $Al_{84.6}Cr_{15.4}$(Ti, Si) and $Al_{74}Cr_{20}Si_6$(Fe, Ti) was described. The authors stated that in a powder fraction of 25–45 µm, phases $Al_{13}Cr_2$, $Al_{82}Fe_{18}$, $Al_{95}Fe_4Cr$ and $Al_{74}Cr_{20}Si_6$ were present, while in a fraction of 100–125 µm only phases $Al_{13}Cr_2$, $Al_{32}Fe_4$ and $Al_{82}Fe_{18}$ were found.[4–6] A quasi-crystalline phase is decomposed at the temperatures around 550 °C.[4,5] It was reported[6] that the compact samples prepared with the methods of cold extrusion, ultra-high pressure (6 GPa) and hot extrusion (480 °C/30 min preheating) had almost no porosity.

The recently developed field-assisted sintering (FAST),[7,8] also known as spark-plasma sintering (SPS),[9–11] or pulsed-electric-current sintering (PECS),[12,13] is a non-conventional powder-consolidation technique used for a very fast densification of ceramic and metal powders. In this method, a powder is placed inside a tool between two pressing punches acting also as electrodes. High-amperage electric-current pulses are passed through the uniaxially pressed powder compact loaded in the tool. The powder is rapidly densified due to a simultaneous application of pressure and heat in accordance with the Joule effect, whereas the grain coarsening is suppressed and the diffusion and decomposition of metastable intermetallics are limited due to the high speed of the process and lower sintering temperatures. The purpose of the present work is to study the compacting of an aluminium-alloy powder using SPS, monitor the changes taking place during the compacting of rapidly solidified powders and compare the structure and phase composition of the obtained samples with the conventional method of hot extrusion.

2 EXPERIMENTAL WORK

The feedstock material for SPS was an atomized (N_2) powder with a composition of AlCr6Fe2(Mn, Si, Ti). The powder was sieved into size fractions of ≤ 32 µm and 160–80 µm. The compacting was carried out in a spark-plasma sintering (SPS) system – model SPS 10-4 (Thermal Technology, USA). The tool system placed inside the vacuum chamber consisted of a graphite punch-and-die unit. The powder was manually poured into the die cavity. The temperature was measured with a NiCr-Ni thermocouple.

Figure 1 is a standard record of a single cycle. The program begins with the evacuation of the chamber. Afterwards, the sample is pre-loaded at 20 MPa, followed by heating with the speed of 100 °C/min, using a pulsed DC source. After reaching the desired process temperature (450, 500 and 550) °C, the sample is loaded to the final compression pressure of 80 MPa. The dwell time at this temperature and pressure is 5 min, as shown in **Figure 1**.

After the dwell time, the DC pulse source is turned off and the sample is cooled down to room temperature with free cooling. After the aeration of the chamber, the graphite tool is opened and the sample is removed. The prepared samples are cylindrical with a diameter of 19 mm and height of 4–6 mm. The porosity of the samples was measured with the Archimedes method. The microstructure was observed in the metallographic cut using a scanning electron microscope EVO MA 15 (Carl Zeiss SMT, Germany, SEM). Both the starting powders, i.e., with the particle sizes smaller than 32 μm and within the range from 160 μm to 180 μm, and the obtained spark-plasma-sintered samples were subjected to X-ray diffraction (XRD) analyses.

The powders were inserted into standard sample holders with the so-called side-loading procedure that minimizes the rise of the preferred orientation. These two samples were measured in the standard Bragg-Brentano geometry with a divergent beam and with a beam knife placed above the samples in order to minimize the effects of air scattering. Since our aim was to further measure the centres of the sintered samples, the irradiated volumes were in the middle of the samples' cross-sections. Therefore, a poly-capillary system and a collimator of 1 mm in diameter were inserted into the primary X-ray beam path changing the originally divergent character into a quasi-parallel one; diffraction CuK_α radiation was detected with a 1D LynxEye detector. The used D8 Discover diffractometer was equipped with a laser system and a compact *x, y, z* stage facilitating precise positioning of the measured surface.

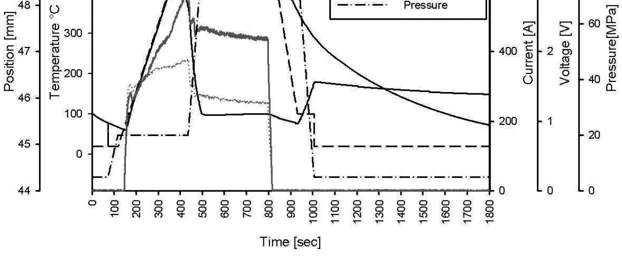

Figure 1: Parameter progress during the sintering of aluminium alloy powder (160–180 μm fraction) at 550 °C (SPS)

Slika 1: Spreminjanje parametrov med sintranjem prahu aluminijeve zlitine (zrnatost 160–180 μm) pri 550 °C (SPS)

3 RESULTS AND DISCUSSION

3.1 Densification behaviour

The diagram in **Figure 1** shows the process parameters during the SPS process at 550 °C for the coarse fraction (160–180 μm). The plots for all the temperatures and fractions are very similar differing only at low temperatures, where a small change in the position can be seen even during the dwell time. The curve of the position, which shows a change in the position of the pistons, indicates that the increasing temperature slightly increases the value of the positions related to thermal heating and auxiliary piston-guide graphite parts. At the temperatures slightly above 300 °C, the softening and deformation of the alloy powder occur (sintering). This temperature is the same for any sintering temperature (450, 500 and 550) °C and powder fraction (32 μm and 160–180 μm).

After reaching the temperature, the pressure increases for one minute, reaching the resulting value of 80 MPa. During the pressure increase, a very sharp reduction in the value of the position is detected, indicating an intensive compaction. After reaching the final pressure, the current values of the temperature and pressure are maintained constant for the duration of 5 min. The sintering temperature of 450 °C leads to a gradual compaction, during the dwell time, of the fraction of the powder smaller than 32 μm but to a smaller extent than for the coarse fraction. This may be related to the fact that the spherical powder alloy has a hard thin oxide layer, whose proportion is smaller in the coarse fraction of the aluminium alloy. This hypothesis is confirmed with the results of the open-porosity measurements, whose values are listed in **Table 1**. The results also show that the sintering temperature of 550 °C results in a very low open porosity, which is almost at the limit of the quantification obtained with the Archimedes method.

Table 1: Open porosity depending on the sintering temperature and powder size

Tabela 1: Odprta poroznost je odvisna od temperature sintranja in od velikosti zrn prahu

	Powder fraction (μm)	Temperature of sintering (°C)	Open porosity (%)
Aluminium alloy	32	450	3.05
Aluminium alloy	32	500	2.63
Aluminium alloy	32	550	0.14
Aluminium alloy	160–180	450	2.88
Aluminium alloy	160–180	500	2.88
Aluminium alloy	160–180	550	0.068

3.2 Microstructure

Figure 2 is a cross-sectional microstructure of the sintered powder fraction of 160–180 μm at 550 °C. The figure shows that the sintered alloy does not contain any visible pores and has a nearly homogeneous structure. In

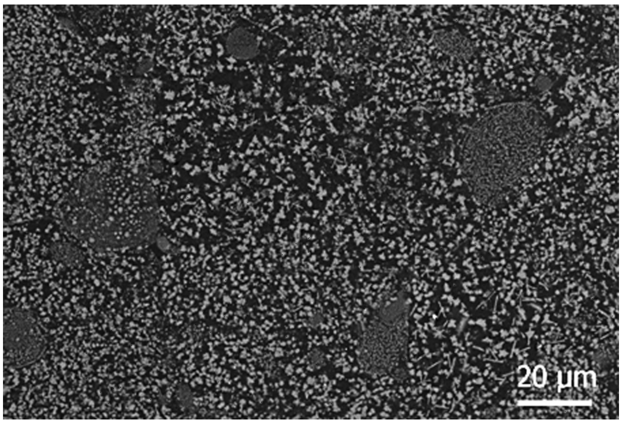

Figure 2: Microstructure of the alloy sintered at 550 °C for 5 min (fraction of 160–180 µm, SEM)

Slika 2: SEM-posnetek mikrostrukture zlitine, sintrane 5 min na 550 °C (zrnatost 160–180 µm)

the microstructure, only some spherical particles can be seen. The structure consists of an aluminium matrix with a small amount of silicon (titanium) in the solid solution, in which $Al_{45}Cr_7$ intermetallic phases consisting of rounded particles with an irregular shape are clearly visible. The observed microstructures are fairly similar at all the compacting temperatures and for both powder fractions.

3.3 XRD – phase analysis

The obtained diffraction patterns are juxtaposed in **Figure 3**. The phase identification revealed, apart from the expected fcc (Fm3m) aluminium solid solution, also aluminium manganese (cubic Pm-3 $Al_{57}Mn_{12}$) and aluminium chromium (monoclinic C12/m1 $Al_{45}Cr_7$) phases. It is clearly seen that the differences between all the SPS-sample diffraction patterns are virtually non-existent and that the peak positions match those of the coarser powder. However, several differences between the diffraction patterns of both powders can be observed (**Figure 4**) and, hence, the sieving led to minor changes in the phase composition.

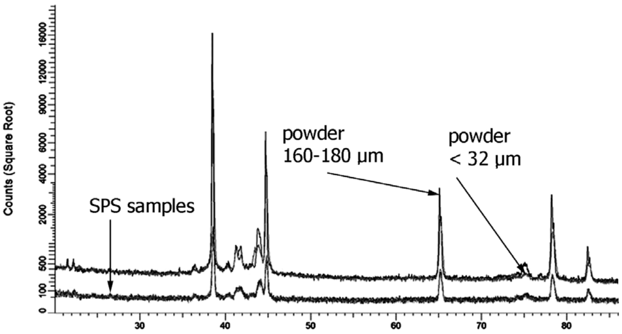

Figure 3: Plain comparison of the obtained diffraction patterns. The substantial difference between the intensities is due to the differences in the irradiated volume of the powders and the centres of the SPS sample cross-sections.

Slika 3: Primerjava dobljenih difrakcijskih vzorcev. Občutna razlika v intenzitetah je zaradi razlik v obsevanem volumnu prahov in sredine prereza SPS-vzorcev.

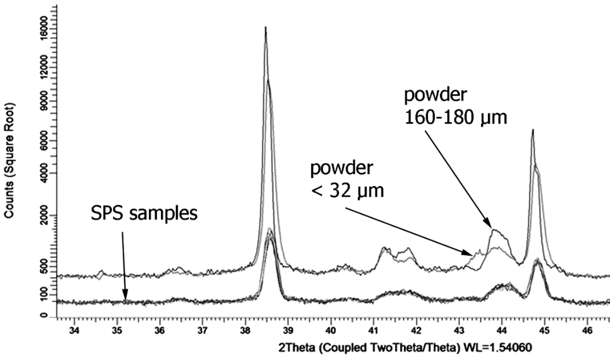

Figure 4: Differences between diffraction-peak positions for the two fractions of the used powder

Slika 4: Razlika med pozicijo difrakcijskih vrhov za dve frakciji uporabljenih prahov

The phase ID of the powder with smaller particles gave hints that the Al-Cr-Mn phase could be present. There are only two such phases in the ICSD database, namely, cubic Im-3 $Al_{12}Cr_{0.5}Mn_{0.5}$ and tetragonal I4/mmm Al_2Cr_3Mn. The latter proved to be the one present according to the Rietveld refinement, which gave the quantity of almost $w = 1$ % of this tetragonal phase. The results of the quantitative Rietveld refinement of both powders are summarized in **Table 2**. Since the diffraction patterns of the sintered samples do not exhibit significant differences, similar information about the phase presence is not relevant and, thus, not provided. Both the Al-Cr (ICSD code of 57652) and Al-Mn (ICSD code of 14374) phases were used for the Rietveld refinement performed in TOPAS 4.2 with sufficiently good matches between the structure model and measured data. There is, however, about the mass fraction 3 % more of the Al-Cr phase in the sintered samples due to various reasons; the difference in the irradiated volume can be one of them.

Table 2: Results of a quantitative Rietveld refinement of both powders

Tabela 2: Rezultati kvantitativnega Rietveldovega udrobljenja obeh prahov

Powder particle fraction	w(Al) /%	$w(Al_{57}Mn_{12})$ /%	$w(Al_{42}Cr_7)$ /%	$w(Al_2Cr_3Mn)$ /%
< 32 µm	63.9	19.0	16.3	0.8
160–180 µm	68.0	9.4	22.6	

mass fraction, *w*/%

4 CONCLUSIONS

Using the SPS method, a compact alloy with a very low open porosity was prepared. The porosity values are dependent on the powder fraction and sintering temperature. The microstructure of the compacted samples is formed using an aluminium-based solid solution with homogeneously dispersed intermetallic particles $Al_{45}Cr_7$ at all the sintering temperatures. The performed evaluation of diffraction data indicates that all the sintered samples are very similar with respect to the phase composition. Moreover, the shapes of diffraction profiles are also the same which means that the real structures, namely, the microstrains and coherent domain sizes, remain virtually the same for all the investigated samples.

It should be noted that the irradiated volumes were in the centre of the cross-sections and, hence, certain differences could occur on the sample surfaces. Nevertheless, we unfolded comparatively significant differences between the phase compositions of both powder fractions. The powder with smaller particles includes almost mass fractions 1 % of the tetragonal Al-Cr-Mn phase, 10 % more of the Al-Mn phase and about 6 % less of the Al-Cr phase. The probable reason for the differences lies in the fact that the powder fractions differ in the cooling rate. Finer powders solidify more rapidly than the coarser ones. This difference can cause changes to the types of intermetallics that are formed. Moreover, the identified phase compositions include more manganese than expected on the basis of the initial chemical composition of the atomized powder. This discrepancy can be explained with, e.g., the substitution of manganese atoms by iron.

The SPS method is a very effective method for compacting alumina-based powders. The sample size is limited by the size of the die. In this case, the whole sample body is heated in accordance with the Joule effect, which enables a production of the samples with almost no porosity at very short dwell times, unlike in the case of hot extrusion. The results of the XRD analysis show that there are almost no observable changes during the SPS compacting process with respect to the phase composition and real structure.

5 REFERENCES

[1] M. J. F. Gándara, Aluminium: the metal of choice, Mater. Tehnol., 47 (**2013**) 3, 261–265

[2] M. Yamasaki, Y. Nagaishi, Y. Kawamure, Inhibition of Al grain coarsening by quasicrystalline icosahedral phase in the rapidly solidified powder metallurgy Al-Fe-Cr-Ti alloy, Scripta Materialia, 56 (**2007**), 785–788

[3] G. Lojen, T. Bončina, F. Zupanič, Thermal stability of Al-Mn-Be Melt-spun ribbons, Mater. Tehnol., 46 (**2012**) 4, 329–333

[4] B. Bártová, D. Vojtěch, J. Verner, A. Gemperle, V. Studnička, Structure and properties of rapidly solidified Al-Cr-Fe-Ti-Si powder alloys, Journal of Alloys and Compounds, 387 (**2005**), 193–200

[5] D. Vojtěch, A. Michalcová, J. Pilch, P. Šittner, J. Šerák, P. Novák, Structure and thermal stability of Al-5.7Cr-2.5Fe-1.3Ti alloy produced by powder metallurgy, Journal of Alloys and Compounds, 475 (**2009**), 151–156

[6] D. Vojtěch, A. Michalcová, F. Průša, K. Dám, P. Šedá, Properties of the thermally stable Al95Cr3.1Fe0.8 alloy prepared by cold-compression at ultra-high pressure and by hot-extrusion, Materials characterization, 66 (**2012**), 83–92

[7] Y. Minamino, Y. Koizumi, M. Tsuji, N. Hirohata, K. Mizuuchi, Y. Ohkanda, Microstructures and mechanical properties of bulk nanocrystalline Fe-Al-C alloys made by mechanical alloying with subsequent spark plasma sintering, Science and Technology of Advanced Materials, 5 (**2004**), 133–143

[8] T. Masao, Handbook of Advanced Ceramics, Chapter 11.2.3 – Spark Plasma Sintering (SPS) Method, System and Applications, Second Edition, 2013, 1149–1177

[9] T. Skiba, P. Haušild, M. Karlík, K. Vanmeensel, J. T. Vleugels, Mechanical properties of spark plasma sintered FeAl intermetallics, Intermetallics, 18 (**2010**), 1410–1414

[10] K. Sastry, Field assisted sintering and characterization of ultrafine and nanostructured aluminium alloys, PhD thesis, Ku Leuven, 2006, p. 255

[11] K. Vanmeensel, A. Laptev, J. Hennicke, J. Vleugels, O. Van Der Biest, Modelling of the temperature distribution during field assisted sintering, Acta Materialia, 53 (**2005**), 4379–4388

[12] J. Zhang, A. Zavaliangos, Jr. J. Groza, Field activated sintering techniques: a comparison and contrast, Powder Metallurgy Science Technology and Application, 5 (**2003**), 17–21

[13] R. Orrú, R. Licheri, A. Locci, A. Cincotti, G. Cao, Consolidation synthesis of materials by electric current activated/assisted sintering, Materials Science and Engineering R, 63 (**2009**), 127–287

UDK 621.791.76/.79:539.4.016:621.785.72
Original scientific article/Izvirni znanstveni članek

ISSN 1580-2949
MTAEC9, 49(1)133(2015)

EFFECT OF TEMPERING ON THE MICROSTRUCTURE AND MECHANICAL PROPERTIES OF RESISTANCE-SPOT-WELDED DP980 DUAL-PHASE STEEL

VPLIV POPUŠČANJA NA MIKROSTRUKTURO IN MEHANSKE LASTNOSTI TOČKASTO VARJENEGA DVOFAZNEGA JEKLA DP980

Fateme Nikoosohbat[1], Shahram Kheirandish[2], Masoud Goodarzi[2], Majid Pouranvari[3]
[1]West Coast Stainless, California, USA
[2]Materials Science and Metallurgical Engineering Department, Iran University of Science and Technology (IUST), Tehran, Iran
[3]Materials and Metallurgical Engineering Department, Dezful Branch, Islamic Azad University, Dezful, Iran
mpouranvari@yahoo.com,

Prejem rokopisa – received: 2014-02-12; sprejem za objavo – accepted for publication: 2014-03-12

This paper aims at investigating the effect of an in-process tempering cycle on the microstructure and mechanical properties of the DP980 dual-phase-steel resistance spot welds. A microstructural characterization, a microhardness test and a quasi-static tensile-shear test were conducted. The results showed that the fusion-zone microstructure of as-welded spot welds mainly consisted of lath martensite. A tempered martensite region was observed in the sub-critical heat-affected zone, producing a relatively soft region compared to the base metal. It was found that applying an in-process tempering for a sufficient time promoted the heat-affected-zone softening and produced a softer fusion zone due to martensite tempering which, in turn, improved the energy-absorption capability of spot welds.

Keywords: resistance spot welding, dual-phase steel, temper, microstructure

Članek opisuje vpliv cikla popuščanja med postopkom točkastega varjenja dvofaznega jekla DP980 na mikrostrukturo in mehanske lastnosti točkastega zvara. Izvršena je bila karakterizacija mikrostrukture, izmerjena mikrotrdota in opravljen kvazi statični natezno-strižni preizkus. Rezultati so pokazali, da je mikrostruktura področja zlivanja točkastega zvara pretežno iz latastega martenzita. V območju podkritične toplotno vplivane cone je bilo opaženo področje popuščenega martenzita, ki je relativno mehko področje v primerjavi z osnovnim materialom. Ugotovljeno je bilo, da uporaba dovolj dolgega popuščanja med postopkom pospešuje mehčanje toplotno vplivane cone in nastanek mehkejše cone zlivanja zaradi popuščnega martenzita, kar hkrati izboljša zmožnost absorpcije energije točkastega zvara.

Ključne besede: uporovno točkasto varjenje, dvofazno jeklo, popuščanje, mikrostruktura

1 INTRODUCTION

Dual-phase (DP) steels exhibit a unique microstructure consisting of soft ferrite and hard martensite that offers a favorable combination of strength, high work-hardening rate, ductility and formability. Due to these features, automotive companies are finding that the use of these steels can enable them not only to reduce the overall weight of an automobile, but also providing an improved crash protection to the vehicle occupants.[1–3]

Resistance spot welding (RSW) is the main joining process of sheet metal, particularly in the automotive industry. Vehicle crashworthiness, which is defined as the capability of a car structure to provide an adequate protection to its passengers against injuries in the event of a crash, largely depends on the spot-weld structural-mechanical behavior.[4–7] Considering the development and commercialization of new DP steels for the application in automotive bodies, there is an increasing need to study the spot-welding behavior of these materials. According to the literature, the problems associated with the resistance spot welding of DP steels can be summarized as follows:[8–15]

(i) High susceptibility to failure in the interfacial failure mode
(ii) High susceptibility to expulsion
(iii) Sensitivity to the formation of shrinkage voids
(iv) High hardness of the fusion zone due to martensite formation. This can have adverse effects on the failure mode under certain loading conditions (e. g., a peel test).

Very high cooling rates in RSW cause a formation of martensite even in low-carbon steels. Tempering can then be performed by adding a post-weld current pulse (the in-process tempering step) to the welding sequence. This tempering step is a relatively simple way of reducing the weld hardness which, in turn, lowers the brittleness of the weld in C-Mn steels.[16] After the weld nugget has been formed, it is held between the electrodes long enough to sufficiently quench to martensite. A subsequent temper pulse is then applied to soften the microstructure of the weld nugget. Steels of varying composition and processing react differently to tempering and it is unknown how some of the newer transformation-hardened steels would react during such tempering.[16]

The objective of the present research is to investigate the effect of a tempering cycle on the microstructure, strength and failure energy of DP980 resistance spot welds.

2 EXPERIMENTAL PROCEDURE

A DP980-steel sheet 2 mm thick was used as the base metal. The chemical composition and mechanical properties of DP980 steel are given in **Tables 1** and **2**, respectively.

Table 1: Chemical composition of the investigated steel in mass fractions (*w*/%)

Tabela 1: Kemijska sestava preiskovanega jekla v masnih deležih (*w*/%)

P	S	Al	Cu	Cr	Si	Mn	C
0.004	0.014	0.036	0.196	0.2	0.13	1.326	0.13

Table 2: Tensile properties of the investigated DP980 steel

Tabela 2: Natezna trdnost preiskovanega jekla DP980

Yield stress (MPa)	Ultimate tensile stress (MPa)	Total elongation (%)
532	990	18

Spot welding was performed using a 120 kVA AC-pedestal-type resistance-spot-welding machine, controlled by a PLC. The welding was conducted using a 45° truncated-cone RWMA Class-2 electrode with an 8 mm face diameter. The welding and tempering were performed in accordance with the schedule given in **Table 3**.

Table 3: Welding and tempering schedule

Tabela 3: Potek varjenja in popuščanja

Squeeze time (cycle)	Welding current (kA)	Welding time (cycle)	Electrode force (kN)	Holding/Cooling time (cycle)	Tempering current (kA)	Tempering time (cycle)
40	9	35	5	40	5	20, 40

The quasi-static tensile-shear test samples were prepared according to ANSI/AWS/SAE/D8.9-97 standard.[17] **Figure 1** shows the sample dimensions used for the tensile-shear tests. The tensile-shear tests were performed at a cross head of 2 mm/min with an Instron universal testing machine, recording the load-displacement curves. The peak load (measured as the peak point in the load-displacement curve) and the failure energy (measured as the area under the load-displacement curve up to the peak load) were extracted from the load-displacement curve.

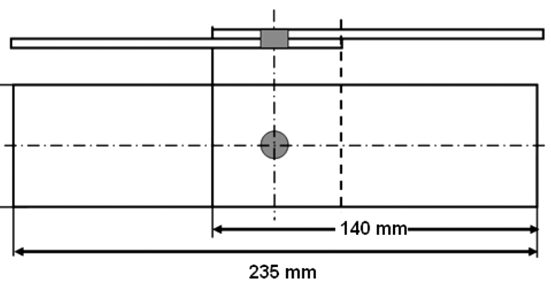

Figure 1: Tensile-shear specimen dimensions

Slika 1: Dimenzije preizkušanca za natezno-strižni preizkus

Light microscopy was used to examine the macrostructures and to measure the weld-fusion-zone (the weld-nugget) size. The microstructures of the samples were also examined with a scanning electron microscope (SEM). The microhardness test, a technique that has proven to be useful in quantifying microstructure/mechanical property relationships, was used to determine the hardness profile parallel to the sheet interface (20 µm away from the weld centerline), using a 100 g load on a Bohler microhardness tester.

3 RESULTS AND DISCUSSION

3.1 Microstructure and hardness profile of as-welded DP980 RSWs

The microstructure and hardness profile of resistance spot welds play important roles in their failure behavior. The rapid heating and cooling induced by resistance-spot-welding thermal cycles significantly alter the microstructure in the joint zone. A typical macrostructure of a

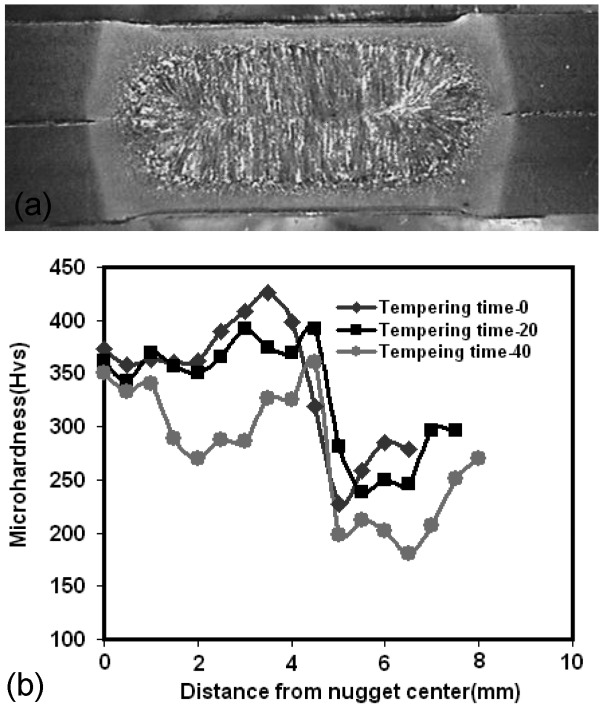

Figure 2: a) Typical macrostructure of an as-welded DP980 joint and b) hardness profile of the DP980 spot weld in the as-welded condition (i.e., tempering time = 0) and after the in-process tempering for the tempering times of 20 and 40 cycles

Slika 2: a) Značilna makrostruktura zvarjenega spoja DP980 in b) profil trdote točkastega zvara DP980 v zvarjenem stanju (čas popuščanja = 0) in po popuščanju med postopkom za čase popuščanja od 20 do 40 ciklov

DP980 spot weld is shown in **Figure 2a** indicating three distinct zones, namely, the fusion zone (FZ), the heat-affected zone (HAZ) and the base metal (BM).

The hardness profile of the DP980 RSW is shown in **Figure 2b**. The hardness variation across the joint can be analyzed in terms of the microstructure of the joint. The DP980 base-metal microstructure, as shown in **Figure 3a**, consists of dispersed martensite islands embedded in a ferrite matrix; the corresponding hardness is 300 HV (**Figure 2b**). As can be seen in **Figure 3b**, the FZ predominantly exhibits lath martensite with the average hardness of 390 HV (**Figure 2b**). The formation of a high-volume fraction of martensite in the FZ explains the higher hardness of the FZ compared to the BM hardness. The martensite formation in the FZ is attributed to the inherently high cooling rate of the resistance-spot-welding process due to the presence of water-cooled copper electrodes and their quenching effect as well as the short welding cycle. Gould et al.[18] developed a simple analytical model predicting the cooling rates of resistance spot welds. According to this model, the cooling rate for a 2 mm thickness is about 2000 K s^{-1}. For steels, the required critical cooling rate to achieve martensite in the microstructure can be estimated using the following equation:[19]

$$\lg v = 7.42 - 3.13\, w(\mathrm{C}) - 0.71\, w(\mathrm{Mn}) - 0.37\, w(\mathrm{Ni}) - 0.34\, w(\mathrm{Cr}) - 0.45\, w(\mathrm{Mo}) \qquad (1)$$

where v is the critical cooling rate (K h^{-1}).

The calculated critical cooling rate for the investigated steel is 280 K s^{-1}. Since the recorded cooling rates in the FZ are significantly higher than the critical cooling rates needed for a martensite formation, it is not surprising that a martensite structure is present in the FZ.

The hardness of the HAZ is higher than the BM hardness due to the formation of non-equilibrium phases. The microstructure of the HAZ is more heterogeneous than that of the FZ, as verified by the hardness profile. The material in the HAZ experiences the peak temperature and cooling rate, inversely proportional to its distance from the fusion line. Thus, the high-thermal cycle gradient coupled with the resulted austenite-grain structure can explain the observed microstructure gradient in the HAZ. One of the interesting features of the DP980 RSW hardness profile is the HAZ softening (i.e., the HAZ hardness reduction with respect to the BM). As can be seen, the HAZ of DP980 welds experiences an approximately 50 HV softening. The HAZ softening during the welding of DP steels was reported in[20–22]. The location of the HAZ softening corresponds to the sub-critical HAZ (i.e., the region in the HAZ that experiences the temperatures below the A_{c1} critical temperature). It is well documented that this phenomenon is due to the tempering of the pre-existing martensite in the sub-critical areas of the HAZ.[22] **Figure 3c** shows a microstructure of this region indicating a presence of the tempered martensite.

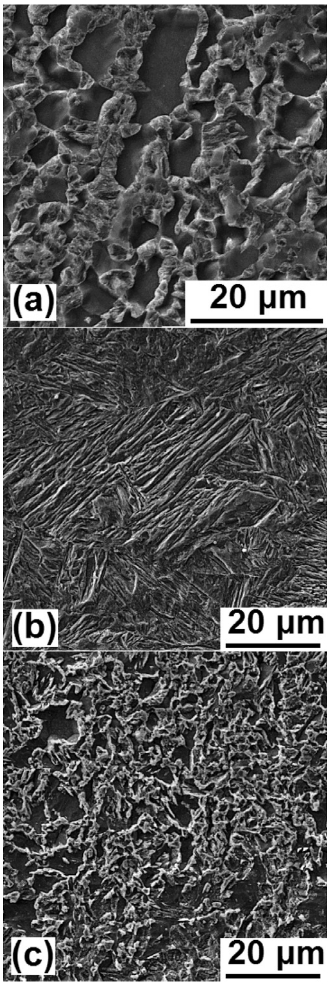

Figure 3: SEM micrographs showing the microstructures of: a) base metal, b) fusion zone, c) HAZ softening region in the as-welded joint
Slika 3: SEM-posnetki mikrostrukture: a) osnovna kovina, b) področje zlivanja, c) HAZ-področje zmehčanja v varjenem spoju

3.2 Criteria for the selection of tempering parameters

The FZ size of the spot welds made with the welding parameters from **Table 3** is about 8 mm, which is well above the conventional recommendation of 4 $t^{0.5}$ and 5 $t^{0.5}$ (t is the sheet thickness (mm)). However, the spot welds produced under the presented welding condition failed in the interfacial-failure mode. As mentioned above, it is well documented that DP steels are more prone to fail in the interfacial-failure mode. The in-process quenching and tempering of welds were used to improve the mechanical properties of the spot welds with interfacial failure.

To perform a proper quenching and tempering treatment on a weldment, the following points should be considered:

(i) The selected quenching time should be such that the weldment cools to a temperature slightly below the martensite-finish temperature (M_f) before being heated for tempering. If this temperature is above M_f, there can be untransformed austenite left in the FZ and it can re-decompose into the untempered martensite upon cooling to room temperature after the tempering.

(ii) In this study, to estimate the temperature distribution during the cooling cycle of spot welding, a simple analytical model predicting the cooling rates of resistance spot welds developed by Gould et al.[16,18] was used. Based on some simplification assumptions, the temperature distribution in the through-thickness direction of a steel sheet after the welding current is turned off, is expressed as follows:

$$T = T_{\mathrm{P}} \frac{1+\left(\frac{2}{\pi}\right)\left(\frac{K_{\mathrm{E}}}{K_{\mathrm{S}}}\right)\left(\frac{t_{\mathrm{S}}}{t_{\mathrm{E}}}\right)\cos\left(\frac{\pi}{2t_{\mathrm{S}}}x\right)}{1+\left(\frac{2}{\pi}\right)\left(\frac{K_{\mathrm{E}}}{K_{\mathrm{S}}}\right)\left(\frac{t_{\mathrm{S}}}{t_{\mathrm{E}}}\right)e^{\frac{\alpha\pi^2}{4t_{\mathrm{S}}^2}t}} \tag{2}$$

where T_{P} is the peak temperature in the spot weld, while t_{S} and t_{E} are the steel-sheet thickness and the electrode face diameter, respectively. K_{S} and K_{E} are the thermal conductivity coefficients of steel and copper, respectively. X is the distance from the weld faying surface to the electrode face, and α is the thermal diffusivity of steel.

Figure 4 shows the calculated temperature distribution for different levels of penetration in the workpiece, ranging from 0 % (the faying surface) to 100 % (the electrode-sheet surface). The temperatures in the weld at the beginning of the cooling range (0-cycle cooling in **Figure 3a**) suggest a full austenization of the weld through thickness. However, the temperatures in the extremities of the weld, approaching the electrode-sheet interfaces, are substantially cooler, being as low as 600 °C. This, of course, is well below the A_3 temperature for the material studied here, suggesting that the peripheral areas of the weld do not achieve even a partial re-austenization and, therefore, are not subjected to local martensite decomposition. Based on **Figure 4**, the quenching time between the welding cycle and the tempering cycle was selected as 40 cycles. Using a quenching time of 40 cycles allows the weldment to cool roughly below the M_{f} temperature, facilitating a transformation into martensite.

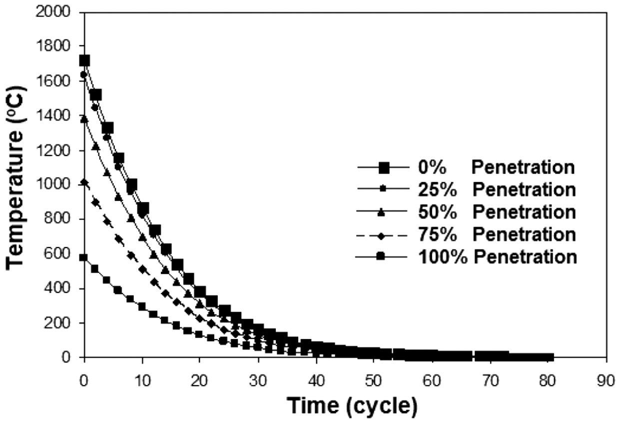

Figure 4: Calculated cooling profiles of a spot weld for different levels of penetration based on the Gould's model[16,18]

Slika 4: Profili ohlajanja točkastega zvara za različne nivoje penetracije, izračunani na osnovi Gouldovega modela[16,18]

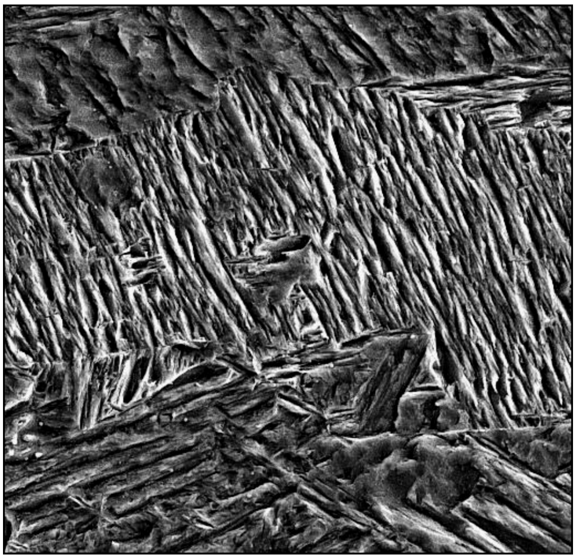

Figure 5: FZ microstructure after 20 cycles of the in-process tempering

Slika 5: Mikrostruktura področja zlivanja (FZ) po 20 ciklih popuščanja med procesom

3.3 *Effect of the tempering cycle on the microstructure and hardness*

Figure 2b shows the effect of the tempering cycle on the weld hardness. According to the hardness values of the FZ, the tempering time of 20 cycles is insufficient for the martensite to decompose. According to **Figure 5**, the FZ microstructure of the welds tempered for the tempering time of 20 cycles is still martensitic.

After a tempering time of 40 cycles a weld exhibits a relatively complex distribution of the hardness (**Figure 2b**). The macrograph of a weld after the tempering time of 40 cycles (**Figure 6a**) shows that the periphery of the weld nugget is surrounded by a narrow shell. The hardness of the weld-nugget centre is higher than that of the shell. Indeed, the weld nugget consists of an untempered fusion zone (UTFZ) and a tempered fusion zone (TFZ). This is caused by a non-uniform temperature distribution inherent during the in-situ tempering. The temperature distribution in the spot weld during the tempering is roughly parabolic in shape, with the peak temperatures always on the weld centerline.[16] Accordingly, the centre of the weld nugget can be overheated and re-austenized during the tempering cycle and, subsequently, retransformed into hard martensite during cooling, as confirmed by the high hardness of the weld center. In the shell of the TFZ, the microstructure shows evidence of tempering as shown in **Figure 6b**. Moreover, according to **Figure 2b**, the tempering cycle resulted in a softer HAZ due to a longer time of tempering the martensite present in the initial microstructure of the BM.

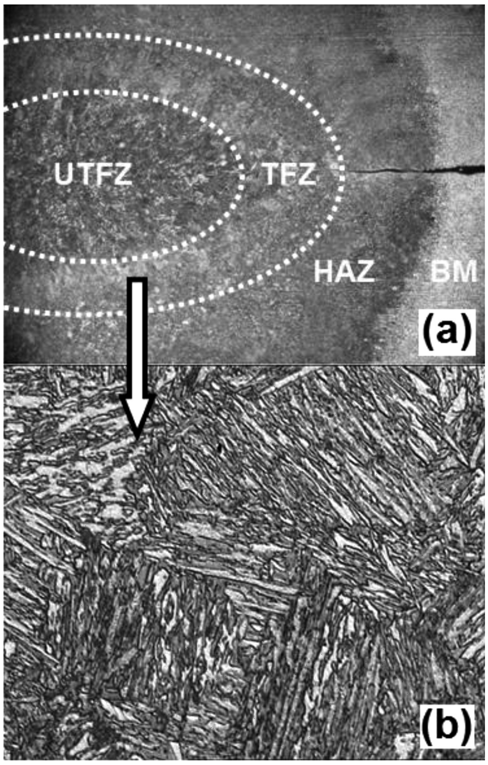

Figure 6: a) Weld-nugget macrograph after 40-cycle in-process tempering showing tempered fusion zone (TFZ) and untempered fusion zone (UTFZ), b) tempered martensite in the TFZ

Slika 6: a) Posnetek makrostrukture jedra zvara po 40 ciklih popuščanja kaže popuščeno področje zlivanja (TFZ) in nepopuščeno področje zlivanja (UTFZ), b) popuščeni martenzit v TFZ

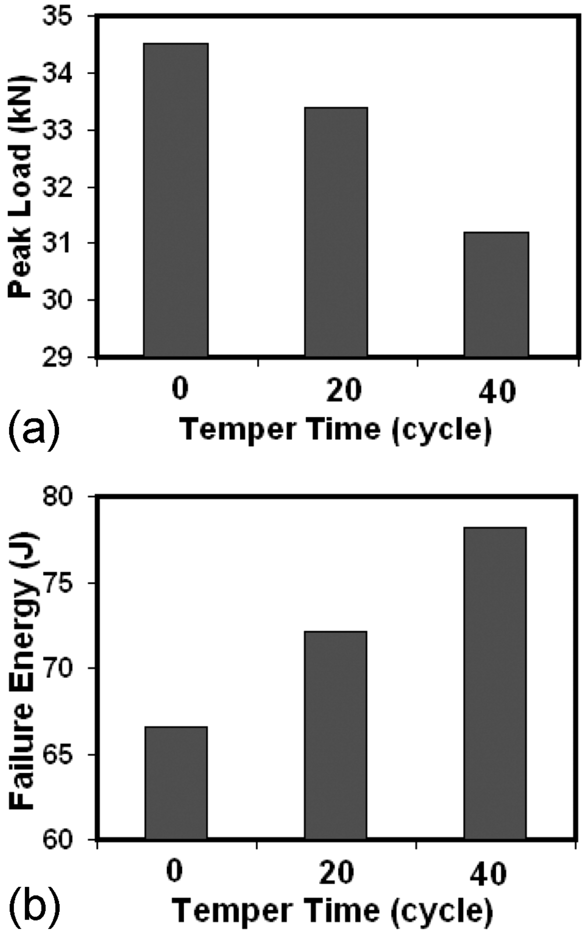

Figure 7: Effect of the tempering cycle on the weld strength and energy

Slika 7: Vpliv cikla popuščanja na trdnost in energijo zvara

3.4 Effect of the tempering cycle on the mechanical properties

The peak load of the spot welds depends on several factors including the physical weld attributes (mainly the FZ size and the indentation depth), the failure mode and the strength of the failure location. The failure energy of spot welds, measured as the area under the load-displacement curve up to the peak point, can be expressed as follows:

$$\mathit{Energyabsorption} = \int_0^{l_{\max}} F\,dl \propto P_{\max} \times l_{\max} \qquad (3)$$

where $P_{\max}$ is the peak load and $l_{\max}$ is the maximum displacement, corresponding to the peak load. The maximum displacement ($l_{\max}$) that represents the ductility of the spot welds depends on the ductility of the failure location. Therefore, the energy absorption depends on the factors governing the peak load and the ductility of the failure location.

Figure 7a shows the tensile-shear peak loads of the welds indicating that the as-welded joint (the untempered condition) exhibits the highest peak load. This can be related to the tensile-shear test configuration, which tends to load the welds in shear. Under the shear loading, any tendency for brittle fracture is minimized.[23] Therefore, the shear strength of the spot welds failed in the IF mode during the tensile-shear test depends on the strength/hardness correlation of the FZ. In the as-welded joint, the fully martensitic microstructure provides the highest peak load. The tempering which softens the FZ microstructure leads to a reduction in the strength of the joints.

Figure 7b shows the failure energy of the welds indicating a positive influence of the tempering cycle on the failure energy of the welds. According to **Figure 7b**, applying a tempering time of 40 cycles improved the weld failure energy. This can be related to the improved ductility of the FZ due to the tempering of the as-welded martensite which, in turn, enhances the energy-absorption capability of the weld. It was shown that there is a direct relationship between the failure energy in the static tensile-shear test and the impact tensile-shear test.[24] Therefore, it can be concluded that the tempering of spot welds that improves the weld energy-absorption capability increases the weld performance reliability against the impact loads such as crash accidents of cars.

4 CONCLUSIONS

1. The FZ of the as-welded spot weld exhibited a lath martensite microstructure. A reduction in the hardness (softening) with respect to the BM was observed in the HAZ due to the tempering of the martensite present in the initial microstructure of the base metal.
2. A short tempering cycle (i.e., a tempering time of 20 cycles) was insufficient for the lamellar martensite microstructure in the FZ to decompose. With the increasing tempering time, the martensite tempering in the FZ increased, resulting in a reduction of the average hardness of the FZ compared with that of the as-welded condition. Moreover, applying a tempering cycle led to an enlargement of the HAZ softening region.
3. It was shown that applying the in-process tempering for a sufficient time generates a pronounced HAZ softening and a softer fusion zone due to martensite tempering that, in turn, improves the energy-absorption capability of the welds.

5 REFERENCES

[1] M. Pouranvari, Influence of welding parameters on peak load and energy absorption of dissimilar resistance spot welds of DP600 and AISI1008 steels, Can Metall Q, 50 (**2001**), 381–88

[2] P. Movahed, S. Kolahgar, S. P. H. Marashi, M. Pouranvari, N. Parvin, The effect of intercritical heat treatment temperature on the tensile properties and work hardening behavior of ferrite–martensite dual phase steel sheets, Mater Sci Eng A, 518 (**2009**), 1–6

[3] M. Delincea, Y. Brechet, J. D. Emburyc, M. G. D. Geersd, P. J. Jacquesa, T. Pardoena, Separation of size-dependent strengthening contributions in fine-grained dual phase steels by nanoindentation, Acta Mater, 55 (**2007**), 2337–50

[4] M. Pouranvari, E. Ranjbarnoodeh, Dependence of the fracture mode on the welding variables in the resistance spot welding of ferrite-martensite DP980 advanced high-strength steel, Mater. Tehnol., 46 (**2012**) 6, 665–671

[5] P. Podrzaj, S. Simoncic, Resistance spot welding control based on fuzzy logic, Int J Adv Manuf Technol., 52 (**2011**), 959–967

[6] P. Podrzaj, S. Simoncic, Resistance spot welding control based on the temperature measurement, Sci Technol Weld Join, 18 (**2013**), 551–557

[7] M. Pouranvari, S. M. Mousavizadeh, Failure Mode of M130 Martensitic Steel Resistance-Spot Welds, Mater. Tehnol., 47 (**2013**) 6, 771–776

[8] M. Pouranvari, S. P. H. Marashi, Critical review of automotive steels spot welding: process, structure and properties, Sci Technol Weld Join, 18 (**2013**), 361–403

[9] M. M. H. Abadi, M. Pouranvari, Failure-mode transition in resistance spot welded DP780 advanced high-strength steel: effect of loading conditions, Mater. Tehnol., 48 (**2014**) 1, 67–71

[10] M. Pouranvari, S. P. H. Marashi, D. S. Safanama, Failure mode transition in AHSS resistance spot welds, Part II: Experimental investigation and model validation, Mater Sci Eng A, 528 (**2011**), 8344–52

[11] M. Pouranvari, H. R. Asgari, S. M. Mosavizadeh, P. H. Marashi, M. Goodarzi, Effect of weld nugget size on overload failure mode of resistance spot welds, Sci Technol Weld Join, 12 (**2007**), 217–25

[12] M. Pouranvari, S. P. H. Marashi, Failure mode transition in AHSS resistance spot welds, Part I, Controlling factors, Mater Sci Eng A, 528 (**2011**), 8337–43

[13] M. Pouranvari, Failure mode transition in similar and dissimilar resistance spot welds of HSLA and low carbon steels, Can Metall Q, 51 (**2012**), 67–74

[14] S. Simoncic, P. Podrzaj, Image-based electrode tip displacement in resistance spot welding, Meas Sci Technol, 23 (**2012**) 6, 065401

[15] X. Sun, E. V. Stephens, M. A. Khaleel, Effects of fusion zone size and failure mode on peak load and energy absorption of advanced high strength steel spot welds under lap shear loading conditions, Eng Fail Anal, 15 (**2008**), 356–67

[16] W. Chuko, J. Gould, Development of Appropriate Resistance Spot Welding Practice for Transformation-Hardened Steels, Report to the American Iron and Steel Institute, 2002

[17] Recommended Practices for Test Methods and Evaluation the Resistance Spot Welding Behavior of Automotive Sheet Steels, ANSI/AWS/SAE D8.9–97, 1997

[18] J. E. Gould, S. P. Khurana, T. Li, Predictions of microstructures when welding automotive advanced high-strength steels, Weld J, 86 (**2006**), 111–6

[19] K. E. Easterling, Modelling the weld thermal cycle and transformation behavior in the heat-affected zone, In: H. Cerjak, K. E. Easterling (Eds.), Mathematical Modelling of Weld Phenomena, 1st ed., Maney Publishing, 1993

[20] F. Nikoosohbat, S. Kheirandish, M. Goodarzi, M. Pouranvari, S. P. H. Marashi, Microstructure and failure behaviour of resistance spot welded DP980 dual phase steel, Mater Sci Technol, 26 (**2010**), 738–44

[21] M. Pouranvari, S. P. H. Marashi, Key factors influencing mechanical performance of dual phase steel resistance spot welds, Sci Technol Weld Join, 15 (**2010**), 149–155

[22] V. H. B. Hernandez, S. K. Panda, M. L. Kuntz, Y. Zhou, Nanoindentation and microstructure analysis of resistance spot welded dual phase steel, Mater Lett, 64 (**2010**), 207–210

[23] R. W. Hertzberg, Deformation and fracture mechanics of engineering materials, 2nd ed, John Wiley & Sons, 1996

[24] M. Zhou, H. Zhang, S. J. Hu, Critical Specimen Sizes for Tensile-Shear Testing of Steel Sheets, Weld J, 78 (**1999**), 305–313

UDK 621.7.01:621.937:519.61/.64
Original scientific article/Izvirni znanstveni članek

ISSN 1580-2949
MTAEC9, 49(1)139(2015)

OPTIMIZATION OF THE PROCESS PARAMETERS FOR SURFACE ROUGHNESS AND TOOL LIFE IN FACE MILLING USING THE TAGUCHI ANALYSIS

OPTIMIZACIJA PROCESNIH PARAMETROV GLEDE NA HRAPAVOST POVRŠINE IN TRAJNOSTNO DOBO ORODJA PRI ČELNEM REZKANJU Z UPORABO TAGUCHIJEVE ANALIZE

Murat Sarıkaya[1], Hakan Dilipak[2], Akın Gezgin[3]

[1]Department of Mechanical Engineering, Sinop University, 57030 Sinop, Turkey
[2]Manufacturing Department, Technology Faculty, Gazi University, 06500 Ankara, Turkey
[3]Mechanical Education, Institute of Science and Technology, Gazi University, 06500 Ankara, Turkey
msarikaya@sinop.edu.tr

Prejem rokopisa – received: 2014-02-13; sprejem za objavo – accepted for publication: 2014-03-12

In this study, the Taguchi method, which is a powerful tool to design quality optimization, is used to find the optimum surface roughness and tool life in milling operations. An orthogonal array, a signal-to-noise (*S/N*) ratio, and an analysis of variance (ANOVA) are employed to investigate the tool life and the surface-roughness characteristics of AISI D3 steel. Accordingly, the lowest surface roughness and the highest tool life were estimated to be 0.436 μm and 434.1 s, respectively and, finally, the Taguchi method allowed the optimization of the system for the verification of the tests.

Further, ANOVA analysis was revealed that the number of cutter insert was the most important parameter influencing the surface roughness with a 75.27 %, and cutting speed was the most important parameter influencing the tool life with a 95 %.

Keywords: material machinability, face milling, Taguchi method, optimization, experimental design

V tej študiji je bila uporabljena Taguchijeva metoda kot močno orodje za ugotavljanje razmer za doseganje optimalne hrapavosti in trajnostne dobe orodja pri rezkanju. Ortogonalna matrika, signal hrupa (*S/N*) in analiza variance (ANOVA) so bili uporabljeni za preiskavo zdržljivosti orodja in hrapavosti površine jekla AISI D3. Na podlagi rezultatov je bila ocenjena najmanjša hrapavost površine 0,436 μm in največja zdržljivost orodja 434,1 s, Taguchijeva metoda pa je omogočila optimizacijo sistema pri verifikaciji preizkusov.

Nadalje je ANOVA analiza odkrila, da je število rezalnih vložkov najbolj pomemben parameter, ki s 75,27 % vpliva na hrapavost površine, hitrost rezanja pa je najpomembnejši parameter, ki s 95 % vpliva na življenjsko dobo orodja.

Ključne besede: obdelovalnost materiala, čelno rezkanje, Taguchijeva metoda, optimizacija, načrtovanje preizkusov

1 INTRODUCTION

Basically, milling is one of the most commonly used chip removal operations in manufacturing processes and machined parts are usually utilized to assembly with other parts in aerospace, die, medical, automotive, defense industry and machine design as well as in manufacturing industries.[1] In addition to the cutting insert, the tool holder, workpiece material, cutting speed (V), feed rate (f), depth of cut (a) and number of milling cutting inserts are the most important cutting parameters that highly affect the performance characteristics such as tool life and surface roughness.

Generally, researchers have focused on the tool deformation, the effects of cutting-tool coatings and environmental conditions using a single insert. The costs of cutting tools are important to manufacturers. The cost factor causes lowering to the minimum level of an implementation with the least number of inserts. In contrast, the increase in the duration of the process is also a well-known factor.[2] The aim of this study is to find out the effects of the cutting parameters (the cutting speed, the feed rate and the number of cutting inserts) on the surface roughness and the tool life at high cutting speeds. The roughness of machined surface is an important quality indicator in machining processes and the various properties of machined parts such as corrosion, wear, friction, and heat transmission are also influenced by surface roughness.[3,4] Most of the process parameters like spindle speed, feed rate, number of insert, depth of cut, tool holder geometry, cutting insert geometry, tool material, cooling condition affect the tool life and surface roughness. Thus, it is difficult to define a general model for tool life and surface roughness.[5] Some statistical methods like Taguchi, Response Surface Methodology (RSM), desirability functional analysis, ANOVA and Grey Relational Analysis (GRA) have been applied for optimization and analysis of process parameters. The optimization using Taguchi method has revealed a unique and powerful optimization tool that differs from traditional applications.[6] For instance, Kivak et al.[7] studied the optimization of drilling parameters based on the Taguchi method to minimize the surface roughness (R_a) and thrust force (F_f). Their study showed that the cutting tool was the most significant parameter for the R_a. Moreover, the results of verification test demonstrated the Taguchi method for drilling operations was successful to obtain the better surface quality of the machined parts. Aslan et al.[8] evaluated the R_a and cutting-tool wear during the machining of AISI 4140 (63 HRC) steel with an experiment according to the Taguchi's L_{27} orthogonal array. From the ANOVA table, it was found out that tool wear is affected by cutting speed with 30 %. They suggested a 250 m/min cutting speed, a 0.25 mm depth of cut and a 0.05 mm/r feed rate to minimize the R_a value. Gunay and Yucel[9] investigated the R_a during the machining of high-alloy white cast iron with an experiment according to the Taguchi L_{18} orthogonal array. According to ANOVA data, they explained that the most important parameter was feed rate for Ni-Hard with 62 HRC although the cutting speed was the most important parameter for Ni - Hard with 50 HRC.

Neseli et al.[10] studied the influence of the tool geometry on the surface finish when turning the AISI 1040 steel with an Al_2O_3/TiC tool using the response-surface methodology (RSM). Their results indicated that the tool-nose radius was the dominant factor for the surface roughness with a 51.45 % contribution to the total variability of the model.

Asilturk and Akkus[11] applied the Taguchi method to minimize the surface roughness, which is R_a and R_z, in turning of hardened AISI 4140 steel (51 HRC) using coated carbide tools. In addition, their study explored the effects of the cutting speed, the feed rate and the depth of cut on the responses. From the ANOVA analysis, it was determined that the feed rate was the most significant parameter on results. Further, it was seen that the optimum machining parameters for R_a and R_z were different. Kacal and Gulesin[12] optimized the machining parameters for the finish turning of austempered cast iron (GJS-400-15). Their experimental investigation was conducted based on Taguchi's L_{18} orthogonal array. Statistical analysis, which was ANOVA, demonstrated that feed rate is the most important factor with 69.5 % for surface roughness (R_a). In addition, they identified the best machining parameters for R_a to be: an austempering temperature of 290 °C, a ceramic tool, a cutting speed of 800 m/min and a feed rate of 0.05 mm/r.

Sarikaya and Gullu[13] studied the Taguchi design and a response-surface-methodology-based analysis of the machining parameters for CNC turning under MQL. It was found that the most effective parameter for the surface roughness is the feed rate. In addition, the cooling conditions also significantly affect the surface roughness. Kadirvel and Hariharan[14] investigated the optimization of the die-sinking micro-edm process for multiple performance characteristics using the Taguchi-based grey relational analysis. Their study indicated that, on the basis of a confirmation test, the improvement in the performance characteristics was found to be as follows: MRR 3.86 %, TWR 4.20 % and SR 3.51 %. Kivak[15] investigated the Taguchi-method-based optimization of drilling parameters when drilling the AISI 316 steel with a PVD monolayer- and multilayer-coated HSS drills. The analysis results revealed that the feed rate was the dominant factor affecting the surface roughness and the cutting speed was the dominant factor affecting the flank wear. Koklu[16] investigated the influence of the process parameters and the mechanical properties of aluminum alloys on the burr height and the surface roughness in dry drilling using the Taguchi method. The analysis of variance and Taguchi techniques were applied in order to determine the effects of the drilling parameters.

The literature survey demonstrates that traditional experimental design procedures are too complicated and not easy to use. A large number of experimental tasks have to be performed when the number of process parameters increases. The Taguchi method uses a special design of orthogonal arrays to study the entire parameter space with only a small number of experiments for solving this problem.[11]

The purpose of this study is to obtain the optimum milling parameters (the cutting speed, the feed rate, the number of cutting inserts) for the minimum surface roughness and the maximum tool life during the milling of AISI D3 steel. The Taguchi parameter-design approach was employed to achieve these goals. Moreover, a statistical analysis (ANOVA) was carried out to see which machining parameter is statistically significant. Finally, confirmation tests were conducted using the optimum cutting conditions determined with the Taguchi optimization method.

2 EXPERIMENTAL PROCEDURE

2.1 Milling experiments

In this study, AISI D3 cold-work tool steel was used as the workpiece material. This steel type is used in many manufacturing industries such as the ones manufacturing cold-extrusion and drilling moulds, mould plates, powder-metallurgy kits, ceramic shaping moulds and cold punches. The dimensions of the workpiece were 100 mm × 48 mm × 300 mm. The chemical composition of the work material is as follows: 1.938 % C; 0.37 % Si; 0.22 % Mn; 10.66 % Cr; 0.22 % Ni; 0.135 % V; 0.062 % W; 0.07 % Cu; 85.82 % Fe. The milling tests were performed using a Johnford VMC 550 model, a three-axis CNC vertical machine centre, equipped with the maximum spindle speed of 8000 r/min and a 10 kW drive motor. The values of process parameters were selected from the manufacturer's handbook recommended and the preliminary experiments for the tested material. Process parameters and their levels are shown in **Table 1**. In all the experiments, the depth of cut was determined as 1 mm. The experiments were carried out under dry cutting conditions. To protect these experiment conditions for each test, a new cutting insert was used for each experi-

Table 1: Chosen factors and their levels
Tabela 1: Izbrani faktorji in njihovi nivoji

Symbol	Cutting parameter	Levels for surface roughness			Levels for tool life		
		1	2	3	1	2	3
A	Cutting speed, *V*/(m/min)	80	120	180	416	500	600
B	Feed rate, *f*/(mm/r)	0.08	0.12	0.18	0.08	0.1	0.125
C	Number of cutting inserts, *z*	1	3	6	1	3	6

Table 2: Standard tool holder and cutting insert
Tabela 2: Standardno držalo orodja in rezalnega vložka

Standard tool holder					Standard cutting insert			
ASX445-080A06R					SEMT13T3AGSN-JM			
D/mm	*d*/mm	*L*/mm	*Z*	a_a/mm	D_1/mm)	S_1/mm)	F_1/mm)	R_e/mm
80	27	50	6	6	13.4	3.97	1.9	1.5

ment. The flowchart for the optimization of the milling parameters is shown in **Figure 1**. In the milling experiments, the coated carbide inserts manufactured by Mitsubishi Carbide were used. Based on the ISO description, they create a SEMT 13T3AGSN tool geometry and a JM-chip-breaker form. In the experiments, the ASX445-080A06R model of the tool holder was used. The geometry of the cutting tool is shown in **Figure 2**. The geometric features of the tools are listed **Table 2**.

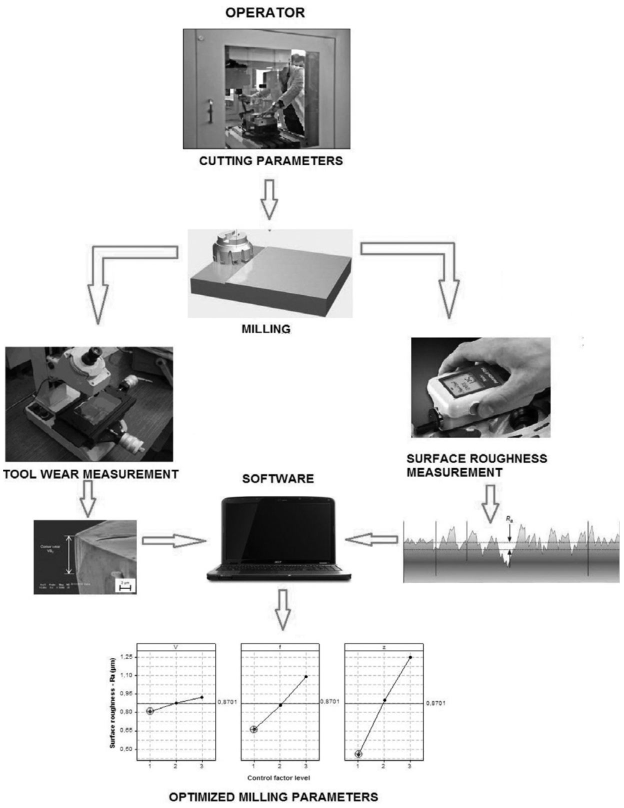

Figure 1: Flowchart for optimization of milling parameters
Slika 1: Diagram poteka optimizacije parametrov rezkanja

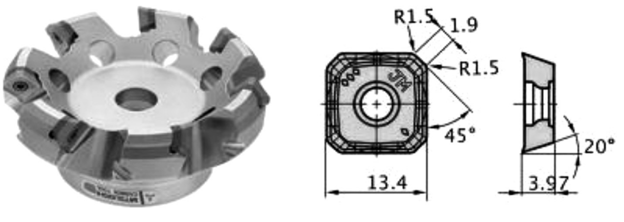

Figure 2: Cutting tool employed in the experiments
Slika 2: Rezalno orodje, uporabljeno pri preizkusih

2.2 Measurements

One of the most important quality indicators of the machined parts is surface roughness or surface quality. According to the standard, the average surface roughness is defined as R_a. In present work, R_a was determined by using a Mahr Perthometer M1 with a cut-off length of 0.8 mm and a sampling length of 5 mm based on ISO 4287 standard. It was considered by measuring the mean of the three roughness results performed from different locations on the workpiece.

Generally, the cutting tool-wear occurs in combination with the predominant wear mode, dependent upon the cutting parameters, cooling/lubrication conditions, workpiece material, cutting tool material and the tool insert geometry. The forms of the cutting-tool wear,

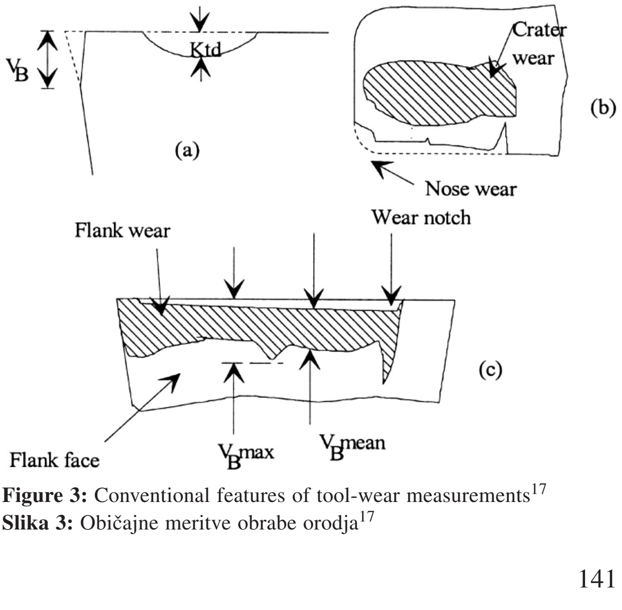

Figure 3: Conventional features of tool-wear measurements[17]
Slika 3: Običajne meritve obrabe orodja[17]

often expressed as the principal types of the tool wear are nose, flank, notch and crater wear types, and **Figure 3** shows how these wear features are usually measured.[17] In the present work, tool deformations were measured and investigated using a Mitutoyo light microscope with a 0.001 mm sensitivity and a capability of magnifying 5 to 10 fold. The experiments revealed that the notch wear was observed during the machining at high cutting speeds. The determination of the machining time was based on ISO 2688-1. When determining the tool life, $VB_{\max}$ was taken as 1 mm. The flank wear on the cutting tools was periodically measured and recorded to determine the tool life.

2.3 Control factors and orthogonal array

The cutting speed V (m/min), feed rate f (mm/r) and number of cutting inserts (z) were selected as the control factors for the surface-roughness and tool-life values, and their levels were determined as shown in **Table 1**. The orthogonal array (OA) enables an effective tool to conduct the test with the small number of studies in the Taguchi experimental method. The total degree-of-freedom (DF_T) is the basis of orthogonal array for experimental design.[18] In present work, because there are three control factors and three levels, the DF_T is given as twenty-six. In order to make the performance comparisons between control factors and its different combinations, an OA having at least nine or twenty-seven test trials ($DF_T + 1$) shoud be selected. Therefore, the standard L_{27} (3^3) OA is selected for the study and the surface-roughness and tool-life values are measured via the experimental design for each combination of the control factors. Determination of the quality characteristics of the measured control factors is provided by the *S/N* ratios.

3 RESULTS AND DISCUSSIONS

3.1 Analysis of the signal-to-noise (S/N) ratio

With the Taguchi method we used the signal-to-noise (*S/N*) ratio as the quality characteristic of choice. In milling operations, a lower surface roughness and larger tool life are indications of a better performance. Therefore, in order to obtain the optimum machining performance, the smaller-the-better (Equation 1) and larger-the-better (Equation 2) ratios were selected for the minimum surface roughness and maximum tool life, respectively:

Table 3: Experimental results, means and corresponding *S/N* ratios
Tabela 3: Eksperimentalni rezultati, povprečja in ustrezna razmerja *S/N*

Exp. No.	Cutting-parameter level			Measured surface roughness, R_a/μm	Calculated (S/N)/dB	Measured tool life, T/s	Calculated, (S/N)/dB
	A Cutting speed, V/(m/min)	B Feed rate, f/(mm/r)	C Number of inserts, z				
1	1	1	1	0.160	15.9176	435	52.7698
2	1	1	2	0.582	4.7015	426	52.5882
3	1	1	3	1.079	–0.6604	403	52.1061
4	1	2	1	0.383	8.3360	401	52.0629
5	1	2	2	0.784	2.1137	365	51.2459
6	1	2	3	1.194	–1.5401	338	50.5783
7	1	3	1	0.586	4.6420	369	51.3405
8	1	3	2	1.109	–0.8986	354	50.9801
9	1	3	3	1.400	–2.9226	328	50.3175
10	2	1	1	0.206	13.7227	266	48.4976
11	2	1	2	0.723	2.8172	236	47.4582
12	2	1	3	1.084	–0.7006	233	47.3471
13	2	2	1	0.456	6.8207	231	47.2722
14	2	2	2	0.869	1.2196	222	46.9271
15	2	2	3	1.261	–2.0143	193	45.7111
16	2	3	1	0.724	2.8052	216	46.6891
17	2	3	2	1.160	–1.2892	210	46.4444
18	2	3	3	1.409	–2.9782	167	44.4543
19	3	1	1	0.303	10.3711	118	41.4376
20	3	1	2	0.708	2.9993	110	40.8279
21	3	1	3	1.104	–0.8594	100	40.0000
22	3	2	1	0.552	5.1612	102	40.1720
23	3	2	2	0.945	0.4914	97	39.7354
24	3	2	3	1.290	–2.2118	86	38.6900
25	3	3	1	0.761	2.3723	97	39.7354
26	3	3	2	1.211	–1.6629	91	39.1808
27	3	3	3	1.449	–3.2214	82	38.2763

Smaller–the–better: $$\frac{S}{N} = -10\log_{10}\left(\frac{1}{n}\sum_{i=1}^{n} y_i^2\right) \quad (1)$$

Larger–the–better: $$\frac{S}{N} = -10\log_{10}\left(\frac{1}{n}\sum_{i=1}^{n} \frac{1}{y_i^2}\right) \quad (2)$$

Here, y_i is the ith measure of the experimental results in a run/row and n gives the number of measurements in each trial/row test.

The *S/N* ratios for the surface roughness and tool life were calculated using Equations 1 and 2, as shown in **Table 3**. The milling parameters were divided by considering different levels and possible effects, according to the selected orthogonal array. According to the experimental results, the mean of the surface roughness was 0.8701 µm and its mean *S/N* ratio was 2.353 dB. The mean value of tool life and its mean *S/N* ratio were also calculated as 232.4 s, and 46.031 dB, respectively. Further, the effects of input parameters on the responses can be analyzed with help of *S/N* ratios. These effects are defined and evaluated according to the total mean values of the experimental-trial results or *S/N* ratios. The minimum surface-roughness and the maximum tool-life values can be calculated from the total mean values of the experimental-trial results for the surface roughness and tool life. An important requirement when calculating the optimum points is to identify the optimum levels of machining parameters. They were defined by assessing different levels of the input parameters, based on the results from combinations produced by the OA. The levels of the control factors were determined for both the surface roughness and tool life, presented in **Table 4**, and *S/N* graphics of these levels were used for the evaluation (**Figures 4** and **5**). As shown in **Figure 4**, the surface roughness is found to be minimal at low cutting speed and feed rate and the minimum number of cutting inserts. The surface roughness increases with a rise in the cutting speed for a given value of the feed rate. Since the temperature increases between the tool material and the workpiece material through the friction under higher cutting speed, the cut chips by the cutting tool stick over the cutting insert with help of the high temperature.[19] Therefore, the surface roughness increases during the experiments at higher cutting speeds. The increased feed rate and number of cutting inserts lead to vibration, generating more heat and, thereby, a higher surface roughness occurs.[20] The tool life based on the wear value of $VB_{\max}$ = 1 mm for all the experiments is drawn. According to **Figure 5**, the longest tool life was obtained at the lowest values of the cutting speed, feed rate and number of cutters. When **Figure 5** is evaluated, it is possible to observe that an increased number of cutting inserts leads to a decreased tool life. This can be explained with the cutting temperature and the vibrations generated at the tool/chip contact when the number of cutting inserts is increased. It is known that a high cutting temperature occurs in the primary deformation zone

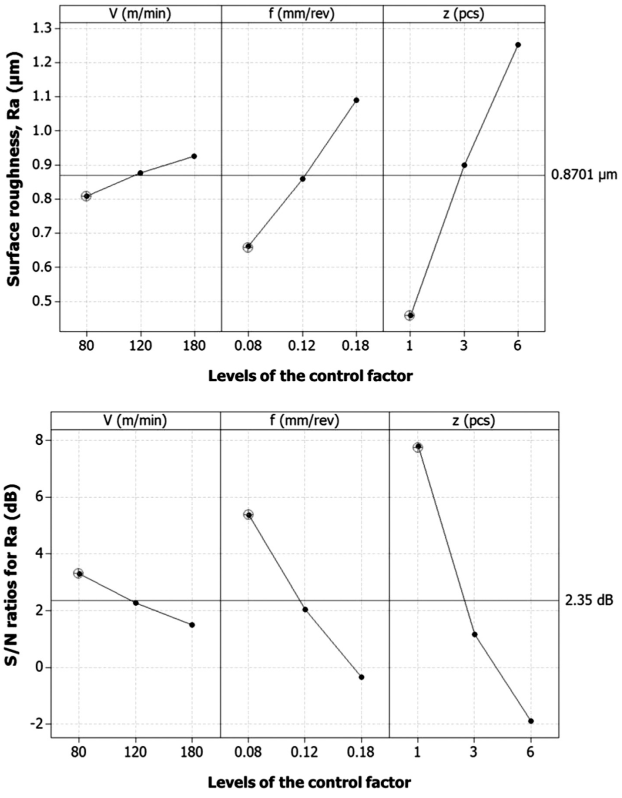

Figure 4: Main effects plot of the factors and *S/N* graph for the surface roughness

Slika 4: Prikaz glavnih faktorjev in odvisnost *S/N* od hrapavosti površine

Table 4: Response table for *S/N* ratios (dB) and means

Tabela 4: Tabela odzivov (dB) za različna razmerja *S/N* in za različna sredstva

Control factors	Surface roughness (R_a)				Tool life (T)			
	Level 1	Level 2	Level 3	Delta	Level 1	Level 2	Level 3	Delta
S/N ratios								
A	3.30	2.26	1.49	1.80	51.55	46.76	39.78	11.77
B	5.37	2.04	–0.35	5.72	47.00	45.82	45.27	1.73
C	7.79	1.16	–1.90	9.69	46.66	46.15	45.28	1.39
Means								
A	0.81	0.88	0.92	0.12	379.89	219.33	98.11	281.78
B	0.66	0.86	1.09	0.43	258.56	226.11	212.67	45.89
C	0.46	0.90	1.25	0.79	248.33	234.56	214.44	33.89

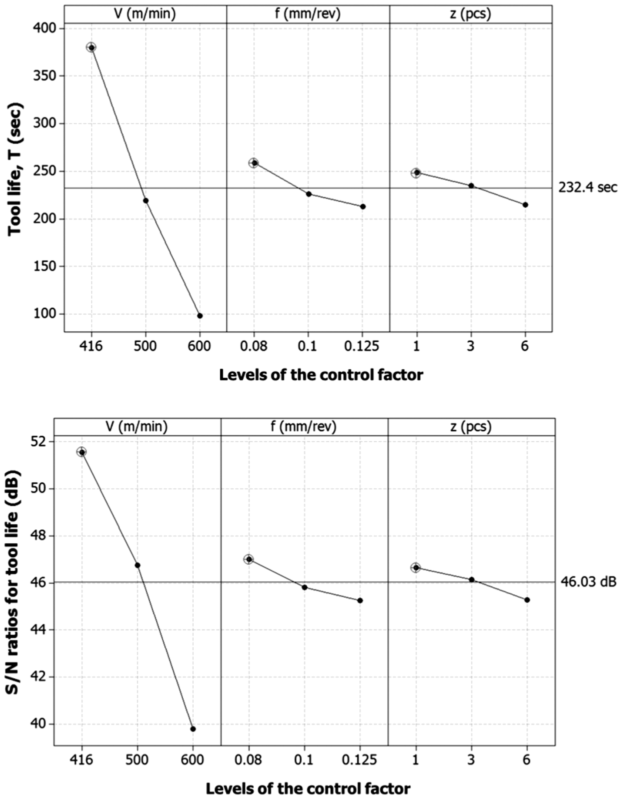

Figure 5: Main effects plot of the factors and *S/N* graph for the tool life

Slika 5: Prikaz glavnih faktorjev in odvisnost *S/N* od zdržljivosti orodja

with the increasing cutting speed. Thus, the wear mechanisms are accelerated and so the tool life is decreased.

The *S/N* ratios of the surface-roughness data obtained from the experimental work, later used to determine the optimum level of each variable, were calculated in **Table 3**. **Figure 4** illustrates the graphs of the *S/N* ratios that were calculated for the surface roughness. As mentioned above, the maximum value of the *S/N* ratios gives the optimum cutting conditions. Thus, the optimum combination for the R_a was determined as $A_1B_1C_1$ (A_1 = 80 m/min, B_1 = 0.08 mm/r, C_1 = 1 cutting insert). The *S/N* ratios for the tool-life data obtained from the experimental results were calculated in **Table 3**. **Figure 5** illustrates the graphs of the *S/N* ratios that were calculated for the tool life. The optimum combination for the tool life was determined as $A_1B_1C_1$ (A_1 = 416 m/min, B_1 = 0.08 mm/r, C_1 = 1 cutting insert).

3.2 Analysis of variance (ANOVA)

The Taguchi method was used for determining the optimum cutting conditions according to the *S/N* ratio, while the control-factor correlation with the experimental results was determined with the help of an analysis of variance (ANOVA). The analysis of variance (ANOVA) was employed through the Minitab 16.0 Program. **Table 5** shows the results of ANOVA for the surface roughness and tool life. In addition to the degree of freedom, the mean of squares (*MS*), the sum of squares (*SS*), the *F*-ratio, *P*-values and the contribution (*PCR*) associated with each factor were presented. This analysis was performed for a confidence level of 95 %. The importance of the input parameters in ANOVA analysis was identified by comparing the *F*-values of each input parameters. The *F*-value determined in the ANOVA table was compared with the value according to standard *F*-tables for a given statistical level of importance.[21] According to the ANOVA table, the *P*-value is effective for all three levels at the reliability level of 95 %, because the results for the surface roughness and tool life are lower than 0.05. As the results of the evaluation of the surface roughness, the percentage contributions of input parameters for *A*, *B* and *C* were determined as: (1.63, 21.96 and 75.27) %, respectively, and the error was 1.14 % (**Table 5**). Thus, it was found that the number of cutting inserts and the feed rate vary significantly more than the cutting speed regarding the surface roughness in milling the AISI D3 steel. The ANOVA table indicates that the variable most significantly affecting the surface-roughness value is the number of cutting inserts with 75.27 % of *PCR*. This result clearly shows the effects of the

Table 5: Results of ANOVA for responses

Tabela 5: Rezultati ANOVA-odzivov

Variation of source	Degree of freedom (*DF*)	Sum of squares (*SS*)	Mean of squares (*MS*)	*F*-ratio	*P*-value	Contribution (%)
Surface roughness (R_a)						
A	2	0.06141	0.03071	14.26	0.000	1.63
B	2	0.82931	0.41466	192.53	0.000	21.96
C	2	2.84270	1.42135	659.97	0.000	75.27
Error (*e*)	20	0.04307	0.00215			1.14
Total	26	3.77650				100
Tool life (*T*)						
A	2	359615	179807	975.62	0.000	95.00
B	2	10018	5009	27.18	0.000	2.65
C	2	5228	2614	14.18	0.000	1.38
Error (*e*)	20	3686	184			0.97
Total	26	378547				100

number of cutting inserts on the surface roughness in milling the AISI D3 steel whose vibration generated a higher frequency between the tool and the workpiece with the increasing number of cutting inserts. The other variable that has an effect on the R_a is the feed rate with 21.96 % of *PCR*. It is known that an increasing feed rate increases the chip volume removed per unit time.[7] Accordingly, **Table 5** shows that the percentage contributions of factors *A*, *B*, and *C* for the tool life are (95.00, 2.65 and 1.38) %, respectively, and the error is 0.97 %. Thus, **Table 5** indicates that the most effective variable for the tool life is the cutting speed (95.00 %). The feed rate and number of cutting inserts do not affect the tool life. In milling operations, the cutting speed is the most effective cutting parameter, reducing the tool life, because an increasing cutting speed increases the cutting temperature in the primary deformation zone. As a result of this situation, the wear mechanisms are accelerated.

3.3 Verification experiments

In the last step of the Taguchi approach, the optimization was confirmed via verification tests then the determination of the parameter levels giving the optimum results. The verification-test results were obtained for the optimum parameter levels ($A_1B_1C_1$) of the surface roughness. Later, the calculation of the predicted minimum surface roughness R_{ap} from Equation 3, taking into consideration individual effects of factors *A*, *B*, *C* and their levels, is as follows:

$$R_{\mathrm{ap}} = T_{\mathrm{Re}} + (A_1 - T_{\mathrm{Re}}) + (B_1 - T_{\mathrm{Re}}) + (C_1 - T_{\mathrm{Re}}) \tag{3}$$

where A_1 is the mean (0.81 μm) of the experimental trials at the first level of factor *A*. B_1 is the mean (0.66 μm) of the experimental trials at the first level of factor *B*. C_1 is the mean (0.46 μm) of the experimental trials at the first level of factor *C*. With Equation 3, the minimum surface roughness was calculated as 0.147 μm. As determined in **Figure 5**, *A*, *B*, *C* and their levels were used for the calculation of the predicted optimum tool life. The equation for the predicted optimum tool life is as follows:

$$T_{\mathrm{p}} = T_{\mathrm{T}} + (A_1 - T_{\mathrm{T}}) + (B_1 - T_{\mathrm{T}}) + (C_1 - T_{\mathrm{T}}) \tag{4}$$

where *A*, *B* and *C* are the means (379.89, 258.56 and 248.33) s of the experimental trials at the optimum levels of these factors. With Equation 4, the maximum tool life was calculated as 441.67 s. The confidence interval (*CI*) was conducted to confirm the output parameters of the verification test. The *CI* for the estimated optimum results was calculated using the following equation:[22]

$$CI = \sqrt{F_{\alpha;1;\mathrm{Ve}} \cdot V_{\mathrm{ep}} \cdot \left(\frac{1}{n_{\mathrm{eff}}} + \frac{1}{r}\right)} \tag{5}$$

where, with respect to $F_{\alpha;1;\mathrm{Ve}}$, *F* is the ratio of significant level α, α is the significance level, $1 - \alpha$ is the confidence level and V_e is the degree of freedom of the pooled error variance. V_{ep} is the pooled error variance, *r* is the number of repeated trials ($r \neq$), *N* is the total number of experimental trials, n_{eff} is the number of effective measured results defined as[22]:

$$n_{\mathrm{eff}} = \frac{N}{1+b} \tag{6}$$

where *b* is total degress of freedom associated with items used in estimate.

In the present investigation, three verification tests ($r = 3$) were made to assess the performance of the experimental study used for the surface roughness at optimum parameters ($A_1B_1C_1$). The value of $F_{\alpha;1;\mathrm{Ve}} = 4.30$ which has a 95 % confidence level for the surface roughness, was found with respect to the values of $\alpha = 0.05$ and $V_e = 20$, based on the look-up table. According to Equations 5 and 6, the confidence interval (*CI*) is calculated as 0.07. The result value of the confirmation test performed for the surface roughness is expected to be in the confidence interval of (0.147 ± 0.07) or (0.077 – 0.217) with a 95 % confidence level.

In the present work, the values of the surface roughness from the three confirmation tests performed with regard to the optimum levels ($A_1B_1C_1$) were measured as (0.159, 0.162 and 0.168) μm. As shown in **Table 6**, the mean of the measurements was 0.163 μm. The mean result of the confirmation tests in the optimum conditions is within the confidence interval ($0.077 < 0.163 < 0.217$). As the mean result falls within this limit, the experiment is considered satisfactory. The optimization of process parameters was achieved using the Taguchi method for the surface roughness at the confidence level of 95 %.

Three confirmation experiments were carried out under the optimum conditions ($A_1B_1C_1$) for the tool life. The value of $F_{\alpha;1;\mathrm{Ve}} = 4.30$ which has a 95 % confidence level for the tool life, was found with respect to the values of $\alpha = 0.05$, and $V_e = 20$, based on the look-up table. According to Equations 5 and 6, the confidence interval (*CI*) is calculated as 21.4 s. The result value of the confirmation test performed for the tool life is expected to be in the confidence interval of (441.7 ± 21.4) or (420.3 – 463.1) with a 95 % confidence level. In this study, the values of the tool life from the three confirmation tests performed with regard to the optimum levels ($A_1B_1C_1$) were measured as (440.2, 436.4 and 425.7) s. As shown in **Table 7**, the mean of the measurements was 434.1 s. The mean result of the confirmation tests in the optimum condition is within the confidence interval ($420.3 < 434.1 < 463.1$). As the mean result falls within this limit, the experiment is considered satisfactory. The optimization of the process parameters was achieved using the Taguchi method for the tool life at the confidence level of 95 %. According to the optimum test and the predicted combination, the comparisons of the surface roughness and tool life, and the combinations

Table 6: Comparisons of surface roughness and tool life
Tabela 6: Primerjave hrapavosti površine in zdržljivosti orodja

Comparison	Surface roughness			Tool life		
	Level	R_a/μm	(*S/N*)/dB	Level	*T*/s	(*S/N*)/dB
Initial combination	$A_2B_1C_2$	0.723	2.82	$A_2B_1C_2$	236	47.45
Optimum combination (Experiment)	$A_1B_1C_1$	0.163	15.9	$A_1B_1C_1$	434.1	52.74
Optimum combination (Prediction)	$A_1B_1C_1$	0.147	16.63	$A_1B_1C_1$	441.67	52.92

Table 7: Comparisons of experimental trials
Tabela 7: Primerjave eksperimentalnih poskusov

Comparison	Surface roughness			Tool life		
	Level	R_a/μm	Quality loss	Level	*T*/s	Quality loss
Initial combination	$A_2B_1C_2$	0.723	–	$A_2B_1C_2$	236	–
Optimum combination (Prediction)	$A_1B_1C_1$	0.147±0.07	–	$A_1B_1C_1$	434.1±21.4	
Optimum combination (Confirmation)	$A_1B_1C_1$	0.163	4.9 %	$A_1B_1C_1$	441.67	29.5 %

($A_2B_1C_2$) selected in the twenty-seven initial trials are given in **Table 6**. According to the comparison table, the surface roughness and tool life are reduced from 0.723 μm to 0.163 μm, and from 236 s to 434.1 s, respectively. The improved efficiency due to the optimum combination was increased for the surface roughness and tool life by up to 77.45 % ((0.723 – 0.163)/0.723) and by up to 45.63 % ((434.1 – 236)/434.1), respectively. The performance comparisons between the initial parameters and the optimum conditions are given in **Table 6**. In addition to, the quality losses are listed in **Table 7**.

The quality losses between the initial and optimum combinations for both the surface roughness and tool life are calculated as follows[18]:

$$\frac{L_{\mathrm{opt}}(y)}{L_{\mathrm{int}}(y)} \approx \left(\frac{1}{2}\right)^{\frac{\Delta_n}{3}} \tag{7}$$

where $L_{\mathrm{opt}}(y)$ and $L_{int}(y)$ are the optimum and initial combinations, respectively. Δ_n is the difference between the *S/N* ratios for the optimal and initial combinations. The differences between *S/N* ratios that can be used to evaluate the quality loss of the optimum combination for the surface roughness and tool life, were found to be 13.08 (Δ_n = 13.08 (= 15.9 – 2.82)) and 5.29 (Δ_n = 5.29 (52.74 – 47.45)), respectively. The quality loss was calculated as 0.049 using Equation 7 for the surface roughness. Thus, the quality loss of the surface roughness for the optimum combination is only 4.9 % of the initial combination. Therefore, the quality losses of the surface roughness were reduced to 95.1 % through the Taguchi application. The quality loss for the tool life was calculated as 0.295, using Equation 7. The quality loss of the tool life for the optimum combination is only 29.5 % of the initial combination. Consequently, the quality losses of the tool life were reduced to 70.5 % through the Taguchi method.

4 CONCLUSIONS

This study focuses on the Taguchi method used for investigating the influence of the cutting parameters on the surface roughness and tool life when face milling the AISI D3 steel. In the milling experiments, different levels of the cutting speed, the feed rate and the number of cutting inserts as the machining parameters are used under dry cooling conditions. The experimental results were evaluated using the analysis of the signal-to-noise ratio, the main effect graphs of means and ANOVA. The optimum operating parameters are determined using the Taguchi method. The results can be drawn as follows:

The optimum levels of the control factors providing a better surface roughness and tool life were: A_1 (the cutting speed, 80 m/min), B_1 (the feed rate, 0.08 mm/r), and C_1 (the number of cutting inserts, 1 insert), and A_1 (the cutting speed, 416 m/min), B_1 (the feed rate, 0.08 mm/r), C_1 (the number of cutting inserts, 1 insert), respectively.

The effects of the process parameters on the surface roughness and tool life were detected by ANOVA analysis. It was revealed that the number of cutting inserts the most important parameter influencing the surface roughness with 75.27 %. Further, cutting speed was the most important parameter influencing the tool life with 95 %.

Through the confirmation experiment, the surface roughness was obtained, with one of the initial combinations, as 0.723 μm, and the surface roughness was improved to 77.45 %. The tool life was obtained, with one of the initial combinations, as 236 s, and it was improved to 45.63 %. The quality losses for the surface roughness and the tool life determined from optimum points were calculated as 4.9 % and 29.5 %, respectively.

The confirmation-experiment results indicated that the observed values were within the calculated confidence interval (*CI*) for the confidence level of 95 %.

The present work demonstrates to industrial users how to apply the Taguchi parameter design for optimizing the machining performance with a minimum cost and time in milling the AISI D3 steel. Moreover, this study considered other factors (the cutting speed, the feed rate, the number of cutting inserts) to find how the control factors affect the surface roughness and tool life. Future works may be extend to analyzing the effects of some additional variables such as different tool holders, tool materials, workpiece materials and cooling conditions (wet, HPC, MQL, cryogenic, etc.).

5 REFERENCES

[1] T. S. Lee, Y. J. Lin, A 3D predictive cutting force model for end milling of parts having sculptured surfaces, Int. J. Adv. Manuf. Tech., 16 (**2000**), 773–783

[2] H. Dilipak, A. Guldas, A. Gezgin, An investigation of the number of ınserts effect on the machining time and metal removal rate during the milling of AISI D3 steel at high cutting speeds, Journal of Mechanical Engineering, 55, (**2009**) 7–8, 438–443

[3] E. Kabakli, M. Bayramoğlu, N. Geren, Evaluation of the surface roughness and geometric accuracies in a drilling process using the Taguchi analysis, Mater. Tehnol., 48 (**2014**) 1, 91–98

[4] H. Durmuş, Optimization of multi-process parameters according to the surface quality criteria in the end milling of the AA6013 aluminum alloy, Mater. Tehnol., 46 (**2012**) 4, 383–388

[5] S. Tamas, Cutting force modeling using artificial neural networks, Journal of Materials Processing Technology, 92 (**1999**), 344–349

[6] M. S. Phadke, Quality engineering using robust design, Prentice Hall, Englewood Cliffs, New Jersey 1989

[7] T. Kivak, G. Samtas, A. Cicek, Taguchi method based optimisation of drilling parameters in drilling of AISI 316 steel with PVD monolayer and multilayer coated HSS drills, Measurement, 45 (**2012**), 1547–1557

[8] E. Aslan, N. Camuscu, B. Birgoren, Design optimization of cutting parameters when turning hardened AISI 4140 steel (63 HRC) with Al2O3 + TiCN mixed ceramic tool, Mater. Des., 28 (**2007**), 1618–1622

[9] M. Gunay, E. Yucel, Application of Taguchi method for determining optimum surface roughness in turning of high-alloy white cast iron, Measurement, 46 (**2013**), 913–919

[10] S. Neseli, S. Yaldız, E. Turkes, Optimization of tool geometry parameters for turning operations based on the response surface methodology, Measurement, 44 (**2011**) 3, 580–587

[11] I. Asilturk, H. Akkus, Determining the effect of cutting parameters on surface roughness in hard turning using the Taguchi method, Measurement, 44 (**2011**), 1697–1704

[12] A. Kacal, M. Gulesin, Determination of optimal cutting conditions in finish turning of austempered ductile iron using Taguchi design method, J. Sci. Ind. Res. India, 70 (**2011**), 278–283

[13] M. Sarikaya, A. Gullu, Taguchi design and response surface methodology based analysis of machining parameters in CNC turning under MQL, Journal of Cleaner Production, 65 (**2014**), 604–616

[14] A. Kadirvel, P. Hariharan, Optimization of the die-sinking micro-edm process for multiple performance characteristics using the Taguchi-based grey relational analysis, Mater. Tehnol., 48 (**2014**) 1, 27–32

[15] T. Kivak, Optimization of surface roughness and flank wear using the Taguchi method in milling of Hadfield steel with PVD and CVD coated inserts, Measurement, 50 (**2014**), 19–28

[16] U. Koklu, Influence of the process parameters and the mechanical properties of aluminum alloys on the burr height and the surface roughness in dry drilling, Mater. Tehnol., 46 (**2012**) 2, 103–108

[17] D. E. Dimla Sr., P. M. Lister, On-line metal cutting tool condition monitoring I: force and vibration analyses, International Journal of Machine Tools & Manufacture, 40 (**2000**), 739–768

[18] Y. T. Liu, W. C. Chang, Y. A. Yamagata, A Study on optimal compensation cutting for an aspheric surface using the Taguchi method, CIRP Journal of Manufacturing Science and Technology, 3 (**2010**), 40–48

[19] V. Savas, C. Ozay, Analysis of the surface roughness of tangential turn-milling for machining with end milling cutter, Journal of Materials Processing Technology, 186 (**2007**), 279–283

[20] I. Korkut, M. Kasap, I. Ciftci, U. Seker, Determination of optimum cutting parameters during machining of AISI 304 austenitic stainless steel, Materials and Design, 25 (**2004**), 303–305

[21] J. Antony, D. Preece, Understanding, Managing and Implementing Quality, Frameworks Techniques and Cases, Routledge, London 2002

[22] R. K. Roy, Design of Experiments Using the Taguchi Approach, John Wiley & Sons, USA 2001

UDK 532.6:669.058.4:669.058.61
Professional article/Strokovni članek

ISSN 1580-2949
MTAEC9, 49(1)149(2015)

THIN TIN MONOSULFIDE FILMS DEPOSITED WITH THE HVE METHOD FOR PHOTOVOLTAIC APPLICATIONS

TANKA PLAST HVE KOSITROVEGA MONOSULFIDA ZA UPORABO V FOTOVOLTAIKI

Naidu Revathi, Sergei Bereznev, Julia Lehner, Rainer Traksmaa, Maria Safonova, Enn Mellikov, Olga Volobujeva

Tallinn University of Technology, Department of Materials Science, Ehitajate tee 5, 19086 Tallinn, Estonia
revathi.naidu@ttu.ee

Prejem rokopisa – received: 2013-10-01; sprejem za objavo – accepted for publication: 2014-02-17

In the present study, thin films of SnS photo-absorbers with two different thicknesses of 0.5 μm and 1 μm were deposited onto molybdenum-covered soda-lime-glass substrates using high-vacuum evaporation (HVE). The changes in the structural, phase-composition, morphological and photo-electrochemical properties depending on the film thickness were studied. The films showed a polycrystalline orthorhombic SnS crystal structure with (040) as the preferred orientation. It was observed that the films showed improved crystallinity with the increase in the film thickness. Raman analysis confirmed the presence of single phase SnS without any other binary phases. Photoconductivity measurements revealed that the layers have the p-type conductivity. The SnS layers grown at a thickness of 1 μm showed a high photosensitivity and could be considered as an absorber layer for solar-cell applications.

Keywords: SnS, thin films, HVE, photo-electrochemical, solar cell

V tej študiji je bila z visokovakuumskim naparevanjem (HVE) nanesena tanka plast SnS fotoabsorberja z dvema debelinama 0,5 μm in 1 μm na z molibdenom prekrito podlago iz natrij-kalcijevega stekla. Preučevane so bile spremembe v strukturi, sestavi faz, morfološke in fotoelektrokemijske lastnosti v odvisnosti od debeline plasti. Te plasti so pokazale polikristalno ortorombično kristalno strukturo SnS z (040) kot prednostno orientacijo. Opaženo je bilo, da se s povečanjem debeline plasti izboljša njena kristaliničnost. Ramanska analiza je potrdila prisotnost samo ene faze SnS brez drugih binarnih faz. Meritve fotoprevodnosti so odkrile, da imajo plasti prevodnost p-tipa. Plasti SnS, ki so zrasle na debelino 1 μm, imajo veliko fotoobčutljivost in so lahko uporabne pri sončnih celicah kot absorpcijska plast.

Ključne besede: SnS, tanke plasti, HVE, fotoelektrokemičen, sončna celica

1 INTRODUCTION

Tin monosulfide (SnS) is a layered compound semiconductor that crystallizes in an orthorhombic structure with the lattice parameters of $a = 0.4329$ nm, $b = 1.1193$ nm and $c = 0.398$ nm.[1] It has a high absorption coefficient with a photon energy threshold of 1.3 eV and exhibits the p-type conductivity.[2] Besides, its constituent elements Sn and S are earth-abundant and nontoxic. SnS has been used in photocondutors,[3] photovoltaic conversion,[1] holographic recording media,[4] solar control,[5] near-infrared detector,[6] etc. Owing to these advantages SnS has to be the promising material in the fabrication of thin-film solar cells. So far, the best reported conversion efficiency for SnS solar cells is about 4.4 %,[7] which is a very low value when compared to CIGS (about 21.7 %)[8] and CZTS (12.6 %) solar cells.[9] The reason for the low efficiency of the SnS solar cells so far has not been understood. In the present study, SnS thin films with two different thicknesses of 0.5 μm and 1 μm were grown on molybdenum (Mo) covered soda-lime-glass substrates and the influence of the preparative parameters of deposition on the microstructural parameters and photocurrent response of the films is reported.

2 EXPERIMENTAL WORK

Thin films of SnS were deposited onto Mo-covered soda-lime-glass substrates with the high-vacuum evaporation technique using BOC EDWARDS Auto 500 systems. The films with two different thicknesses of 0.5 μm and 1 μm were deposited at a constant substrate temperature (T_s) of 300 °C, with a deposition rate of 0.5 nm/s. The deposition was carried out in a vacuum chamber at a pressure of around 1.33×10^{-6} mbar with a deposition source-to-substrate distance of ≈ 25 cm. The crystalline-phase identification and phase-composition determination were done with a Bruker D5005 X-ray diffractometer and a Horiba LabRam HR spectrometer, respectively. The surface morphology of the as-deposited layers was observed using high-resolution scanning electron microscopy (HR-SEM Zeiss ULTRA 55) and an atomic force microscope (AFM, Bruker Nanoscope V controller with the application module MultiMode 8.10). The type of conductivity of the prepared SnS films was identified by performing the photo-electrochemical measurements in a background electrolyte solution of 0.1 M H_2SO_4.

3 RESULTS AND DISCUSSION

Figure 1 shows X-ray diffraction (XRD) profiles of the SnS thin films deposited onto Mo-coated glass substrate at a substrate temperature of 300 °C and a detailed XRD pattern of the (040) peak is shown in the inset. XRD profiles of all the layers had diffraction peaks at $2\theta \approx$ (26.12°, 31.96° and 39.04°), corresponding to the polycrystalline orthorhombic crystal structure of SnS with (040) as the dominant peak and being in agreement with the JCPDS data (card no. 39-0354). The strong-characteristic (040) diffraction peak could be due to the fact that most of the SnS crystallites grew preferentially along the (010) crystal plane that has the lowest surface energy,[10] with its orientation parallel to the substrate. At a thickness of 1 μm, the (040) plane of the as-deposited SnS film showed an enhanced intensity. The average crystallite size of the films was calculated using the full width at half maximum (FWHM) of the (040) plane with Scherrer's relation.[11] The FWHM of the (040) peak decreased with the film thickness, which indicates that the film crystallinity had improved. The evaluated average crystallite size of the prepared SnS films was found to be 18.9 nm and 58.9 nm for the thicknesses of 500 nm and 1 μm, respectively. The observed increase in the crystallite size at the higher thickness may be due to a decrease in the disorderness and microstrain in the thicker films. Analogous results for nanocrystalline SnS thin films prepared with electron-beam evaporation were also reported by Shaaban et al.[12] The microstrains of SnS thin films were calculated from equation[13] and the calculated values are 0.00183 and 0.00061 for the thicknesses 500 nm and 1 μm, respectively.

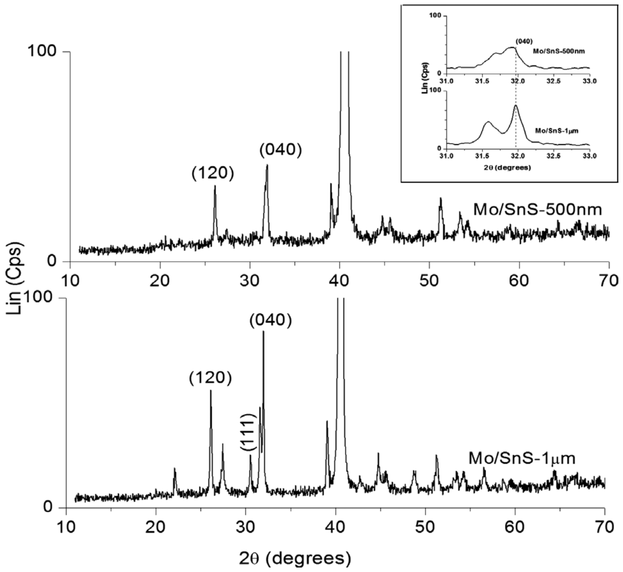

Figure 1: XRD patterns of SnS thin films (the inset: detailed (040) peak profiles)
Slika 1: XRD-posnetka tankih plasti SnS (vložek: podrobnejši profil vrhov (040))

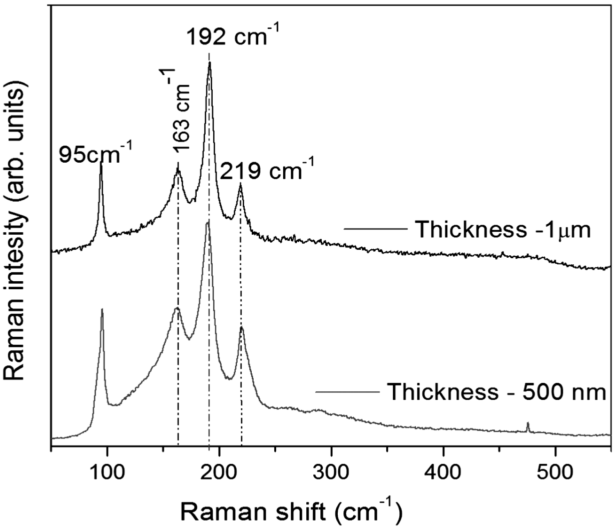

Figure 2: Raman spectra of SnS films at the thicknesses of 500 nm and 1 μm
Slika 2: Ramanska spektra plasti SnS pri debelinah 500 nm in 1 μm

Raman measurements were performed to get detail information of the phase composition of the films. The room-temperature Raman spectra of the SnS thin films were measured in a wavenumber range of 50–550 cm^{-1} and are shown in **Figure 2**. The peaks at (96, 163, 192

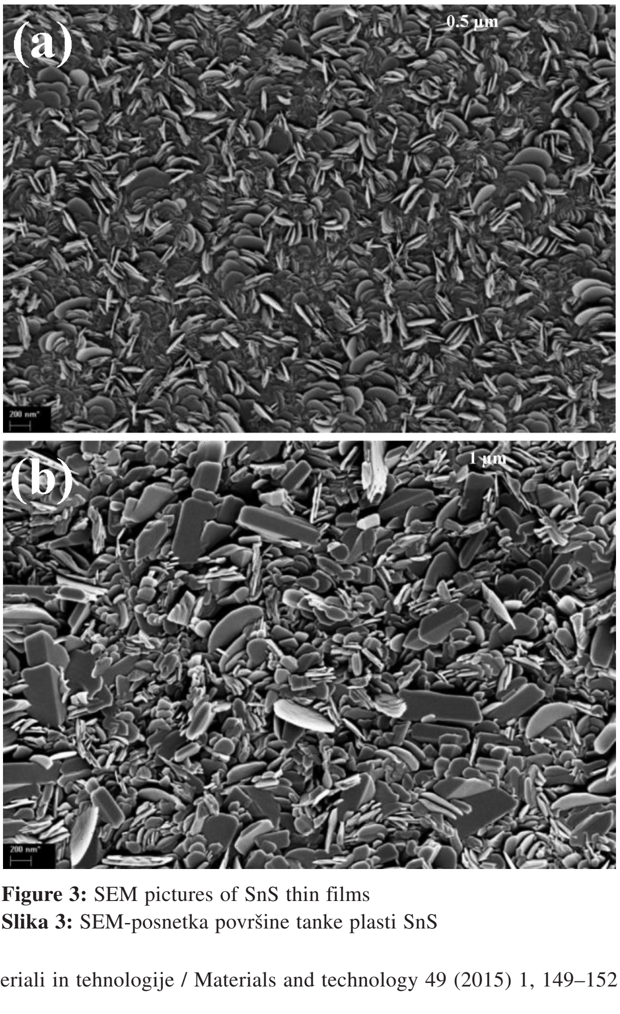

Figure 3: SEM pictures of SnS thin films
Slika 3: SEM-posnetka površine tanke plasti SnS

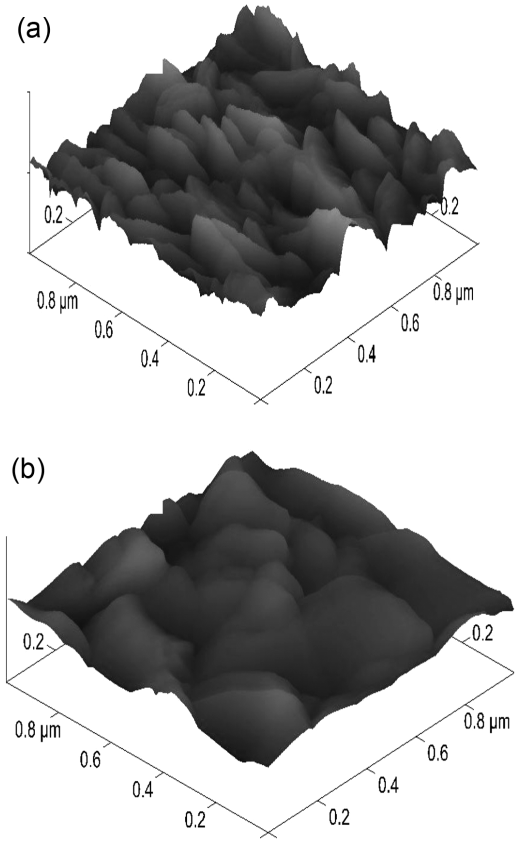

Figure 4: AFM images of SnS films of: a) 0.5 µm and b) 1 µm
Slika 4: AFM-posnetka plasti SnS: a) 0,5 µm in b) 1 µm

and 220) cm^{-1} can be attributed to the orthorhombic SnS. The Raman modes observed at (96, 192 and 220) cm^{-1} belong to the A_g mode whereas the band line at 163 cm^{-1} can be ascribed to the B_2g mode.[14] The spectra do not indicate the presence of traces of SnS_2 or Sn_2S_3 phases in the films.

The HR-SEM images of the SnS thin films deposited at the thicknesses of 0.5 µm and 1 µm are presented in **Figure 3**. The surfaces of the films are composed of densely packed flake-like particles with the average diameters of about 179 nm and 429 nm for the thicknesses of 500 nm and 1 µm, respectively.

Figure 4 shows the AFM micrographs of the SnS thin films that were scanned over an area of 1 µm × 1 µm. It is clear from the images that the thinner films (500 nm) have smoother surfaces compared to the thicker films (1 µm). The root-mean-square roughness (R_q) and the mean-value roughness (R_a) for the film with the 500 nm thickness are 20.6 nm and 16.7 nm, whereas for the thicker film (1 µm) the values of R_q and R_a are about 25.8 nm and 20.3 nm, respectively. The average grain size of the as-deposited SnS films increased from 24 nm to 60 nm with the increase in the film thickness.

Figure 5 shows the photocurrent response of the SnS thin films, taken under illumination in the background electrolyte. The photocurrent was found to be increased towards the negative region of the applied potential, confirming that the films exhibit the p-type electroconductivity. The results indicate that the best photosensitivity was obtained with the SnS absorber layer with a thickness of 1 µm.

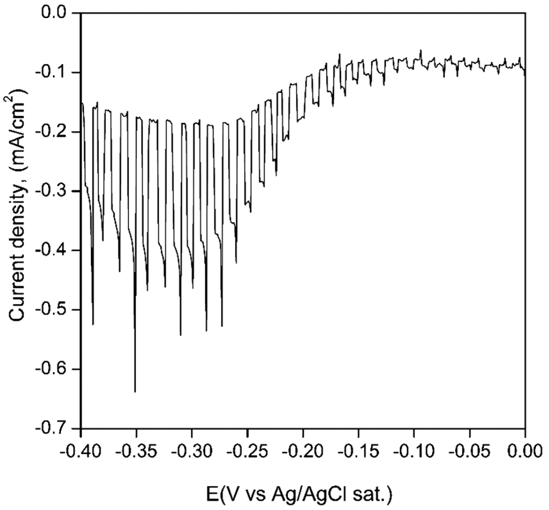

Figure 5: PEC measurements of a SnS film deposited with a thickness of 1 µm
Slika 5: PEC-meritev nanesene plasti SnS z debelino 1 µm

The above studies revealed that the SnS thin films deposited at a thickness of 1 µm showed a larger crystallite size of 58.9 nm with a surface roughness of 25.8 nm and a high photosensitivity. These results are promising for the fabrication of complete solar-cell structures based on a SnS photo-absorber.

4 CONCLUSIONS

Thin films of SnS were successfully deposited onto a Mo-coated soda-lime-glass substrate using the HVE technique with two different thicknesses of 500 nm and 1 µm. The XRD and Raman analysis showed that the films have a single-phase SnS orthorhombic crystal structure without any other binary traces of SnS_2, Sn_2S_3, etc. The layers deposited with a thickness of 1 µm compared with the layers with a thickness of 0.5 µm show an improved crystallinity, a uniform and densely packed surface morphology and a high surface roughness. They exhibit the p-type conductivity and high photosensitivity. Therefore, the prepared SnS photo-absorber layers could be applied in complete solar-cell structures.

Acknowledgements

Estonian Centre of Excellence in Research Project TK117T "High-technology Materials for Sustainable Development", Estonian Energy Technology Program (project AR 10128), Estonian Ministry of Higher Education and Science (targeted project T099) and Estonian Science Foundation (MJD213, G8147) are acknowledged for the financing of the research.

5 REFERENCES

[1] B. Gosh, M. Das, P. Banerjee, S. Das, Semicond. Sci. Technol., 24 (**2009**) 2, 025024

[2] J. Vidal, S. Lany, M. d'Avezac, A. Zunger, A. Zakutayev, J. Francis, J. Tate, Appl. Phys. Lett., 100 (**2012**) 3, 032104

[3] G. H. Yuea, W. Wanga, L. S. Wanga, X. Wanga, P. X. Yanb, Y. Chena, D. L. Peng, J. Alloy Compd., 474 (**2009**) 1–2, 445–449

[4] G. Valiukonis, D. A. Guseinova, G. Krivaite, A. Sileica, Phys. Stat. Sol. B, 135 (**1986**), 299–307

[5] A. Ortiz, J. C. Alonso, M. Garcia, J. Toriz, Semicond. Sci. Technol., 11 (**1996**) 2, 243–247

[6] N. Koteswara Reddy, K. T. Ramakrishna Reddy, G. Fisher, R. Best, P. K. Dutta, J. Phys. D: Appl. Phys., 32 (**1999**) 9, 988–990

[7] P. Sinsermsuksakul, L. Sun, S. W. Lee, H. H. Park, S. B. Kim, C. Yang, R. G. Gordon, Adv. Energy Mater., 4 (**2014**) 15, 1400496

[8] ZSW sets 21.7 % thin film efficiency record: http://www.pv-magazine.com/news/details/beitrag/zsw-sets-217-thin-film-efficiency-record_100016505/#axzz3OhYBRNbe (accessed 22 September 2014)

[9] W. Wang, M. T. Winkler, O. Gunawan, T. Gokmen, T. K. Todorov, Y. Zhu, D. B. Mitzi, Adv. Energy Mater., 4 (**2014**) 7, 1301465

[10] W. G. Pu, Z. Z. Lin, Z. W. Ming, G. X. Hong, C. W. Qun, H. Tanamura, M. Yamaguchi, H. Noguchi, T. Nagatomo, O. Omoto, 24th IEEE PV Specialists Conference, 1 (**1994**), 365–368

[11] B. E. Warren, X-ray Diffraction, Reprint, Dover Publications, Inc., New York 1990, 253

[12] E. R. Shaaban, M. S. Abd El-Sadek, M. El. Hagary, I. S. Yahia, Phys. Scr., 86 (**2012**) 1, 015702

[13] K. Santhosh Kumar, C. Manoharan, L. Amalraj, S. Dhanapandian, G. Kiruthigaa, K. Vijayakumar, Cryst. Res. Technol., 47 (**2012**) 7, 771–779

[14] P. M. Nikolic, Lj. Miljkovic, P. Mihajlovic, B. Lavrencic, J. Phys. C: Solid State Phys., 10 (**1977**) 11, L289–L292

UDK 669.14.018.8:658.567.1:620.172
Professional article/Strokovni članek

ISSN 1580-2949
MTAEC9, 49(1)153(2015)

MECHANICAL PROPERTIES OF THE AUSTENITIC STAINLESS STEEL X15CrNiSi20-12 AFTER RECYCLING

MEHANSKE LASTNOSTI AVSTENITNEGA NERJAVNEGA JEKLA X15CrNiSi20-12 PO RECIKLIRANJU

Alen Delić[1], Omer Kablar[2], Almir Zulić[1], Džemal Kovačević[1], Nusmir Hodžić[1], Enis Barčić[1]

[1]CIMOS TMD Automobilska industrija, d. o. o., Sarajevska 62, Gradačac, Bosnia and Herzegovina
[2]ArcelorMittal Zenica, Steel Plant Department, Bulevar Kralja Tvrtka I, no. 17, Zenica, Bosnia and Herzegovina
alen.delic@cimos.eu

Prejem rokopisa – received: 2013-11-21; sprejem za objavo – accepted for publication: 2014-03-28

X15CrNiSi20-12 is a steel that has excellent resistance to corrosion and heat as well as good strength at room and elevated temperatures. According to EN 10095, the forged steel is used for products resistant to hot gases and combustion products at temperatures above 550 °C. As annealed, the steel is nonmagnetic, but becomes slightly magnetic after cold working. Typical uses include furnace parts, heating elements, aircraft and jet-engine parts, heat exchangers, carburizing and annealing boxes, sulfite liquor-handling equipment, kiln liners, boiler baffles, refinery and chemical processing equipment, and auto-exhaust parts.

The influence of re-melted back (waste) materials on the quality of X15CrNiSi20-12 steel was determined for re-melted (MM) and re-alloyed (AM) material with tensile strength tests using two standard test specimens at room temperature and 740 °C. The tensile properties were used for the analysis and a comparison of the features in order to obtain suitable material for recycling.

Keywords: austenitic stainless steel, mechanical properties, re-alloying, recycling

Jeklo X15CrNiSi20-12 je toplotno obstojno, z odlično odpornostjo proti koroziji in visoki temperaturi ter z dobro trdnostjo pri sobni in pri povišanih temperaturah. Skladno s standardom EN 10095 se jeklo uporablja za odkovke, ki so odporni proti vročim plinom in produktom zgorevanja pri temperaturah nad 550 °C. Žarjeno jeklo je nemagnetno in pri hladni predelavi postane rahlo magnetno. Značilna uporaba je za dele peči, grelne elemente, letalstvo in dele reaktivnih motorjev, za toplotne izmenjevalce, škatle za naogljičenje in žarjenje, za opremo, ki pride v stik z raztopino sulfita, vodila v ogrevnih pečeh, za špirale kotlov, v rafinerijah, v opremi kemijske procesne industrije in za dele avtomobilskih izpušnih sistemov.

Vpliv pretaljevanja odpadkov materiala na kvaliteto jekla X15CrNiSi20-12 je bil določen na pretaljenem (MM) in na dodatno legiranem (AM) materialu z nateznim preizkusom materiala z navadnimi vzorci za natezne preizkuse pri sobni temperaturi in pri 740 °C. Natezne lastnosti so bile uporabljene za analizo in za določitev, kakšen material je primeren za recikliranje.

Ključne besede: avstenitno nerjavno jeklo, mehanske lastnosti, ponovno legiranje, recikliranje

1 INTRODUCTION

X15CrNiSi20-12 steel is resistant to corrosion and is generally considered to be a fire-proof alloy, with the temperature for the destructive loss of weight being about 1093 °C. The standard EN 10095 lists the requirements for the chemical composition of the austenitic stainless steel X15CrNiSi20-12. **Table 1** shows the chemical composition of the raw material (RM), the re-melted material without re-alloying (MM) and the material with re-alloying (AM).[1] The examinations were performed with a SPECTRO LAB LAVM10 metal analyzer.

1.1 Mechanical and working properties

The basic requirements for these steels involve their applications at elevated temperatures and at higher loads. The X15CrNiSi20-12 steel has a stable austenitic microstructure and it can be used up to 1000 °C. The occurrence of undesirable δ-ferrite is possible only in exceptional cases, when the contents of the elements that stabilize the ferrite are at the upper limit of the allowable content, with a low content of austenite-stabilizing elements that stabilize the austenite, especially in the case of low contents of carbon and nitrogen[2].

Table 1: Chemical composition of the X15CrNiSi20-12 steel according to EN 10095[1]
Tabela 1: Kemijska sestava jekla X15CrNiSi20-12 skladno z EN 100095[1]

Material condition	Chemical composition (mass fractions, w/%)							
	C	Mn	Si	Cr	Ni	N	P	S
EN 10095	<0.20	<2.00	1.5–2.5	19–21	11–13	<0.11	<0.04	<0.030
Raw – RM	0.149	1.89	1.53	19.33	11.39	0.061	0.028	0.002
Remelted – MM	0.130	1.59	1.34	19.30	11.44	0.065	0.029	0.013
Realloyed – AM	0.133	1.76	1.50	19.28	11.34	0.066	0.030	0.020

Austenitic steels show very good ductility and large elongations at low temperatures. Furthermore, the tensile strength is significantly increased at low temperatures. These properties make austenitic steels suitable for use at low temperatures. However, when increasing the temperature the strength properties are decreased. The influence of delta ferrite can also not be ignored, as it increases the tensile strength and also the dispersion-hardening mechanism that increases the yield strength[3].

Table 2 lists the basic mechanical properties according to the EN 10095 standard.

Table 2: Mechanical properties of the austenitic stainless steel X15CrNiSi20-12[1]
Tabela 2: Mehanske lastnosti avstenitnega nerjavnega jekla X15CrNiSi20-12[1]

Yield strength $R_{p0.2}$ /MPa	> 230
Yield strength $R_{p1.0}$ /MPa	> 270
Tensile strength R_m/MPa	500–750
Elongation A/%)	> 28
Hardness, HB	< 223

2 EXPERIMENTAL

2.1 Tensile properties at 20 °C and 740 °C

The tensile strength of the re-melted (MM) and re-alloyed (AM) steel after annealing was determined at room temperature and at 740 °C. The results showed that the tensile properties of both melts are uniform and within standard limits[4]. A metallographic analysis showed an austenitic microstructure with carbide precipitates at the grain boundaries. In the re-melted steel (MM) the grains are coarser due to the longer holding time at the quenching temperature[5]. The hardness testing was carried at room temperature and the results are given in **Table 3**.

Figure 1 provides a graphical representation of the tensile strength at room temperature and at 740 °C and the values prescribed in the standard EN 10095 for room temperature. The tensile properties at 740 °C are not prescribed by this standard.

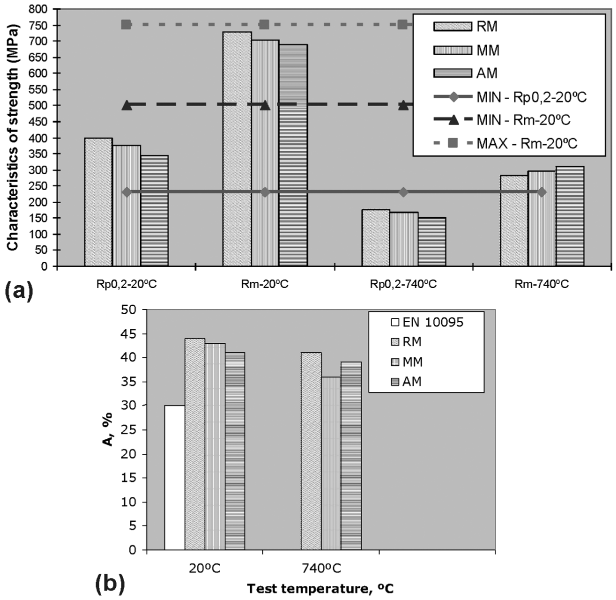

Figure 1: Tensile tests at temperatures of 20 °C and 740 °C: a) $R_{p0.2}$, R_m, b) A
Slika 1: Natezni preizkusi pri temperaturah 20 °C in 740 °C: a) $R_{p0.2}$, R_m, b) A

The test results show that all the tensile strengths at 20 °C are within the limit values of the EN 10095 standard. The tensile strengths of the raw and re-melted steel are similar and close to the maximum prescribed in the standard[6]. The highest strength was obtained for the raw steel (RM) 730 MPa, followed by the re-melted steel (MM) 703 MPa, and the lowest value of 689 MPa for the re-alloyed steel (AM) (**Figure 2**).

The tensile strength at the test temperature of 740 °C shows a reverse trend, from 281 MPa for the raw steel, followed by the re-melted steel without re-alloying at 297 MPa, and finally for the re-alloyed steel a value of 311 MPa. The elongation shows the same behavior as the tensile strength for all three steels. The highest value of 44 % was for the raw steel, for the re-melted steel with-

Table 3: Results of the tensile tests at temperatures of 20 °C and 740 °C
Tabela 3: Rezultati nateznih preizkusov pri temperaturah 20 °C in 740 °C

Steel condition X15CrNiSi20-12	20 °C				740 °C		
	$R_{p0.2}$/MPa	R_m/MPa	A/%	HB	$R_{p0.2}$/MPa	R_m/MPa	A/%
EN 10095	> 230	500–750	> 28	< 223	–	–	–
Raw – RM	400	730	44	194	177	281	41
Remelted – MM	376	703	43	190	168	297	36
Realloyed – AM	345	689	41	180	150	311	39

Table 4: Tensile properties at 20 °C for the melted and re-alloyed steel, cast and annealed
Tabela 4: Lastnosti pri nateznem preizkusu pri 20 °C za staljeno in ponovno legirano jeklo, ulito in žarjeno

Steel condition X15CrNiSi20-12	Remelted steel - MM			Realloyed steel - AM		
	$R_{p0.2}$/MPa	R_m/MPa	A/%	$R_{p0.2}$/MPa	R_m/MPa	A/%
Casted	628	813	28	367	696	42
Annealed	403	717	41	346	691	38

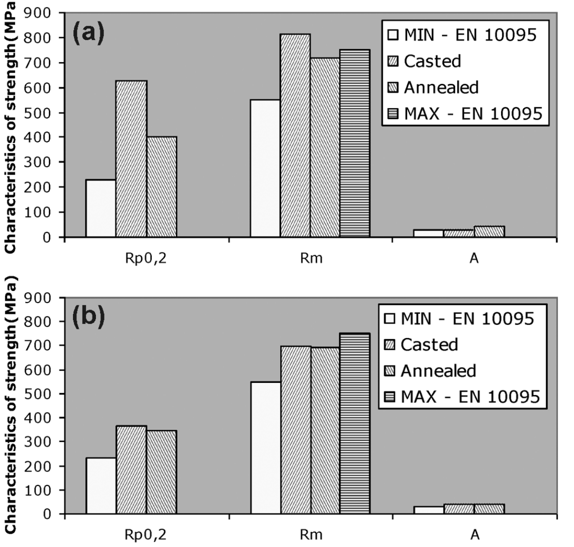

Figure 2: Results of tensile tests at 20 °C in the as-cast and annealed conditions for: a) re-melted and b) re-alloyed steel

Slika 2: Rezultati nateznih preizkusov pri temperaturi 20 °C v litem in žarjenem stanju za: a) pretaljeno in b) ponovno legirano jeklo

out re-alloying the value was 43 % and for the re-melted and re-alloyed steel it is 41 %. The elongation at 740 °C is above the prescribed value for room temperature and it is not prescribed in the standard.

Figure 2 shows the results of tensile tests for the re-melted and re-alloyed steel, cast and annealed, and in **Table 4** are the results of the tensile tests for the cast and annealed, re-melted and re-alloyed steel.

A comparison of the results in **Table 4** indicates that the properties of the re-melted (MM) and the re-alloyed (AM) steel are reduced after annealing and are much closer and more balanced than the re-alloyed steel. The thermal annealing treatment was performed to obtain the same conditions as were present for the raw steel.

The hardness values are the values prescribed by the standard for all steels and the maximum hardness is 223 HB. The hardness of the steel is the highest for raw steel, HB 194, for the re-melted steel it is 190 HB, and it is the lowest value, 180 HB, for the re-melted and re-alloyed steel.

2.2 Metallographic analysis

The microstructure was examined with a light microscope, OLYMPUS, BX60M, according to ASTM E 407[7]. **Figure 3** shows the microstructure of the raw steel (RM), the re-melted (MM) and the re-alloyed steel (AM) after quenching with a magnification of 100-times and 500-times is shown after etching with the Kalling reagent[8].

For all three steels the microstructure consists of an austenitic base and carbide precipitates in the interior and boundaries of the austenite grains. **Figure 3** reveals the difference in the amount of carbides. In the re-alloyed material a certain amount of carbides are inside the grains. This may be regarded as a consequence of the cooling rate. Considering the location and the size of the carbide it is assumed that these are complex chromium carbides[9]. The composition of complex chromium carbides can be found in a number of references.

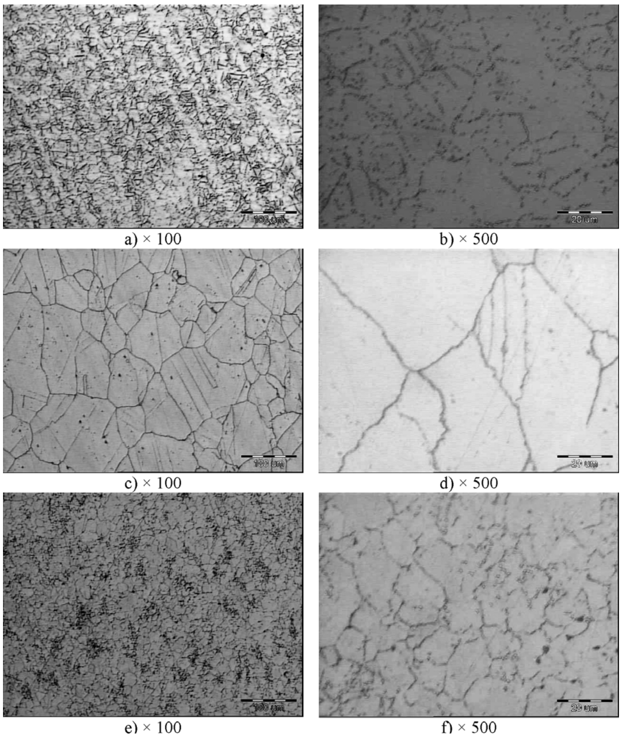
a) × 100
b) × 500
c) × 100
d) × 500
e) × 100
f) × 500

Figure 3: Microstructure of: a), b) the raw steel (RM), c), d) re-melted steel (MM) and e), f) re-alloyed steel (AM)

Slika 3: Mikrostruktura: a), b) jeklo (RM), c), d) pretaljeno jeklo (MM), e), f) dolegirano jeklo (AM)

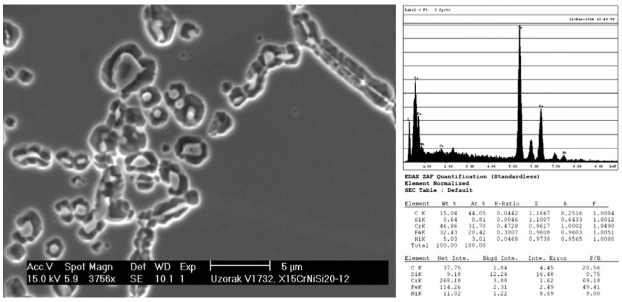

```
EDAX ZAF Quantification (Standardless)
Element Normalized
SEC Table : Default

Element   Wt %    At %    K-Ratio    Z       A       F
  C K     15.04   44.05   0.0442   1.1667  0.2516  1.0004
  SiK      0.64    0.81   0.0046   1.1007  0.6433  1.0012
  CrK     46.86   31.70   0.4728   0.9617  1.0002  1.0490
  FeK     32.43   20.42   0.3007   0.9608  0.9603  1.0051
  NiK      5.03    3.01   0.0468   0.9738  0.9565  1.0000
 Total   100.00  100.00

Element  Net Inte.   Bkgd Inte.   Inte. Error    P/B
 C K       37.75        1.84         4.45        20.56
 SiK        9.18       12.24        16.48         0.75
 CrK      268.18        3.88         1.62        69.18
 FeK      114.26        2.31         2.49        49.41
 NiK       11.02        1.22         8.69         9.00
```

Figure 4: EDS analysis of carbides in re-alloyed steel (AM)

Slika 4: EDS-analiza karbidov v dolegiranem jeklu (AM)

The examinations were performed with a Philips XL-30 Scanning Electron Microscope. **Figure 4** shows the analysis of the carbides in the re-alloyed steel. **Figure 4** shows the results of the EDS analysis of the carbides in the re-alloyed steel that confirms the presence of chromium carbides.

3 CONCLUSIONS

Based on an analysis of the literature data and the conducted experimental studies, as well as the results of laboratory tests, the possibility of recycling the revert scrap of the austenitic stainless steel X15CrNiSi20–12 was investigated.

Re-melted (MM) steel and re-melted steel with re-alloying (AM) were processed into square rods of 36 mm, and quenched to obtain the same condition and dimensions as the raw steel (RM). The tensile properties and microstructure of both melts X15CrNiSi20-12 were examined with forging and rolling deformation and subsequent heat treatment of the experimental melts, approximately equal raw steels were obtained and then used for comparative laboratory tests. All the technical parameters of the heating, deformation and heat treatment were fixed.

The mechanical properties were tested at room and elevated temperatures. The mechanical properties at room temperature show that the tensile strength of raw steel (RM), of re-melted steel (MM) and of (AM) are fairly uniform and are close to the upper prescribed limit of 750 MPa in the standard EN 10095. The highest strength is obtained for the raw steel (RM), then the re-melted steel (MM) and the lowest value of 689 MPa for the re-melted and re-alloyed steel (AM). The same trend of results is present for the yield stress $R_{p0.2}$ and the elongation. At elevated temperatures the strength shows the opposite trend, with the maximum value of 311 MPa for re-melted and re-alloyed steel (AM) and for the raw steel (RM) a value of 281 MPa. For the yield stress $R_{p0.2}$ the trend is reversed with the largest value of 177 MPa for the (RM) to a minimum of 150 MPa for the AM. The high tensile properties are due to the austenitic structure and the carbide precipitates at the austenite grain boundaries.

The experimental results show that with the recycling process for X15CrNiSi20-12 steel it is possible to obtain the steel properties required by the standard EN 10095. The obtained results can be used with recycling technology in industrial conditions. The proper recycling process can ensure competitive products by the use of an accurate regime of re-melting, processing and heat treatment.

4 REFERENCES

[1] EN 10095 Standard, Heat resisting steels and nickel alloys, 1999

[2] F. Rakoski, Nichtmetallische Einschlüsse in Stählen, Stahl und Eisen, 114 (**1994**) 7, 71–76

[3] A. Gigović - Gekić, Kvantifikacija uticaja alfa-gama obrazujućih elemenata na mehaničke osobine i pojavu delta ferita kod nehrđajućeg austenitnog čelika NITRONIC 60, Doktorska disertacija, Fakultet za metalurgiju i čelike, Univerzitet u Zenici, 2010

[4] M. Oruč, M. Rimac, O. Beganović, A. Delić, New Materials as Base for Development of Modern Industrial Technologies, 13th Inernational Research/Expert Conference Trends in the Development of Machinery and Associated Technology, TMT 2009, Hammamet, Tunisia, 2009

[5] J. D. Verhoeven, Metallurgy of Steel for Bladesmiths & Others who Heat Treat and Forge Steel, Iowa State University, 2005, 66–68

[6] M. Torkar, M. Lamut, A. Millaku, Recycling of steel chips, Mater. Tehnol., 44 (**2010**) 5, 289–292

[7] ASTM E 407 Standard, Standard Practice for Microetching Metals and Alloys, 2007

[8] H. Šuman, Metalografija, Tehnološko metalurški fakultet, Univerzitet u Beogradu, Beograd, 1989

[9] H. K. D. H. Bhadeshia, R. W. K. Honeycombe, Steels Microstructure and Properties, Third Edition, Elsevier Ltd, 2006, 264–266

UDK 621.74.045:666.76
Professional article/Strokovni članek

ISSN 1580-2949
MTAEC9, 49(1)157(2015)

COMPARISON OF REFRACTORY COATINGS BASED ON TALC, CORDIERITE, ZIRCON AND MULLITE FILLERS FOR LOST-FOAM CASTING

PRIMERJAVA OGNJEVZDRŽNIH PREMAZOV NA OSNOVI SMUKCA, KORDIERITA, CIRKONA IN MULITNIH POLNIL ZA ULIVANJE V FORME Z IZPARLJIVIM MODELOM

Zagorka Aćimović-Pavlović[1], Anja Terzić[2], Ljubiša Andrić[3], Marko Pavlović[1]
[1]University of Belgrade, Faculty of Technology and Metallurgy, Karnegy st. 4, 11000 Belgrade, Serbia
[2]Institute for Materials Testing, Vojvode Mišića Bl. 43, 11000 Belgrade, Serbia
[3]Institute for Technology of Nuclear and Other Raw Mineral Materials, Franchet d'Esperey 86, 11000 Belgrade, Serbia
anja.terzic@institutims.rs

Prejem rokopisa – received: 2013-12-23; sprejem za objavo – accepted for publication: 2014-01-15

This study presents the results of an investigation of high-temperature materials – refractory coatings based on different refractory fillers including talc, cordierite, zircon and mullite applied in the lost-foam casting process. Design and optimization of a coating composition with controlled rheological properties and synthesis were achieved by applying different coating components, suspension agents and fillers and by altering the coating-production procedure. A morphological and microstructural analysis of the fillers was carried out with scanning electron microscopy. An X-ray diffraction analysis was applied to determine and monitor the phase-composition changes of the refractory fillers. The particle size and shape were assessed with the PC software application package OZARIA 2.5. To assess the effects of the applications of individual refractory coatings, a detailed investigation of the structural and mechanical properties of the mouldings obtained was performed. Highlight was placed on revealing and analyzing surface and volume defects present on the mouldings. Radiographic moulding tests were carried out with an X-ray device, SAIFORT type-S200. The attained results are essential for the synthesis of the refractory coatings based on high-temperature fillers and their applications in the lost-foam casting process for manufacturing the mouldings with in-advance-set properties.

Keywords: high-temperature materials, refractory coatings, talc, cordierite, zircon, mullite, lost-foam casting

Ta študija predstavlja rezultate raziskave visokotemperaturnih materialov – ognjevzdržnih premazov na osnovi različnih ognjevzdržnih polnil, smukca, kordierita, cirkona in mulita, uporabljenih pri postopku ulivanja v forme z izparljivim modelom. Načrtovanje in optimizacija sestave premazov s kontroliranimi reološkimi lastnostmi in sintezo sta bila dosežena z uporabo različnih komponent premaza, sredstev za suspenzijo in polnil ter s spreminjanjem postopka izdelave premaza. Morfološka in mikrostrukturna analiza polnil sta bili izvršeni z vrstično elektronsko mikroskopijo. Rentgenska difrakcijska analiza je bila uporabljena za ugotavljanje in kontrolo sprememb fazne sestave ognjevzdržnih sestavin. Velikost in oblika zrn sta bili določeni s PC programskim paketom OZARIA 2.5. Za ugotovitev vpliva posameznega ognjevzdržnega premaza je bila izvršena podrobna analiza strukturnih in mehanskih lastnosti form. Pozornost je bila namenjena ugotavljanju in analizi površine ter volumenskih napak v formah. Rentgenski pregledi form so bili opravljeni z rentgensko napravo SAIFORT type-S200. Dobljeni rezultati so pomembni za sintezo ognjevzdržnih premazov na osnovi visokotemperaturnih polnil in njihovo uporabo pri postopku ulivanja z izparljivimi modeli za izdelavo form z vnaprej določenimi lastnostmi.

Ključne besede: visokotemperaturni materiali, ognjevzdržni premazi, smukec, kordierit, cirkon, mulit, ulivanje z izparljivimi modeli

1 INTRODUCTION

The most important characteristic of the lost-foam casting process is the fact that the patterns and the mould gating made of polymers remain in a cast until the liquid-metal inflow. In contact with the liquid metal the polymer is decomposed and evaporated in a relatively short time. The previously described process is accompanied by moulding crystallization[1–3]. In order to achieve a high-quality and profitable moulding production using the lost-foam method, it is necessary to reach a balance in the system involving evaporable polymer pattern – liquid metal – refractory coat – sand mould during the phases of metal inflow, decomposition and evaporation of the polymer pattern, and formation and solidification of castings (**Figure 1**).[4] This requires systematic researches of the complex appearances and processes occurring in the pattern, the metal and the cast as well as the appearances and processes in the contact zone metal involving pattern and metal – refractory coating – sand.[5–8]

Polymer decomposition is an endothermic process which starts with a liquid-metal inflow. The pattern-decomposition kinetics is the function of the liquid-metal temperature with which the polymer gets in contact. During the inflow stage, while the metal passes through the polymer pattern, 70–90 % of the products is liquid. During the process, the decomposed liquid products are being pushed towards the casting-cavity upper surface, afore the liquid-metal front. In the case of a minor permeability of the refractory coating and the sand for modelling, these liquid products of the polymer decom-

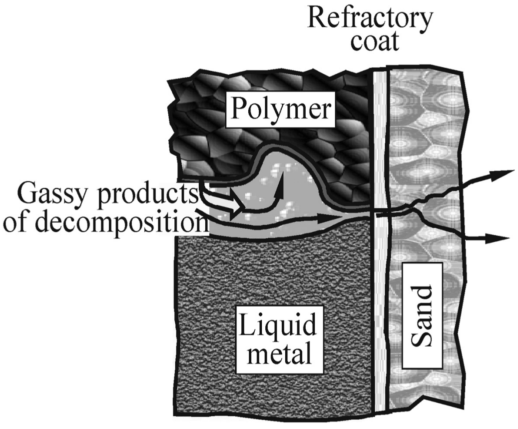

Figure 1: Lost-foam-process system balance: liquid metal – refractory coating – pattern – sand

Slika 1: Postopek z izparljivim modelom – ravnotežje sistema: talina – ognjevzdržna obloga – izparljiv model – pesek

position remain in the upper parts of the mouldings causing surface, subsurface and volume defects. A further decomposition of the liquid phase occurs due to evaporation (the creation of boiling phase layer) forming a solid residue of the polymer chain, monomer and benzene, small quantities of toluene and ethyl benzene.[9–11]

Important factors influencing the pattern decomposition and evaporation process, besides the temperature and the pattern density, are: the type and thickness of the refractory coating layer covering the evaporable polymer, the type and size of the sand grain for modelling, the respective permeability of the sand for modelling, the mouldings and the gating of the mould construction. The pattern density and permeability of the refractory coating and the sand mould determine the polymer evaporation velocity. The velocity of the liquid metal entering the mould and its contact with the pattern are controlled with a proper definition of the mould gating[12–20].

In order to obtain the mouldings of the required quality, critical process parameters should be determined for each particular polymer pattern, as well as the type of the alloy for casting. This requires long-lasting researches aimed to achieve the optimization of the lost-foam casting process and to obtain the mouldings with previously specified properties. In order to correctly understand the optimization of the lost-foam casting process, it is necessary to know the various types of moulds and their properties[21–28]. Beside this necessity to obtain the mouldings with the previously specified properties, the fundamental structure dependence on the technology should also be determined by applying the control of the critical process parameters and the control of the useful moulding properties. Thus, in this work a special consideration was dedicated to this correlation.

Figure 2: Lost-foam-process phases: a) coating-excess removal from the pattern and layer equalizing on the pattern surface, b) coating-layer drying, c) staged probe prepared for casting, d) easy coating removal from the casts

Slika 2: Faze postopka ulivanja z izparljivim modelom: a) odstranjevanje odvečnega premaza iz modela in izenačenje nanosov na površini modela, b) sušenje plasti nanosa, c) forma, pripravljena za ulivanje, d) enostavna odstranitev premaza iz ulitka

Table 1: Compositions of the refractory-coating series A, B, C and D

Tabela 1: Sestava ognjevzdržnih premazov vrste A, B, C in D

Coat type	Refractory filler		Bonding agent	Coating maintenance material	Solvent for the coating density, 2 g/cm^3
	Granulation, µm	Quantity, %			
A	talc		bentonite 3.5–5 % bindal H 8 %	dextrin 0.3–0.5 % lucel 0.3–0.5 %	water
	30–35	85–88			
B	cordierite		bentonite 1–3 % bindal H 5–7 %	dextrin 0.5 % lucel 0.5 %	water
	35–40	88–90			
C	zircon		sodium silicate (water glass) 2–4 %	dextrin 0.5 % lucel 0.5 %	water
	35–40	90–95			
D	mullite		bentonite 4 % bindal H 2–4 %	dextrin 0.5 % lucel 0.5 %	water
	40–45	88–90			

2 MATERIALS AND METHODS

Four series of experiments were carried out to analyze the possibilities of applying the refractory coatings based on talc (series mark A), cordierite (series mark B), zircon (series mark C) and mullite (series mark D) (**Table 1**) and the methods for preparing the coating components were determined. The grinding of the refractory fillers including talc, cordierite, zircon and mullite was conducted in a mill with the balls of Cr-Ni steel (the Retsch-PM4 type), with a capacity of 20 kg/h, a mill load of 70 % and the grinding time of 45–60 min.

Refractory talc, cordierite, zircon and mullite powders used for both the coating production and the application in the lost-foam casting process depend crucially on the rheological coating quality and the sedimentary coating stability. Both, the coating compositions and their preparation procedures were altered to achieve the specified coating properties. While applying a refractory coating on the polymer pattern with the techniques of immersion into the tank containing the coating, overflowing and coating with a brush, a special attention was given to the coating quality control. The basic criteria for the quality evaluation of this type of refractory products were: the pertinence of the application, the drying behaviour, the resistance to attrition, the sedimentation and the penetration.

The experimental parameters of the lost-foam casting process (the selection of the composition and preparation of the refractory coats) were determined as presented in **Table 2**.

The lost-foam-process phases are showed in **Figure 2**.

Table 3 shows the process parameters for all the series of the refractory-coating production, the methods of the coating application on the patterns and drying.

3 RESULTS AND DISCUSSION

In **Figures 3** to **6** the results of the XRD phase analysis of samples A to D are presented. The results of XRD show that talc is dominant in sample A (**Figure 3**)[29], cordierite is dominant in sample B where spinel and

Table 2: Experimental parameters of the lost-foam casting process
Tabela 2: Eksperimentalni parametri postopka ulivanja z izparljivim modelom

Parameter	Parameter description
Tested alloy	AlSi10Mg
Preparation methods for the liquid die	-refinement with the compounds of NaCl and KCl with a quantity of 0.1 % of the die mass; -degasification with briquette C_2Cl_6 with a quantity of 0.3 % of the die mass; -modification with sodium with a quantity of 0.05 %.
Casting temperature (°C)	735; 760; 795
Evaporable polystyrene pattern	-density (kg/m^3): 20; 25 -pattern construction: a plate of 200 mm × 50 mm × 20 mm and a staged probe with different wall-thickness values (mm): 10; 20; 30; 40; 50 -polystyrene grain size of 1–1.5 mm
Mounting pattern for the casting	a cluster of four pattern plates set on the central runner gate and a cluster of two staged probes set on the central runner gate
Gating of the moulds	-central runner gate of 40 mm × 40 mm × 400 mm -ingates of 20 mm × 20 mm × 10 mm, 2 pieces
Dry quartz sand for the cast production	Grain size (mm): 0.17; 0.26; 0.35

Table 3: Optimum process parameters of the production and preparation of the coating, the lining and coat drying on polystyrene patterns
Tabela 3: Optimalni procesni parametri pri izdelavi premaza, podlage in sušenju premaza na polistirenskem modelu

Parameter	Parameter description
Coat density	2 g/cm^3
Coat temperature	25 °C
Removing the coat excess from the pattern after pulling it out of the tank for lining	the coat is being seeped for 5–10 s while the pattern is in the vertical position and then kept for 5 s at an angle of 45° in order for the coat layers on the pattern surface to become even
Slow mixing of the coat in the tank while applying the coat on the pattern	- velocity of 1 r/min
Methods of applying the coat on the pattern	-cluster immersion into the tank with the coating - overflowing -coating with a brush
Drying	- first layer for 1.5 h - final layer for 24 h
Thickness of the coat layer on the pattern after drying (mm)	0.5; 1; 1.5

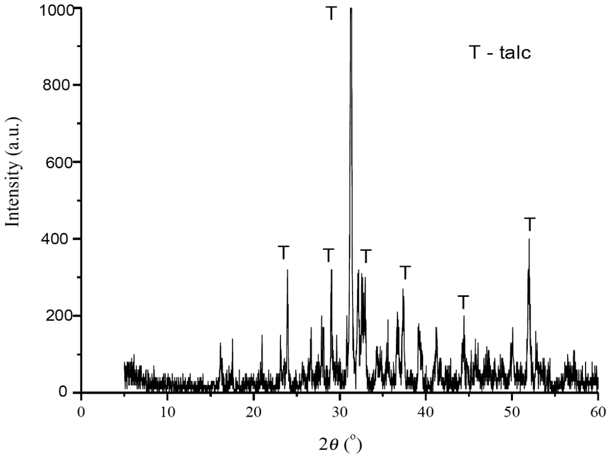

Figure 3: Diffractogram of the filler based on talc
Slika 3: Difraktogram polnila na osnovi smukca

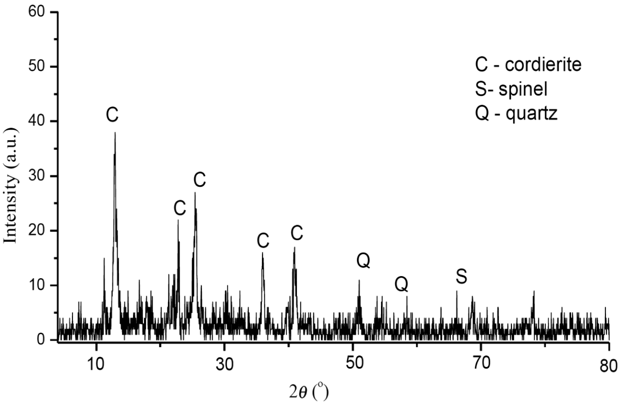

Figure 4: Diffractogram of the filler based on cordierite
Slika 4: Difraktogram polnila na osnovi kordierita

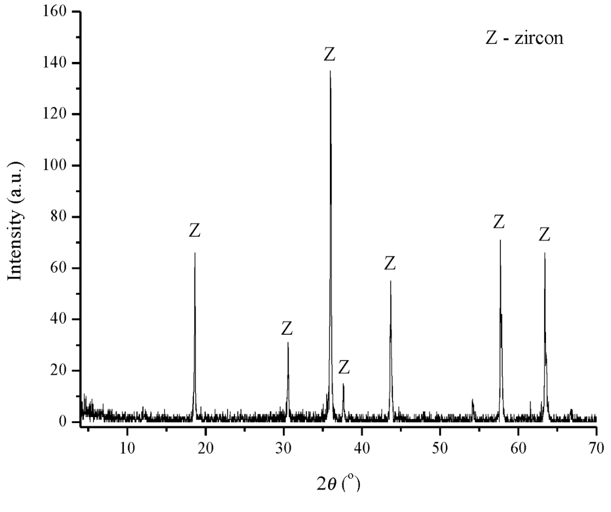

Figure 5: Diffractogram of the filler based on zircon
Slika 5: Difraktogram polnila na osnovi cirkona

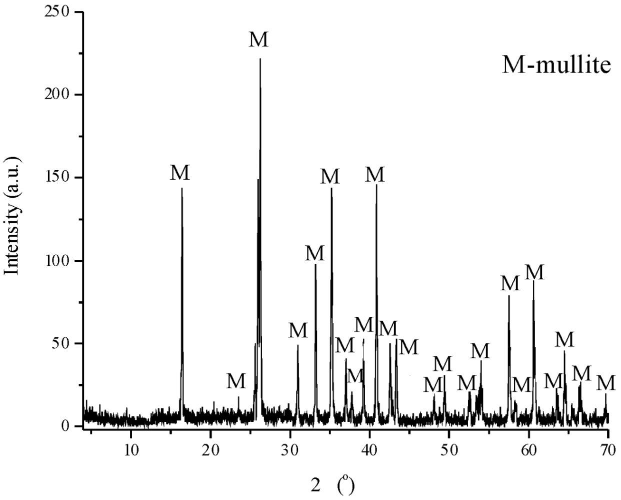

Figure 6: Diffractogram of the filler based on mullite[30]
Slika 6: Difraktogram polnila na osnovi mulita[30]

quartz are also present (**Figure 4**), zircon is dominant in sample C (**Figure 5**) and mullite is dominant in sample D (**Figure 6**)[30].

Figures 7 and **8** show the diagrams of the grain-size and grain-shape factors of samples A to D. The mean grain size of the refractory filler is between 35–40 μm and the mean grain-shape factor is 0.63–0.75, which means that the grains are elongated rounds (the shape factor of 0 corresponds to the needle shape and the factor of 1 corresponds to the circle). SEM microphotographs show that grains are in fact irregularly shaped with a large number of angles that strengthen the locking of the particles in the coating mixture and are preferable for obtaining a homogeneous coating mixture. This conclusion is in accordance with the previous investigations[22,23] emphasizing the fact that the filler particle size and shape are crucial for the quality of casting coatings. The conditions of the filler particle size, shape and surface depend on the type of the mill. The roughness of the surfaces of filler particles may cause an increased absorp-

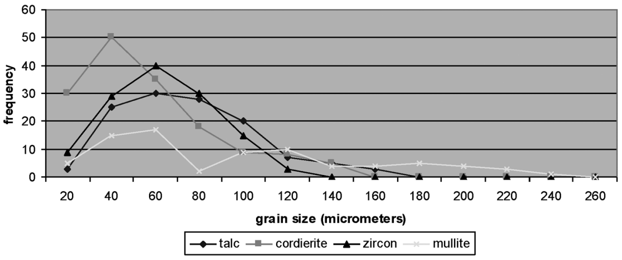

Figure 7: Histogram of the grain sizes of samples A to D
Slika 7: Razporeditev velikosti zrn vzorcev od A do D

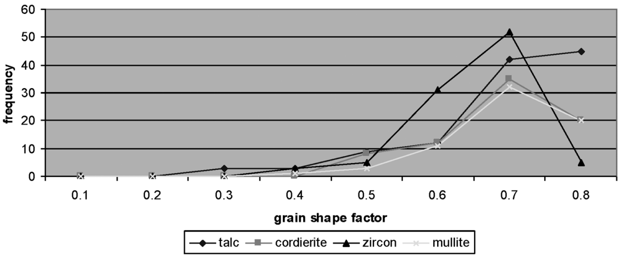

Figure 8: Histogram of the grain-shape factors of samples A to D
Slika 8: Histogram faktorja oblike zrn vzorcev od A do D

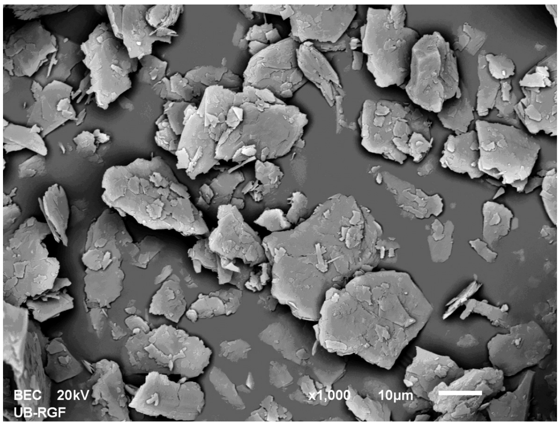

Figure 9: Microphotograph of the refractory filler based on talc
Slika 9: Posnetek ognjevzdržnega polnila na osnovi smukca

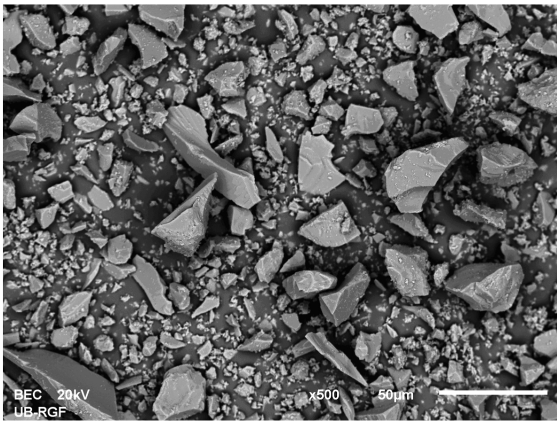

Figure 11: Microphotograph of the refractory filler based on zircon
Slika 11: Posnetek ognjevzdržnega polnila na osnovi cirkona

tion of the liquid metal onto the coating surface, which deteriorates the coating quality.

Figures 9 to **12** show the shapes of fillers A to D. The ceramic-powder particles have similar morphologies but different particle sizes. This is favourable since the particles of diverse granulations contribute to the formation of an even and continuous coating layer on the polymer pattern, due to a better harmony among the particles. For the mullite-sample preparation, a longer grinding time was required (approximately 90 min) to achieve a particle granulation of less than 40 μm. **Figure 9** shows that the talc-based filler consists of proper foliate aggregates. The morphology of the cordierite sample (**Figure 10**) shows that cordierite particles have improper forms and different sizes. The zircon-powder particles also have improper forms with a typical shell-like break and different sizes (**Figure 11**). The mullite sample (**Figure 12**) shows improper forms and different sizes of the particles. Pursuant to the previous work[31], it was showed that an application of the talc-based filler with elongated and smooth particles contributed to the production of the coatings of a higher quality, easily adherent to the patterns and not forming sintered sand faults on the mouldings. Applying the coating of zircon flour plus colloidal silica[13,17], thin coating layers with a high gas permeability were obtained, while the silica-amount increase contributed to the reduction of the metal penetration into the mould. Surveying the references, no application of cordierite as a refractory filler was recorded. Referencing earlier works[22,23], this research used different filler granulations that were proved to be appropriate for obtaining homogenous coating layers and achieving a better coating adherence to the pattern surface. Further, the bentonite quantity was reduced, i.e., the carboxymethyilcellulose (CMC) quantity increased causing a reduction in the cracks in dried coating layers, in accordance with[18,21,25].

The control of the critical process parameters for the refractory-coating production and the control of the coating properties determine that the coatings of all the series comply with the conditions for the application in the lost-foam process. It was determined that the coatings were easily applied on the polymer patterns, being evenly lined during the overflowing and immersion, were easy to be coated with a brush, without any marks of brushing, leakage, drops or clots. After drying, the coating surface was smooth; the coating layers were of equal

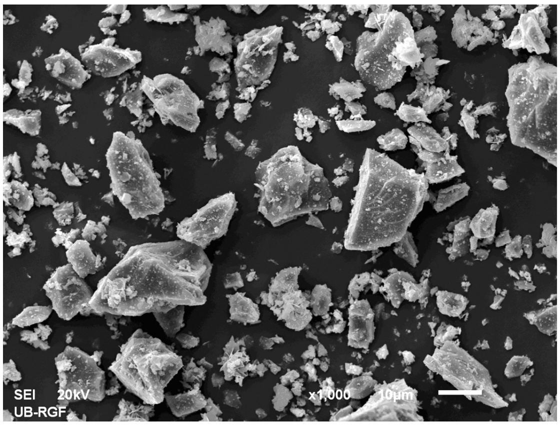

Figure 10: Microphotograph of the refractory filler based on cordierite
Slika 10: Posnetek ognjevzdržnega polnila na osnovi kordierita

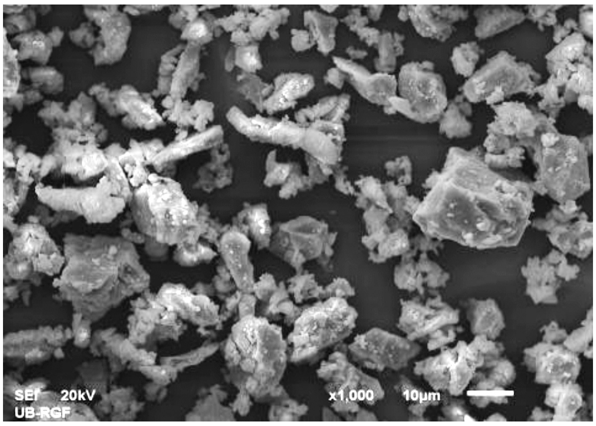

Figure 12: Microphotograph of the refractory filler based on mullite
Slika 12: Posnetek ognjevzdržnega polnila na osnovi mulita

thickness everywhere on the pattern surface, without bubbles, crazing, peelings or attrition. The coating quality and the refractory-filler homogeneity of the coating depend on the coating preparation. To achieve an even coat-layer thickness on the pattern surfaces, it is necessary to slowly and constantly mix the coating during its application on the patterns, maintaining the defined density (2 g/cm^3) and temperature (25 °C) of the coating, otherwise the coating composition becomes non-homogeneous.

In the case of applying a coating layer of a higher thickness that dried out fast, crazing and tweaking emerged on dried coating layers, having negative effects on the mould-surface quality (uneven surface, roughness, sintered sand, cracks, folds, as seen on **Figures 13a** and **13c**) and there were the risks of a liquid-metal penetration into the cast and the sinking of the cast (**Figure 13b**). The coating-layer perforation and metal penetration into the cast were also noticed on the series of the casts with the coating layers of a lower thickness (0.5 mm) on the moulding part, with a wall thickness larger than 40 mm, and applied at higher casting velocities. When the coating layers of a higher thickness were applied (above 1 mm) this fault did not emerge on the mouldings.

To observe the effects of the casting process, evaluate certain operation phases and analyse the refractory-coating influence, a visual control of the obtained mouldings was carried out, testing their structural and mechanical properties. After pulling the formed "clusters" from the mould, their surfaces are covered with a coating layer that is easy to remove so the cleaning is not necessary, which significantly reduces the production costs. The refractory coatings of all the series demonstrated positive effects on the surface quality – shiny and smooth moulding surfaces were obtained. The mouldings were true copies of the patterns (dimensionally accurate) indicating a total decomposition and evaporation of the polystyrene pattern and a satisfactory gating of the moulds. It was noticed that the lower moulding parts of all the series have flat and sharp edges, clean and shiny surfaces. In the cases of some mouldings from the series with the coating layer of a higher thickness (above 1.5 mm) the upper moulding surfaces are slightly uneven and folded, and on certain moulding parts surface roughness also appears, more often on the mouldings from the series with a pattern density greater than 20 kg/m^3.

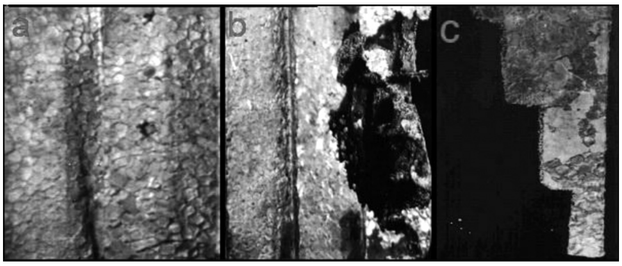

Figure 13: Defects on castings: a) casting lumpiness of the surface reproduced from the pattern, surface porosity, fold, b) metal penetration into the sand, c) sintered sand on the casting surface

Slika 13: Napake na ulitkih: a) odtis površine iz izparljivega modela, poroznost površine, guba, b) prodor taline v pesek, c) sintrani pesek na površini ulitka

The results of the investigations of the moulding structural and mechanical characteristics were within the limits predicted by the standards for this type of alloys. These included the mouldings from the series with the used polystyrene patterns of up to 20 kg/m^3, refractory coatings of a lower layer thickness, below 1 mm, quartz sand for modelling with its grain size larger than 0.26 mm, the casting temperature within the limits of 760–780 °C and the casting velocity which enabled even decomposition and evaporation of polystyrene with a complete elimination of the gassy products from the patterns, without the cast falling in or the liquid metal penetrating into the sand (**Figure 14**).

On the other hand, the mouldings from the series with the applied patterns with the densities greater than 20 kg/m^3 and the coat thickness greater than 1.5 mm exhibited subsurface and also volumetric porosity (**Figure 15**). This indicates that the reasons for these types of defects are, primarily, the polystyrene pattern, followed by the refractory coating and the high casting velocity. This is in accordance with[6,17,24,26,27] showing that a success of the lost-foam casting process may be achieved with the polymer patterns with a density of less than 20 kg/m^3 and with an application of thinner layers of refractory coatings of different compositions based on silicondioxide[31], zircon[17], talc[31], mica[26], with various components within the coating composition, an application of polysaccharide and an increased amount of CMC (1–5 %). Contrary to our research where pure components for the refractory fillers were used, the works[32,33] showed that a combination of different refractory fillers, such as zircon flour, alumina, silica, magnesite, clays, talc, chromite, mica, together with various suspension agents for the control of the system rheology, may be used to attain the significant effects of an increase in both the coating refractoriness and gas permeability. All

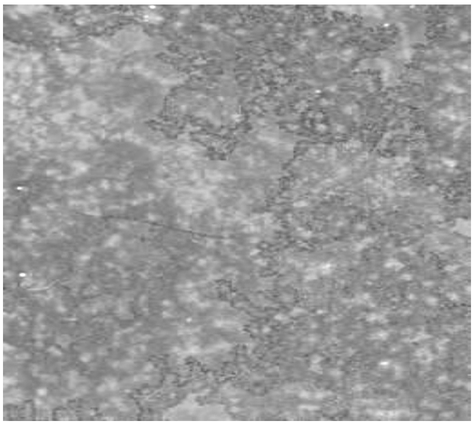

Figure 14: Characteristic sample radiogram: a casting without porosity

Slika 14: Značilen radiogram vzorca: ulitek brez poroznosti

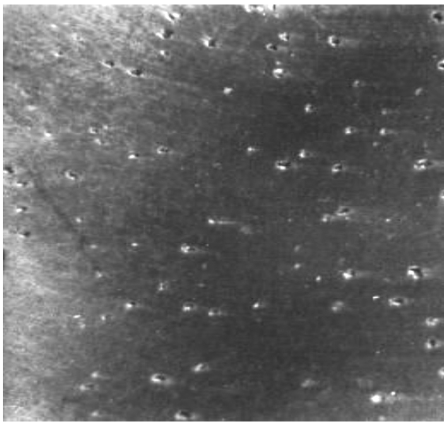

Figure 15: Characteristic sample radiogram: a casting with expressed porosity, a higher pattern density and a coating layer with a higher thickness

Slika 15: Značilen radiogram vzorca: ulitek s poroznostjo, večjo gostoto modela in večjo debelino premaza

of these contributed to achieving an increased quality of the surfaces of the lost-foam mouldings. To apply this type of coating on large and complex forms, a flow coating method was successively developed.

4 CONCLUSION

Utilization of refractory talc, cordierite, zircon and mullite powders for a coating production and application in the lost-foam casting process depends, crucially, on the rheological properties of the coatings, and, respectively, on the sedimentary coating stability. The presented research results show the optimum coating compositions and their preparation procedures with the goal of achieving positive effects on the moulding quality. Shiny and smooth moulding surfaces are obtained without detectable defects and volumetric porosity, folds, sintered sand in the series of casting with polymer patterns of a lower density, application of refractory coating layers of a lower thickness and quartz sand for the casts of a higher permeability. The achieved results of applying refractory coatings on the mullite base are the initial ones. Further studies should be done with the goal to determine the correlations between the coating composition and the layer thickness, and the moulding structural and mechanical characteristics. By developing refractory coatings on talc, cordierite, zircon and mica bases and optimizing the technological parameters of the lost-foam casting process, the mouldings with the previously defined quality, i.e., desired properties could be obtained with significantly lower costs with respect to the mouldings based on sand.

Acknowledgements

This investigation was supported and funded by the Ministry of Education, Science and Technological Development of the Republic of Serbia and Projects 33007, 172057 and 45008.

5 REFERENCES

[1] R. Monroe, Expandable Pattern Casting, AFS Inc., Des Plaines, Illinois, USA 1992, 71

[2] H. Mae, X. Teng, Y. Bai, T. Wierzbicki, Comparison of ductile fracture properties of aluminum castings: Sand mold vs. metal mold, International Journal of Solids and Structures, 45 (**2008**), 1430–1444

[3] G. W. Powell, The fractography of casting alloys, Materials Characterization, 33 (**1994**), 275–293

[4] A. Prstić, Z. Aćimović-Pavlović, M. Đurić, A. Terzić, Lj. Pavlović, Synthesis, Characterization and Application of the Filler Based on Corundum for Obtaining the Ceramic Coats in Foundry, Metalurgia International, 17 (**2012**), 83–87

[5] R. E. Moore, Refractories, Structure and Properties, Encyclopedia of Materials: Science and Technology, Pergamon Press, Oxford 2001, 8079–8099

[6] Y. Motoyama, H. Takahashi, Y. Inoue, K. Shinji, M. Yoshida, Development of a device for dynamical measurement of the load on casting and the contraction of the casting in a sand mold during cooling, Journal of Materials Processing Technology, 212 (**2012**), 1399–1405

[7] M. Daniel, K. Jarrett New, J. Dantzig, A sand surface element for efficient modeling of residual stress in castings, Applied Mathematical Modeling, 25 (**2001**), 825–842

[8] D. G. Eskin, L. Katgerman, Contraction behavior of aluminum alloys during solidification, International Foundry Research, 59 (**2007**), 8–13

[9] L. Y. Pio, S. Sulaiman, A. M. Hamouda, M. Mohamad, H. M. Ahmad, Grain refinement of LM6 Al–Si alloy sand castings to enhance mechanical properties, Journal of Materials Processing Technology, 162–163 (**2005**), 435–441

[10] D. Apelian, G. K. Sigworth, K. R. Whaler, Assessment of Grain Refinement and Modification of Al–Si Foundry Alloys by Thermal Analysis, American Foundrymen's Society, Inc., 1984, 99297–99307

[11] U. C. Nwaogu, T. Poulsen, R. K. Stage, C. Bischoff, N. S. Tiedje, New sol–gel refractory coatings on chemically-bonded sand cores for foundry applications to improve casting surface quality, Surface and Coatings Technology, 205 (**2011**), 4035–4044

[12] J. R. Brown, The Foseco Foundryman's Handbook, Pergamon Press, Oxford 2000

[13] F. L. Pirkle, D. A. Podmeyer, Zircon: Origin and Uses, Transactions, vol. 292, Society for Mining, Metallurgy and Exploration, Inc., USA 1988, 62

[14] B. Schillinger, E. Calzada, C. Eulenkamp, G. Jordan, W. W. Schmahl, Dehydration of moulding sand in simulated casting process examined with neutron radiography, Nuclear Instruments and Methods in Physics Research A, 651 (**2011**), 312–314

[15] J. L. Li, R. S. Chen, W. Ke, Microstructure and mechanical properties of Mg-Gd-Y-Zr alloy cast by metal mould and lost foam casting, Transactions of Nonferrous Metals Society of China, 21 (**2011**), 761–766

[16] A. Wróbel, E. Kulej, B. Kucharska, The Effect of Corrosion Wear on the Recorded Texture of a Clad Al-Si Coating, Archives of Metallurgy and Materials, 4 (**2011**), 897–902

[17] M. Karimian, A. Ourdjini, M. H. Idris, T. Chuan, H. Jafari, Process Control of Lost Foam Casting using Slurry Viscosity and Dipping Time, Journal of Applied Sciences, 11 (**2011**), 3655–3658

[18] W. D. Griffiths, P. J. Davies, The permeability of Lost Foam pattern coatings for Al alloy castings, Journal of Materials Science, 43 (**2008**), 5441–5447

[19] A. Charchi, M. Rezaei, S. Hossainpour, J. Shayegh, S. Falak, Numerical simulation of heat transfer and fluid flow of molten metal in MMA–St copolymer lost foam casting process, Journal of Materials Processing Technology, 210 (**2010**), 2071–2080

[20] M. Khodai, N. Parvin, Pressure measurement and some observation in lost foam casting, Journal of Materials Processing Technology, 206 (**2008**), 1–6

[21] F. W. Pursall, Coatings for Moulds and Cores, In: K. Straus (Ed.), Applied Science in the Casting of Metals, Pergamon Press, Oxford 1970

[22] Lj. Trumbulovic, Z. Acimovic-Pavlovic, Z. Gulisija, Lj. Andric, Correlation of technological parameters and quality of castings obtained by the EPC method, Materials Letters, 56 (**2004**), 1726–1731

[23] Z. Aćimović, Lj. Pavlović, Lj. Trumbulović, Lj. Andrić, M. Stamatović, Synthesis and characterization of the cordierite ceramics from nonstandard raw materials for application in foundry, Materials Letters, 57 (**2003**), 2651–2656

[24] T. Hübert, S. Svoboda, B. Oertel, Wear Resistant Alumina Coatings Produced by a Sol-Gel Process, Surface and Coatings Technology, 201 (**2006**), 487–491

[25] W. Gasior, P. Fina, Z. Moser, Modeling of the Thermodynamic Properties of Liquid Fe-Ni and Fe-Co Alloys From the Surface Tension Data, Archives of Metallurgy and Materials, 1 (**2011**), 13–23

[26] D. Gan, S. Lu, C. Song, Z. Wang, Physical Properties of Poly(ether ketone ketone)/Mica Composites: Effect of Filler Content, Materials Letters, 48 (**2001**) 5, 299–302

[27] P. L. Jain, Principle of Foundry Technology, 4th Edition, McGraw-Hill, New Delhi 2006

[28] D. A. Caulk, A foam melting model for lost foam casting of aluminum, International Journal of Heat and Mass Transfer, 49 (**2006**), 2124–2136

[29] Lj. Andrić, A. Terzić, Z. Aćimović-Pavlović, Lj. Pavlović, M. Petrov, Comparative Analysis of Process Parameters of Talc Mechanical Activation in Centrifugal and Attrition Mill, Physicochemical Problems of Mineral Processing, 50 (**2013**), 433–452

[30] Z. Aćimović, A. Terzić, Lj. Andrić, Lj. Pavlović, M. Pavlović, Synthesizing a new type of mullite lining, Mater. Tehnol., 47 (**2013**) 6, 777–780

[31] M. Yekeler, U. Ulusoy, C. Hicyilmaz, Effect of particle shape and roughness of talc mineral ground by different mills on the wettability and floatability, Powder Technology, 140 (**2004**), 68–78

[32] U. C. Nwaogu, N. S. Tiedje, Foundry Coating Technology: A Review, Materials Science and Applications, 2 (**2011**), 1143–1160

[33] D. Kascheev, N. Yu. Novozhilov, E. V. Tsarevskii, V. A. Perepelitsyn, V. A. Ryabin, N. F. Seliverstov, Refractory Coatings for Foundry Moulds and Cores, Journal of Refractories and Ceramics, 23 (**1982**), 36–139

UDK 621.791.92:539.375.6:539.92
Professional article/Strokovni članek

ISSN 1580-2949
MTAEC9, 49(1)165(2015)

SELECTION OF THE MOST APPROPRIATE WELDING TECHNOLOGY FOR HARDFACING OF BUCKET TEETH

IZBIRA NAJBOLJ PRIMERNE TEHNOLOGIJE TRDEGA NAVARJANJA ZOBA ZAJEMALKE

Vukić Lazić[1], Aleksandar Sedmak[2], Ružica R. Nikolić[1], Milan Mutavdžić[3], Srbislav Aleksandrović[1], Božidar Krstić[1], Dragan Milosavljević[1]

[1]University of Kragujevac, Faculty of Engineering, Sestre Janjić 6, 34000 Kragujevac, Serbia
[2]University of Belgrade, Faculty of Mechanical Engineering, Kraljice Marije 16, 11000 Belgrade, Serbia
[3]Company for Road Construction Kragujevac, Tanaska Rajića 16, 34000 Kragujevac, Serbia
vlazic@kg.ac.rs

Prejem rokopisa – received: 2014-01-02; sprejem za objavo – accepted for publication: 2014-01-15

A possibility of extending the service life of the working parts of construction machinery with particular attention to hardfacing of loader bucket teeth was investigated. In the first part of this paper the tribological processes typical for this machinery is analysed. Worn excavator parts are made of conditionally weldable cast steel that requires a special hardfacing technology, so numerous investigations were performed to obtain the most appropriate technology. In the experimental part of the paper, the selection of the optimum hardfacing technology for bucket teeth and the procedure of the manual arc hardfacing are presented. The samples were first hardfaced using different techniques and technologies and then the microstructure and microhardness of characteristic hardfaced layers were studied. Specially prepared samples were used for tribological investigations. The results of experimental investigations enabled the selection of the most suitable hardfacing technology and its application to real parts. The bucket teeth, with their hardfaced layers applied vertically, horizontally or in a honeycomb pattern were mounted onto a loader bucket, alternated with the new non-hardfaced teeth and their performance during the operation was regularly monitored. After a certain period, the degrees of the wear for the non-hardfaced and differently hardfaced teeth were measured. Taking into account both technical and economic factors, the most suitable hardfacing technology was determined.

Keywords: hardfacing, wear, loader bucket teeth, hardness, microstructure, friction coefficient

Izvršena je bila analiza podaljšanja zdržljivosti delov na gradbenih strojih s posebno pozornostjo na trdem navarjanju na zobeh zajemalke. V prvem delu tega članka so analizirani tribološki procesi, ki se pojavijo pri teh strojih. Pri kopačih so deli, ki se obrabljajo, izdelani iz pogojno varivega litega železa, ki zahteva posebno tehnologijo nanašanja, zato so bile izvršene številne raziskave, da bi dobili najprimernejšo tehnologijo. V eksperimentalnem delu članka je predstavljena optimalna tehnologija nanašanja trdih slojev na zobe zajemalke in predstavljen je postopek za ročno varjenje. Na vzorce so bili naneseni različni trdi sloji z različnimi tehnikami in tehnologijami in preučevane so bile mikrostrukture in mikrotrdote trdih nanosov. Preiskani so bili posebno pripravljeni vzorci za tribološke preizkuse. Rezultati eksperimentov so omogočili izbiro najprimernejše tehnologije nanašanja trdega sloja in njeno uporabo na realnih delih. Zobje zajemalke z vertikalnim, horizontalnim ali satastim nanosom trdega sloja so bili nameščeni skupaj z novimi, neobdelanimi zobmi na nakladalnik in redno je bilo spremljano njihovo vedenje med delom. Po določenem času je bila izmerjena obraba zob z različnimi nanosi in obraba neobdelanih zob. Z upoštevanjem tehničnih in ekonomskih faktorjev je bila določena najprimernejša tehnologija nanašanja trdih plasti.

Ključne besede: trdo navarjanje, obraba, zobje zajemalke nakladalnika, trdota, mikrostruktura, koeficient trenja

1 INTRODUCTION

During operation, certain parts of the road-construction machinery are exposed to different abrasive materials that cause most of the damage of the parts in direct contact with the stone aggregate causing abrasive wear. Hard and sharp-edged particles of stone materials are highly abrasive and they damage the working parts of bucket teeth.

The working parts exposed to the abrasive wear due to occasional medium-impact loads include: the bucket teeth of loaders, trenchers and excavators, the blades of concrete- and asphalt-cutting devices, the blades and rippers of bulldozers and graders, the leading rings and blades of rock-drill bits, the spindles of screw conveyors, etc. The greatest abrasive wear occurs on bucket teeth. For that reason, our experimental investigations were conducted on the loader bucket teeth.

The studies of the causes for the damage of some parts of machines and devices revealed that in more than 50 % of the cases the damage was the result of tribological processes under more or less regular operating conditions[1–6]. The damaged parts can be either replaced with new ones or, in most cases, they can be hardfaced. Both reparatory and production hardfacing reduce downtime and costs because new parts are expensive. Hardfacing is economically justified especially in the cases of large-sized parts or when there are many equal parts. However, there are occasions when reparatory hardfacing has to be performed regardless of the costs, for example, when unique machines and devices have to be repaired or no spare parts are available[7–11].

2 DAMAGE DUE TO TRIBOLOGICAL CAUSES

Wear is generally considered to be the result of friction or a combination of friction, thermal, chemical, electrochemical and other factors on the elements of a tribo-mechanical system. When studying friction, one has to consider the factors dominant in each particular case, such as the material, working-surface properties, the contact-surface quality and properties, properties of the medium between the contact surfaces, characteristics of the relative motion between the working surfaces, the load, the temperature, the quantity and properties of the particles produced due to the wear, etc.[1–6]

During the surface contact between two tribo-elements, elastic and plastic deformations occur. They depend on the load intensity, friction conditions, material mechanical properties and micro-geometry of the contact surfaces. When two rough surfaces interact, a momentary loss of the contact may occur due to the micro-roughness caused by their elastic and plastic deformations. The process of micro-wear involves a plurality of such micro-deformations and a destruction of the surface roughness peaks. Experimental investigations[1–6] showed that the process of the final wear is in fact a fatigue process. Different authors give different classifications of the wear, but all of them are based on the way the contact between two bodies is realized. Therefore, the following types of wear can be distinguished: adhesive, abrasive, erosive, fatigue, cavitation, vibrational and corrosive wear. Since the aim of this research was to study and estimate also the filler materials used for hardfacing the parts exposed to the abrasive wear, the abrasive wear under moderate to medium impact loads was considered.

According to several authors[1–6], abrasive wear accounts for approximately half of all the wear. The elements most exposed to abrasive wear are the parts of construction, mining and agricultural machinery, elements of transport devices, working parts of the equipment in metallurgy, some parts of tool machines, parts of railway and tram equipment, impellers of hydraulic and gas turbines, oil-well drilling bits, and parts of the equipment for sandblasting.

Experimental investigations showed that the resistance to abrasive wear is linearly dependent on the metal mechanical properties[1,4]. Therefore, the wear behaviour of a metal can be predicted on the basis of its mechanical properties, primarily the hardness. The penetration depth of foreign particles in the coupled machine elements is inversely proportional to the hardness of the surface layers. However, the resistance to wear of the alloys of the same hardness can vary depending on the chemical composition and structure of the alloy. Hence, the wear is influenced not only by the hardness, but also by the shape, the size and the structural component arrangement. There is no agreement on the most favourable type of structure in relation to the resistance to abrasive wear. Some authors believe that the austenite-carbide is the most favourable, while others prefer the martensite-carbide structure[1–6]. This disagreement stems from a great variety of abrasive-wear types and a wide range of working conditions[1].

Abrasive materials penetrate the metal-surface layers causing surface damage. How deep the abrasive particles penetrate into the metal depends on the shape and hardness of the grains. For example, sharp-edged particles of relatively soft abrasive materials can cause greater damage than rounded particles of hard abrasive materials. Investigations[1] showed that the bigger the size of the particles, the more abrasive they are. Other factors of influence include the length of the wear path, the specific pressure, the relative humidity and the chemical environment.

The wear-resistance level is influenced by each structural component of steel, but the level of influence depends on its hardness and its presence in the structure. Abrasive wear primarily depends on the possibility of abrasive materials to penetrate into the surface of steel and on the strength of the bonds between the structural components at the metal grain boundaries. This means that the quenched and tempered steel is more resistant than the steel with a ferrite-pearlite structure. Experiments showed that pure martensite structures, even those of a lower hardness, exhibit a greater resistance than martensite-carbide structures. Furthermore, if the martensite amount is reduced at the expense of the retained austenite in a martensite-carbide structure, the resistance to wear is increased despite a decrease in the hardness. It is the austenite-carbide structure that has the highest resistance to wear and not the martensite-carbide one, as might have been expected because of the hardness. This is due to the fact that the grain-boundary bonds are stronger in austenite-carbide structures than in a combination of martensite and carbide. In other words, abrasive particles pull carbides more easily out of a martensite matrix than out of an austenite base, whose crystal-lattice parameter is similar to the carbide-lattice parameter[1–6].

The change in operating conditions brings about a change in the intensity and mechanisms of abrasive wear. These conditions include the properties of abrasive materials, the shape and size of grains, the type of bonds, the specific pressure at the contact surfaces, the relative sliding speed, the wear-path length, the humidity, the chemical aggressiveness of the working environment, etc.

3 SELECTION OF THE PROCEDURE, FILLER MATERIAL AND HARDFACING TECHNOLOGY

The role of bucket teeth (**Figure 1a**) is to separate and crush stone material and to protect the bucket against wear. The number and shape of teeth depends on the application (trench digging, gravel digging, material loading, etc.) and the size of the bucket, varying from three (trencher buckets) to fifteen teeth (buckets of bigger loaders). They can be installed in two ways: bolted directly to a bucket or their holder can be welded to a bucket and the teeth are bolted onto the holder. Teeth are made of cast steel or cast iron; their mass ranges from 3 kg to 15 kg per piece.

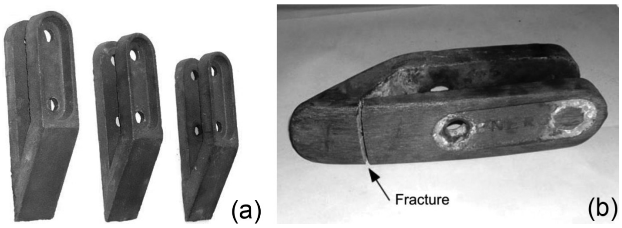

Figure 1: Loader bucket teeth: a) new parts, b) damaged part
Slika 1: Zobje zajemalke: a) novi deli, b) poškodovani del

Two problems were noticed during the operation of the bucket teeth: the tougher and less hard teeth are subjected to plastic deformation and intensive wear, while the teeth made of brittle materials of high hardness break at higher impact loads (**Figure 1b**). A special problem is encountered with the construction machines operating in quarries or open-pit mines of ore and coal, where a piece of a broken tooth can get into the crushers and cause damage. Broken bucket teeth can also get into the equipment used for asphalt and concrete production and cause major damage and downtime.

An analysis of the chemical composition of the teeth material showed they were made of cast steel ČL3134 (JUS) (**Table 1**). A broken tooth was cut to be used for an investigation of the hardness and microstructure of the base material. The hardness ranged from 340 HV1 to 420 HV1, while the microstructure was martensite with retained austenite. This microstructure was not resistant enough because the teeth wore out quickly, especially under the conditions of severe abrasion. For that reason, instead of installing new teeth, it was decided to try to extend the service life of both worn and new teeth with reparatory and production hardfacing.

Hardfacing was performed with the manual arc-welding method using a high-alloy rutile electrode with the properties from **Table 2**, as #1. According to the manufacturer, the layers hardfaced with this electrode exhibit a high resistance to intensive abrasive wear and can withstand moderate impact loads during operation. The layers are very hard and can be grinded. This electrode is especially suited for hardfacing the parts of the machinery exposed to the metal-to-mineral wear. They include bulldozer blades, excavator bucket teeth, excavator shovels, parts of conveyors and crushing machines for various applications, blades and parts of mixers, etc. The reparatory hardfacing of these parts should be produced with the interlayer deposition using an electrode (**Table 2**). The hardfacing parameters, given in **Table 3**, were chosen in accordance with the recommendations in[11–15].

Table 1: Chemical composition, mechanical properties and notation of steel ČL3134[5,8]
Tabela 1: Kemijska sestava, mehanske lastnosti in oznaka jekla ČL3134[5,8]

	Chemical composition, w/%					Mechanical properties					Relation to other standards
	C	Si	Mn	P	S	R_m MPa	R_{eH} MPa	A_5 %	Hardness HV1	Microstructure	DIN
Prescribed	0.45	0.50	1.80	0.040	0.040	780–930	390	7	340–430*	Martensite-bainite and retained austenite	GS-36MnS
Analyzed	0.35	0.20	1.65	0.020	0.020	–	–	–	340–420	Martensite-bainite and retained austenite	

Table 2: Properties of filler materials[5,8]
Tabela 2: Lastnosti dodajnega materiala[5,8]

Electrode notation			Chemical composition, w/%					Current type	Mechanical properties of the hardfaced layer	Application
FIPROM Jesenice		DIN	C	Si	Mn	Cr	Ni			
1	ABRADUR 58	DIN 8555 E 10-UM-60-GR	3.6	–	–	32	–	~ = (+)	57–62 HRC	For hardfacing the parts exposed to severe abrasive wear from minerals in the cold state
2	INOX B 18/8/6	DIN 8556 E 18 8 6 Mn B 20+	0.12	0.8	7	19	9	= (+)	$KV > 80$ J	Interlayer austenite basic electrode

Table 3: Parameters of hardfacing with the MMA welding method
Tabela 3: Parametri trdega navarjanja z metodo varjenja MMA

Electrode notation			Electrode core diameter d_e/mm	Welding current I/A	Voltage U/V	Hardfacing speed v_z/(cm/s)	Input heat q_l/(J/cm)
FIPROM Jesenice		DIN					
1	ABRADUR 58	E 10-UM-60-GR	3.25	130	25	0.124	20968
2	INOX B 18/8/6	E 18 8 6 Mn B 20+	3.25	100	24	0.136	14118

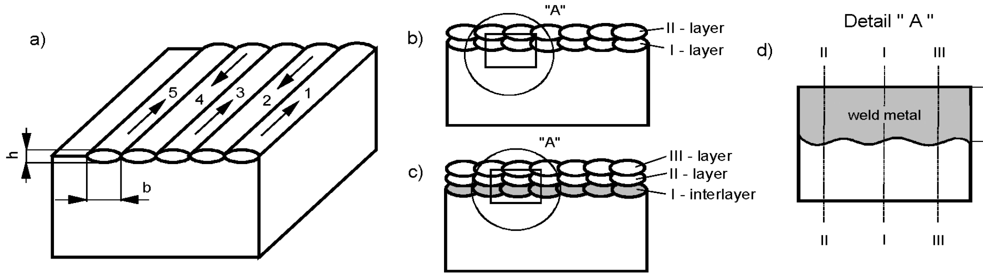

Figure 2: Order of hardfaced-layer deposition: a) 1st layer, b) 2nd layer, c) 3rd layer, d) metallographic sample (block)
Slika 2: Zaporedje trdih navarov: a) 1. sloj, b) 2. sloj, c) 3. sloj, d) vzorec za metalografijo

4 EXPERIMENTAL INVESTIGATIONS ON MODELS AND BUCKET TEETH

4.1 Model investigations

4.1.1 Investigations of the hardness and microstructure of the hardfaced-layer zones

The aim of these experimental investigations was to establish the optimum hardfacing technology. The specimens were hardfaced in a single pass or several passes (layers) (**Figures 2a** to **2c**), either with or without preheating. Hardfaced samples were cut into metallographic samples for tribological investigations (**Figure 2d**). Their hardness was measured along three different directions (see detail "A" in **Figure 2d**) and the microstructure of characteristic hardfaced-layer zones was estimated. The hardfaced-layer hardness was 551 to 742 HV1, while the microstructure was estimated as martensite-ledeburite with retained austenite and excreted carbides at the grain boundaries. The microstructure of the heat-affected zone (HAZ) was martensite with transitions into interphase structures, and the hardness was from 465 HV1 to 613 HV1. The microstructure of the interlayer was austenite-carbide, while its hardness was about 482 HV1. The hardness distribution and the microstructures of the characteristic zones are shown in **Figure 3** for the three-layer hardfacing and in **Figure 4** for the two-layer hardfacing with preheating[5–8].

4.1.2 Tribological investigations

Tribological investigations were performed for a block-on-disk contact, on a TPD-93 tribometer (**Figure 5**) made at the Faculty of Engineering in Kragujevac. The aim of these investigations was to evaluate the resistance to wear of the base materials and deposited layers. Three prismatic samples (two from the hardfaced layer and one from the base material) were prepared for tribological investigations (6.5 mm × 15 mm × 10 mm).

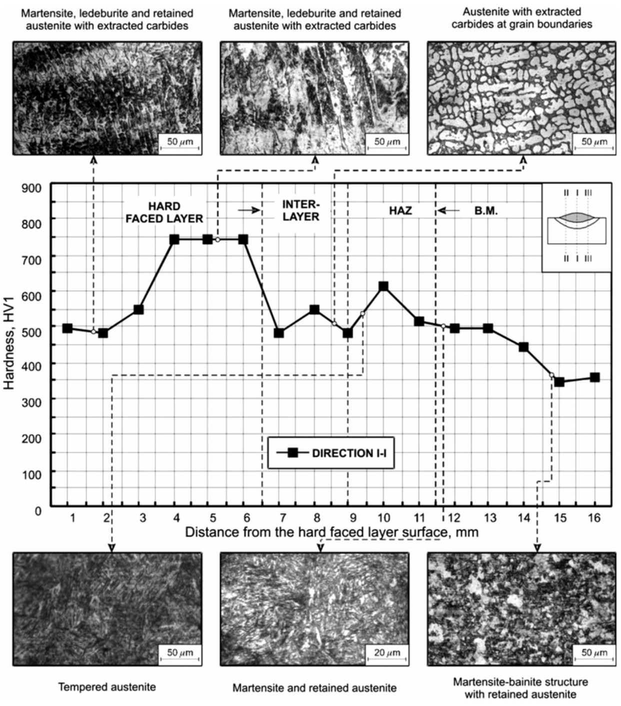

Figure 3: Hardness distribution and microstructures of characteristic hardfaced-layer zones (interlayer + two layers, T_o = 20 °C)
Slika 3: Razporeditev trdote in mikrostruktura področja trdega navara (vmesna plast + dva sloja, T_o = 20 °C)

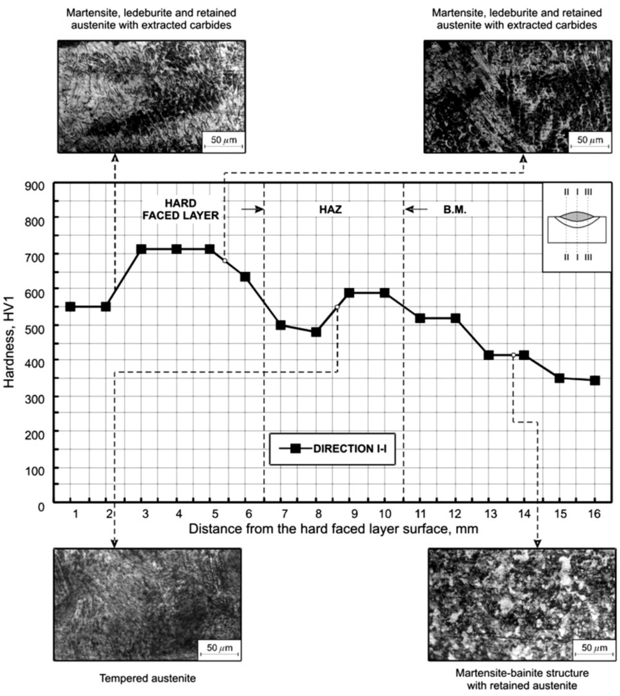

Figure 4: Hardness distribution and microstructures of characteristic hardfaced-layer zones (two layers, T_p = 200 °C)
Slika 4: Razporeditev trdote in mikrostruktura področij značilnih trdih navarov (dva sloja, T_p = 200 °C)

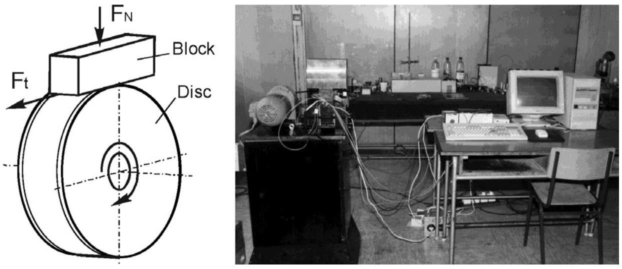

Figure 5: Tribometer TPD-93 and other measuring equipment for the performance of tribological tests
Slika 5: Tribometer TPD-93 in druga merilna oprema za izvajanje triboloških preizkusov

During the investigations, the line block-on-disk contact was realized. The external variables of the tested samples were the contact forces, the sliding speed and the lubricant (motor oil GLX 2 SAE 15-W-40)[4,5,8].

Prior to the investigations, the surface topography of blocks and discs was assessed with the computer measuring system Talysurf 6. The force F_N = 300 N and sliding speed v_{kl} = 1 m/s were adopted. During the contact time of ≈ 60 min, the friction-coefficient variation was registered (**Figure 6**). When the contact was terminated, the surface topography was assessed again and the wear-scar widths of the blocks were measured (**Figure 7**). The wear-scar width was measured using a universal microscope UIM-21, with a magnification of 50 times[4–9].

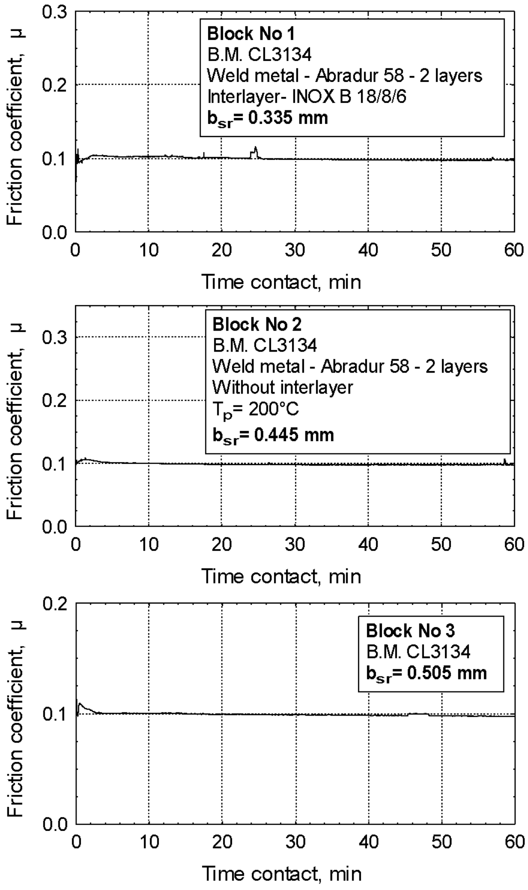

Figure 6: Friction-coefficient variation during the contact of 60 min (blocks 1, 2 and 3)
Slika 6: Spreminjanje koeficienta trenja med stikom 60 min (blok 1, 2 in 3)

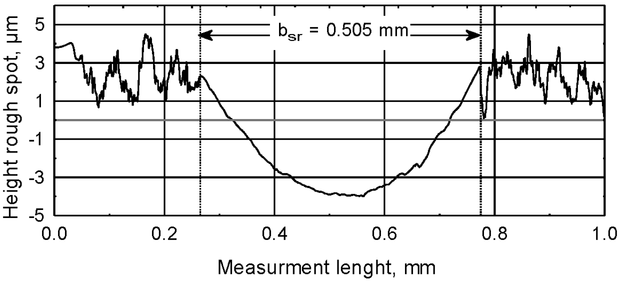

Figure 7: Wear scar – block No. 3 (after the contact of 60 min)
Slika 7: Brazgotina zaradi obrabe – blok št. 3 (po stiku 60 min)

Based on the results obtained with tribological investigations, the macroscopic and microscopic damages of the damaged blocks from **Figure 8** were assessed.

4.2 Hardfacing of real parts with different methods of hardfaced-layer deposition

The measurements of the wear-scar widths showed that hardfaced layers have a significantly higher resistance to wear (especially those hardfaced without preheating) than the base material. This illustrates the importance of selecting the right hardfacing technology and filler materials for excavator/loader bucket teeth.

After the samples had been hardfaced and tribologically investigated, the optimum technology was selected and applied to the real parts. Taking into consideration the limitations imposed by the base-material thickness, the hardfaced-layer height and electrode diameter, the

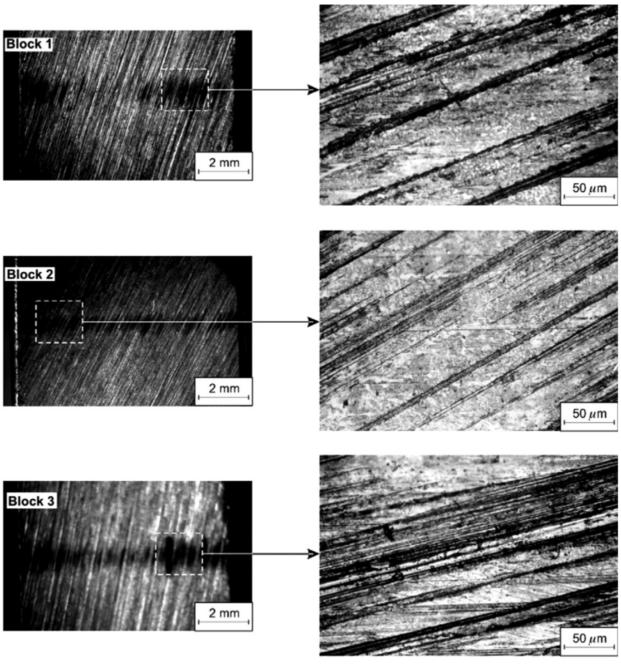

Figure 8: Wear of block Nos. 1, 2 and 3
Slika 8: Obraba na bloku št. 1, 2 in 3

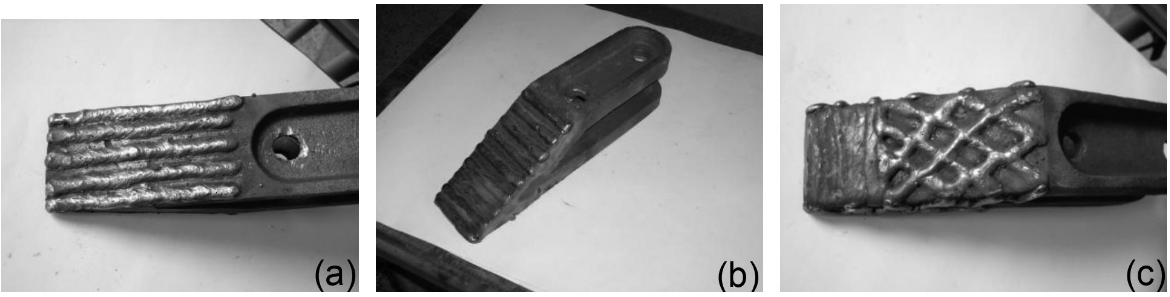

Figure 9: Hardfaced teeth with the layers deposited: a) longitudinally, b) horizontally and c) in a honeycomb pattern
Slika 9: Zob s trdim navarom, položenim: a) vzdolžno, b) vodoravno in c) satasto

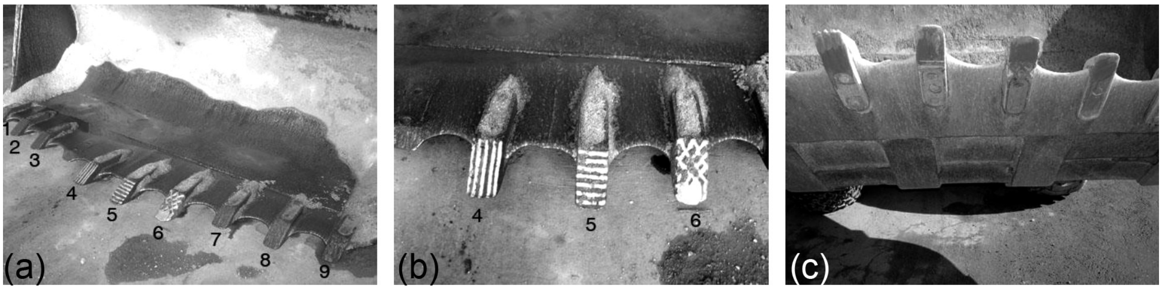

Figure 10: Bucket-tooth mounting sequence: a) front surface, b) back surface, c) teeth surface after 360 h of operation
Slika 10: Zaporedje namestitve zob zajemalke: a) zgornja površina, b) spodnja površina, c) zobje po 360 h dela

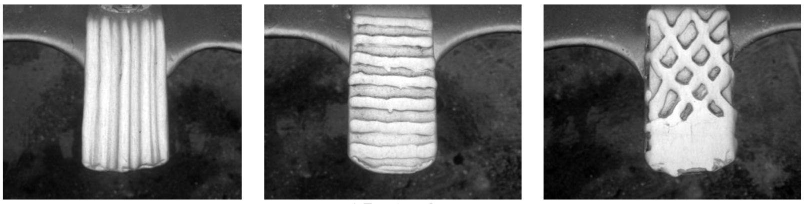

a) Front surface

b) Back surface

Figure 11: Hardfaced teeth after 1600 h of operation: a) front surface, b) back surface
Slika 11: Zob s trdim navarom po 1600 h dela: a) zgornja površina, b) spodnja površina

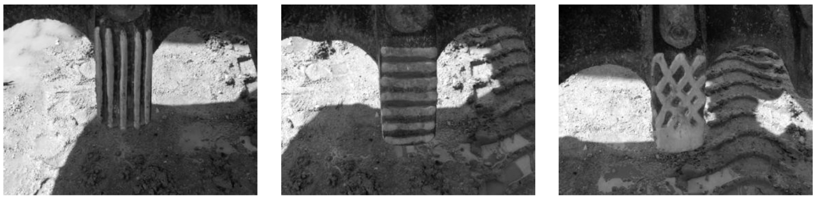

a) Front surface

b) Back surface

Figure 12: Hardfaced teeth after 3200 h of operation: a) front surface, b) back surface
Slika 12: Zob s trdim navarom po 3200 h dela: a) zgornja površina, b) spodnja površina

Table 4: Results of mass measurements before and after the teeth were put into operation for 3200 h
Tabela 4: Merjenje mase zob pred 3200 h dela in po njem

Tooth type	New (non-hardfaced) teeth			Hardfaced teeth with the layers deposited*			New (non-hardfaced) teeth		
Tooth number	1	2	3	4	5	6	7	8	9
Tooth mass before the operation, kg	8.60	8.58	8.62	9.02	9.05	9.62	8.67	8.60	8.64
Tooth mass after the operation, kg	7.75	7.72	7.84	8.80	8.65	9.22	7.62	7.74	7.82
Mass loss, kg	0.85	0.86	0.78	0.22	0.50	0.40	0.95	0.86	0.82
Mass-loss percentage, %	9.88	10.02	11.09	2.44	5.46	4.16	11.08	10.00	9.49

*Tooth #4 hardfaced vertically; tooth #5 hardfaced horizontally; tooth #6 hardfaced in a honeycomb structure

three-layer hardfacing (with an interlayer) was chosen. Hardfaced layers were deposited at the front and back sides – vertically over a tooth (**Figure 9a**), horizontally across a tooth (**Figure 9b**) or in a honeycomb pattern (**Figure 9c**). The width of the hardfaced layers was from 10 mm to 12 mm and the height was about 4 mm. Then, the hardfaced teeth were installed onto the central part of the bucket with the most intensive abrasive wear (**Figure 10a**, teeth 4, 5 and 6). The end teeth mounted on both sides were new (1, 2, 3 and 7, 8, 9).

The wear area was monitored and inspected after 360 h (**Figures 10a** to **10c**), after 1600 h (**Figures 11a** and **11b**) and finally after 3200 h of operation (**Figures 12a** and **12b**)[5,8].

5 DISCUSSION

The teeth mass was measured before they were installed. After the teeth were used under real operating conditions for about 3200 hours, they were dismounted and their mass was measured again (**Table 4**). **Figure 13** gives the diagrams of mass losses for the new (non-hardfaced) and hardfaced teeth.

The examination of the damaged-tooth geometries and the measurements of the material depth in the wedge parts of the teeth revealed that the wear degree of the lower (back) surfaces was about 3 times higher than that of the upper (front) surfaces of the teeth. This can be ascribed to the friction of the back surfaces in contact with the abrasive material[5,8].

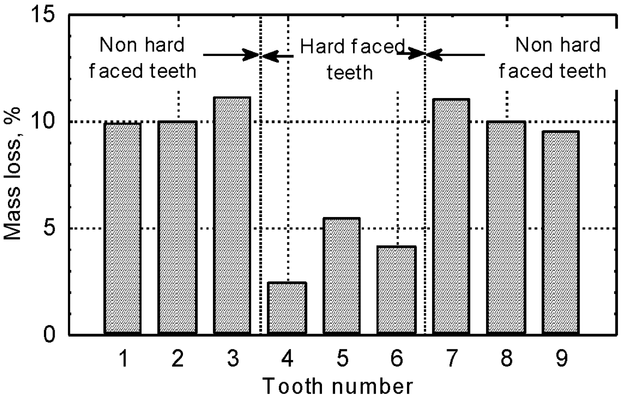

Figure 13: Diagram of mass losses for the non-hardfaced and hardfaced teeth
Slika 13: Prikaz izgube mase za neobdelane in trdo navarjene zobe

The greatest resistance to the abrasive wear (loading of crushed stone material) was exhibited by the teeth with the hardfaced layers applied vertically, followed by the teeth with the hardfaced layers deposited in a honeycomb structure, while the teeth with the horizontal hardfaced layers showed the least wear resistance. The best hardfacing patterns for the other conditions of the abrasive wear require a further investigation[5,8].

On the basis of the knowledge acquired in practice and from the literature, the criterion for a worn-tooth replacement was established, stating that teeth should be replaced after 6400 h of operation (two seasons) or when the mass loss is about 20 %[5,8,16,17]. Considering the last rows of **Table 4** and **Figure 13**, one can notice that the hardfaced teeth were worn significantly less than the new ones, by about 2 to 4 times. Thus, one can conclude that the expected service life of the hardfaced teeth would be 2–4 times longer than the service life of the non-hardfaced teeth, depending on the applied hardfacing method.

The techno-economic analysis[4,5,7,15,16] showed that the production and reparatory hardfacing of the working parts of construction machinery is cost-effective. Especially the production hardfacing of parts was studied in detail. Taking into consideration the costs for repair, the costs for new parts and the service life, it can be concluded that the savings reach up to 225 %, while for the repair hardfacing, they reach up to, or even exceed, 300 %[5,8].

6 CONCLUSION

Through the experimental investigations of the hardness and microstructure of hardfaced-layer characteristic zones, as well as tribological investigations of hardfaced layers, the optimum hardfacing technology was determined.

Based on these models and other experimental investigations, as well as the tests of real parts in operating conditions, it was concluded that the optimum production-hardfacing technology should consist of the following steps:

- Proper selection of the filler material (the right type of electrodes);
- Selection of the hardfacing parameters (welding current, voltage, welding speed, input heat);
- Number and order of deposited layers;
- Direction of the hardfaced-layer deposition;
- Thermal treatment prior to hardfacing (preheating) or deposition of a buffer interlayer.

The right choice of the hardfacing technology and its proper application ensure numerous advantages and benefits over the installation of new non-hardfaced parts. Hardfacing extends the service life by two to four times, increases productivity, shortens downtime, reduces the inventory of spare parts, i.e., reduces the production costs in general.

Although hardfacing represents an almost unique process, requiring the technology to be modified for each particular part, the general procedure applicable to similar parts of construction, mining and agricultural machineries has been determined in this paper. This technology can be applied to both manufacturing new teeth (or parts in general) and repairing the worn ones. The techno-economic benefits are the same.

It has also been shown that the choice of the hardfacing technology is closely related to the complex procedure of hardfaced-layer quality control. This means that this type of work can be performed only in specialized facilities with adequate equipment and skilled staff. In other words, successful hardfacing can be performed only by expert teams specialized in the technical system maintenance.

7 REFERENCES

[1] S. Marković, Lj. Milović, A. Marinković, T. Lazović, Tribological Aspect of Selecting Filler Metal for Repair Surfacing of Gears by Hard facing, Structural Integrity and life, 11 (**2011**) 2, 127–130

[2] J. Dzubinski, A. Klimpel, Hard facing and thermal spraying, WNT, Warsaw 1983, 7–19

[3] M. Gierzynska, Friction life and lubrication in plastic metal processing, WNT, Warsaw 1983, 35–39

[4] V. Lazić, Optimization of hard facing process from the aspect of tribological characteristics of the hard faced layers and residual stresses, PhD thesis, Faculty of Mechanical Engineering, Kragujevac, 2001

[5] M. Mutavdzić, Reparatory hard facing of machine parts and devices in civil engineering, MS Thesis, Faculty of Mechanical Engineering, Kragujevac, 2007

[6] L. Gusel, R. Rudolf, N. Romčević, B. Buchmeister, Genetic programming approach for modelling of tensile strength of cold drawn material, Optoelectron. Adv. Mater. Rapid Commun., 6 (**2012**) 3/4, 446–450

[7] B. Nedeljković, M. Babić, M. Mutavdžić, N. Ratković, S. Aleksandrović, R. Nikolić, V. Lazić, Reparatory hard facing of the rotational device knives for terrain leveling, Journal of the Balkan Tribological Association, 16 (**2010**) 1, 46–75

[8] M. Jovanović, V. Lazić, M. Mutavdžić, D. Adamović, Selection of optimal technology for reparatory hard facing of bucket teeth, Welding and welded structures, 50 (**2005**) 1, 11–20

[9] V. Lazić, M. Mutavdžić, D. Milosavljević, S. Aleksandrović, B. Nedeljković, P. Marinković, R. Čukić, Selection of the most appropriate technology of reparatory hard facing of working parts on universal construction machinery, Tribology in Industry, 33 (**2011**) 1, 18–27

[10] K. M. Mashloosh, T. S. Eyre, Abrasive wear and its application to digger teeth, Tribology International, 18 (**1985**) 5, 259–266

[11] J. D. Verhoeven, A. H. Pendray, H. F. Clark, Wear tests of steel knife blades, Wear, 265 (**2008**) 7/8, 1093–1099

[12] R. F. Smart, J. C. Moore, Materials selection for wear resistance, Wear, 56 (**1979**) 1, 55–67

[13] V. Lazić, M. Jovanović, D. Milosavljević, M. Mutavdžić, R. Čukić, Choosing of the most suitable technology of hard facing of mixer blades used in asphalt bases, Tribology in Industry, 30 (**2008**) 1–2, 3–10

[14] Standards: JUS, ASTM, DIN, EN

[15] Catalogues of filler material producers: SŽ Fiprom Jesenice-Slovenia, Lincoln Electric-USA, Esab-Sweden

[16] R. Wasserman, How to save millions by reducing inventories of spare parts, 1st ed., Eutectic-Castolin Institute for the Advancement of Maintenance and Repair Welding Techniques, New York 1971, 11–23

[17] R. Čukić, Techno-economic analysis of production and reparatory hard facing of various parts of machine systems, PhD thesis, University of Belgrade, 2010

UDK 537.533:66.017:620.3
Professional article/Strokovni članek

ISSN 1580-2949
MTAEC9, 49(1)173(2015)

CHARACTERIZATION OF TiO_2 NANOPARTICLES WITH HIGH-RESOLUTION FEG SCANNING ELECTRON MICROSCOPY

KARAKTERIZACIJA NANODELCEV TiO_2 Z VISOKOLOČLJIVOSTNO FEG VRSTIČNO ELEKTRONSKO MIKROSKOPIJO

Zoran Samardžija[1], Domen Lapornik[2], Ksenija Gradišek[2], Dejan Verhovšek[2], Miran Čeh[1]

[1]Jožef Stefan Institute, Department for Nanostructured Materials, Jamova cesta 39, 1000 Ljubljana, Slovenia
[2]Cinkarna Celje, d. d., Metalurško-kemična industrija Celje, Kidričeva 26, 3001 Celje, Slovenia
zoran.samardzija@ijs.si

Prejem rokopisa – received: 2014-01-16; sprejem za objavo – accepted for publication: 2014-03-04

Ultrafine titanium dioxide powder (UF-TiO_2) has many applications as a result of its nanometer particle size and semiconducting electric properties. An upgraded method for synthesis of UF-TiO_2 was developed, with the ability to control the characteristics of the nanoparticles, i.e. their size, shape and crystal structure. In order to determine the correlation between the various synthesis parameters and the final form of the TiO_2 nanoparticles, their size and morphology were analyzed using high-resolution field-emission-gun scanning electron microscopy (FEGSEM). The UF-TiO_2 specimens for the FEGSEM high-magnification observations were prepared using three different routes. Micrographs were recorded with an inside-the-lens secondary electron detector and additionally using scanning transmission (STEM) mode. We found that coating the specimens with carbon or Au-Pd did not improve the image quality. Carbon coating was inappropriate because it filled the gaps between the nanoparticles giving the appearance of a smoothed, agglomerated surface. The TiO_2 nanoparticles sputtered with Au-Pd were observed to have better contrast; however, they were falsely enlarged due to the Au-Pd nano-layer around them. The best results were obtained with the uncoated specimens, where TiO_2 nanoparticles sized 5–10 nm were clearly visible at a magnification of 300 000-times. With STEM mode we were able to distinguish the TiO_2 nanoparticles relatively easily; however with different image contrast than when using standard SEM mode.

Keywords: titanium dioxide, nanoparticles, FEGSEM

Prah titanovega dioksida z nanodelci (UF-TiO_2) ima vsestranske aplikacije, ki izhajajo iz majhne velikosti delcev in njegovih polprevodniških električnih lastnosti. Nadgrajena je bila metoda za sintezo UF-TiO_2 z možnostjo kontrole lastnosti nanodelcev: njihove velikosti, oblike in kristalne strukture. Za določanje vpliva različnih parametrov sinteze na končno obliko nanodelcev TiO_2 je bila preiskovana njihova velikost in oblika z visokoločljivostnim vrstičnim elektronskim mikroskopom s katodo na poljsko emisijo (FEGSEM). Vzorci UF-TiO_2 so bili pripravljeni za analize FEGSEM na tri različne načine. Posnetki so bili narejeni z detektorjem sekundarnih elektronov, nameščenim v objektni leči mikroskopa in dodatno v presevnem načinu (STEM). Ugotovljeno je, da prevodne plasti ogljika ali Au-Pd, ki so bile nanesene na površino vzorcev, ne izboljšajo kakovosti slike. Nanos amorfne plasti ogljika je bil neprimeren, ker je zapolnil prostor med nanodelci, dajajoč vtis zglajene, aglomerirane površine. Nanodelci v vzorcu, ki je bil napršen z Au-Pd, so bili vidni z boljšim kontrastom, vendar so bili navidezno večji, kot so v resnici, zaradi dodane plasti Au-Pd okoli njih. Najboljši rezultati so bili dobljeni z opazovanjem nenapršenega vzorca, kjer so bili osnovni nanodelci TiO_2 z velikostjo od 5 nm do 10 nm jasno vidni pri 300 000-kratni povečavi. S STEM je relativno enostavno razločiti nanodelce TiO_2, vendar z drugačnim slikovnim kontrastom v primerjavi s standardnim SEM-načinom.

Ključne besede: titanov dioksid, nanodelci, FEGSEM

1 INTRODUCTION

Ultrafine, nanometer-grade titanium dioxide (UF-TiO_2) is known for its versatile applications, originating from its very high specific surface due to the nano-sized particles and its semiconducting electric properties. The range of use for TiO_2 nanoparticles in its two crystalline forms, anatase or rutile, is very wide: photocatalytic applications, UV absorbing transparent coatings, plastics additive, cosmetics UV blockers, photo-electrochromic windows, DSSCs ("dye-sensitized solar cells") and many more.[1–3] The production of TiO_2 material with a high specific surface is one of the core development activities in the factory Cinkarna Celje, with a strategic orientation towards the production of UF-TiO_2 in water-suspension form. For that reason the gel-sol synthesis method was employed and upgraded to obtain anatase and/or rutile TiO_2 nanoparticles.[4] To study the influence of various reaction parameters of the gel-sol synthesis on the characteristics of the final UF-TiO_2 product it is necessary to perform fast and reliable analyses of the samples of TiO_2 powders that consist of nanoparticles. Namely, it is necessary to have reliable data on the particle size and the morphology of the ultrafine powders after each synthesis protocol in order to establish the correct correlation between the processing parameters and the material's characteristics according to a specific application. A modern field-emission-gun scanning electron microscope (FEGSEM) with a very-high-brightness cathode is one of the analytical tools that can be used for the characterization of nanoparticles. The very small, focused, electron-probe diameter in the FEGSEM makes it possible to observe the specimens with an ultimate resolution of about 1 nm.[5] In this work we implemented advanced methods of FEGSEM microscopy to study the ultrafine, nano-sized TiO_2 powders and to determine the morphology and the size of both the agglomerates and the constituent TiO_2 nanoparticles.

2 EXPERIMENTAL

For the FEGSEM analyses the powder specimens with ultrafine TiO_2 nanoparticles were prepared in three different ways. Initially, the TiO_2 nanoparticles were dispersed from properly diluted suspensions using an ultrasonic device and then deposited and dried on polished aluminum holders. The first-type specimens were uncoated, the second-type specimens were coated with an amorphous carbon layer 4 nm and the third-type specimens were coated with a layer 3 nm of Au-Pd alloy. The coatings were applied in a Gatan PECS 682 ion-beam coating apparatus with specimen rotation up to 20 r/min, tilt up to 25° and a rocking speed of 10° s^{-1}. The specimens were observed using two FEGSEM microscopes: a JEOL JSM-7600F and a Zeiss Sigma VP. The FEGSEM experimental set-ups were adjusted and optimized according to the individual specimen and the desired final magnification, with an emphasis on the preferential application of low-voltage high-resolution microscopy.[6] Thus the applied SEM accelerating voltages were set in the range 2–10 kV with electron-beam currents of 20–100 pA and working distances of 3–10 mm. An inside-the-lens secondary-electron detector was used for the imaging. All the images were recorded without noise-reduction tools. In addition, the SEM scanning-transmission (STEM) mode was used at 30 kV with samples that were prepared by the direct dispersion of the nanoparticles on a thin carbon-membrane.

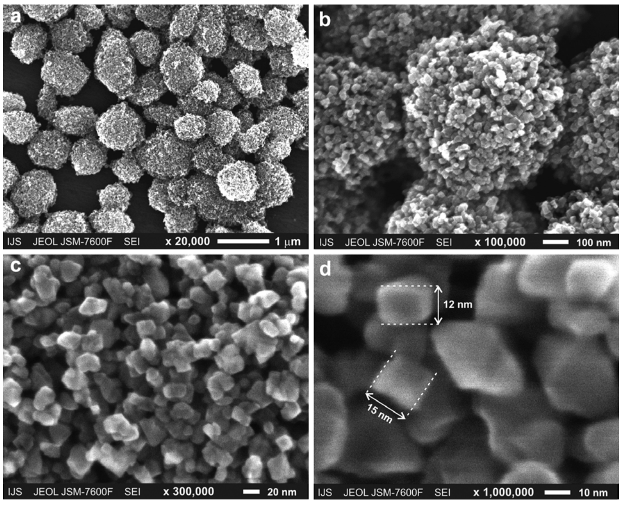

Figure 1: FEGSEM micrographs of the ultrafine anatase TiO_2: a) submicrometer-sized agglomerates of the nanoparticles, b), c) basic anatase nanoparticles in the agglomerates at 100 000-times and 300 000-times magnifications, d) the image of the anatase nanocrystallites at highest accessible 1 000 000-times magnification

Slika 1: FEGSEM-posnetki zelo finega prahu anatasa TiO_2: a) submikrometrsko veliki aglomerati nanodelcev, b), c) osnovni nanodelci anatasa v aglomeratih, posneti pri povečavah 100 000-krat in 300 000-krat, d) posnetek nanokristalitov anatasa pri največji možni povečavi 1 000 000-krat

3 RESULTS AND DISCUSSION

The high-resolution FEGSEM micrographs of the uncoated specimen of the ultra-fine TiO_2 anatase powder were recorded using a sequence of magnifications, as shown in **Figure 1**. The rounded agglomerates of the particles with a size of ≤ 1 μm remained stable, even after applied ultrasonic dispersion, as displayed in **Figure 1a**. The micrographs at higher magnifications of 100 000-times and 300 000-times (**Figures 1b** and **1c**) clearly revealed, angularly shaped, constituent anatase nanocrystallites within the agglomerates. From these images the size of the crystallites was easily estimated to be up to 20 nm. Furthermore, exploiting the limits of the microscope by operating under specially optimized imaging conditions, we were able to record the images of the basic nanocrystallites at an ultimate, maximum magnification of 1 000 000-times, as presented in **Figure 1d**. Dimensional measurements were then performed directly on the image and these confirmed that the size of the anatase nanocrystallites is in the range 10–20 nm. Moreover, the shape of some nanocrystallites was recognized as being similar to octahedra, which is typical for the anatase crystal structure.[7]

Two samples of crystalline UF-TiO_2, rutile and anatase, were prepared employing identical sample preparation routes and then examined using the same FEGSEM set-up with a final magnification of 100 000-times. The micrograph presented in **Figure 2** shows rutile nanoparticles in the form of "wheat-like" grains with a size of 20–40 nm, also exhibiting a narrow size distribution as a consequence of the inherent monodispersed nature of the rutile precursor within the applied synthesis procedure.[8] In contrast, the anatase sample looks different, revealing the presence of nano-agglomerates that consisted of very small, basic nanoparticles with a size

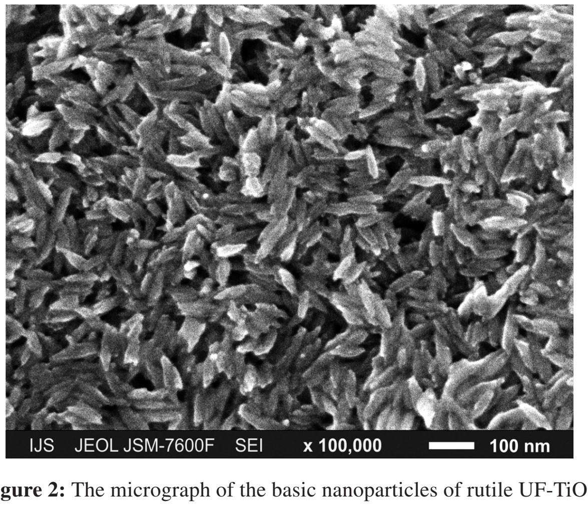

Figure 2: The micrograph of the basic nanoparticles of rutile UF-TiO_2
Slika 2: Posnetek osnovnih nanodelcev UF-TiO_2 rutila

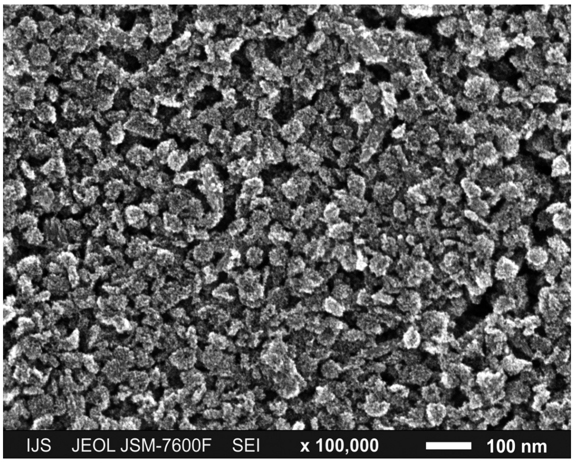

Figure 3: The micrograph of nanometer-sized agglomerates of anatase UF-TiO_2

Slika 3: Posnetek aglomeratov nanodelcev UF-TiO_2 anatasa

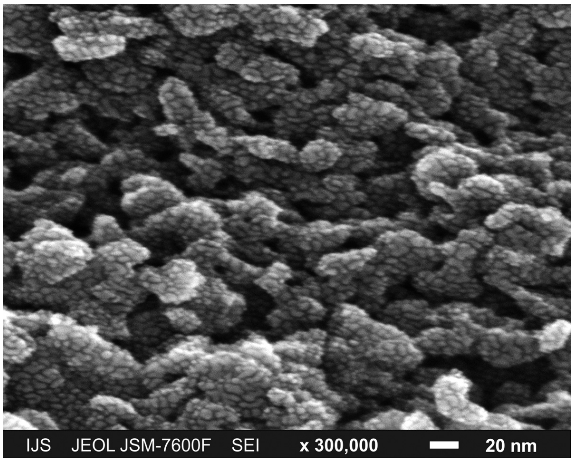

Figure 5: The high-resolution micrograph of the details of nanometer-sized anatase agglomerates; specimen coated with Au-Pd layer

Slika 5: Visokoločljivostni posnetek detajla nanometrskih aglomeratov anatasa; vzorec, napršen s plastjo iz zlitine Au-Pd

below 10 nm, as shown in **Figure 3**. The size of these agglomerates was between 20 nm and 40 nm only.

In order to get a more detailed view of the constituent anatase nanoparticles the specimens were additionally treated using the three preparation routes mentioned in the experimental part. An ultra-high-magnification 300 000-times micrograph of the uncoated anatase specimen is shown in **Figure 4** and clearly reveals the authentic structure of the nano-agglomerates, which consist of the basic TiO_2 nanoparticles sized 5–10 nm. In the case of the uncoated sample, surface charging was avoided by operating at a properly selected accelerating voltage, with lower beam currents and using faster scanning speeds for the recording. A similar image of the specimen coated with a Au-Pd nanolayer shown in **Figure 5** provides basically the same information as given in **Figure 4**; however, due to applied coating the agglomerates seem somewhat rounded and also the nanoparticles are falsely slightly larger. The imaging of the Au-Pd-coated anatase specimen was easier to perform than for the uncoated specimen, because the sample was more stable under the electron-beam and was sufficiently conductive to avoid charging artifacts, thus allowing us to operate at higher beam currents. Also, the image contrast and signal-to-noise ratio were better using higher currents and because of the high secondary-electron yield of the Au-Pd material. If one would neglect these artificial changes to the morphology due to the Au-Pd coating, these prepared samples are acceptable, especially because of the easier FEGSEM high-magnification imaging. In comparison with the uncoated and the Au-Pd-coated samples the third anatase sample that was coated with carbon appeared very different, as shown in **Figure 6**. An amorphous carbon layer covered the surface of the agglomerates, filling the gaps between the nanoparticles. Therefore, the agglomerates look

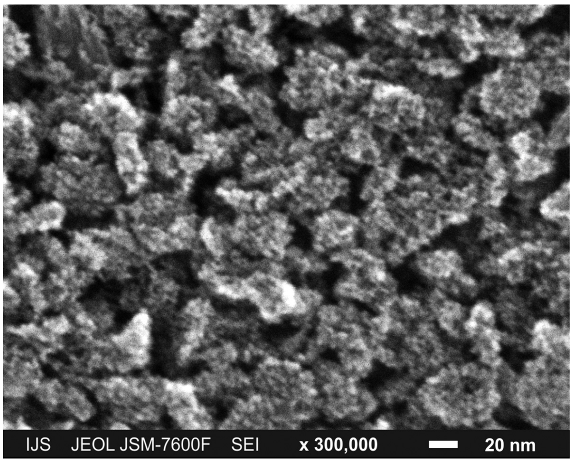

Figure 4: The high-resolution micrograph of the details of nanometer-sized anatase agglomerates with constituent TiO_2 nanoparticles sized 5–10 nm; uncoated specimen

Slika 4: Visokoločljivostni posnetek detajlov nanometrskih aglomeratov anatasa z osnovnimi nanodelci TiO_2 z velikostjo 5–10 nm; nenapršen vzorec

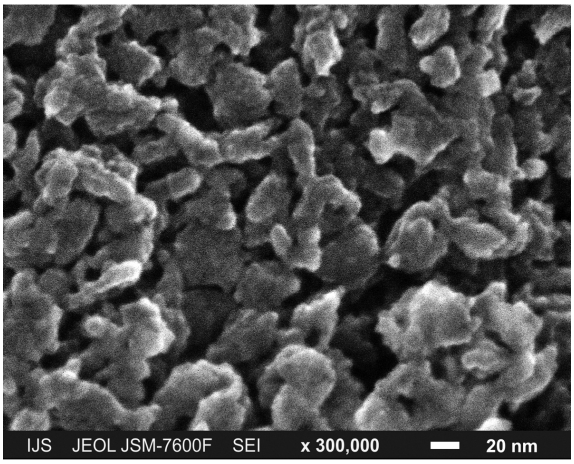

Figure 6: The high-resolution micrograph of nanometer-sized anatase agglomerates; specimen coated with amorphous carbon layer

Slika 6: Visokoločljivostni posnetek nanometrskih aglomeratov anatasa; vzorec, napršen z amorfno plastjo ogljika

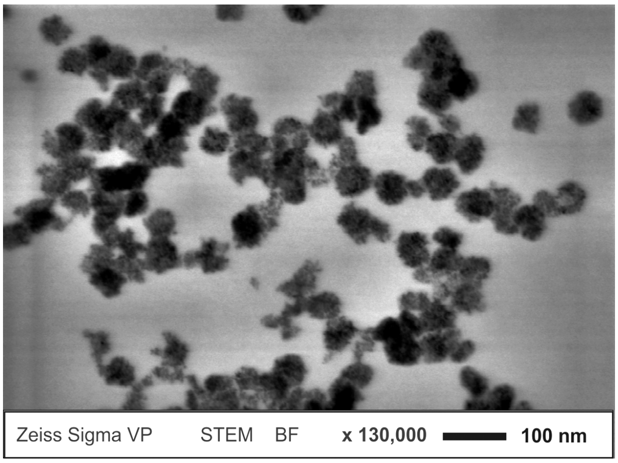

Figure 7: STEM bright-field image of nanometer-sized anatase agglomerates
Slika 7: STEM-posnetek v svetlem polju nanometrskih aglomeratov anatasa

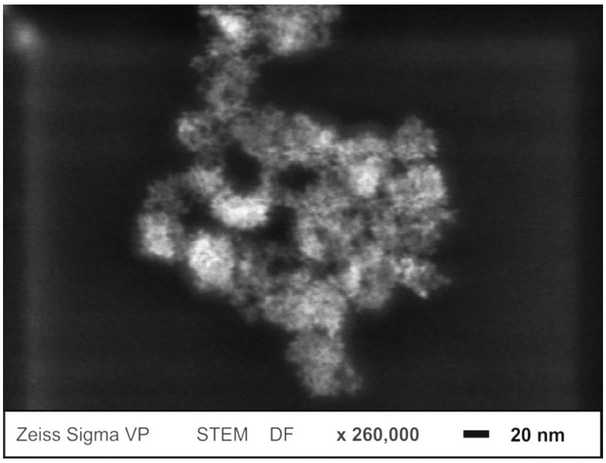

Figure 8: STEM dark-field image of nanometer-sized anatase agglomerates and nanoparticles
Slika 8: STEM-posnetek v temnem polju nanometrskih aglomeratov in nanodelcev anatasa

falsely smooth and in this case it was not possible to resolve the basic TiO_2 nanoparticles.

A complementary bright-field (BF) STEM image of agglomerated anatase nanoparticles is presented in **Figure 7**. Because of the high applied accelerating voltage (30 kV) the issues related to accurate astigmatism correction and precise electron-beam centering are less pronounced, although they are very important in the standard imaging mode. The contours of the agglomerates are sharp and visible, thus allowing a straightforward estimation of their size. The drawback of the STEM observation is rapid sample contamination and the subsequent loss of image contrast. Once the area of interest is found, the STEM images have to be recorded as quickly as possible so as to reduce the contamination and to keep the image contrast at the desired level. The basic anatase nanoparticles were also visible in STEM mode. In this case dark-field (DF) imaging was used at higher magnifications, as shown in **Figure 8**. The bright spot in the upper-left corner of the image and the visible traces of the grey frame arise from the contamination that occurred within several seconds of exposure under the electron-beam.

4 CONCLUSIONS

The morphology, size and size distribution of the ultrafine titanium dioxide powders consisting of nanoparticles were successfully analyzed using a high-resolution FEGSEM with useful images attained at magnifications up to 1 000 000-times. By comparing the images of the differently prepared samples we found that sputtered conductive layers of either carbon or Au-Pd do not improve the quality of the FEGSEM micrographs. The best micrographs were obtained on genuine, uncoated specimens where TiO_2 nanoparticles sized 5–10 nm were clearly revealed at a 300 000-times magnification. Carbon coating was found to be inappropriate because it filled the gaps between the nanoparticles, making the agglomerates artificially smooth. The nanoparticles in the specimen coated with Au-Pd could be observed easily with better contrast; however, they appeared slightly bigger because of the coating. Using the STEM mode we were able to see agglomerated anatase nanoparticles relatively easily, albeit with a different image contrast. The best images for the characterization of the morphology and the size of TiO_2 nanoparticles were recorded using the inside-the-lens secondary electron detector and the appropriate FEGSEM set-ups optimized for ultra-high-magnification observation.

Acknowledgements

This work was supported by the Slovenian Research Agency (ARRS) within the project J2-4237 "Electron microscopy and microanalysis of materials on submicrometer scale".

5 REFERENCES

[1] Z. Zhang, C. C. Wang, R. Zakaria, J. Y. Ying, J. Phys. Chem. B, 102 (**1998**), 10871–10878

[2] A. L. Linsebigler, G. Lu, J. T. Yates Jr., Chem. Rev., 95 (**1995**), 735–758

[3] B. O'Regan, M. Gratzel, Nature, 353 (**1991**), 737–740

[4] T. Sugimoto, X. Zhou, A. Muramatsu, J. Colloid Interface Sci., 259 (**2003**), 43–52

[5] J. I. Goldstein, D. E. Newbury, D. C. Joy, C. E. Lyman, P. Echlin, E. Lifshin, L. Sawyer, J. R. Michael, Scanning Electron Microscopy and X-Ray Microanalysis, 3rd ed., Kluwer Academic Publishers, New York 2003, 34

[6] S. Asahina, T. Togashi, O. Terasaki, S. Takami, T. Adschiri, M. Shibata, N. Erdman, Microscopy and Analysis, 26 (**2012**), S12–S14

[7] Y. Li, T. J. White, S. H. Lim, J. Solid State Chem., 177 (**2004**), 1372–1381

[8] J. Park, V. Priman, E. Matijević, J. Phys. Chem. B, 105 (**2001**), 11630–11635

Erratum

G. Novak, J. Kokošar, A. Nagode, D. Steiner Petrovič, Correlation between the excess losses and the relative permeability in fully finished non-oriented electrical steels, Mater. Tehnol., 48 (**2014**) 6, 997–1001

The Editor-in-Chief declared by mistake the article as professional article, correct is original scientific article, as evident from the reviewers report.

A/Prof. Dr. Matjaž Torkar
Editor-in-Chief